



Politecnico
di Bari

Repository Istituzionale dei Prodotti della Ricerca del Politecnico di Bari

Seismic microzonation by means of finite element approaches

This is a PhD Thesis

Original Citation:

Seismic microzonation by means of finite element approaches / Falcone, Gaetano. - (2017).
[10.60576/poliba/iris/falcone-gaetano_phd2017]

Availability:

This version is available at <http://hdl.handle.net/11589/100163> since: 2017-03-27

Published version

Politecnico di Bari
DOI: 10.60576/poliba/iris/falcone-gaetano_phd2017

Terms of use:

Altro tipo di accesso

(Article begins on next page)



POLITECNICO DI BARI

D.R.R.S.

05
2017

Doctor of Philosophy in Risk and Environmental, Territorial and Building Development

Coordinator: Prof. Michele Mossa

XXIX CYCLE

Curriculum: Geotechnical earthquake engineering

DICATECh

Department of Civil, Environmental, Building Engineering and Chemistry

Seismic microzonation by means of finite element approaches

Prof. Angelo Amorosi
Department of Structural and Geotechnical Engineering
Sapienza University of Rome, Rome, Italy

Prof. Daniela Boldini
Department of Civil, Chemical, Environmental and Materials Engineering
University of Bologna, Bologna, Italy

Gaetano Falcone



POLITECNICO DI BARI

D.R.R.S.

05

Dottorato di Ricerca in Rischio, Sviluppo
ambientale, territoriale ed edilizio

2017

Coordinatore: Prof. Michele Mossa

XXIX CICLO
Curriculum: Geotecnica Sismica

DICATECh

Dipartimento di Ingegneria Civile, Ambientale,
del Territorio, Edile e di Chimica

**Microzonazione Sismica mediante approcci agli
elementi finiti**

Angelo Amorosi
Dipartimento di Ingegneria Strutturale e Geotecnica
Sapienza Università di Roma

Daniela Boldini
Dipartimento di Ingegneria Civile, Chimica, Ambientale e dei Materiali
Università di Bologna

Gaetano Falcone

EXTENDED ABSTRACT

When an earthquake occurs, seismic waves radiate away from the source and travel rapidly through the earth's crust. The motion recorded at the ground surface of an area could be really different, in terms of duration and frequency content, from the reference outcrop motion due to the following site conditions: sequence of soil layers, velocity contrast between soil layers, thickness of each layer, dynamic behaviour of the soils, topography and geometry of the sub-interface.

Concerning the site-effects, it is possible to discuss about one-dimensional (1D) effects, two-dimensional (2D) and three-dimensional (3D) ones. One-dimensional effects are induced in case of horizontally layered deposits with a horizontal ground surface (vertically heterogeneous media). Two-dimensional site-effects are generated in case of a complex stratigraphic sequence (vertically and laterally heterogeneous media) and/or in case of an uneven ground surface. In presence of stratigraphic and topographical surface varying in any direction (vertically, laterally and transversally heterogeneous media), it is necessary to refer to three-dimensional site-effects.

Seismic microzonation (SM) studies are used to assess local geological and geotechnical site conditions and to identify earthquake characteristics. A SM study can be undertaken according to three different levels of details, as reported in the Italian guidelines. In particular, numerical analyses are requested for a level III SM to quantify the reference motion modification.

This work aims to evaluate complex site-effects for a real case study, i.e. the Bovino village, located in South of Italy. This case study has been chosen due to the

presence of a soft soil valley surrounded by rock outcrop hills. As a consequence complex site-effects are expected.

Essential ingredients for predicting site effects are: topography, stratigraphy, interface between soil layers and dynamic soil behaviour. Moreover it is necessary to select the reference seismic event and to define properly the input motion used in the numerical analyses.

The present thesis addresses how to perform a site response analysis using the finite element (FE) method. Two different FE codes, in the time domain, have been used: QUAKE/W, based on the equivalent-linear approach, and PLAXIS 3D, which adopts a non-linear Hardening Soil model with small strain stiffness (HSs).

At first, some numerical approaches to simulate 1D site response are defined with reference to ideal case studies. These approaches have been validated by comparison with results obtained with the code EERA, which is based on an equivalent-linear approach in the frequency domain. 1D schemes have also been used to clarify the definition of reference motion and numerical input motion.

The numerical simulations of seismic site response for the Bovino case study are then presented. Before discussing the results of these analyses, local geology and topography are described. The geotechnical model is subsequently defined, based on field investigations and laboratory data. The reference outcrop motion is then selected, according to the Italian probabilistic seismic hazard maps. Seven real accelerograms have been selected as reference outcrop motions.

The results of the 2D analyses performed using QUAKE/W, with reference to 22 sections, are presented first. The results of the 2D analyses are compared with those of 1D analyses performed with reference to 42 soil columns, extracted along two sections.

Finally, results of 1D, 2D and 3D analysis performed with PLAXIS 3D, assuming two reference motions, are discussed. The analyses allowed to identify the effects of dimensional scheme to seismic site response, the dependency of each amplification pattern to the selected reference motion, the ground motion modification due to dif-

ferent topography and soil layers interface, the comparison between different constitutive approaches to the same problem (i.e. linear equivalent and non-linear).

key words: seismic site response, numerical simulation, site effects, finite element, seismic microzonation

EXTENDED ABSTRACT

Il manifestarsi di un evento sismico comporta la generazione di onde sismiche che dalla sorgente si propagano attraverso la crosta terrestre sino a raggiungere i depositi di terreno più superficiali. Le registrazioni accelerometriche, in corrispondenza del piano campagna di un dato sito, possono risultare significativamente differenti tra loro, in termini di durata e contenuto in frequenza, rispetto a quello di riferimento registrato all'affioramento in piano della formazione rocciosa a causa delle seguenti condizioni locali: stratigrafia, contrasto di rigidità tra gli strati di terreno, spessore di ogni strato, comportamento dinamico dei materiali, topografia e morfologia dei passaggi di strato.

È possibile fare riferimento ad effetti di sito mono-dimensionali (1D), bi-dimensionali (2D) e tri-dimensionali (3D). Gli effetti mono-dimensionali sono generati da depositi caratterizzati da piano campagna e passaggi di strato tutti orizzontali (mezzi eterogenei in direzione verticale). Gli effetti bi-dimensionali sono generati in presenza di complesse condizioni stratigrafiche (depositi verticalmente e lateralmente eterogenei) e/o in caso di piano campagna non orizzontale. In caso di superficie topografica e passaggi di strato variabili in ogni direzione (verticalmente, lateralmente e trasversalmente eterogenei), è necessario fare riferimento allo studio degli effetti tri-dimensionali.

Gli studi di Microzonazione Sismica (SM) hanno l'obiettivo di razionalizzare la conoscenza sulle condizioni geologiche e geotecniche locali e dell'effetto di queste sullo scuotimento sismico in superficie. Uno studio di MS può essere redatto secondo tre livelli di dettaglio, come indicato nelle linee guida Italiane. In particolare, il livello III de-

ve essere basato su analisi numeriche per la determinazione delle caratteristiche del moto sismico in superficie.

Il presente lavoro è basato sulla valutazione degli effetti di sito in condizioni locali variabili lungo ogni direzione, con riferimento all'area urbana di Bovino, comune dell'Italia meridionale. Tale area è stata selezionata in quanto caratterizzata da una condizione di valle e dall'affioramento in rilievo della formazione rocciosa di base. Per quanto sopra detto, è richiesto lo studio degli effetti di sito mediante approcci numerici avanzati.

Lo studio degli effetti di sito richiede una conoscenza dettagliata delle seguenti condizioni: topografia, stratigrafia, passaggi di strato e comportamento dinamico dei terreni. Inoltre, è necessario selezionare gli eventi sismici di riferimento e definire l'input dinamico per le simulazioni numeriche.

Obiettivo del presente lavoro di tesi è la definizione di un'adeguata procedura numerica, basata sul metodo agli elementi finiti (FE), per lo studio della risposta sismica locale. Due differenti codici di calcolo FE, nel dominio del tempo, sono stati utilizzati: QUAKE/W, basato sull'approccio lineare equivalente, e PLAXIS 3D, per il quale è stato selezionato il modello non lineare *Hardening Soil model with small strain stiffness* (HSs).

Dapprima, sono stati valutati gli approcci numerici per lo studio della risposta sismica locale con riferimento a casi ideali 1D. Il confronto dei risultati ottenuti da tali approcci con quelli relativi al codice EERA, basato sull'analisi lineare equivalente nel dominio delle frequenze, ha permesso di validare degli stessi approcci. Gli schemi 1D, inoltre, hanno permesso di chiarire la differenza tra segnale di riferimento e moto di input per le simulazioni numeriche.

In seguito, sono riportati i risultati delle simulazioni numeriche per lo studio della risposta sismica locale per il sito di Bovino. Dapprima, sono descritte la geologia e la topografia locali. Sulla base delle indagini in sito e delle prove di laboratorio disponibili per l'area in esame, è stato definito il modello geotecnico. 7 segnali di riferimento all'affioramento della formazione rocciosa sono stati selezionati sulla base dello mappa di pericolosità sismica nazionale dell'Istituto Nazionale di Geologia e Vulcanologia.

Per quanto riguarda le simulazioni numeriche, dapprima, sono riportati i risultati di analisi 2D eseguite, per 22 sezioni, con il codice QUAKE/W. Questi risultati sono confrontati con quelli di analisi 1D relativi a 42 colonne stratigrafiche, determinate lungo 2 sezioni rappresentative dell'area oggetto di studio.

Infine, selezionati due eventi di riferimenti, sono mostrati i risultati ottenuti attraverso analisi 1D, 2D e 3D eseguite con il codice PLAXIS 3D. Le analisi proposte hanno permesso di evidenziare gli effetti dello schema geometrico sulla risposta sismica locale, la dipendenza del fattore di amplificazione dal segnale di riferimento considerato, le modifiche che il segnale sismico subisce per effetto delle condizioni topografiche e stratigrafiche locali e di confrontare diversi approcci numerici (i.e. lineare equivalente e non lineare) per la soluzione di uno stesso problema.

key words: risposta sismica locale, analisi numeriche, effetti di sito, elementi finiti, microzonazione sismica

INDEX

<i>Introduction</i>	11
<i>Chapter 1. Seismic site response</i>	17
<i>Chapter 2. 1D numerical modelling of the seismic site response</i>	45
<i>Chapter 3. Seismic microzonation: a case study</i>	99
<i>Conclusions</i>	203
<i>References</i>	207
<i>Appendix</i>	213
<i>Curriculum vitae</i>	359

INTRODUCTION

The assessment of the seismic risk can play a crucial role in the definition of a governance policy aimed at preserving people safety. In general, when referring to any event, risk (R) is defined as the product of two quantities:

$$R=P \times D \quad 1$$

where P is the probability of occurrence of an event and D is the magnitude losses related to the same event. With particular reference to the seismic risk, P is the probability of occurrence of a seismic event and D is the corresponding magnitude of losses.

Seismic hazard analyses allow to estimate the probability of occurrence of an earthquake at the regional scale. The seismic events, resulting from the seismic hazard analysis, should be considered in structural design, are assumed to be the reference ones recorded at the horizontal ground surface of the outcropping rock, i.e. at the surface of an ideal homogenous rigid half-space.

The magnitude of losses can be related to three different factors: earthquake characteristics, local geological and geotechnical conditions, structural design and construction features of civil buildings. Seismic microzonation (SM) is aimed at assessing the role of the first two factors. As a matter of fact, it is used to evaluate the modifications of the reference ground motion due to site conditions.

It is well known that the motion recorded at the surface of an area could differ significantly, in terms of duration and frequency content, from the reference ground motion due to following site conditions: stratigraphy, velocity contrast between upper

and lower portions of each soil layers, dynamic behaviour of the soils, and geometrical characteristics of both surface and layers' interfaces.

Site-effects are characterised by one- (1D), two- (2D) and three-dimensional (3D) effects. 1D effects are observed in case of horizontally layered soil sequence and horizontal ground surface (i.e. they occur in vertically heterogeneous soil deposits only). 2D site-effects are generated in a more complex stratigraphic geometrical sequence (vertically and laterally heterogeneous media) and/or in case of irregular ground surface. When the above variability is three-dimensional, corresponding 3D site-effects are likely to occur.

Given the increasing political and scientific interest in seismic risk management, the Technical Committee on earthquake geotechnical engineering (TC4) of the International Society of Soil Mechanics and Geotechnical Engineering (TC4-ISSMGE 1993) produced the first guideline for seismic microzonation studies. Three grades of approach to zonation are described in these guidelines:

- grade-1, based on existing information about historical earthquakes, geological maps and interviews with local residents;
- grade-2, aimed at improving the quality of previous grade, by making use of additional data. For example, the microtremor measurements can be used to obtain more detailed information on subsurface stratigraphy or amplification characteristics of ground motions;
- grade-3, based on additional site investigation whose findings may be incorporated into computer-aided analyses of seismic ground response.

The Italian department for Civil Protection published its Guidelines for Seismic Microzonation, named "*Indirizzi e criteri per la microzonazione sismica*", in 2008.

These guidelines, similarly to those published by TC4, recommended that a SM study could be developed according to three different levels of detail. Level I provides a qualitative indication of the seismic effects due to local conditions. Level II includes an estimation of ground motion modifications based on simplified empirical approaches. Numerical analyses simulating wave propagation are requested at level III of the SM, to estimate the reference ground motion modifications due to topo-

graphic and stratigraphic conditions. The results of such a detailed study should be summarised into contour maps, drawing the factors that quantify the amplification or de-amplification of the reference seismic signal.

1D and 2D site response were deeply investigated by previous authors. Ground motion modification due to local site conditions were studied with reference to ideal case studies and real case histories. The mechanical soil behaviour was taken into account by means of simplified constitutive models or advanced hypotheses in order to describe the material non-linear response.

3D seismic response analyses, rarely reported in the literature, should allow to investigate ground motion modifications in presence of very peculiar soil conditions. The currently works available in the literature are generally based on ideal case studies or simplified case histories. In particular, the constitutive assumptions and site conditions are generally simplified in order to be suitable for the actual computer facilities.

The aim of this work is to analyse complex site-effects for a real case study by means of 1D, 2D and 3D numerical approaches using different computer codes and adopting simple and advanced constitutive models.

Additionally, in order to define microzonation procedures, studies based on seismic response analyses are necessary. At this end, numerical analyses have been undertaken following the typical prescriptions of a level III SM study. Additionally, up to date numerical approaches, which are currently under development in the geomechanical research field, were adopted.

The area of interest analysed heren, named Bovino, is located in the northern part of the Apulia region, in southern Italy. It has been chosen because it is characterised by a soft soil valley and outcropping rock hills, i.e. a rather inhomogeneous environment. Topography of the area, stratigraphic sequence and dynamic behaviour of the soil deposits have been included in the modelling. Moreover, it is necessary to select the reference signals and to properly adapt them to be used as input motion in the numerical analyses. It is worth noting that the input motion, implemented in the FE

model in terms of prescribed displacement or stress time history, could differ from the reference one.

The thesis is divided into four chapters. The first one presents an overview of different approaches to seismic site response analyses. 1D approaches are initially discussed, for which the analytical solutions are recalled with reference to a homogeneous linear elastic soil deposit over rigid bedrock. The cases of elastic bedrock, vertically heterogeneous media and non-linear soil material are also discussed, and a critical literature review of the 2D and 3D effects is finally reported.

The second chapter focuses on the strategies used to model site response effects by means of finite element (FE) analyses. In particular, two different FE codes, both solving the problem in the time domain, are illustrated: *QUAKE/W*, based on the equivalent-linear approach, and *PLAXIS 3D*, adopting a non-linear hysteretic elastoplastic constitutive model. The chapter also includes a discussion on the appropriate boundary conditions to be adopted when FE numerical approaches are employed. At this scope, simple 1D problems have been analysed to validate the numerical assumptions against the available analytical solutions and well established numerical linear-equivalent ones, the latter obtained by the code *EERA*. A 1D scheme has also been considered in order to clarify the definition of reference ground motion and input motion.

The first part of the third chapter briefly covers the historical evolution of seismic zonation in Italy. The rest of the chapter is centred on the numerical simulation of the seismic site response for the Bovino case study. The local geology and topography are described first. The geotechnical model is then defined, based on the available field and laboratory data, together with the reference seismic motions used in the analyses, which are based on the Italian probabilistic seismic hazard study. In particular, seven real accelerograms are selected as reference motions.

The analyses of the case study have been first carried out, considering simplified 2D conditions, with the code *QUAKE/W*, with particular reference to 22 plane strain sections. The resulting amplification factors are determined by comparing the numerically predicted surface ground motions against the reference accelerograms.

The results of these 2D analyses have been compared with those relative to 42 soil columns, i.e. 1D analyses, extracted from two sections. The results of 1D, 2D and 3D analyses, performed by means of code PLAXIS 3D assuming two reference motions, are finally discussed.

The overall results obtained by the different codes and under different geometric assumptions (1,2 or 3D) allow to address the following different aspects of the problem under study: the effects of the different dimensional schemes to seismic site response, the dependency of each amplification pattern to the selected reference motion, the ground motion modification due to different topography and stratigraphic interface, the comparison between different constitutive approaches to the same problem (i.e. linear equivalent and non-linear).

CHAPTER 1. SEISMIC SITE RESPONSE

1.1. Introduction

When an earthquake occurs, seismic waves radiate away from the source and travel rapidly through the earth's crust. When these waves reach the ground surface, they produce shaking that may last from seconds to minutes. Strength and duration of shaking, at a particular site, depend on size and location of the earthquake and on the characteristics of the site. Since soil conditions often vary over short distances, levels of ground shaking can vary significantly within a small area of 1 km².

Given a certain earthquake, different damages can be observed for different buildings close with each other due to different local conditions.

The earthquake occurred in Mexico in 1985 was considered the first event which widely illustrated the effects of local soil conditions on ground motion modification. Its epicentre has been sited off Pacific Coast, but many damages occurred over 360 km away in Mexico City. This event encouraged subsequent studies to better understand the dynamic properties of fine-grained soils and how they affect the seismic site response.

When an earthquake occurs, two types of seismic waves are produced: body waves and surface waves.

Body waves are of two types: p-waves and S-waves (see, Fig. 1). P-waves induce particle movement parallel to the direction of wave propagation, while S-waves produce particle movement perpendicular to the wave direction, then causing shear

strains. The direction of particle movement can be used to divide S-waves into two components, SV (vertical plane movement) and SH (horizontal plane movement). Surface waves result from the interaction between body waves and the ground surface. The most important surface waves, for engineering purposes, are Rayleigh waves and Love waves (see, Fig. 1). Rayleigh waves, produced by the interaction of p- and SV-waves with the earth's surface, involve both vertical and horizontal particle motion. Love waves result from the interaction of SH-waves with a soft surficial layer and have no vertical component of particle motion.

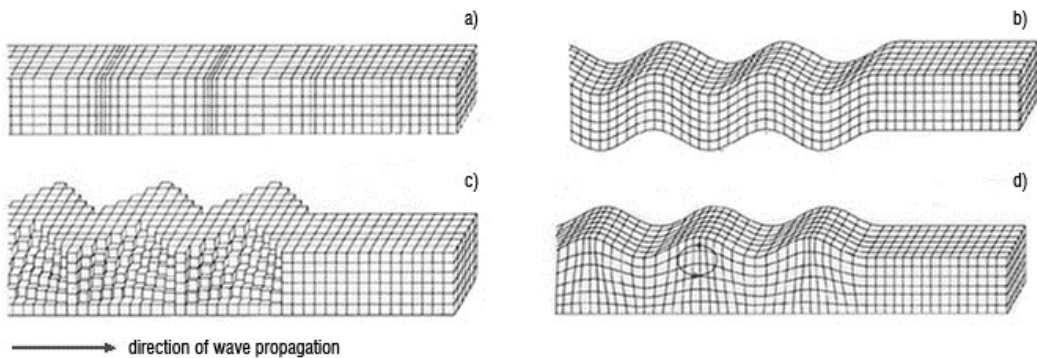


Fig. 1 Deformation produced by a) p-, b) S-, c) Love and d) Rayleigh waves

The wave front travelling from the source to the bedrock-soft soil interface passes through different rock layers (Fig. 2a). For engineering purpose it is possible to assume the upper layer is less stiff than the deeper one. According to Snell's law, waves traveling from stiffer material into less stiff material will be refracted closer to the normal to the interface, (see Fig. 2b and c). Considering only the S-wave for the purpose of this work, the Snell's law could be simplified as following:

$$\frac{\sin \beta}{V_{S,n}} = \frac{\sin \alpha}{V_{S,n-1}} \quad 2$$

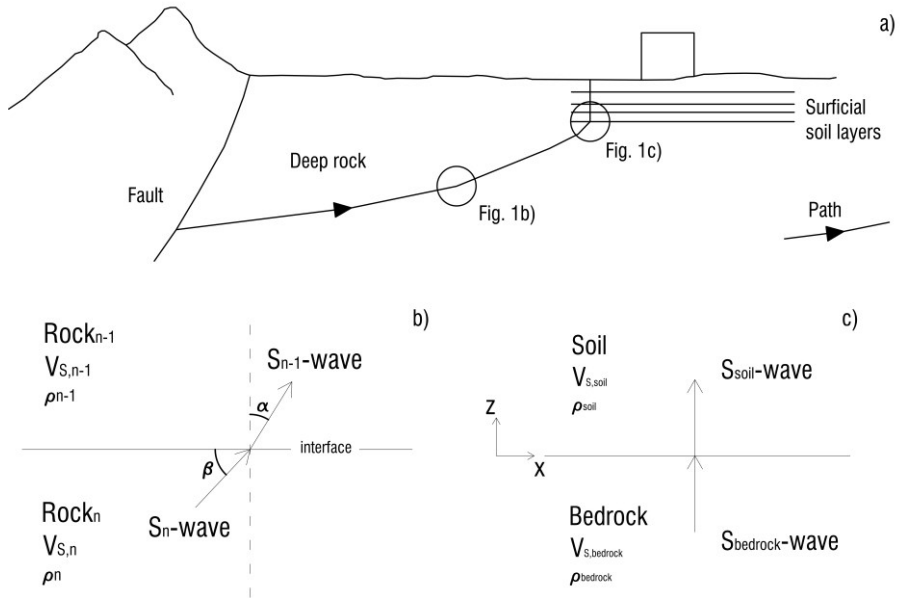


Fig. 2 Seismic wave path: a) refraction process that produces nearly vertical propagation near the ground surface, b) Refracted S_{n-1} -wave resulting from incident S_n -wave travelling through deep rock and c) S-wave, polarized in x direction, vertically propagating

Due to Snell's law, when dealing with vertically layered deposits, ground response can be analysed by means of 1D schemes.

Several terms, that are used in the next, will be defined. With reference to Fig. 3, the motion at the surface of a soil deposit, far enough from the lateral boundaries, will be referred to as free-field motion (point S). The motion at the base of the soil deposit, i.e. at the interface bedrock-soft soil, will be referred to as bedrock motion (point R). The motion at a location far enough from the lateral soil-rock interface, where bedrock is exposed at the ground surface, will be referred to as outcrop motion (point A). The following section is dedicated to the mechanical behaviour of geo-materials under cyclic loading.

Additionally, in this chapter, the analytical solution of ideal case studies will be presented as first approach to seismic site response analysis. It is worth noting that the analytical solutions allow to test multiple Finite Element codes that are capable of predicting linear and non-linear seismic site response with various constitutive models.

Thus, the analytical results will be considered as the reference target to be simulated using different numerical approaches.

At least it is presented a literature review about 2D and 3D effects highlighting the difference from 1D effects.

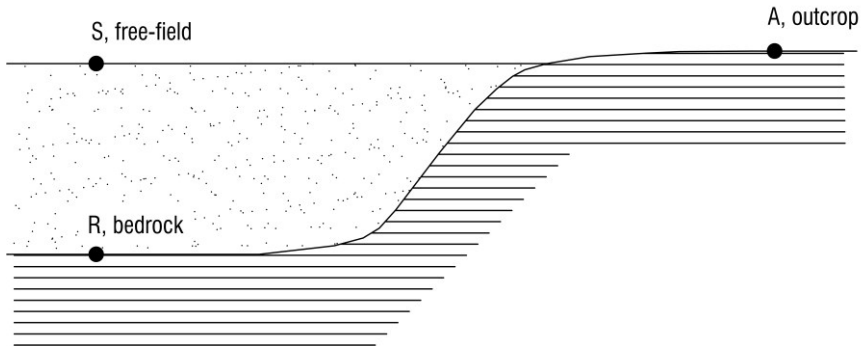


Fig. 3 Ground response nomenclature (Kramer 1996)

1.2. Dynamic soil properties

An element of soil subjected to a symmetric shear cyclic loading might exhibit a hysteresis loop of the type shown in Fig. 4.

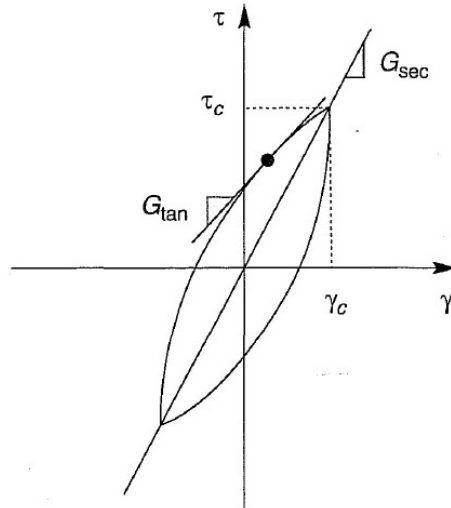


Fig. 4 Hysteresis loop of a soil element under symmetric shear cyclic loading

The main features of a hysteresis loop are inclination and breadth. The inclination of the loop depends on the soil stiffness, which can be described by the tangent shear modulus, G_{\tan} :

$$G_{\tan} = \frac{\delta\tau}{\delta\gamma} \quad 3$$

The average value over the entire loop corresponds to the secant shear modulus, G_{\sec} :

$$G_{\sec} = \frac{\tau_c}{\gamma_c} \quad 4$$

where τ_c and γ_c , shown in Fig. 4, are the shear stress and shear strain amplitudes of the cycle, respectively. Thus, G_{\sec} describes the general inclination of the hysteresis loop. The breadth of the hysteresis loop is related to the area included by the loop which, as a measure of energy dissipation, can conveniently be described by the damping ratio, D :

$$D = \frac{W_D}{4\pi W_S} = \frac{A_{\text{loop}}}{2\pi G_{\sec} \gamma_c^2} \quad 5$$

where W_D is the dissipated energy, W_S the maximum strain energy, and A_{loop} the area of the hysteresis loop. G_{\sec} and D are often referred to as equivalent linear material parameters.

Laboratory tests have shown that soil stiffness is influenced by cyclic strain amplitude, void ratio, mean principal effective stress, plasticity index, overconsolidation ratio, and number of loading cycles. At low strain amplitude, the secant shear modulus is high, but it decreases as the shear strain amplitude increases. The secant shear modulus at zero cyclic strain amplitude, i.e. at lowest shear strain amplitude, is called G_{\max} or G_0 . At greater cyclic strain amplitudes, the modulus ratio G_{\sec}/G_{\max} drops to values less than 1.

After reviewing experimental results from a broad range of materials, Dobry and Vucetic in 1991 concluded that the shape of the modulus reduction curve is influenced more by the plasticity index than by the void ratio and presented curves of the type shown in Fig. 5.

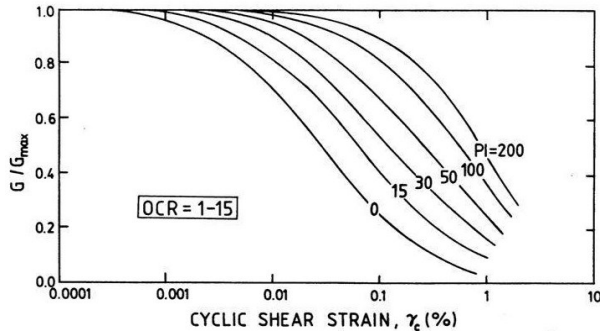


Fig. 5 Modulus reduction curves for fine grained soils of different plasticity (Vucetic & Dobry 1991)

This properties also affect the damping behaviour, but the damping ratio increases with the strain amplitude, as shown in Fig. 6.

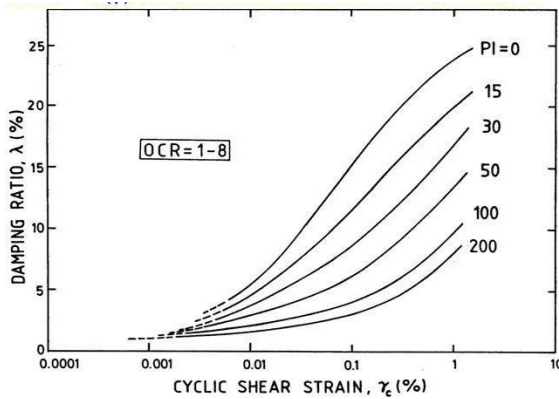


Fig. 6 Variation of damping ratio for fine-grained soils with cyclic shear strain amplitude and plasticity index (Vucetic & Dobry 1991)

For practical purposes, a single set of G_{max} , $G(\gamma)/G_{max}$ and $D(\gamma)$ is generally considered for each deposit. Nevertheless, the G_{max} of real soil deposit varies as depth increases. More general, maximum value of tangent shear modulus is considered as a function of void ratio, overconsolidation ratio and mean principal effective stress. According to the widely used relationship proposed by Viggiani and Atkinson in 1995, G_{max} is a function of plasticity index (PI), mean principal effective stress and overconsolidation ratio according to the following equation:

$$\frac{G_{\max}}{p_r} = A \left(\frac{p'}{p_r} \right)^n R^m \quad 6$$

where p_r is a reference pressure, A , m and n are depending on PI and p' is the mean principal effective stress.

Fig. 7 shows ideal trends of G_{\max} with depth, dashed line for homogeneous soil layer and continuous one for heterogeneous soil deposit. Furthermore, real deposits are characterised by non-linear trends of G_{\max} with depth starting from no-zero value at the ground surface, as represented by the dots in Fig. 7.

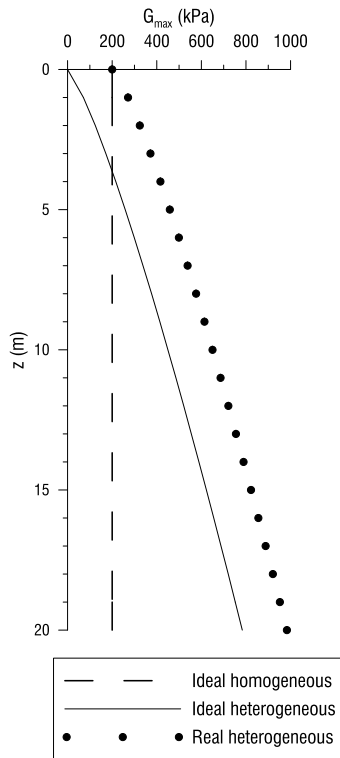


Fig. 7 Maximum value of tangent shear modulus against depth for homogeneous and heterogeneous soil deposits

The shear modulus is related to the shear wave propagation velocity, V_s , through the mass density, ρ :

$$G = V_s^2 \rho \quad 7$$

1.2. 1D approach. Homogenous undamped linear elastic deposit over rigid bedrock

The comparison between free-field and bedrock motions (S/R) or between free-field and outcrop motions (S/A) allows to quantify site effects related to local seismic response.

For sake of simplicity the analytical solution has been determined with reference to a sinusoidal input motion of frequency f :

$$u(t) = A \sin(\omega t + \phi) \quad 8$$

where A is the maximum displacement induced by the vertical propagating wave front from the source and $\omega = 2 \pi f$ and ϕ are the circular frequency and the phase of the motion respectively.

Equation 8 is referred to the displacement induced by a sinusoidal wave propagating vertically in an infinite space characterised by an infinitely large shear modulus. More generally, referring to a homogeneous elastic deposit, the displacement at time t and depth z can be described by means of the following expression:

$$u(z, t) = A e^{i(kz + \omega t)} + B e^{i(-kz + \omega t)} \quad 9$$

where $k = \omega/V_s$ is the wave number, while A and B are two constants defined with respect to the boundary conditions. Equation 9 means that the displacement in the homogenous deposit is depending on the wave propagating upwards from the bedrock and the wave reflected at the ground surface which propagates downwards.

Considering a soil deposit of thickness H and shear wave velocity $V_{s,soil}$, the absolute value of the ratio between soil displacement at free-field and soil displacement at bedrock can be defined as Amplification function A_{daf} and corresponds to:

$$A_{daf} = \frac{1}{|\cos(k_{soil} H)|} \quad 10$$

As $k_{soil} H = \omega H/V_{s,soil}$ approaches $\pi/2 + n\pi$, the denominator of equation 10 approaches zero, which implies that infinite amplification, i.e. resonance, will occur, as shown in Fig. 8. The above consideration suggests that resonance will occur by applying at the base of the soil layer, an input motion of frequency $f_{r,n}$:

$$f_{r,n} = (2n-1) \frac{V_{S,soil}}{4H}, \quad n = 1, 2, \dots, \infty \quad 11$$

The first value of resonance frequency obtained for $n = 1$ is called fundamental frequency:

$$f_{r,1} = \frac{V_{S,soil}}{4H} \quad 12$$

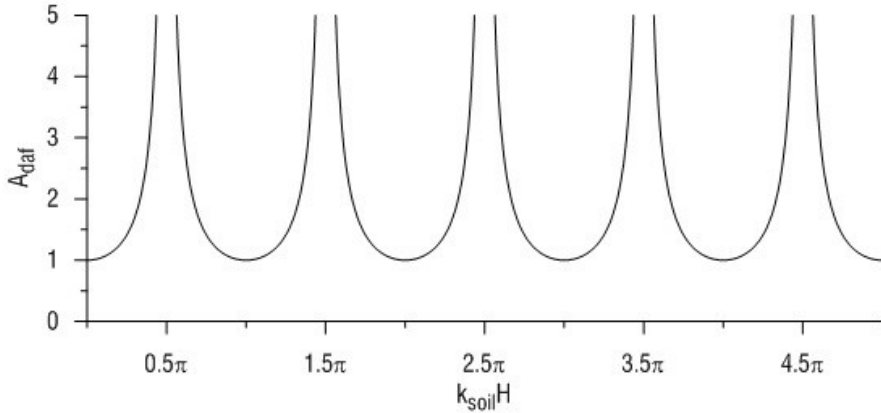


Fig. 8 Amplification function A_{daf} (S/R) for a homogeneous undamped linear elastic soil deposit over rigid bedrock

In the same manner, if the frequency of the input motion applied at the base of the soil layer is f then the resonance will occur if the thickness of the soil deposit is $H_{r,n}$:

$$H_{r,n} = (2n-1) \frac{V_{S,soil}}{4f}, \quad n = 1, 2, \dots, \infty \quad 13$$

The amplification function could also be defined as the ratio between displacement at free-field and displacement at the outcrop:

$$A_{dbf} = \frac{1}{\sqrt{\cos^2(k_{soil}H) + \frac{1}{I^2} \sin^2(k_{soil}H)}} \quad 14$$

where I is the impedance ratio, defined as:

$$I = \sqrt{\frac{\rho_{bedrock} \cdot V_{S,bedrock}}{\rho_{soil} \cdot V_{S,soil}}} \quad 15$$

It is worth noting that equation 14 becomes equal to equation 10, in fact, $1/l^2$ can be considered equal to zero when $V_{S,bedrock}$ is infinitely large.

By combining equations 10 and 14 it is possible to obtain the Amplification function as a ratio between soil displacement at the outcropping rock and displacement at the bedrock:

$$A_{dabf} = \sqrt{1 + \frac{1}{l^2} \tan^2(k_{soil}H)} \quad 16$$

It is possible to notice that the bedrock motion is equal to the rock outcropping motion when a rigid bedrock is considered, i.e. when $V_{S,bedrock}$ is infinitely large.

1.3. 1D approach. Homogenous undamped linear elastic deposit over elastic bedrock

Considering again a motion described by equation 8, a soil deposit of thickness H and shear wave velocity $V_{S,soil}$, and a finite value for the shear wave velocity $V_{S,bedrock}$ of the bedrock (elastic bedrock), the absolute value of the ratio between free-field displacement (point S in Fig. 2) and bedrock displacement (point R in Fig. 2) is described by equation 10.

The amplification function defined as the ratio between displacement registered at free-field and displacement at the outcropping rock is described by equation 14. In this case $1/l^2 > 0$, then resulting in $1 \leq A_{dbf} < \infty$. As one can notice from Fig. 9, the amplification function has finite values for its peaks due to radial damping at the soft soil-bedrock interface. The smaller is the impedance ratio, the bigger is the radial damping, the smaller are the peaks of the amplification function (see Fig. 9).

As described by equation 16, the bedrock motion is equal to the rock outcropping motion if $\tan^2(k_{soil}H)$ is equal to zero. This condition can be satisfied if H or f reach the “steady-state” value, which is determined according to equations 17 and 18 respectively:

$$H_{ss,n}(A_{dabf} = 1) = \frac{n V_{S,soil}}{2 \cdot f}, \quad n = 0, 1, \dots, \infty \quad 17$$

$$f_{ss,n} (A_{dabf} = 1) = \frac{n \cdot V_{s,soil}}{2 \cdot H}, \quad n = 0, 1, \dots, \infty \quad 18$$

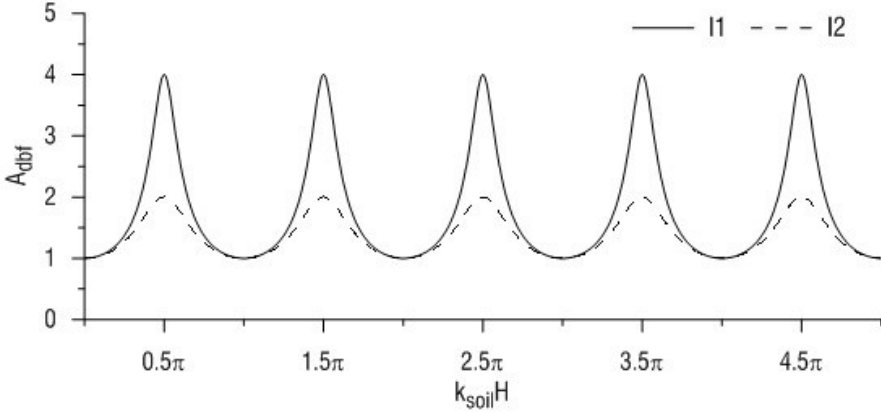


Fig. 9 Amplification function A_{dabf} (S/A) for a homogeneous undamped linear elastic soil deposit over elastic bedrock

Assuming, for sake of convenience, $f = 0.001\text{Hz}$ as the smallest frequency that can be sampled, and normalizing equation 17 by $H_{ss,f1} = H_{ss}(f = 0.001\text{Hz})$ the following equation can be obtained:

$$\frac{H_{ss}(f)}{H_{ss,f1}} = \frac{0.001\text{Hz}}{f} \quad 19$$

whose representation is shown in Fig. 10.

Considering, for instance, $V_{s,soil} = 200\text{m/s}$ and a frequency content of $1 \leq f \leq 10\text{Hz}$, equation 17 gives:

$$n \cdot 100 \geq H_{ss,n} \geq n \cdot 10 \text{ m}, \quad n = 0, 1, \dots, \infty \quad 20$$

Equation (20) suggests that, in general, the bedrock motion is different from that at the outcrop.

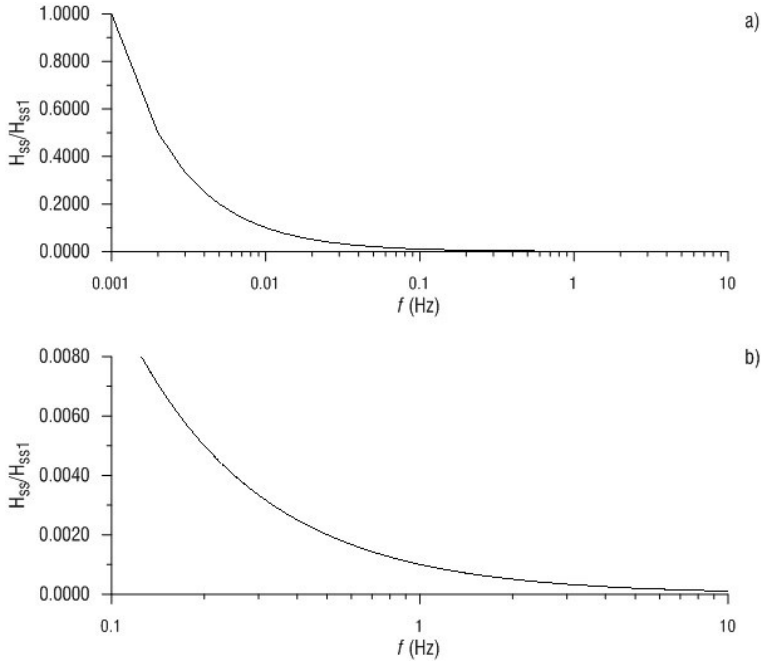


Fig. 10 Normalized steady state thickness of soil deposit against frequency for a) $0.001 \leq f \leq 10\text{Hz}$ and b) $0.1 \leq f \leq 10\text{Hz}$

1.4. 1D approach. Homogenous damped linear elastic deposit over rigid bedrock

Soil material has been assumed to have the shearing characteristics of a Kelvin-Voigt solid in order to account for damping (Kramer 1996), i.e. energy dissipation.

Considering the same motion 8, a soil deposit of thickness H , of shear wave velocity $V_{s,soil}$ and of damping ratio D over a rigid bedrock, the absolute value of the ratio of soil displacement registered at free-field (point S in Fig. 3) to that at bedrock (point R in Fig. 3) is represented by the following equation:

$$A_{daf} = \frac{1}{\sqrt{\cos^2(k_{soil}H) + (Dk_{soil}H)^2}} \quad 21$$

The amplification function A_{daf} , shown in Fig. 11, has no infinite values for the peaks, contrarily to what has been observed for a homogenous undamped linear elastic deposit over rigid bedrock. Furthermore, by increasing the damping ratio D , the peak values of A_{daf} decrease (see Fig. 11).

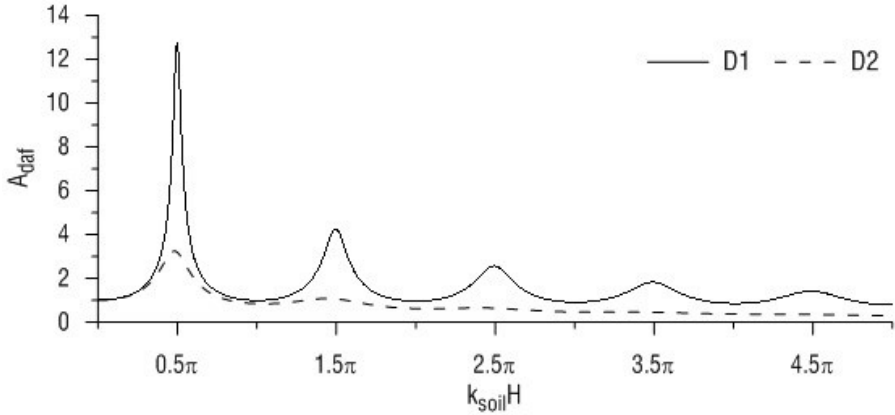


Fig. 11 Amplification function A_{daf} (S/R) for a homogeneous damped linear elastic soil deposit over rigid bedrock

Before outlining the effect of heterogeneity and of non-linear behaviour of real soil on seismic site response, it is worth to noticing that, with the respect to the above case studies, the maximum values of the amplification functions A_{daf} and A_{dbf} are observed for the same frequency factors $k_{soil}H$, as it can be observed by comparing Fig. 8, Fig. 9 and Fig. 11.

1.5. Seismic response of real soil deposits by means of 1D scheme

With regards to a homogeneous damped linear elastic half-space over elastic bedrock, the amplification function A_{daf} can be described by equation 21. However, in this case, no analytical solution to determine the amplification function A_{dbf} is available. Nevertheless, it is possible to notice that the peak values of A_{dbf} are smaller than those characterising a homogeneous damped linear elastic deposit over rigid bedrock, as shown in Fig. 12. This figure shows the maximum value of A_{dbf} against impedance ratio for different damping ratios.

Fig. 13 shows different amplification functions related to different heterogeneous soil deposits (Gazetas 1982). Results are reported for different amplification ratios, D , and for deposit with different level of heterogeneity, where α is a factor describing the heterogeneity grade. In particular, the bigger is α , the bigger is the heterogeneity of the deposit, that is the variation of G_{max} with depth. Given the same α , the bigger is D ,

the smaller is the peak value of A_{daf} . For the same value of damping ratio, the bigger is α , the bigger is the value of the fundamental frequency and the bigger is the peak value of A_{daf} .

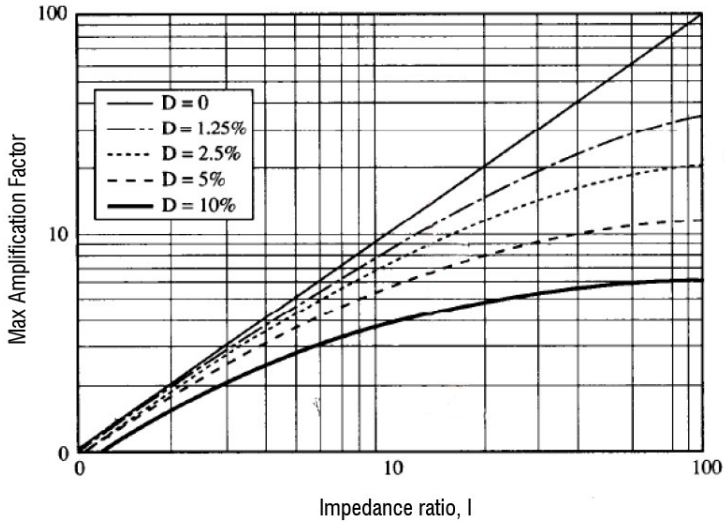


Fig. 12 Peak value of amplification function in case of a homogeneous damped linear elastic half-space over elastic bedrock (Lanzo & Silvestri 1999)

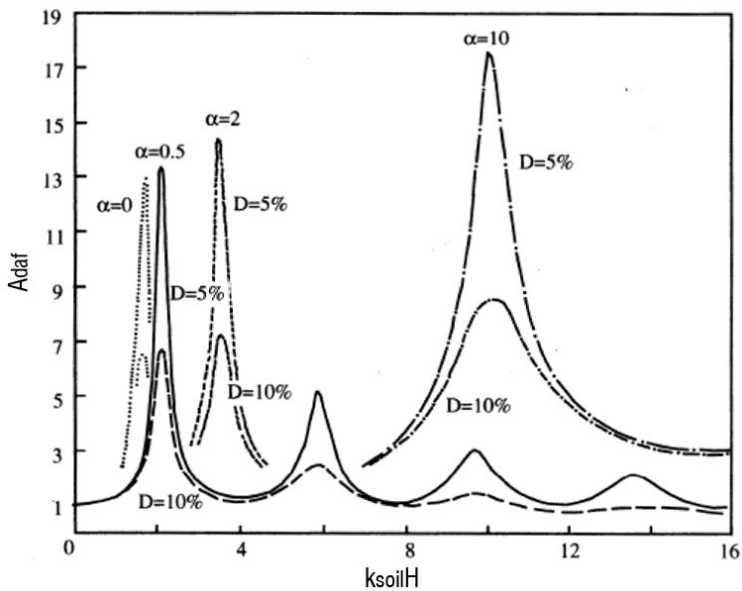


Fig. 13 Amplification function A_{daf} against $k_{soil}H$ relating to different value of D and of α (Gazetas 1982)

Fig. 14 shows more detailed effects of the heterogeneity on seismic site response. As stated above, the fundamental frequency and the peak value increase with the heterogeneity of the deposit. Furthermore, the other resonance frequencies are smaller compared to the case of homogeneous deposit.

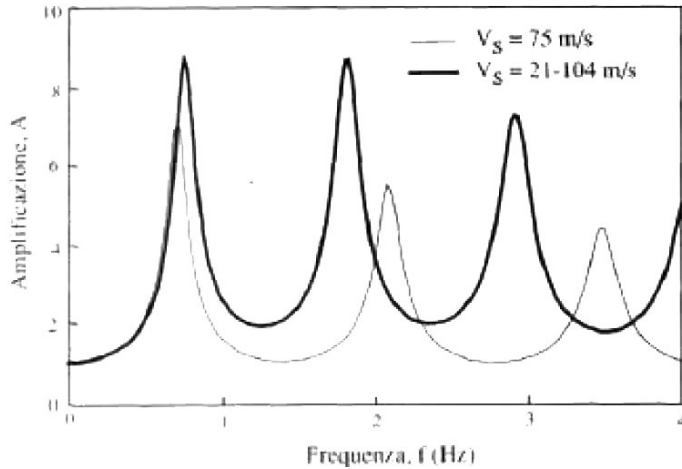


Fig. 14 Amplification function A_{daf} against f relating to homogeneous and heterogeneous deposit (Lanzo & Silvestri 1999)

Finally, when a non-linear deposit is considered, one can observe that the maximum deformation induced by the seismic event reduces both resonance frequencies and peak values of amplification function Fig. 15.

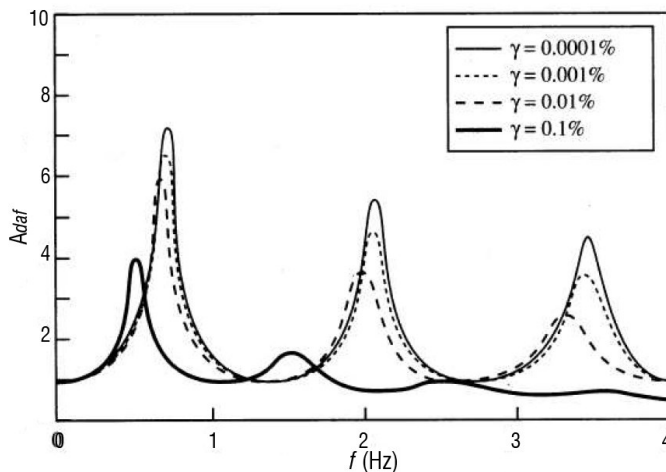


Fig. 15 Amplification functions of a non-linear soil deposit relating to different input motion (Lanzo & Silvestri 1999)

1.6. Concluding remarks on seismic site response by means of one dimensional approach

It is possible to study seismic site response by means of 1D approach if the following conditions are satisfied:

- horizontal ground surface;
- homogeneous soil deposit or horizontally layered soil deposit (vertically heterogeneous soil deposit);
- horizontal soil-bedrock interface;
- vertically propagating seismic waves.

The amplification function A_{daf} (absolute value of the ratio between soil displacement registered at free-field and at bedrock) of an undamped homogeneous linear elastic soil deposit shows infinite peak value with reference to the resonance frequencies. These frequencies are related to the shear wave velocity of the soil and to the thickness of the deposit. The amplification function is independent from the input signal.

With respect to the previous case study, the effects of different soil behaviour are listed in the following:

- damping reduces the peak values of amplification function;
- heterogeneity increases the value of fundamental frequencies and reduces the value of other resonance frequencies respect to homogeneous soil deposit. Additionally heterogeneity increases peak values of amplification function;
- adopting non-linear soil behaviour, by increasing input motion amplitude decreases resonance frequencies and peak values of amplification function. The amplification function of a non-linear soil deposit depends on the input signal.

Furthermore it was shown that in the case of rigid bedrock the signal at bedrock is equal to the outcrop motion. In case of elastic bedrock the signal at bedrock, in general, differs from the outcrop motion.

1.7. Two dimensional effects on seismic site response

The vertically propagating wave front from the deep rock intersecting a non-horizontal soft soil-bedrock interface is refracted in the upper soil according to the Snell's law

represented by the equation 2. If a vertically propagating wave front intersects a non-horizontal ground surface it is reflected downward according to the Snell's law. The seismic site response should be studied by means of 2D approach both in case of vertically propagating waves from bedrock into a laterally heterogeneous media and in case of a homogeneous half-space characterized by an uneven topography. Aki e Larner published the work "Surface motion of a layered medium having an irregular interface due to incident plane SH waves" in 1970. An analytical method to predict the motion at the ground surface is presented. With reference to Fig. 16, plane SH-waves are considered, polarized in the y direction, normally to the x-z plane, with circular frequency ω and incident parallel to the x-z plane at the angle θ_0 from the z direction. It is referred to very large and deep soft basin. For example, in Fig. 17a) a valley large 50 km and deep 1 km is sketched.

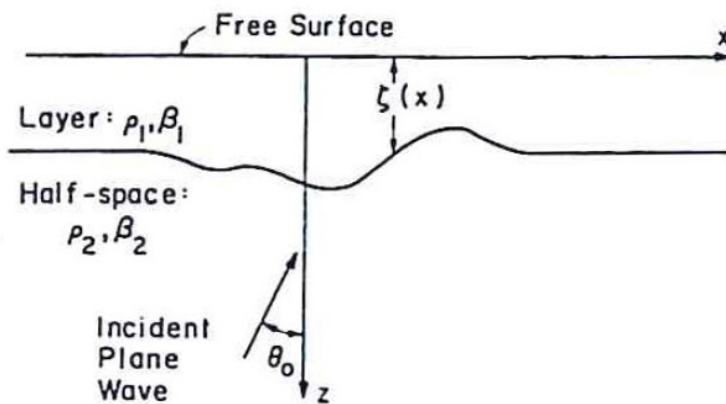


Fig. 16 Schematic cross section displaying the layered-medium configuration and coordinate axes (Aki et al. 1970)

Scattered waves with horizontal phase velocities, i.e. Love wave, different from that of the incident waves are generated at the non-plane interface between rigid half-space and layer.

The Fig. 17 shows comparison between Aki e Larner solution (named approximate solution) and flat layer response for two different kinds of basin. Flat-layer theory is referred to the stratification directly beneath each observation point.

So long as the interface slope is small, the flat-layer theory gives a satisfactory result as shown in Fig. 17a). As the interface becomes more irregular, the effect of lateral interface becomes more important.

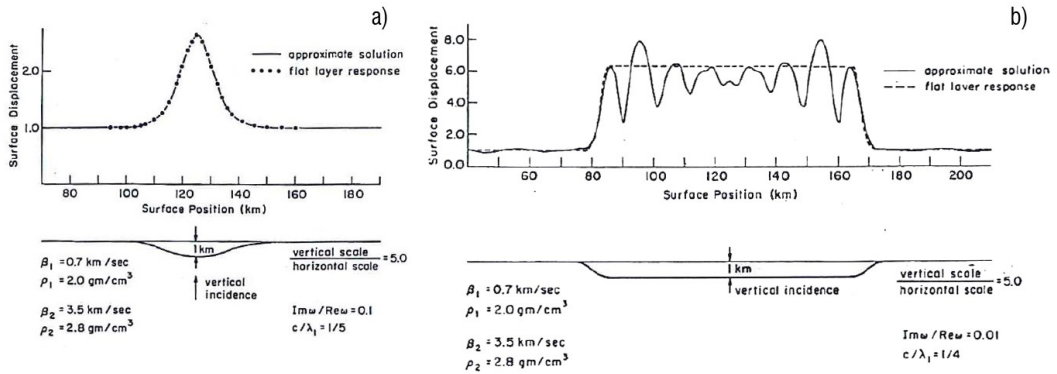


Fig. 17 Displacement at the surface of soft basin (Aki et al. 1970)

The authors also investigated the effect of incidence angle of the propagating direction of the wave front. Fig. 18 depicted the incidence angle effect. The difference between approximate solution and flat layer response increases when increasing the incidence angle of the propagating wave front.

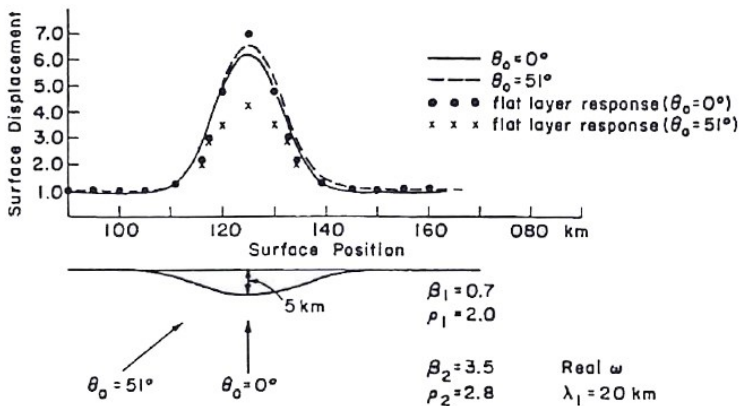


Fig. 18 Normalized displacement amplitudes at the ground surface of a soft basin for two directions of incidence of long wavelength waves (Aki et al. 1970)

Thanks to the work of Aki e Larnar, they were studied the effects on surface ground motion due to irregular interface and to the incidence angle of the S-wave normally

polarized to the plane section. It was demonstrate the importance of lateral interference relating to Love waves generated at the surficial interface.

Most of study has been focused on 2D site effects with reference to soft valley (M. D. Trifunac 1971; Mihailo D. Trifunac 1971; Bard & Bouchon 1980a) and to irregular ground surface (Bouchon 1973; Wong 1982; Geli et al. 1988; Sánchez-Sesma & Campillo 1991).

With reference to acceleration time histories it is possible to enlighten another 2D effect: the length of ground surface signal is bigger than the reference one as shown in the left side of Fig. 19 (Bard & Bouchon 1980b). In the left side, the traces represent the horizontal displacements at surface receivers, spaced from 0 to 6.0 km from the valley centre. The bottom trace would be the surface displacement signal without the valley. In the right side, diagrams showing the spatial and temporal evolution of the surface displacement components are depicted. The dots indicate the location of the site where the seismograms are computed.

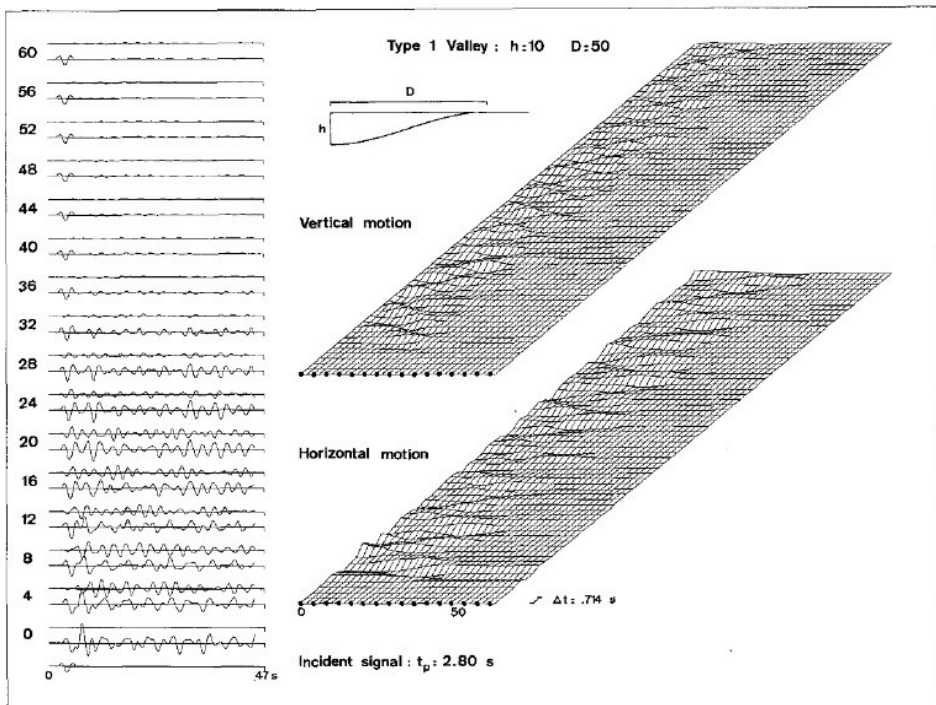


Fig. 19 Response of a high-contrast type 1 valley of maximum depth 1km, and half-width 5km, and an SV Richer wavelet with characteristic period $t_p=2.8$ s. (Bard & Bouchon 1980b)

Jibson published a report on the topographic amplification of earthquake effects shaking on slope stability in 1987 showing the site effects by means of real recorded signals. As presented in Fig. 20, the peak ground acceleration reaches its peak at the crest of the hill.

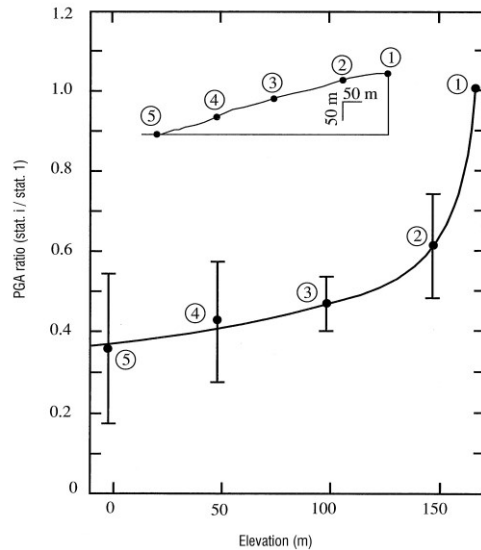


Fig. 20 Ratio of stations' PGA to PGA of station 1 versus station elevation (Jibson 1987)

Referring to the reference system sketched in Fig. 16, recent studies have shown the 2D site effects due to vertically propagating S-waves polarized in x direction.

The paper of Bouckovalas and Papadimitriou published in 2005 presents numerical results, obtained by means of the Finite Difference method, of the seismic response for a step-like ground slopes in uniform visco-elastic soil. The main results (for example see the Fig. 21) are summarised in the following:

- even a purely horizontal excitation, as vertically propagating S-wave, results in considerable (parasitic) vertical motion, i.e. Rayleigh wave, at the ground surface near the slope;
- the topography aggravation of the horizontal ground motion (ground surface acceleration against free-field acceleration) fluctuates intensely with distance away from the crest of the slope, alternating between amplification and de-amplification within very short horizontal lengths;

- the horizontal ground motion is de-amplified at the toe of the slope and amplified near the crest.

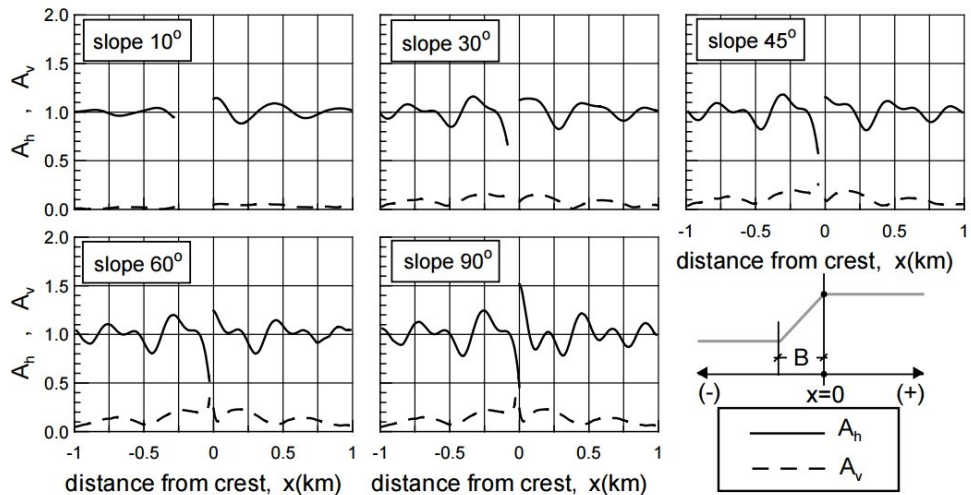


Fig. 21 Effect of slope inclination i on the amplification of peak horizontal A_h and parasitic vertical A_v acceleration, as a function of distance x from the crest of a step-like slope (Bouckovalas & Papadimitriou 2005)

A similar study as Bouckovalas and Papadimitriou has been carried out by Rizzitano et al. in the 2014 with regards to Finite Element method. The authors obtained the same results of Bouckovalas and Papadimitriou, validating the numerical approach. The work of Gatmiri and Arson, published in 2008, shows the site effects by means of a parametric study. It is referred to the scheme of Fig. 22 and an incident Ricker input signal, polarized in x direction, with a predominant frequency equal to 2 Hz.

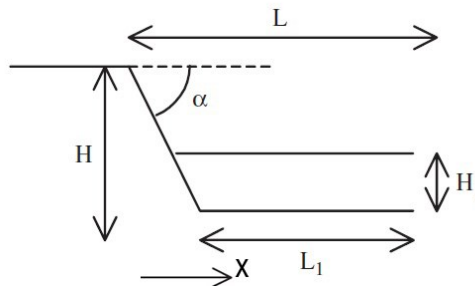


Fig. 22 Main geometrical parameters characterizing the half of a symmetric alluvial basins (Gatmiri & Arson 2008)

The authors delineate that in a canyon, assuming $H_1 = 0$, horizontal displacements tend to be attenuated at the centre and slightly amplified at the edge. On the contrary, in an alluvial basin, $H_1 = H$, horizontal displacements are amplified at the centre and can be locally attenuated near the edge if depth is large enough.

Assuming as reference motion that registered at the outcrop, Fig. 23 presents typical results for the above case study. In general, the 2D effects depends on the shape of the valley. In particular, Fig. 23a and c) are referred to the horizontal ground motion. While, Fig. 23b and d) point out the presence of a “parasitic” vertical motion at the ground surface.

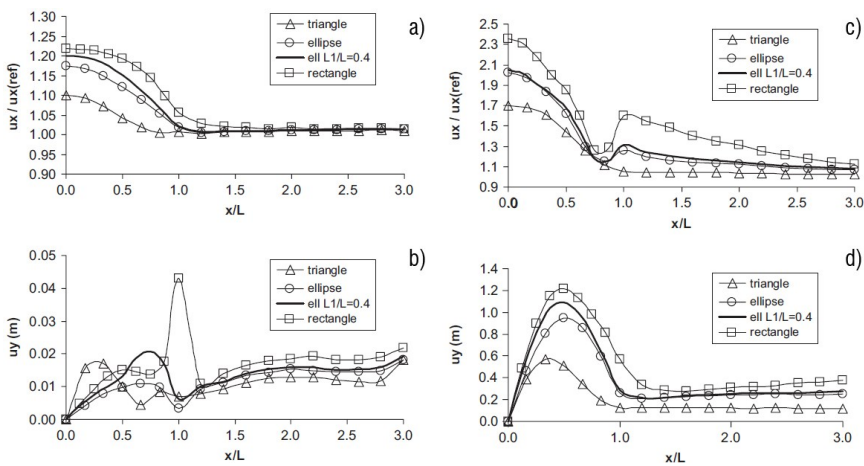


Fig. 23 Influence of shape on horizontal (a, c) and vertical (b, d) displacements at the surface of full alluvial valleys: $H/L = 0.2$ (a, b) and $H/L = 0.6$ (c, d) (Gatmiri & Arson 2008)

Fig. 24 shows the results of seismic site response analyses by means of finite element method with reference to an area characterised by a soft soil valley surrounded by rock hills (Falcone et al. 2015). A real accelerogram was selected as the reference outcrop motion. The response spectra and peak ground acceleration of the ground surface motion have been compared against the reference one. 1D and 2D analyses have been performed. The 1D analyses refer to soil columns extracted from the 2D section represented in Fig. 24 by black, red and green lines. It is possible to recognize the 2D site effects: a bigger amplification of the reference motion at centre of the valley and at the crest of the rock hill.

As 2D response is dominated by stratigraphic effect, 1D and 2D amplification factors are in good agreement, e.g. between $0 \leq x \leq 500\text{m}$. As 2D response is dominated by geometric effects due to irregular interface and/or irregular topography, 2D amplification factors differ from 1D ones, e.g. between $500 < x < 800\text{m}$ and $1000 < x < 1200\text{m}$.

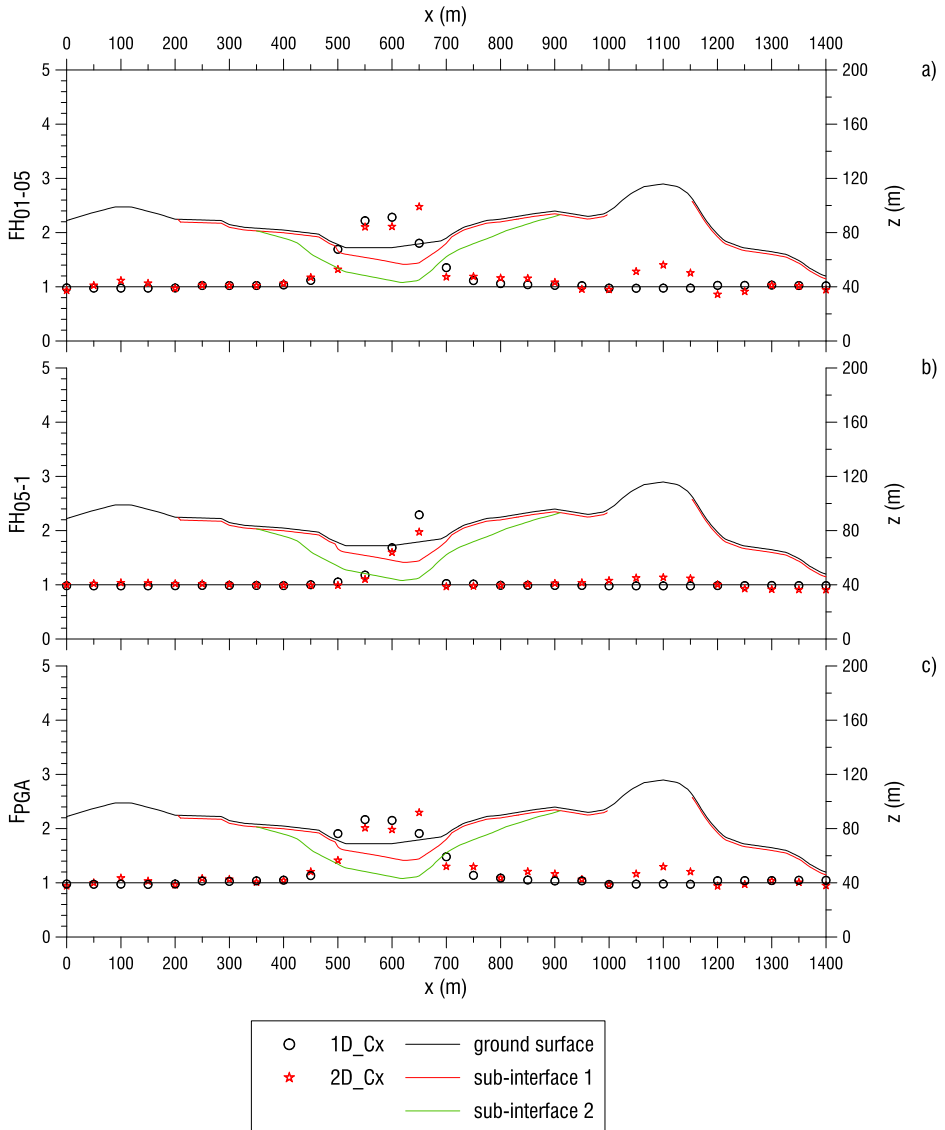


Fig. 24 Comparison of seismic site response referring to a real site by means of 1D and 2D approaches (Falcone et al. 2015)

1.8. Concluding remarks on seismic site response by means of two dimensional approach

If at least one of the following conditions is satisfied, the seismic site response needs to be studied by means of two dimensional approach:

- irregular ground surface of a homogeneous half-space;
- laterally heterogeneous media, i.e. irregular sub-interface;
- the presence of a structure in the area of interest. All studies presented in the previous section was focused on the free-field response, that is the motion expected at the ground surface far away from any surficial or underground structure. For example, the seismic response of a homogeneous half-space with horizontal ground surface could be studied by means of 1D approach but the presence of a regular building makes it a 2D case study.

The main 2D effects are summarised in the following:

- greater amplification at the centre of alluvial valleys and at the crest of outcropping rock hills due to the focalization of refracted S-waves;
- the amplification pattern depends on the input signal features, geometry of interface between soil layers and topography;
- the duration of the signal at the ground surface is bigger than that of the reference outcrop motion;
- the generation of surficial Rayleigh or Love waves;
- the generation of “parasitic” vertical ground surface motion.

At least it should be noted that all presented case studies are related to great valley condition (depth and length over 1 and 5 km, respectively) and simplified input signal, for example Richer pulse or sinusoidal wave, characterised by a frequency content minor than 5 Hz.

1.9. Three dimensional effects on seismic site response

The seismic site response has to be studied by means of 3D approach both in case of vertically propagating wave from bedrock into a laterally and transversally hetero-

geneous media and in case of a homogeneous deposit characterized by an irregular topographic surface in any direction.

A lot of work has been published from 1988 about 3D effects relative to both ideal case study (e.g. Jiang & Kuribayashi 1988; Ohori et al. 1992; Sahar & Narayan 2015) and real case history (e.g. Hisada et al. 1993; Fäh et al. 2006; Lee et al. 2009; Pitilakis et al. 2011; Landolfi 2013).

The work of Makra & Chávez-García (2016) was related to the seismic response of a soft basin, 5 km wide and 15 km long, with maximum sediment thickness reaching about 410 m, imposing a flat ground surface, i.e. topography was not included. The chosen input motion was the Gabor pulse characterised by a frequency content up to 4 Hz; the different dimensional models, 2D and 3D, were excited by this vertical incident plane shear waves. The authors highlighted that, in general, ground motion simulated using 2D models is very similar to that computed from a full 3D model; 3D model does not introduce additional phenomena relative to 2D, however, in that case basin response becomes more dependent on the characteristics of the exciting motion.

With reference to a point on ground surface, in general, the seismic site response is studied comparing acceleration time histories and amplification function obtained using different dimensional approaches; for example, with reference to the centre point of section 1 shown in Fig. 25, the results are presented in Fig. 26a and b). Additionally it is possible to qualitatively compare the acceleration time histories along the ground surface of the whole section as proposed in Fig. 26c).

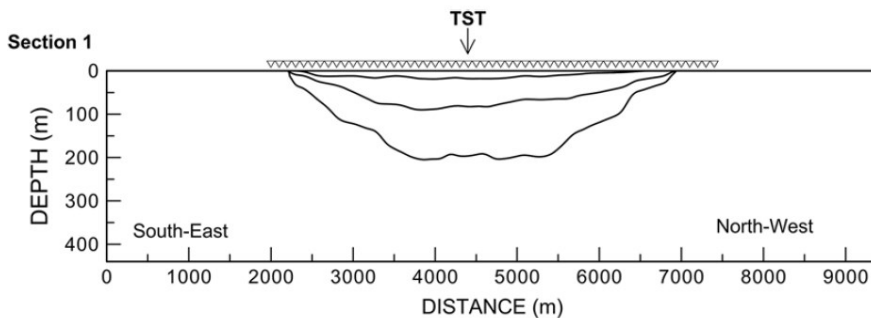


Fig. 25 Section of study from the work of Makra and Chávez-García (2016)

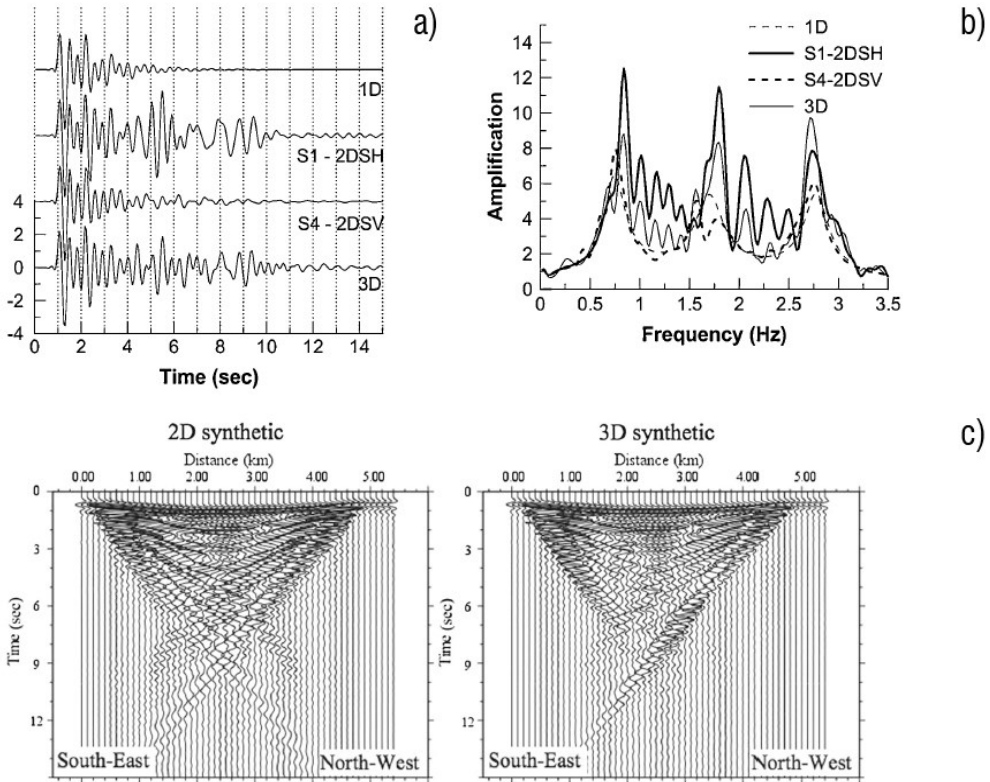


Fig. 26 Results of seismic site response referring to work of Makra and Chávez-García (2016)

In a more detailed way, Ohori et al. (1992) outlined that the comparison among 1D, 2D, and 3D amplification factors at the centre of the basin shows that the higher the dimensionality of the analysis, the higher the dominant frequency and the larger the maximum amplitude (see Fig. 27).

Furthermore, the 3D approach makes possible to include in a unique numerical model the following layout: geological and geotechnical model, topography, source of the seismic waves. For example, the paper of Smerzini et al. (2011) shows the importance of 3D modelling when the coupling of seismic source and complex site effects plays a dominant role in spite of a reduced resolution at high frequency mainly due to the size of the numerical domain. It is worth noting that in this study the numerical model was constructed by combining the kinematic seismic source model of

the seismic event proposed by Hernandez et al. (2004) and linear visco-elastic material behaviour, allowing to propagate seismic motion up to $f = 3$ Hz.

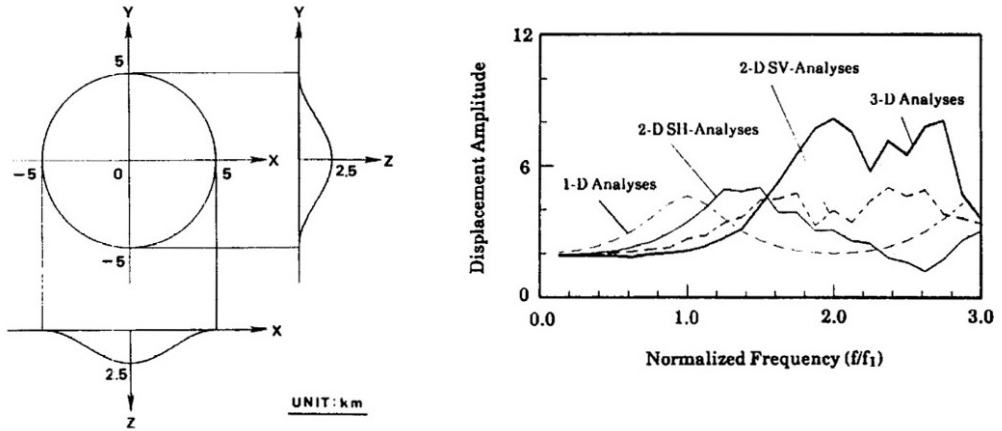


Fig. 27 Right: a 3D basin model and Left: the 1D, 2D, and 3D amplification factors at the center of the basin due to vertical incident plane wave (Ohori et al. 1992)

3D model, including the seismic source, allows to study the so called source effects. These effects could be implemented in the 2D model by varying the intensity, frequency content and travelling direction of the input motion. Instead, the 1D scheme accounts for source effects only in terms of intensity and frequency content of the seismic input.

As reported in the introduction to this chapter, the present thesis is focused on the site response analyses with reference to horizontal input motion then no more detailed results have been shown about source effects.

At least, it is recalled one of the main learning from the Euroseistest Verification and Validation Project (Maufroy et al. 2016): no ground motion simulation code accounting for wave propagation in complex media can be considered as press-button. The most common case states that, without iterations and cross-checking, different codes provide significantly different results when applied to the same case study.

1.10. Concluding remarks on seismic site response by means of three dimensional approach

If at least one of the following conditions is satisfied, the seismic site response needs to be studied by means of three dimensional approaches:

- ground surface of an homogeneous half-space uneven in any direction;
- laterally and transversally heterogeneous media, i.e. irregular sub-interface;
- the presence of an irregular structure in the area of interest.

The above mentioned works about 3D geometric schemes have outlined that no-additional phenomena are observed with reference to that enlighten by the 2D simulations respect to 1D. The 1D approach allows to evaluate stratigraphic effect, that is ground motion modification in terms of amplitude and frequency content. Seismic site response using 2D scheme allows to highlight the geometric effects, named valley and topographic effects. They consist on ground motion modification in terms of amplitude and frequency content and greater signal duration respect to that computed using 1D approach and the generation of a parasitic vertical component.

In general the 1D and 2D numerical analyses could underestimate the ground motion evaluated by means of 3D approach. 3D numerical results could be three times bigger than the one achieved by means of 1D and 2D analyses.

At least, it should be noted that the 2D and 3D studies are often related to ideal case studies, linear visco-elastic material behaviour and simplified seismic motion characterised by a frequency content up to $f = 4$ Hz; the problem of major interest in civil engineering requires to study the seismic response of non-linearly behaving material and referring to the propagation of seismic waves characterised by a frequency content up to 10 Hz. Further investigation are aimed to better understand the seismic response of a real site by means of 3D dimensional approach.

CHAPTER 2. 1D NUMERICAL MODELLING OF THE SEISMIC SITE RESPONSE

The site response analysis is characterised by a significant number of variables, each of which might play a significant role in the solution of the problem, as recently well highlighted by an international benchmark on this topic, named PRENOLIN (Régnier et al. 2016). This latter was specifically focused on the 1D site effects, for which the correct definition of the input motion and the boundary conditions might be as important as the specific constitutive assumption adopted.

Analytical solutions allow to determine the motion at the free-surface of a soil deposit only for simple constitutive soil behaviour, assuming the acceleration time history recorded at the bedrock or at the outcrop as the input motion. In fact, as already discussed in § 1, generally, the bedrock motion differs from that at the outcrop.

Another key aspect of the numerical analysis of this class of problems is that of the input motion, which is typically applied at the base of the model and should be defined consistently with the adopted boundary conditions. In general, it is possible to consider boundary conditions in terms of prescribed displacements or stresses. Assuming an acceleration time history applied at the base of the numerical model corresponds to prescribe the base displacements, as such that boundary should be considered as a perfectly reflecting base. On the other hand, the so called compliant base condition requires the application of a stress time history, together with the activation of dashpots at the base of the model; the base displacements and accelerations are

thus an outcome of the analysis, i.e. they are obtained as a response of the numerical simulation.

In standard practice, the accelerograms to be adopted in a seismic site response analysis are selected as compatible, on average, to a probabilistic-based definition of the design spectrum. Such a procedure is carried out with reference to an ideal horizontal outcropping bedrock, thus the accelerograms are defined consistently with this idealisation. As a consequence, it is crucial to properly transfer those input motions to the depth at which they will be applied to the model, this holding for both analytical and numerical simulations. This issue will be also addressed in this chapter, together with the definition of further ingredients of the numerical problem at hand, as the size of the finite elements (Kuhlemeyer & Lysmer 1973), the time step of analyses (Bathe 1996), the size of the mesh (Amorosi et al. 2008; Amorosi et al. 2010).

In what follows, simplified ideal cases are analysed under 1D conditions using PLAXIS 3D (PLAXIS 2016) and QUAKE/W. The numerical assumptions are verified against available analytical solutions and well established linear-equivalent ones, those latter obtained by the code EERA (Bardet et al. 2000).

The following canonical cases are considered:

- homogeneous linear elastic half-space;
- homogeneous linear elastic soil deposit;
- homogeneous non-linear elastic soil deposit;

With reference to all the above cases, it is worth noting that one-dimensional conditions implies:

- horizontal ground surface;
- laterally and transversally unbounded media. The homogeneous half-space also implies no base bounded media;
- vertically propagating waves.

All these conditions have to be implemented in the numerical model. Obviously it is not possible to create an unbounded finite element mesh. Thus it is necessary to define both the size and boundary conditions in order to correctly approximate the 1D hypotheses. The codes PLAXIS 3D and QUAKE/W require the implementation of

three-dimensional and two-dimensional bounded models, respectively. A one-dimensional one is implemented in the more basic code EERA.

Referring to vertically propagating S-waves, the soil particles experience only horizontal motion, while they are fixed along the vertical direction.

Considering a Cartesian coordinate system, it is assumed:

- z as the direction of vertical propagating seismic wave front;
- particle motion of soil in x direction;
- y direction normal to the xz plane.

For the sake of brevity, all the analyses reported in this chapter were carried out with reference to the same signal, assumed as known at the outcrop and characterised by the features listed in Table 1. The signal is scaled up to 0.22g.

Earthquake ID	Station ID	Earthquake Name	Date	Mw	PGA (g)	Component
80	ST45	Calabria	11/03/1978	5.2	0.07616	y

Table 1 Features of the selected input accelerogram at the rock outcrop

The elements' size should be smaller than one eighth of the wave length associated with the maximum frequency component f_{max} of the outcrop signals. In order to avoid excessively thin elements, the selected event was filtered to cut-off frequencies higher than 10 Hz.

Fig. 28 shows the accelerogram, Fourier spectrum and response Spectra (structural damping 5%) in terms of pseudo-relative velocity and pseudo-absolute acceleration of the scaled and filtered signal.

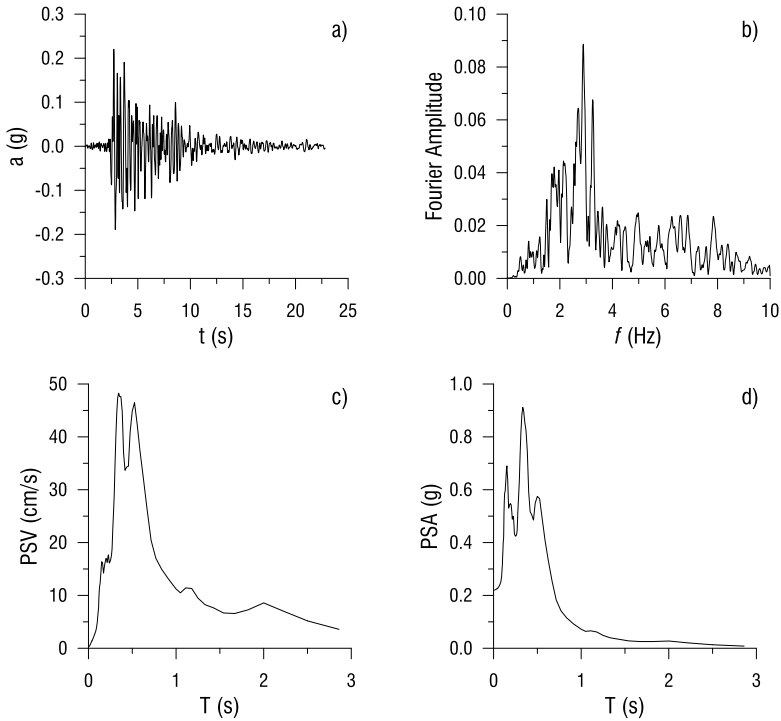


Fig. 28 Reference motion a) time history of acceleration, b) Fourier spectrum, c) pseudo-velocity and d) pseudo-absolute acceleration response spectra

2.1. Homogeneous linear elastic half-space

In the following the seismic response of a homogeneous half space is modelled through a soil deposit of thickness H whose physical and mechanical properties are those of the bedrock.

Concerning this case, some lessons learned from the analytical solutions are summarized in the following:

- the amplification function between outcrop and bedrock motions, according to equation 16 and for $l = 1$, becomes equal to 1 only for values of frequency f and depth H determined according to equations 18 and 17, respectively. Assuming, for example, $V_s = 1200$ m/s and the frequency of a sinusoidal input equal to $f = 5$ Hz, outcrop and bedrock motion will be the same, i.e. $A_{dabf} = 1$, for $H_{ss,n} = n \cdot 120$ m ($n = 0, 1, 2, \dots, \infty$). If $A_{dabf} \neq 1$ it results that the outcrop motion differs from the bedrock one;

- if the fundamental frequency, determined according to equation 12, is much larger than the maximum frequency of the bedrock signal ($f_{r,1} \gg f_{max}$), it results $A_{daf} (f < f_{max}) \approx 1$. For example it is possible to consider a stiff material, $V_s = 1200$ m/s, and an half-space analytical model of depth 10 m; it results that $f_{r,1} = 30$ Hz $\gg f_{max} = 10$ Hz. Therefore, the bedrock and the free-field motions will be nearly the same;
- therefore, for the case of the homogeneous half-space, there is no physical difference between outcrop and free-field conditions as defined in the introduction of chapter 1. This condition is confirmed by equation 14 which provides $A_{dbf} = 1$.

The above features should be considered in a numerical simulation of this ideal case. To verify it, three different soil materials are selected (Table 2) and three different geometrical models of the deposit (Table 3 and Fig. 29) are implemented in the adopted codes.

Soil	V_s (m/s)	ν	γ (kN/m ³)	G (MPa)
1	1200	0.25	18	2642
2	600	0.25	18	661
3	200	0.25	18	73

Table 2 Physical and mechanical properties of the homogeneous linear elastic half-space

Model	$Z_{PLAXIS\ 3D} = Z_{QUAKE/W} = Z_{EERA}$ (m)	$X_{PLAXIS\ 3D} = X_{QUAKE/W}$ (m)	X_{EERA} (m)	$Y_{PLAXIS\ 3D}$ (m)	$Y_{QUAKE/W} = Y_{EERA}$ (m)
A	18	144	/	2	/
B	55	440	/	2	/
C	110	880	/	2	/

Table 3 Sizes of the models implemented in the adopted codes, simulations of 1D seismic wave propagation

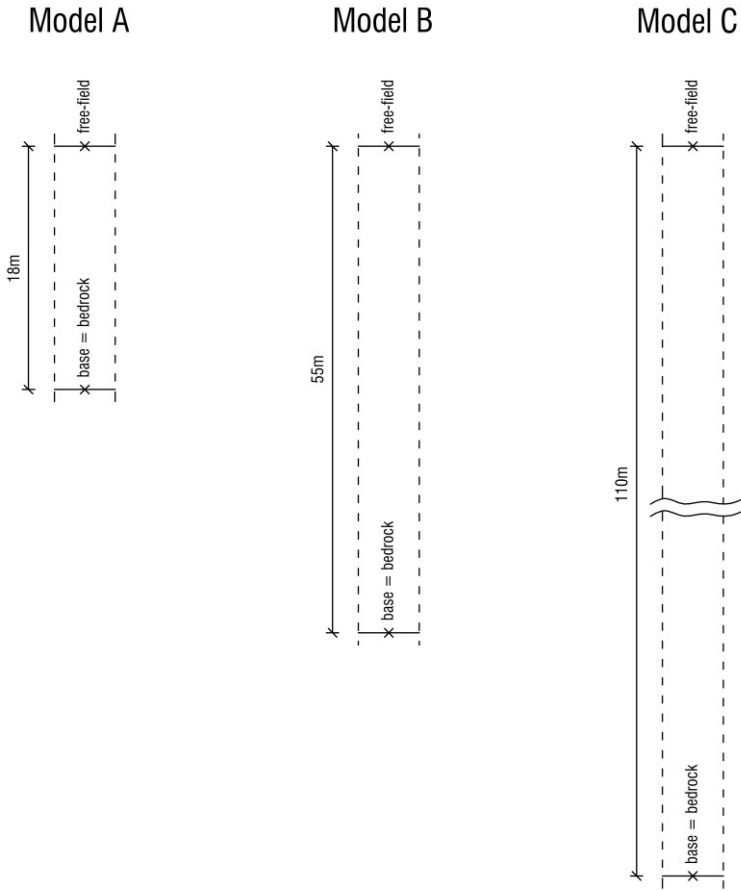


Fig. 29 Three different models implemented for seismic site response analyses

For sake of convenience, the nomenclature suggested in § 1 is adopted in the following; the free-field and bedrock points are located at the ground surface and at the base of the half-space numerical model, respectively.

The results obtained using the EERA code are first discussed. The comparison between outcrop, free-field and bedrock motions for Soil 1 are shown in Figs. 30-32 for Models A, B and C. Free-field and outcrop motion are the same, as predicted by the analytical solutions. Additionally, the first resonance frequency of this deposit is $f_{r,1}$ (Soil 1 model A) = 16.66 Hz, a value larger than the maximum frequency of the signal $f_{\max} = 10$ Hz. As a consequence, as predicted by the analytical solutions, the bedrock and the free-field motions are very similar to each other.

The free-field and outcrop motions, for Models B and C, are very similar to each other. Instead, free-field and outcrop motions show a divergence in the spectral response for the following resonance frequencies determined according to analytical solutions, i.e. equation 11:

- $f_{r,1} = 5.45$ Hz for model B (see Fig. 31b);
- $f_{r,1} = 2.72$ Hz and $f_{r,2} = 8.18$ Hz for model C (see Fig. 32b).

A key result of this set of analyses is in the great difference between outcrop motion and inside one, Fig. 31 and Fig. 32, even in the case of the stiff material ($V_s = 1200$ m/s). This proves that it is not acceptable to apply the outcrop time history of the accelerations directly at the deep base of the FE model in order to simulate the seismic site response of an homogenous half-space. This leads to the crucial necessity, when a rigid boundary condition is adopted at the base of the model, to define the time history to be applied at the bedrock prior to proceed with the analysis. As an alternative, different boundary conditions can be applied, as for example the flexible one, here defined as condition 2.

Comparing the free-field acceleration time history to the outcrop one, Fig. 31a) and Fig. 32a): it can be detected a negligible delay of the first peak due to physical propagation of waves from the base of the model to the ground surface . In fact, assuming $t(a_{\max, \text{FF}})$ and $t(a_{\max, \text{outcrop}})$ as the time of peak free-field and outcrop acceleration, respectively, it is verified the following equation:

$$\begin{cases} \Delta t_{\text{signal}} = t(a_{\max, \text{FF}}) - t(a_{\max, \text{outcrop}}) \\ \Delta t_{\text{propagation}} = \frac{H}{V_s} \end{cases} \Rightarrow \Delta t_{\text{signal}} = \Delta t_{\text{propagation}} \quad 22$$

where V_s is the shear wave velocity of the linear elastic half space and H is the thickness of the model implemented in the FE code.

For example, referring to Soil 1 Model C, Δt_{signal} (equal to 0.09 s) is the same as $\Delta t_{\text{propagation}} = 110 \text{ m}/(1200 \text{ m/s}) = 0.09 \text{ s}$.

As such, it is more significant a comparison carried out in terms of Fourier or response spectra rather than with reference to the time histories.

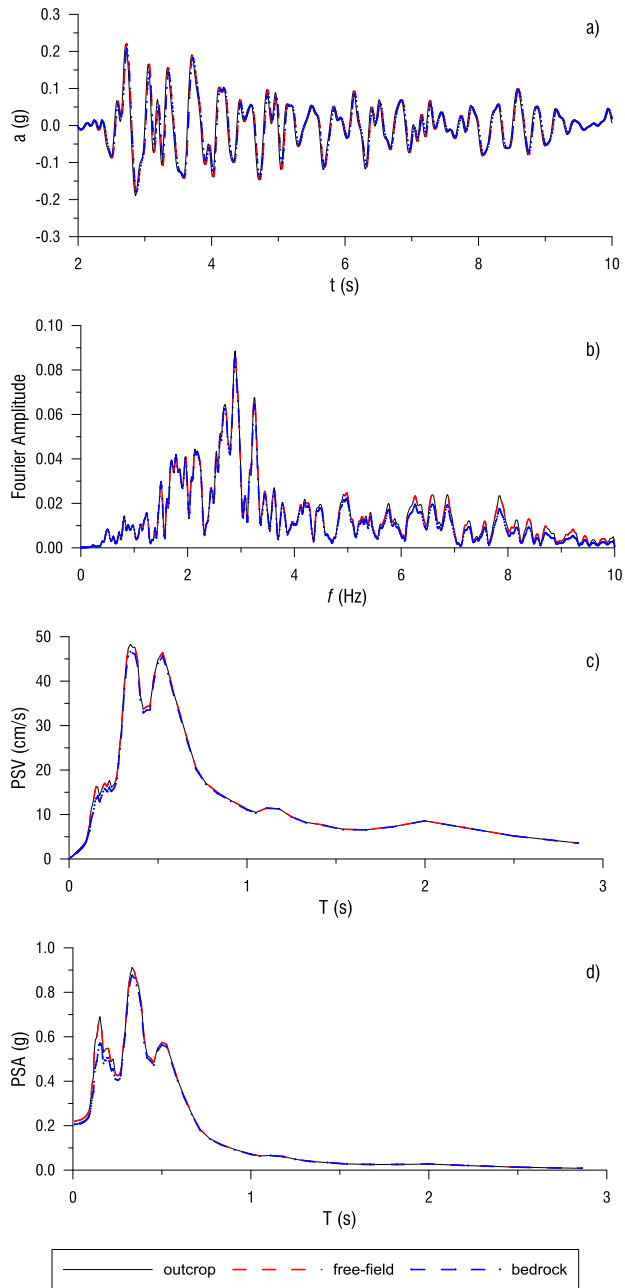


Fig. 30 a) time history of acceleration, b) Fourier spectrum, c) pseudo-velocity and d) pseudo-absolute acceleration response spectra obtained by means of code EERA for Soil 1-Model A

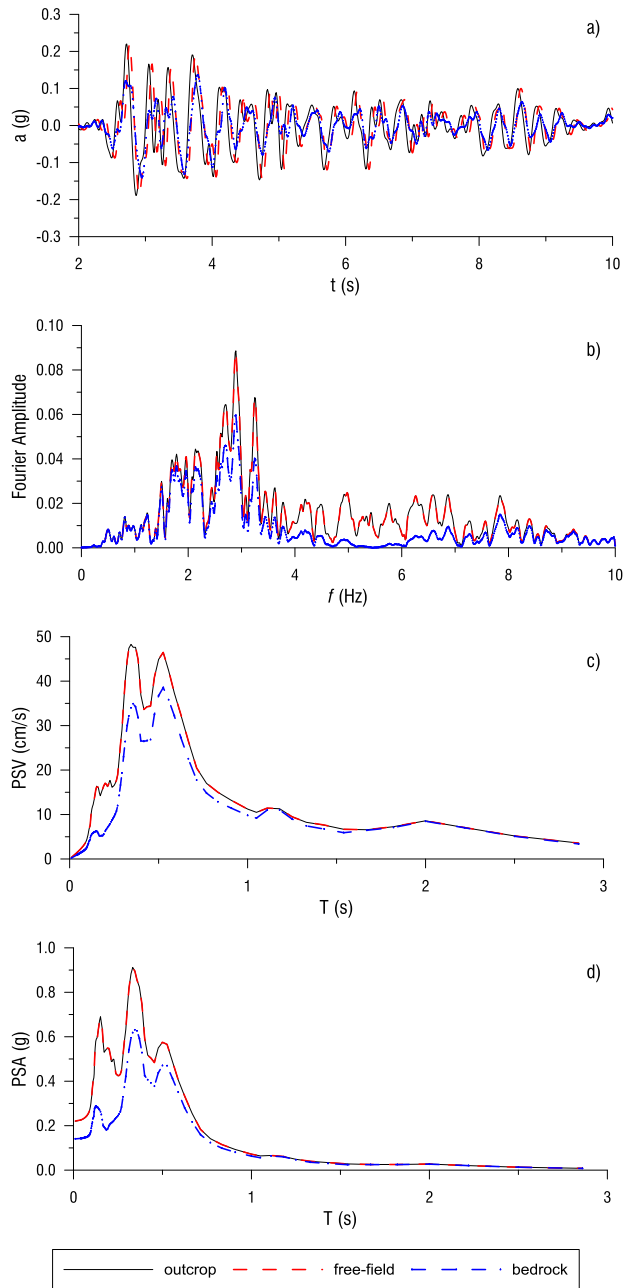


Fig. 31 a) time history of acceleration, b) Fourier spectrum, c) pseudo-velocity and d) pseudo-absolute acceleration response spectra obtained by means of code EERA for Soil 1- Model B

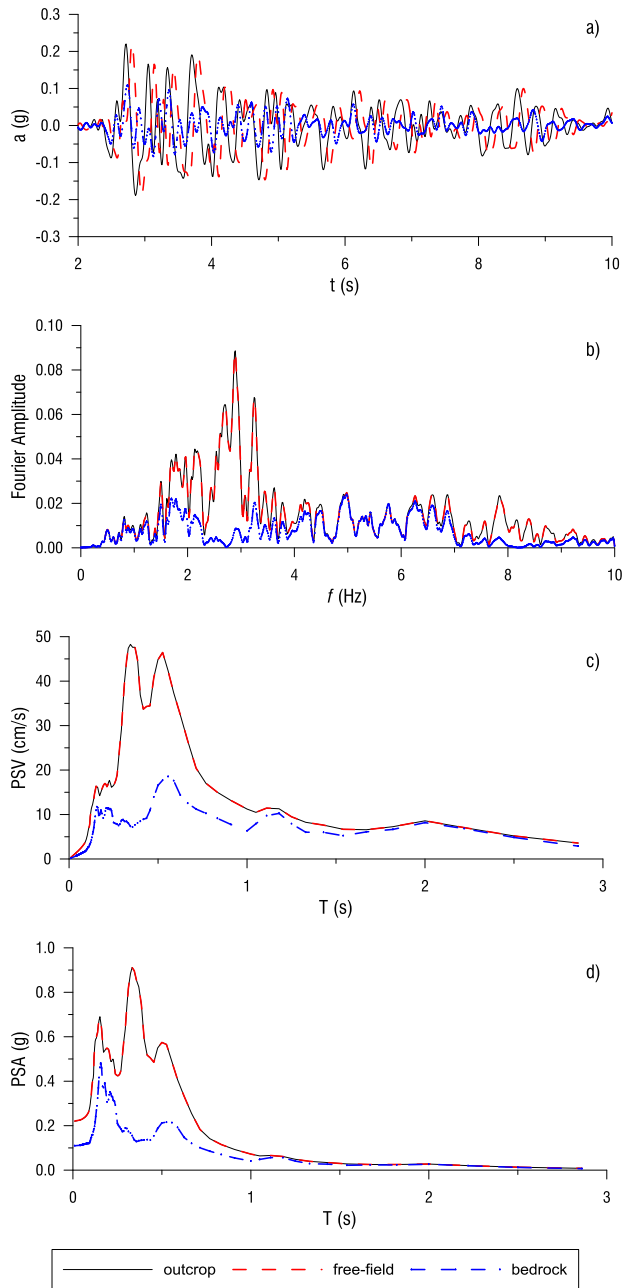


Fig. 32 a) time history of acceleration, b) Fourier spectrum, c) pseudo-velocity and d) pseudo-absolute acceleration response spectra obtained by means of code EERA for Soil 1-Model C

With reference to the results obtained by the code EERA, the comparison between outcrop, free-field and bedrock motion for Soil 2 is shown in Fig. 33, Fig. 34 and Fig. 35 for Models A, B and C respectively.

As previously observed for Soil 1, the free-field and outcrop motion are very similar to each other. The bedrock motion is different from that of the outcrop in all the analysed models. Greater differences are visible for the following frequencies:

- $f_{r,1} = 8.33$ Hz for model A (see Fig. 33b);
- $f_{r,1} = 2.73$ Hz and $f_{r,2} = 8.18$ Hz for model B (see Fig. 34b);
- $f_{r,n} = (2n - 1) \cdot 1.36$ Hz with $n = 1,2,3,4$ for model C (see Fig. 35b).

where $f_{r,n}$ are computed according to equation 11.

With regard to model B and C, the comparison between the acceleration time histories relative to the free-field and the outcrop motion, Fig. 33a), Fig. 34a) and Fig. 35a), shows more significant differences than model A due to physical propagation of waves through a softer material.

A similar pattern is also observed for Soil 3 (Fig. 36-Fig. 38). In particular, free-field and outcrop motions are very similar to each other. The bedrock motion is different from that of the outcrop in all the analysed models. Greater differences are visible for the following resonance frequencies:

- $f_{r,1} = 2.78$ Hz and $f_{r,2} = 8.83$ Hz for model A (see Fig. 36b);
- $f_{r,n} = (2n - 1) \cdot 0.91$ Hz with $n = 1$ to 6 for model B (see Fig. 37b);
- $f_{r,n} = (2n - 1) \cdot 0.45$ m with $n = 1$ to 11 for model C (see Fig. 38b).

The comparison between acceleration time histories relative to free-field and outcrop motion, Fig. 36a), Fig. 37a) and Fig. 38a), shows greater delay of the first peak than soil 1 and 2 due to physical propagation of waves in a soft material.

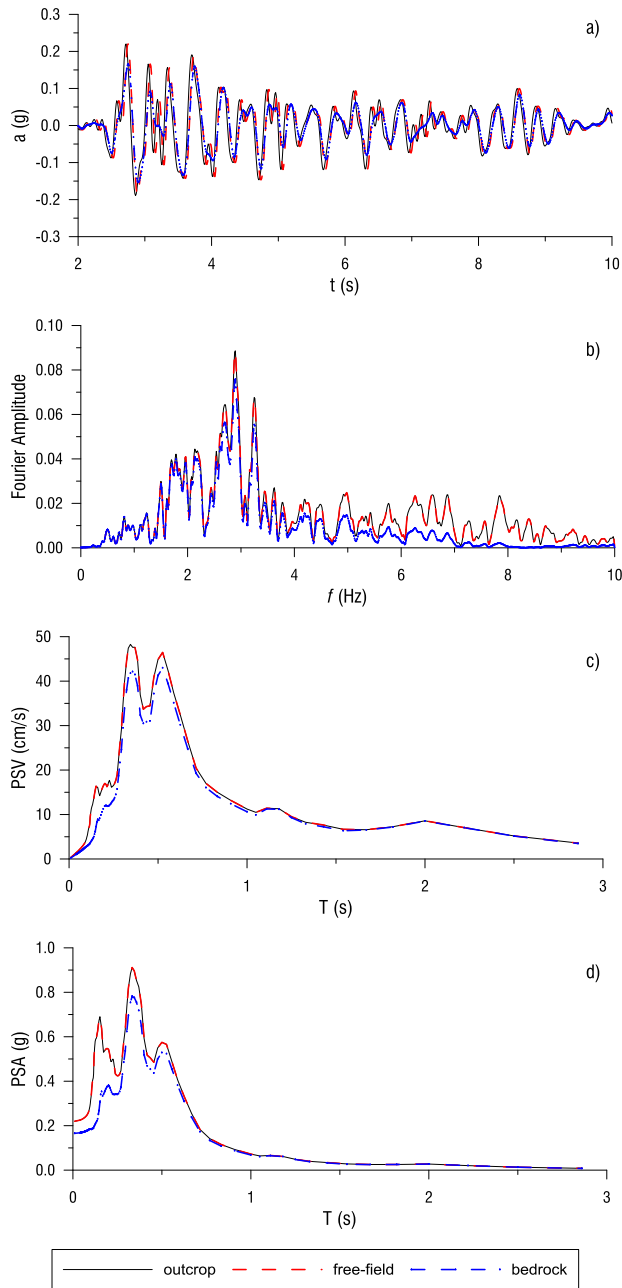


Fig. 33 a) time history of acceleration, b) Fourier spectrum, c) pseudo-velocity and d) pseudo-absolute acceleration response spectra obtained by means of code EERA for Soil 2- Model A

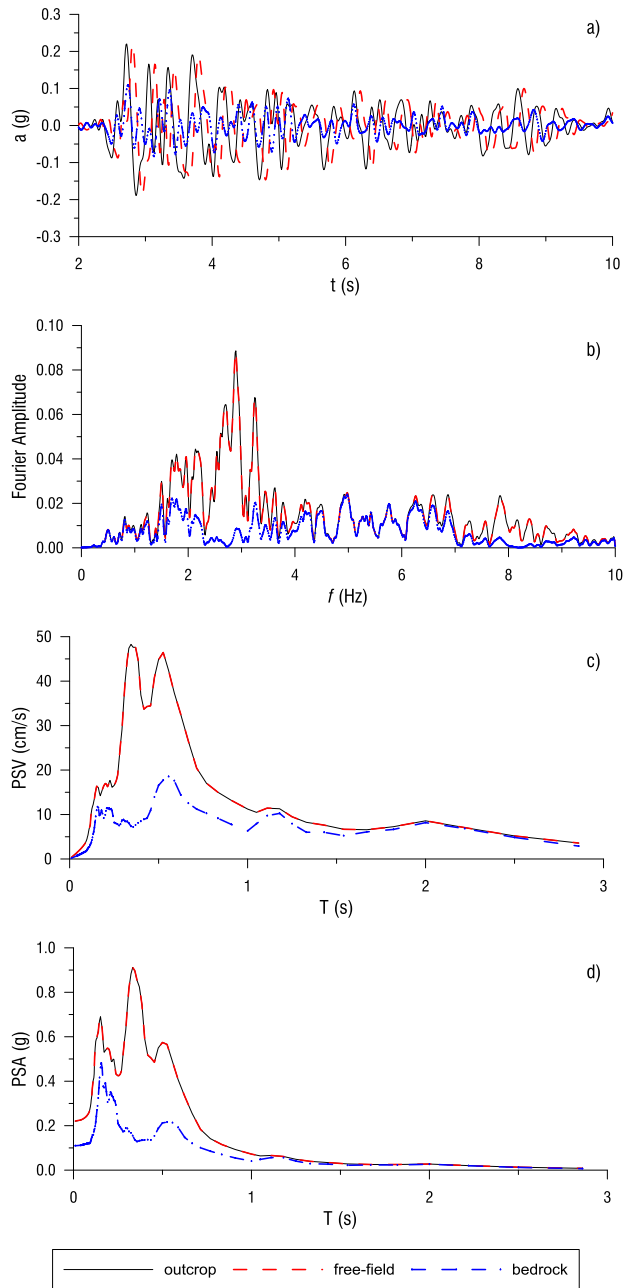


Fig. 34 a) time history of acceleration, b) Fourier spectrum, c) pseudo-velocity and d) pseudo-absolute acceleration response spectra obtained by means of code EERA for Soil 2- Model B

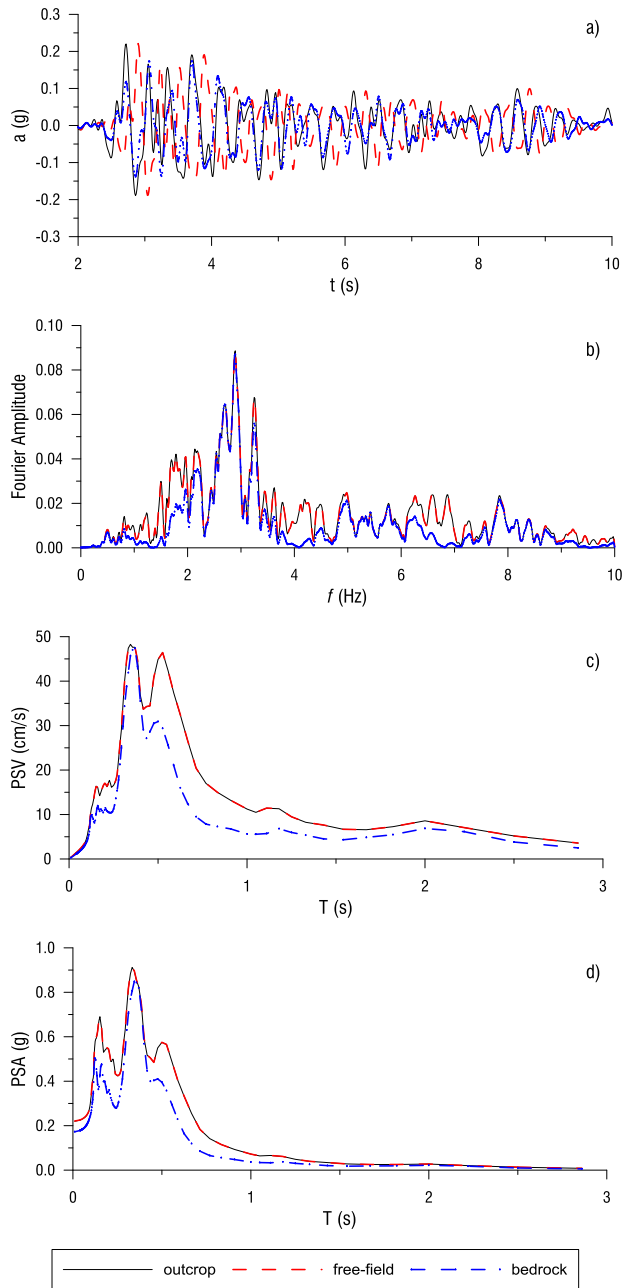


Fig. 35 a) time history of acceleration, b) Fourier spectrum, c) pseudo-velocity and d) pseudo-absolute acceleration response spectra obtained by means of code EERA for Soil 2- Model C

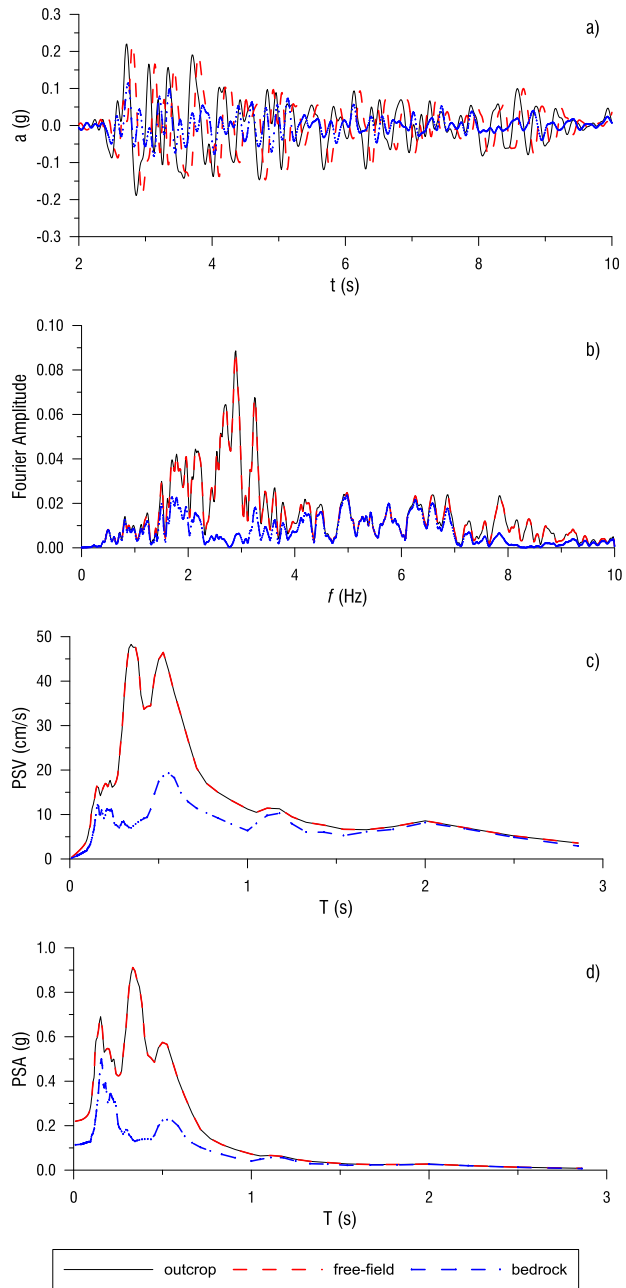


Fig. 36 a) time history of acceleration, b) Fourier spectrum, c) pseudo-velocity and d) pseudo-absolute acceleration response spectra obtained by means of code EERA for Soil 3- Model A

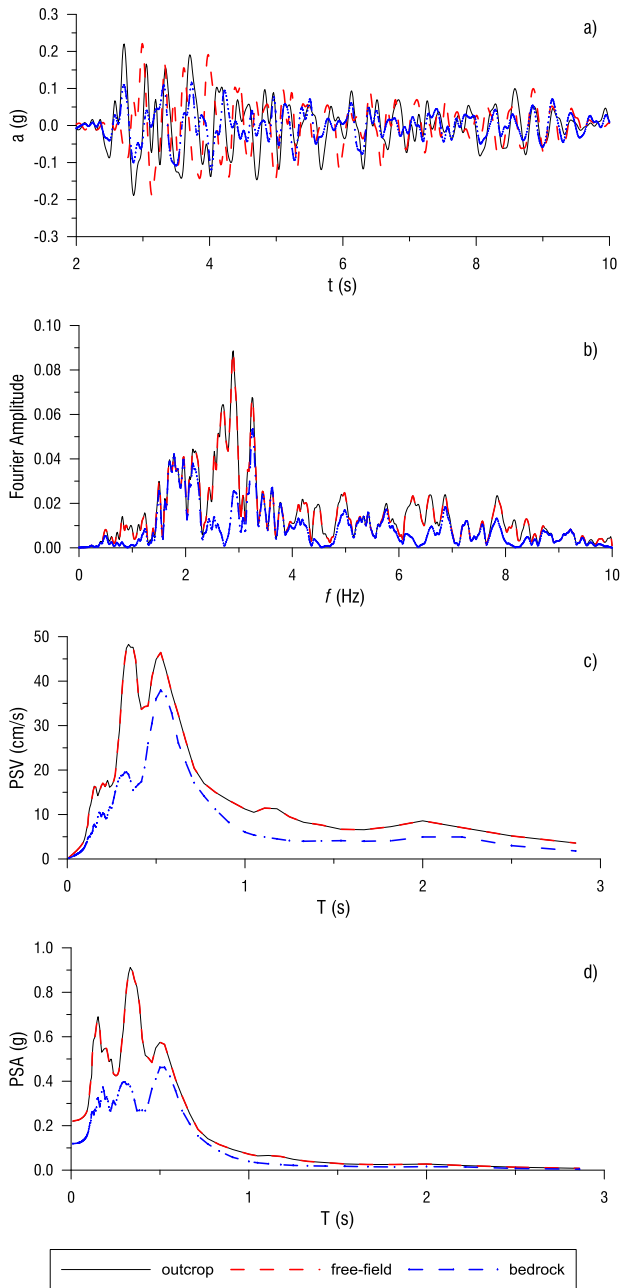


Fig. 37 a) time history of acceleration, b) Fourier spectrum, c) pseudo-velocity and d) pseudo-absolute acceleration response spectra obtained by means of code EERA for Soil 3- Model B

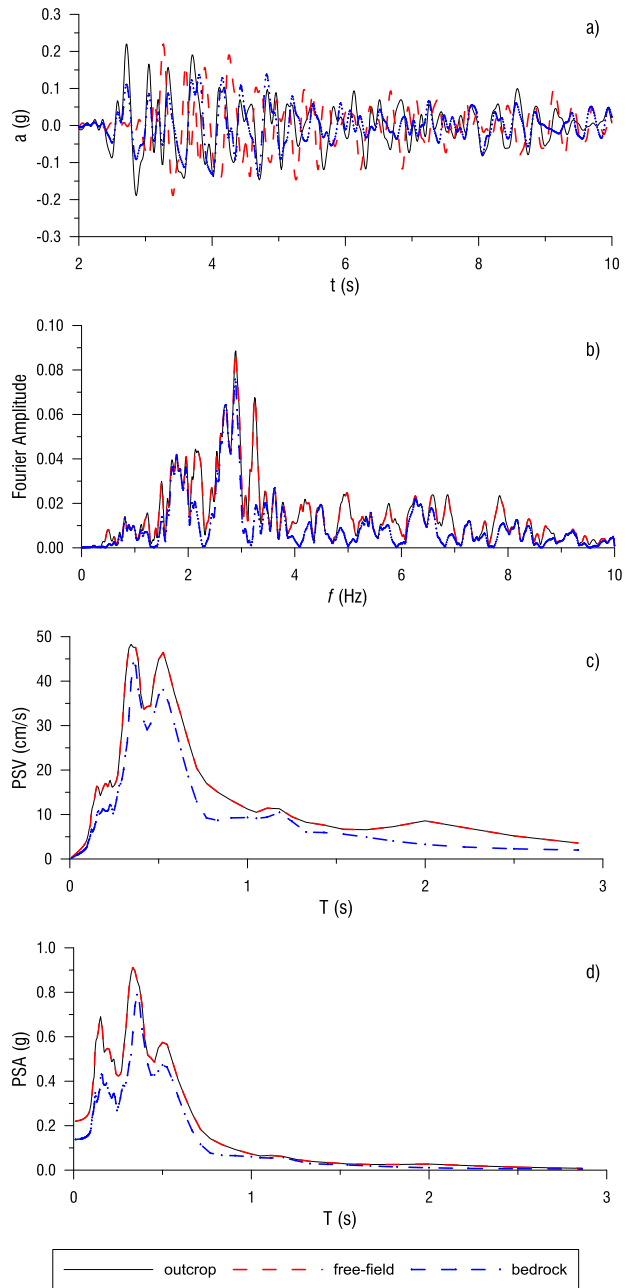


Fig. 38 a) time history of acceleration, b) Fourier spectrum, c) pseudo-velocity and d) pseudo-absolute acceleration response spectra obtained by means of code EERA for Soil 3- Model C

The same seismic response analyses were repeated using QUAKE/W and PLAXIS 3D. The numerical models were created taking into account the following constraints. The length of each model in the x direction is defined as eight times the relative depth, in the z direction, in order to avoid wave reflection along the vertical side (Amorosi et al. 2008).

For each numerical model, the maximum finite element size, h_{max} , was determined according to the well-known relationship proposed by Kuhlemeyer & Lysmer (1973):

$$h_{max} = \frac{V_s}{6 \div 8 \cdot f_{max}} \quad 23$$

where V_s is the shear wave velocity of the soil and f_{max} is the maximum frequency of the reference signal.

The two FE codes generate automatically unstructured meshes, composed by 3-node triangular and 10-node tetrahedral elements for QUAKE/W and PLAXIS 3D, respectively.

The time step of each numerical analysis is assumed as equal to the sample time of the reference motion (Bathe 1996).

Table 4 and Table 5 summarise the adopted boundary conditions for PLAXIS 3D and QUAKE/W respectively.

Boundary Condition	Code	Vertical side	Horizontal base	Ground surface
1	PLAXIS 3D	$u_x = \text{free}$ $u_y = u_z = 0$	$a_x(z, t) = a_{\text{bedrock}}(z, t)$ $a_y = a_z = 0$	$u_x = u_y = u_z = \text{free}$
		free-field (PLAXIS 2016)		
2	PLAXIS 3D	$u_x = \text{free}$ $u_y = u_z = 0$	$a_x(t) = 0.5 \cdot a_{\text{outcrop}}(t)$ $a_y = a_z = 0$	$u_x = u_y = u_z = \text{free}$
		free-field (PLAXIS 2016)	compliant base (PLAXIS 2016)	

Table 4 Boundary conditions for PLAXIS 3D, 1D simulations

Boundary Condition	Code	Vertical side	Horizontal base	Ground surface
1	QUAKE/W	$u_x = \text{free}$ $u_z = 0$	$a_x(z, t) = a_{\text{bedrock}}(z, t)$ $a_z = 0$	$u_x = u_z = \text{free}$
2	QUAKE/W	$u_x = \text{free}$ $u_y = u_z = 0$	$\tau_x(t) = 2 \cdot \tau_{\text{bedrock}}(t)$ (Mejia & Dawson 2006) $\tau_z = 0$	$u_x = u_z = \text{free}$
			nodal damping (Krahn 2004)	

Table 5 Boundary conditions for QUAKE/W, 1D simulations

The letter u and a listed in Table 4 and Table 5 indicate displacements and accelerations, respectively. The subscripts are related to the direction of application.

The free-field PLAXIS conditions (PLAXIS 2016) are applied along the vertical boundary surfaces normal to the x axis. The free-field boundary simulates the propagation of waves into the far field with minimum reflection at the boundary. Free field elements can be modelled at all vertical of the main domain and are characterised by the same properties of the soil layers inside the mesh. The free field motion is transformed from the free field elements to the main domain by applying the equivalent normal and shear forces. Two dashpots are added, in the normal and shear directions, at each node of the vertical model boundary, to adsorb the waves reflected from the internal structures.

The compliant base PLAXIS condition (PLAXIS 2016) simulates the continuation of waves into the deep soil with minimum reflection at the base boundary. It is made up of a combination of a surface prescribed displacement and a viscous boundary. As for the free-field condition, a surface element is added at the base of the model which allows to internally transform the prescribed displacement history into a load history. The viscous boundary consists of applying a series of dashpots, in the normal and shear directions, at each node of the base, to adsorb downward propagating compressive and shear waves. The compliant base and the free-field boundary conditions are based on the same principle. However, the compliant base is allowed only at the

base of the geometry model because the reaction of the dashpot is multiplied by a factor of 2 since half of the input is adsorbed by the viscous dashpot.

The quantity $\tau_{\text{bedrock}}(t)$, listed in Table 5, is defined as following:

$$\tau_{\text{bedrock}}(t) = 0.5 \cdot V_{S,\text{bedrock}} \cdot \rho_{\text{bedrock}} \cdot v_{\text{outcrop}}(t) \quad 24$$

where ρ_{bedrock} is the mass density of the bedrock and v_{outcrop} is the time history of the velocity recorded at the outcrop.

The QUAKE/W nodal damping (Krahn 2004) condition consists of nodal dashpot which provides a resisting force proportional to velocity generally expressed as:

$$F_{\text{damping}} = D_{\text{nodal}} \cdot v_{\text{base}}(t) \quad 25$$

$$D_{\text{nodal}} = \rho_{\text{bedrock}} \cdot V_{S,\text{bedrock}} \cdot L_{\text{node}} \cdot 1 \quad 26$$

where D_{nodal} is the material nodal damping ($D_{\text{dashpot}} = \rho_{\text{bedrock}} \cdot V_{S,\text{bedrock}}$) times a nodal contributing area ($L_{\text{nodal}} \cdot 1$) and $v_{\text{base}}(t)$ is the velocity of the base node at time t . L_{nodal} is the distance between the nodes of the base and, in particular, for the corner nodes is one half the same distance.

For the sake of brevity, the boundary condition 2 of Table 4 and Table 5 are referred to as compliant base. The shear stress time history, defined according to equation 24, is applied at the base of the numerical model and the base acceleration time history is an outcome of the numerical analysis. On the contrary, the boundary condition 1, named rigid base, allows the simulation of a perfect reflecting boundary; the bedrock acceleration time history is applied as the input motion. The bedrock accelerogram should be known from field record at the desired depth or determined through deconvolution of outcrop signal.

The results obtained adopting geometrical model A and C and using the boundary condition 2 are presented in the following.

Figs. 39-46 show the comparison between the seismic response analyses carried out by means of three adopted codes: EERA, QUAKE/W and PLAXIS 3D. It is possible to observe the very good agreement among the three sets of results, thus demonstrating the reliability of the FE approaches in reproducing the well-established frequency domain solution provided by EERA.

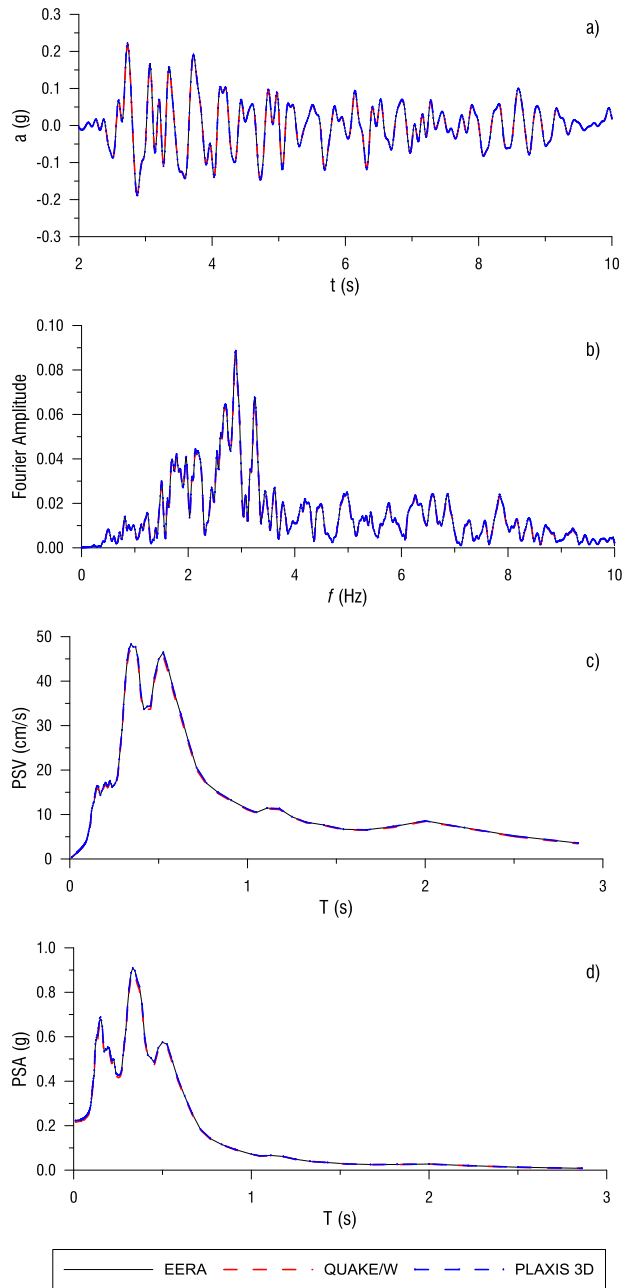


Fig. 39 a) time history of acceleration, b) Fourier spectrum, c) pseudo-velocity and d) pseudo-absolute acceleration response spectra obtained by means of three adopted codes for Soil 1- Model A at the free-field

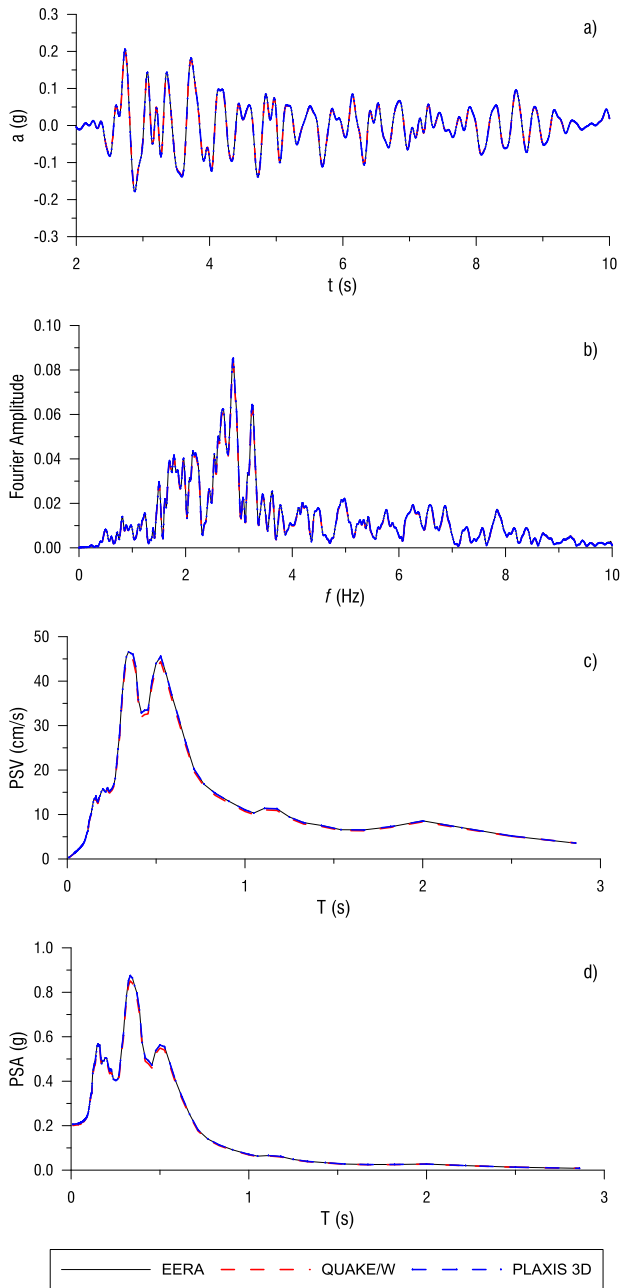


Fig. 40 a) time history of acceleration, b) Fourier spectrum, c) pseudo-velocity and d) pseudo-absolute acceleration response spectra obtained by means of three adopted codes for Soil 1- Model A at the bedrock

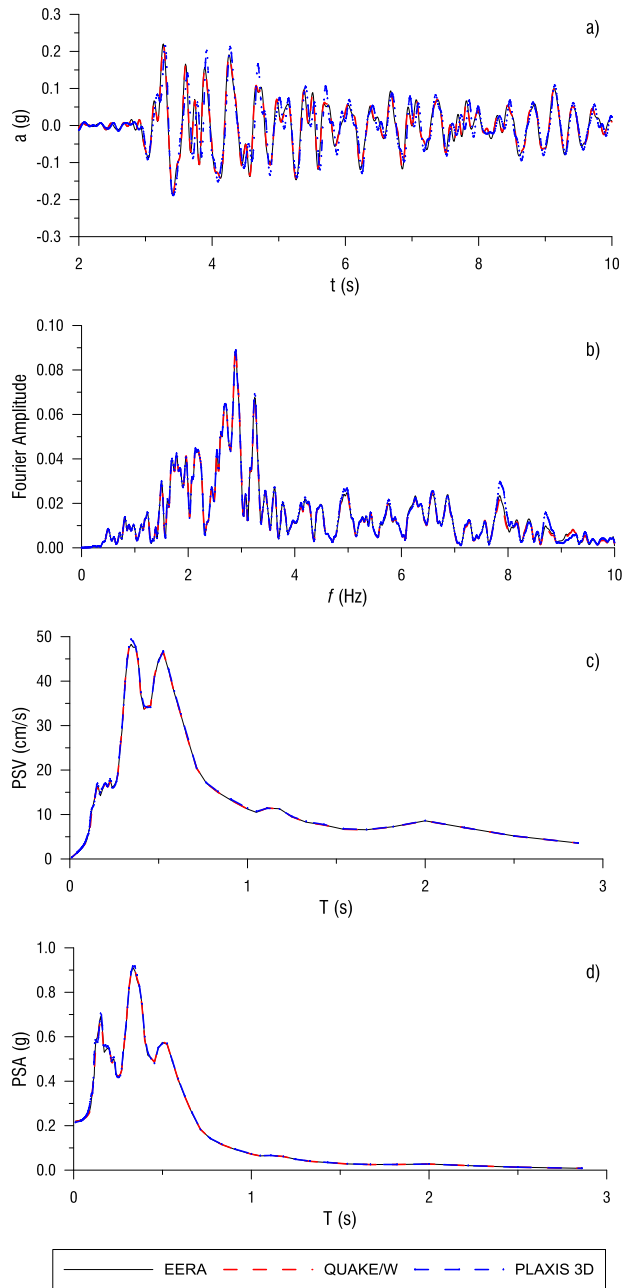


Fig. 41 a) time history of acceleration, b) Fourier spectrum, c) pseudo-velocity and d) pseudo-absolute acceleration response spectra obtained by means of three adopted codes for Soil 3- Model A at the free-field

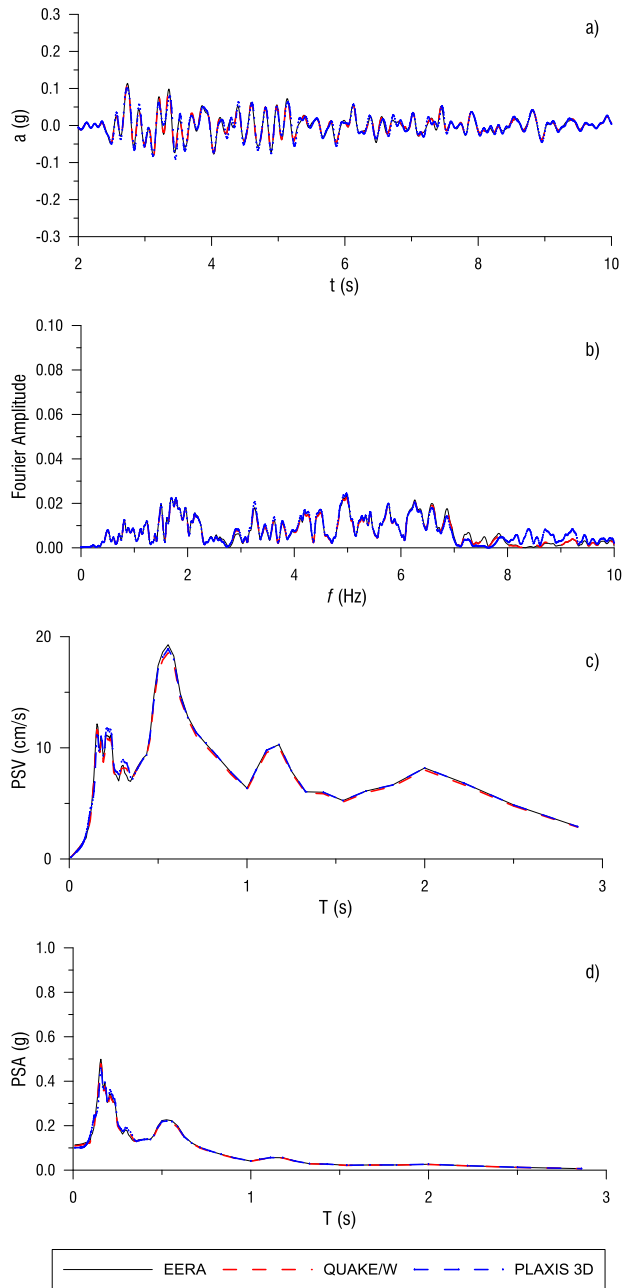


Fig. 42 a) time history of acceleration, b) Fourier spectrum, c) pseudo-velocity and d) pseudo-absolute acceleration response spectra obtained by means of three adopted codes for Soil 3- Model A at the bedrock

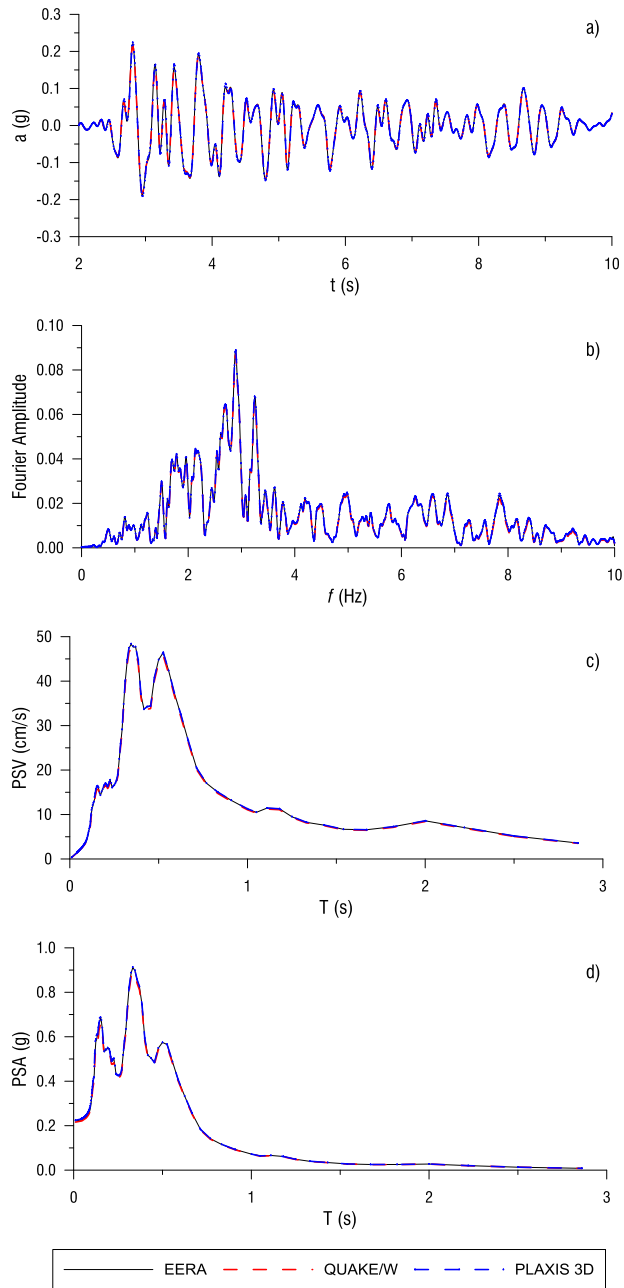


Fig. 43 a) time history of acceleration, b) Fourier spectrum, c) pseudo-velocity and d) pseudo-absolute acceleration response spectra obtained by means of three adopted codes for Soil 1- Model C at the free-field

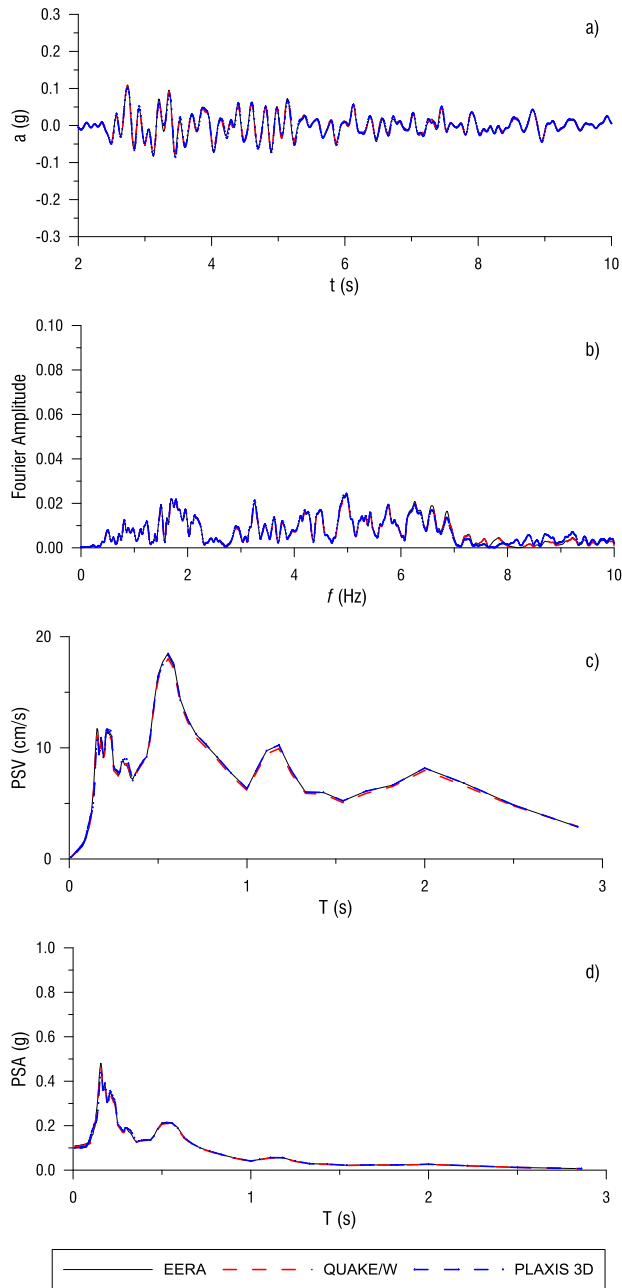


Fig. 44 a) time history of acceleration, b) Fourier spectrum, c) pseudo-velocity and d) pseudo-absolute acceleration response spectra obtained by means of three adopted codes for Soil 1- Model C at the bedrock

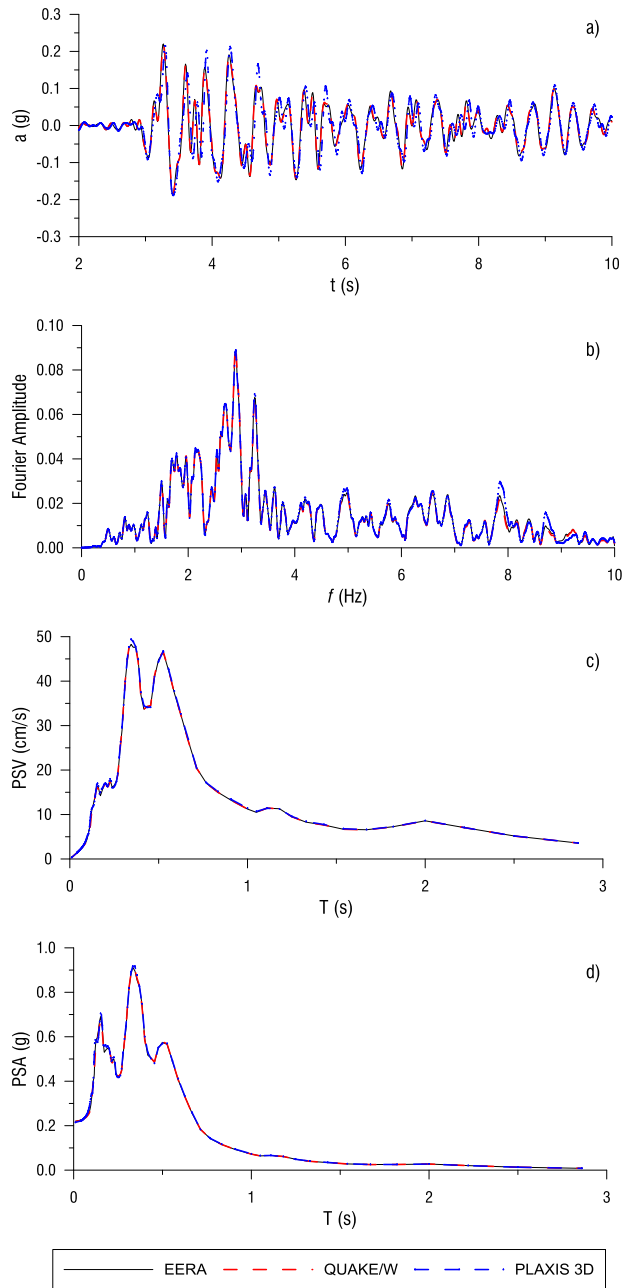


Fig. 45 a) time history of acceleration, b) Fourier spectrum, c) pseudo-velocity and d) pseudo-absolute acceleration response spectra obtained by means of three adopted codes for Soil 3- Model C at the free-field

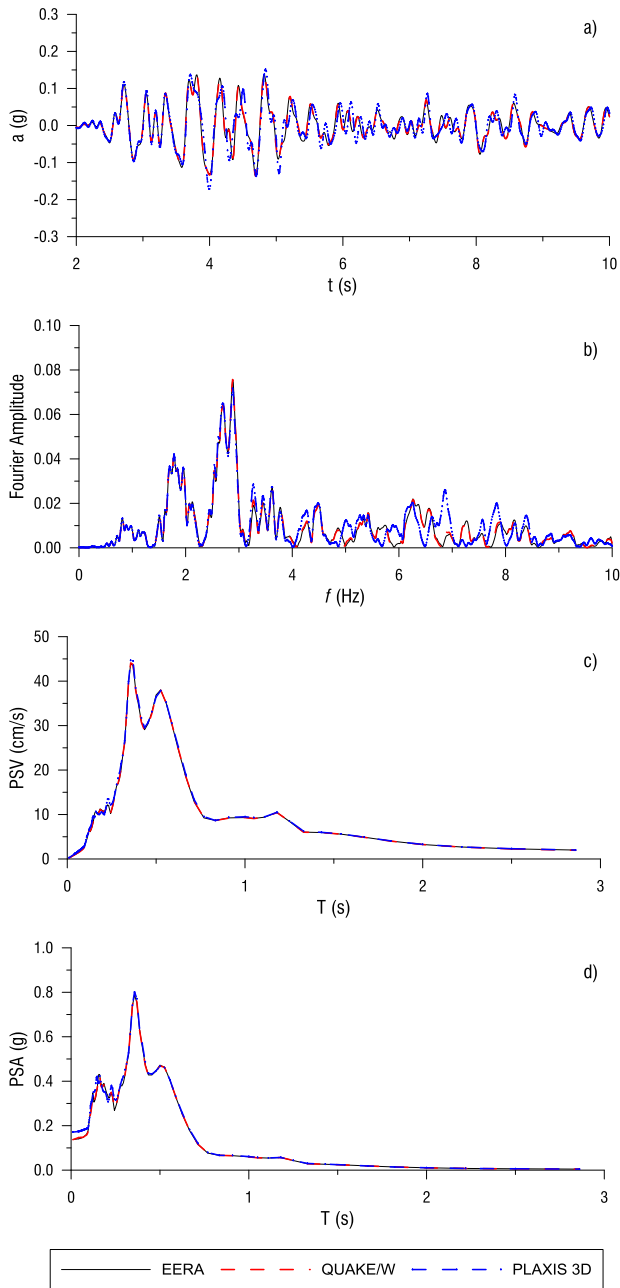


Fig. 46 a) time history of acceleration, b) Fourier spectrum, c) pseudo-velocity and d) pseudo-absolute acceleration response spectra obtained by means of three adopted codes for Soil 3- Model C at the bedrock

2.2. Homogeneous linear visco-elastic deposit

Two different soil material, named 2 and 3 (Table 6), were considered for the following seismic site response analyses.

Soil	V_s (m/s)	ν	γ (kN/m ³)	G (MPa)	D %
1	1200	0.25	18	2642	/
2	800	0.25	18	661	0.1
3	200	0.25	18	73	0.1

Table 6 Physical and mechanical properties of the homogeneous linear elastic soil deposit

Soil 1 (Table 6) was assumed as the bedrock.

Table 7 reports the sizes of the deposit as implemented in the codes.

Deposit	$Z_{\text{PLAXIS 3D}} = Z_{\text{QUAKE/W}} = Z_{\text{EERA}}$ (m)	$X_{\text{PLAXIS 3D}} = X_{\text{QUAKE/W}}$ (m)	X_{EERA} (m)	$Y_{\text{PLAXIS 3D}}$ (m)	$Y_{\text{QUAKE/W}} = Y_{\text{EERA}}$ (m)
A	20	160	/	2	/

Table 7 Dimensions of the deposit, simulations of 1D propagation

The boundary conditions adopted for the FE models are those called boundary condition 2 and listed in Table 4 and Table 5, i.e. considering a compliant base, as already discussed for the case of a homogeneous half-space.

The comparison between the numerical results obtained by means of three adopted codes is carried out in terms of free-field and bedrock motions.

Figs. 47-50 illustrate the main results, highlighting a good agreement between the three sets of results. In general, it can be assessed that the seismic behaviour of a linear elastic deposit is well simulated using the numerical models implemented in the FE codes (QUAKE/W and PLAXIS 3D).

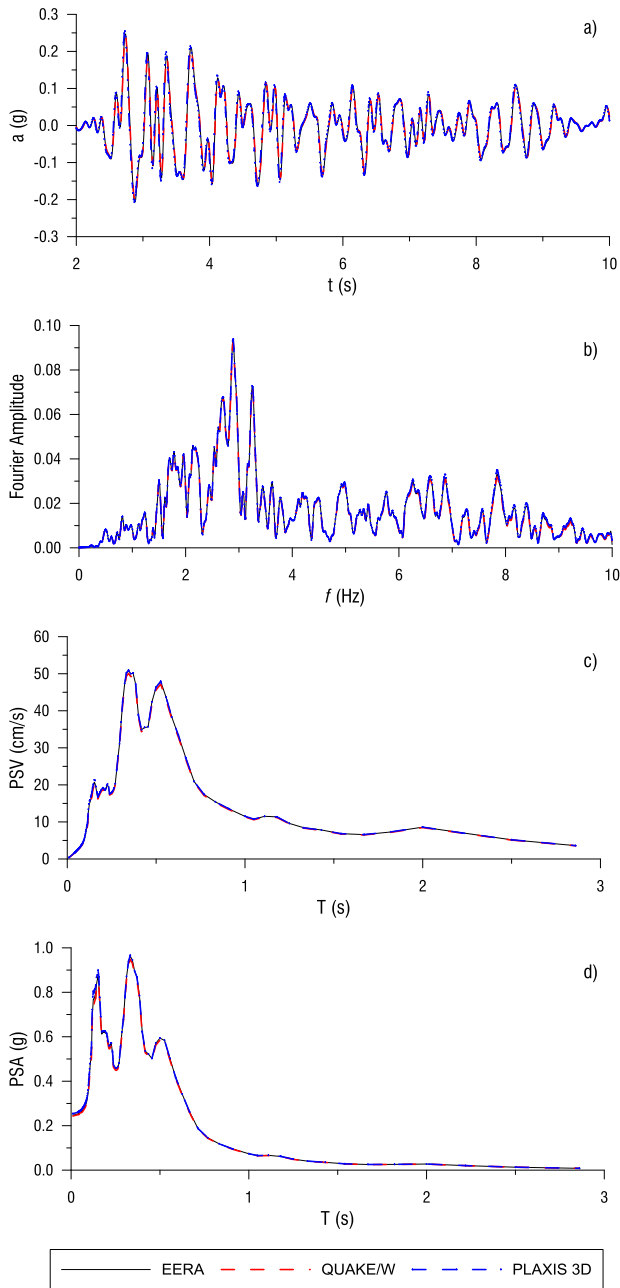


Fig. 47 a) time history of acceleration, b) Fourier spectrum, c) pseudo-velocity and d) pseudo-absolute acceleration response spectra obtained by means of three adopted codes for linear visco-elastic Soil 2 deposit at the free-field

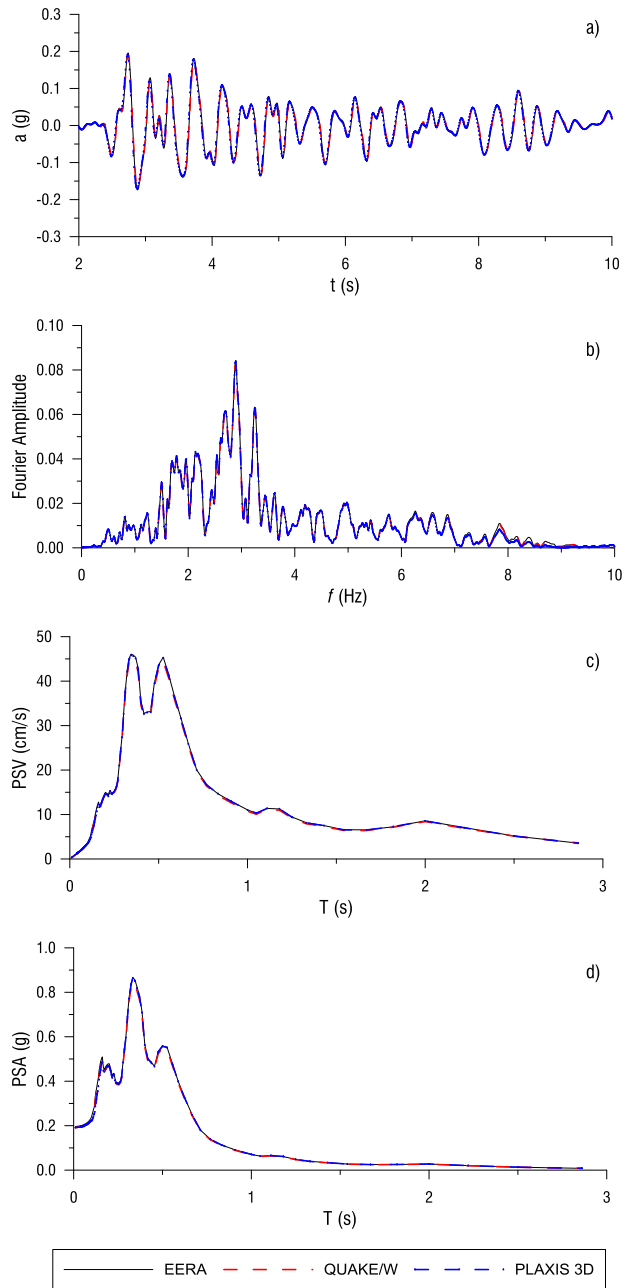


Fig. 48 a) time history of acceleration, b) Fourier spectrum, c) pseudo-velocity and d) pseudo-absolute acceleration response spectra obtained by means of three adopted codes for linear visco-elastic Soil 2 deposit at the bedrock

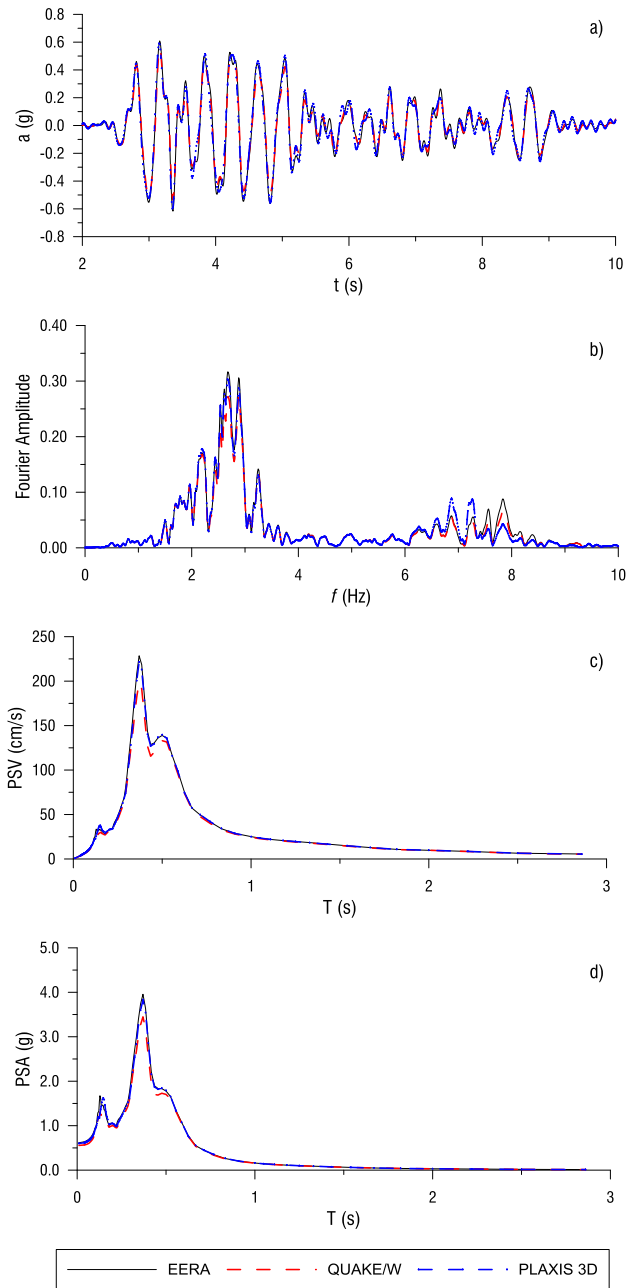


Fig. 49 a) time history of acceleration, b) Fourier spectrum, c) pseudo-velocity and d) pseudo-absolute acceleration response spectra obtained by means of three adopted codes for linear visco-elastic Soil 3 deposit at the free-field

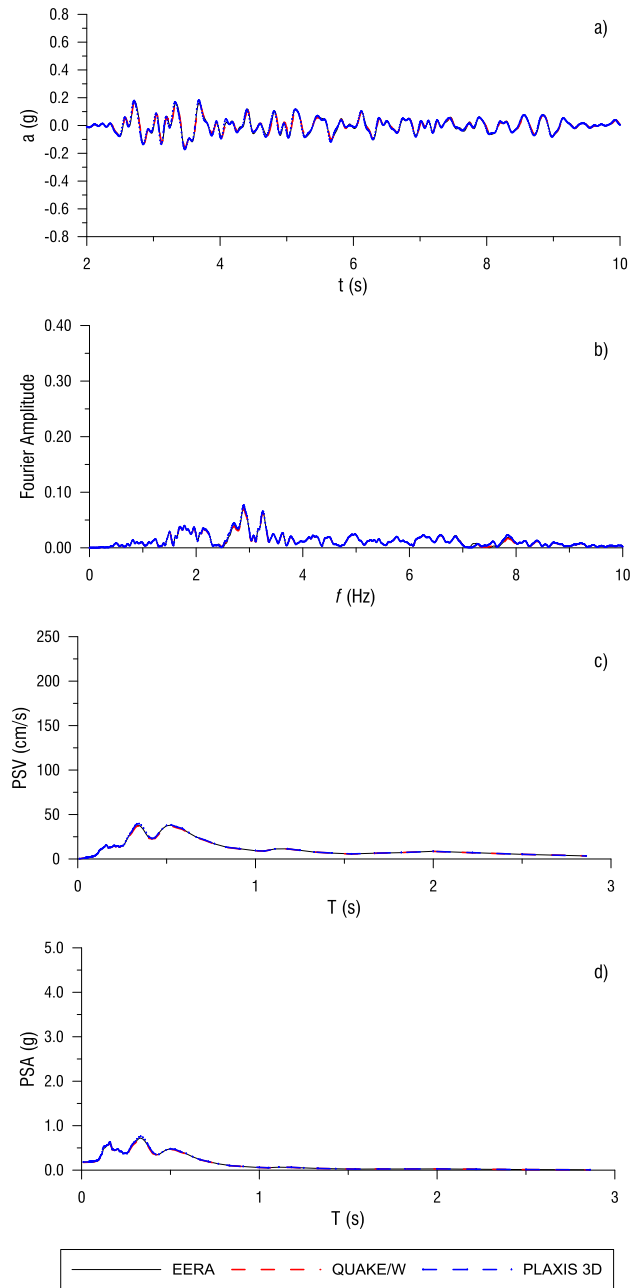


Fig. 50 a) time history of acceleration, b) Fourier spectrum, c) pseudo-velocity and d) pseudo-absolute acceleration response spectra obtained by means of three adopted codes for linear visco-elastic Soil 3 deposit at the bedrock

2.3. Homogeneous non-linear visco-elastic deposit

Two different soil materials, called 2 and 3, were defined for the seismic site response analyses of a non-linear deposit. The physical and mechanical properties relative to small strains are summarized in Table 8.

Soil	V_s (m/s)	ν	γ (kN/m ³)	G_0 (MPa)	D_0 %	Non-linear curves
1	1200	0.25	18	2642	/	/
2	800	0.25	18	661	1	Fig. 51
3	200	0.25	18	73	1	Fig. 51

Table 8 Physical and mechanical properties of the homogeneous non-linear elastic deposit

As in the previous case, Soil 1 (Table 6) was assumed as the bedrock.

The constitutive models to simulate the non-linear behaviour of deposit are:

- linear equivalent as provided in the library of QUAKE/W;
- Hardening Soil Model with small strain stiffness (Benz 2006; Benz et al. 2009), also known as HSsmall, available in the material model library of PLAXIS 3D. HSsmall is an isotropic hardening elastoplastic hysteretic model and allows to take into account the non-linear behaviour of soil even at very small strain, introducing a pre-yield para-elastic hysteretic scheme, which controls the shear modulus degradation and the corresponding variation of the damping ratio.

Non-linear behaviour of the soil materials 2 and 3 is represented by the secant shear modulus decay, $G(\gamma)/G_0$, and damping, $D(\gamma)$, curves shown in Fig. 51. The black lines, considered as the reference curves, are directly implemented both in EERA and QUAKE/W by means of the corresponding set of data points.

The dashed red lines refer to the HSsmall model as calibrated to mimic the black lines (di Lernia 2014; Amorosi et al. 2016). The corresponding set of parameters is reported in Table 9.

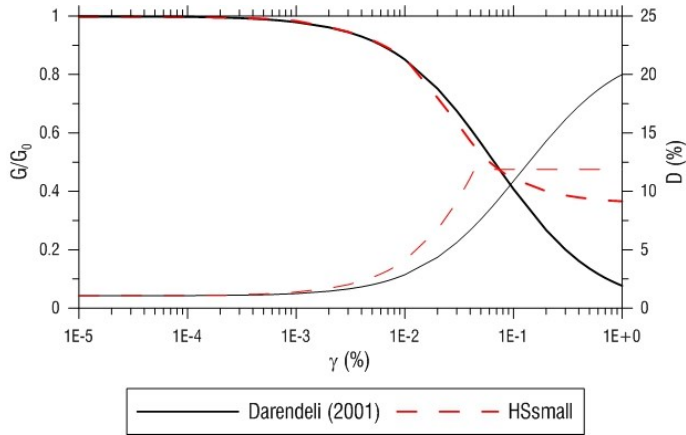


Fig. 51 Non-linear behaviour of soil material 2 and 3

Parameter	Soil 2	Soil 3
a	0.385	0.385
$\gamma_{0.7}$ (%)	0.025	0.025
G_{ur} (kPa)	419397	26212
G_0^{ref} (kPa)	1174312	73394
ρ (kg/m ³)	1.83	1.83
V_s (m/s)	800	200
γ kN/m ³	18	18
γ_{cut_off} (%)	0.044	0.044
m	0	0
P_{ref}^i (kPa)	100	100

Parameter	Soil 2	Soil 3
ν_{ur}	0.25	0.25
E_{ur}^{ref} (kPa)	1048493	65531
E_{oed}^{ref} (kPa)	349498	21844
E_{50}^{ref} (kPa)	349498	21844
c' (kPa)	1.E+35	1.E+35
ϕ' (°)	89	89
$D_{Rayleigh}$ (%)	1.053	1.053
f_m (Hz)	1.00	1.00
f_n (Hz)	10.00	10.00
α_R	0.12027	0.12027
β_R	0.00030	0.00030

Table 9 HSs parameters for soil 2 and 3

To consistently compare the numerical results obtained by the two FE codes, which are related to different soil constitutive models, the yield and strength parameters of the HSsmall model were fixed at their highest possible values, so that the corresponding formulation results scaled down to that of a purely hysteretic para-elastic model (i.e. no plastic strain are generated throughout the analyses) (di Lernia 2014).

The dimensions of the soil deposit as implemented in the codes are listed in Table 7.

The boundary conditions adopted for the FE model are the boundary condition 2 (Table 4 and Table 5), including the compliant base, as adopted for all the previous examined cases.

The comparison between the numerical results obtained by means of three adopted codes are given in terms of free-field and bedrock motions.

Figs. 52-55 illustrate the main results, highlighting again the good agreement among the three sets of results.

The above results indicate that the FE codes, when referring to boundary condition 2, i.e. compliant base, are capable to reproduce the expected (i.e. EERA-based) seismic behaviour of a non-linear elastic deposit.

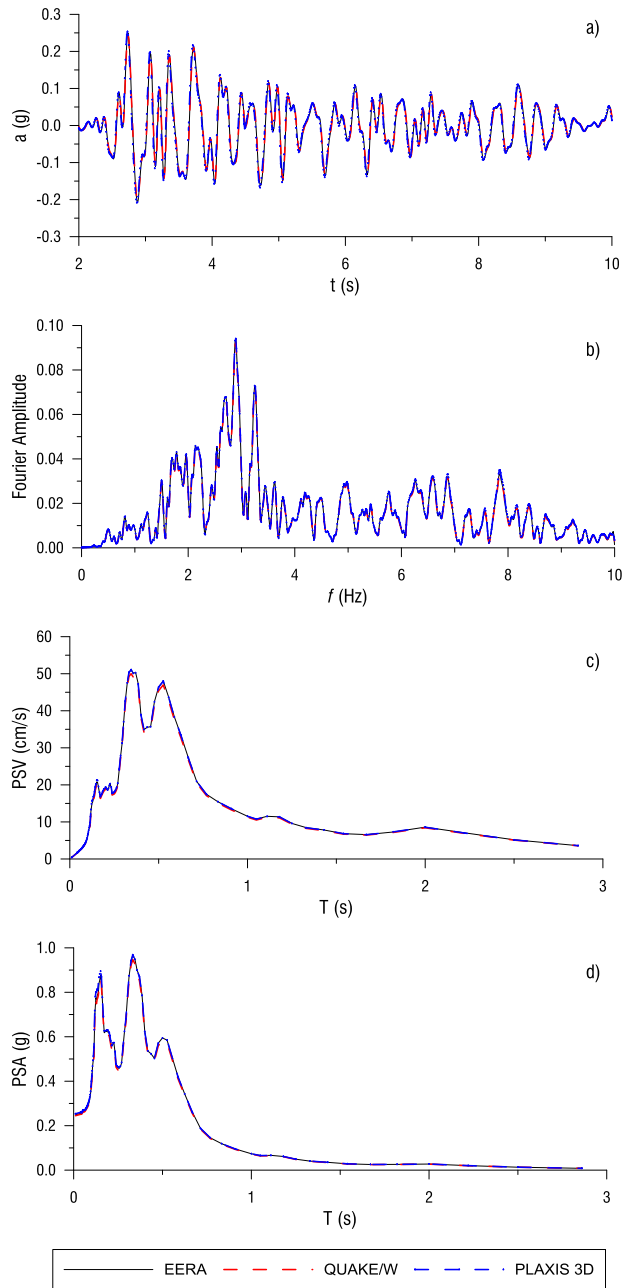


Fig. 52 a) time history of acceleration, b) Fourier spectrum, c) pseudo-velocity and d) pseudo-absolute acceleration response spectra obtained by means of three adopted codes for non-linear visco-elastic Soil 2 deposit at the free-field

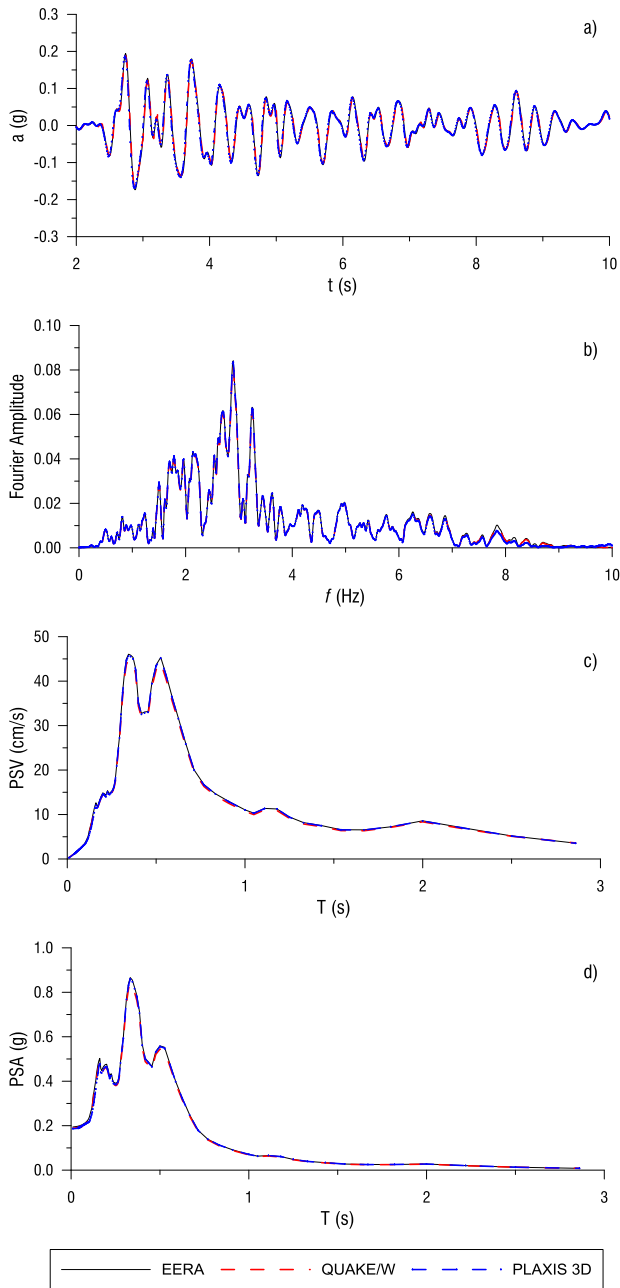


Fig. 53 a) time history of acceleration, b) Fourier spectrum, c) pseudo-velocity and d) pseudo-absolute acceleration response spectra obtained by means of three adopted codes for non-linear visco-elastic Soil 2 deposit at the bedrock

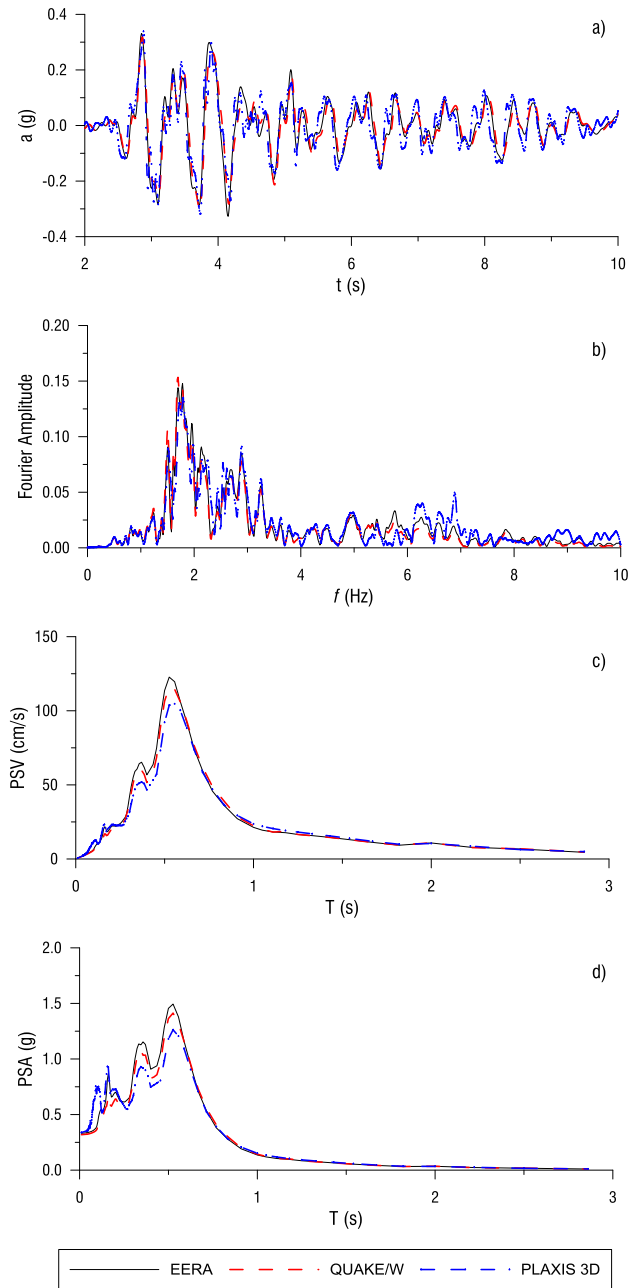


Fig. 54 a) time history of acceleration, b) Fourier spectrum, c) pseudo-velocity and d) pseudo-absolute acceleration response spectra obtained by means of three adopted codes for non-linear visco-elastic Soil 3 deposit at the free-field

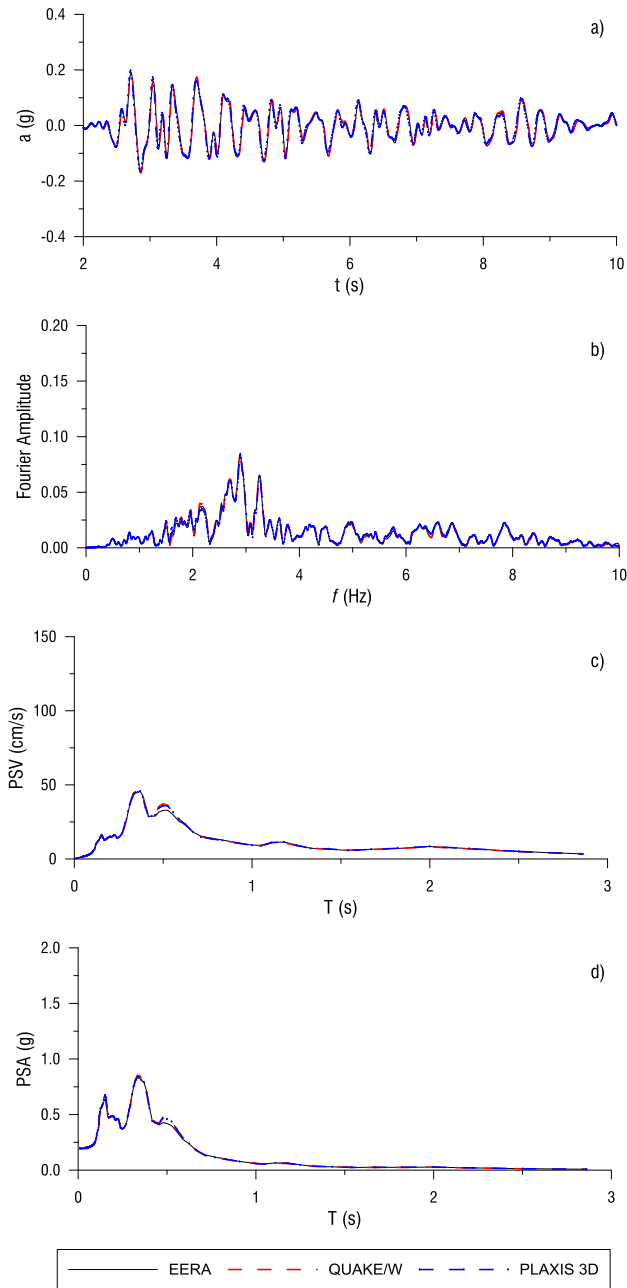


Fig. 55 a) time history of acceleration, b) Fourier spectrum, c) pseudo-velocity and d) pseudo-absolute acceleration response spectra obtained by means of three adopted codes for non-linear visco-elastic Soil 3 deposit at the bedrock

All the previous FE numerical models were characterised by a zero thickness bedrock. In the next, the influence of the thickness of the bedrock implemented in the numerical models will be discussed. With reference to the same reference motion, two different bedrock thicknesses are considered and the results are thus compared with that relative to the zero thickness assumption. In Fig. 56 the three models implemented in the FE codes are sketched; it is worth to note that only for Model 1 the bedrock condition overlaps with the base of the numerical model.

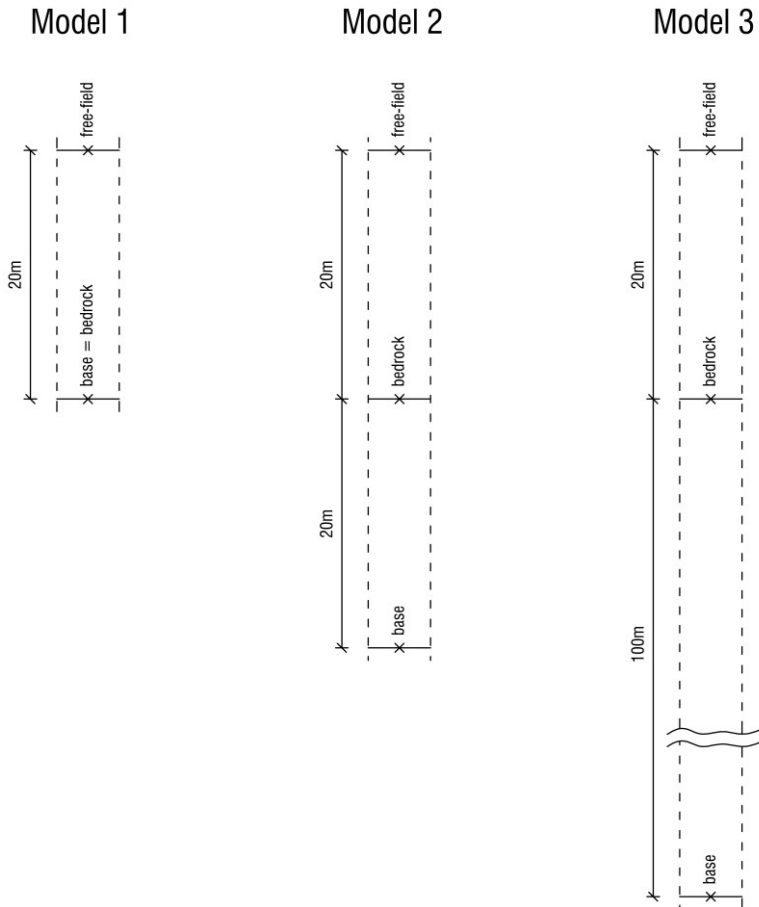


Fig. 56 Three different thickness bedrock models implemented for seismic site response analyses

The results obtained by means of PLAXIS 3D and referring to a 20 m thick deposit of Soil 3 (see Table 7-Table 8-Table 9) are shown in Fig. 57-Fig. 58 for the free-field and

bedrock points (Fig. 56) respectively. All the results show an overall good agreement. As a consequence, the results based on the compliant base boundary condition are not influenced by the thickness of bedrock included in the FE model.

Consistently with what already discussed for all the previous cases, when referring to the acceleration time history a delay of the first peak is to be expected, due to the time lag related to the physical propagation of seismic waves in the soil deposit.

Finally, Fig. 59 shows the comparison between the three model results for the base point. The base motion depends on the features of the model implemented in the FE code. Varying the thickness of the bedrock included in the numerical model causes different base motion outcomes from the numerical simulation.

It should be clear that the shear stress time history is requested by the compliant base boundary condition as the input motion; the acceleration time history of the base model is a result of the numerical calculation. On the contrary, when a non-compliant base is adopted, the input motion is applied as an acceleration or displacement time history then the base motion should results equal to the input motion.

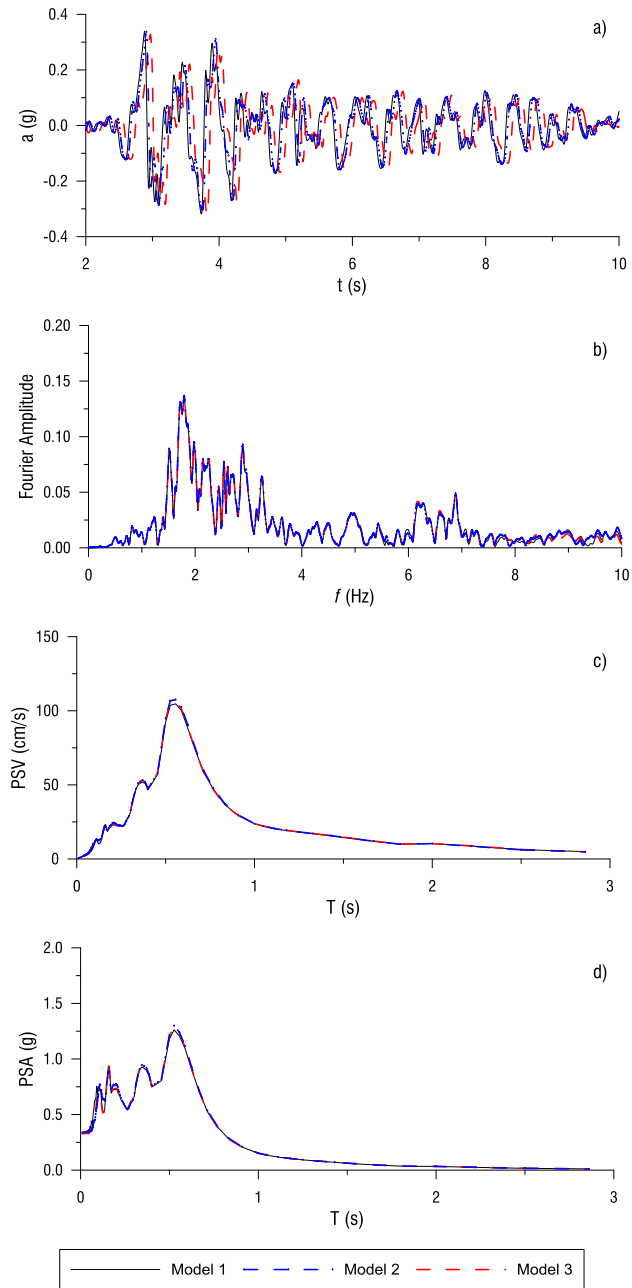


Fig. 57 a) time history of acceleration, b) Fourier spectrum, c) pseudo-velocity and d) pseudo-absolute acceleration response spectra obtained by means of three adopted codes for non-linear visco-elastic Soil 3 deposits at the free-field

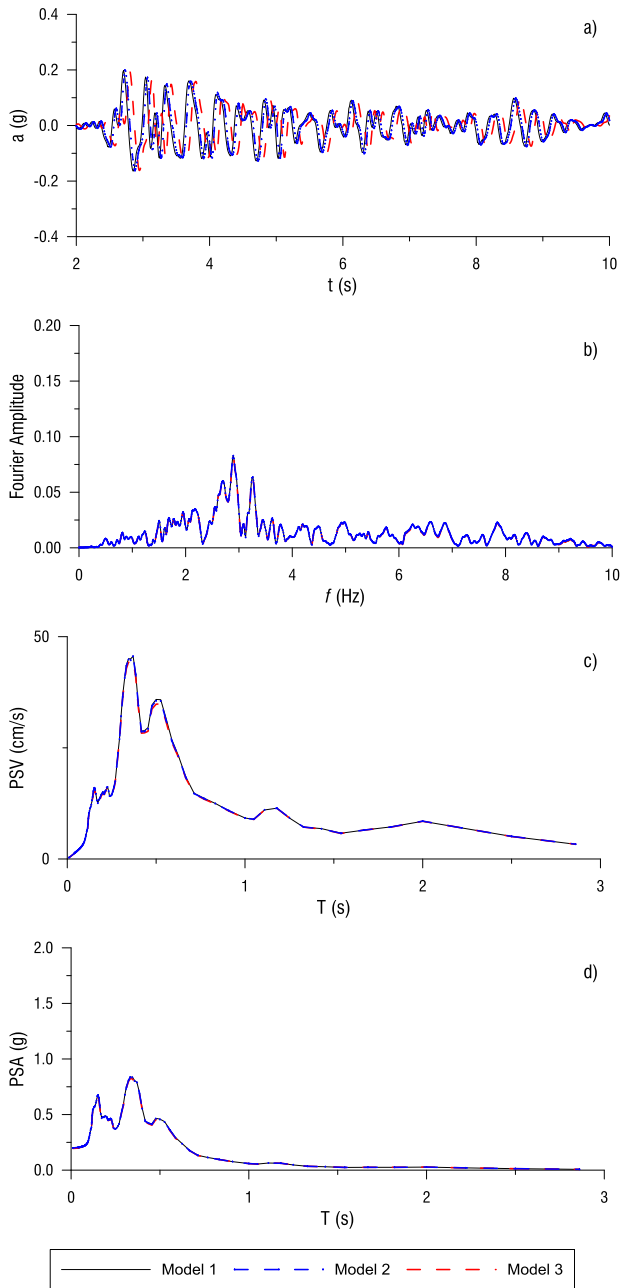


Fig. 58 a) time history of acceleration, b) Fourier spectrum, c) pseudo-velocity and d) pseudo-absolute acceleration response spectra obtained by means of three adopted codes for non-linear visco-elastic Soil 3 deposits at the bedrock

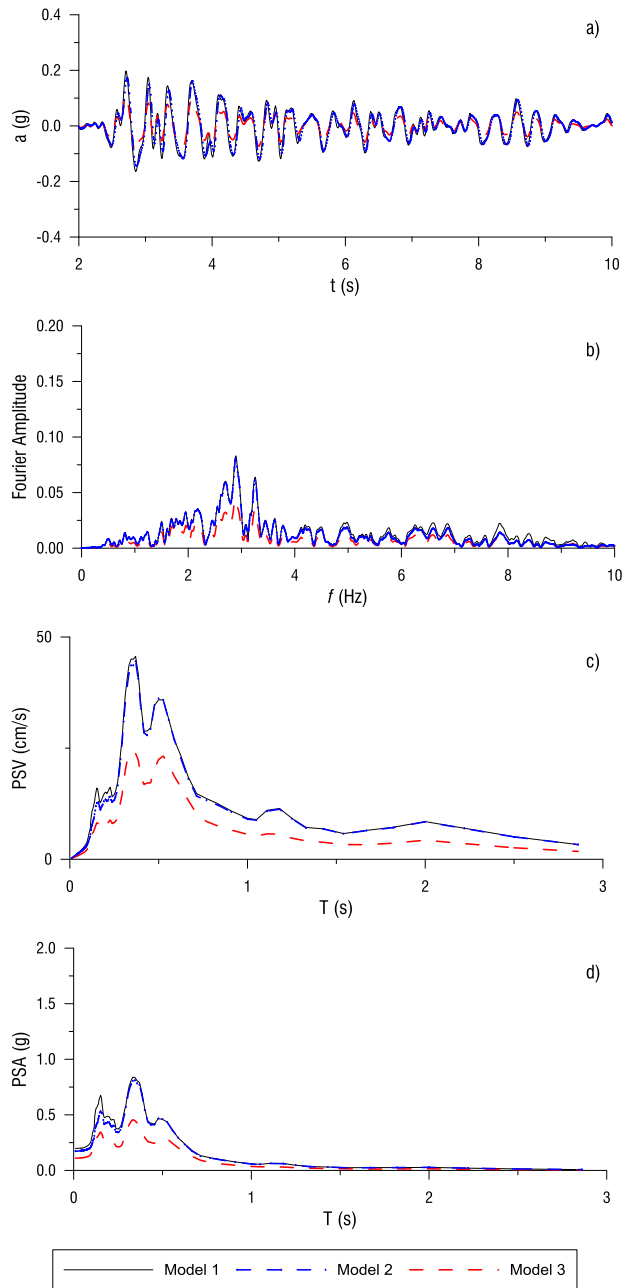


Fig. 59 a) time history of acceleration, b) Fourier spectrum, c) pseudo-velocity and d) pseudo-absolute acceleration response spectra obtained by means of three adopted codes for non-linear visco-elastic Soil 3 deposits at the base of the models

2.4. Concluding remarks on 1D numerical simulations

In this Chapter the three adopted codes proved to be capable of simulating the earthquake-induced shear wave propagation process in linear elastic half-space, linear elastic and non-linear visco-elastic deposits of finite thickness.

In detail, assuming the free-field, bedrock and outcrop definitions stated in the chapter 1, and adopting as an input signal depending on the one defined at the outcrop, it can be stated that:

- adopting the compliant base boundary condition, the input motion is defined as a function of the outcrop signal. A shear stress time history is applied at the base of the numerical model and the base acceleration time history is an outcome of the numerical analysis;
- free-field and outcrop accelerograms of an homogeneous half-space should be the same. As a consequence, the homogeneous half-space condition requires that the analytical and numerical solutions return the same accelerogram at free-field and outcrop points. In addition, a finite value of the thickness deposit should be included in the analytical and numerical model despite to the condition of vertically unbounded media. With reference to the results shown in this chapter, the FE approach, if a compliant base is adopted, allows to simulate the seismic response of an homogeneous half-space at ground surface;
- motions inside the half-space, for example at the base of the numerical model, could differ from that at the outcrop and at free-field and depend on the thickness of the half-space simulated in the numerical model;
- with reference to seismic site response of a deposit, time history of acceleration at free-field and bedrock points are not influenced by the thickness of bedrock implemented in the FE codes provided the compliant base condition is adopted. The motion at the base of the FE models is related to the thickness of the bedrock and generally depends on the size of the overlying deposit.

2.5. On the base boundary condition for 2D and 3D numerical simulation

As fixed in the previous sections, it is really important to highlight that the accelerogram at the base of the soil deposit generally differs from the outcrop one, depending on mechanical behaviour and thickness of the same soil deposit.

Referring for example to an ideal 3D semi-ellipsoidal homogeneous basin, see Fig. 60a), of which one half of two 2D sections are sketched in Fig. 60b), it is worth considering three generic boreholes, reported in Fig. 60c), as 1D different stratigraphic conditions. Physical and mechanical parameters of Soil 3 and 1, listed in Table 8, are considered for the basin and bedrock, respectively.

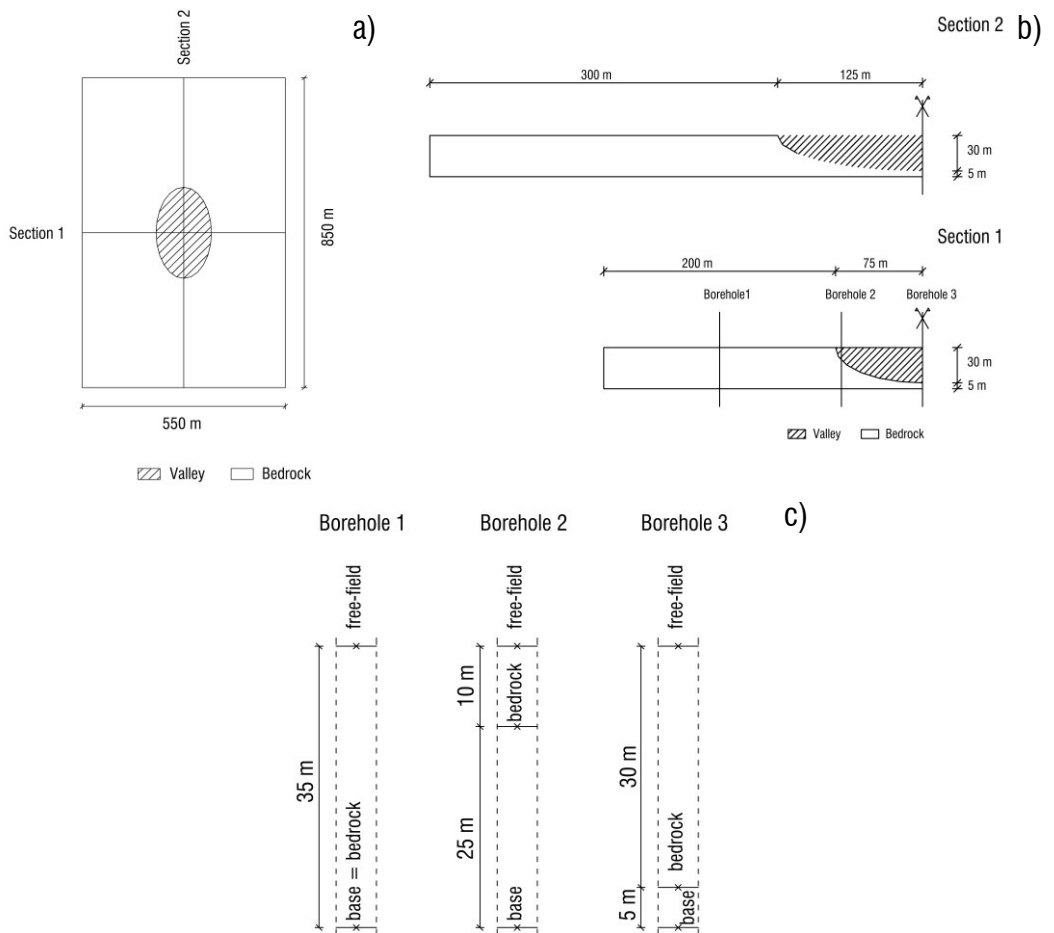


Fig. 60 a) plane view of a 3D semi-ellipsoidal basin b) 2D sections and c) stratigraphy relative to three different boreholes

1D analyses, using compliant base boundary condition, were performed assuming the three stratigraphic conditions sketched in Fig. 60c). Fig. 61 shows the comparison among base motions referred to the three boreholes. The results different one from each other.

Thus, even considering the simplified case of Fig. 60 it is not possible to define a unique time history of accelerations to be applied at the base of the 2D and 3D numerical models. It is worth noting that the compliant base boundary condition allows to define a unique shear stress time history base input; the acceleration time history is an outcome of the numerical simulation and will result different motions at the base of 1D models and varying along the base of the 2D and 3D models.

Fig. 62 and Fig. 63 show the comparison between base motion at three different abscissa for 2D and 3D schemes, respectively. The resulting motions are different from each other. Furthermore, Figs. 64-66 show the comparison between 1D, 2D and 3D base motions for the considered abscissa. Thus, the base motions inside the valley area, see Fig. 66, obtained as an outcome of the numerical simulations, is depending on the adopted dimensional scheme.

In conclusions, the numerical simulation of site response by means of 2D and 3D approaches requires to define the base boundary condition according to the so called compliant base.

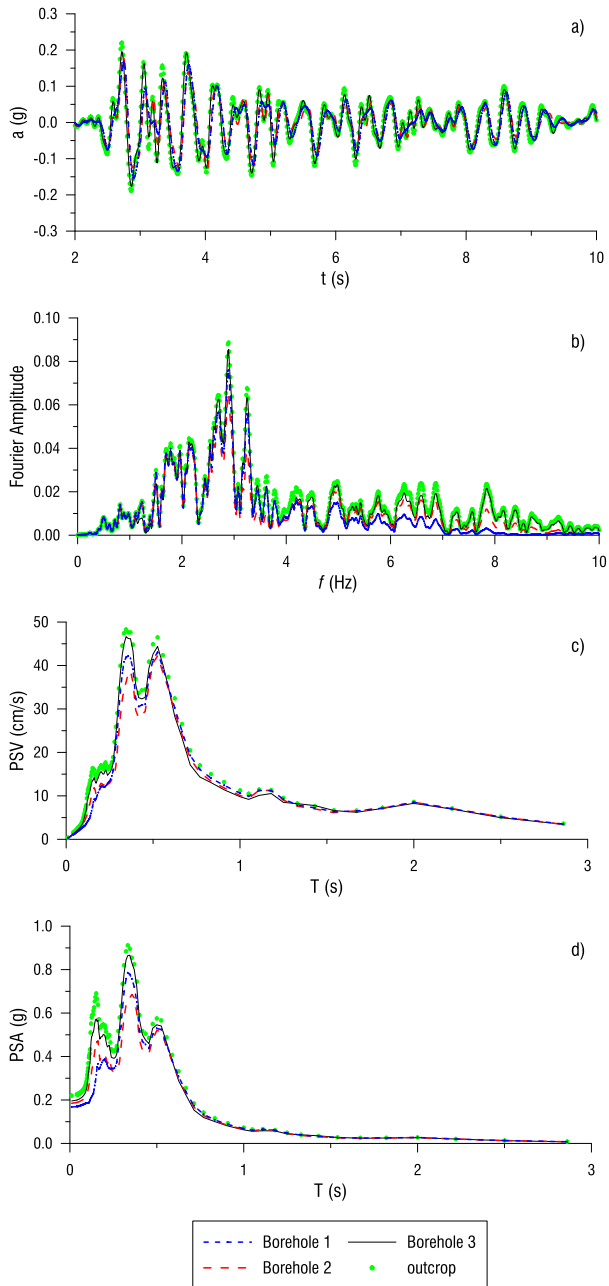


Fig. 61 a) time history of acceleration, b) Fourier spectrum, c) pseudo-velocity and d) pseudo-absolute acceleration response spectra obtained by means of three adopted code for non-linear visco-elastic Soil 3 valley at the base of the 1D models

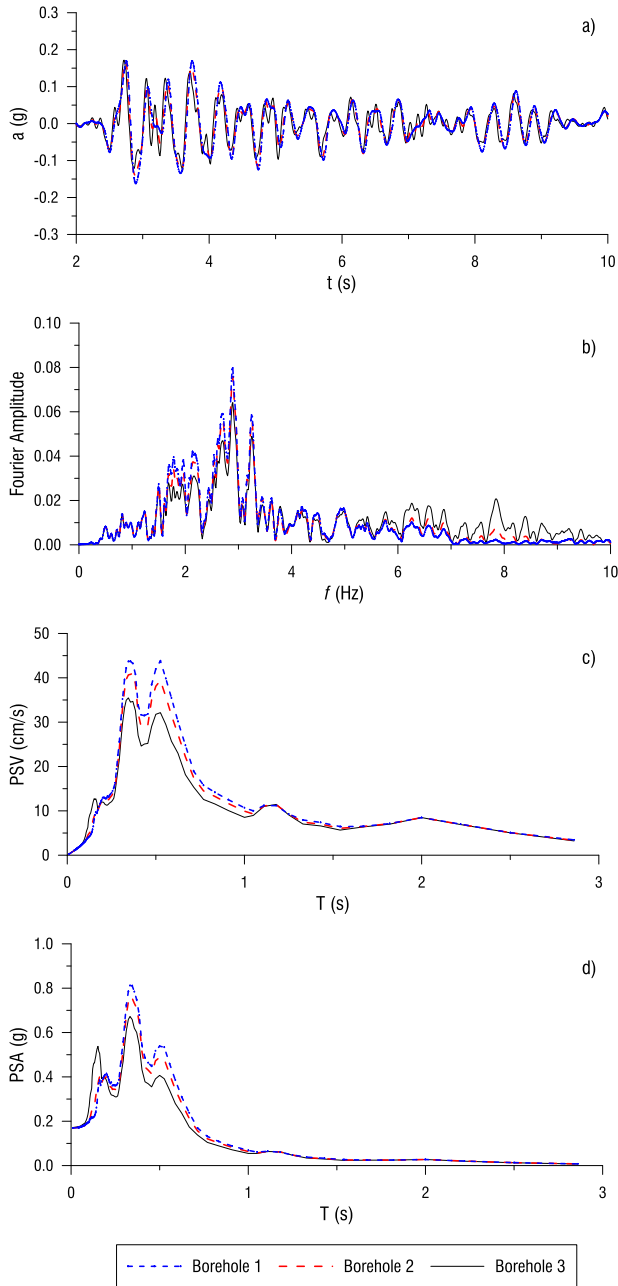


Fig. 62 a) time history of acceleration, b) Fourier spectrum, c) pseudo-velocity and d) pseudo-absolute acceleration response spectra obtained by means of three adopted code for non-linear visco-elastic Soil 3 valley along the base of the 2D model

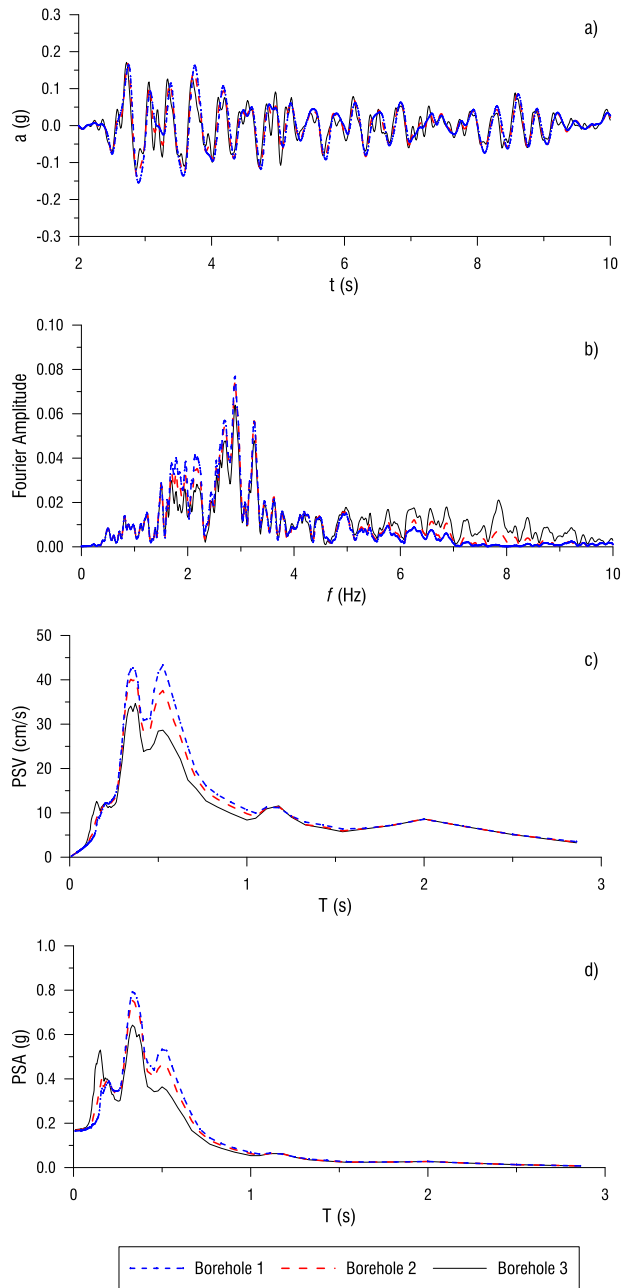


Fig. 63 a) time history of acceleration, b) Fourier spectrum, c) pseudo-velocity and d) pseudo-absolute acceleration response spectra obtained by means of three adopted code for non-linear visco-elastic Soil 3 valley along the base of the 3D model

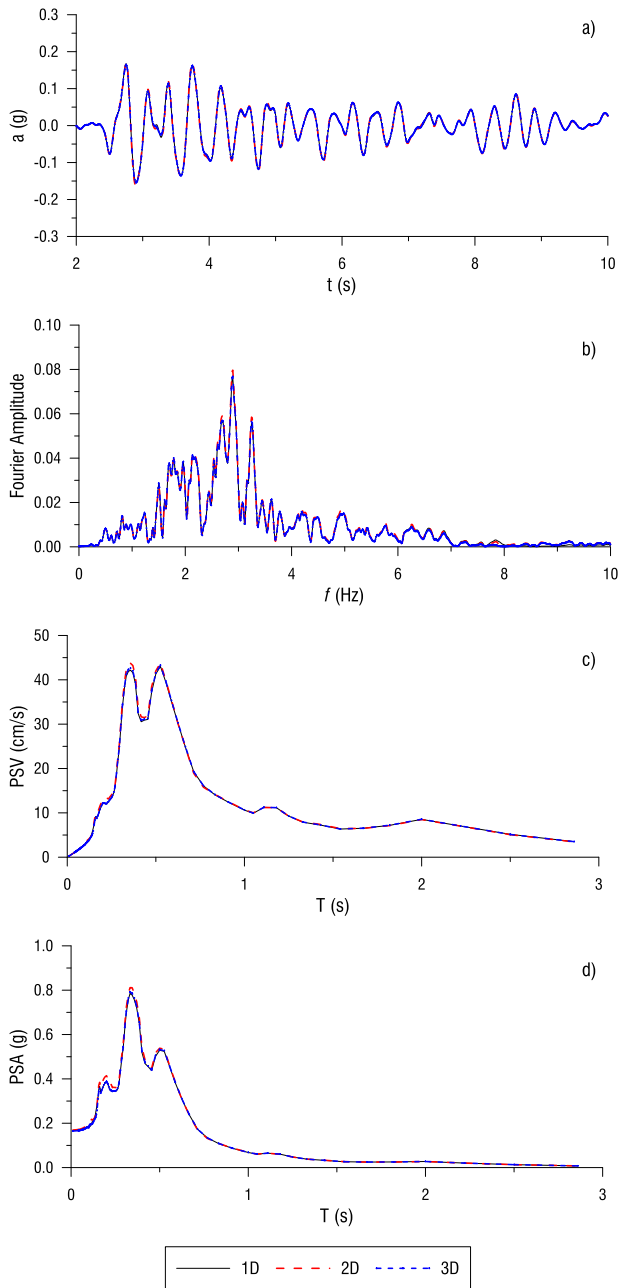


Fig. 64 a) time history of acceleration, b) Fourier spectrum, c) pseudo-velocity and d) pseudo-absolute acceleration response spectra obtained by means of three adopted code for non-linear visco-elastic Soil 3 valley at the borehole 1 base of the 1D, 2D and 3D models

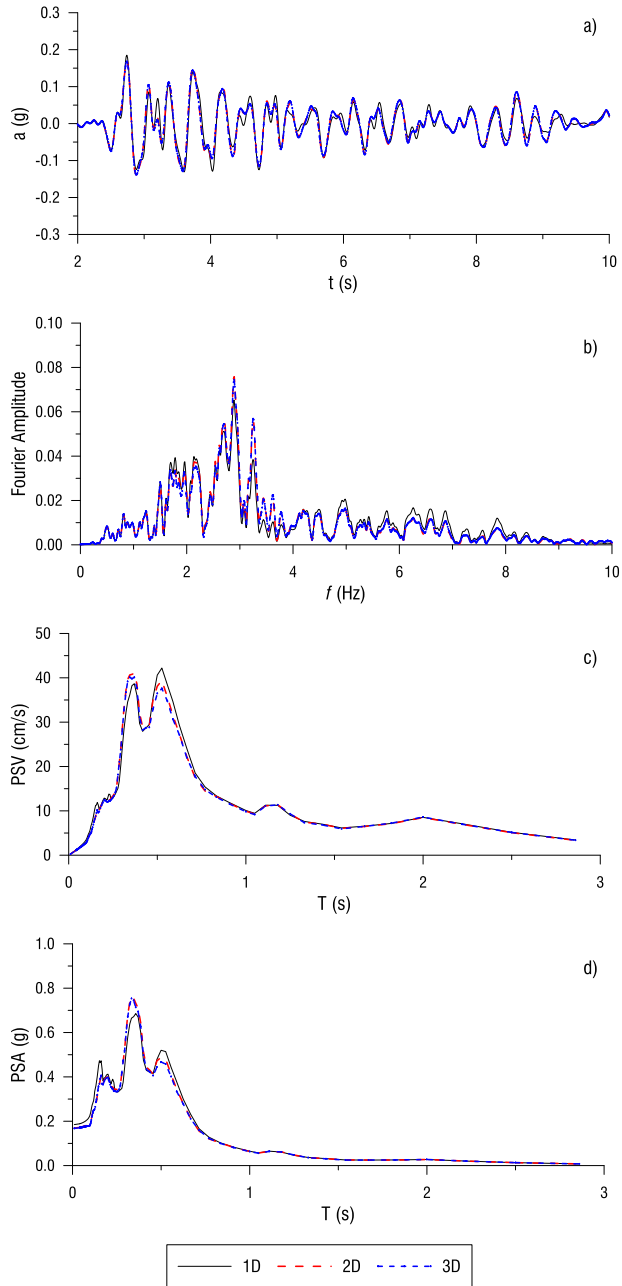


Fig. 65 a) time history of acceleration, b) Fourier spectrum, c) pseudo-velocity and d) pseudo-absolute acceleration response spectra obtained by means of three adopted code for non-linear visco-elastic Soil 3 valley at the borehole 2 base of the 1D, 2D and 3D models

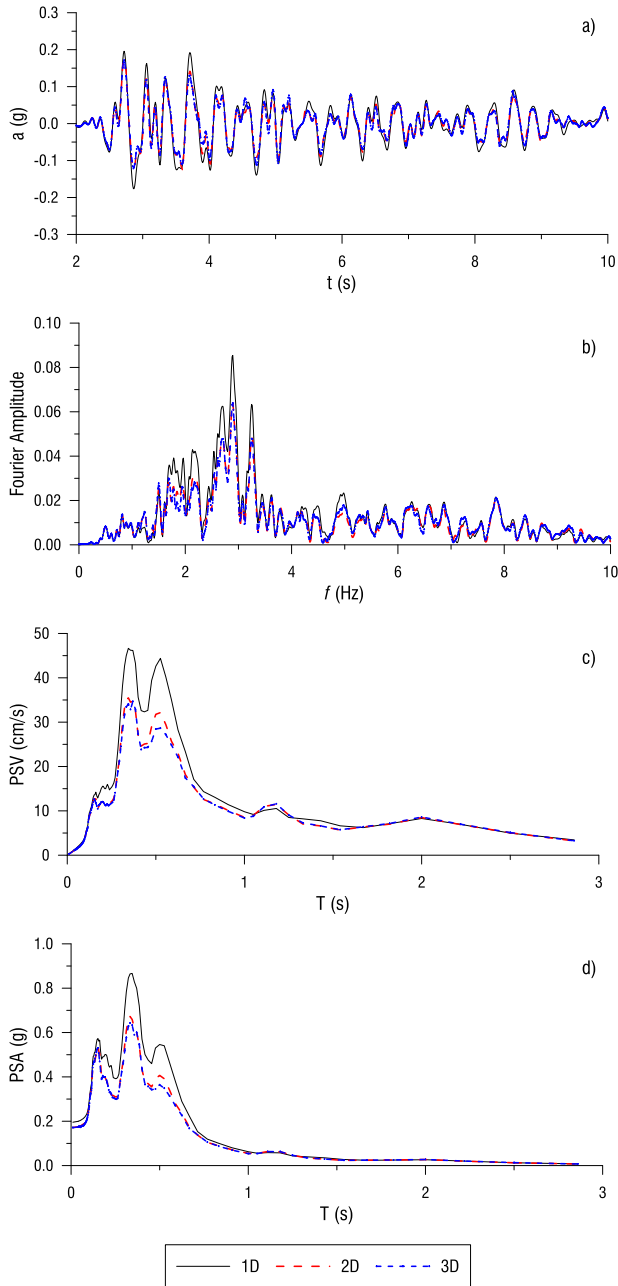


Fig. 66 a) time history of acceleration, b) Fourier spectrum, c) pseudo-velocity and d) pseudo-absolute acceleration response spectra obtained by means of three adopted code for non-linear visco-elastic Soil 3 valley at the borehole 3 base of the 1D, 2D and 3D models

CHAPTER 3. SEISMIC MICROZONATION: A CASE STUDY

3.1. General

The first part of the present chapter briefly summarises the historical evolution of Seismic Zonation in Italy and describes the main aspects of the Italian Guidelines for Seismic Zonation (briefly IGSM). A more accurate description of the Italian history of Seismic Zonation has been reported by De Marco et al. (2000), while a thorough description of the guidelines for Seismic Zonation currently valid in Italy can be found in reports published by "Gruppo di Lavoro" in 2004 and "Gruppo di Lavoro MS" in 2008. This second part is focused on a specific seismic microzonation case study. The selected area is that of a village called Bovino, located in the Apulia region, southern Italy, nearby the local portion of the Apennine Chain. The interest towards this location was triggered by a pre-existing level 1 seismic microzonation, carried out by the regional authority under the supervision of a specialised team of geologists. The outcome of this activity led to the classification of the area as prone to seismic local amplification (Palladino 2001). Consequently, further detailed analyses were required to investigate in detail the seismic response of such an area. The peculiar aspects that made this the ideal case to be studied in this work were essentially the complex topography and the rather articulated stratigraphy, which would have helped illustrating the corresponding effects, already discussed in a general form in the chapter 1. An agreement between the Department of Civil, Environmental, Land, Construction Engineering, and Chemistry of Technical University of Bari and the Basin Authority of

Apulia Region was then set up, aiming at upgrading to a level 3 the SM of the Bovino urban area.

The activity, whose this research work has contributed to, was thus developed consistently with the Italian Guidelines (Gruppo di Lavoro MS 2008). Those latter stating clearly that numerical analyses had to be carried out to evaluate in detail the seismic site response of the area, though without providing any specific indication concerning the detail to be adopted in such “advanced” analyses.

In general, earthquake-induced permanent soil deformation, including liquefaction and slope instability, should be included in a microzonation study, but they will not be discussed here, as considered out of the scope of this research work.

Focusing more on the numerical modelling of seismic site response, it is worth recalling what discussed by Santucci de Magistris et al. (2014): the Authors classified such activity as either aimed at analysing retrospectively an observed damaged area after a recent strong-motion earthquake, or at predicting the likely effects of ‘expected’ scenario earthquakes, to be then properly mapped. In light of what above, the SM of Bovino has to be considered as a predictive study.

As stated in the chapter 1, when tackling the SM problem for a level 3 analysis, numerical models can be generated with reference to three different geometrical schemes to represent the site conditions, namely 1D, 2D or 3D. This latter is to be preferred in case of an area characterised by complex geometrical characteristics at both the surface (topography) and the sub-layers interfaces.

On the other hand, a 3D FE analysis can be rather complex to be set up and very time consuming. As such, it is scientifically worth asking whether a simpler approach, based on 1D or 2D analyses, would lead to substantially different results or not. This is one of the question this chapter is aimed at finding an answer, at least with reference to the rather complex selected case study.

As a first step, the validation of the dynamic performance of the code PLAXIS 3D is carried out performing some simplified analyses under 1D and 2D conditions and comparing their results to those obtained solving the same problems by means of the well-established code QUAKE/W. This verification phase is considered satisfied if the

different codes return similar results. After such a validation stage, all the remaining analyses are carried out solely by PLAXIS 3D, so that the simplified 1D and 2D schemes for the case under study could be directly compared to those obtained by the more complete 3D model.

3.2 Historical evolution of Seismic Zonation in Italy

The Reggio Calabria – Messina earthquake, occurred in 1908, caused 80,000 victims. After this tragic event, a number of cities characterised by high seismicity was listed and reported in the Italian Royal Decree n. 193, which was approved in 1908 and can then be considered as the first Italian Seismic Zonation attempt. This decree, despite allowing for aseismic building design, considered building damage assessment from field observations and prevented the construction of new buildings in high risk zones, such as unstable or very steep slopes, marshy areas and laterally heterogeneous deposits.

After the 1927 Colli Albani (Lazio) earthquake, the countries damaged by the seismic event was grouped into two levels of seismicity.

The Ancona earthquake in 1972 triggered the idea of quantifying the seismicity of an area and two years later, with the Italian act n. 64, the prescriptions for Seismic National Zonation were defined.

The “Geodinamica” project, carried out by the Italian National Research Council, contains the first proposal for the Italian Seismic Zonation, which was finally accepted in 1984 by the Italian Ministry of Public Work.

In 1997, the Italian Department of Civil Protection commissioned a review of the existing National Seismic Zonation, which was approved in 1999 and carried out on the basis of three parameters. Two parameters are probabilistic, i.e. the peak ground acceleration, characterised by a 10% of exceedance in 50 years, and the Housner intensity. The third parameter is deterministic and corresponds to the maximum intensity experienced in the last thousand years.

3.3 Guidelines for Seismic Microzonation in Italy

The Italian guidelines for Seismic Microzonation, published by Gruppo di Lavoro MS in 2008, stress the importance of evaluating in detail seismic hazard at both local and regional scale. The evaluation of regional seismic hazard is summarised in the Italian seismic hazard map (Gruppo di Lavoro 2004), shown in Fig. 67, which refers to the motions at the outcropping rock. On the other hand, the evaluation of local seismic hazard, which corresponds to the estimation of the ground motion modifications with respect to the outcrop motion, requires additional studies.

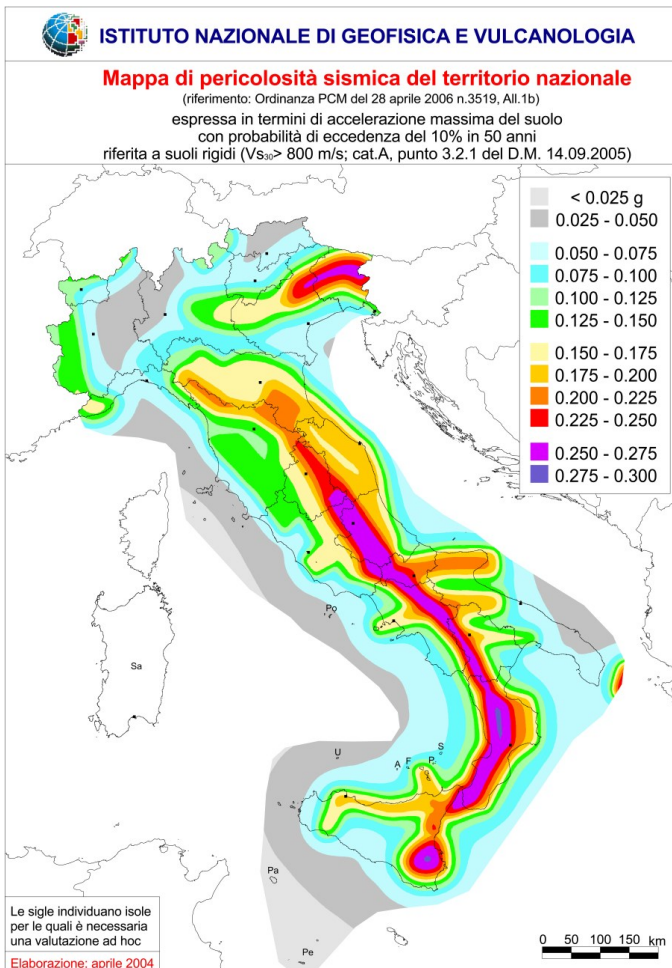


Fig. 67 National Seismic Hazard map (Gruppo di Lavoro 2004)

Seismic risk evaluations, which include Seismic Microzonation Studies, are now requested to perform urban and emergency planning and to design structures and infrastructure under safe conditions. Seismic Microzonation, in particular, aims at evaluating seismic homogeneous areas, such as stable areas, stable areas subjected to local seismic amplification, and unstable areas. More specifically, stable areas are zones where the motion expected at the horizontal surface of the outcropping rock will not be modified as consequence of amplification phenomena and no landslides are expected.

Based on the above mentioned Italian guidelines, Seismic Microzonation studies can be carried out according to three levels of detail:

- level 1, which consists of a collection of existing data and a qualitative identification of homogeneous seismic microzones;
- level 2, based on new and more detailed site investigations and laboratory data, which aims at quantifying the seismic response of an area using simplified method;
- level 3, which requires numerical simulations of local site response.

Fig. 68 shows the links between levels of Seismic Microzonation studies and their use in structure and infrastructure design and urban planning, as reported in the IGSM (Gruppo di Lavoro MS 2008).

The key ingredients for a level 3 seismic microzonation are: geotechnical model, reference motion and numerical analyses.

The geotechnical model is based on the identification of the morphological and lithological characteristics of the area analysed, with particular reference to the thickness of the soil layers and the depth of the seismic bedrock. The model also needs to include the dynamic soil behaviour of each geotechnical unit. A level 3 microzonation then requires site investigations (e.g. cross-holes and down-holes) and laboratory tests, (e.g. resonant column or cyclic shear tests) in order to determine the parameters of the constitutive model used to describe the dynamic behaviour of the materials.

IGSM recognises three different approaches to select the reference motion: deterministic (using recorded accelerograms), stochastic (identifying the motion through the Green’s functions) and probabilistic (starting from uniform hazard spectra). It is generally recommended to use real accelerograms characterised by uniform hazard response spectra. For instance, real accelerograms might be selected considering magnitude and epicentral distance that generally affect the area under investigation and in order to be compatible with the design spectrum of the same area. This procedure represents a good compromise between deterministic and probabilistic approaches and has been used already by other authors (e.g. Silvestri & D’Onofrio 2014; Santucci de Magistris et al. 2014).

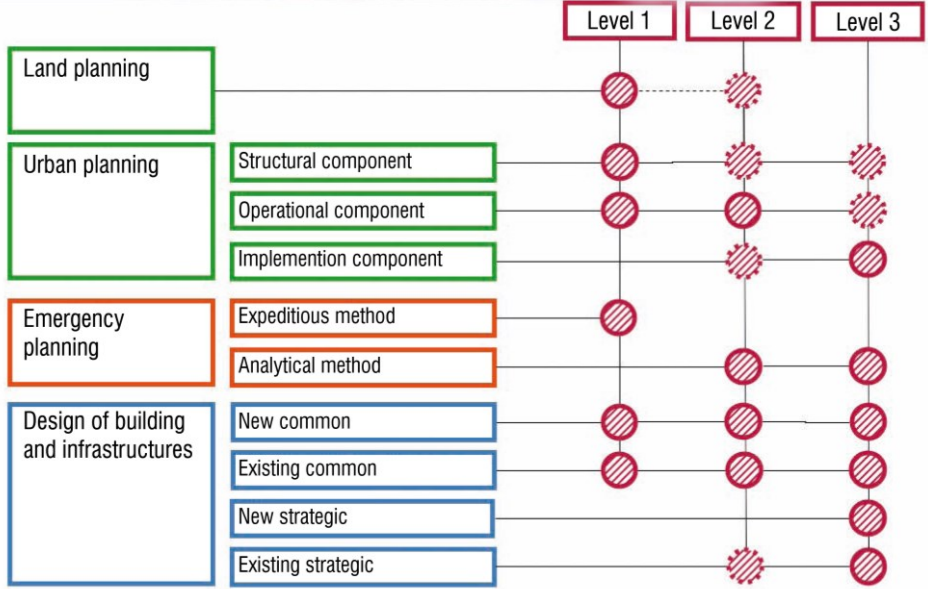


Fig. 68 Levels of Seismic Microzonation studies related to urban and emergency planning and to structure and infrastructure design (from Gruppo di Lavoro MS 2008)

The numerical analyses should simulate the seismic wave propagation through the surficial soil layers. As highlighted in Chapter 1, when areas have complex stratigraphical and topographical characteristics, different dimensional schemes can lead to very different results, so it is of paramount importance to select a dimensional scheme that suits the site conditions.

It is finally worth noticing that IGSM defines some amplification factors (AF) to quickly identify ground motion modifications with respect to the outcrop motion, but no mandatory indications are made in the IGSM about the choice of AF. Given that regional hazard is related to three parameters, two of which are peak ground acceleration and Housner intensity, AF in terms of the same parameters can be used for consistency.

3.4. Site investigations and laboratory data. Geological and Geotechnical models

The available site investigations, carried out for level 1 SM, are localised in Fig. 69. Twelve continuous coring boreholes, 10 to 40 m deep, were carried out in the studied area, together with eight shear wave profiles, determined by means of down-hole prosecutions and eight measurement of horizontal to vertical spectral ratio (HVSr in the following). Moreover, thirty-two undisturbed soil samples were retrieved during the drilling of the continuous boreholes.

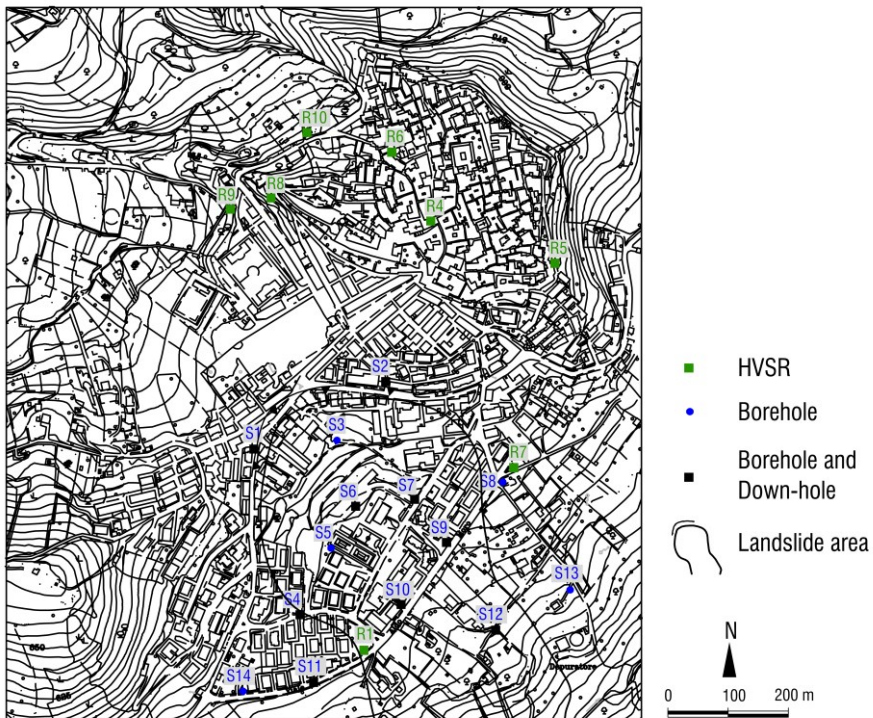


Fig. 69 Site investigation map of Bovino urban area

Table 22 and Table 23, listed in the appendix, summarise the physical and mechanical properties of the soil strata within the urban area of the Bovino village.

The geological model described in the present chapter derives from the one proposed by Petti (2010) and Cotecchia et al. (2016). This geological setting was improved by the borehole data available from the in-situ investigations reported in Fig. 69. The same figure highlight the contour of a major landslide, which partly affects the village. In the following this stability problem will not be discussed, as being out of the scope of this work.

As shown in Fig. 70, the old town of Bovino is built up on the rock part of the Bovino Synthem (briefly BOV in the following) which is a Pliocene sedimentary succession formed by silty clays with sands, lying on grain-supported conglomerates and sandstones. BOV is located to the East of a North-East verging thrust fault, South-West dipping, where it overlies unconformably the Faeto Flysch Formation (Miocene; as FAE hereafter).

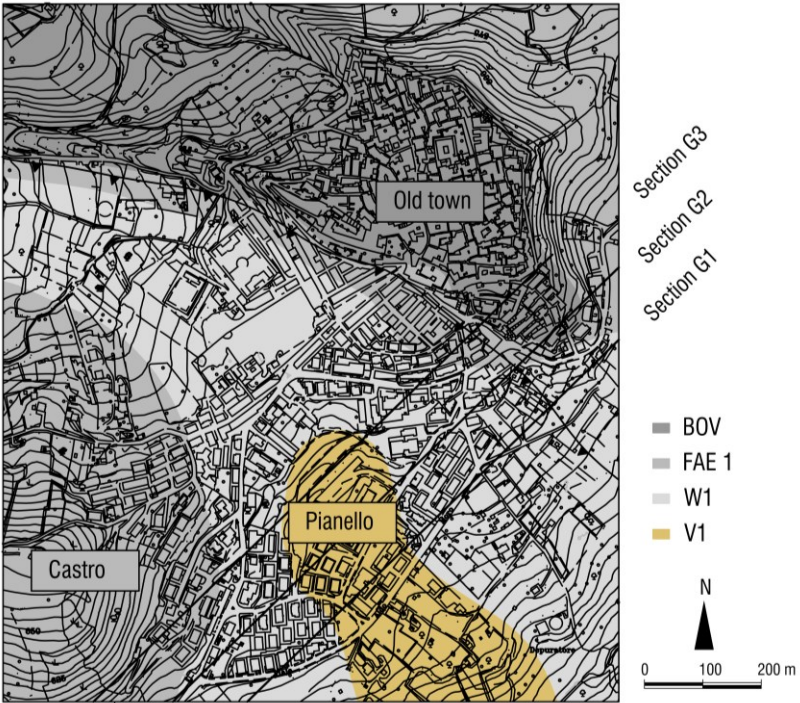


Fig. 70 Outcropping geological units map of Bovino urban area

According to Di Nocera e Torre (1987), the FAE consists of an upper marly-calcareous member (FAE1) and a lower clayey-marly one (FAE2). In particular, in the study area, the FAE1 is present in the old town area, below the pliocenic conglomerate, and at Mount Castro, whereas FAE2 outcrops in the Pianello slope. FAE1 consists of calcarenites and calcareous marls interbedded with a few clayey levels, while FAE2 is formed by high plasticity, locally sheared, clays interbedding few and thin calcareous strata. The lithological transition between these two members is gradual, and moving up-slope, both to North-Est and to North-West of the Pianello hill, the thickness and the frequency of the rock interbeddings increase. Moving down to depth, FAE2 gradually passes to the Red Flysch Formation (Cretaceous-Miocene; FYR herein), which outcrops at South, outside the studied area (Pieri et al. 2011).

The FAE3 unit, identified below FAE2, is the transition unit from FAE to FYR. Clays including either sandy levels, or intensely fractured rock strata, W1 in Fig. 70, are found to overlies extensively FAE2. This observation suggests that they represent the effects of either shallow landsliding or weathering within FAE2, or remoulding due to tectonic movements. Based on the available lithological data, the thickness of this unit changes from few meters up to 20 m. Finally, higher plasticity clays, that appear to be the result of further fluvial remoulding of FAE2 clays, are found to cover the W1 clays (i.e. V1 in Fig. 70).

The three geological section, corresponding to the traces sketched in Fig. 70 and derived from the works of Santaloia et al. (in prep.) and Cotecchia et al. (2016), are shown in Fig. 71.

In general, the geological model is the pivot model on the base of which should be the geotechnical model defined. In other word, the geological soil units could differ from the geotechnical ones related to phenomena under investigation.

With specific reference to the seismic behaviour the key features of a soil material are: weight of saturated soil volume, shear wave velocity, shear stiffness degradation and damping ratio curves against shear strain. The geotechnical model was defined according to these parameters.

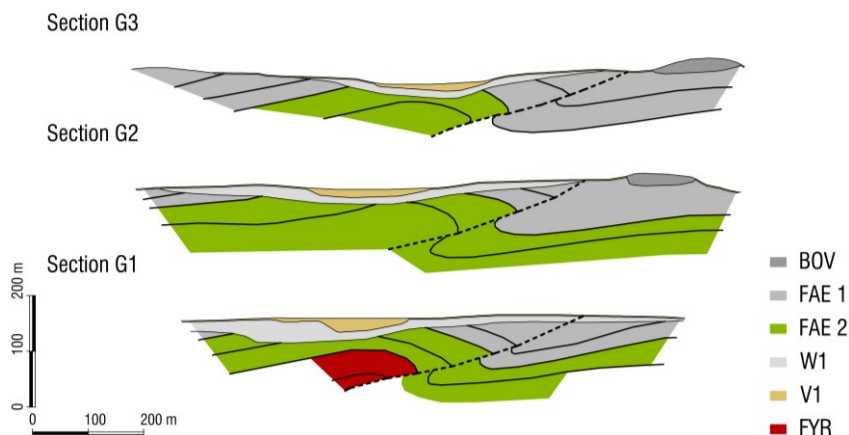


Fig. 71 Geological sections of Bovino urban area

Fig. 72 depicts the shear wave profile from all the available down-hole investigations. They could be divided into two groups as outside (S1, S2, S4, S7, S9, S12) and inside or nearby (S6, S10, S11) the main landslide area, drawn in Fig. 69, which characterises the Bovino urban area (Petti 2010; Cotecchia et al. 2016). It is possible to recognise three different soil strata with reference to the first group (Fig. 72a). These materials are characterised by mean shear wave velocities equal to 200 m/s, 800 m/s and 1200 m/s. The second group of boreholes (Fig. 72b), show only one dynamic soil material which exhibits a shear wave velocity equal to 200m/s on average.

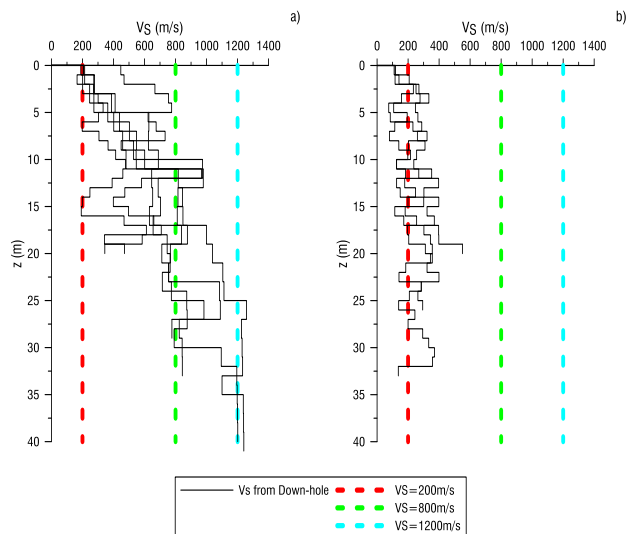


Fig. 72 Shear wave profiles from down-holes with reference to boreholes a) outside and b) inside the main landslide body

With regard to four boreholes, Fig. 73 shows a comparison between the geological units (namely V1, W1 and FAE) and the shear wave velocity profile, $V_s(z)$, resulted from the down-hole logging. With reference to S9 and S12 boreholes, Fig. 73a) and b), it is possible to assess that the geological units V1, W1 and FAE are characterised by mean values of shear wave velocity equal to 200 m/s, 800 m/s and 1200 m/s respectively. On the other hand, along the S10 and S11 boreholes, Fig. 73c) and d), both the geological units V1 and W1 look as characterised by a mean value of shear wave velocity equal to 200 m/s.

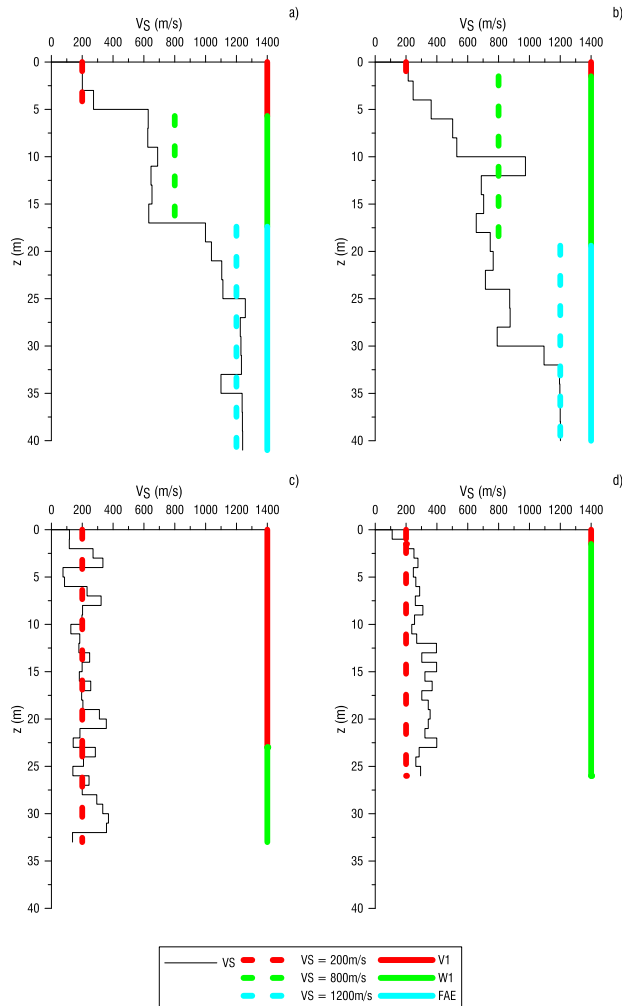


Fig. 73 Comparison between geological units and shear wave profile from Down-hole with reference to boreholes a) S9, b) S12, c) S10 and d) S11

Different values of mean shear wave velocity related to unit W1 does not represent an inconsistency in the available data; in fact, Bovino urban area is strongly affected by landsliding (Petti 2010; Cotecchia et al. 2016). The boreholes S9 and S12 are outside the main landslide area while boreholes S10 and S11 are placed within and nearby, respectively, the main landslide body of Bovino. The remoulding due to landsliding movement could be considered as a possible explanation for the differences existing between the above apparent inconsistencies of the mean value of shear wave velocity of geological unit W1 within and outside the landslide area.

Two HVSR results from ambient noise record, related to the measurements R4 and R6 (localised in Fig. 69), are represented in Fig. 74. The results do not show a meaningful peak and, as a consequence, are in good agreement with the geological hypothesis of outcropping rock in the old town area (SESAME 2004; Albarello & Castellaro 2011).

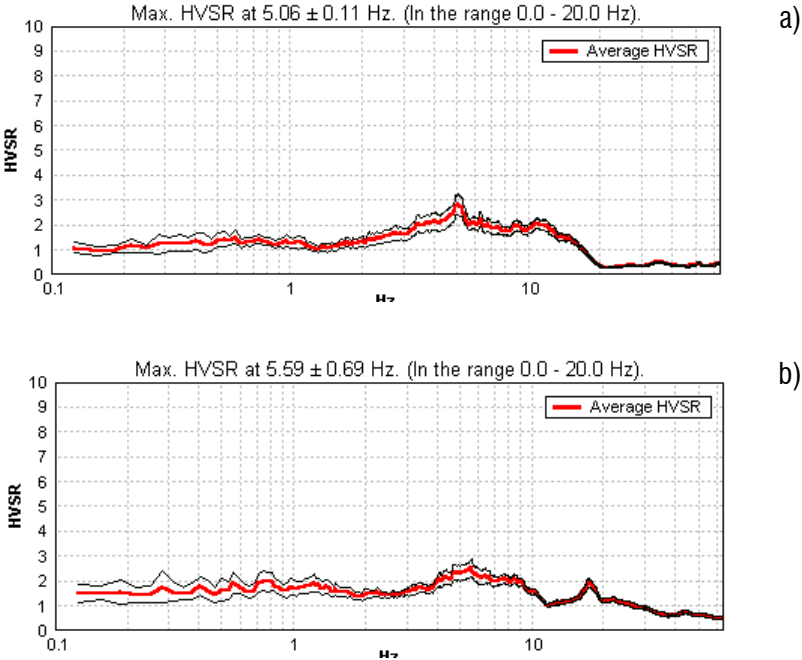


Fig. 74 HVSR measurements within Bovino old town a) R4 and b) R6

With reference to the geological model previously described and the above shear wave velocity profiles, the following soil materials were recognised as the main ones in the Bovino urban area:

- geological unit BOV could be considered as outcropping rock characterised by a high value of shear wave velocity. For sake of convenience it is assumed $V_s = 1200$ m/s;
- unit FAE is characterised by a mean value of shear wave velocity equal to 1200m/s;
- unit W1, apart from the landslide area, is identified as a dynamic unit characterised by a mean value of shear wave velocity $V_s = 800$ m/s;
- unit W1 within the main landslide area and unit V1 are regarded as unique dynamic unit characterised by a mean shear wave velocity $V_s = 200$ m/s.

Table 10 summarises the mean value of the saturated weight, plasticity index and shear wave velocity related to the soil strata previously identified. The constitutive parameters and mechanical properties are assumed constant with depth within each soil layer.

Geological Unit	Dynamic Unit	γ_{sat} (kN/m ³)	V_s (m/s)	ν	IP (%)
V1, W1	1	18	200	0.25	22
W1	2	18	800	0.25	22
FAE, BOV	3	18	1200	0.25	/

Table 10 Mean value of physical and mechanical properties of the dynamic units within Bovino urban area

The outcropping dynamic units map is sketched in Fig. 75. The above geological section showed in Fig. 71 and modified taking into account the geotechnical features are sketched in Fig. 76.

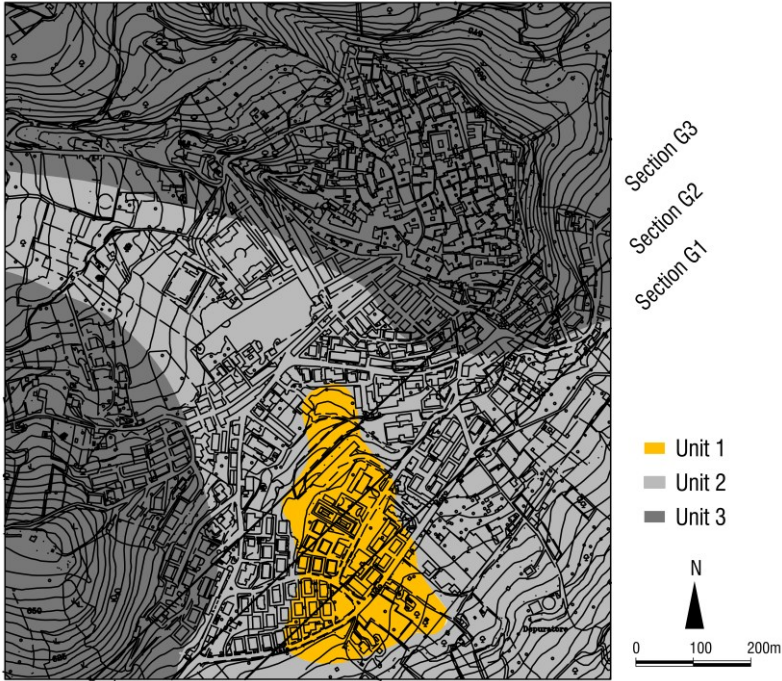


Fig. 75 Outcropping geotechnical units map of Bovino urban area

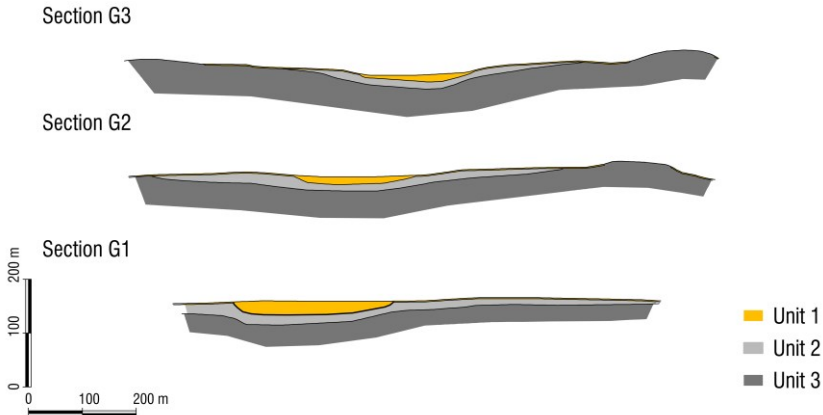


Fig. 76 Geotechnical sections of Bovino urban area

Due to the lack of specific laboratory tests, the $G(\gamma)/G_0$ and $D(\gamma)$ curves are assumed from the literature with reference to plasticity index $PI = 22\%$. In particular, the analytical expression proposed by Darendeli (2001) was calibrated against the values pro-

posed by Vucetic & Dobry (1991) for soils having PI = 15% and PI = 30%. The Darendeli expression provides an analytical solution for the shear stiffness degradation and damping ratio curves, which could be conveniently implemented in the numerical codes.

In Fig. 77 the black and red dots represent the values related to PI = 15% and PI = 30%, respectively, while the adopted curves for units 1 and 2 are the continuous black.

The dynamic unit 3, considered as the elastic seismic bedrock, is assumed to behave linearly.

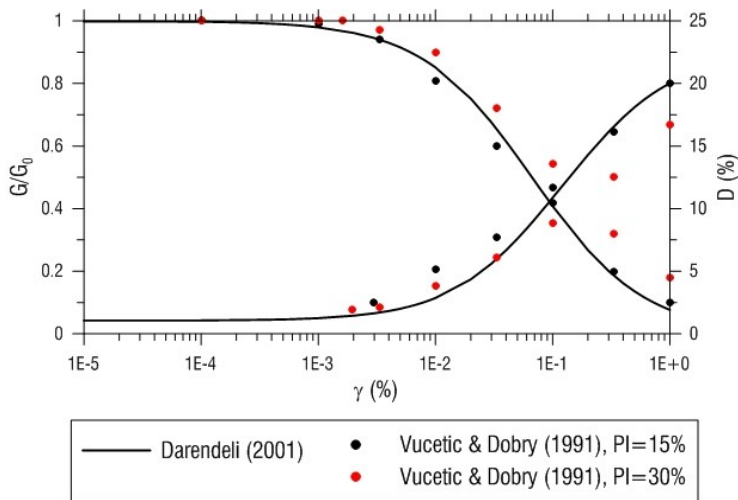


Fig. 77 Shear stiffness degradation and damping ratio curves for dynamic unit 1 and 2

3.5. Reference motion

The reference motion could be selected according to the following approaches:

- stochastic by means of seismological criteria;
- deterministic according to real recorded event;
- probabilistic based on the regional seismic hazard map.

In the following a probabilistic approach was adopted, as its reliability for this class of study has already been proved by many authors (e.g. Lanzo et al. 2011; Silvestri & D'Onofrio 2014; Santucci de Magistris et al. 2014).

The value of maximum outcrop acceleration, $a_{\max} = 0.22 \text{ g}$, for the area under investigation is defined with reference to the data summarised in Table 11 and obtained by means of seismic hazard map of the National Institute of Geophysics and Volcanology (<http://esse1-gis.mi.ingv.it/>) which is sketched in Fig. 78.

N	E	Exceedance probability in 50 years	Percentile	Return period
(°)	(°)	(%)	(%)	(year)
41.15	15.21	10	50	475

Table 11 Data for regional hazard analyses

The reference values in terms of return period have been selected according to the Italian guidelines for seismic microzonation (Gruppo di Lavoro MS 2008) and to similar studies carried out in the past (e.g. Lanzo et al. 2011; Silvestri & D’Onofrio 2014; Santucci de Magistris et al. 2014). The value of geographical reference are related to Bovino urban area. The Fig. 81 shows the standard design response spectrum for soil A and topography T1 as suggested by the Italian building code.

A set of real accelerograms were then be selected by means of code REXEL v3.5 (Iervolino et al. 2009) taking into account the main features of the seismic source which mainly contributes to the hazard of Bovino urban area. With regard to the disaggregation analysis for this area, illustrated in Fig. 79, it is possible to consider the $0 \leq R \leq 10 \text{ km}$ and $4.5 \leq M_w \leq 6.5$ as the range value of the epicentral distance and moment magnitude of the most important seismic source.

When approaching a seismic microzonation study it is important to account for the characteristics of the most diffuse building in the examined area, for example by means of their natural period of vibration. This should lead to the selection of input motions and interpretative parameters that has to be consistent with the building environment under study. The old village of Bovino is mostly characterised by two floors

masonry structures, while the more recently urbanised area is made out of reinforced concrete structures up to six floors tall. The natural periods of these two kind of structures are in general in the range $0.1 \leq T \leq 0.5$ s.

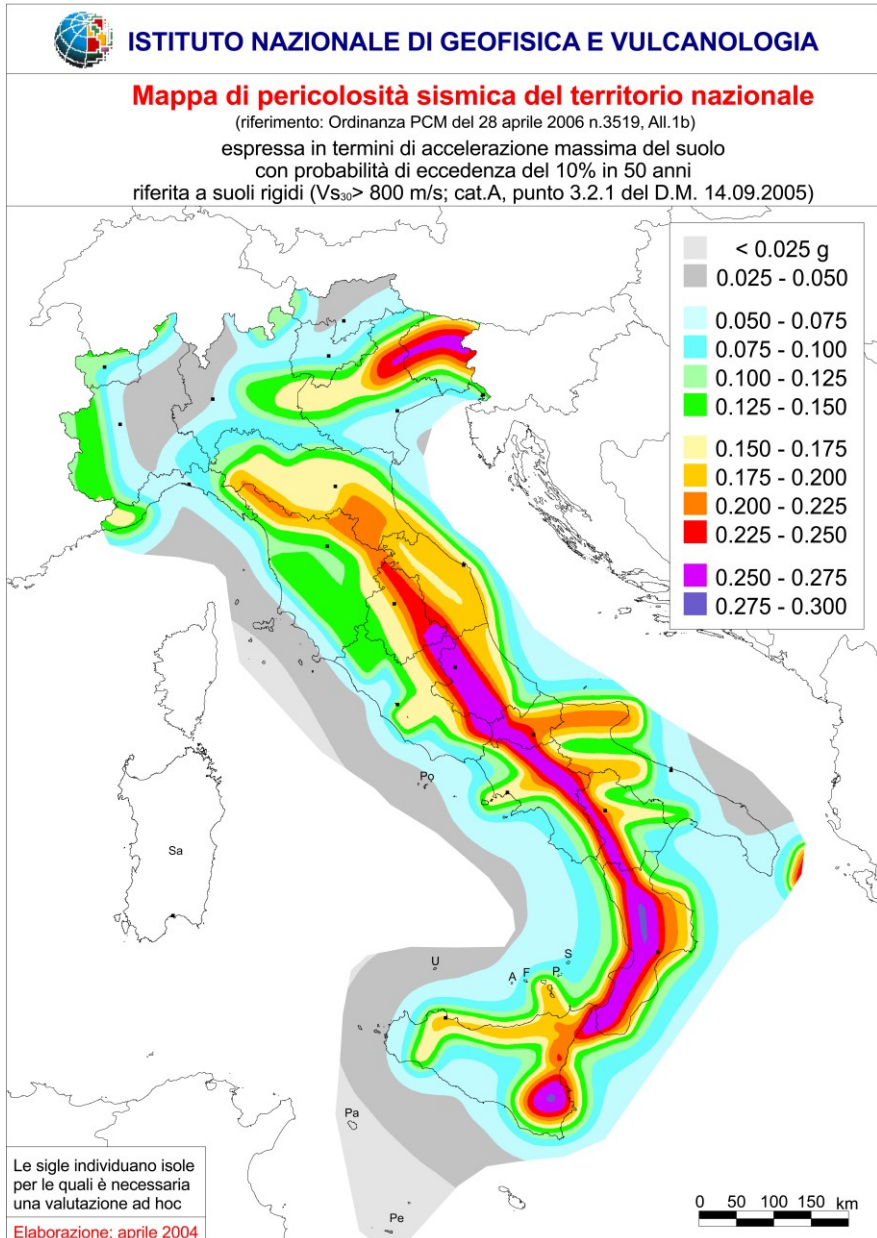


Fig. 78 National Seismic Hazard map (Gruppo di Lavoro 2004)

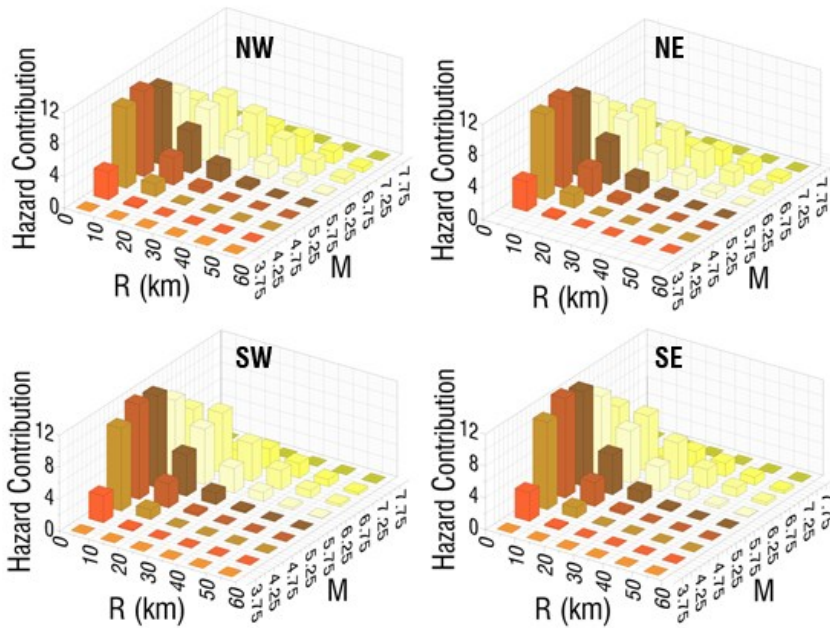
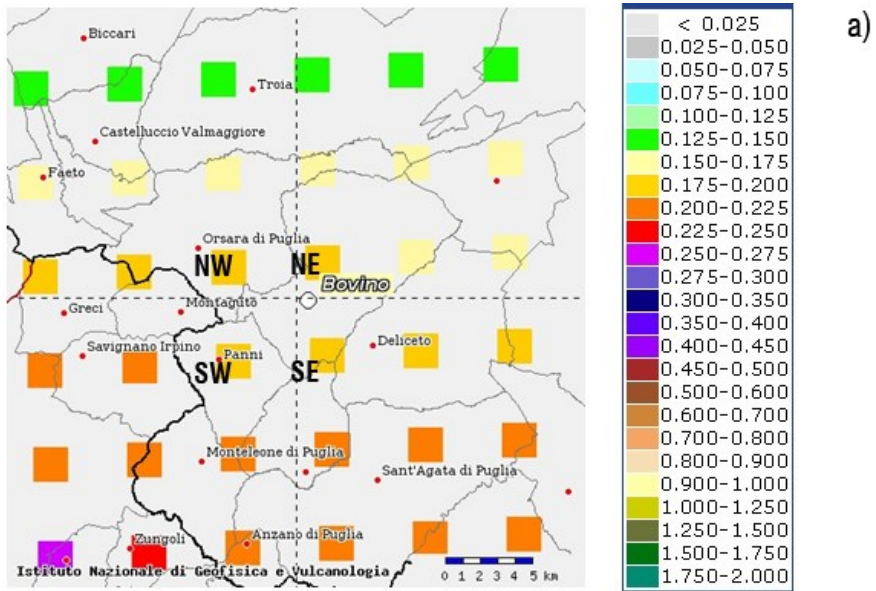


Fig. 79 Disaggregation analysis for Bovino urban area (Gruppo di Lavoro 2004)

Based on the previous considerations, seven real scaled accelerations have been selected as compatible with outcrop design spectrum defined with reference to the Italian building code based on the input data reported in Table 11 (NTC 2008). The spectrum compatibility was determined in the period range $0.1 \leq T \leq 0.5$ s assuming a 10% tolerance. The mean value of the scale factor was imposed equal to 2 in order to select the most representative reference motions according to literature recommendation (Bommer & Acevedo 2004; Silvestri & D’Onofrio 2014).

In Table 12 the main characteristics of the seven reference signals are summarised. With reference to the NTC 2008, the site class is A for all the events which are thus regarded as outcrop motions.

Signal ID	Earthquake ID	Station ID	Earthquake name	Date	Site class	M_w	Scale factor	Spectrum compatible component
C1	1635	ST486	South Iceland	17/06/2000	A	6.5	0.71	x
C2	350	ST236	Umbria Marche	03/10/1997	A	5.3	1.21	y
C3	80	ST45	Galabria	11/03/1978	A	5.2	2.92	y
C4	153	ST120	Campano Lucano	16/01/1981	A	5.2	3.54	y
C5	175	ST140	Lazio Abruzzo	07/05/1984	A	5.9	2.06	y
C6	2142	ST2558	South Iceland	21/06/2000	A	6.4	0.27	y
C7	1635	ST2486	South Iceland	17/06/2000	A	6.5	0.67	y

Table 12 Main features of the seven reference spectrum-compatible motions

A low-pass filter, assuming $f_{\max} = 10$ Hz, was applied to the seven scaled reference motions in order to avoid much too small finite elements, according to equation (14) of chapter 2.

The above scaled and filtered outcrop motions in terms of acceleration time history, Fourier spectrum and response spectra (conventional 5% structural damping) are rep-

resented in Fig. 80. In the next, for brevity, the seven outcrop spectrum-compatible motions will be called reference motions.

Fig. 81 shows the response spectrum obtained as the mean of the seven reference response spectra together with the standard design one for soil A and topography T1 as suggested by the Italian building code, in red and black lines respectively.

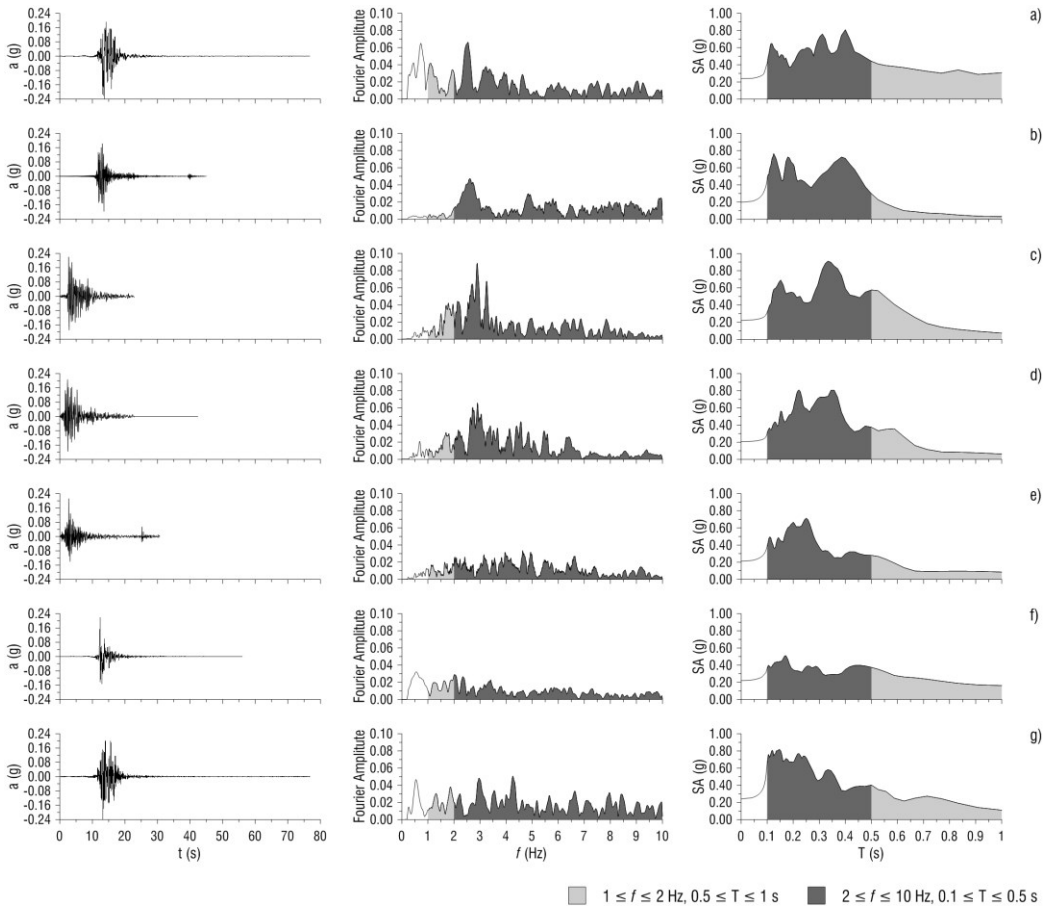


Fig. 80 From the left to the right, acceleration time history, Fourier spectrum and response spectrum for the seven reference motion: a) I1, b) I2, c) I3, d) I4, e) I5, f) I6 and g) I7

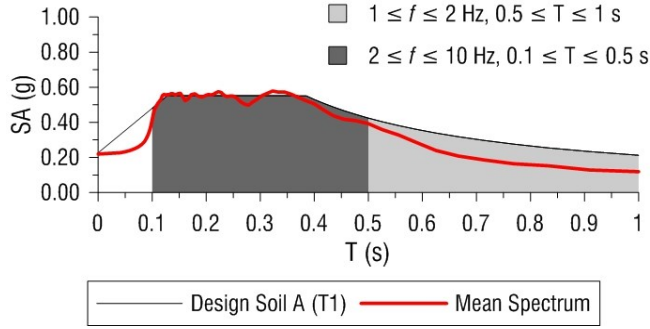


Fig. 81 Mean response spectrum of the seven reference motions and design response spectrum

3.6. Amplification factors

The evaluation of the site effects computed with the different numerical approaches was also carried out in terms of different amplification factors, briefly AF, as proposed in several studies (Gruppo di Lavoro MS 2008; Lanzo et al. 2011; Silvestri & D’Onofrio 2014; Santucci de Magistris et al. 2014; Pagliaroli, Moscatelli, et al. 2014; Pagliaroli, Quadrio, et al. 2014).

In particular, with reference to the point at the ground surface, for example of coordinates (x, y, z) , the adopted amplification factors are:

$$FH_{01-05}(x, y, z) = \frac{\int_{0.1}^{0.5} PSV_o(x, y, z) dT}{\int_{0.1}^{0.5} PSV_i dT} \quad 27$$

$$FH_{05-1}(x, y, z) = \frac{\int_{0.5}^1 PSV_o(x, y, z) dT}{\int_{0.5}^1 PSV_i dT} \quad 28$$

$$F_{PGA}(x, y, z) = \frac{PGA_o(x, y, z)}{PGA_i} \quad 29$$

where $PGA(x, y, z)$ is the peak ground acceleration and $PSV(x, y, z)$ is the pseudo-spectral velocity (5% structural damping) referred to motion determined at the above mentioned point of coordinates (x, y, z) and T is the period. The subscripts i and o are referred to outcrop signal, the reference one, and to the output signal, predicted at the ground surface by means of numerical analyses. The subscripts 01-05 and 05-1 of

the amplification factors defined in Eq. 27 and 28 indicate the period intervals considered in the computation of the integral quantities.

The FH_{01-05} proves to be the most important one for Bovino urban area because it is representative of the expected amplification in the range of natural period of vibration of the most common buildings, at most six floor tall, in the area under investigation.

Additionally, with reference to the point at the ground surface, for example of coordinates (x, y, z) it is possible to also define the following resulting relationships, which represent the mean result for the selected Amplification Factor as evaluated by the 7 different signals:

$$FH_{01-05}(x, y, z) = \frac{\sum_{n=1}^7 [FH_{01-05}(x, y, z)]_n}{7} \quad 30$$

$$FH_{05-1}(x, y, z) = \frac{\sum_{n=1}^7 [FH_{05-1}(x, y, z)]_n}{7} \quad 31$$

$$F_{PGA}(x, y, z) = \frac{\sum_{n=1}^7 [F_{PGA}(x, y, z)]_n}{7} \quad 32$$

assuming $[F(x, y, z)]_n$ the amplification factor related to the outcrop motion n . The above relationships, 30-32, are referred to as mean values of amplification factors.

3.7. Site response analysis. QUAKE/W

In this section the results obtained by means of code QUAKE/W are first discussed.

The Bovino urban area was subdivided into 22 sections, according to the grid shown in Fig. 82. The local reference system for the examined sections, together with their 3D surface patterns, are reported in Fig. 83. In particular, sections 1-7, aligned along the x-axis, develop along the SW-NE direction, while sections 8-22, oriented as the y axis, follow a NW-SE direction. The first set of sections covers a length of 1400 m, while in the second group a variable extension, up to 1000 m, was considered to ac-

count for the variable dimension of the village. The outcome of the analyses in terms of motion was recorded at 438 points, identified in Fig. 83, at the ground surface. The topography of the surface model was derived by the Apulia Region's Digital Terrain Model with a cell-size resolution of 8m (<http://www.sit.puglia.it>).

The 2D sections were defined in terms of stratigraphy based on a more general 3D-shear wave velocity model, this latter being defined starting from the geological and geotechnical models as discussed in § 3.4 and simplified in order to be suitable for the implementation in the adopted numerical codes. In Fig. 84 the ground level, in black line, and interface between soil layers, the red and green lines, are sketched with reference to some section; it is possible to enlighten the complex topographical surface and stratigraphic succession which characterise the Bovino urban area. In the next, the ground level and stratigraphy will be shown for each of the 22 sections.

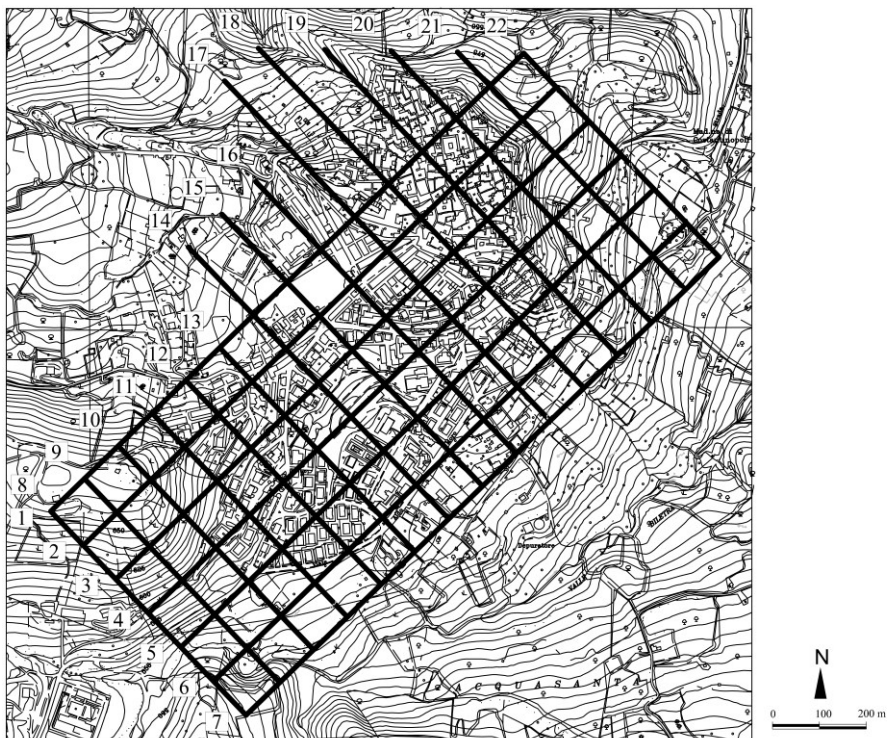
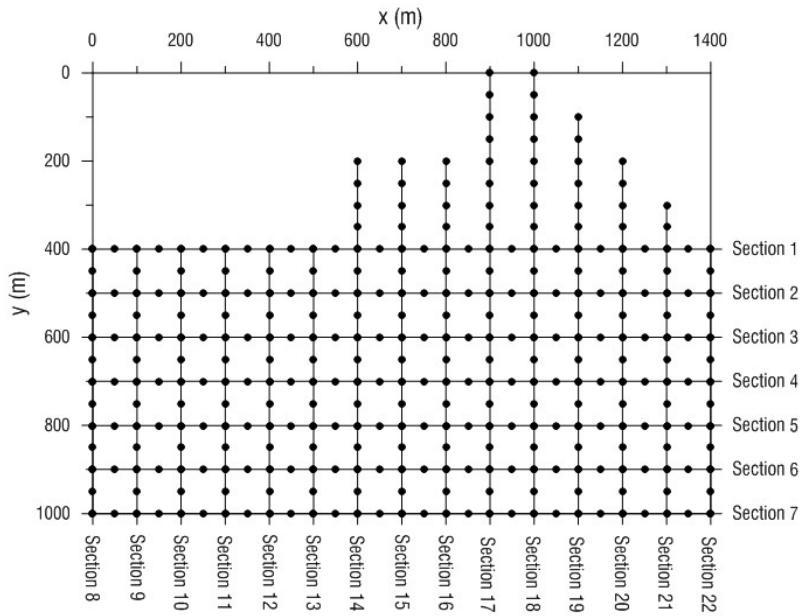
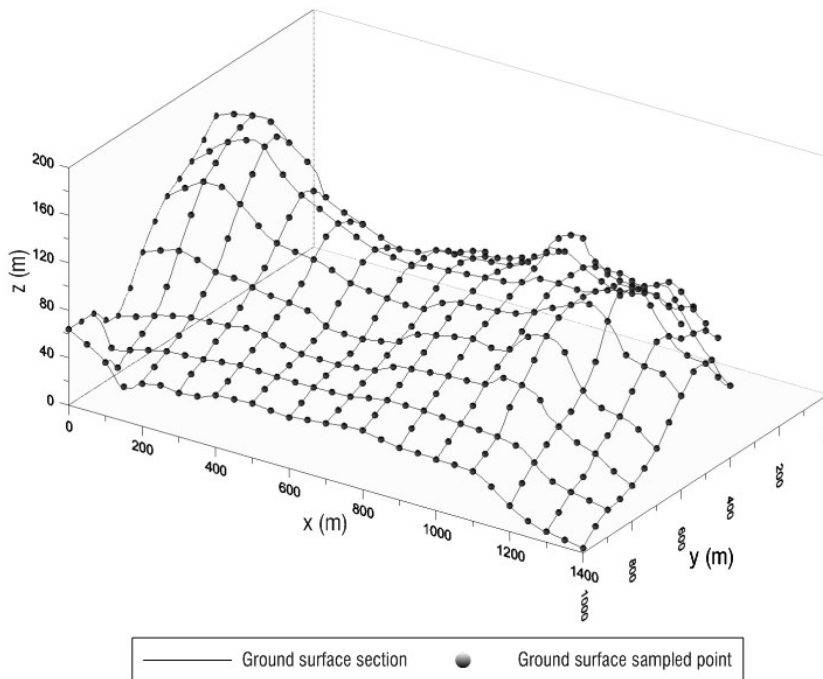


Fig. 82 Bovino urban area and studied area



a)



b)

Fig. 83 Studied sections (QUAKE/W) and sampled points within Bovino urban area. a) plane view, b) 3D view

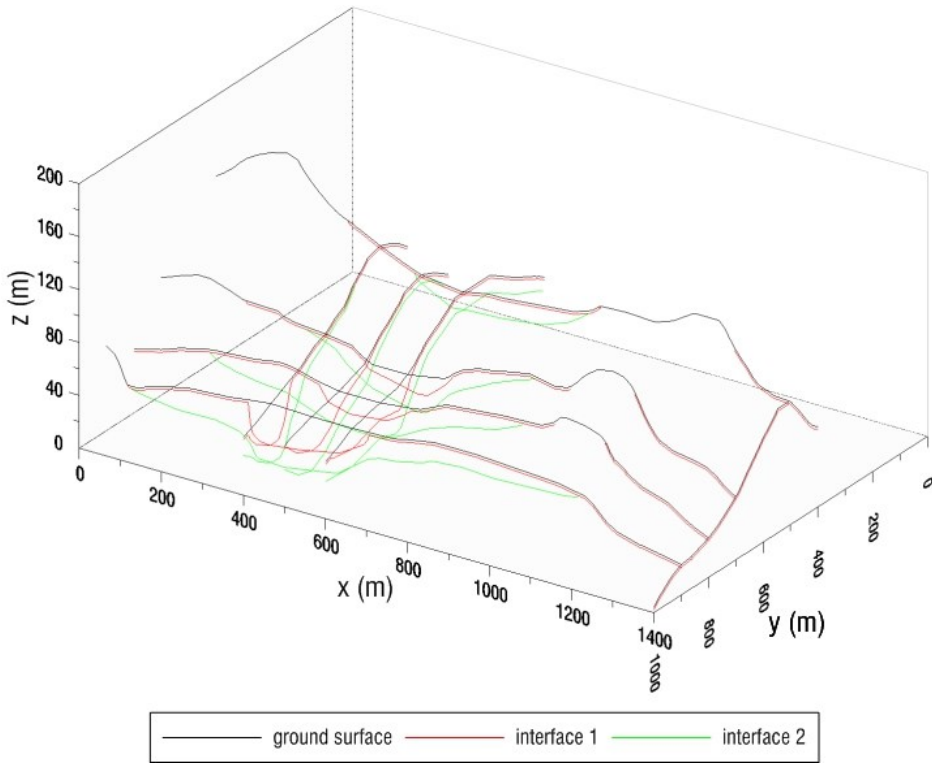


Fig. 84 Succession stratigraphy for some representative sections of the studied area

The numerical simulations of the seismic site response were carried out with reference to 1D and 2D schemes. As discussed in the chapter 2, assuming the reference motion recorded at the outcrop, the use of compliant base boundary condition is recommended for 1D simulations, while it is necessary for 2D schemes. Additionally, the input motion depends on the outcrop acceleration time history and physical and mechanical properties of the bedrock, regardless of the depth of model base. Thus, the so-called compliant base allows to assume a very limited value of bedrock thickness to be implemented in the numerical model. Reducing the size of the mesh leads to faster calculation. At the same time, as stated in the chapter 2, adopting such a boundary condition makes the thickness of the bedrock having no influence on the motion of the entire deposit.

The adopted boundary conditions are listed in Table 13, where u is the displacement in the direction indicated by the subscript letter and τ is the shear stress time history defined according to equation (15) of chapter 2.

Vertical boundary	Horizontal base	Ground surface
$u_x = \text{free}$ $u_z = 0$	$\tau_x(t) = 2 \cdot \tau_{\text{bedrock}}(t)$ (Mejia & Dawson 2006) $\tau_z = 0$	$u_x = u_z = \text{free}$
	edge damping (Krahn 2004)	

Table 13 Boundary conditions for QUAKE/W analyses

The equivalent linear elastic constitutive model was assumed for the three dynamic units described in the § 3.4. Unit 3 is considered as the seismic bedrock but for sake of necessity it assumed to be a QUAKE/W equivalent linear elastic material with $G(\gamma)/G_0 = 1$ and $D(\gamma) = 0.01\%$ (the shear stiffness decay and damping ratio curves respectively). The curves for units 1 and 2 adopted in QUAKE/W analyses are shown in Fig. 85.

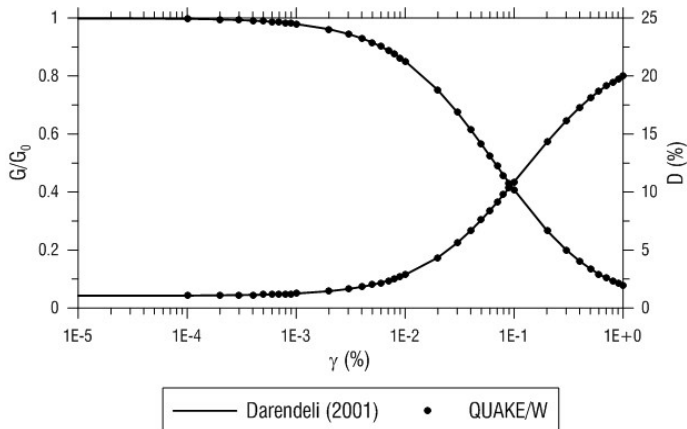


Fig. 85 $G(\gamma)/G_0$ and $D(\gamma)$ curves from Darendeli (2001) and as implemented in QUAKE/W

Due to equivalent linear hypothesis, it is necessary to define the ratio R between the mean shear strain induced by the earthquake, γ_{eff} , and its maximum value, γ_{max} , recorded during the whole event. R is assumed as a linear function of the Magnitude:

$$R = \frac{\gamma_{\text{eff}}}{\gamma_{\text{max}}} = \frac{M-1}{10} \quad 33$$

The damping is based on the following Rayleigh formulation:

$$\eta = \frac{\alpha + \beta \cdot \omega^2}{2\omega} \quad 34$$

where ω is the general angular velocity $\omega = 2 \cdot \pi \cdot f$. α and β are two scalars called Rayleigh damping coefficients and are determined according to the subsequent relationships:

$$\alpha = 2D \frac{\omega_m \cdot \omega_n}{\omega_m + \omega_n} \quad 35$$

$$\beta = \frac{2D}{\omega_m + \omega_n} \quad 36$$

D is the target damping, while ω_m and ω_n are related to the frequencies f_m and f_n respectively. In the procedure adopted by the code QUAKE/W these two frequencies are the lowest and second lowest system frequencies.

The size of the mesh, the max size of the finite element, i.e. the max distance between two nodes of the same element, and the time step of analyses were defined according to what discussed in the § 2.1. Fig. 86 sketches a typical mesh adopted in the analyses, to enlighten the variation in size of the elements. The area under investigation is the L_{sec_6} but it is laterally increased in order to avoid reflection of seismic wave along the vertical boundary of the mesh (Amorosi et al. 2008).

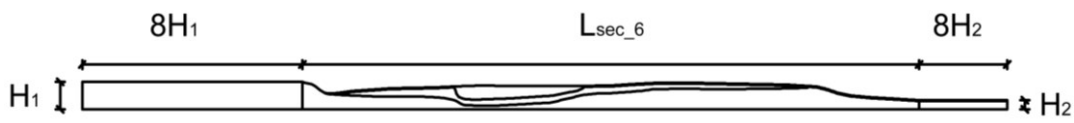


Fig. 86 Type-mesh to enlighten the oversize with respect to the area under investigation

At first, the results obtained by means of 1D and 2D analyses are shown with reference to sections 4 and 14.

A qualitative and synthetic representation of the numerical results obtained with the numerical analyses is presented in Figs. 87-90 for section 4 and 14 in terms of acceleration time histories predicted at the ground surface. The reference motion is also included for the sake of comparison at the top. The position of each control point at the ground surface, fifty meters apart from each other, is evident thanks to the geotechnical section shown on the left side on the figure. The black line indicates the topographic surface, while the red and green lines represent the interfaces among the geotechnical units 1, 2 and 3.

Figs. 87-90 are related to the reference signal C3. It is possible to observe that 1D analyses, Fig. 87 and Fig. 89, do not catch any amplification due to the presence of the hill (between $1000 \leq x \leq 1200$ m for section 4 and $350 \leq x \leq 550$ m for section 14), while the motion is amplified at the ground surface of the valley (between $500 \leq x \leq 700$ m for section 4 and $650 \leq x \leq 1000$ m for section 14). On the other hand, the 2D results, Fig. 88 and Fig. 90, enlighten the amplification on the ground surface of the hill, e.g between $1000 \leq x \leq 1200$ m for section 4, and at the valley. The sections 4 and 14 seems to be characterised by similar amplification pattern irrespective of the geometrical schematization adopted in the numerical simulation, thus indicating a prevailing stratigraphic influence on the computed amplification factors.

The profile of amplification factors along the section were determined in order to quantify and to assess in a more clear way the modification of the reference motion due to local site conditions. The 2D numerical analyses related to the twenty-two sections have been performed for each one of the 7 reference motions. All profiles of amplification factors are listed in the appendix.

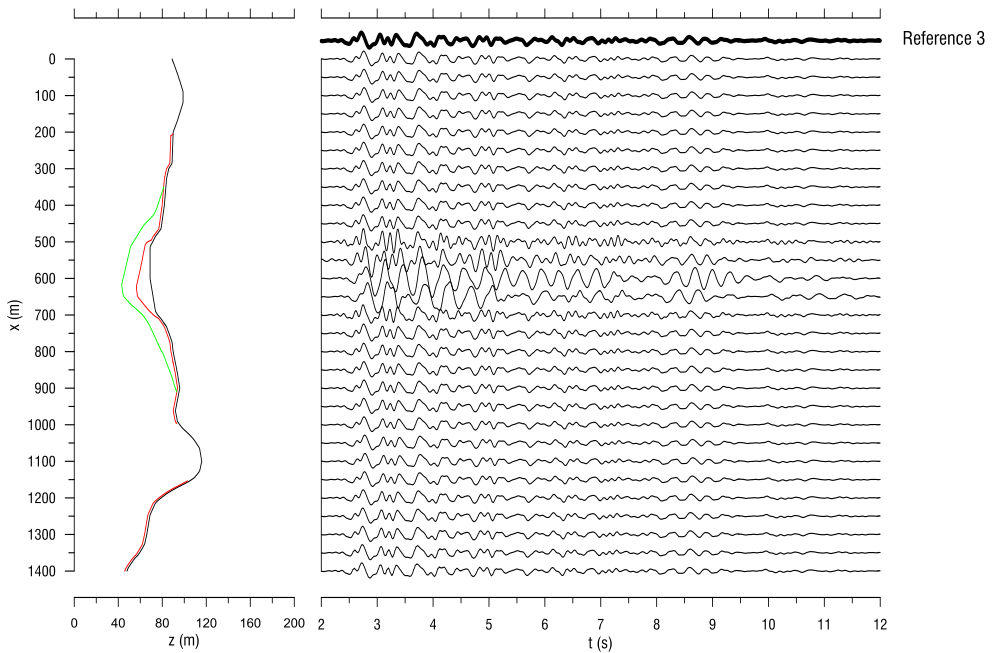


Fig. 87 Accelerograms predicted at the ground surface of section 4 by means of QUAKE/W with reference to 1D analysis, signal 3

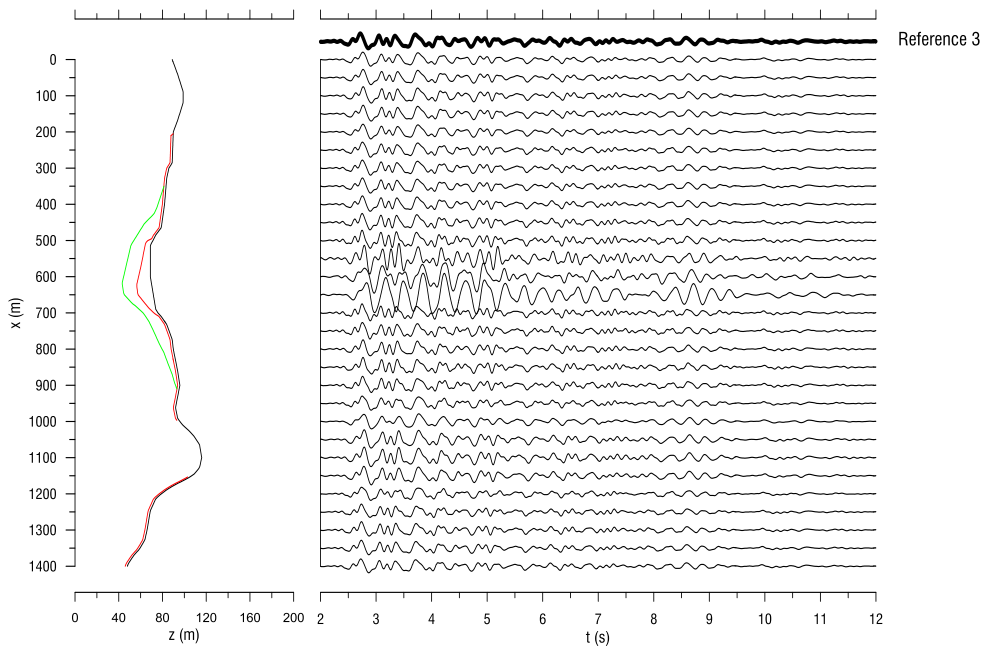


Fig. 88 Accelerograms predicted at the ground surface of section 4 by means of QUAKE/W with reference to 2D analysis, signal 3

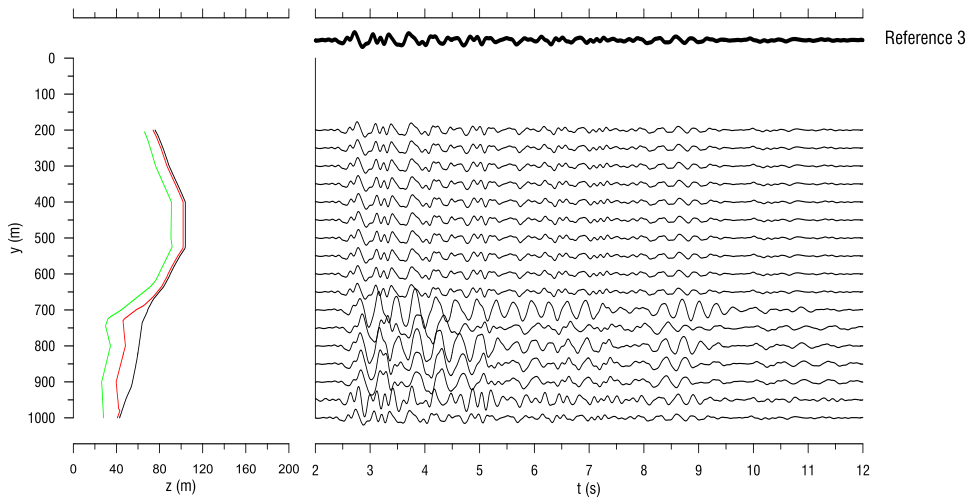


Fig. 89 Accelerograms predicted at the ground surface of section 14 by means of QUAKE/W with reference to 1D analysis, signal 3

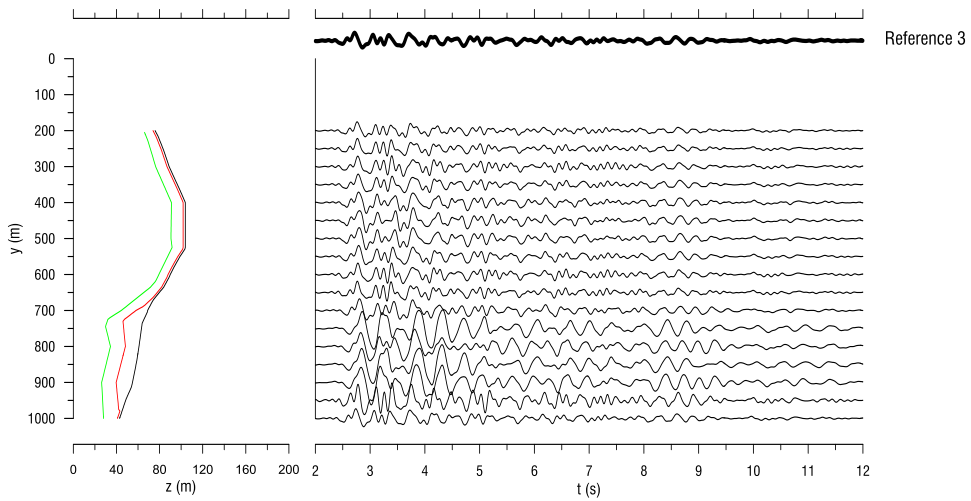


Fig. 90 Accelerograms predicted at the ground surface of section 14 by means of QUAKE/W with reference to 2D analysis, signal 3

The amplification factors obtained by 1D and 2D analyses carried out for each of the seven reference motions are shown in Figs. 91-96 again for the sections 4 and 14. The script $Cn_x_Cn_y_a_i$ (where $n = 0-7$, m and $i = x, y$), used to define the amplification factors profiles, is composed of three part. The first two parts, Cn_x and Cn_y , are related to the input motion considered in the x and y direction, respectively. The third one, a_i , is referred to the recorded output. For example, $C0_x_C2_y_a_y$ stays for: no motion applied in the x direction, input motion C2 applied along y direction and ground surface acceleration determined along the y direction. It is worth noting that input motion C2 is the shear stress time history determined according to equation 24, reported in chapter 2, and assuming the reference motion C2.

The condition $n = m$ stays for profile of mean value.

Furthermore, in Figs. 91-96 the black bold continuous and the red bold dashed lines, separately, represent the mean values of 1D and 2D amplification factors calculated at each surface point of coordinates (x, y, z) . In both cases it is possible to observe that the F_{PGA} is the most depending on the reference motion as compared to the FH_{01-05} and FH_{05-1} . This observation is consistent to what already discussed in the related literature (Madiai & Simoni 2013; Lanzo et al. 2011; Silvestri & D'Onofrio 2014).

With reference to 1D results, as stated in chapter 1, increasing the thickness of the soft soil material reduces the fundamental frequency of the deposit (increases the fundamental period of the deposit). In fact, FH_{01-05} , Fig. 91 and Fig. 94, shows peak values for unit 1 thickness from 4 to 10 m. On the contrary, FH_{05-1} gains the peak value with reference to the borehole characterised by the greater unit 1 thickness.

The 2D analyses, Fig. 92 and Fig. 95, predict amplification factors greater than 1 along the ground surface of the hill and the greatest values at the centre of the valley area.

The comparison between the 1D and 2D mean value profiles of amplification factors, Fig. 93 and Fig. 96, shows that the 2D analysis allows to catch the amplification due to the presence of the hill (topographic effect). In particular, value of about $FH_{01-05} = 1.5$ is gained at the crest. Instead, the 1D amplification factor is always equal to

1 in presence of the outcropping rock or in case of a really thin unit 1 layer, $\Delta H \leq 2\text{m}$, overlying the stiffer materials.

With reference to the mean amplification factors along the ground surface of the valley, it might be recognised different patterns obtained by 1D and 2D analyses (Fig. 93 and Fig. 96). This discrepancy is related to the geometric amplification, due to the geometry of the interface between soil layers (i.e. valley effect). Taking for example the sampled point at $x = 650\text{ m}$ of section 4 (Fig. 93), it results that the mean amplification factor $FH_{01-05}(x = 650\text{m}, 1\text{D})$ obtained by 1D analysis is equal to 1.80, while the one computed by 2D simulation $FH_{01-05}(x = 650\text{m}, 2\text{D})$ is equal to 2.48.

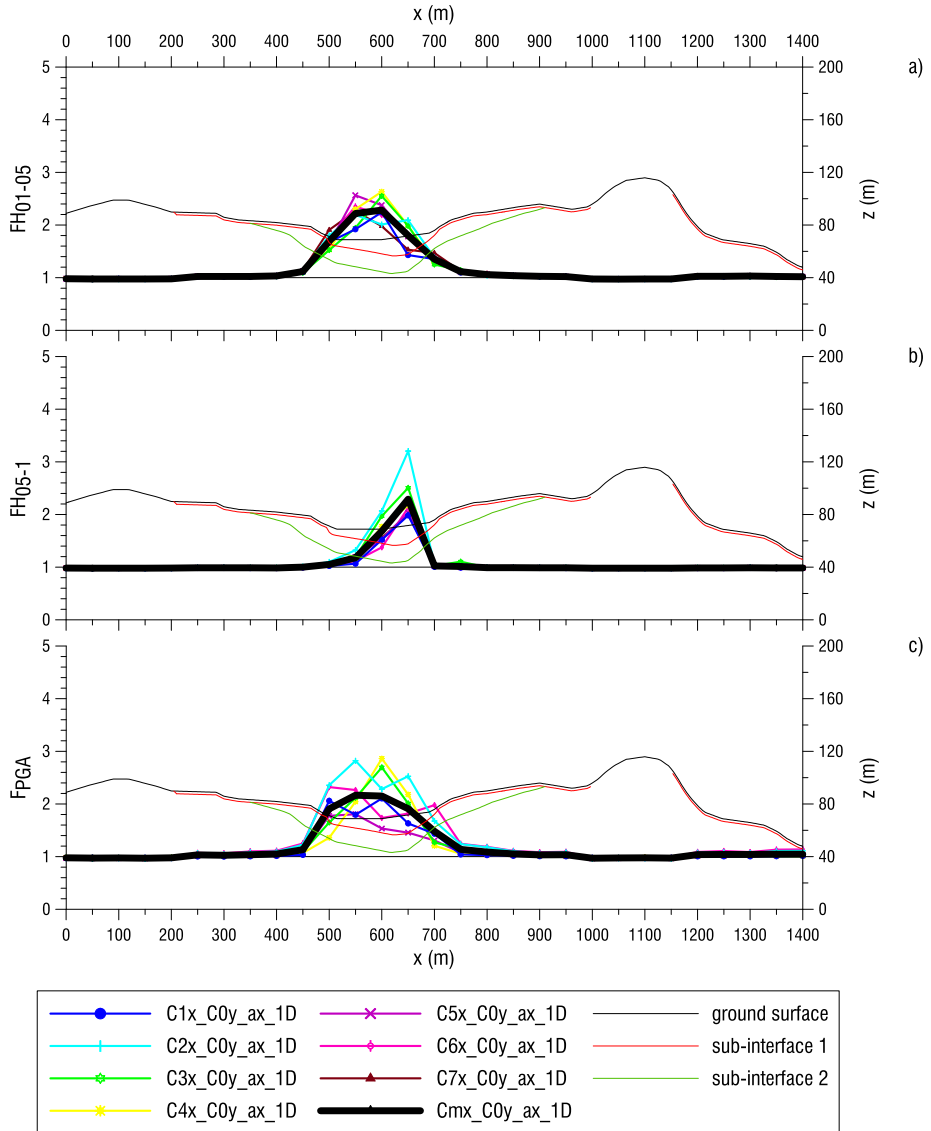


Fig. 91 Amplification factors profiles by means of 1D analyses for section 4 a) FH_{01-05} , b) FH_{05-1} , b) F_{PGA}

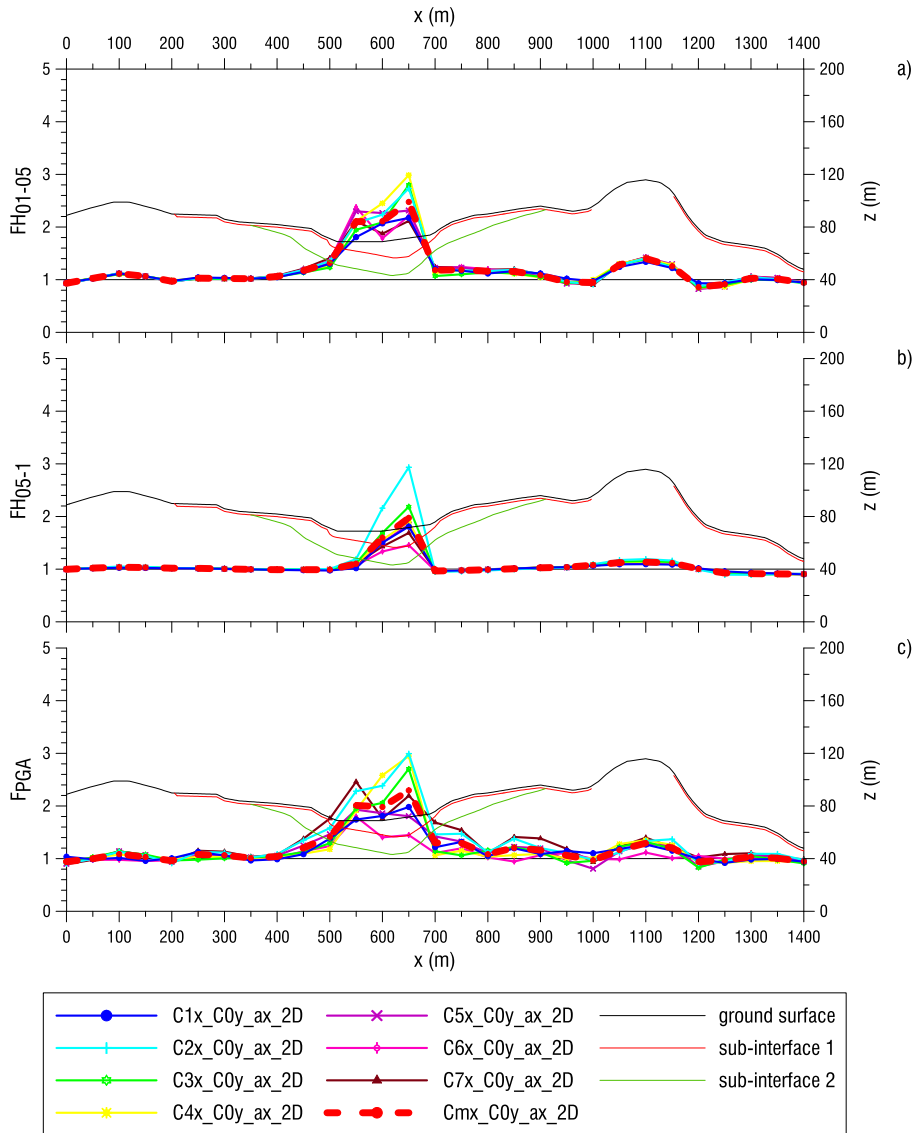


Fig. 92 Amplification factors profiles by means of 2D analyses for section 4 a) FH_{01-05} , b) FH_{05-1} , c) F_{PGA}

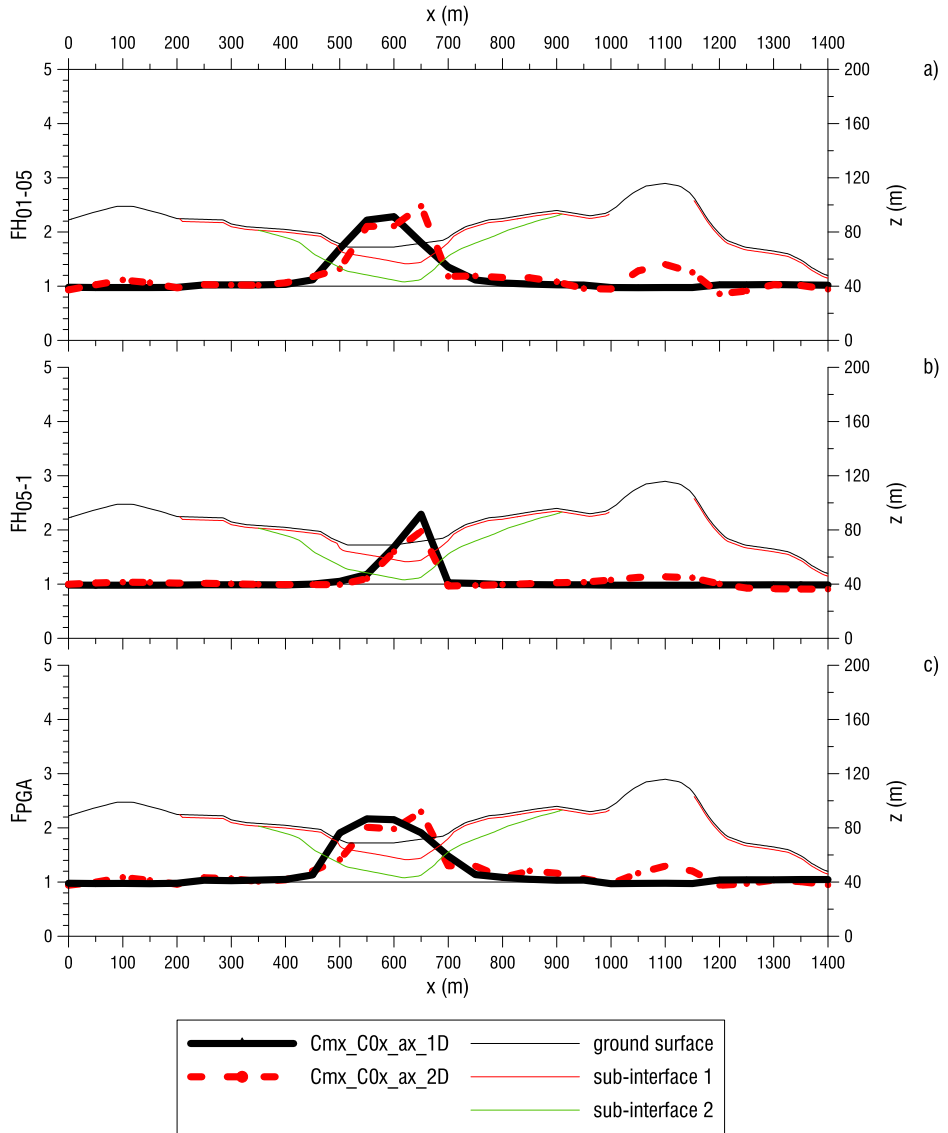


Fig. 93 Comparison between 1D and 2D mean values for section 4 a) $F_{H_{01-05}}$, b) $F_{H_{05-1}}$, c) F_{PGA}

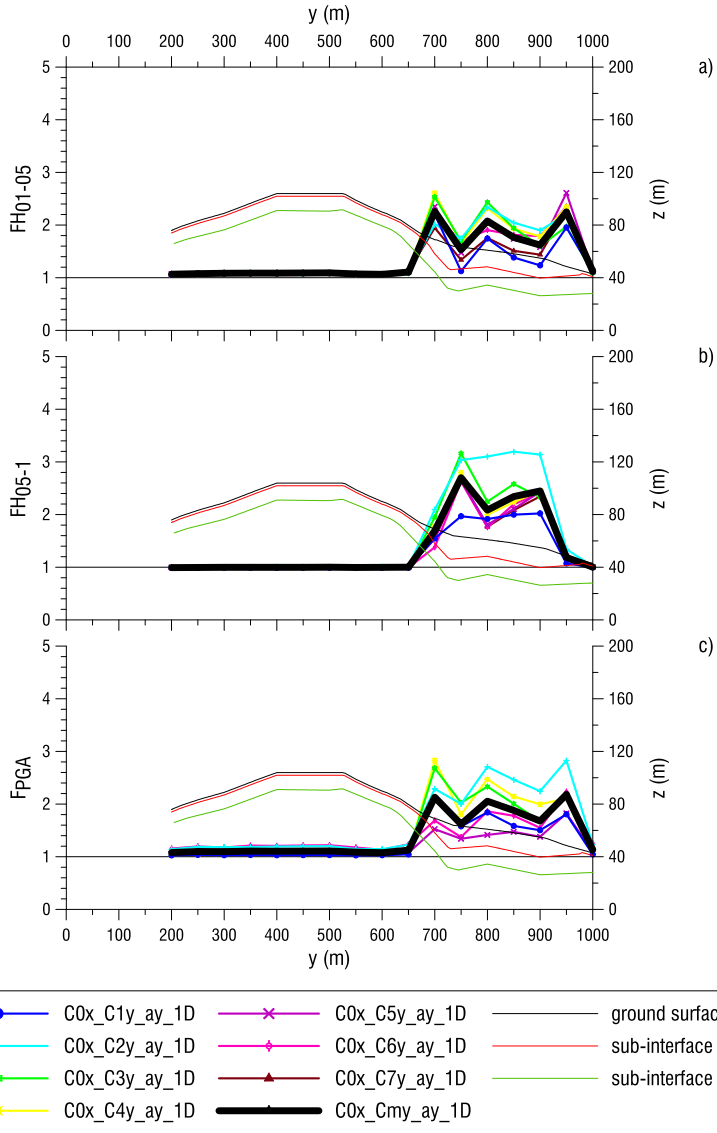


Fig. 94 Amplification factors profiles by means of 1D analyses for section 14 a) FH_{01-05} , b) FH_{05-1} , c) F_{PGA}

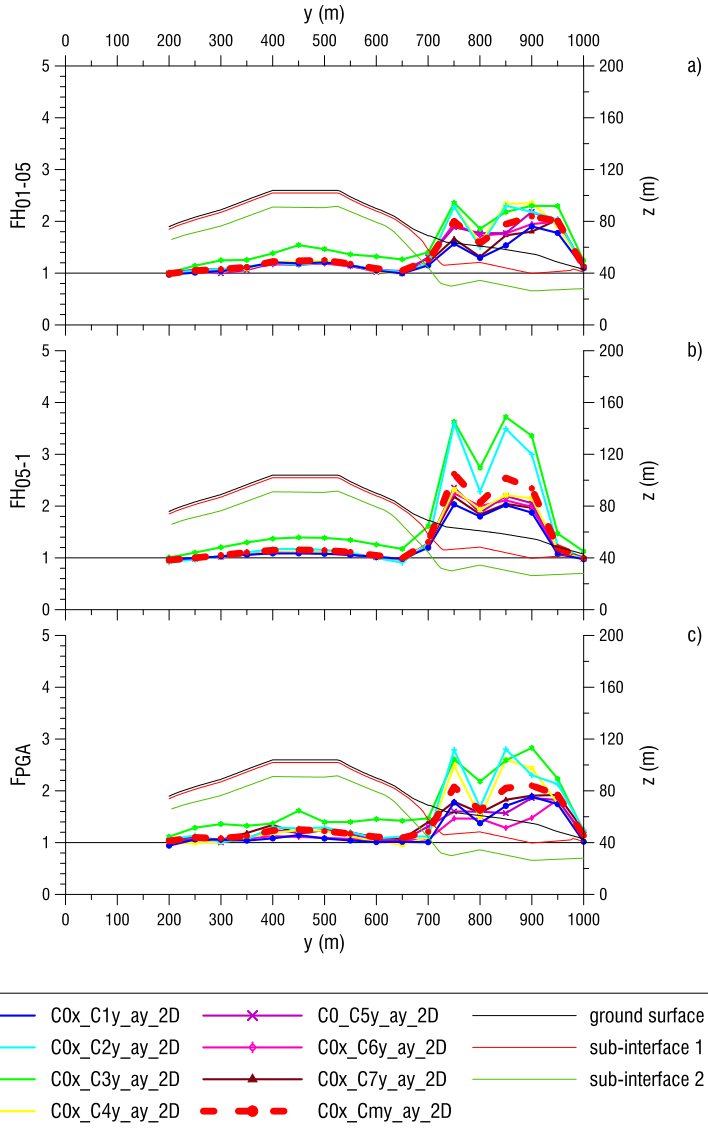


Fig. 95 Amplification factors profiles by means of 2D analyses for section 14 a) FH_{01-05} , b) FH_{05-1} , b) F_{PGA}

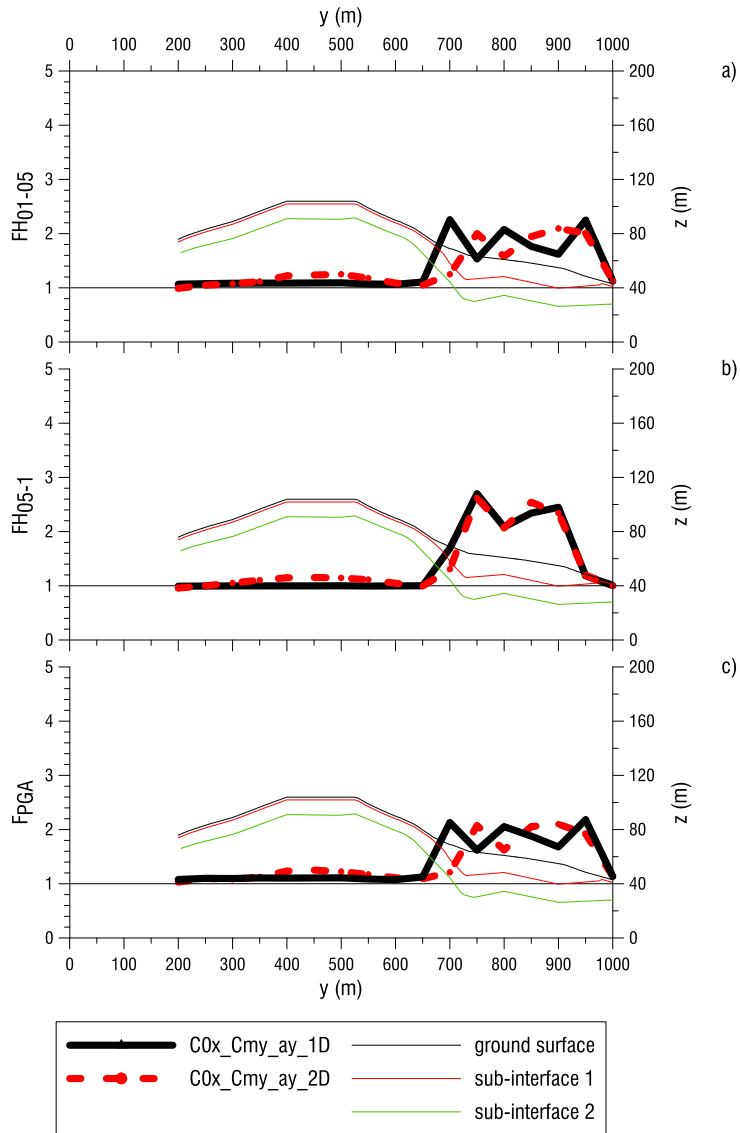


Fig. 96 Comparison between 1D and 2D mean values for section 14 a) FH_{01-05} , b) FH_{05-1} , c) F_{PGA}

The profiles of amplification factors obtained by 2D analyses for each of the seven reference motions and related to all the remaining twenty sections are reported in the appendix, Figs. 150-173.

The above comments made with reference to sections 4 and 14 can be extended to all the other analysed sections. In general:

- in presence of thick soft layer, $H_1 > 4$ m, the amplification factors F_{PGA} are more dependent on the reference motion as compared to the other FH_{01-05} and FH_{05-1} , as stated by other authors (Madiari & Simoni 2013; Lanzo et al. 2011; Silvestri & D'Onofrio 2014). In presence of outcropping units 2 and 3, or in the case of thin soft layer, $H_1 < 4$ m, the F_{PGA} related to the seven reference motions are similar to each other;
- the presence of the bedrock outcropping hill determines amplification factors slightly greater than 1. The greater is the slope of the hill the larger is the ground motion amplification; at most, a value equal to 1.5 is gained at the crest. At the same time a slight deamplification of the reference signal, i.e. amplification factor lower than 1, takes place at the toe of the hill;
- the largest amplification is induced by the presence of the soft soil valley. In this case the amplification pattern depends on the shape and size of valley. It is possible to observe that amplification factors profile of sections 3, 4, 5, 7 and 12, display one peak, instead sections 6, 13 and 14 are characterised by two peak values of amplification factors.

With reference to the above mentioned sections, Table 14 and Table 15 summarize the maximum value of thickness H and width L of the valley. The H/L ratio is also listed. It is not possible to find a clear correlation between the H/L ratio and the amplification pattern; it is worth to note that the motion recorded at the ground surface also depends on the locally irregular geometry of the topographic surface and of the subsurface strata interfaces.

- in the soft soil valley area it might be recognised different patterns obtained by 1D and 2D analyses. In more detail, related to amplification factor FH_{01-05} and F_{PGA} , looking carefully at each sampled point it is possible to deduce that the 2D analysis leads to different values with respect to the 1D.

Section	H (m)	L (m)	H/L
3	10	70	0.14
4	15	151	0.10
5	15	225	0.07
7	13	95	0.14
12	35	154	0.23

Table 14 Size of the valley characterized by one peak value of amplification factors

Section	H (m)	L (m)	H/L
6	31	295	0.11
13	27	194	0.14
14	18	295	0.06

Table 15 Size of the valley characterized by two peak values of amplification factors

With reference to 2D scheme, the Figs. 174-194 listed in the appendix report the profiles of the mean values of the amplification factors obtained with reference to the section sketched in each figure together with the corresponding values obtained at the same point along by the cross section analysis, in red dashed line and black triangles respectively.

For example, in Fig. 97 Cmx_C0y_ax_2D represents the mean value of amplification factors obtained with reference to section 2. C0x_Cmy_ay_2D is related to the mean values obtained at the intersection points between section 2 and sections from 8 to 22 determined with reference to all these one by one.

It is possible to observe that the greater differences between amplification factors obtained with reference to the section along x direction and those related to y direction take place where the topographic surface and/or the interface between soil layers are really complex in any direction.

At the intersection point between sections 2 and 22, $x = 1400$ m in Fig. 97 and $y = 500$ m in Fig. 98, is possible to observe the greater difference between $C_{mx_C0y_ax_2D}$ and $C_{0x_Cmy_ay_2D}$ due to the topography of the ground surface, which varies along all the directions.

The effect of the complex geometry interface between soil layers is enlighten for $400 \leq x \leq 700$ m in Figs. 99-101 and $700 \leq y \leq 900$ m in Figs. 102-104.

In Fig. 105 sections 2, 4, 5, 6, 12, 13, 14, 22 are sketched to point out the shape of ground surface and sub-interfaces which causes the above different results from 2D analyses along x and y directions. For example point (1400, 500) is located at the crest of the section 22 but it is at the sub-horizontal ground surface of the section 2 or point (500, 900) is at the center of the valley of section 6 but it is nearby the border of the valley of section 13.

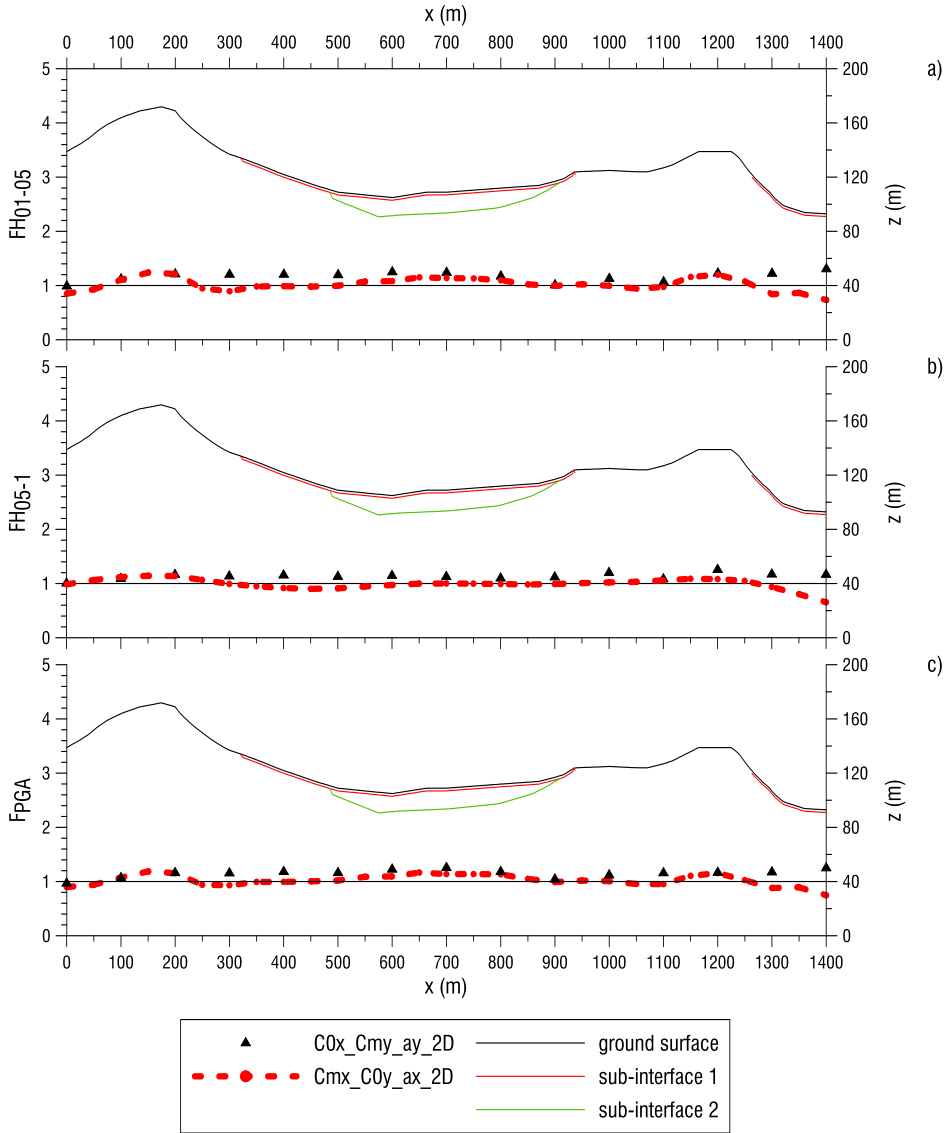


Fig. 97 Comparison between 2D mean values for section 2 and that obtained by transversal sections a) FH₀₁₋₀₅, b) FH₀₅₋₁, c) F_{PGA}

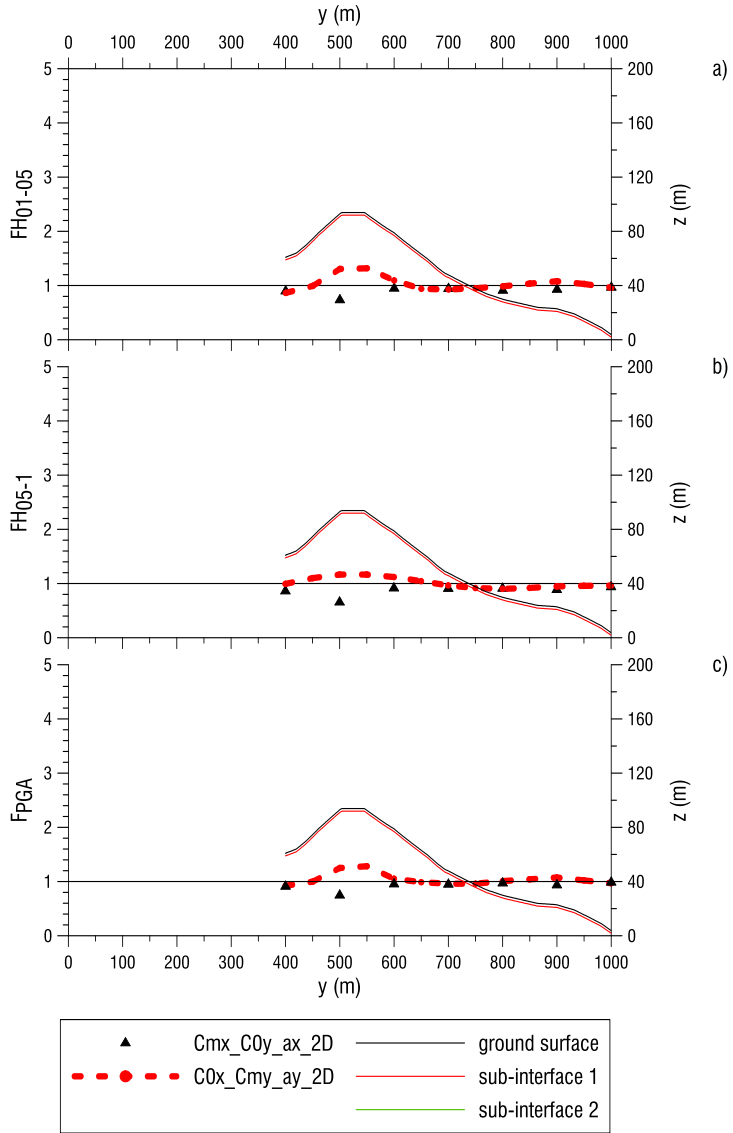


Fig. 98 Comparison between 2D mean values for section 22 and that obtained by transversal sections
a) FH_{01-05} , b) FH_{05-1} , c) F_{PGA}

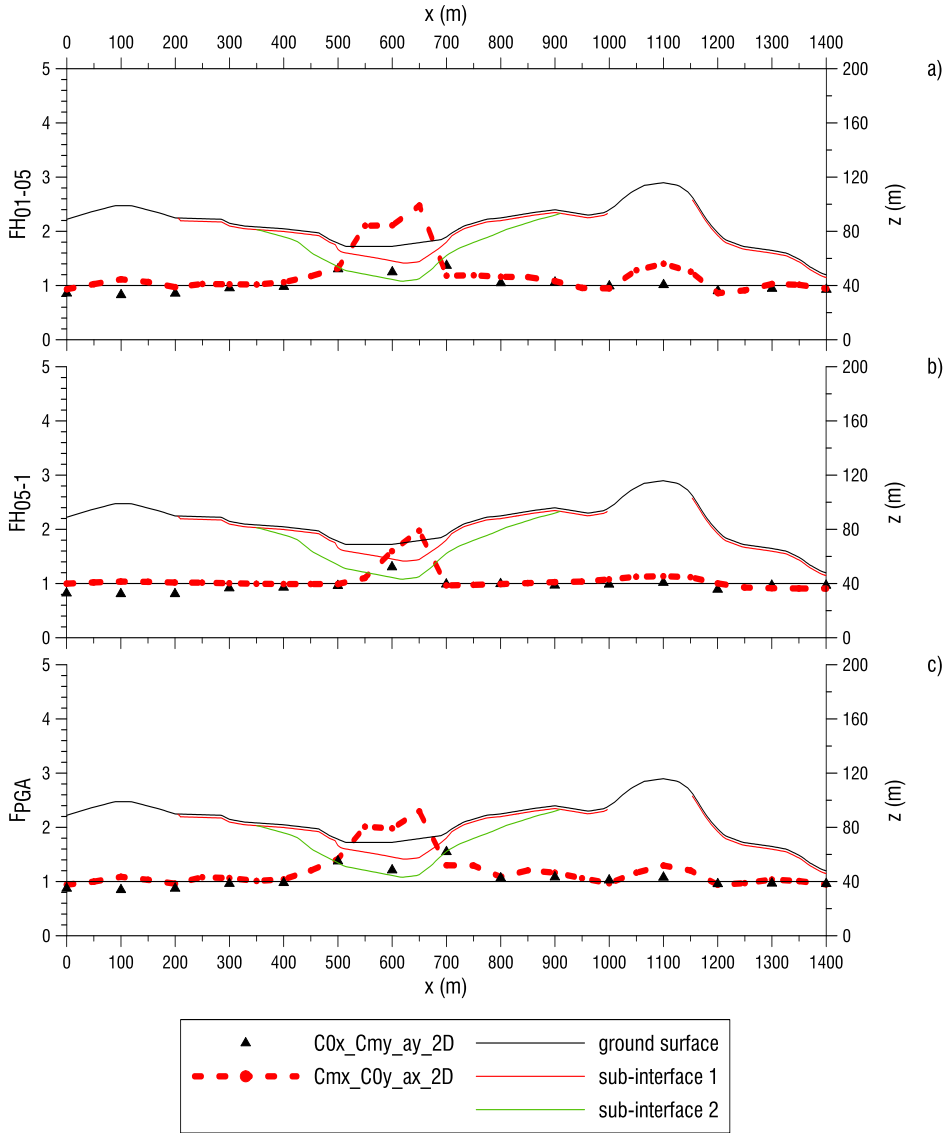


Fig. 99 Comparison between 2D mean values for section 4 and that obtained by transversal sections a) FH_{01-05} , b) FH_{05-1} , c) F_{PGA}

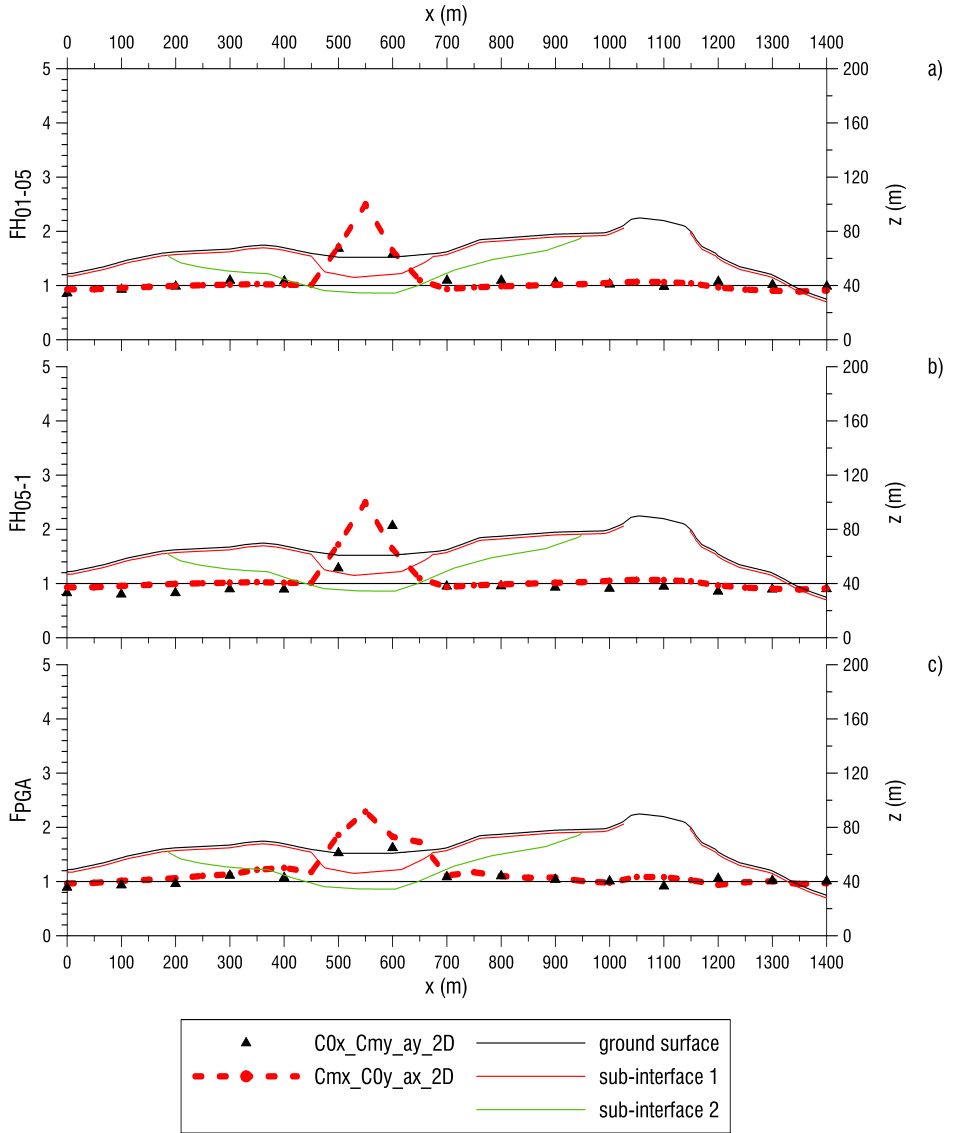


Fig. 100 Comparison between 2D mean values for section 5 and that obtained by transversal sections
a) FH_{01-05} , b) FH_{05-1} , c) F_{PGA}

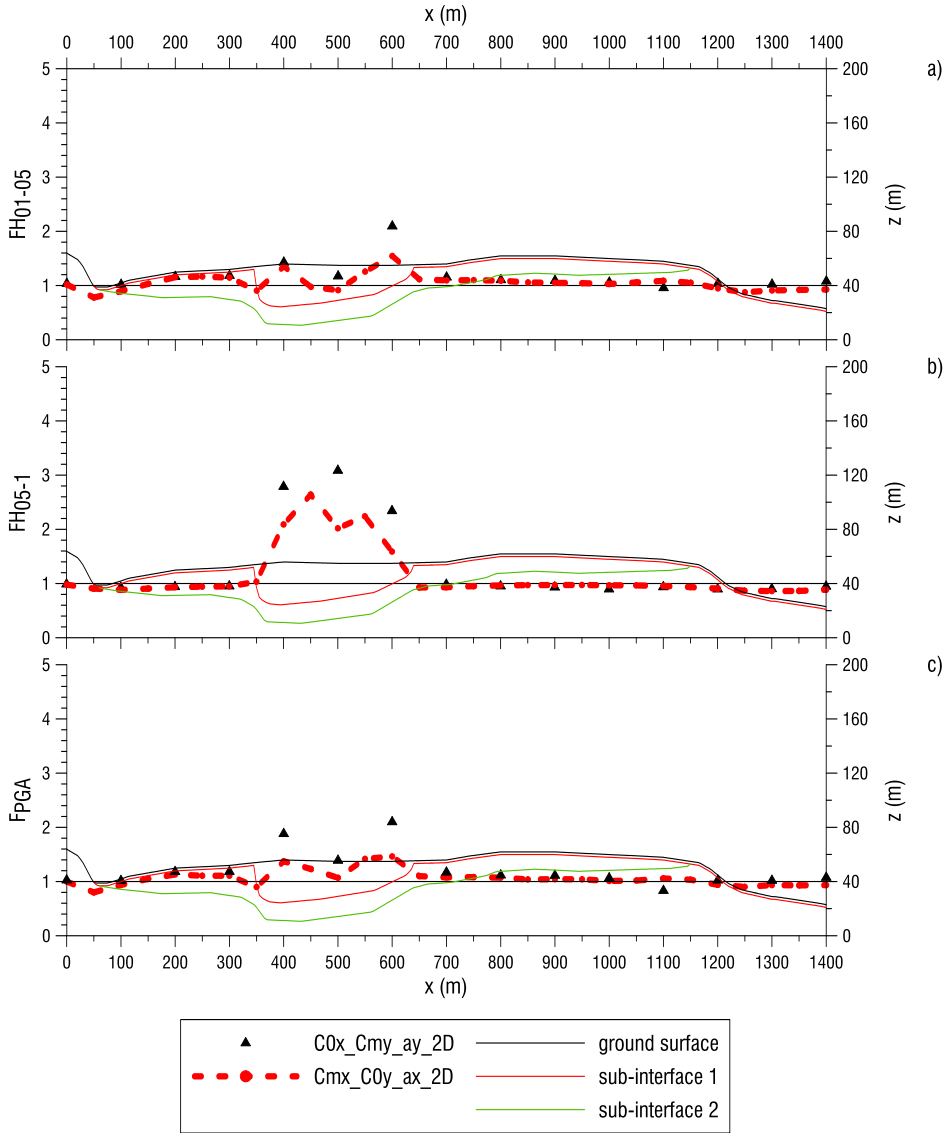


Fig. 101 Comparison between 2D mean values for section 6 and that obtained by transversal sections
 a) FH_{01-05} , b) FH_{05-1} , c) F_{PGA}

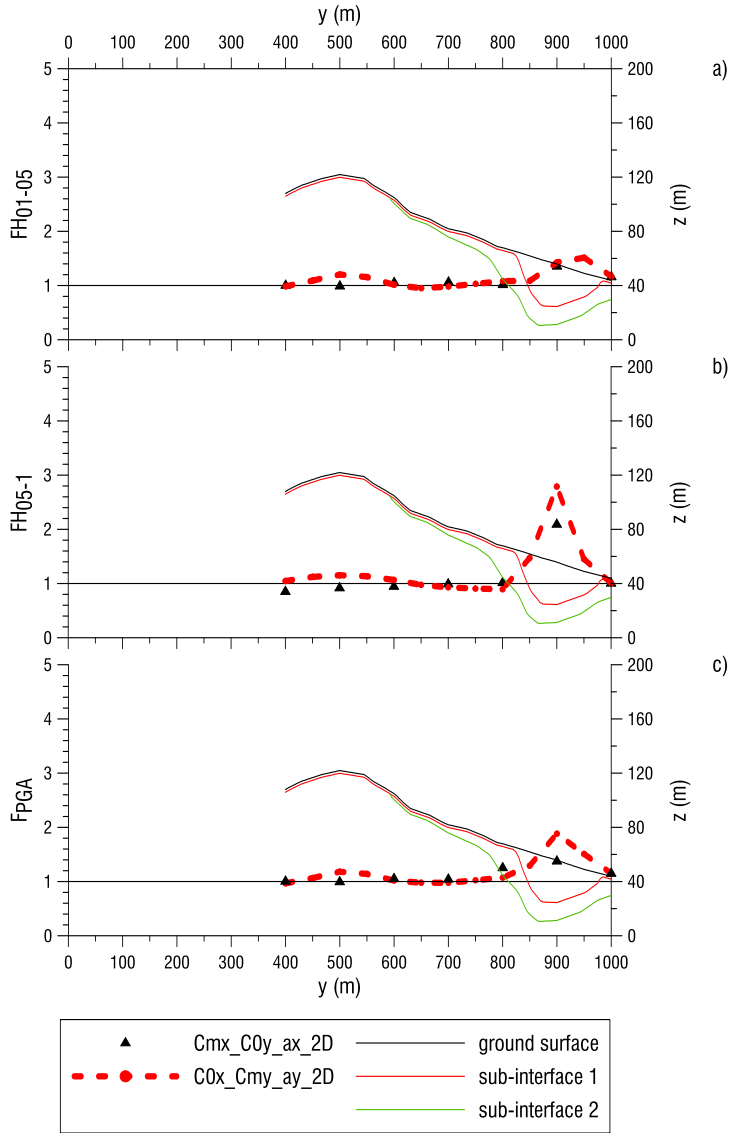


Fig. 102 Comparison between 2D mean values for section 12 and that obtained by transversal sections
a) FH_{01-05} , b) FH_{05-1} , c) F_{PGA}

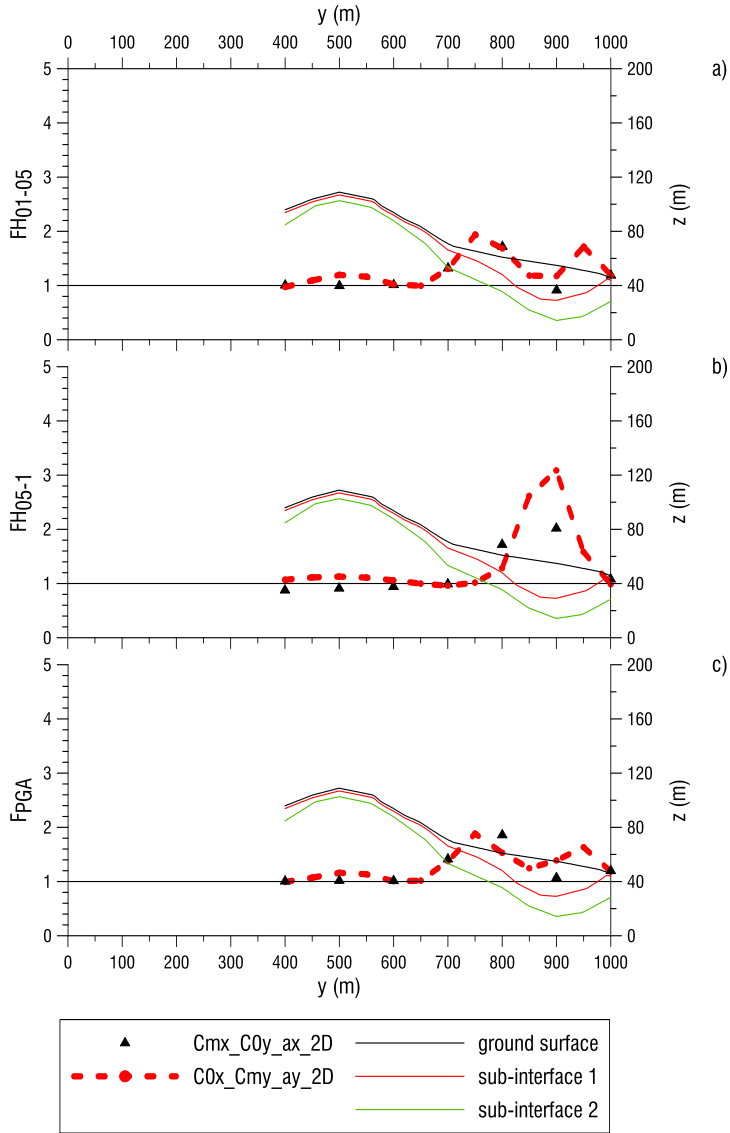


Fig. 103 Comparison between 2D mean values for section 13 and that obtained by transversal sections
a) FH_{01-05} , b) FH_{05-1} , c) F_{PGA}

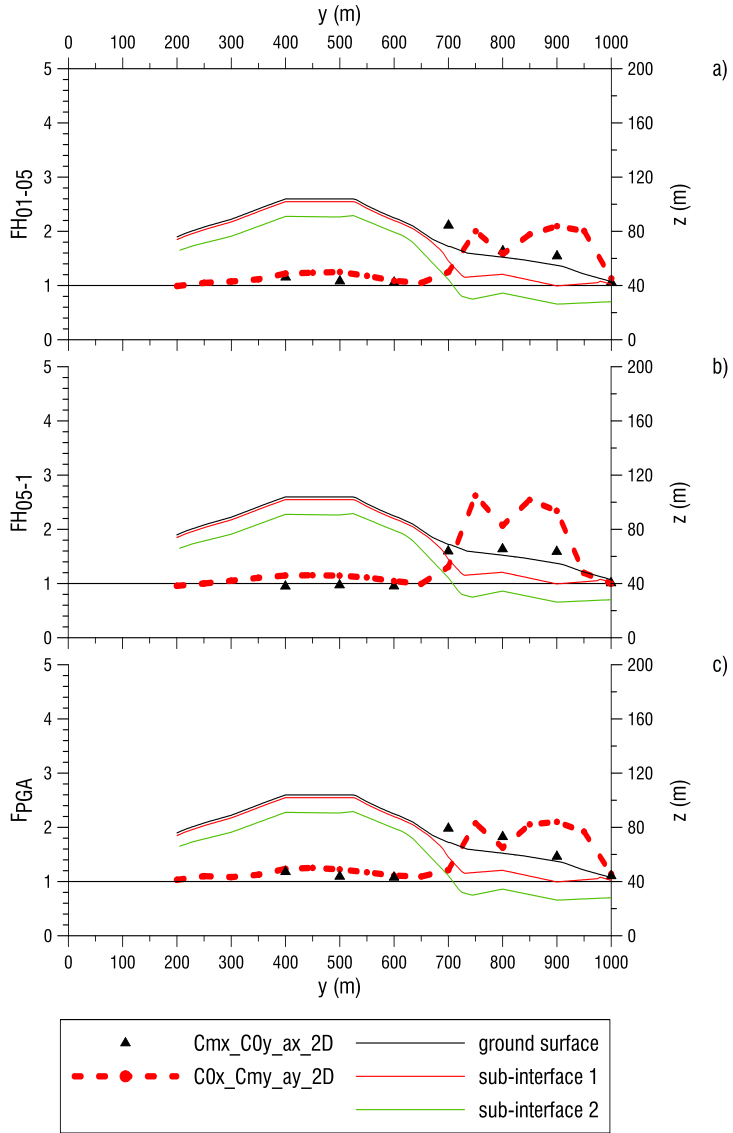


Fig. 104 Comparison between 2D mean values for section 14 and that obtained by transversal sections
 a) FH_{01-05} , b) FH_{05-1} , c) F_{PGA}

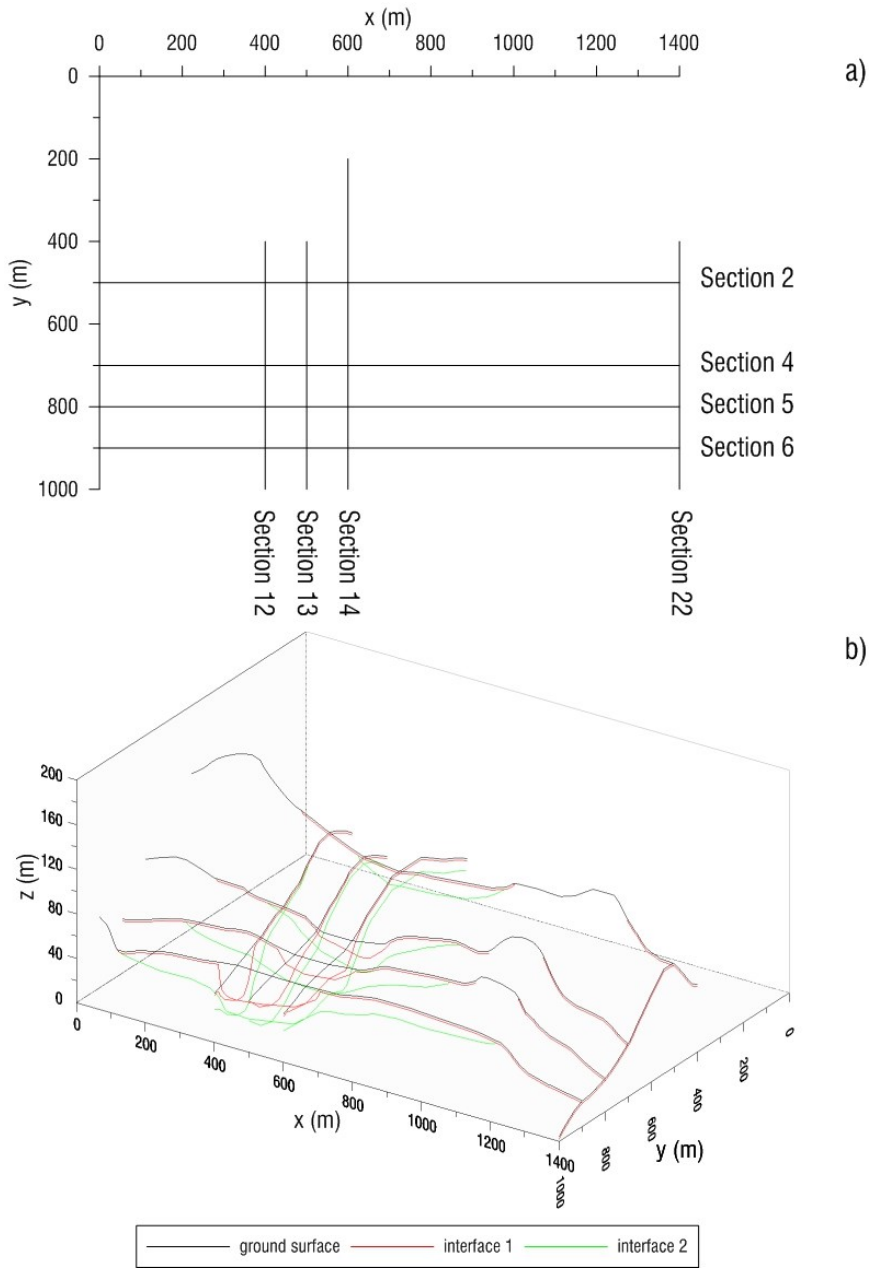


Fig. 105 Studied sections which enlighten the 2D issue. a) plane view, b) 3D view

All the previous data must be collected to create the Seismic Microzonation maps. Before showing these maps, it is worth looking at Fig. 106 where the thickness of unit 1 is graphically reported. That unit is the one characterised by the softest material in the area under investigation. It is worth noting that the portion of the studied area characterized by the valley condition (filled with unit 1) is about 250 m x 300 m with a maximum depth minor than 30 m, i.e. it is relatively small as compared to the whole studied area. Furthermore, it is characterised by a rather irregular interface separating it from the underlying stiffer soils.

The Seismic Microzonation maps, based on the 2D amplification determined along x and y directions, are reported in Figs. 107-109. The same figures also show the topographic surface of Bovino urban area and the Unit 1 thickness map.

All the previous suggestions, related to the profiles of amplification factors for any sections viewed separately, are confirmed:

- the largest amplification is due to the presence of the soft soil valley. FH_{01-05} and F_{PGA} attain their maximum values at the centre of the valley area. It should be observed that, due to the really complex geometry of interfaces between soil layers, the centre of the valley does not correspond to the projection on the ground surface of the deepest point of the unit 1 layer. Furthermore, the mean amplification factor FH_{05-1} becomes greater for increasing thickness of the valley (unit 1);
- for all the three selected amplification factors, values slightly greater than one are due to topographic effect in presence of outcropping unit 3;
- a somewhat de-amplification of the reference motion is observed at the toe of the hill.

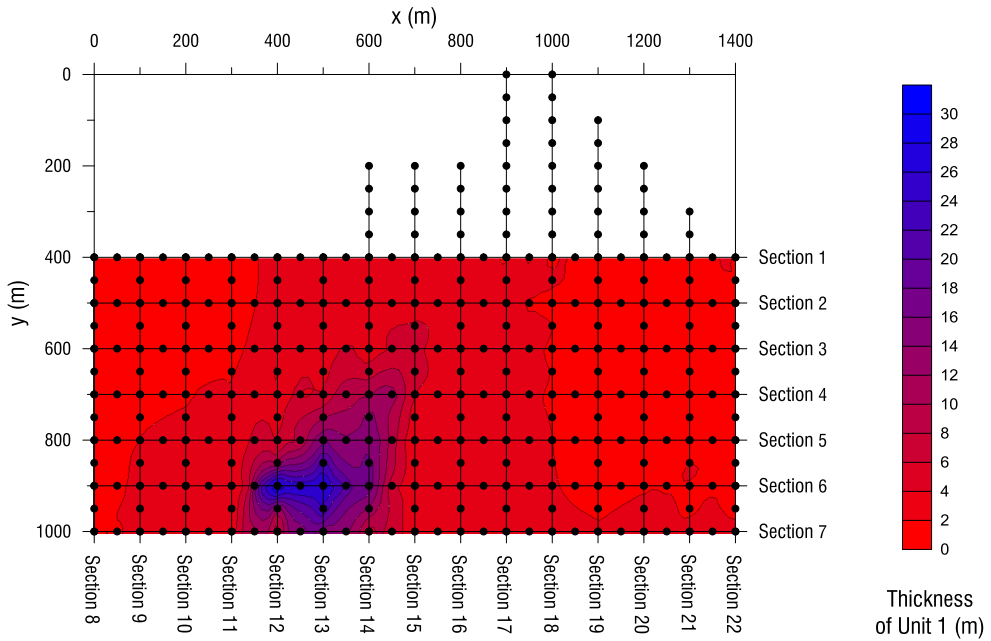


Fig. 106 Unit 1 thickness map

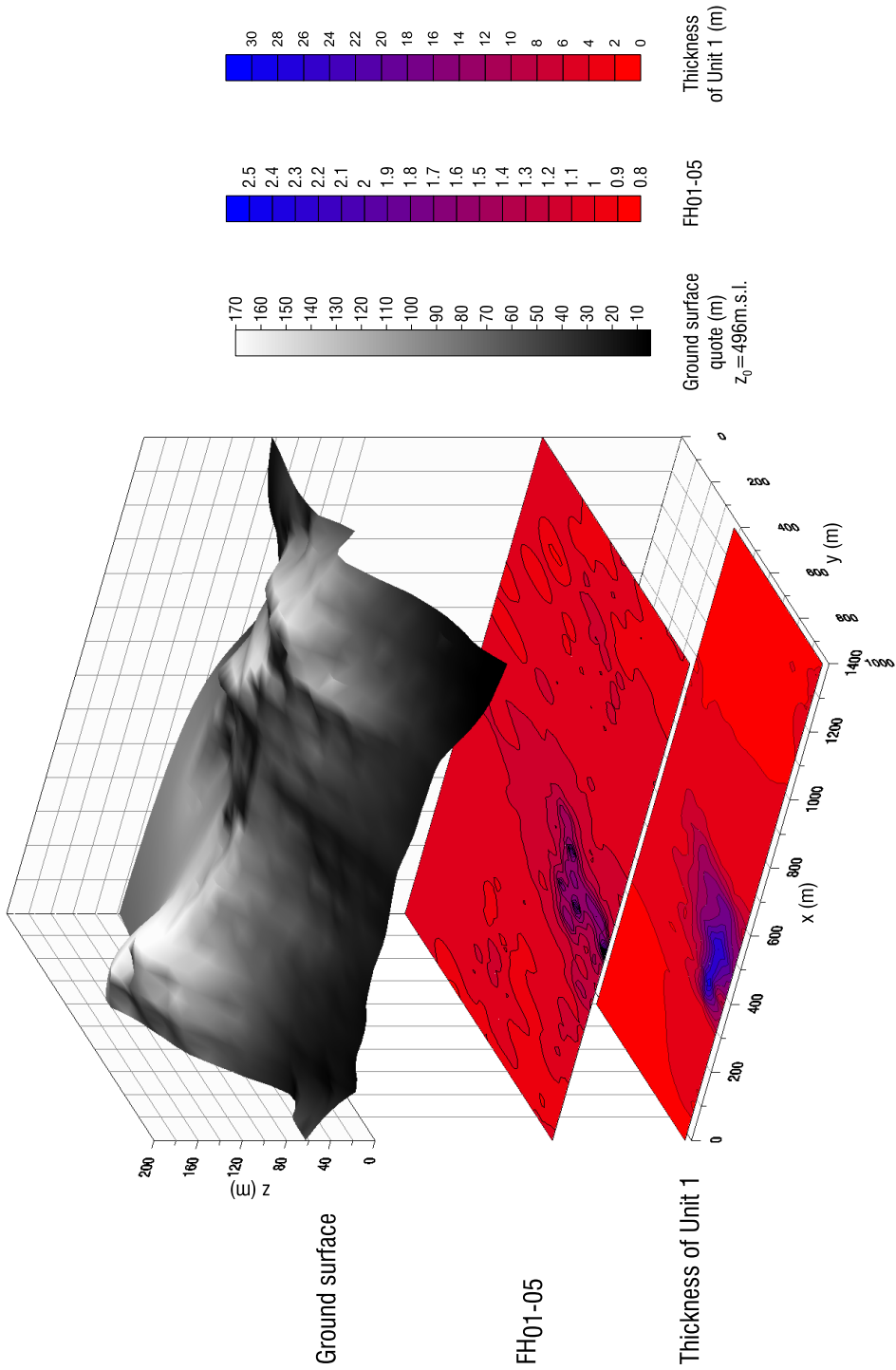


Fig. 107 Topography of Bovino urban area, Seismic Microzonation map related to FH₀₁₋₀₅ (QUAKE/W) and map of the unit 1 thickness

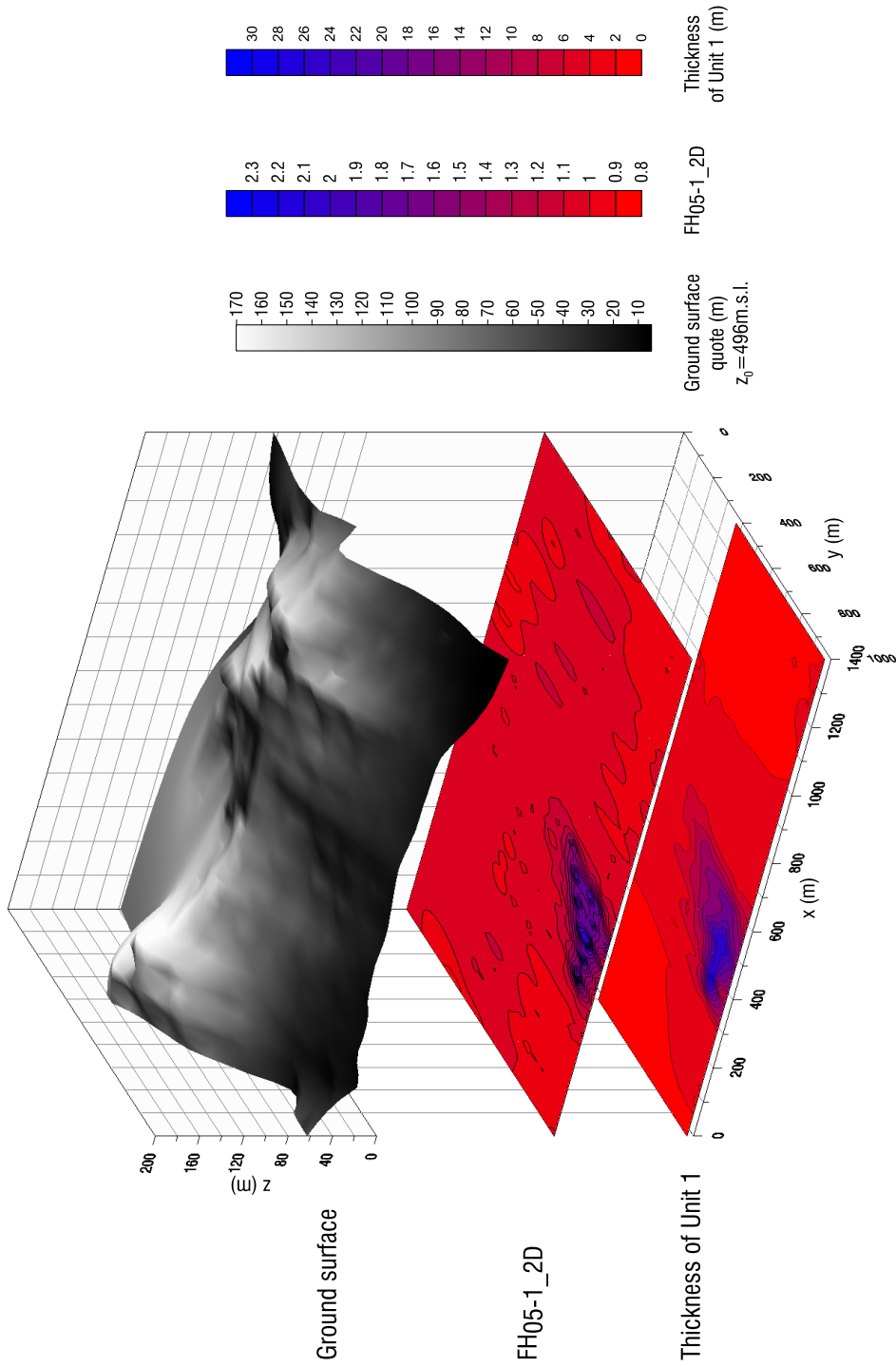


Fig. 108 Topography of Bovino urban area, Seismic Microzonation map related to FH₀₅₋₁ (QUAKE/W) and map of the unit 1 thickness

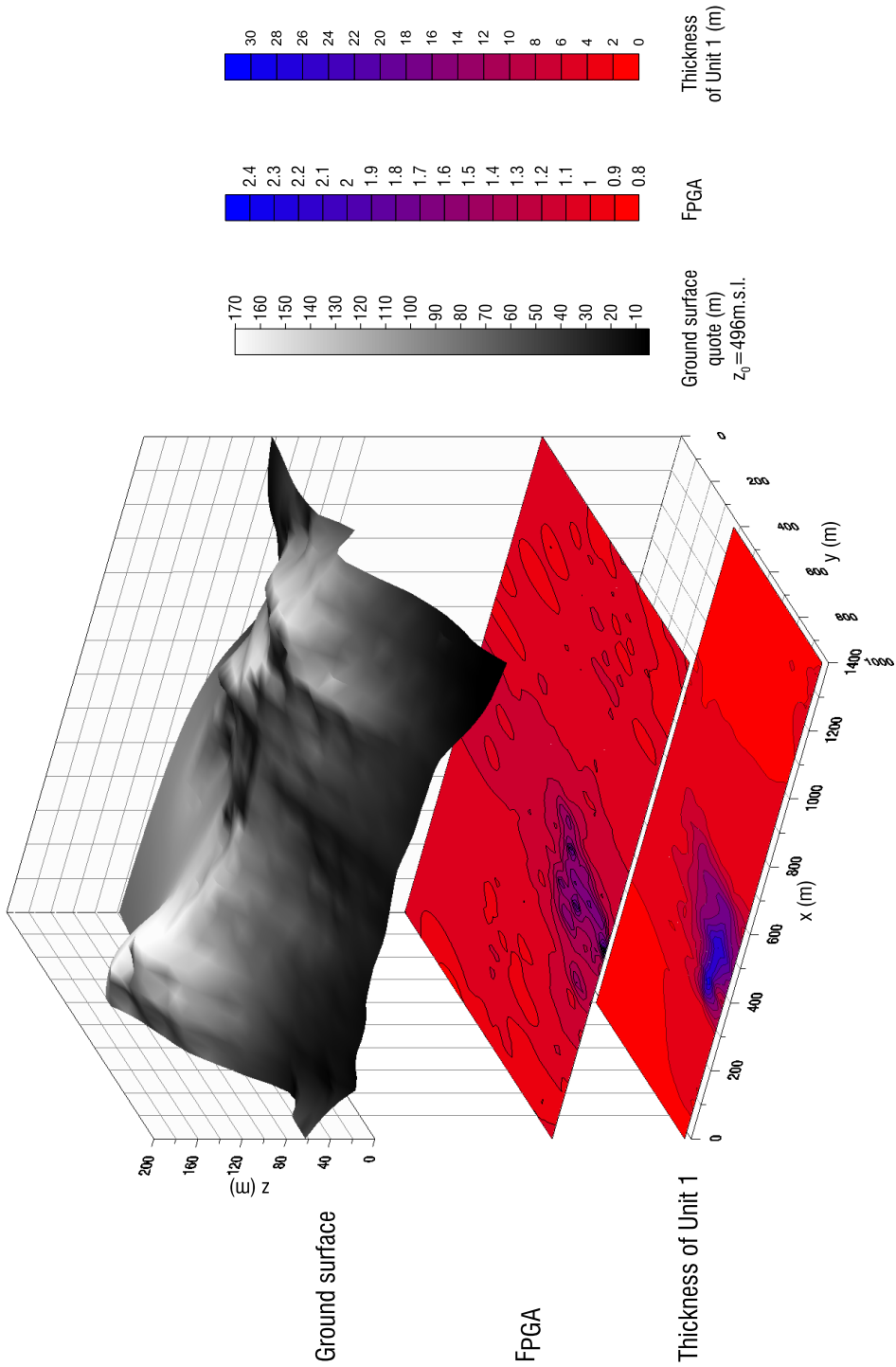


Fig. 109 Topography of Bovino urban area, Seismic Microzonation map related to F_{PGA} (QUAKE/W) and map of the unit 1 thickness

3.8. Site response analysis. PLAXIS 3D

In this section the results obtained by the code PLAXIS 3D are discussed. This code version was used to perform site response numerical analyses using 1D, 2D and 3D schemes. In the next, for sake of brevity, the code version PLAXIS 3D will be referred to as PLAXIS.

It is worth noting that the increase in the 3D model size requires more powerful hardware system and long-time calculation. Relating to Bovino urban area the examined portion reproduced in the PLAXIS model, shown in Fig. 110, was reduced with respect to the QUAKE/W one (Fig. 83). The 2D analyses were performed only for sections 2, 3, 4, 5, 6, 11, 12, 13, 14, 15, 16 and 21. The 3D model is delimited by the section 1, 22, 7 and 8 (Fig. 110a).

The fifty sampled points represented in Fig. 110 are the same for 1D, 2D and 3D schemes. Additional two-thousand sampled points were considered in the 2D analyses; as a consequence, the acceleration time history was determined at ground surface with respect to point located 5 ÷ 25 m apart from each other along x or y directions.

The adopted boundary conditions are the same discussed in the chapter 2. In particular, referring to an input motion applied along x or y direction the boundary conditions are summarised in Table 16 and Table 17. Moreover, related to a 3D analysis simulating the case of horizontal components applied along x and y directions at the same time, the boundary conditions are reported in Table 18.

Viscous boundary were also considered. This boundary condition corresponds to a situation in which viscous dampers are activated in the x and y direction along the boundary, providing a resistant force in the normal and tangential direction that is proportional to the velocity in the near-boundary material (Lysmer & Kuhlemeyer 1969).

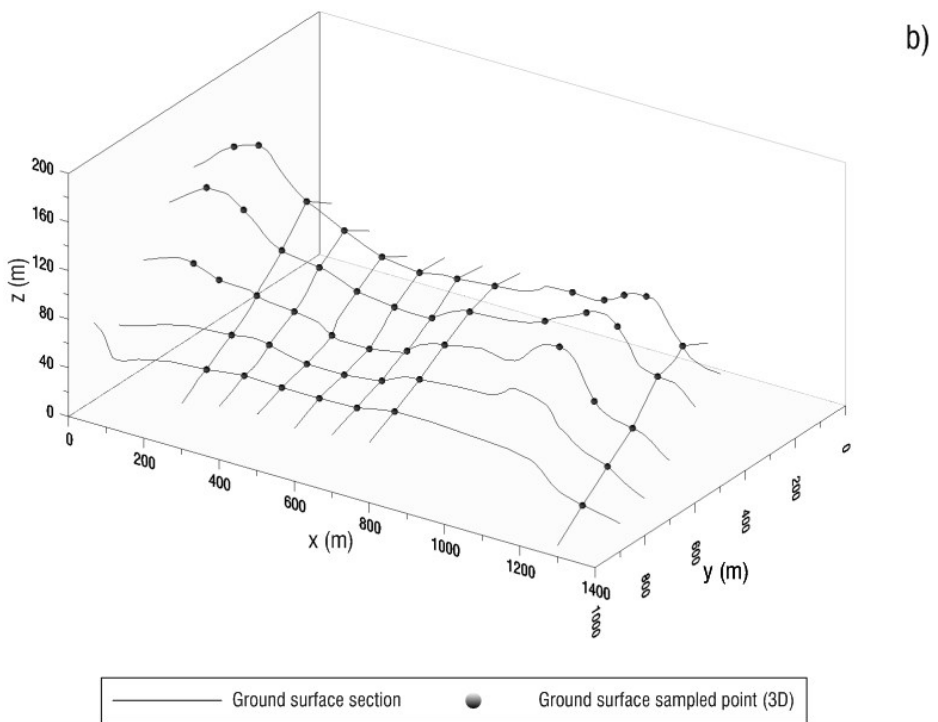
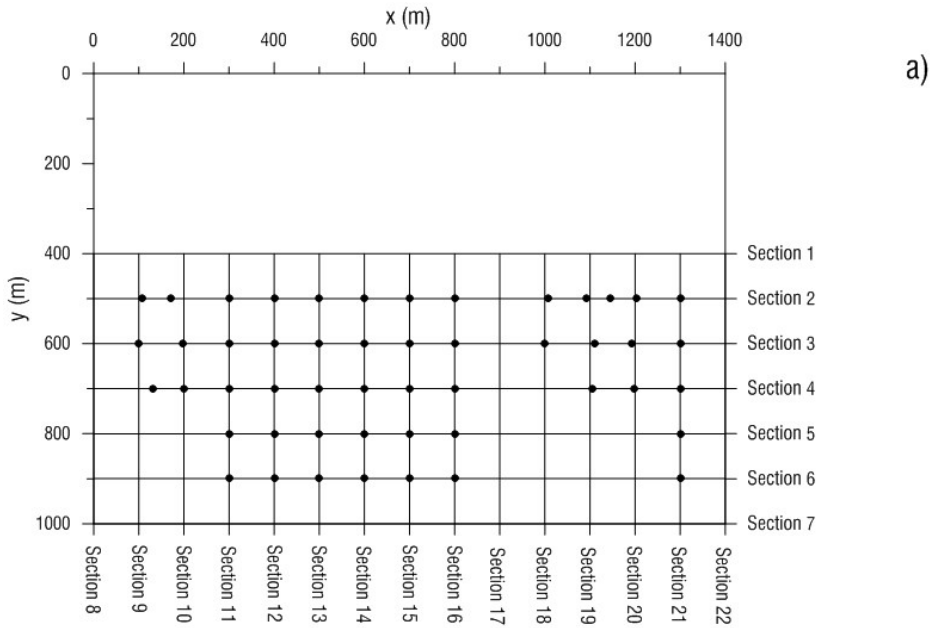


Fig. 110 Sections (PLAXIS 3D) and sampled points considered for the Bovino urban area. a) plane view, b) 3D view

Vertical boundary	Horizontal base	Ground surface
$u_x = \text{free}$ $u_y = u_z = 0$	$a_x(t) = 0.5 \cdot a_{\text{outcrop}}(t)$ $a_y = a_z = 0$	$u_x = u_y = u_z = \text{free}$
free-field (PLAXIS 2016)	compliant base (PLAXIS 2016)	

Table 16 Boundary conditions for PLAXIS analyses, x horizontal component as input

Vertical boundary	Horizontal base	Ground surface
$u_y = \text{free}$ $u_x = u_z = 0$	$a_y(t) = 0.5 \cdot a_{\text{outcrop}}(t)$ $a_x = a_z = 0$	$u_x = u_y = u_z = \text{free}$
free-field (PLAXIS 2016)	compliant base (PLAXIS 2016)	

Table 17 Boundary conditions for PLAXIS analyses, y horizontal component as input

Vertical Boundary	Horizontal base	Ground surface
$u_x = u_y = \text{free}$ $u_z = 0$	$a_x(t) = 0.5 \cdot a_{x,\text{outcrop}}(t)$ $a_y(t) = 0.5 \cdot a_{y,\text{outcrop}}(t)$ $a_z = 0$	$u_x = u_y = u_z = \text{free}$
viscous (PLAXIS 2016)	compliant base (PLAXIS 2016)	

Table 18 Boundary conditions for PLAXIS analyses, two horizontal components

It should be outlined that a verification of all the above boundary conditions were carried out with reference to canonical case study but it is not showed here for sake of brevity.

The linear elastic model was considered for unit 3 (the seismic bedrock).

The non-linear behaviour of units 1 and 2 was simulated by the Hardening Soil Model with small strain stiffness (HSsmall in the following) which is available in the library of code PLAXIS (Benz 2006; Benz et al. 2009; di Lernia 2014; Amorosi et al. 2016; PLAXIS 2016).

In Table 19 the parameters adopted for HSsmall are summarised.

As a first step it was necessary to compare the results obtained under 1D and 2D conditions to those discussed in the previous paragraph (i.e. obtained by QUAKE/W). To compare the numerical results obtained with the two FE codes and related soil constitutive models, the strength parameters of the HSsmall model were fixed at their highest possible values, so that plasticity would not be activated during the analyses and the response would only be characterised by the para-elastic formulation of the HSsmall model. Similarly, the initial dimension of the shear hardening yielding surface was artificially enlarged, by simulating loading and unloading phases, to obtain a purely non-linear response in the calculations (di Lernia 2014).

Parameter	Unit 1	Unit 2
A	0.385	0.385
$\gamma_{0.7}$ (%)	0.025	0.025
G_{ur} (kPa)	26212	419397
G_0^{ref} (kPa)	73394	1174312
ρ (kg/m ³)	1.83	1.83
V_s (m/s)	200	800
γ (kN/m ³)	18	18
γ_{cut_off} (%)	0.044	0.044
M	0	0
p'_{ref} (kPa)	100	100

Parameter	Unit 1	Unit 2
v_{ur}	0.25	0.25
E_{ur}^{ref} (kPa)	65531	1048493
E_{oed}^{ref} (kPa)	21844	349498
E_{50}^{ref} (kPa)	21844	349498
c' (kPa)	1.E+35	1.E+35
ϕ' (°)	89	89
$D_{rayleigh}$ (%)	1.053	1.053
f_m (Hz)	1.00	1.00
f_n (Hz)	10.00	10.00
α_R	0.12027	0.12027
β_R	0.00030	0.00030

Table 19 HSs parameters for Unit 1 and 2

The adopted shear stiffness degradation and damping curves are shown in Fig. 111. In the same figure the Darendeli (2001) curves are also reported.

Rayleigh damping was also implemented to provide an additional small amount of damping ($D_{\text{Rayleigh}} = 1.05\%$) as suggested in the work of Régnier et al. (2016). PLAXIS allows to select two Rayleigh control frequencies, the value of which are reported in the previous Table 19.

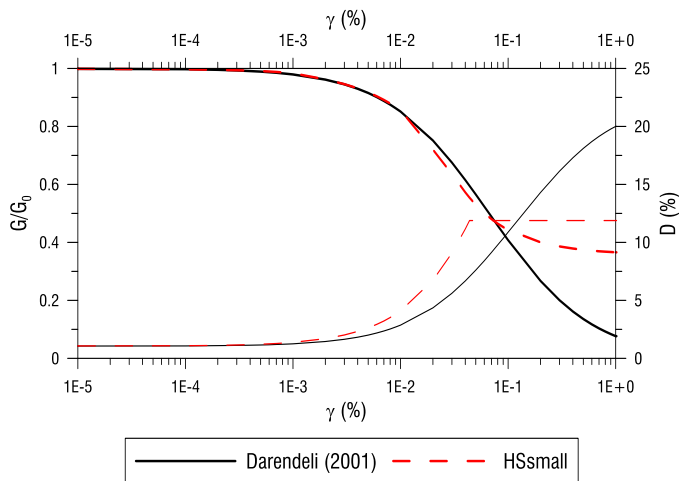


Fig. 111 $G(\gamma)/G_0$ and $D(\gamma)$ curves from Darendeli (2001) and as implemented in PLAXIS

As stated for QUAKE/W analyses, the maximum size of the finite element and the time step of analyses have been defined how reported in the chapter 2.

Differently from the QUAKE/W analyses, for the PLAXIS models the size of the mesh has not been increased with respect to the area under investigation, thanks to the adopted vertical boundary conditions, listed in Table 16-Table 18.

The comparison between QUAKE/W and PLAXIS results is now discussed.

The analyses performed by PLAXIS are related to two signals whose main features are listed in Table 20. It is enlightened that the signal called Cx is the same C3 of Table 12. This signal was chosen for this verification exercise as being the shortest one (thus reducing the computational time) and because the profiles of amplification factors obtained by it in the QUAKE/W analyses are the most similar to the mean profile. Thus the results obtained assuming the reference signal C3 as outcrop motion could

be considered representative of the mean seismic response of the examined area. A low-pass filter, assuming $f_{\max} = 10$ Hz, was applied to the two scaled reference motions. Acceleration time history, Fourier spectrum and response spectrum (5% structural damping) of the filtered and scaled signals are sketched in Fig. 112.

Signal ID	Earthquake ID	Station ID	Earthquake name	Date	Site class	M_w	Scale factor	Spectrum compatible component
Cx	80	ST45	Calabria	11/03/1978	A	5.2	2.92	y
Cy	80	ST45	Calabria	11/03/1978	A	5.2	2.92	x

Table 20 Main features of the reference outcrop motion selected for PLAXIS simulation

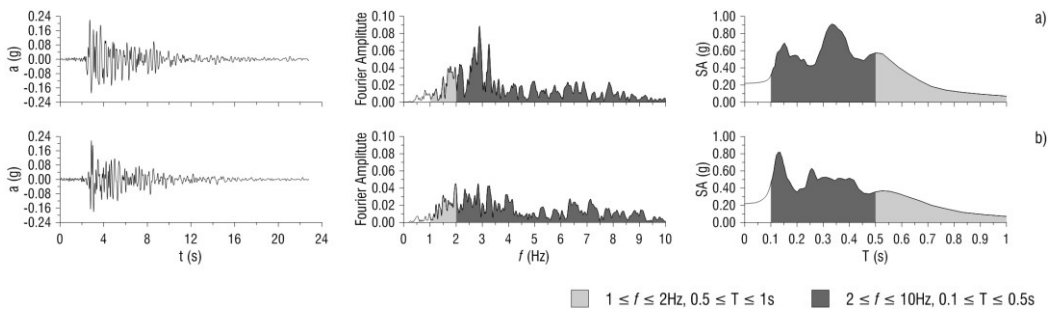


Fig. 112 Acceleration time history, Fourier spectrum and response spectrum for the two reference motion: a) Cx and b) Cy

Figs. 113-115 show a comparison between QUAKE/W and PLAXIS results obtained for the 2D models of sections 2, 4 and 5. The results related to the two FE codes are in satisfactory agreement. Thus, the PLAXIS numerical approach should be considered as verified and, as such, the code could then be used as the unique tool to perform all the following analyses, not only limited to the 1D and 2D cases but obviously allowing to extend the model to the 3D one.

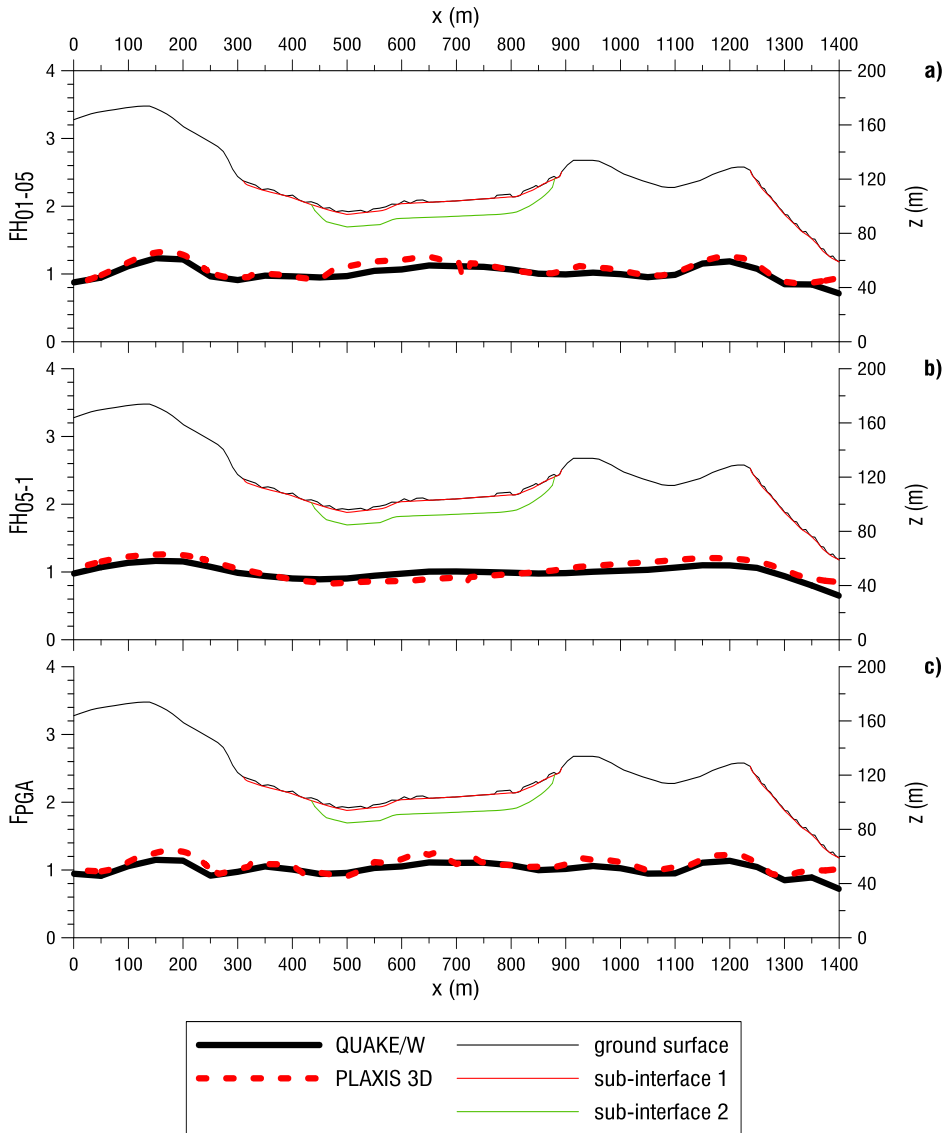


Fig. 113 Comparison between 2D profile of amplification factors for section 2 obtained by means of QUAKE/W and PLAXIS, a) $F_{H_{01-05}}$, b) $F_{H_{05-1}}$, b) F_{PGA}

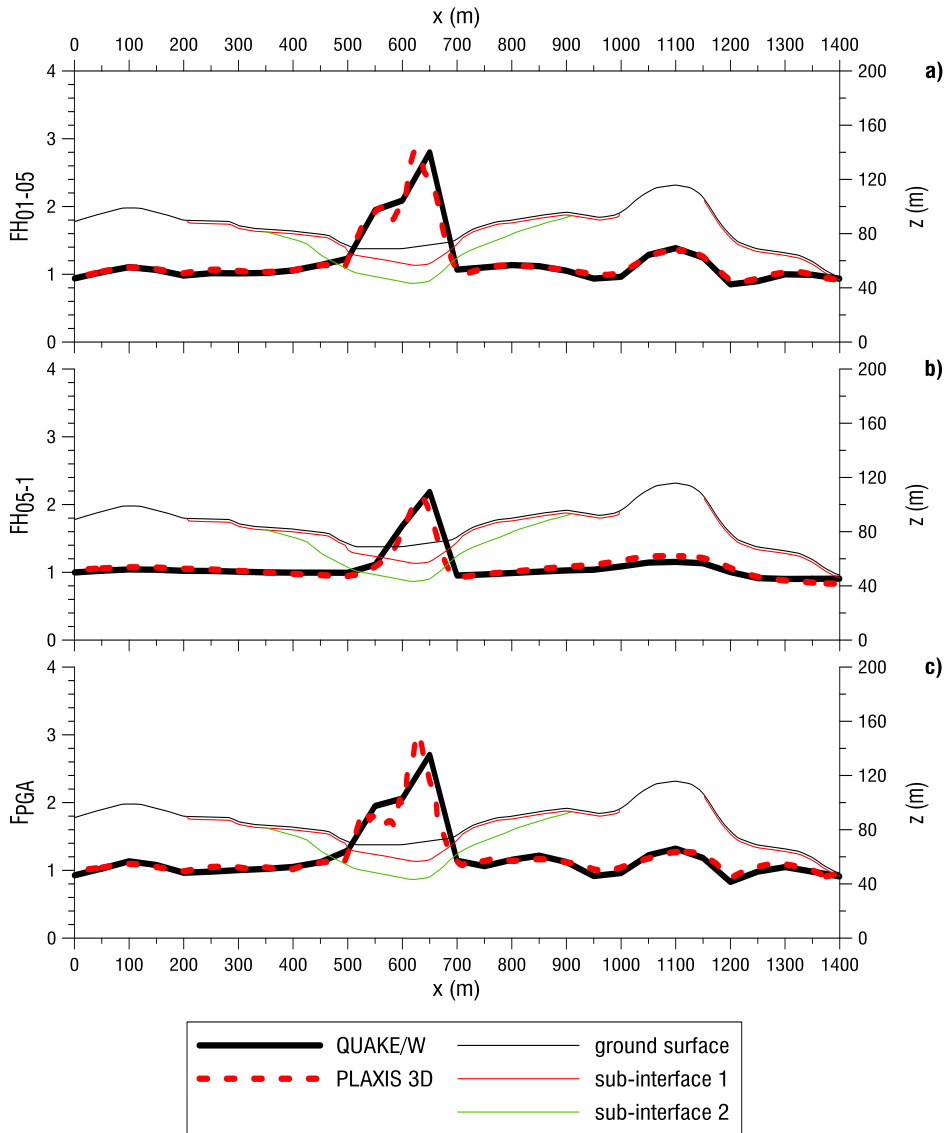


Fig. 114 Comparison between 2D profile of amplification factors for section 4 obtained by means of QUAKE/W and PLAXIS, a) $F_{H_{01-05}}$, b) $F_{H_{05-1}}$, c) F_{PGA}

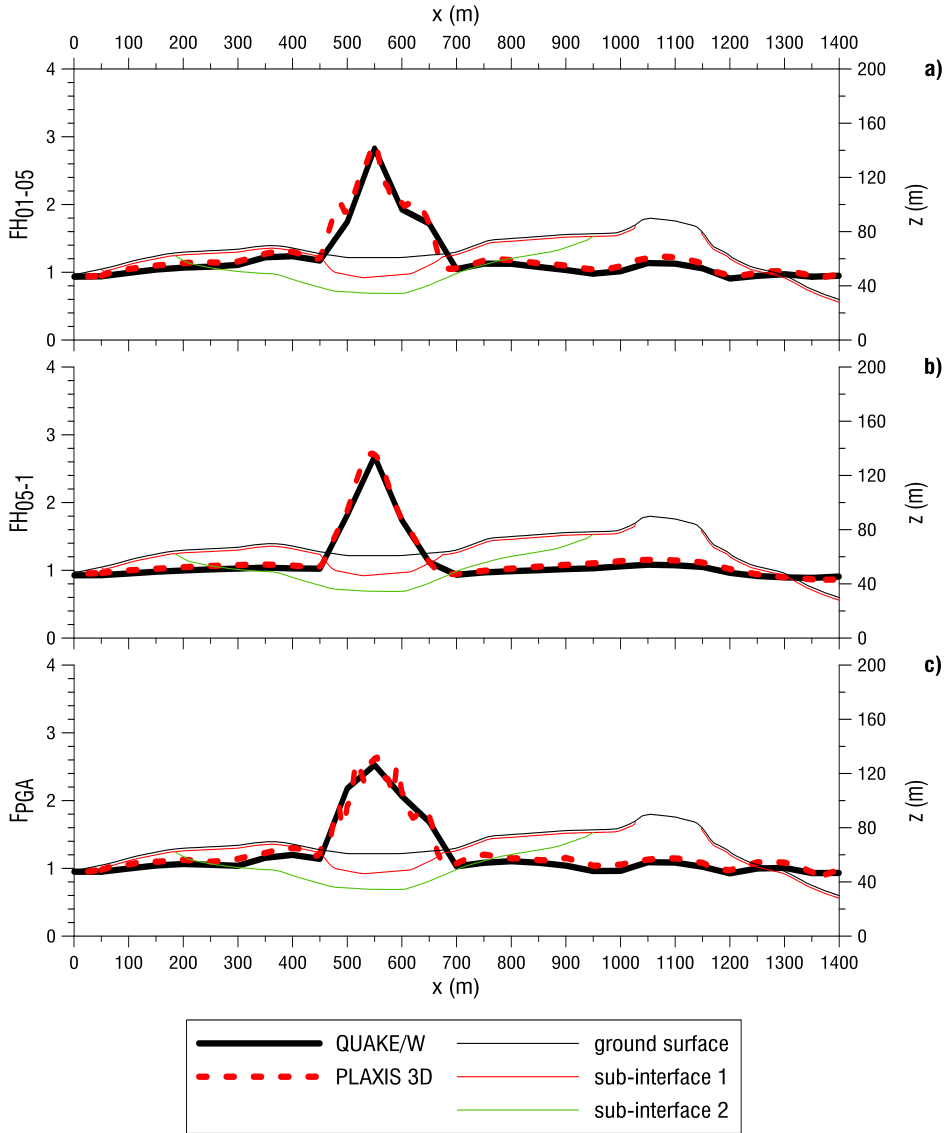


Fig. 115 Comparison between 2D profile of amplification factors for section 5 obtained by means of QUAKE/W and PLAXIS, a) FH_{01-05} , b) FH_{05-1} , b) F_{PGA}

In the next, the results of all the analyses according to 1D, 2D and 3D schemes carried out using PLAXIS are shown.

The script Ckx_Cky_ai (where k = 0, x, y and i = x, y), used to define the amplification factors profiles, is composed of three part. The first two parts, Ckx and Cky, are related to the input motion considered in the x and y direction, respectively. The third one, ai, is referred to the recorded output. For example, C0x_Cxy_ay stays for: no motion applied in the x direction, reference motion Cx applied along y direction and ground surface acceleration determined along the y direction. Table 21 lists the performed analyses and the recorded output used to determine the AF.

Analysis ID	Scheme	Input Signal ID	Direction of input motion	Output
A1	1D	Cx	/	Cx_a
A2	1D	Cy	/	Cy_a
A3	2D	Cx	x	Cxx_C0y_ax
A4	2D	Cy	x	Cyx_C0y_ax
A5	2D	Cx	y	C0x_Cxy_ay
A6	2D	Cy	y	C0x_Cyy_ay
A7	3D	Cx	x	Cxx_C0y_ax
A8	3D	Cy	x	Cyx_C0y_ax
A9	3D	Cx	y	C0x_Cxy_ay
A10	3D	Cy	y	C0x_Cyy_ay
A11	3D	Cx	x	Cxx_Cyy_ax
		Cy	y	Cxx_Cyy_ay

Table 21 Performed numerical analyses by means of PLAXIS

The subsequent comparisons are proposed and the corresponding figures are listed in the appendix:

- A1 vs A3 vs A7 and A2 vs A4 vs A8 to point out the difference between the results assuming the same reference motion for different dimensional schemes (1D, 2D and 3D) of analysis (Figs. 196-219);
- A3 vs A5 and A4 vs A6 to assess the dependency of amplification factors by the direction of input motion referring to 2D site response analysis (Figs. 220-243);
- A7 vs A9 and A8 vs A10 to compare the 3D seismic response related to different direction of the input motion (Figs 244-267);
- A7 vs A11 and A10 vs A11 to enlighten the effects due to the simultaneous application of two input motions as compared to the one by one case (Figs. 268-291).

The comparison A1 vs A3 vs A7 and A2 vs A4 vs A8 (i.e. 1D vs 2D vs 3D) results in good agreement for that portion of the studied area characterised by really thin layer of material 1 or by sub-horizontal ground surface of outcropping rock. On the other hand, the larger is the depth of material 1 and the dimension of the valley, the more intense is the amplification of 3D model as compared to the 2D and 1D ones. In more detail, FH_{05-1} from 3D is greater than 2D for the case of a large and deep valley (section 6, Fig. 118 and Fig. 119), while FH_{01-05} and F_{PGA} gain highest value from 3D for the case of thin and deep valley (section 12, Fig. 120 and Fig. 121). Thus, the major differences between 1D and 2D or 3D results are related to the thickest unit 1 layer. Referring, for example, to section 6 (Fig. 118 and Fig. 119) and section 13 (Fig. 122 and Fig. 123), where the thickness of unit 1 is about 30 m, the 1D AF is slightly greater than 1, while the 2D AF might attain a value up to 3, because of the geometric amplification. Furthermore, the three-dimensionality of the geometry generally enhances the seismic waves focalization at the ground surface of the valley area. For example, with reference to the ground surface point at $x = 500$ m of section 6 (Fig. 118), the 2D mean amplification factor $FH_{01-05}(x = 500\text{m}, 2\text{D})$ is equal to 1.25, while the one computed by 3D simulation $FH_{01-05}(x = 500\text{m}, 3\text{D})$ achieves a value of 1.88.

With reference to A3, A4, A5 and A6 analyses, as already observed for QUAKE/W simulations, for increasing complexity of the sub-interface and the ground surface

shapes, the amplification strongly depends on the direction of the considered 2D section. For example, at the intersection point between section 2 and 21 ($x = 1300$ m in Fig. 124 and Fig. 125, $y = 900$ m in Fig. 130 and Fig. 131) it is possible to observe a slightly de-amplification or amplification by applying the motion along x direction or y direction respectively. In fact, at $x = 1300$ m is the toe of the right side hill in section 2, but $y = 900$ m is related to the crest of section 21. The effect of sub-interface shape is enlightened with reference to intersection points between sections 5 and 6 with sections 12, 13 and 14. As an example, $x = 500$ m is at the centre of the ground surface of the deep and large valley of section 6 (Fig. 126 and Fig. 127) but the corresponding $y = 900$ m is at ground surface of the narrow valley of section 13 (Figs. 128-129); it results that by applying the input motion along the y direction the amplification results higher than by applying the input along x direction.

All the above issues raised with reference to the 2D results, depending on input motion direction, have also been observed with reference to 3D model (A7, A8, A9 and A10 analyses). The greatest difference takes place, in terms of F_{PGA} , at the intersection point between section 6 ($x = 400$ m in Figs. 132-133) and 12 ($y = 900$ m in Figs. 134-135).

Furthermore, 3D scheme (e.g. Fig. 132) allows to reduce those differences between the 2D amplification patterns of FH_{01-05} and FH_{05-1} (e.g. Fig. 126), obtained by separately applying the input motion along the x or y direction.

In Fig. 136 sections 2, 4, 5, 6, 12, 13, 14, 22 are sketched to point out the shape of the ground surface and sub-interfaces which causes the above different results from 2D and 3D analyses carried out by applying the input motion along x or y directions. The three dimensional scheme allows to take into account the overall geometry of the examined area, showing different site amplification with respect to the two-dimensional analyses, but at the same time still requires to choose the earthquake scenario (i.e. the direction of its application) in order to carry out a SM study.

Comparing the results obtained by applying only one horizontal component of a seismic event with that related to the two horizontal components acting at the same time, that is A7 vs A11 and A10 vs A11, the A11 amplification results greater than A7 and

A10 (e.g. Figs. 137-138 and Figs. 139-140). To clarify the reason of this effect it is interesting to observe that by applying the input motion along one direction, for example x, it results in “parasitic” horizontal ground motion along the transversal direction, that is y. This “parasitic” motion brings up a greater amplification by comparing A11 with A7 and A10.

A quick way to display the above “parasitic” component is to sketch the horizontal motion, that is acceleration along x and y direction, at ground surface. With reference to the fifty sampled point, Figs. 141-143 are related to analyses called A7, A10 and A11. It is possible to observe, by a qualitatively evaluation, that the presence of both the hill and the valley generates the “parasitic” motion and that the large amplification of the reference signal and the most intense “parasitic” acceleration take place in the valley area, as shown in Fig. 141 and Fig. 142. Relating to Fig. 143 it is less intuitive to separate the “parasitic” component from the amplification effects.

An additional phenomenon should be recognised in the 3D valley, related to the constitutive assumptions. The valley material is a soft non-linear soil, for which the HSsmall constitutive model was considered. By applying simultaneously two horizontal components of motion, the HSsmall model responds in a more stiff and less dissipative fashion as compared to the case of only one horizontal input motion; this feature, that was first reported in the works of di Lernia 2014 and Amorosi et al. 2016, might contribute to the differences observed in the seismic responses obtained for single-directional and multi-directional input data.

With reference to the points of coordinates (600.2, 801, 51.21) and (600.8, 799.3, 55.6) at about 10 m and 5 m deep inside the valley area, shear stress-strain paths, in terms of $\tau_{zx}-\gamma_{zx}$, are sketched in Fig. 116c) and d), respectively, for the time interval $2 \leq t \leq 4$ s; black and red lines are referred to the solution obtained by means of A7 (i.e. single component of input motion) and A11 analyses (i.e. two components input motion acting simultaneously), respectively. The reference motions are also shown in Fig. 116a) and c). It is worth noting that for $0 \leq t \leq 2.75$ s, the base input motion should straight act along the x axis.

A11 shear stress-strain path highlights a more stiff and less dissipative behaviour as compared to the A7 path, due to multi-directional condition induced by the input signal. Furthermore the A7 response is also affected by a multi-directional motion due to the “parasitic” component generated by the 3D effect.

The above consideration should also be considered reliable in terms of shear stress-strain paths $\tau_{zy}-\gamma_{zy}$ which are shown in Fig. 117.

This material behaviour involves a greater amplification of A11 analysis (multi-directional input motion) with respect to the A7 and A10 simulations (single-directional input motion).

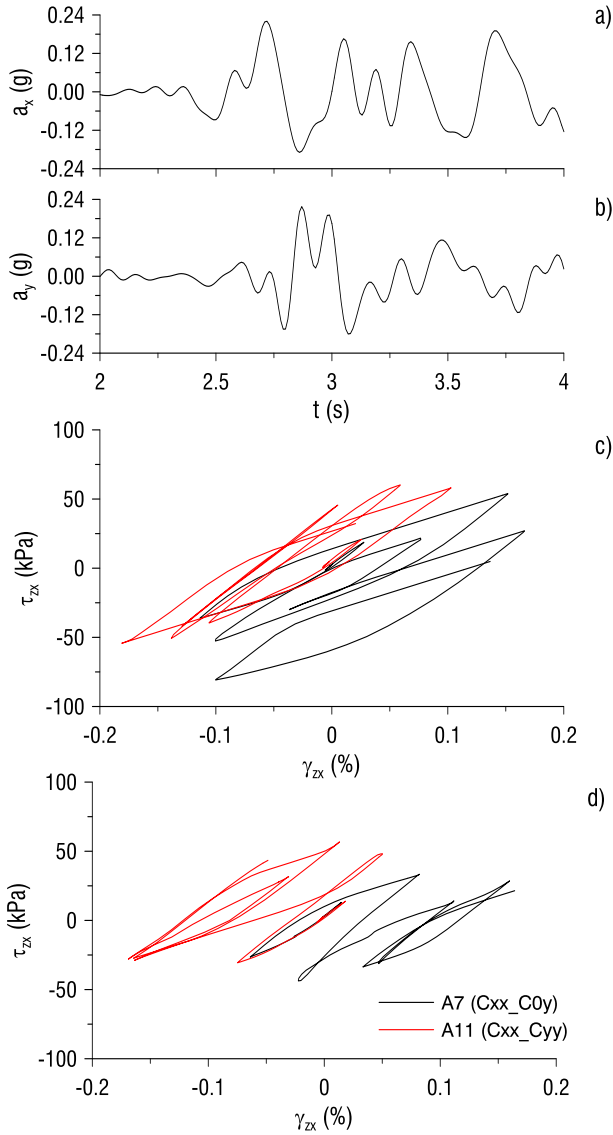


Fig. 116 a) reference motion Cx, b) reference motion Cy, c) and d) shear stress-strain paths (τ_{zk} - γ_{zk}) at the stress points, in the valley area, of coordinates (600.2, 401, 51.21) and (600.8, 399.3, 55.6), respectively

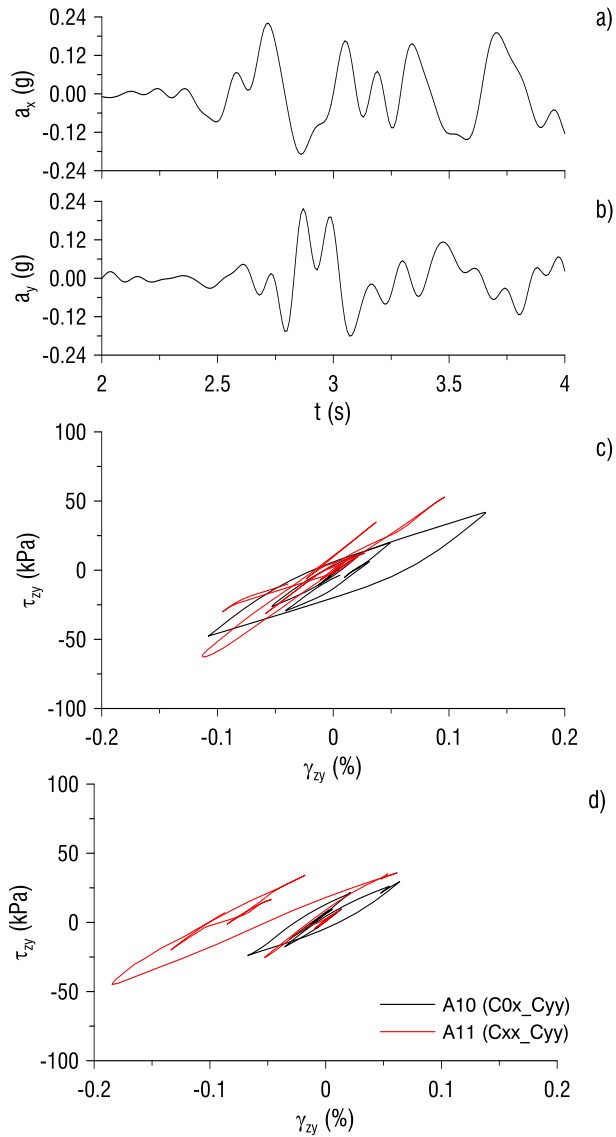


Fig. 117 a) reference motion Cx, b) reference motion Cy, c) and d) shear stress-strain paths (τ_{zy} - γ_{zy}) at the stress points, in the valley area, of coordinates (600.2, 401, 51.21) and (600.8, 399.3, 55.6), respectively

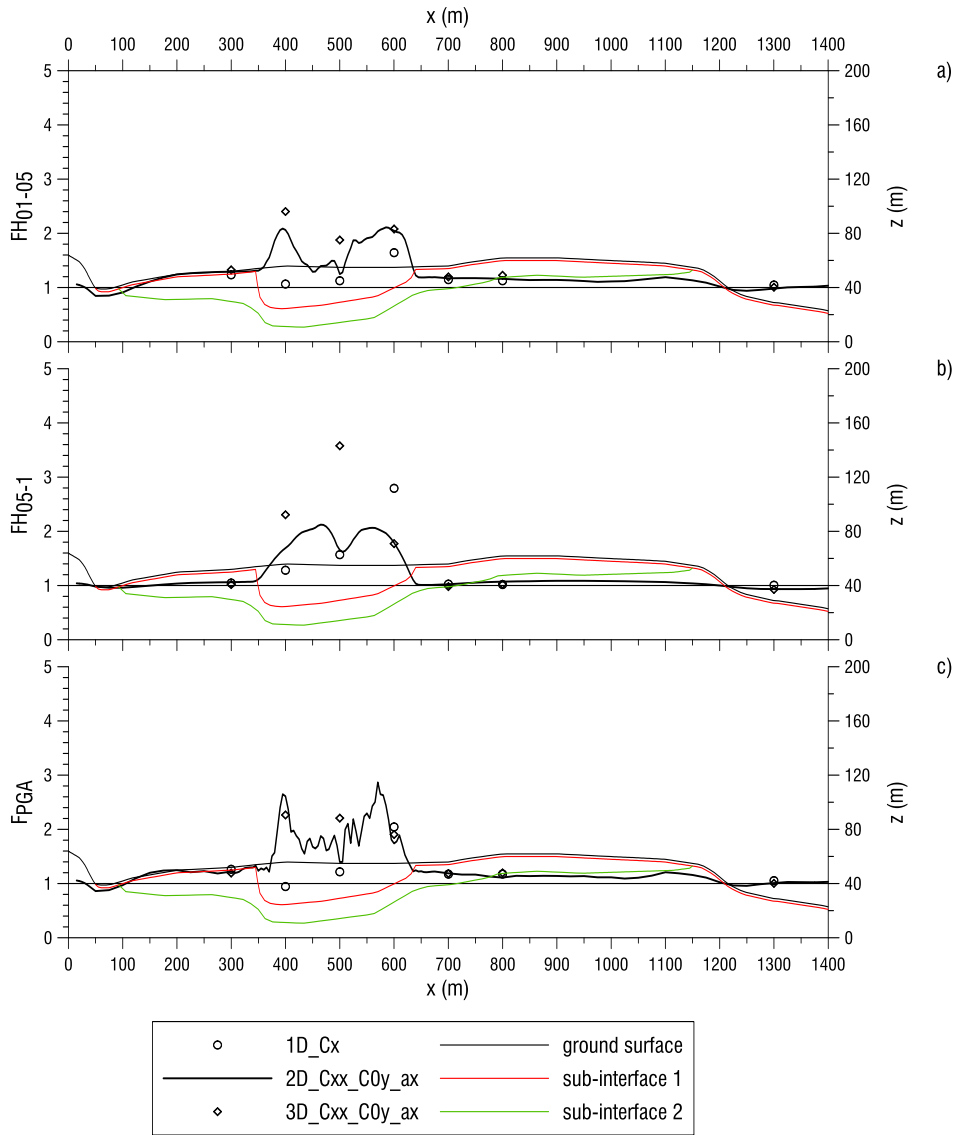


Fig. 118 Comparison A1-A3-A7 with reference to section 6, a) $F_{H_{01-05}}$, b) $F_{H_{05-1}}$, b) F_{PGA}

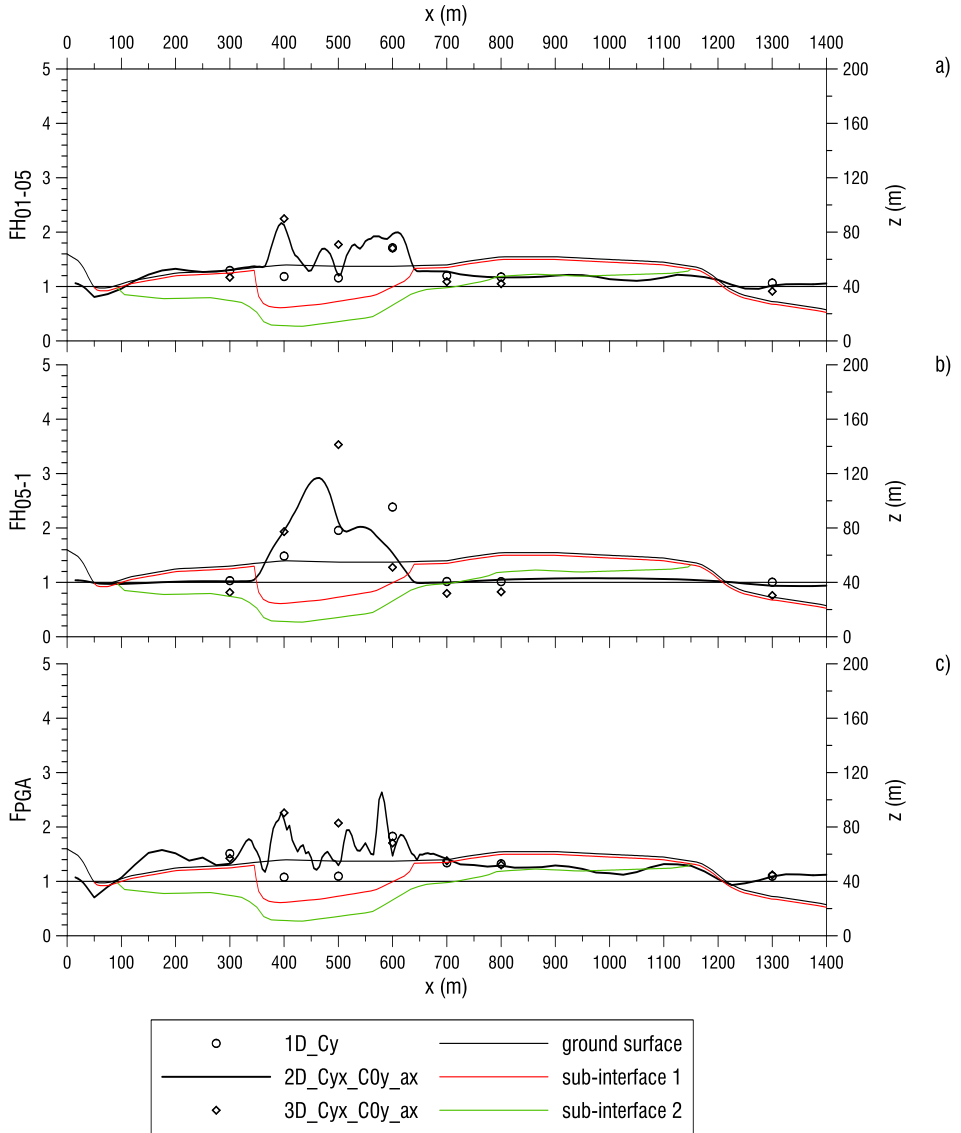


Fig. 119 Comparison A2-A4-A8 with reference to section 6, a) FH_{01-05} , b) FH_{05-1} , c) F_{PGA}

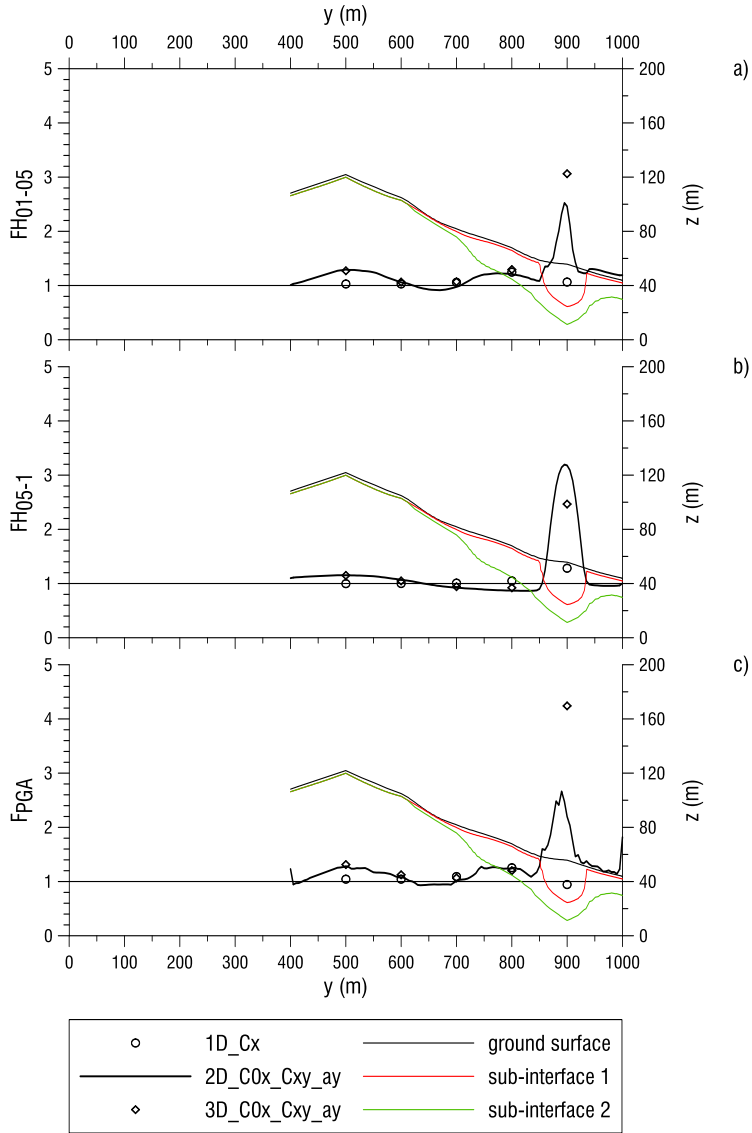


Fig. 120 Comparison A1-A3-A7 with reference to section 12, a) FH_{01-05} , b) FH_{05-1} , b) F_{PGA}

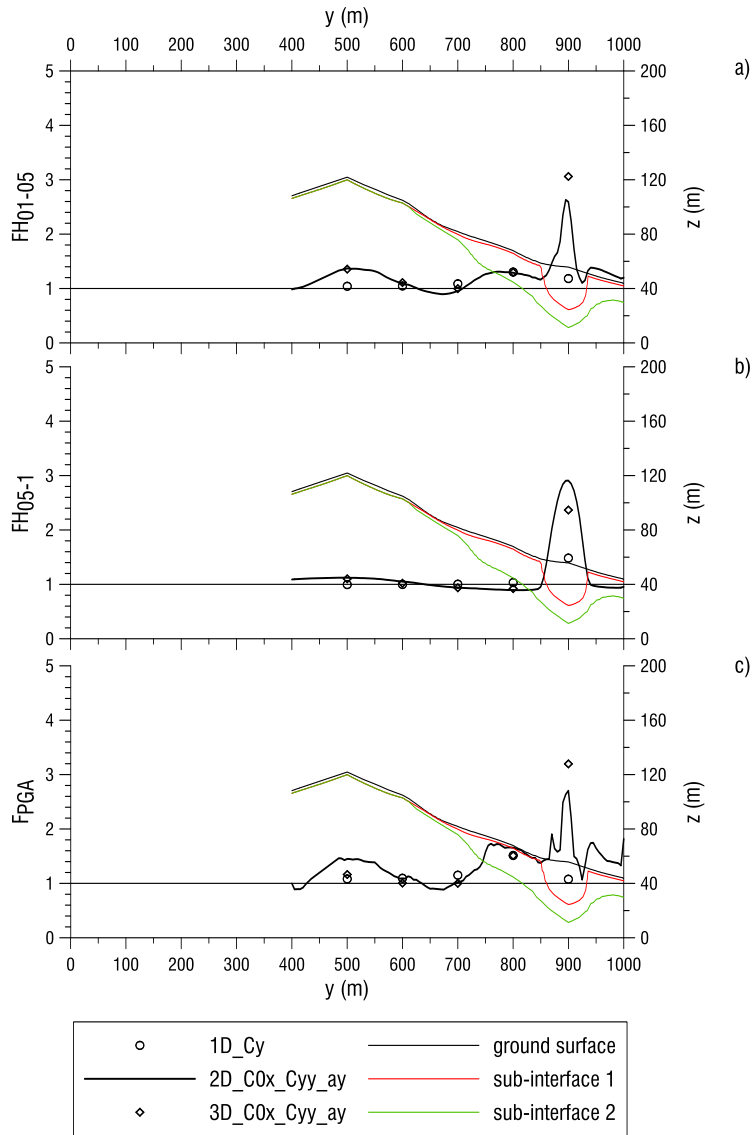


Fig. 121 Comparison A2-A4-A8 with reference to section 12, a) FH_{01-05} , b) FH_{05-1} , b) F_{PGA}

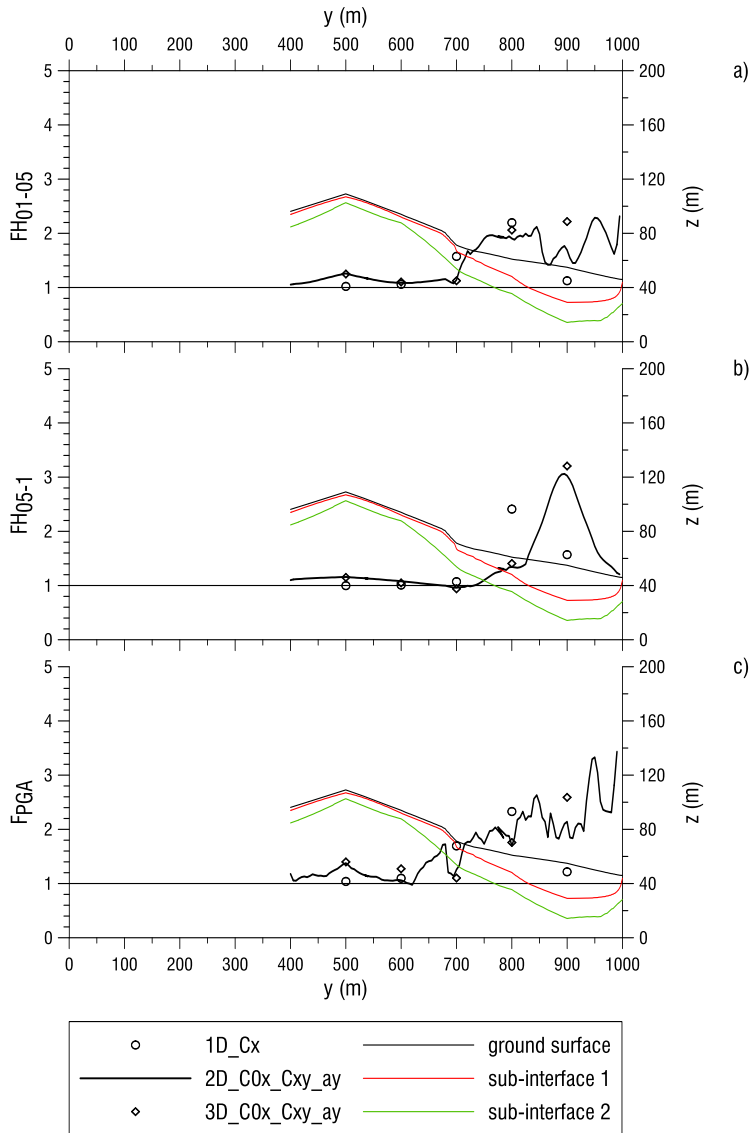


Fig. 122 Comparison A1-A3-A7 with reference to section 13, a) FH_{01-05} , b) FH_{05-1} , b) F_{PGA}

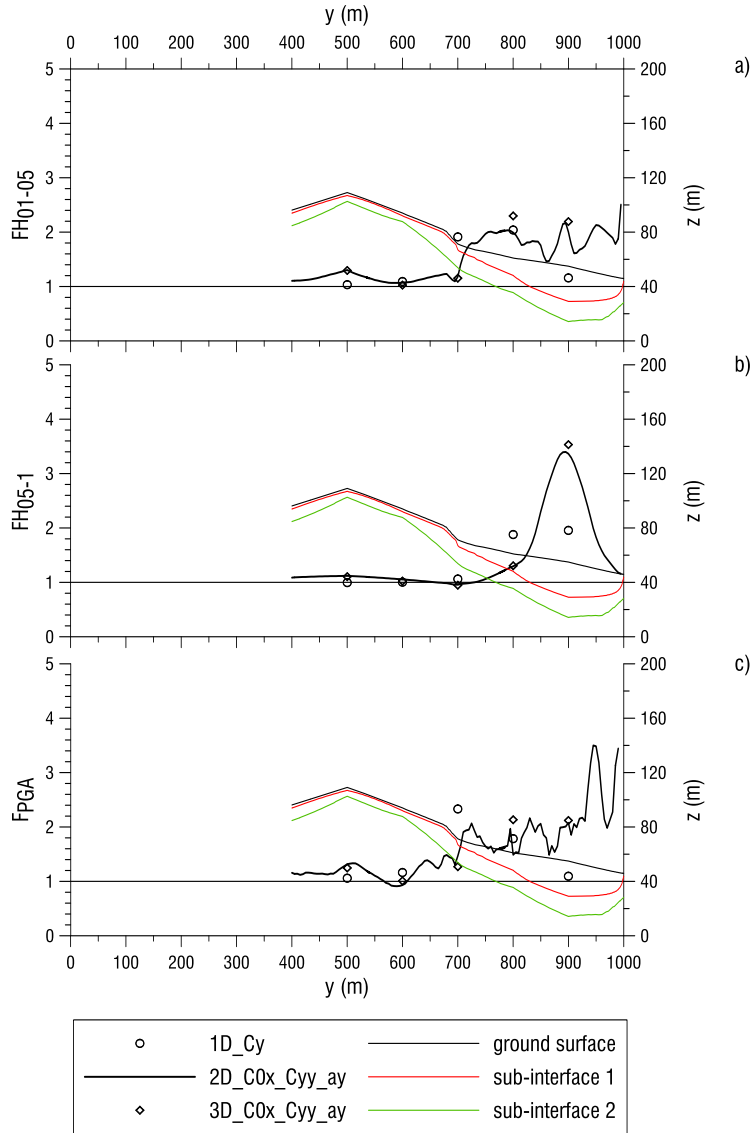


Fig. 123 Comparison A2-A4-A8 with reference to section 13, a) FH_{01-05} , b) FH_{05-1} , b) F_{PGA}

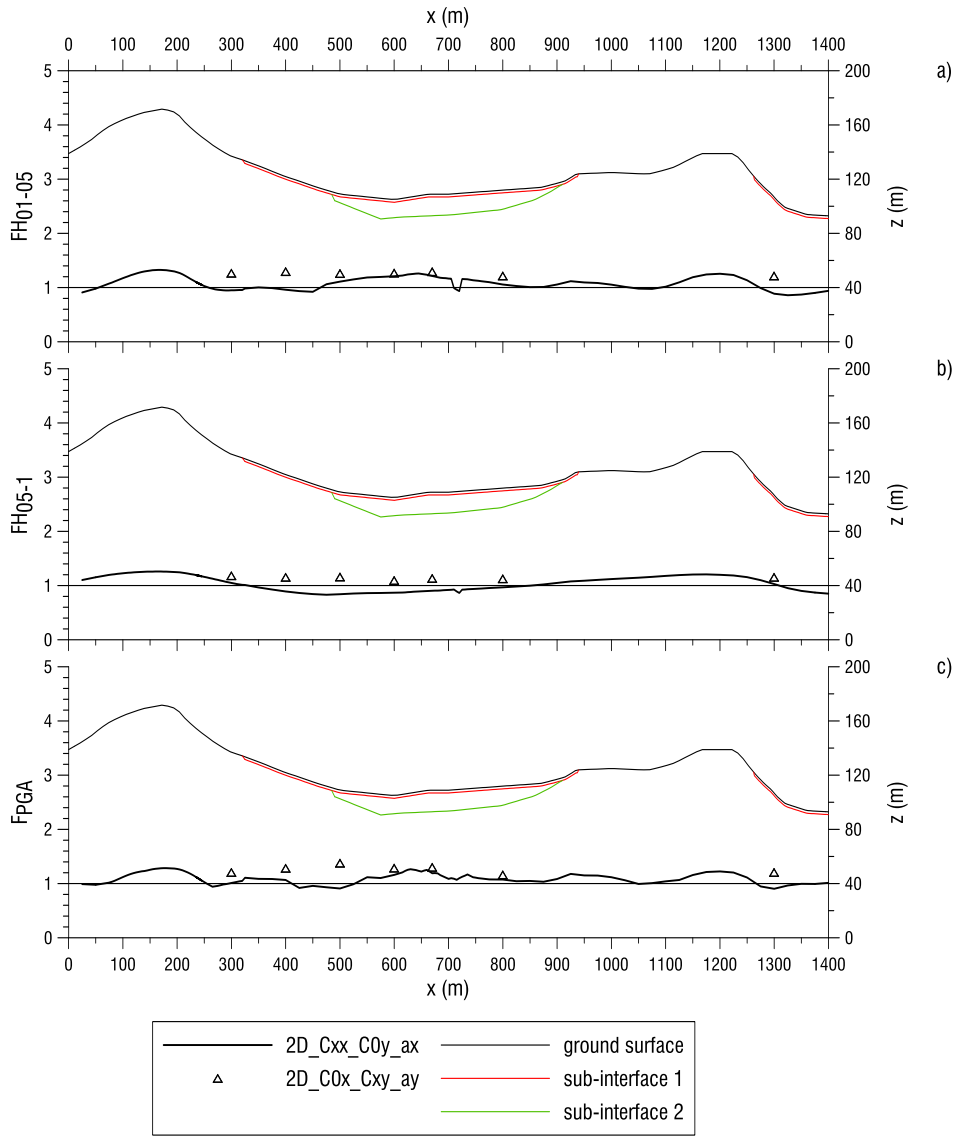


Fig. 124 Comparison A3-A5 with reference to section 2, a) F_{H01-05} , b) F_{H05-1} , b) F_{PGA}

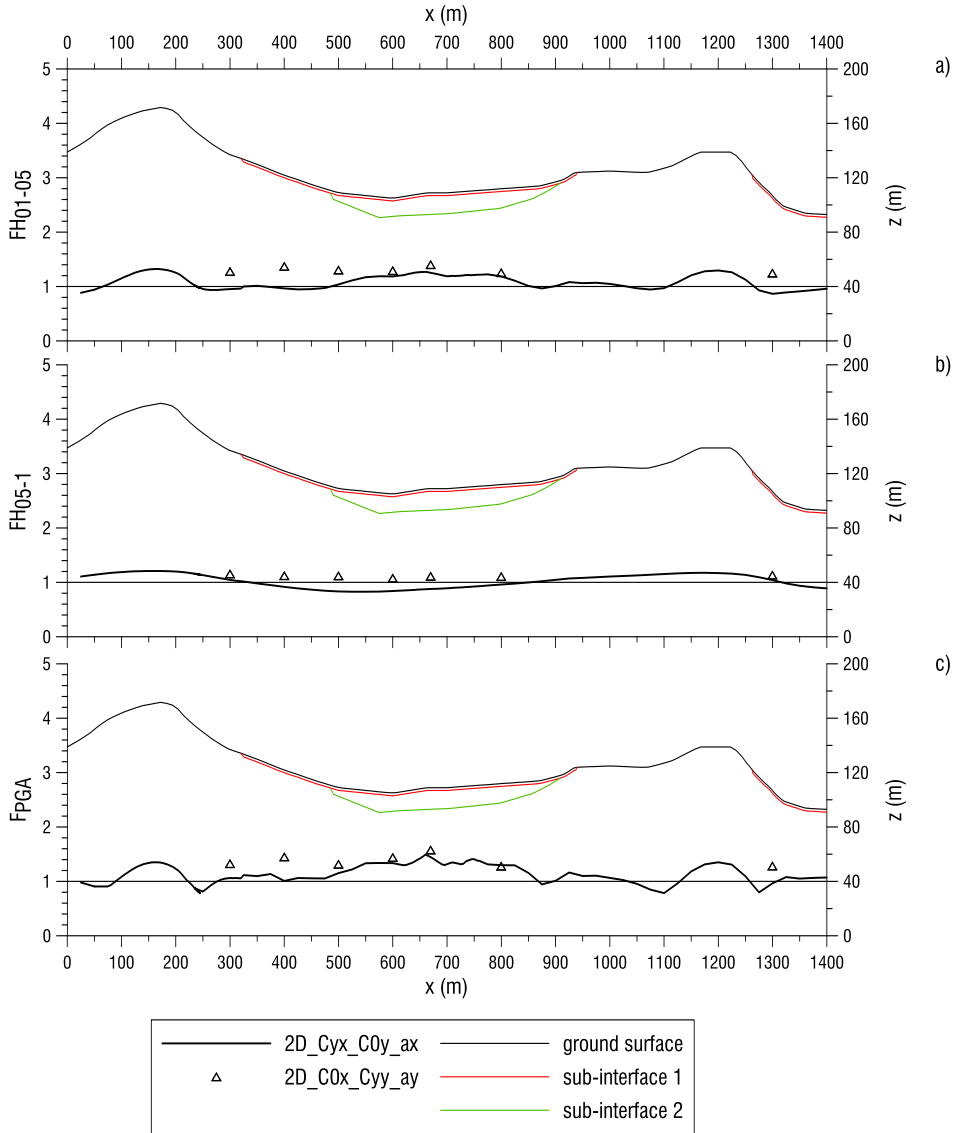


Fig. 125 Comparison A4-A6 with reference to section 2, a) FH₀₁₋₀₅, b) FH₀₅₋₁, c) F_{PGA}

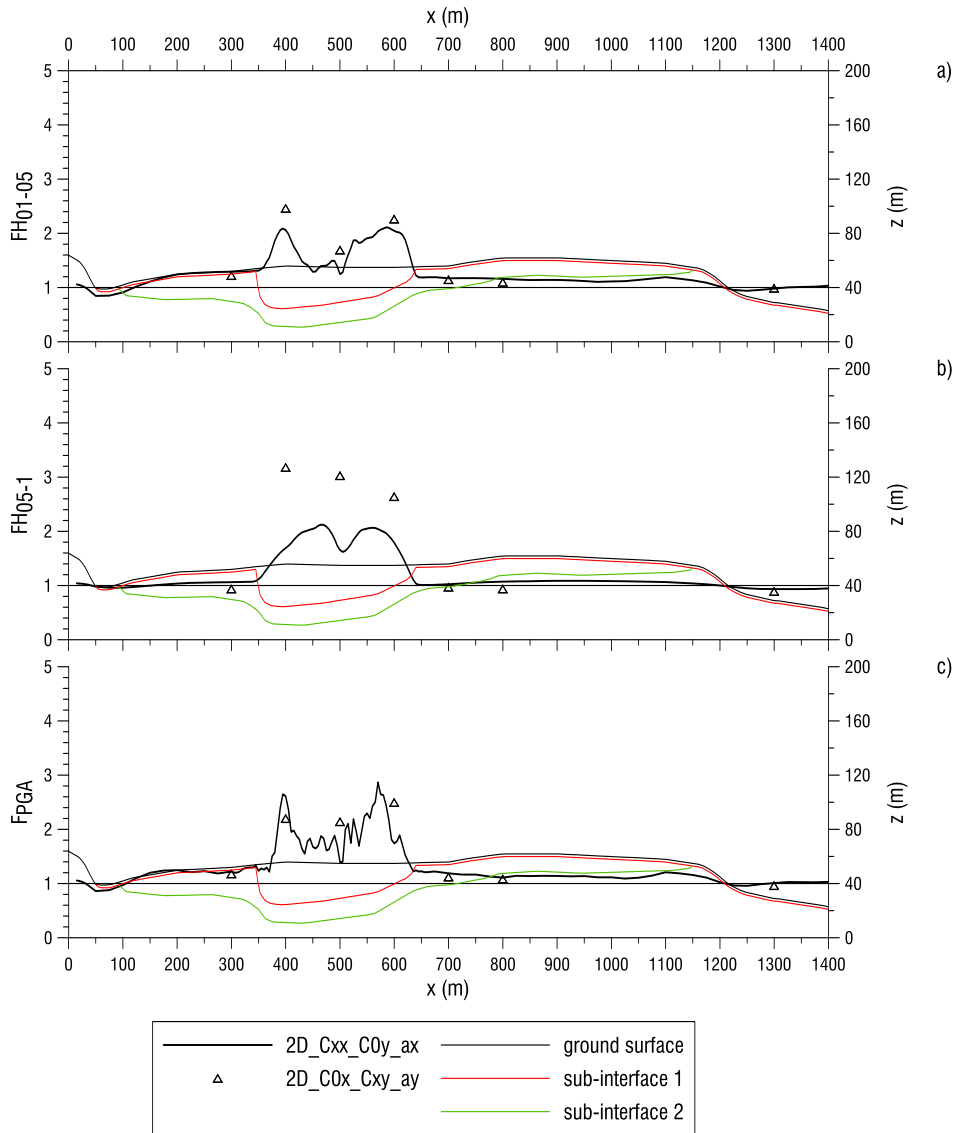


Fig. 126 Comparison A3-A5 with reference to section 6, a) F_{H01-05} , b) F_{H05-1} , c) F_{PGA}

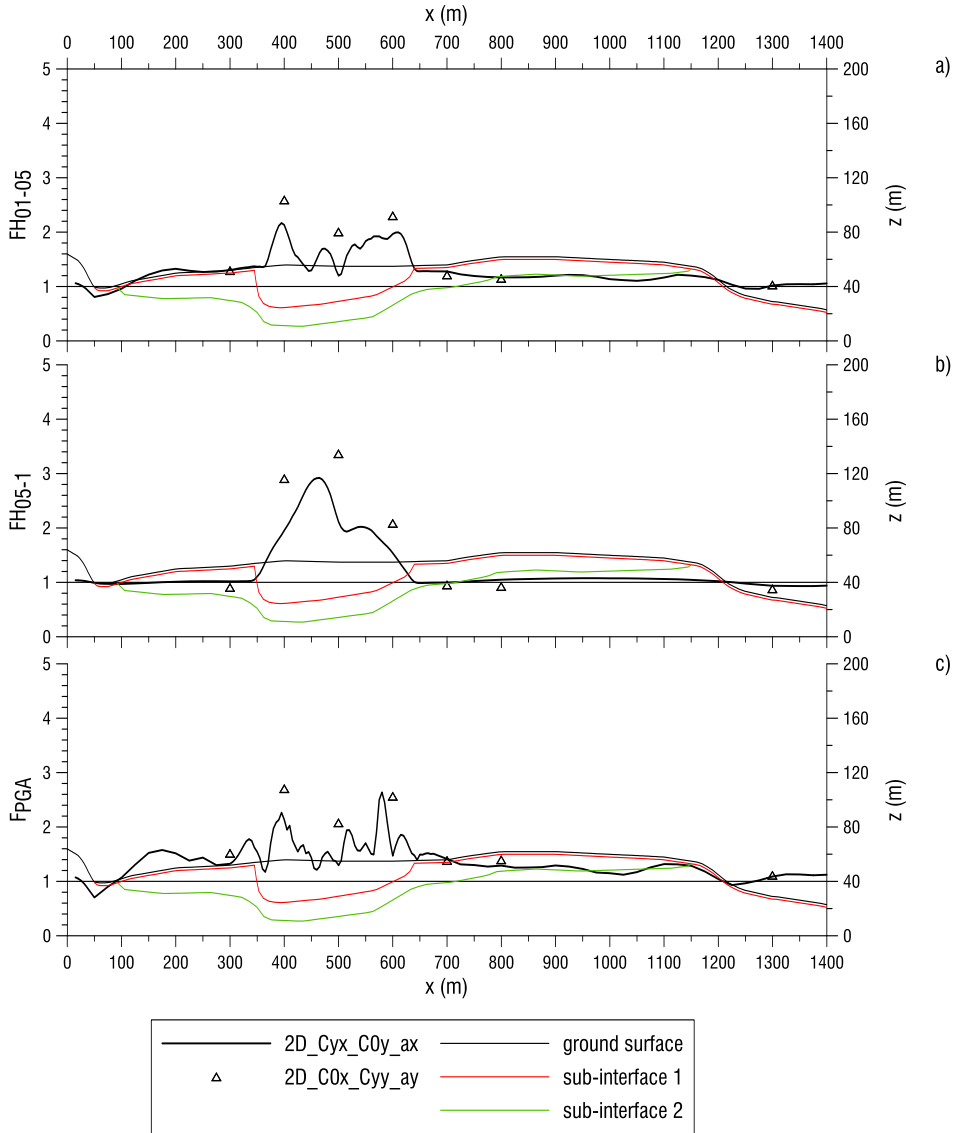


Fig. 127 Comparison A4-A6 with reference to section 6, a) FH_{01-05} , b) FH_{05-1} , b) F_{PGA}

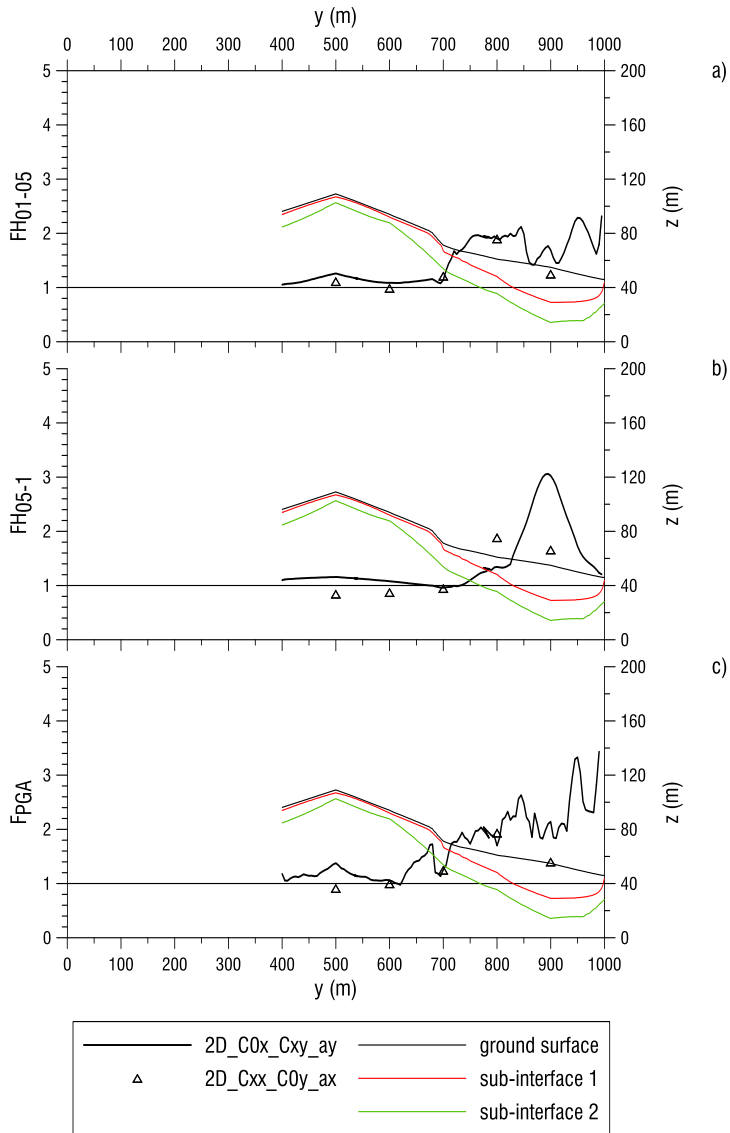


Fig. 128 Comparison A3-A5 with reference to section 13, a) FH_{01-05} , b) FH_{05-1} , c) F_{PGA}

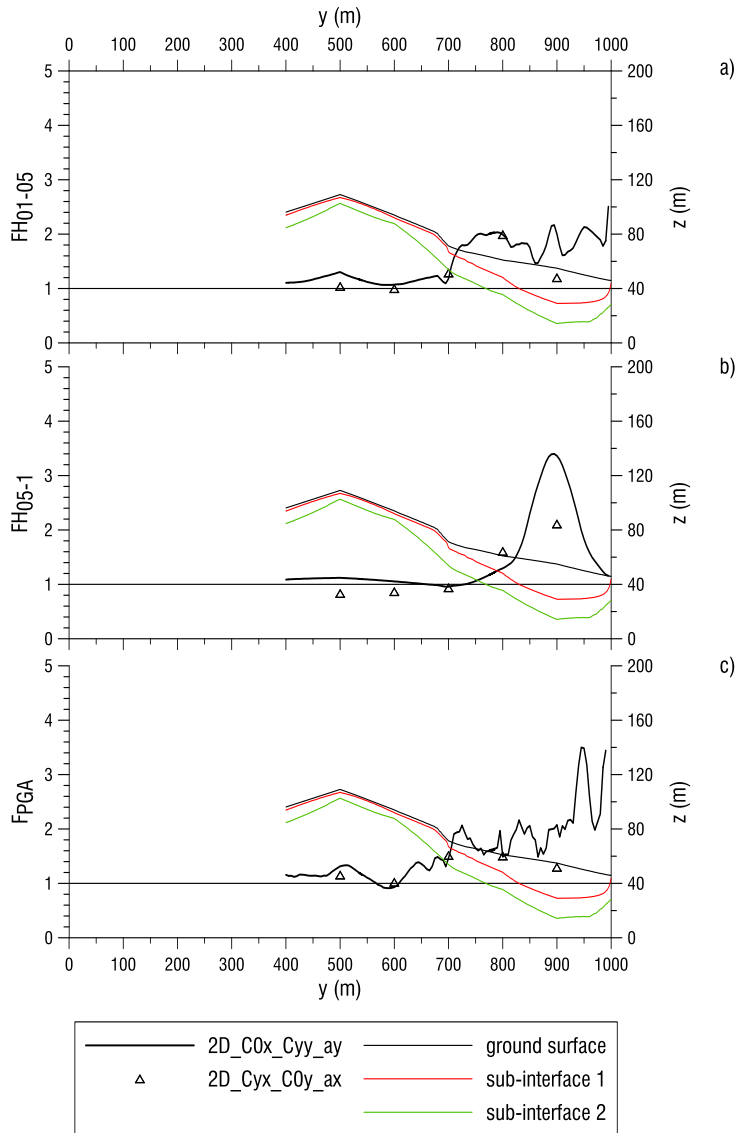


Fig. 129 Comparison A4-A6 with reference to section 13, a) FH_{01-05} , b) FH_{05-1} , c) F_{PGA}

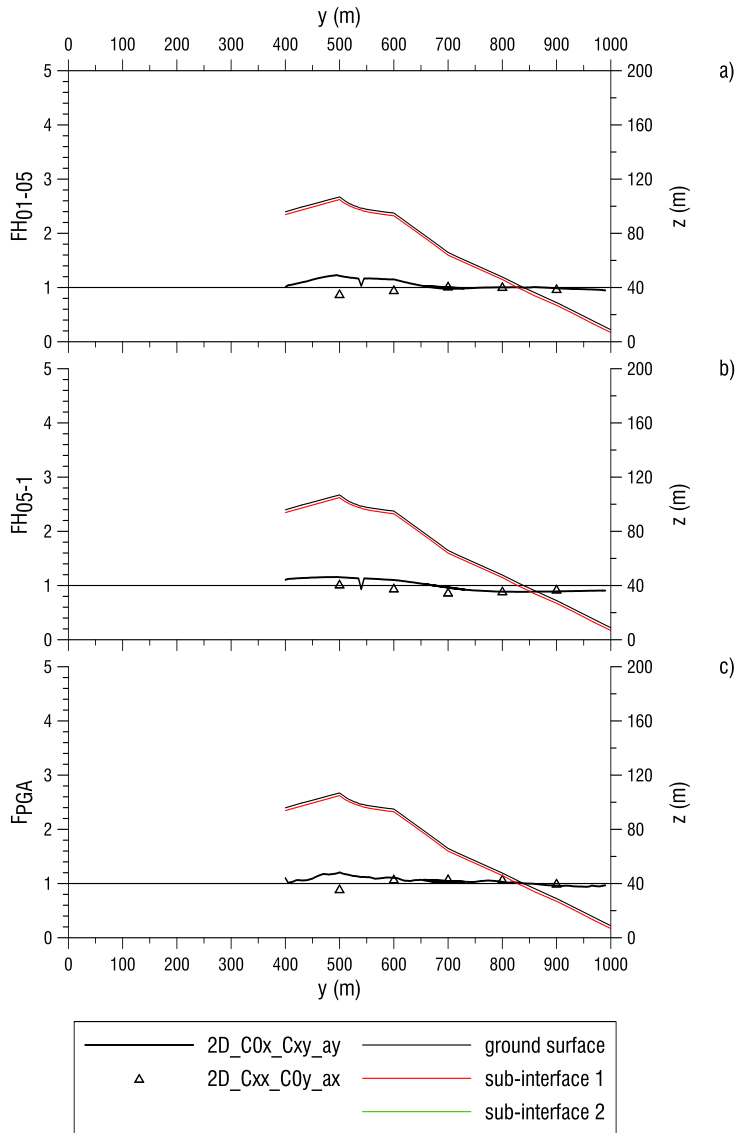


Fig. 130 Comparison A3-A5 with reference to section 21, a) FH_{01-05} , b) FH_{05-1} , b) F_{PGA}

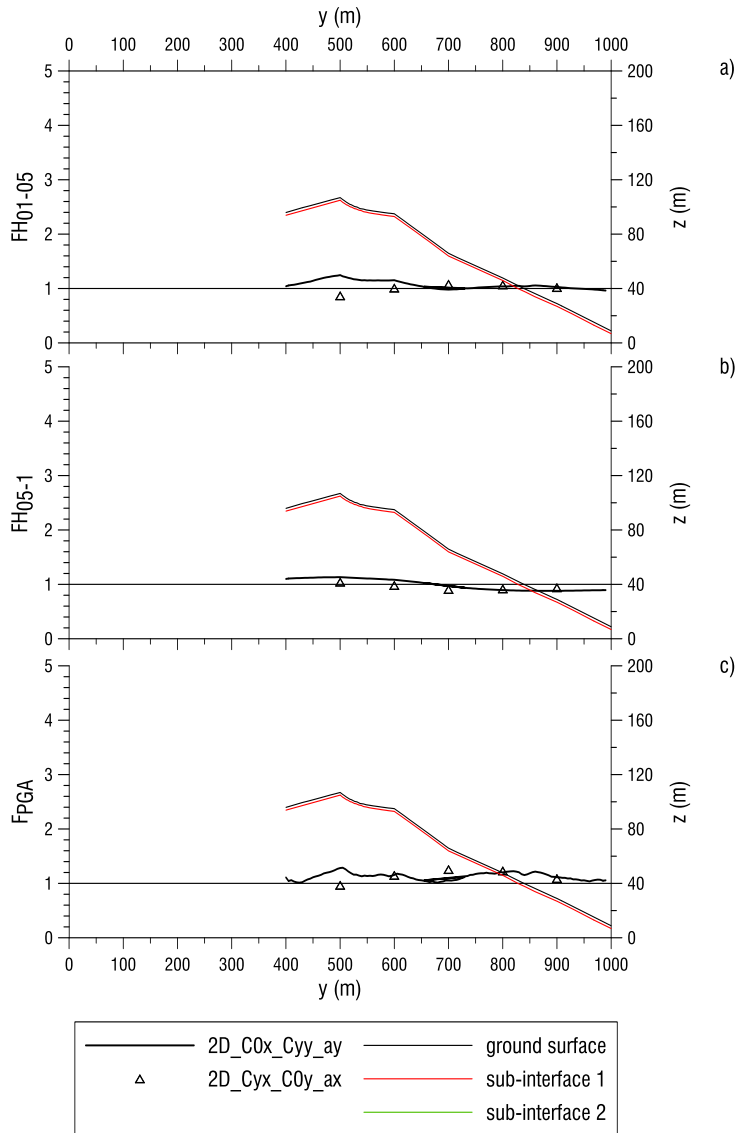


Fig. 131 Comparison A4-A6 with reference to section 21, a) FH_{01-05} , b) FH_{05-1} , c) F_{PGA}

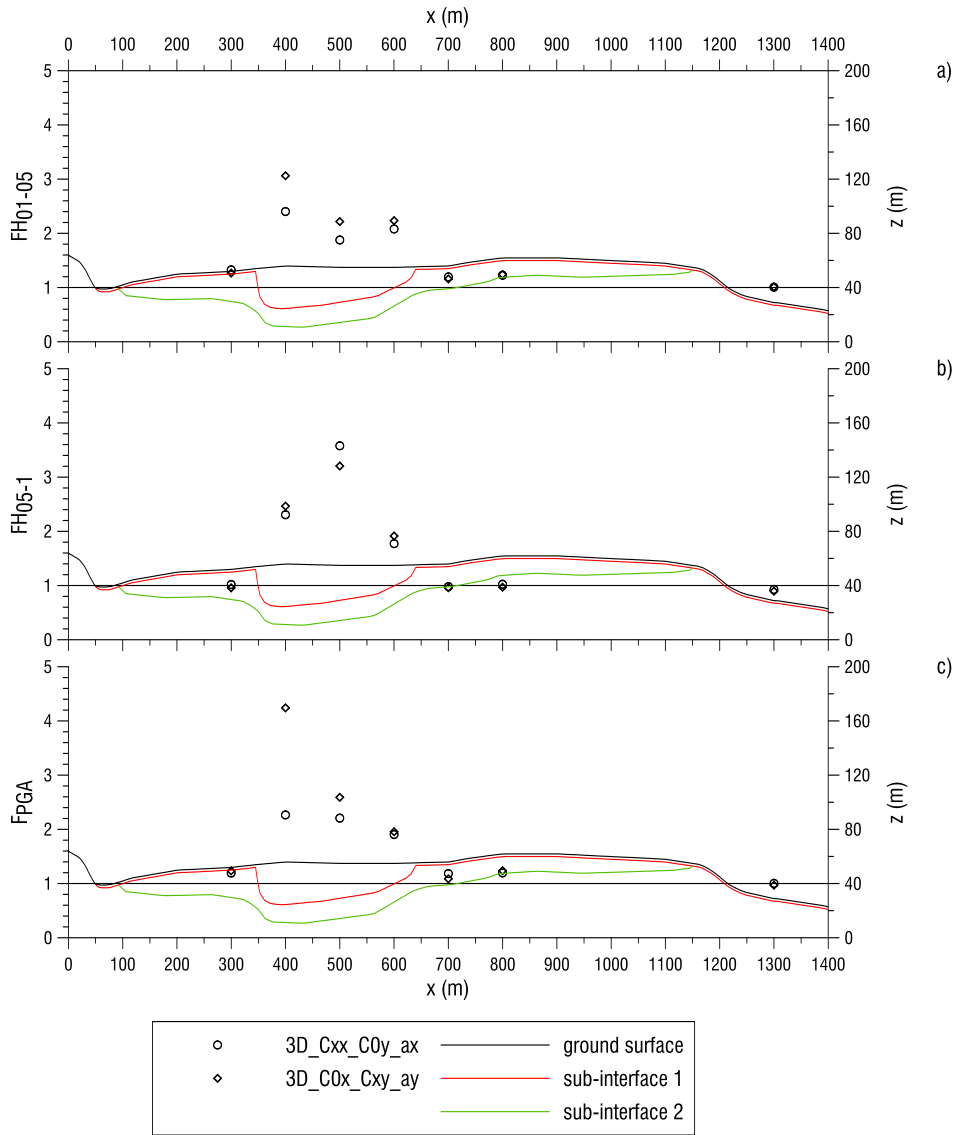


Fig. 132 Comparison A7-A9 with reference to section 6, a) FH_{01-05} , b) FH_{05-1} , c) F_{PGA}

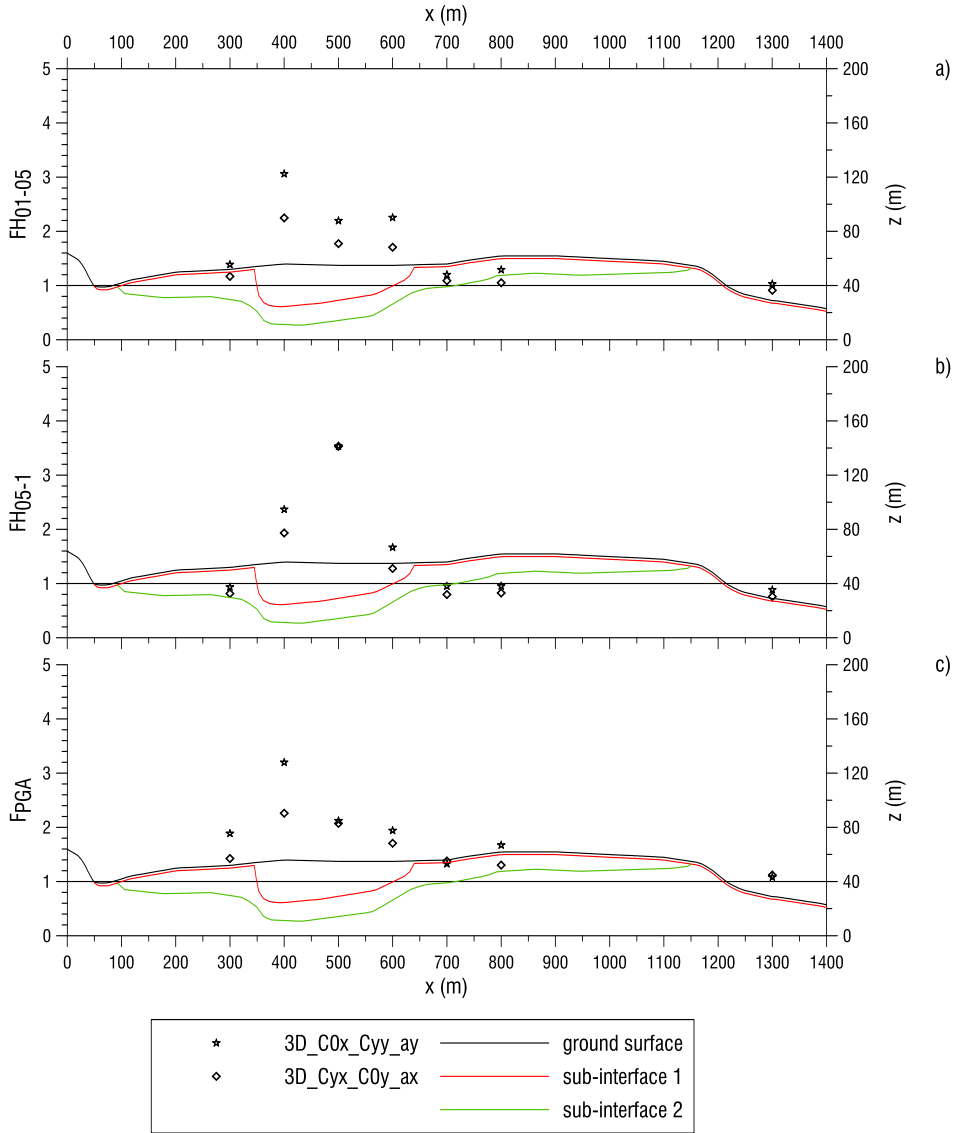


Fig. 133 Comparison A8-A10 with reference to section 6, a) F_{H01-05} , b) F_{H05-1} , c) F_{PGA}

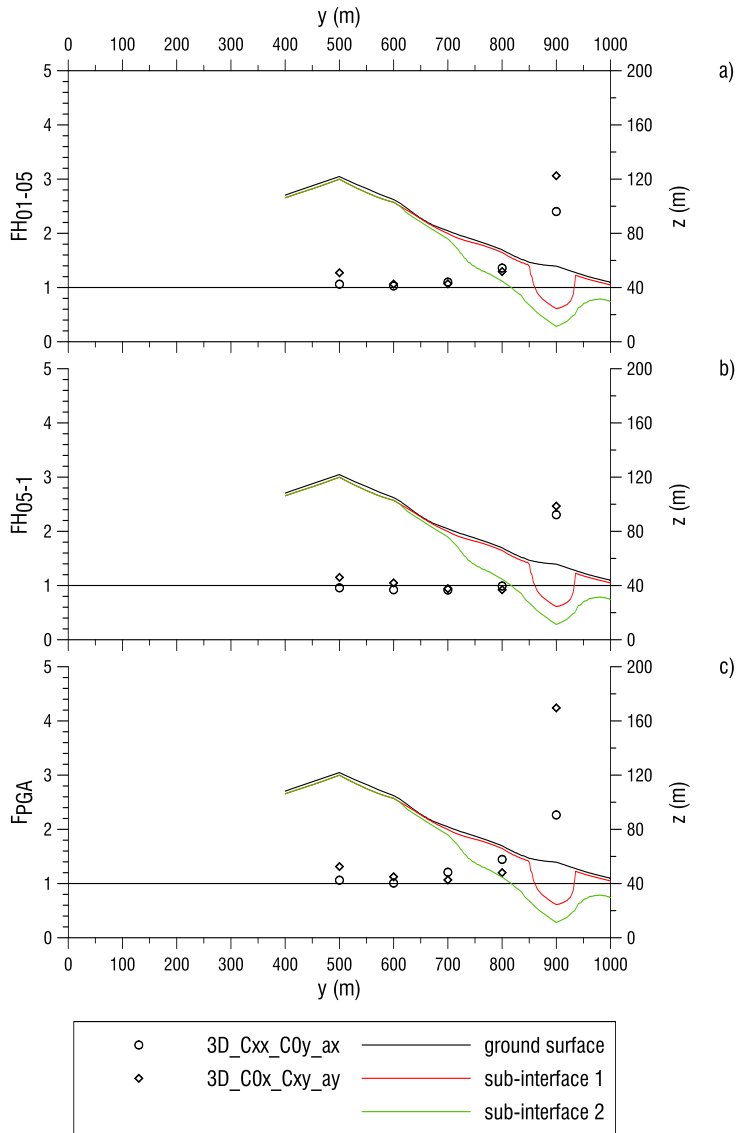


Fig. 134 Comparison A7-A9 with reference to section 12, a) FH_{01-05} , b) FH_{05-1} , b) F_{PGA}

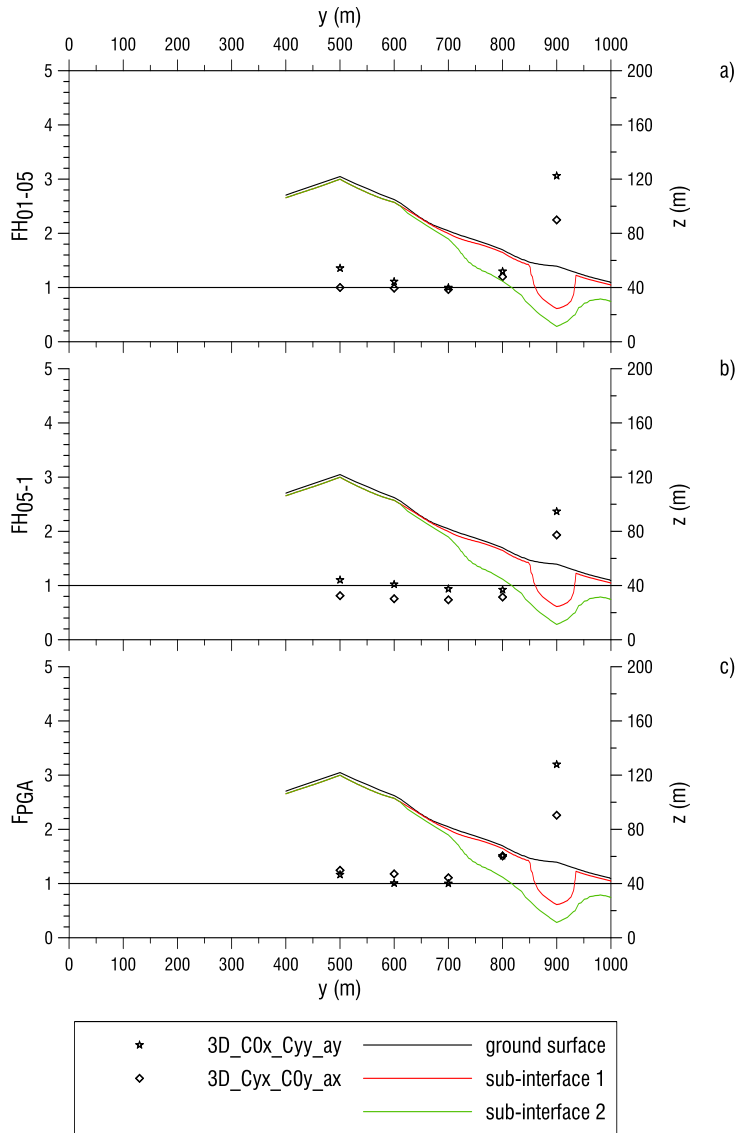


Fig. 135 Comparison A8-A10 with reference to section 12, a) $F_{H_{01-05}}$, b) $F_{H_{05-1}}$, c) F_{PGA}

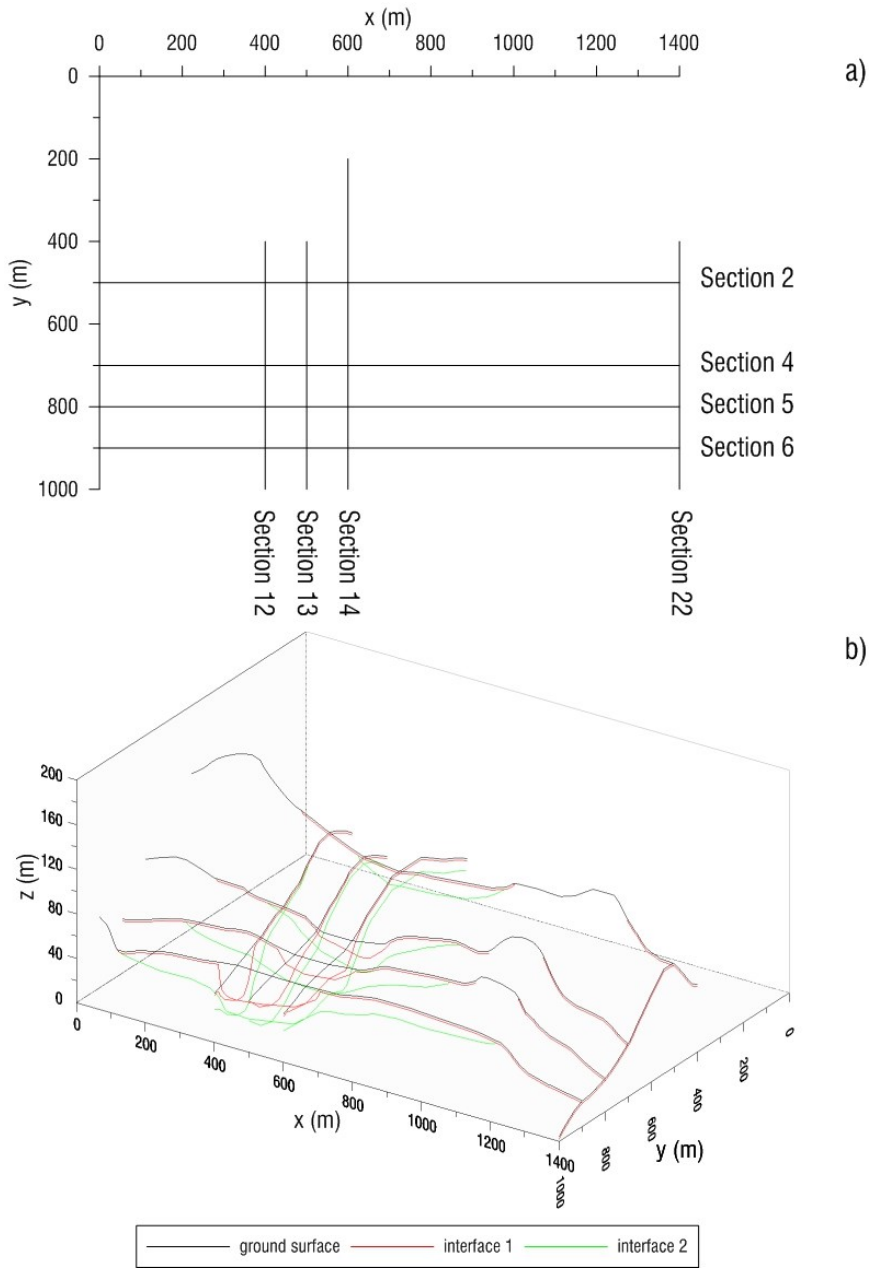


Fig. 136 Studied sections which enlighten the 3D issue. a) plane view, b) 3D view

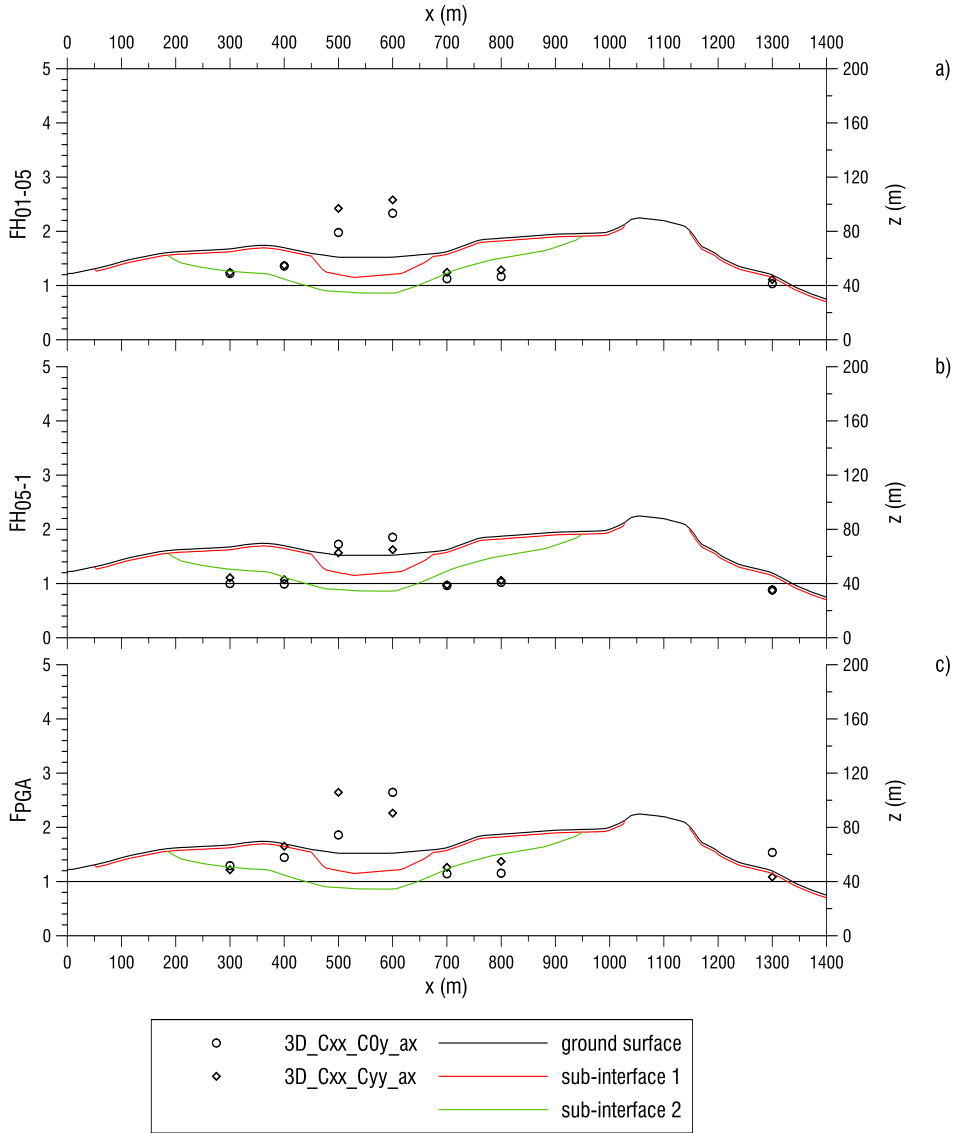


Fig. 137 Comparison A7-A11 with reference to section 5, a) F_{H01-05} , b) F_{H05-1} , c) F_{PGA}

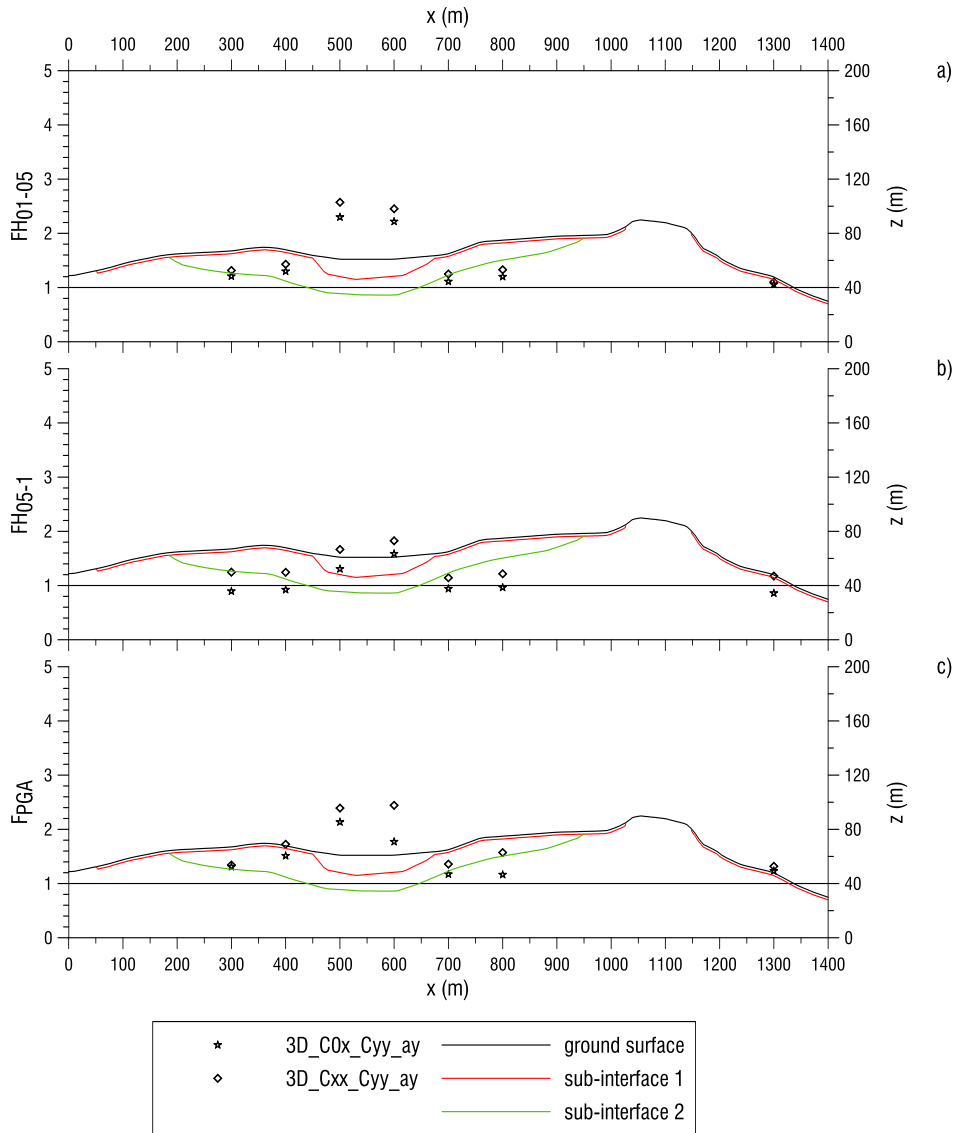


Fig. 138 Comparison A10-A11 with reference to section 5, a) FH_{01-05} , b) FH_{05-1} , c) F_{PGA}

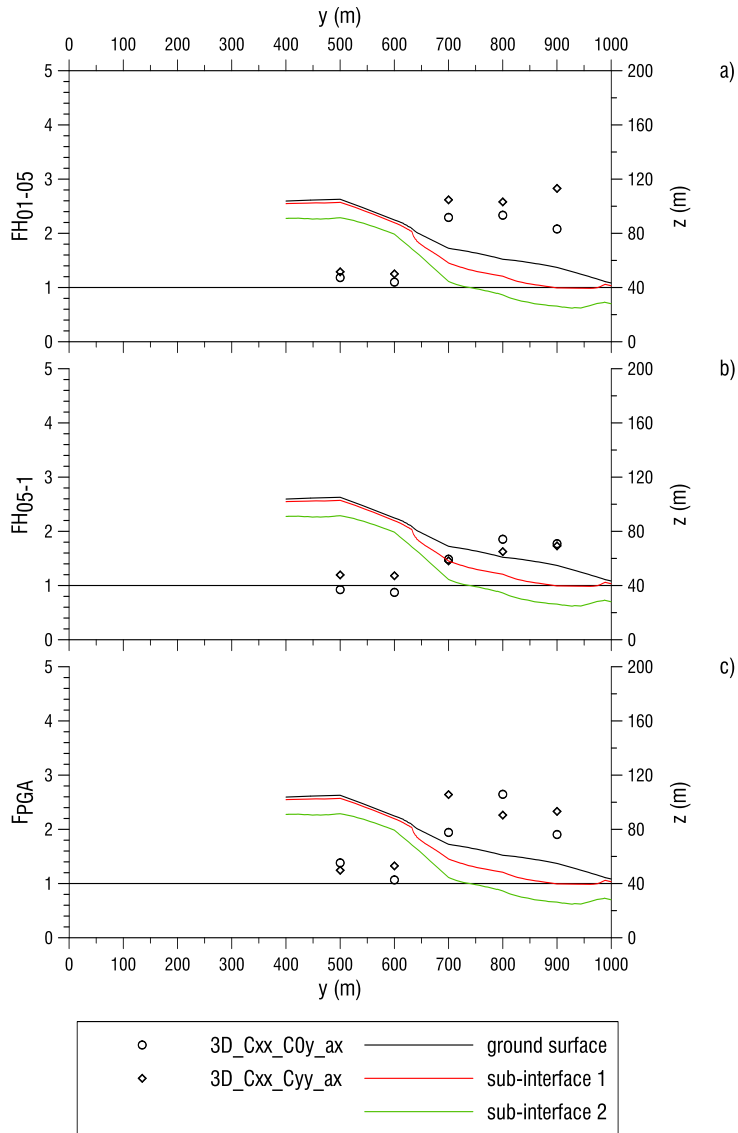


Fig. 139 Comparison A7-A11 with reference to section 14, a) FH_{01-05} , b) FH_{05-1} , b) F_{PGA}

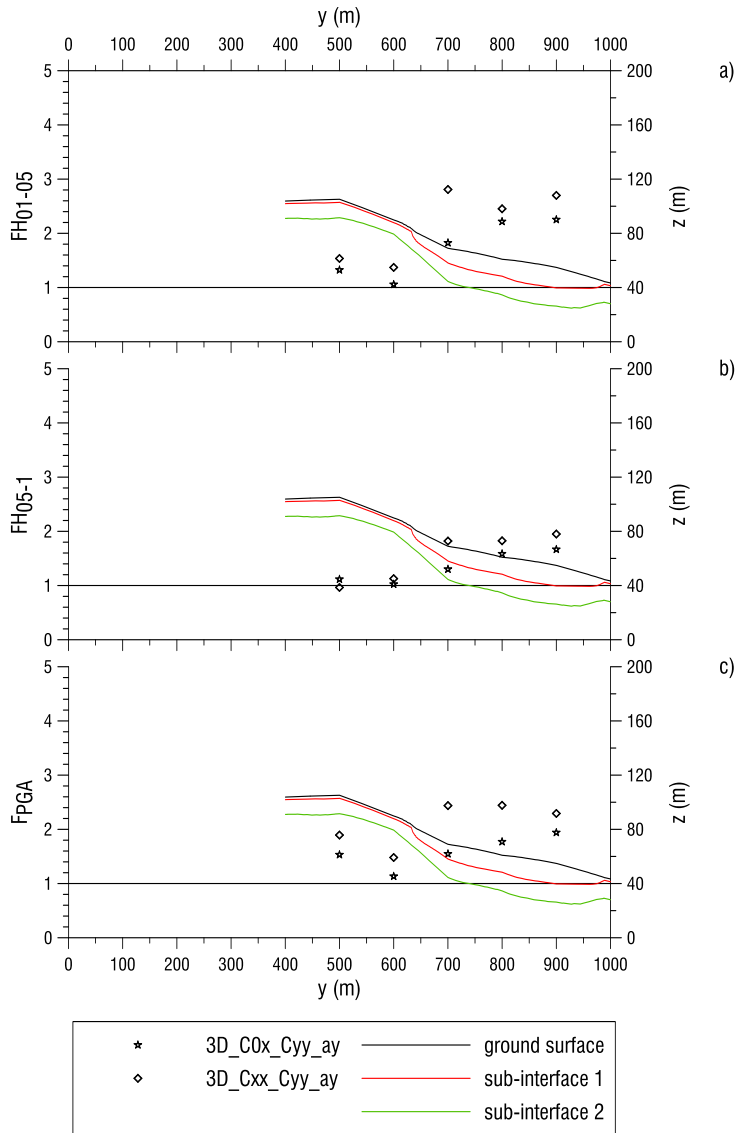


Fig. 140 Comparison A10-A11 with reference to section 14, a) FH_{01-05} , b) FH_{05-1} , c) F_{PGA}

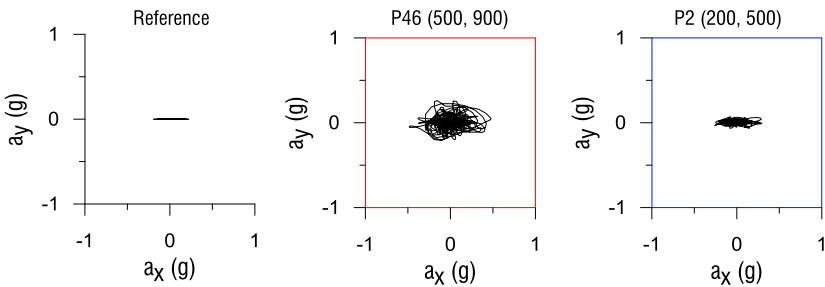
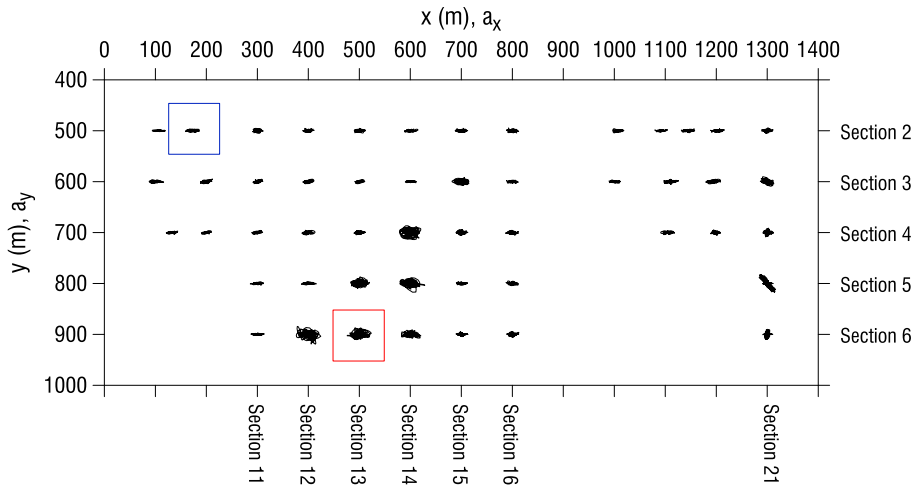
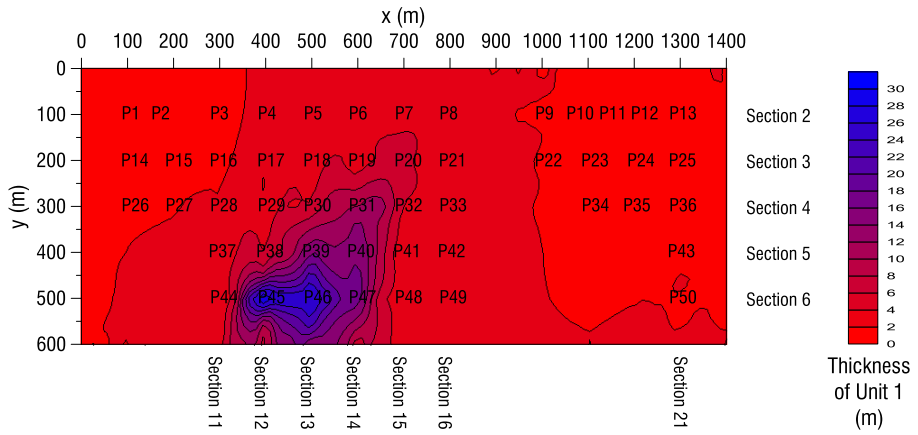


Fig. 141 Ground surface horizontal motion related to A7 analysis

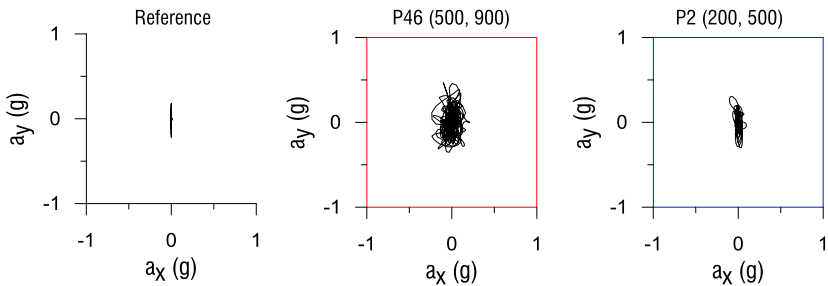
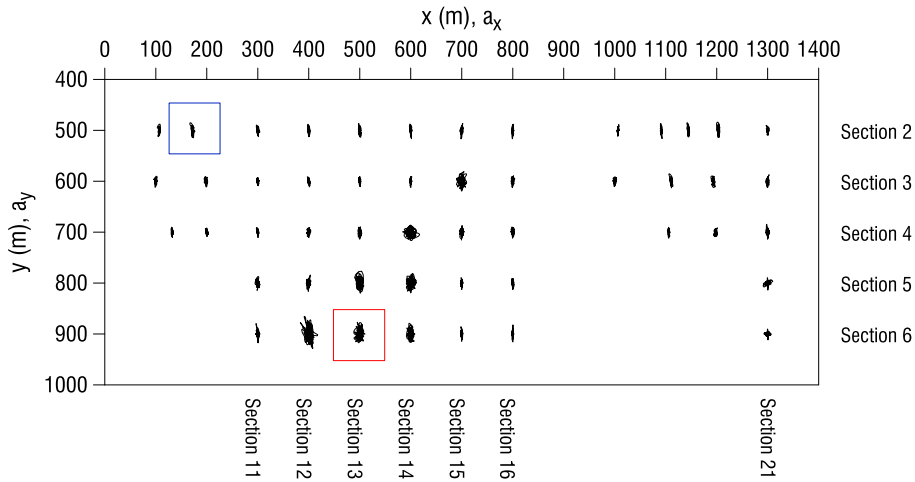
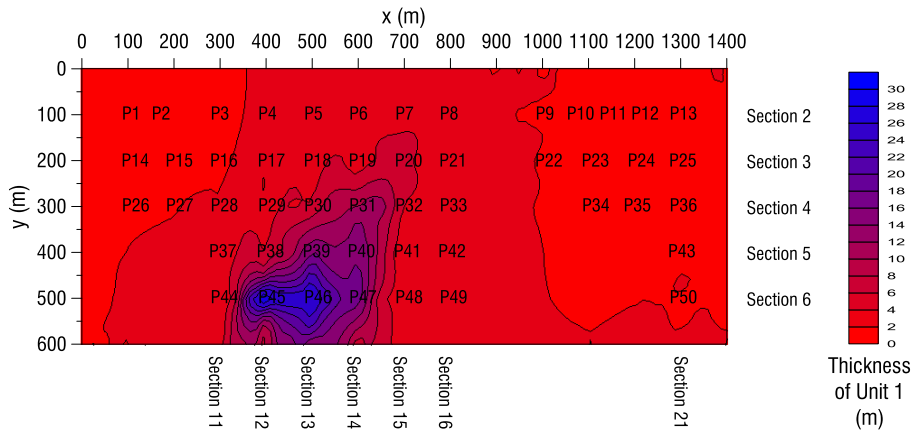


Fig. 142 Ground surface horizontal motion related to A10 analysis

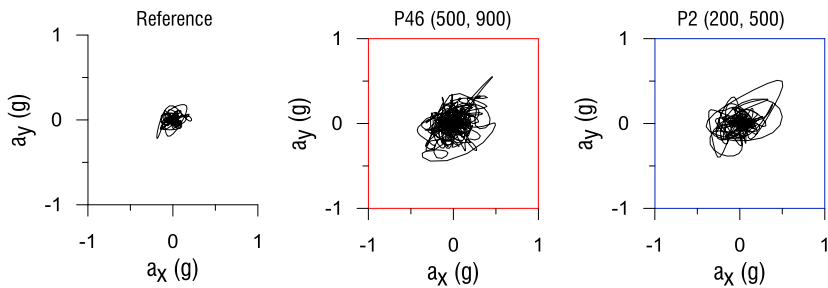
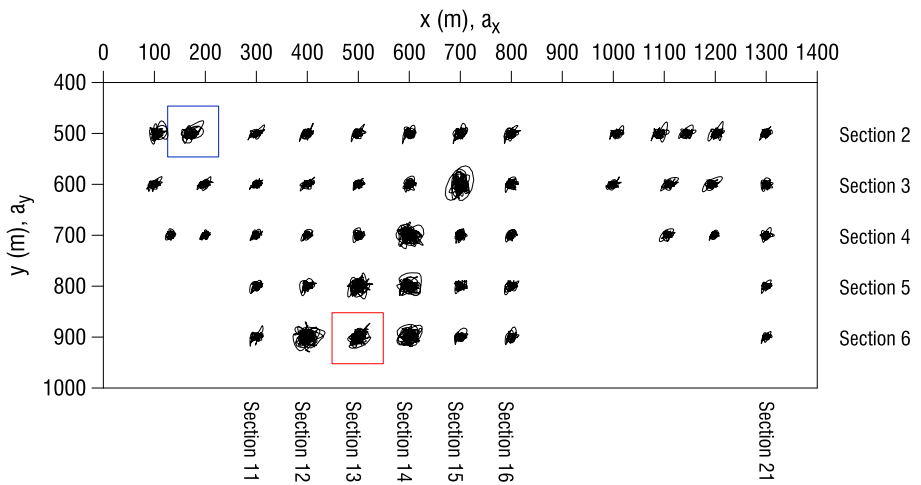
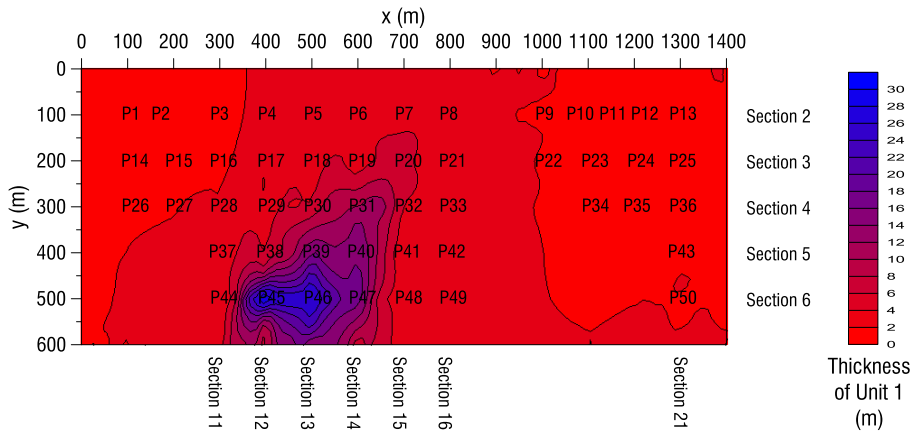


Fig. 143 Ground surface horizontal motion related to A11 analysis

Thanks to all data, referring to the amplification factors determined along x and y directions obtained by numerical 2D analyses, it is possible to sketch up the Seismic Microzonation maps shown in the Figs. 144-146. As for the case of QUAKE/W results, it is possible to assert that:

- the greatest amplification takes place in the valley area;
- the presence of the hill causes amplification factor greater than 1;
- at the toe of the hill the reference motion is slightly de-amplified.

Before comparing PLAXIS and QUAKE/W results it should be considered that the SM maps reported in § 3.7 are referred to mean value of amplification factors obtained by 2D QUAKE/W numerical simulations. In Figs. 147-149 the QUAKE/W maps related to the only reference motion C3, i.e. Cx for PLAXIS analyses, are shown.

The results obtained by the two FE codes are in good agreement. Thanks to the greatest resolution of PLAXIS maps (about 2500 sampled points) as compared to that of QUAKE/W (about 500 points) it is possible to define in a more accurate way the area characterised by topographical amplification. In general the shape of the contour in valley area results very similar when comparing the maps related to the QUAKE/W and PLAXIS two-dimensional results. In fact, it should be remarked that numerical results, for the examined case study, are in satisfactory agreement (see Figs. 113-115), in spite of the constitutive assumptions implemented in the adopted FE codes.

The 3D simulations highlighted a different ground motion amplification with respect to the 2D analyses. Nevertheless, due to the scarce amount of retrieved output data by 3D numerical simulations, it was not possible to create Seismic Microzonation maps based on these data.

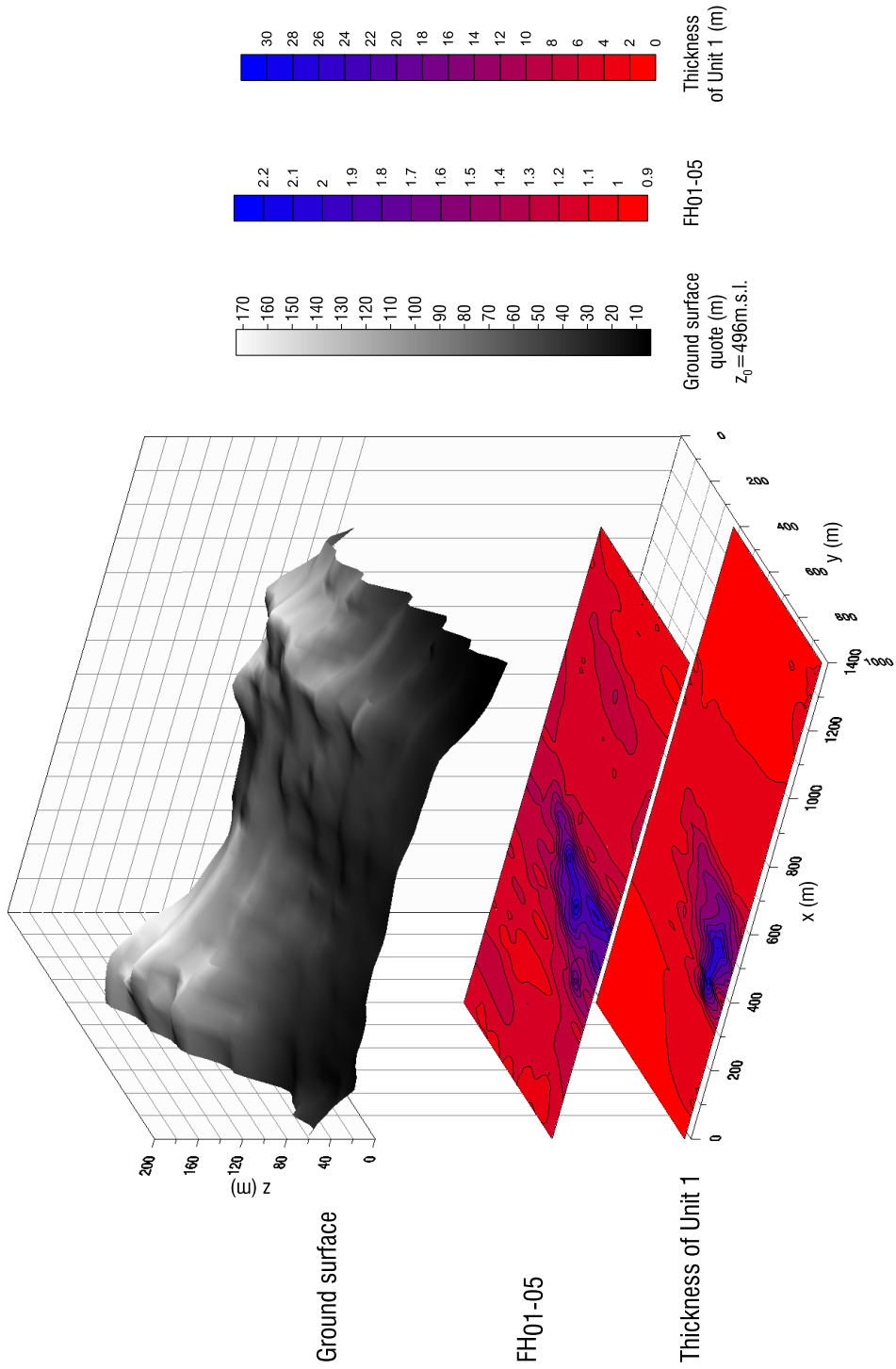


Fig. 144 Topography of Bovino urban area, Seismic Microzonation map related to FH₀₁₋₀₅ (PLAXIS, Cx) and map of the unit 1 thickness

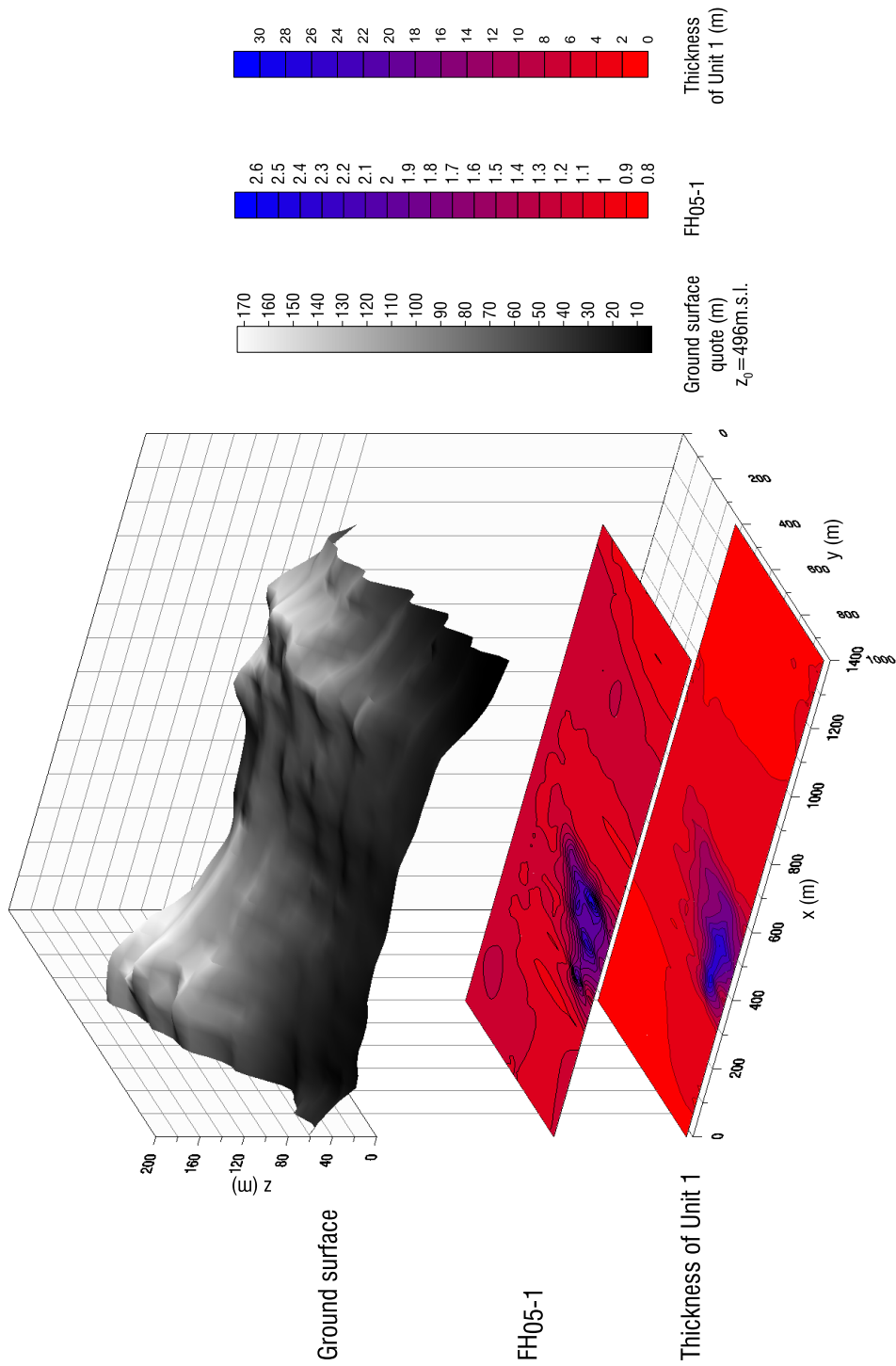


Fig. 145 Topography of Bovino urban area, Seismic Microzonation map related to FH₀₅₋₁ (PLAXIS, Cx) and map of the unit 1 thickness

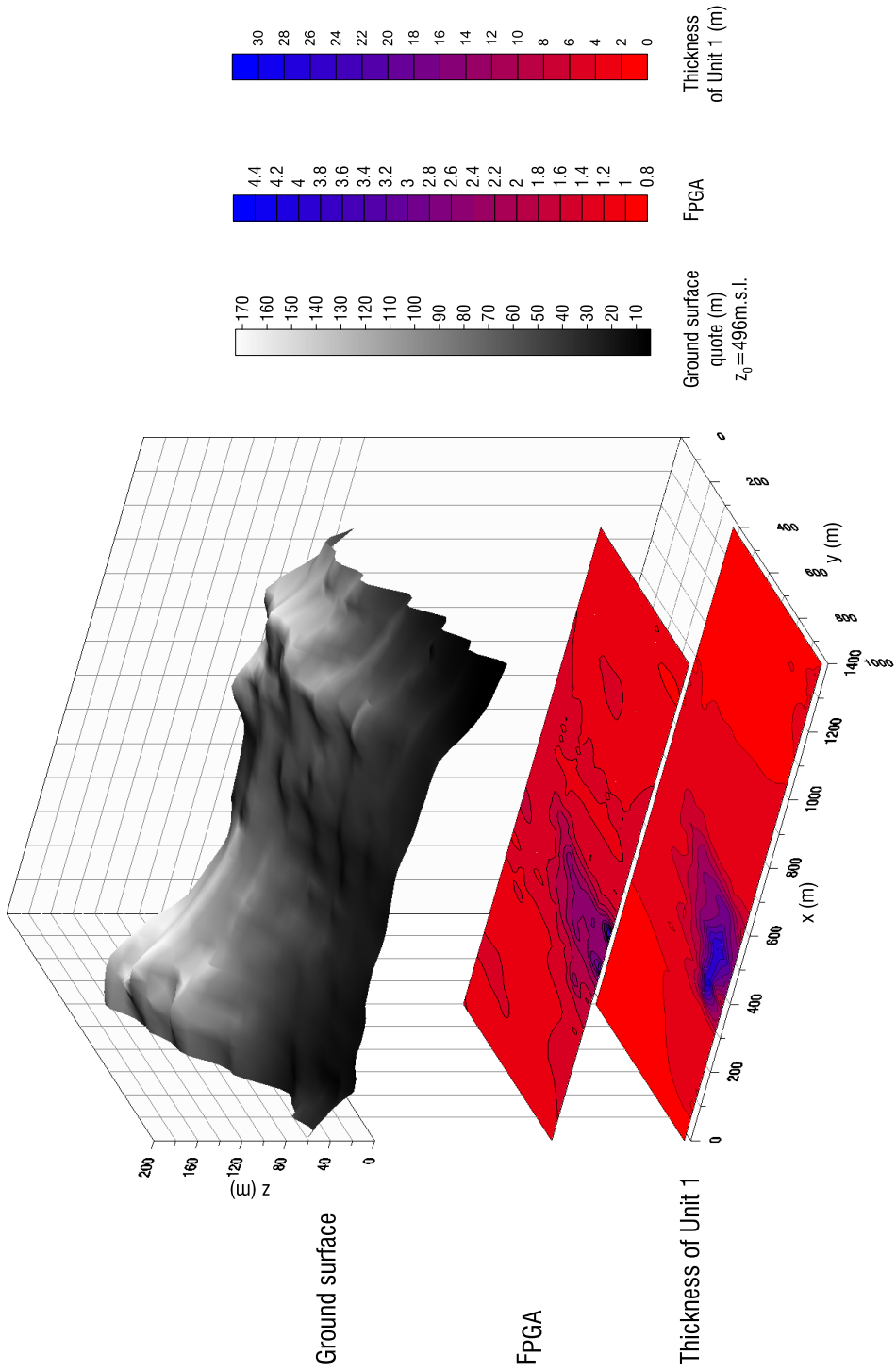


Fig. 146 Topography of Bovino urban area, Seismic Microzonation map related to F_{PGA} (PLAXIS, Cx) and map of the unit 1 thickness

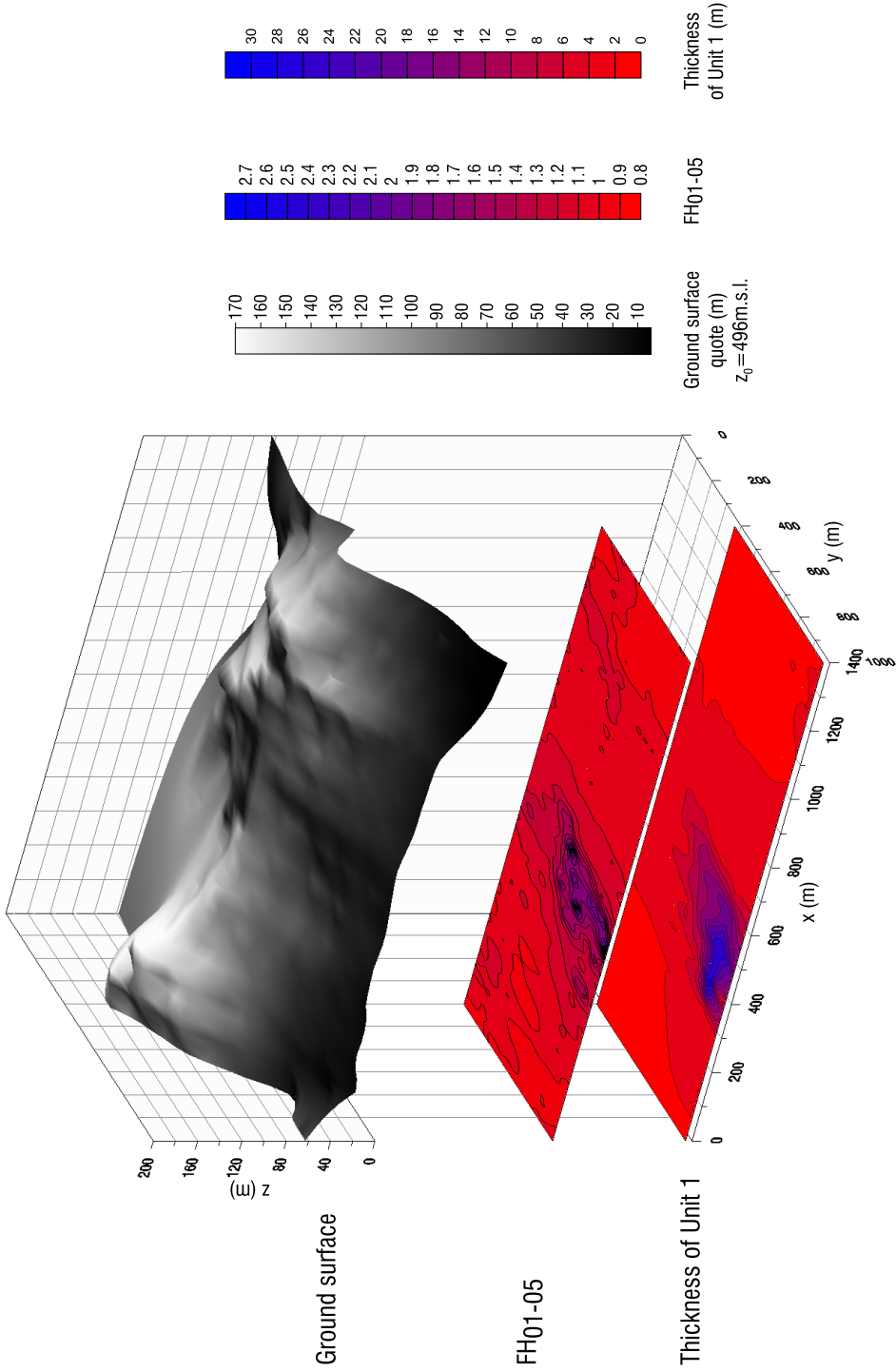


Fig. 147 Topography of Bovino urban area, Seismic Microzonation map related to FH₀₁₋₀₅ (QUAKE/W, I3) and map of the unit 1 thickness

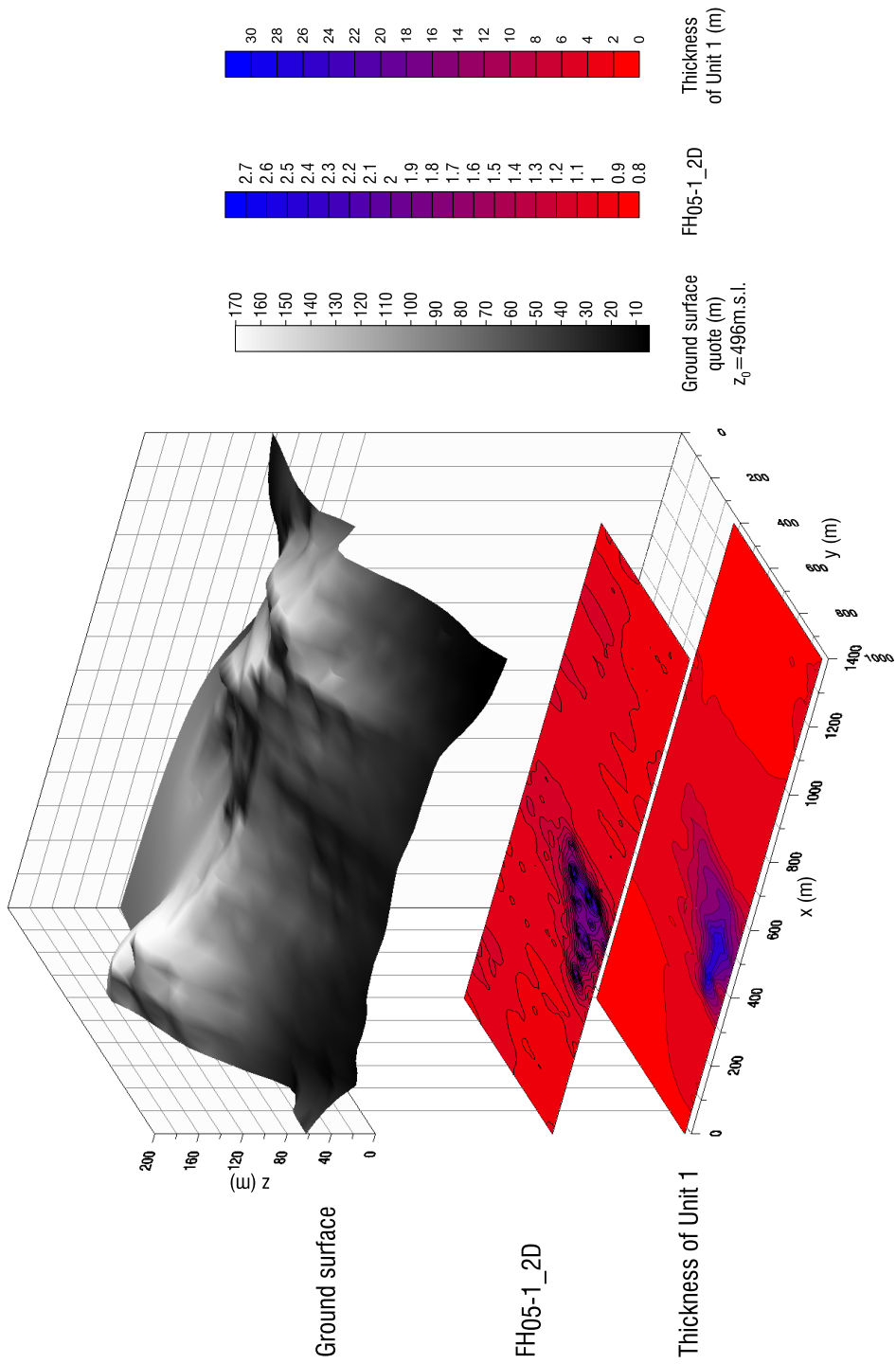


Fig. 148 Topography of Bovino urban area, Seismic Microzonation map related to FH₀₅₋₁ (QUAKE/W, I3) and map of the unit 1 thickness

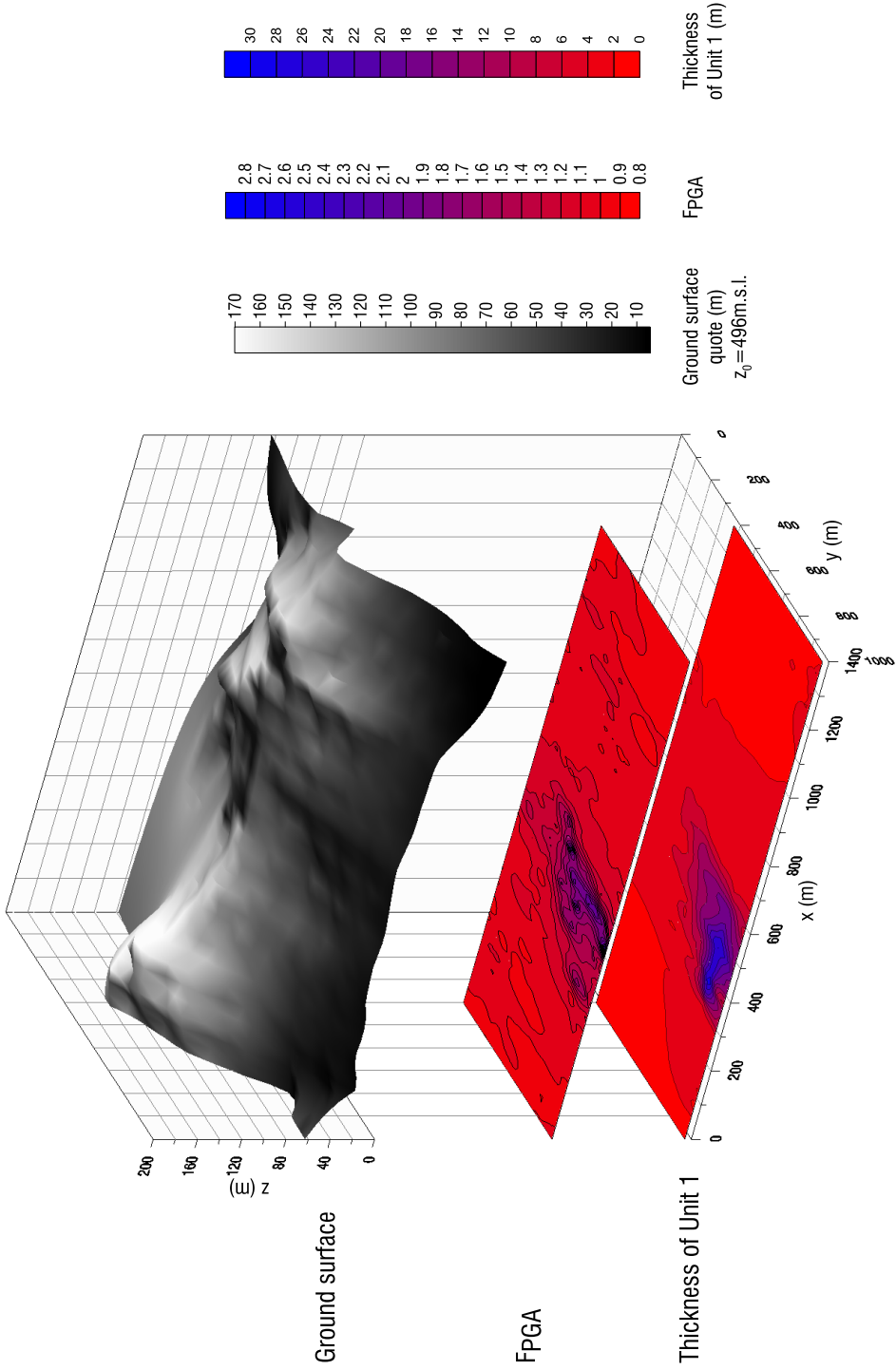


Fig. 149 Topography of Bovino urban area, Seismic Microzonation map related to F_{PGA} (QUAKEW, I3) and map of the unit 1 thickness

CONCLUSIONS

The present work is focused on the numerical prediction of seismic site response obtained using two finite element codes: QUAKE/W and PLAXIS 3D.

The numerical simulation of wave propagation requires the application of the input motion at the base of the numerical model in terms of either acceleration or shear stress time history, i.e. referring to rigid and compliant base, respectively.

The base accelerogram should be computed through deconvolution of outcrop signal or measured in situ by means of deep seismometer arrays.

The shear stress time history is determined as a linear function of the physical and mechanical parameters of the bedrock and of the outcrop signal; the base accelerogram is an outcome of the numerical analysis. Thus, the compliant base allows to define a unique input motion in terms of shear stress time history, regardless of bedrock depth and bedrock thickness simulated in the numerical model.

The compliant base boundary condition was adopted for all numerical simulation performed in this study.

The constitutive models adopted to simulate the non-linear soil behaviour are summarized in the following:

- linear equivalent model as provided in the library of QUAKE/W;
- Hardening Soil Model with small strain stiffness (HSsmall), available in the material model library of PLAXIS 3D. HSsmall is an isotropic hardening elasto-plastic hysteretic model which allows to take into account the non-linear soil behaviour. The model has a pre-yield para-elastic hysteretic scheme

which controls the shear modulus degradation and the corresponding variation of the damping ratio.

Vertical propagating S-waves from the bedrock were only considered in the analyses. The numerical approaches adopted were validated with reference to ideal 1D cases. The motion determined at the bedrock and at the ground surface by means of the adopted FE codes were compared with the available analytical solutions and well established numerical linear-equivalent ones, the latter obtained with the code EERA. The following ideal cases were considered: homogeneous linear elastic half-space, homogeneous linear elastic soil deposit and homogeneous non-linear elastic soil deposit.

Very good agreement among the different sets of results was obtained, thus demonstrating the reliability of the FE approaches in reproducing the frequency domain solution provided by EERA.

The 1D analyses demonstrated that the numerical simulations provide the same results regardless of the bedrock thickness. Additionally, it was not possible to define a base input in terms of acceleration time history for 2D and 3D numerical model, so the compliant base boundary condition was applied in order to perform multi-dimensional seismic site response analyses.

The Bovino case study was finally analysed, with the aim of evaluating the site response in presence of complex local conditions, both stratigraphic and topographic, by means of mono and multi-dimensional analyses. Some prescriptions proposed by Italian guidelines for seismic microzonation were considered in the analyses, in order to provide the greatest detailed level-III seismic microzonation study.

The Bovino village, located in South of Italy, was chosen due to the presence of a soft soil valley surrounded by rock outcrop hills, which allows to investigate complex site-effects.

Firstly, the local geology and topography were described and the geotechnical model was defined on the basis of the available field and laboratory data. The reference seismic motions used in the analyses, based on the Italian probabilistic seismic haz-

ard study, were also described. In particular, seven real accelerograms were selected as reference motions.

1D and 2D analyses were carried out using the code QUAKE/W and assuming the seven reference signals. Subsequently, 1D, 2D and 3D analyses were performed by means of PLAXIS 3D, assuming two reference motions.

Ground motion modifications were evaluated in terms of amplification factors, which were determined by comparing the numerically predicted surface ground motions against the reference accelerograms, in order to highlight the range of periods affected by the greatest amplifications.

The seismic site response was found to be strictly dependent on the dimensional assumption adopted.

1D analyses do not allow to evaluate topographic effects; on the other hand, multi-dimensional analyses showed peak values of the amplification factors at the crest of the outcropping hill and a slightly de-amplification of the reference signal at the toe of the hill. Furthermore, with reference to soil columns extracted from superficial valley, 1D results showed peak values of amplification factor profiles. Instead, amplification factors about equal to 1 were obtained for a valley depth of about 30m maximum.

Multi-dimensional analyses allowed to evaluate valley effects due to uneven interfaces between soil material. The greatest amplification factors were obtained in the valley area. 2D results are depending more on the horizontal direction of the input motion compared to the 3D ones. Additionally, with reference to 3D schemes, it was observed that the application of the input motion along one direction, for example "x", resulted in "parasitic" horizontal ground motion along the transversal direction, that is "y". This "parasitic" motion induces a greater amplification, as observed when comparing the results obtained by the application of the input motion along one direction with those obtained by the simultaneous application of the input motion along two directions.

An additional phenomenon was recognised in the 3D valley, with particular reference to the constitutive assumptions. The valley material is a soft non-linear soil, for which the HSsmall constitutive model was considered. By applying simultaneously two hori-

zontal components of motion, the HSsmall model responds in a stiffer and less dissipative fashion as compared to the case of only one horizontal input motion.

In general, the amplification factor profiles were observed to depend on the following ingredients: sequence of soil layers, velocity contrast between soil layers, thickness of each layer, dynamic behaviour of the soils, topography, geometry of the sub-interface and mechanical behaviour of the soils.

The seismic microzonation maps (in which seismic homogeneous areas were recognised) were finally proposed, together with the definition of reliable seismic microzonation procedures. In particular, the outcomes of the present work encourage the use of advanced 2D and 3D dynamic numerical analyses for the seismic site response investigation and the definition of seismic microzonation maps.

REFERENCES

- Aki, K., Larner, K.L. & Jennings, P.C., 1970. Surface motion of a layered medium having an irregular interface due to incident plane SH waves. *Journal of Geophysical Research*, 75(5), pp.933–954.
- Albarello, D. & Castellaro, S., 2011. Tecniche sismiche passive: indagini a stazione singola. *Ingegneria Sismica*, 2, p.32.
- Amorosi, A., Boldini, D. & Elia, G., 2010. Parametric study on seismic ground response by finite element modelling. *Computers and Geotechnics*, 37(4), pp.515–528.
- Amorosi, A., Boldini, D. & di Lernia, A., 2016. Seismic ground response at Lotung: Hysteretic elasto-plastic-based 3D analyses. *Soil Dynamics and Earthquake Engineering*, 85, pp.44–61.
- Amorosi, A., Boldini, D. & Sasso, M., 2008. Modellazione numerica del comportamento dinamico di gallerie superficiali in terreni argillosi - AMS Acta - AlmaDL Università di Bologna.
- Bard, P.-Y. & Bouchon, M., 1980a. The seismic response of sediment-filled valleys. Part 1. The case of incident SH waves. *Bulletin of the Seismological Society of America*, 70(4), pp.1263–1286.
- Bard, P.-Y. & Bouchon, M., 1980b. The seismic response of sediment-filled valleys. Part 2. The case of incident P and SV waves. *Bulletin of the Seismological Society of America*, 70(5), pp.1921–1941.
- Bardet, J.P., Ichii, K. & Lin, C.H., 2000. *EERA - A Computer Program for Equivalent-Linear Earthquake Site Response Analysis of Layered Soil Deposits* U. of S. C. D. of C. Engineering, ed.,
- Bathe, K.-J., 1996. *Finite Element Procedures* 2nd ed., Upper Saddle River, N.J.: Prentice Hall.
- Benz, T., 2006. *Small-Strain Stiffness of Soils and its numerical consequences*. PhD

Thesis. University of Stuttgart.

- Benz, T., Vermeer, P.A. & Schwab, R., 2009. A small-strain overlay model. *International Journal for Numerical and Analytical Methods in Geomechanics*, 33(1), pp.25–44.
- Bommer, J.J. & Acevedo, A.B., 2004. The use of real earthquake accelerograms as input to dynamic analysis. In *Journal of Earthquake Engineering*. pp. 43–91.
- Bouchon, M., 1973. Effect of topography on surface motion. *Bulletin of the Seismological Society of America*, 63(2), pp.615–632.
- Bouckovalas, G.D. & Papadimitriou, A.G., 2005. Numerical evaluation of slope topography effects on seismic ground motion. *Soil Dynamics and Earthquake Engineering*, 25(7–10), pp.547–558.
- Cotecchia, F. et al., 2016. Slow landslides in urbanised clayey slopes: an emblematic case from the south of Italy. In C. Press, ed. *Landslides and Engineered Slopes. Experience, Theory and Practice*. pp. 691–698.
- Darendeli, M.B., 2001. Development of a new family of normalized modulus reduction and material damping curves. PhD Thesis. The University of Texas at Austin.
- Fäh, D. et al., 2006. The earthquake of 250 a.d. in Augusta Raurica, A real event with a 3D site-effect. *Journal of Seismology*, 10(4), pp.459–477.
- Falcone, G. et al., 2015. Microzonazione sismica di livello 3 di un comune della daunia: analisi preliminari. In *Proceedings of the conference IARG 2015*. Cagliari, Italy.
- Gatmiri, B. & Arson, C., 2008. Seismic site effects by an optimized 2D BE/FE method II. Quantification of site effects in two-dimensional sedimentary valleys. *Soil Dynamics and Earthquake Engineering*, 28(8), pp.646–661.
- Gazetas, G., 1982. Vibrational characteristics of soil deposits with variable wave velocity. *International journal for numerical and analytical methods in geomechanics*, 6, pp.1–20.
- Geli, L., Bard, P.-Y. & Jullien, B., 1988. The effect of topography on earthquake ground motion: A review and new results. *Bulletin of the Seismological Society of America*, 78(1).
- Gruppo di Lavoro, 2004. Redazione della mappa della pericolosità sismica prevista dall'Ordinanza PCM del 20 marzo 2003, Rapporto conclusivo per il Dipartimento della Protezione Civile.
- Gruppo di Lavoro MS, 2008. Indirizzi e criteri per la microzonazione sismica.
- Hernandez, B. et al., 2004. Rupture history of the 1997 Umbria-Marche (Central Italy) main shocks from the inversion of GPS, DInSAR and near field strong motion data. *Annals of Geophysics*, 47(4).
- Hisada, Y., Aki, K. & Teng, T.-L., 1993. 3-D simulations of surface wave propagation

- in the kanto sedimentary basin, japan part 2: application of the surface wave BEM. *Bulletin of the Seismological Society of America*, 83(6), pp.1700–1720.
- Iervolino, I., Galasso, C. & Cosenza, E., 2009. REXEL: computer aided record selection for code-based seismic structural analysis. *Bulletin of Earthquake Engineering*, 8(2), pp.339–362.
- Jiang, T. & Kuribayashi, E., 1988. The three-dimensional resonance of axisymmetric sediment-filled valleys. *Soils and Foundations*, 28(4), pp.130–146.
- Jibson, R.W., 1987. *Summary of research on the effects of topographic amplification of earthquake shaking on slope stability*, Mnlo Park, California.
- Krahn, J., 2004. Dynamic modeling with QUAKE/W: an engineering methodology.
- Kramer, S., 1996. *Geotechnical earthquake engineering*, Upper Saddle River N.J.: Prentice Hall.
- Kuhlemeyer, R.L. & Lysmer, J., 1973. Finite Element Method Accuracy for Wave Propagation Problems. *Journal of the Soil Mechanics and Foundations Division*, 99(5), pp.421–427.
- Landolfi, L., 2013. *Analisi della risposta sismica locale in condizioni complesse di sottosuolo: il caso di Castelnuovo (AQ)*. PhD Thesis. Università degli studi di Napoli Federico II.
- Lanzo, G. et al., 2011. Site response studies and seismic microzoning in the Middle Aterno valley (L'aquila, Central Italy). *Bulletin of Earthquake Engineering*, 9(5), pp.1417–1442.
- Lanzo, G. & Silvestri, F., 1999. *Risposta sismica locale*. Hevelius, Benenvento.
- Lee, S.-J. et al., 2009. Effects of Realistic Surface Topography on Seismic Ground Motion in the Yangminshan Region of Taiwan Based Upon the Spectral-Element Method and LiDAR DTM. *Bulletin of the Seismological Society of America*, 99(2A), pp.681–693.
- di Lernia, A., 2014. *Interazione dinamica terreno-struttura mediante approcci non lineari tridimensionali agli elementi finiti*. PhD Thesis. Politecnico di Bari.
- Lysmer, J. & Kuhlemeyer, R.L., 1969. Finite Dynamic Model For Infinite Media. *Journal of the Engineering Mechanics Division*, 95(4), pp.859–878.
- Madiai, C. & Simoni, G., 2013. Analyses of the basin geometry effects across the Aterno Valley in Petogna (L'Aquila), Italy. *Rivista Italiana di Geotecnica*, 4, pp.24–37.
- Makra, K. & Chávez-García, F.J., 2016. Site effects in 3D basins using 1D and 2D models: an evaluation of the differences based on simulations of the seismic response of Euroseistest. *Bulletin of Earthquake Engineering*, 14(4), pp.1177–1194.
- Maufroy, E. et al., 2016. Earthquake Ground Motion in the Mygdonian Basin, Greece:

- Latest Lessons from the E2VP Verification and Validation Project. *Soil Dynamics and Earthquake Engineering*.
- Mejia, L.H. & Dawson, E.M., 2006. Earthquake deconvolution for FLAC. In *4th International FLAC Symposium on Numerical Modeling in Geomechanics*. Minneapolis: Itasca Consulting Group.
- NTC, 2008. '*Norme Tecniche per le Costruzioni*', Italia: D.M. 14 Gennaio 2008.
- Ohori, M., Koketsu, K. & Minami, T., 1992. Seismic Responses of Three-Dimensionally Sediment-Filled Valleys due to Incident Plane Waves. *J. Phys. Earth*, 40, pp.209–222.
- Pagliaroli, A., Quadrio, B., et al., 2014. Numerical modelling of site effects in the Palatine Hill, Roman Forum, and Coliseum Archaeological Area. *Bulletin of Earthquake Engineering*, 12(3), pp.1383–1403.
- Pagliaroli, A., Moscatelli, M., et al., 2014. Seismic microzonation of the central archaeological area of Rome: results and uncertainties. *Bulletin of Earthquake Engineering*, 12(3), pp.1405–1428.
- Palladino, G., 2001. Relazione Tecnica e illustrativa – Progetto di Microzonazione sismica di I livello dei Centri abitati della Provincia di Foggia. , pp.69–75.
- Pitilakis, K. et al., 2011. *Earthquake Data in Engineering Seismology* S. Akkar, P. Gülkan, & T. van Eck, eds., Dordrecht: Springer Netherlands.
- PLAXIS, 2016. Reference Manual.
- Régnier, J. et al., 2016. International Benchmark on Numerical Simulations for 1D, Nonlinear Site Response (PRENOLIN): Verification Phase Based on Canonical Cases. *Bulletin of the Seismological Society of America*, 106(5), pp.2112–2135.
- Rizzitano, S., Cascone, E. & Biondi, G., 2014. Coupling of topographic and stratigraphic effects on seismic response of slopes through 2D linear and equivalent linear analyses. *Soil Dynamics and Earthquake Engineering*, 67, pp.66–84.
- Sahar, D. & Narayan, J.P., 2015. Quantification of focusing effects of the semi-spherical and semi-cylindrical synclinal basement topography on ground motion characteristics. *Journal of Seismology*, 20(1), pp.167–183.
- Sánchez-Sesma, F.J. & Campillo, M., 1991. Diffraction of P, SV, and Rayleigh waves by topographic features: A boundary integral formulation. *Bulletin of the Seismological Society of America*, 81(6), pp.2234–2253.
- Santaloia, F. et al., Failure mechanism and slope evolution of a slow-moving landslide. (*in prep.*).
- Santucci de Magistris, F. et al., 2014. Lessons learned from two case histories of seismic microzonation in Italy. *Natural Hazards*, 74(3), pp.2005–2035.

- SESAME, 2004. *Guidelines for the implementation of the H/V spectral ratio technique on ambient vibrations*,
- Silvestri, F. & D'Onofrio, A., 2014. Risposta sismica e stabilità di centri abitati e infrastrutture. In AGI, ed. *La Geotecnica nella difesa del territorio e delle infrastrutture dalle calamità naturali*. pp. 5–60.
- Smerzini, C., Paolucci, R. & Stupazzini, M., 2011. Comparison of 3D, 2D and 1D numerical approaches to predict long period earthquake ground motion in the Gubbio plain, Central Italy. *Bulletin of Earthquake Engineering*, 9(6), pp.2007–2029.
- Trifunac, M.D., 1971. Surface motion of a semi-cylindrical alluvial valley for incident plane SH waves. *Bulletin of the Seismological Society of America*, 61(6), pp.1755–1770.
- Trifunac, M.D., 1971. Surface motion of a semi-cylindrical alluvial valley for incident plane SH waves. *Bulletin of the Seismological Society of America*, 61(6), pp.1755–1770.
- Viggiani, G. & Atkinson, J.H., 1995. Stiffness of fine-grained soil at very small strains. *Géotechnique*, 45(2), pp.249–265.
- Vucetic, M. & Dobry, R., 1991. Effect of soil plasticity on cyclic response. *Journal of geotechnical engineering*, 117(1), pp.89–107.
- Wong, H.L., 1982. Effect of surface topography on the diffraction of P, SV, and Rayleigh waves. *Bulletin of the Seismological Society of America*, 72(4), pp.1167–1183.

Appendix

survey S	sample	gravel	sand	silt	clay	direct shear		triaxial		ELL	k _m cm/s	E kPa	penetrometer kPa
		(%)	(%)	(%)	(%)	φ' (°)	c' (kPa)	φ' (°)	c' (kPa)	c _u kPa			
1	1	1.53	3.90	60.34	34.23					167			275
1	2	0.21	4.75	86.37	8.67								450
2	1	0.17	6.92	71.35	21.56								358
2	2	0.60	9.14	77.41	13.39					363			442
3	1	5.49	3.03	76.27	15.21	28.28	19.80				1.38E-07	3528	83
3	2	2.78	6.89	73.00	17.32			21.63	15.00		1.75E-06	3571	333
4	1	9.91	18.28	61.59	10.22	24.32	25.97				2.49E-07	4665	367
4	2	8.89	10.65	65.08	15.38			23.89	18.32				458
5	1	1.08	5.96	68.06	24.91	17.03	20.13				4.06E-08	5583	242
5	2	0.37	2.02	59.90	37.71	12.50	39.14				1.43E-07	7709	342
5	3	3.40	7.52	58.95	30.09			20.36	12.32		7.67E-07	7124	308
6	1	6.75	13.66	56.06	23.53	18.26	15.94						292
6	2	0.19	12.75	61.32	25.74	18.06	0.16			71	5.70E-08	718	208
6	3	10.00	9.50	64.76	15.75					122			233
6 BIS	1	1.11	2.54	59.17	37.18			20.95	15.32	245			283
7	1	1.79	10.37	58.57	29.28	25.17	4.02						133
7	2	5.14	11.32	55.91	27.63	23.31	14.74						163
7	3	0.00	0.80	77.84	21.36			23.65	18.23				383
8	1	0.00	3.53	61.49	34.98								325
9	1	0.19	4.56	63.26	31.99			22.95	14.95		1.74E-08	6830	317
9	2	0.24	13.76	58.93	27.07								408
10	1	0.51	4.34	65.48	29.67	14.92	24.24				1.12E-07	5733	217
10	2	1.31	4.98	61.85	31.86					98			217
11	1	0.06	1.17	70.41	28.36						6.78E-08	36364	292
11	2	1.54	2.59	78.96	16.91					69			450
12	1	2.65	11.33	53.04	32.98					232			267
12	2	6.78	11.51	53.60	28.11					238			267
12	3	0.45	10.89	72.71	15.95					285			450
12 BIS	3	4.51	3.42	61.02	31.05					264			308
13	1	0.00	1.11	75.69	23.20						4.97E-07	3719	367
13	2	1.61	4.06	85.92	8.40								500
14	1	1.62	1.26	54.02	43.10			18.53	10.23				400

Table 23 Physical and mechanical properties of the soils within Bovino urban area, part 2

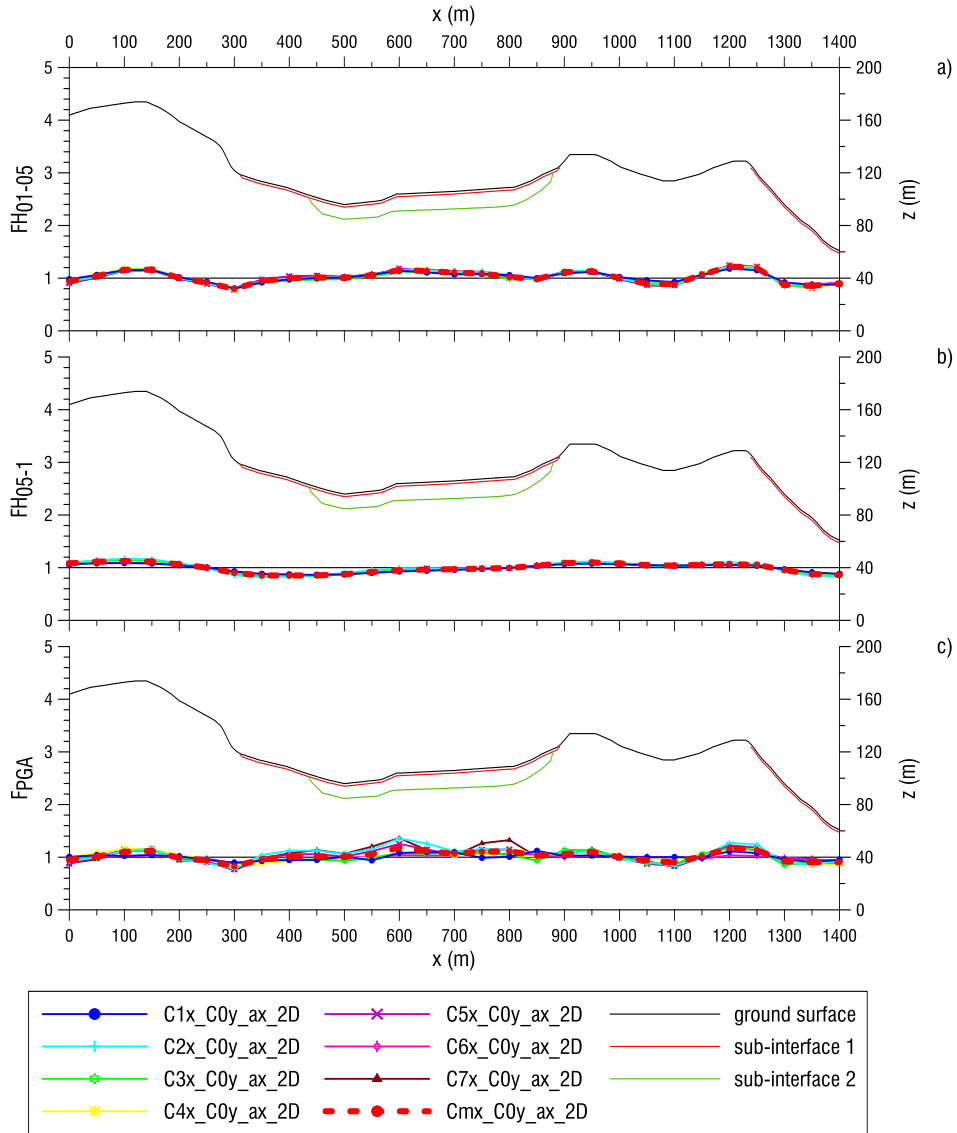


Fig. 150 Amplification factors profiles by means of 2D analyses for section 1 a) FH_{01-05} , b) FH_{05-1} , c) F_{PGA}

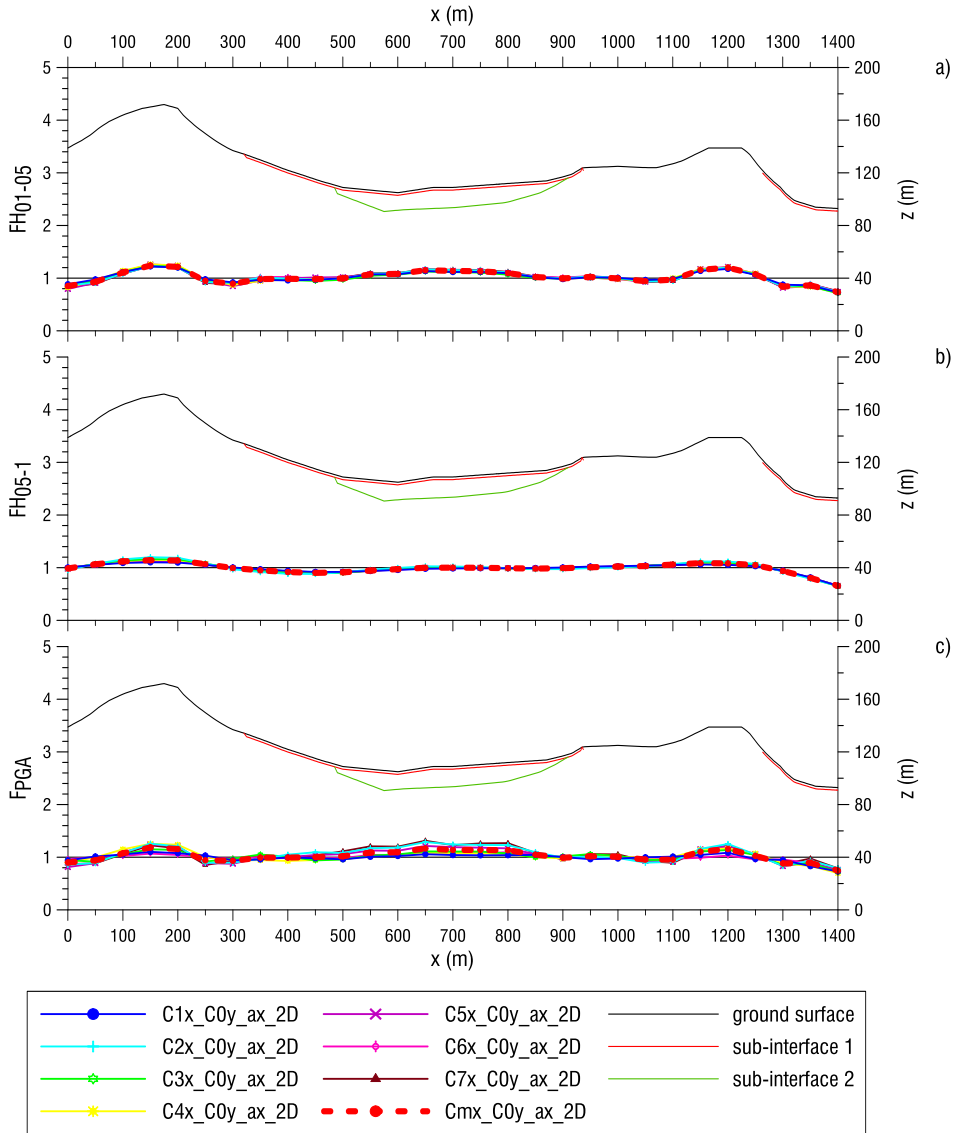


Fig. 151 Amplification factors profiles by means of 2D analyses for section 2 a) $F_{H_{01-05}}$, b) $F_{H_{05-1}}$, c) F_{PGA}

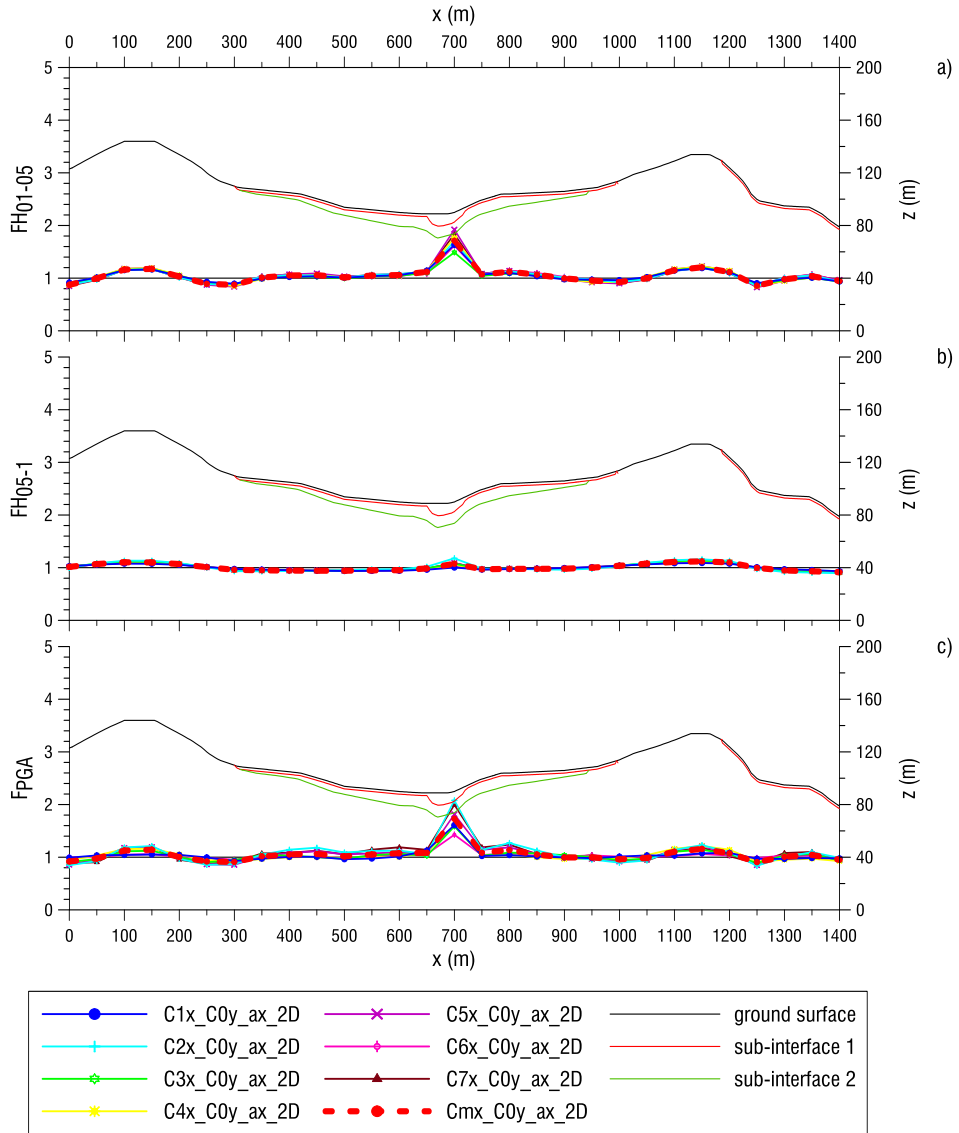


Fig. 152 Amplification factors profiles by means of 2D analyses for section 3 a) FH_{01-05} , b) FH_{05-1} , b) F_{PGA}

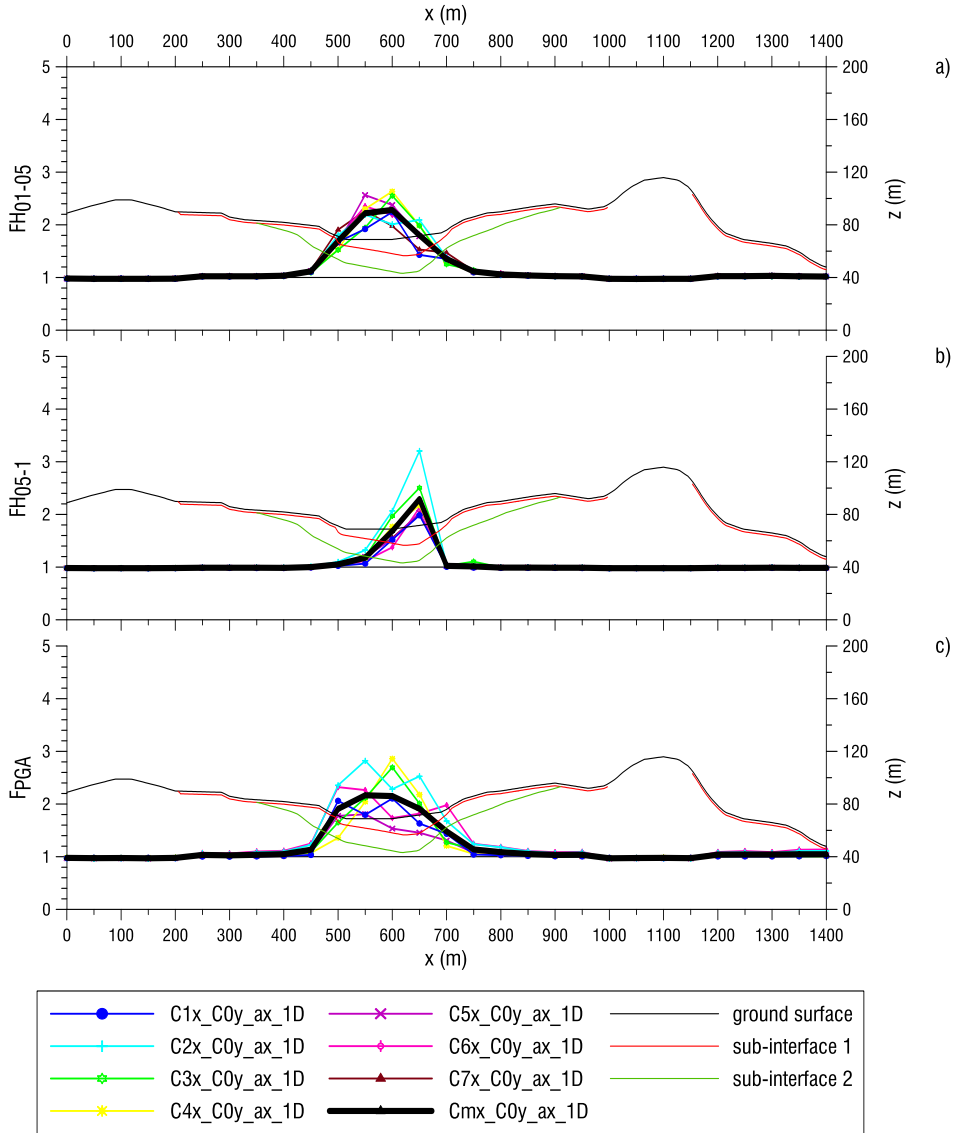


Fig. 153 Amplification factors profiles by means of 1D analyses for section 4 a) FH_{01-05} , b) FH_{05-1} , c) F_{PGA}

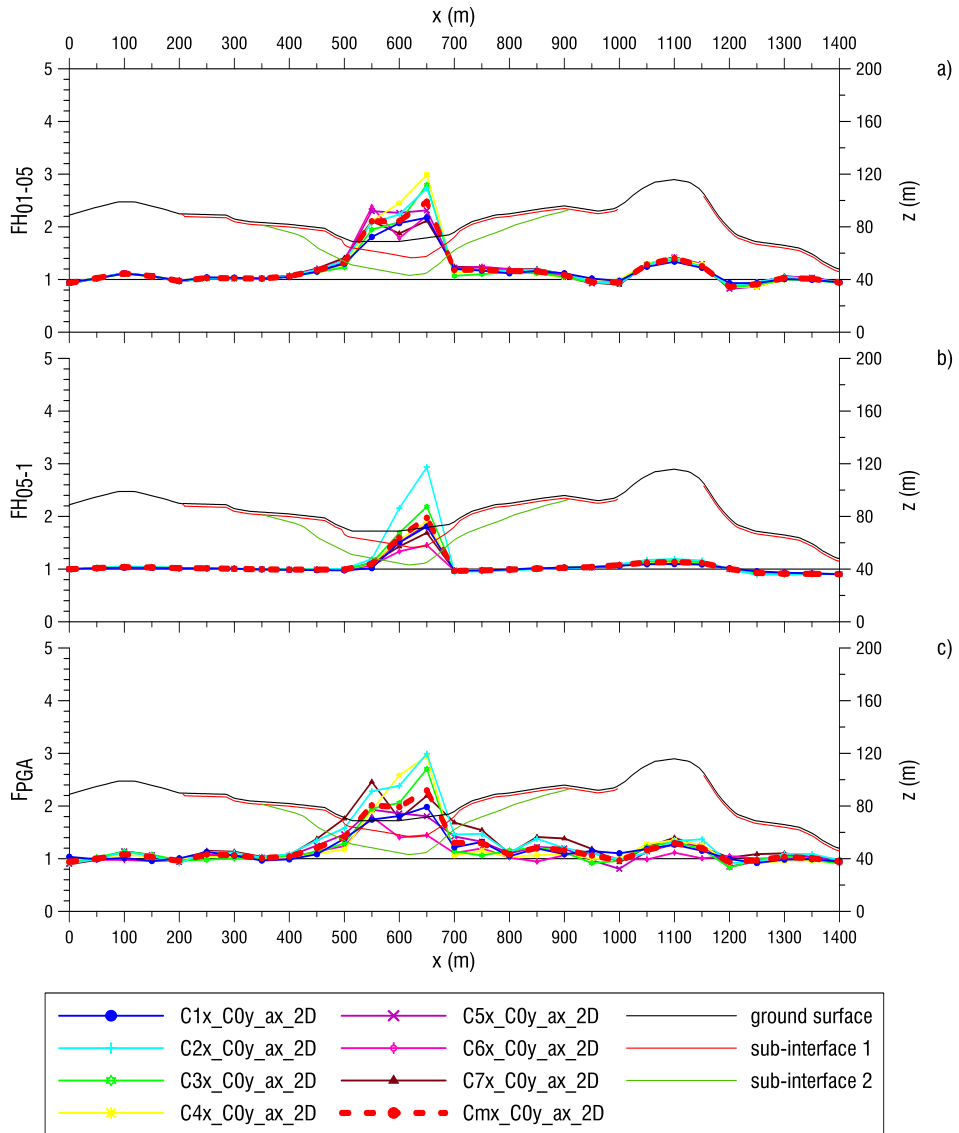


Fig. 154 Amplification factors profiles by means of 2D analyses for section 4 a) FH_{01-05} , b) FH_{05-1} , b) F_{PGA}

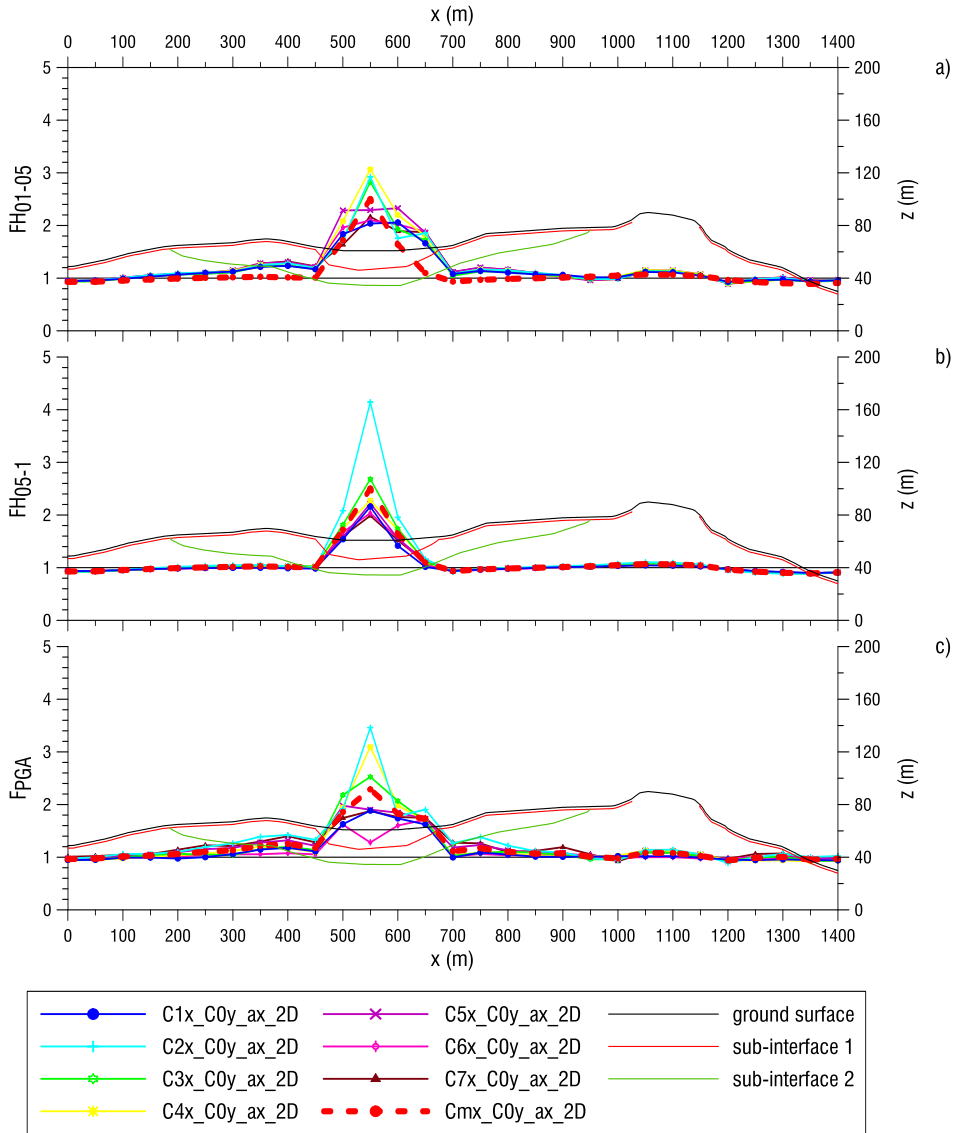


Fig. 155 Amplification factors profiles by means of 2D analyses for section 5 a) FH_{01-05} , b) FH_{05-1} , c) F_{PGA}

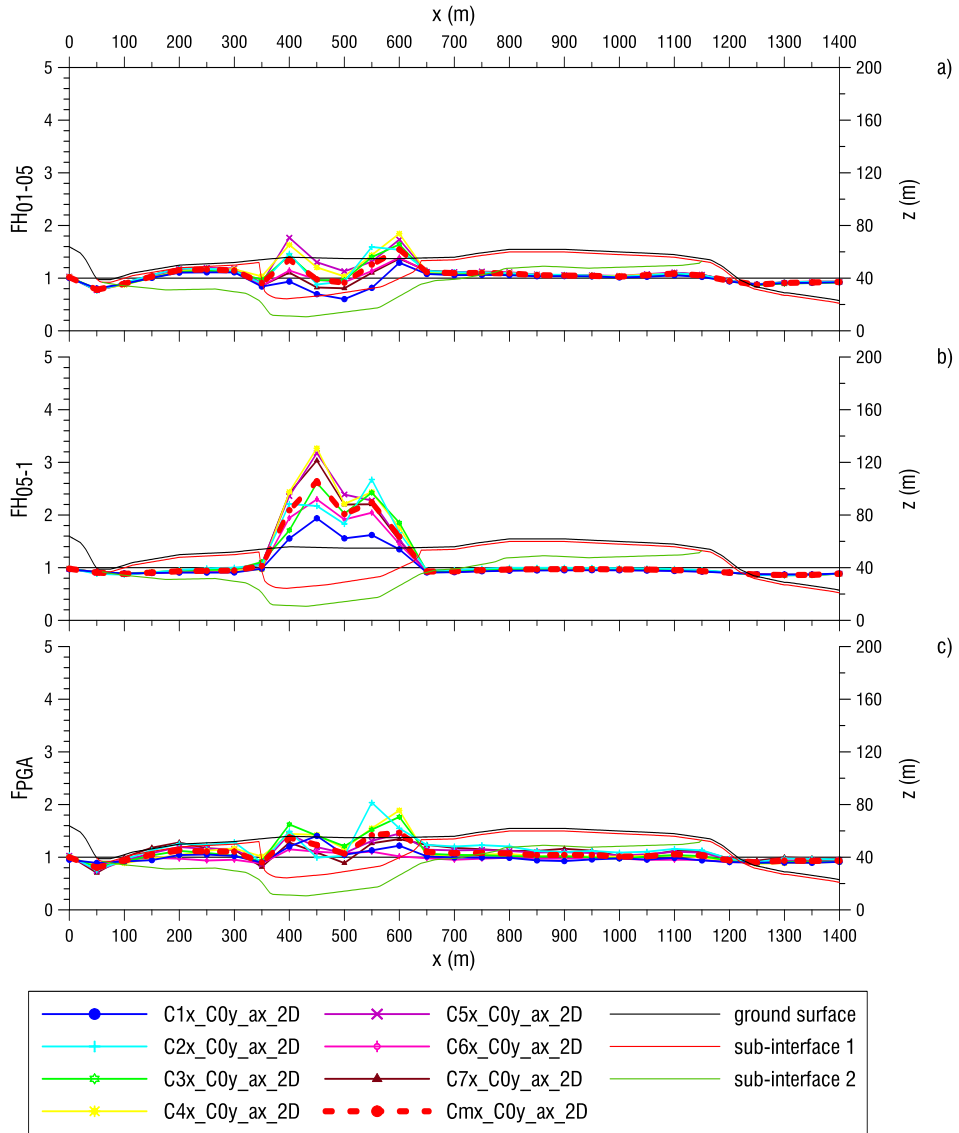


Fig. 156 Amplification factors profiles by means of 2D analyses for section 6 a) FH_{01-05} , b) FH_{05-1} , c) F_{PGA}

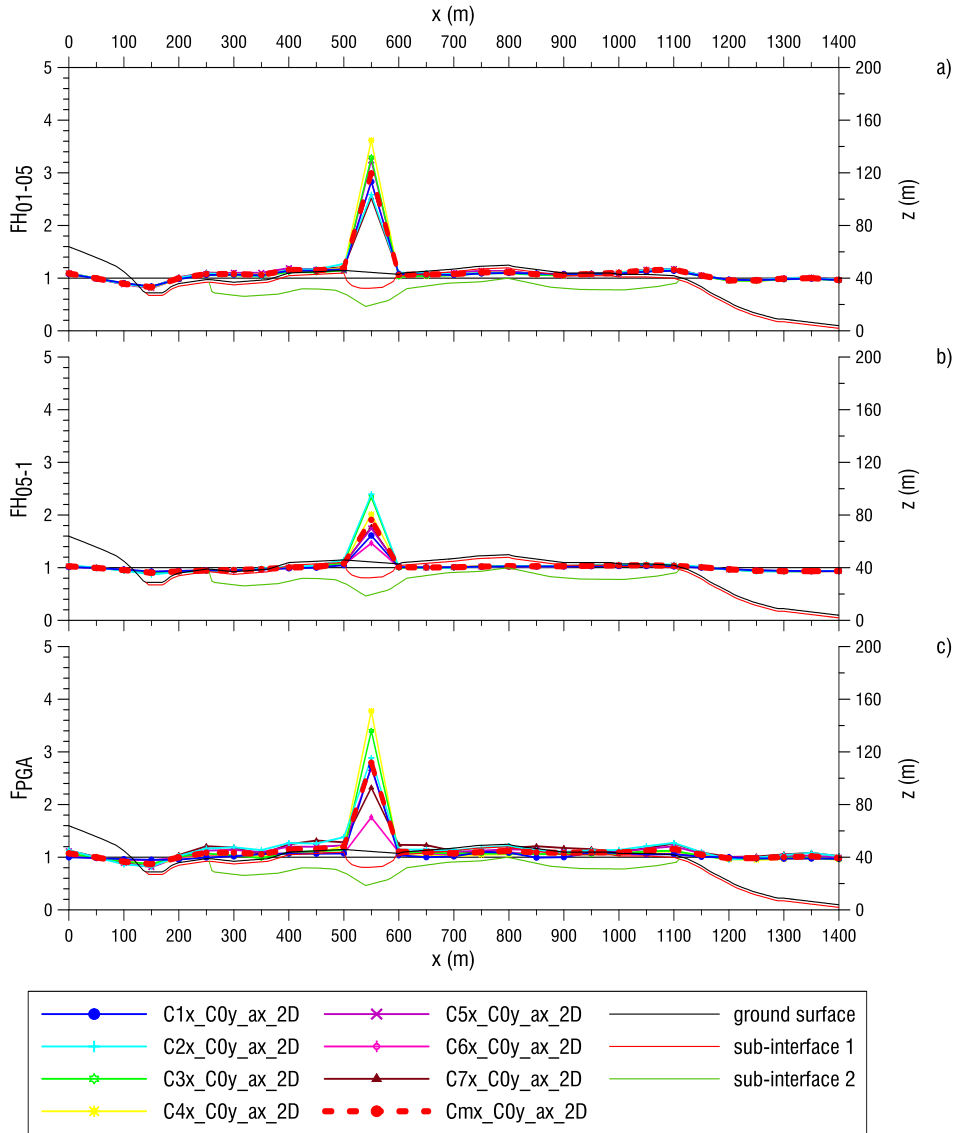


Fig. 157 Amplification factors profiles by means of 2D analyses for section 7 a) FH_{01-05} , b) FH_{05-1} , c) F_{PGA}

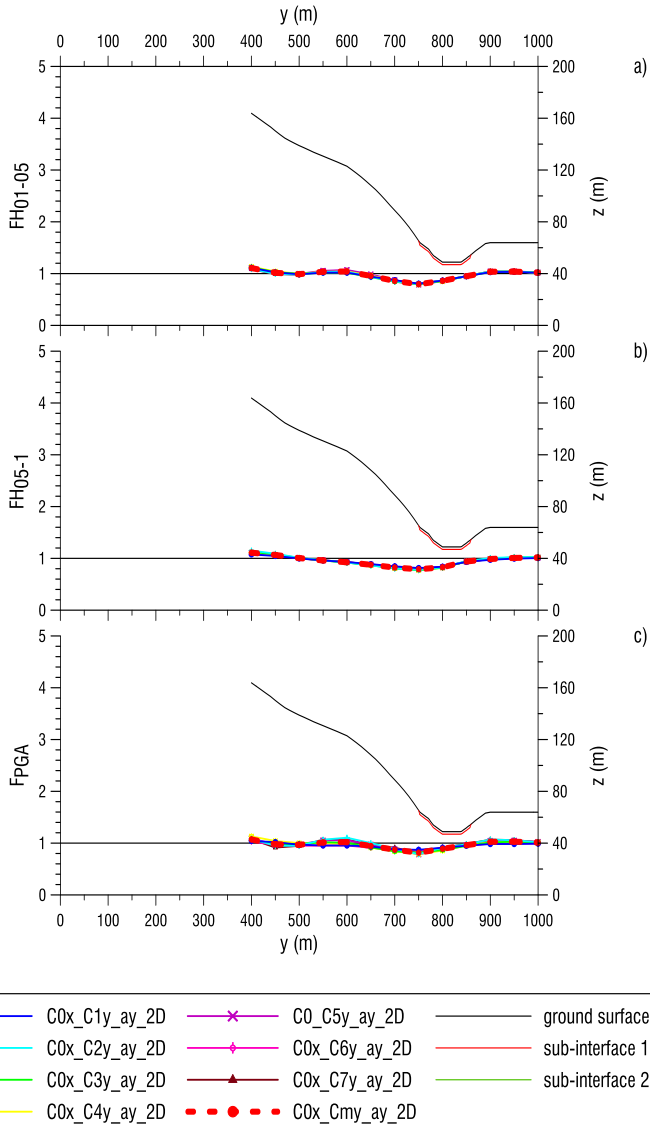


Fig. 158 Amplification factors profiles by means of 2D analyses for section 8 a) FH₀₁₋₀₅, b) FH₀₅₋₁, b) F_{PGA}

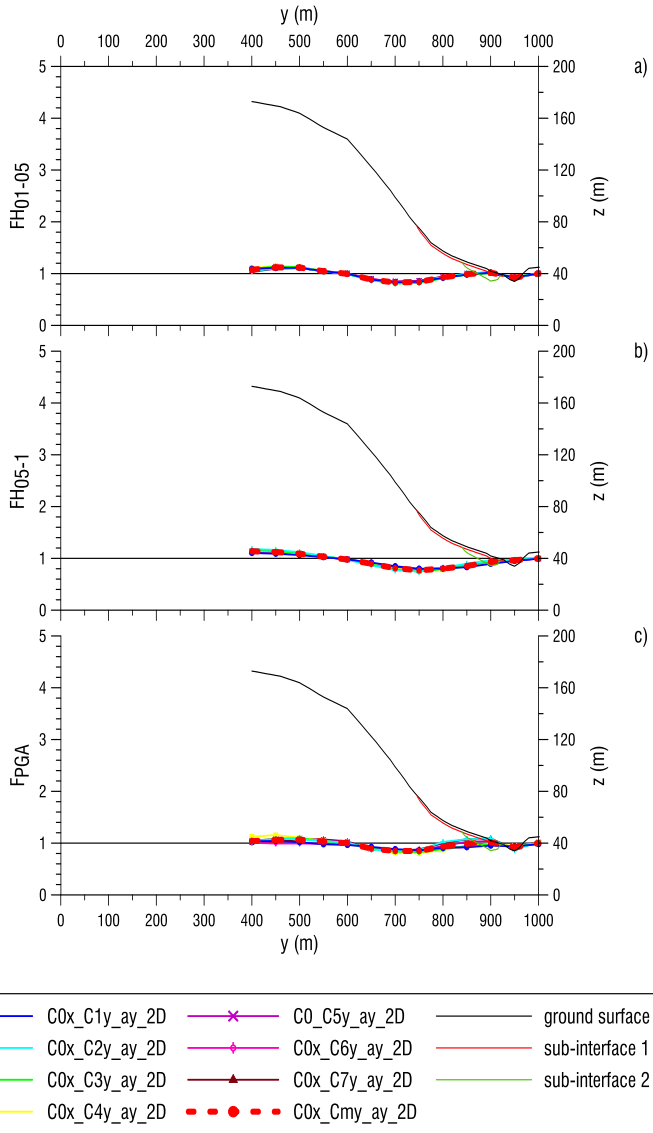


Fig. 159 Amplification factors profiles by means of 2D analyses for section 9 a) FH₀₁₋₀₅, b) FH₀₅₋₁, b) F_{PGA}

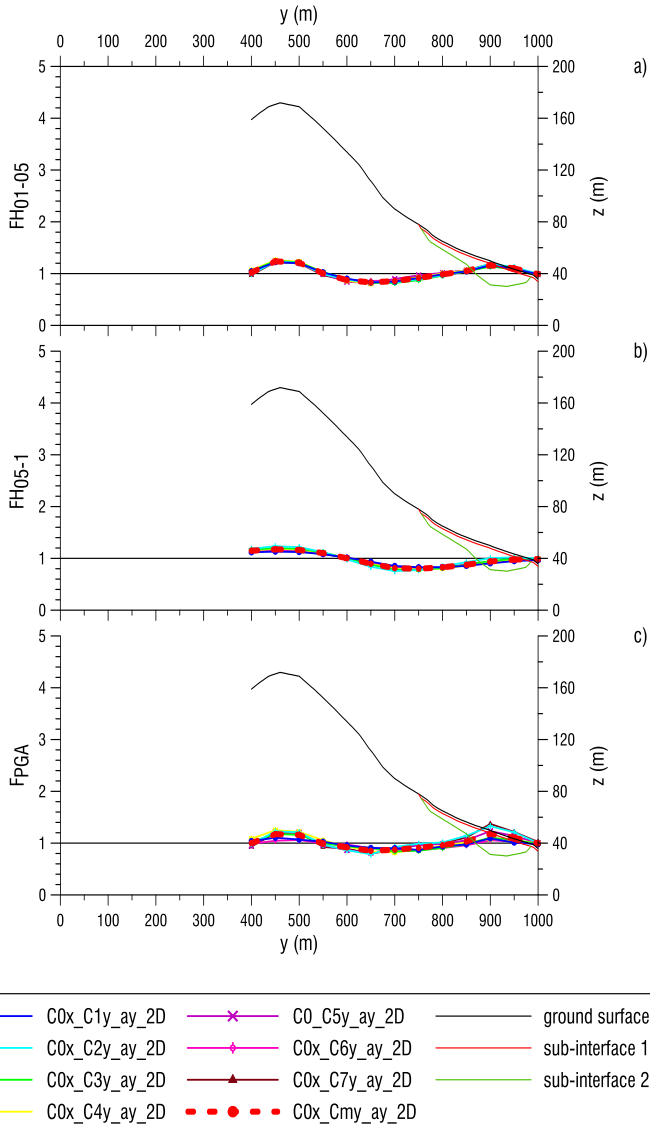


Fig. 160 Amplification factors profiles by means of 2D analyses for section 10 a) F_{H01-05} , b) F_{H05-1} , c) F_{PGA}

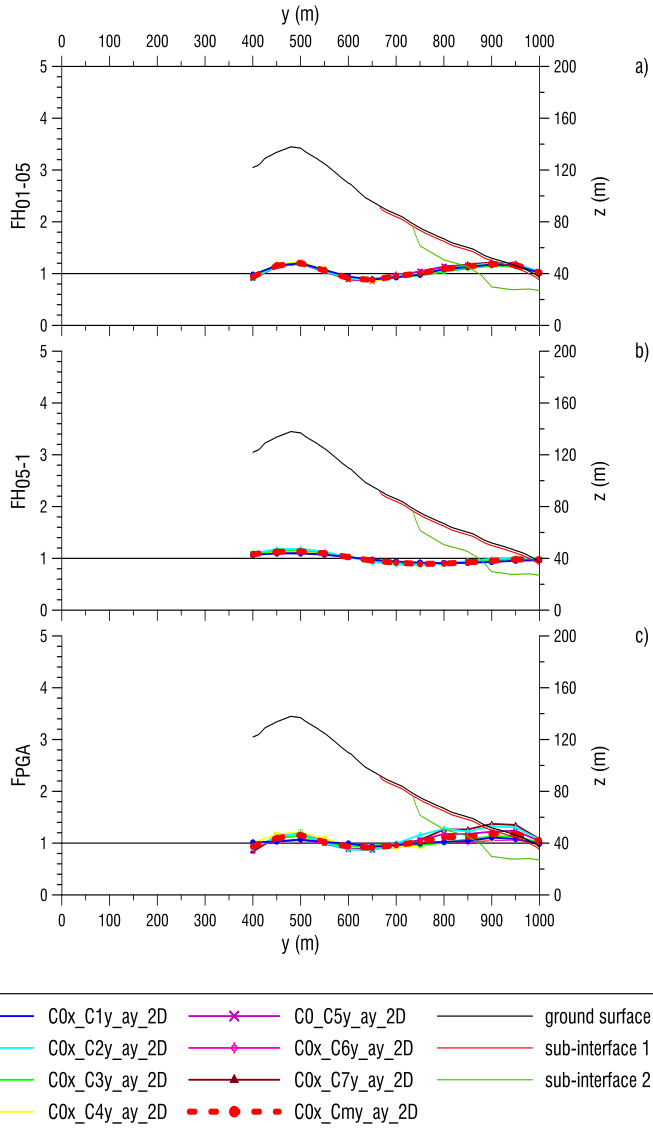


Fig. 161 Amplification factors profiles by means of 2D analyses for section 11 a) F_{H01-05} , b) F_{H05-1} , c) F_{PGA}

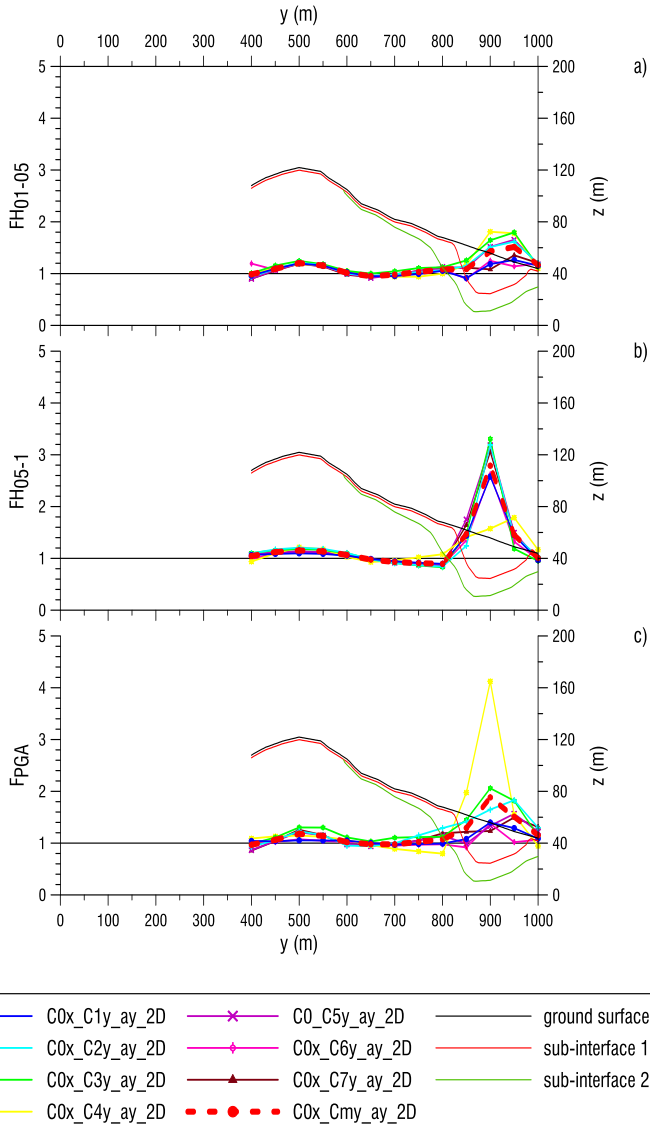


Fig. 162 Amplification factors profiles by means of 2D analyses for section 12 a) F_{H01-05} , b) F_{H05-1} , c) F_{PGA}

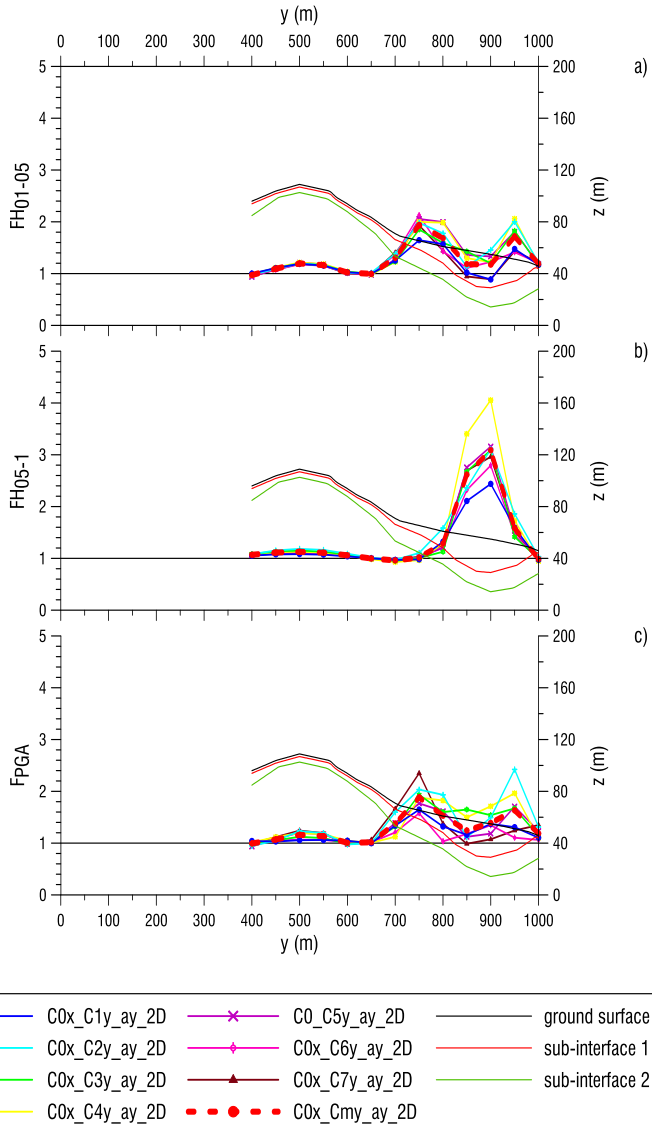


Fig. 163 Amplification factors profiles by means of 2D analyses for section 13 a) FH_{01-05} , b) FH_{05-1} , c) F_{PGA}

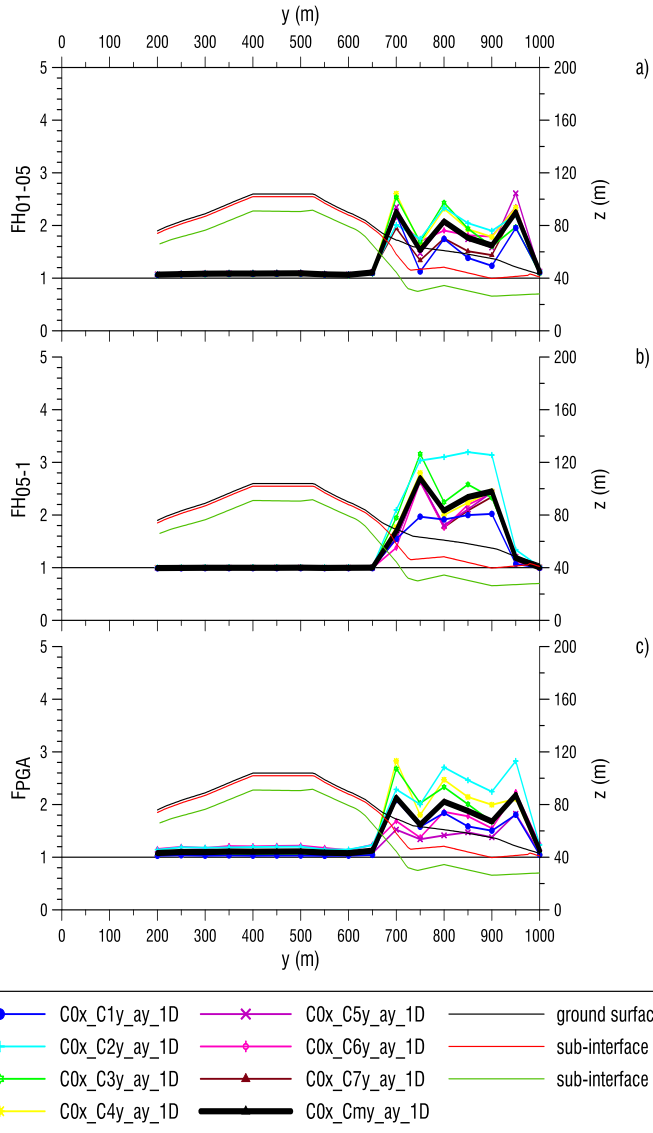


Fig. 164 Amplification factors profiles by means of 1D analyses for section 14 a) F_{H01-05} , b) F_{H05-1} , c) F_{PGA}

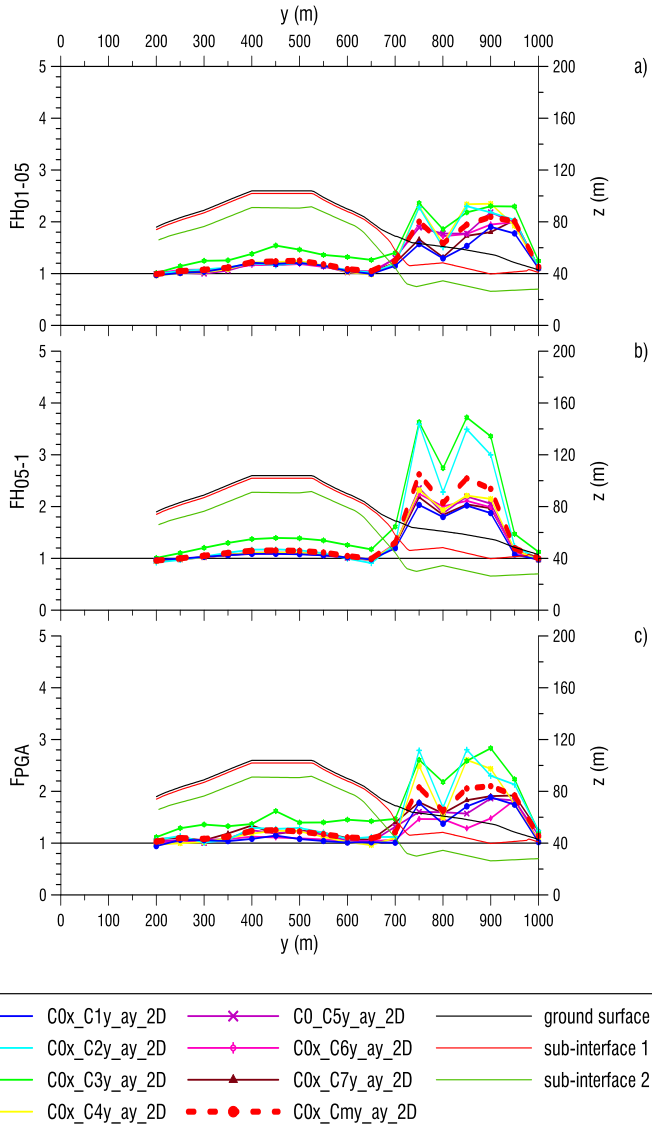


Fig. 165 Amplification factors profiles by means of 2D analyses for section 14 a) F_{H01-05} , b) F_{H05-1} , c) F_{PGA}

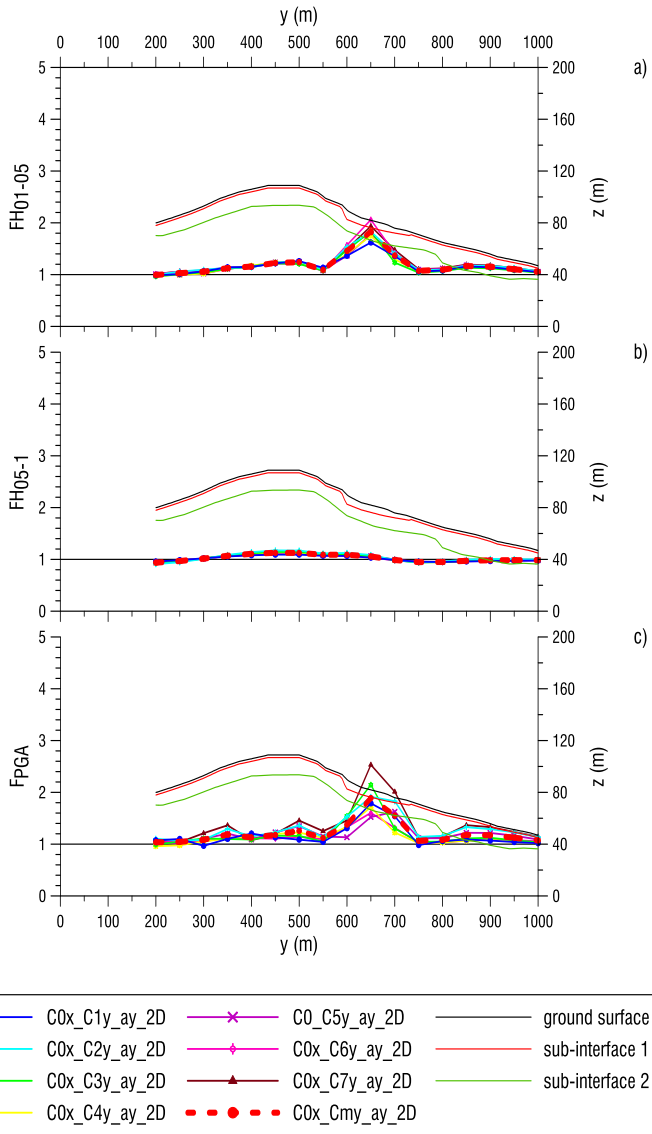


Fig. 166 Amplification factors profiles by means of 2D analyses for section 15 a) $F_{H_{01-05}}$, b) $F_{H_{05-1}}$, c) F_{PGA}

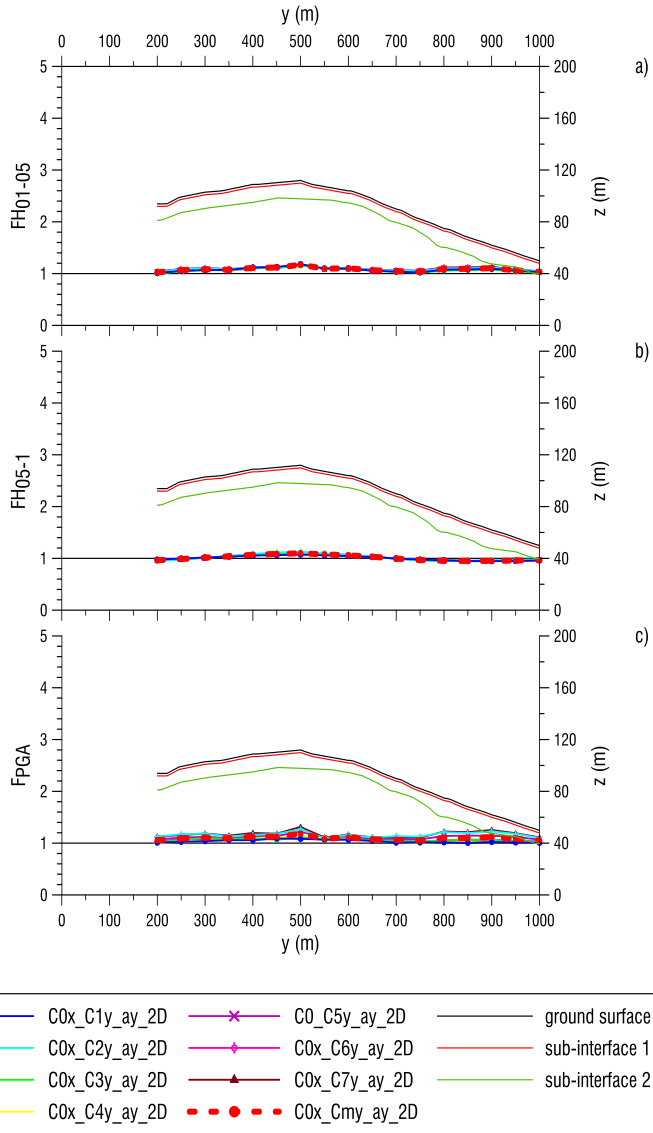


Fig. 167 Amplification factors profiles by means of 2D analyses for section 16 a) F_{H01-05} , b) F_{H05-1} , c) F_{PGA}

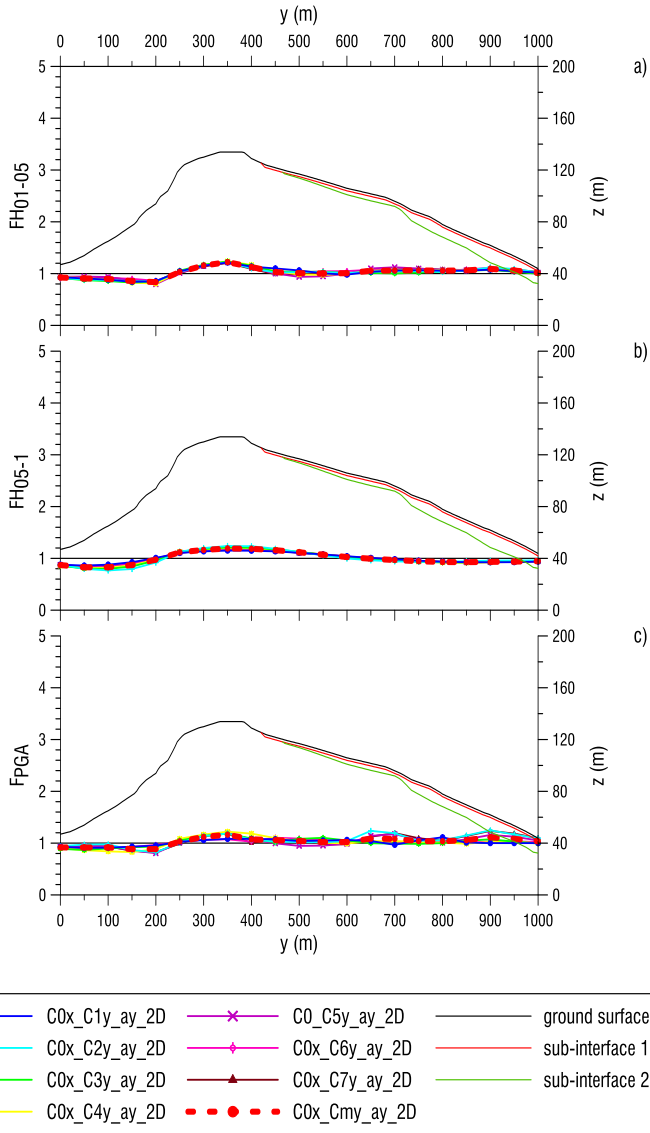


Fig. 168 Amplification factors profiles by means of 2D analyses for section 17 a) FH_{01-05} , b) FH_{05-1} , c) F_{PGA}

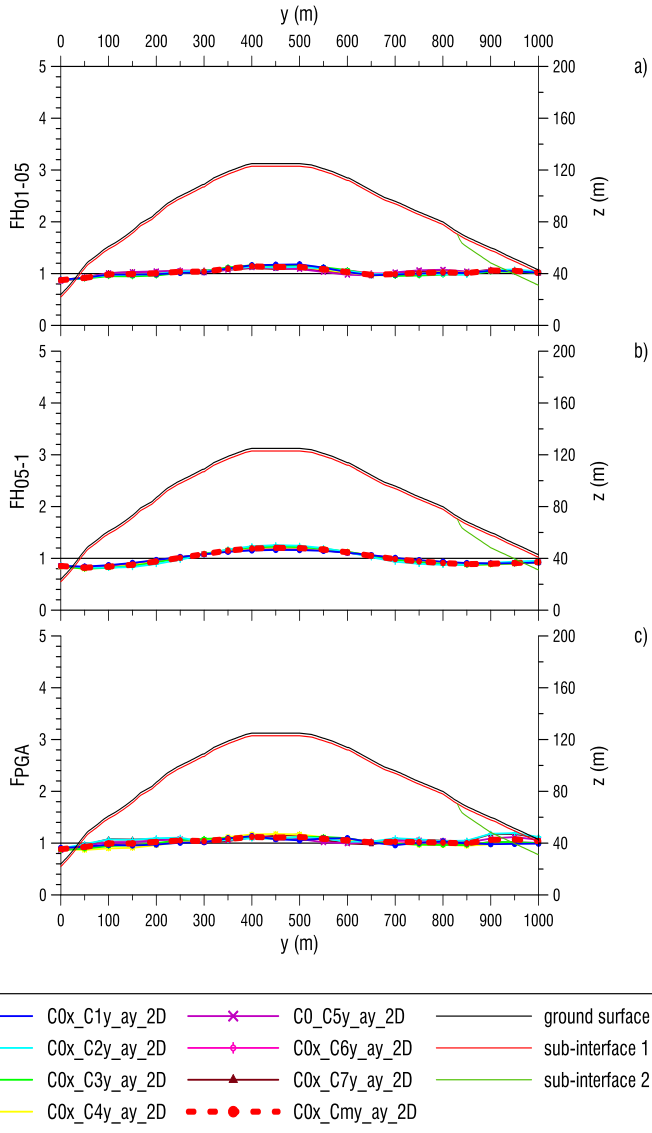


Fig. 169 Amplification factors profiles by means of 2D analyses for section 18 a) $F_{H_{01-05}}$, b) $F_{H_{05-1}}$, c) F_{PGA}

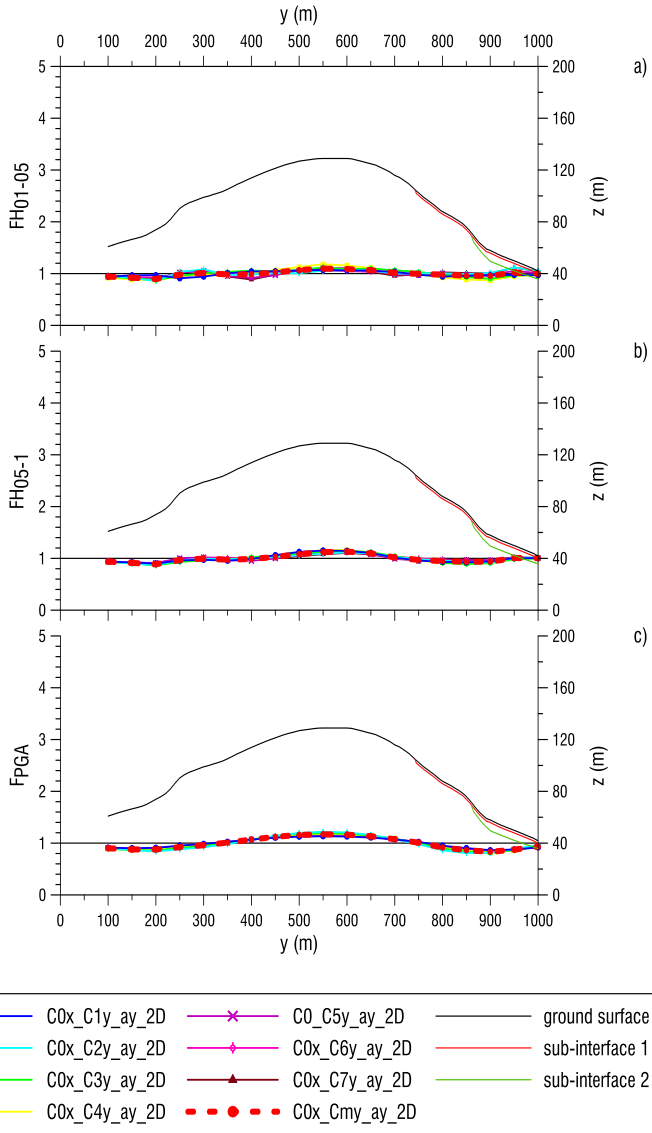


Fig. 170 Amplification factors profiles by means of 2D analyses for section 19 a) $F_{H_{01-05}}$, b) $F_{H_{05-1}}$, c) F_{PGA}

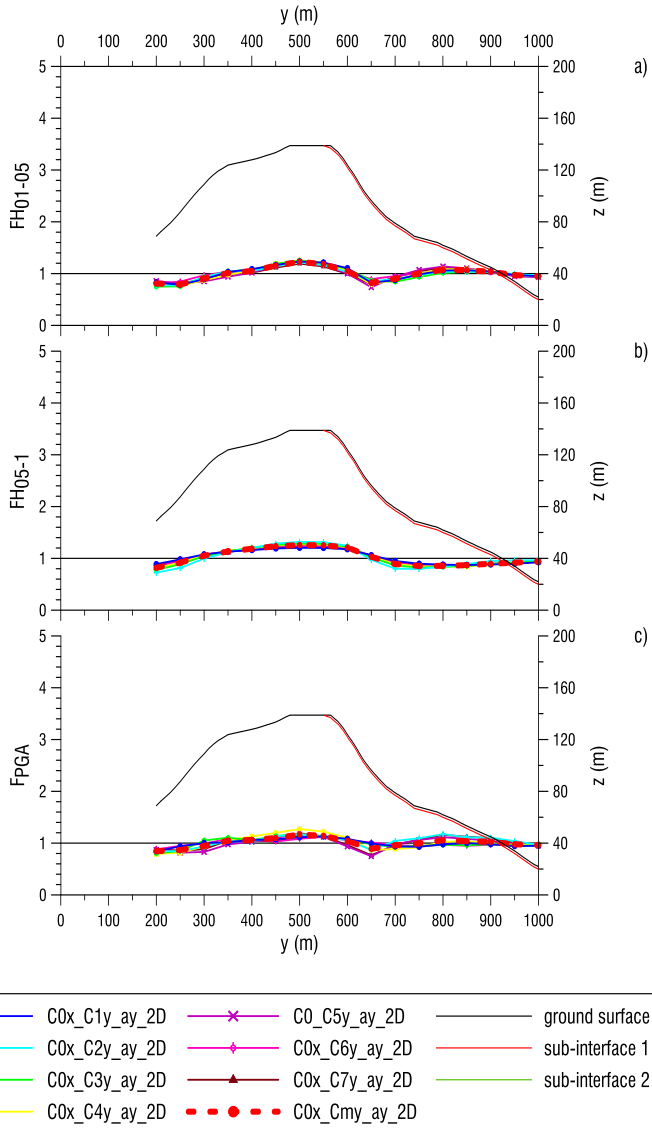


Fig. 171 Amplification factors profiles by means of 2D analyses for section 20 a) F_{H01-05} , b) F_{H05-1} , c) F_{PGA}

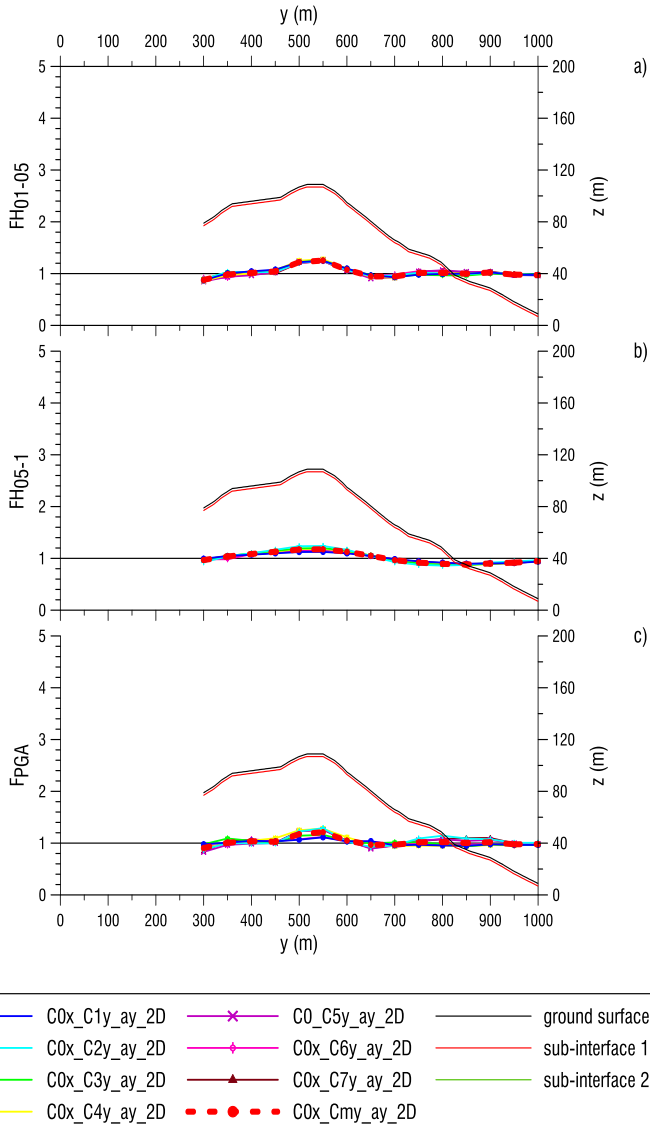


Fig. 172 Amplification factors profiles by means of 2D analyses for section 21 a) F_{H01-05} , b) F_{H05-1} , c) F_{PGA}

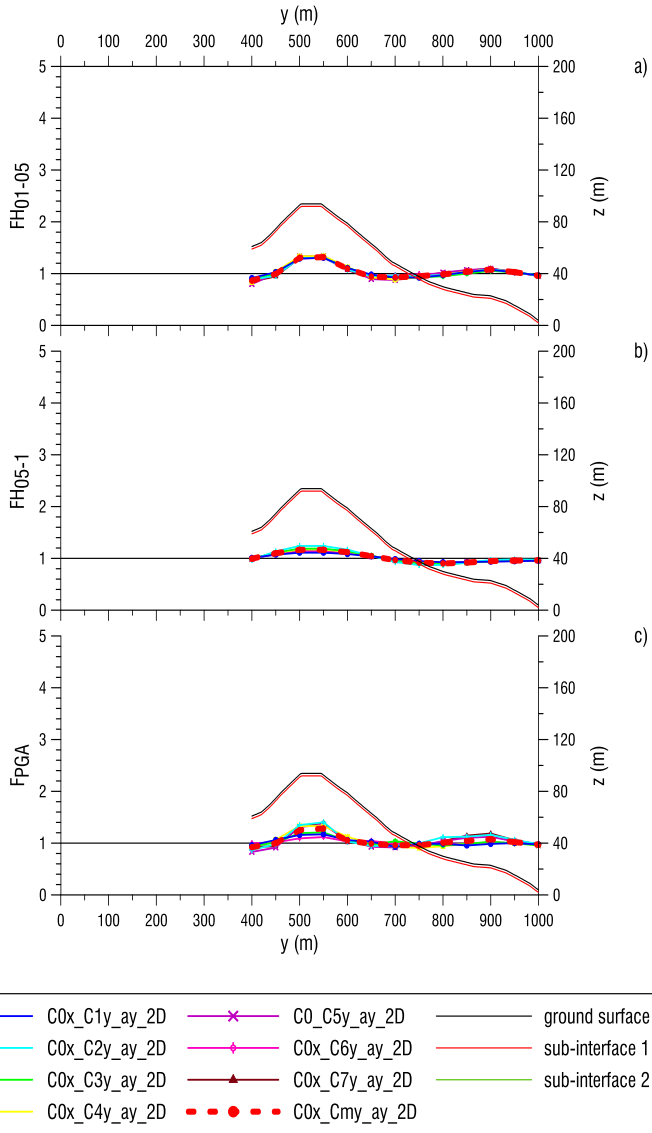


Fig. 173 Amplification factors profiles by means of 2D analyses for section 22 a) $F_{H_{01-05}}$, b) $F_{H_{05-1}}$, c) F_{PGA}

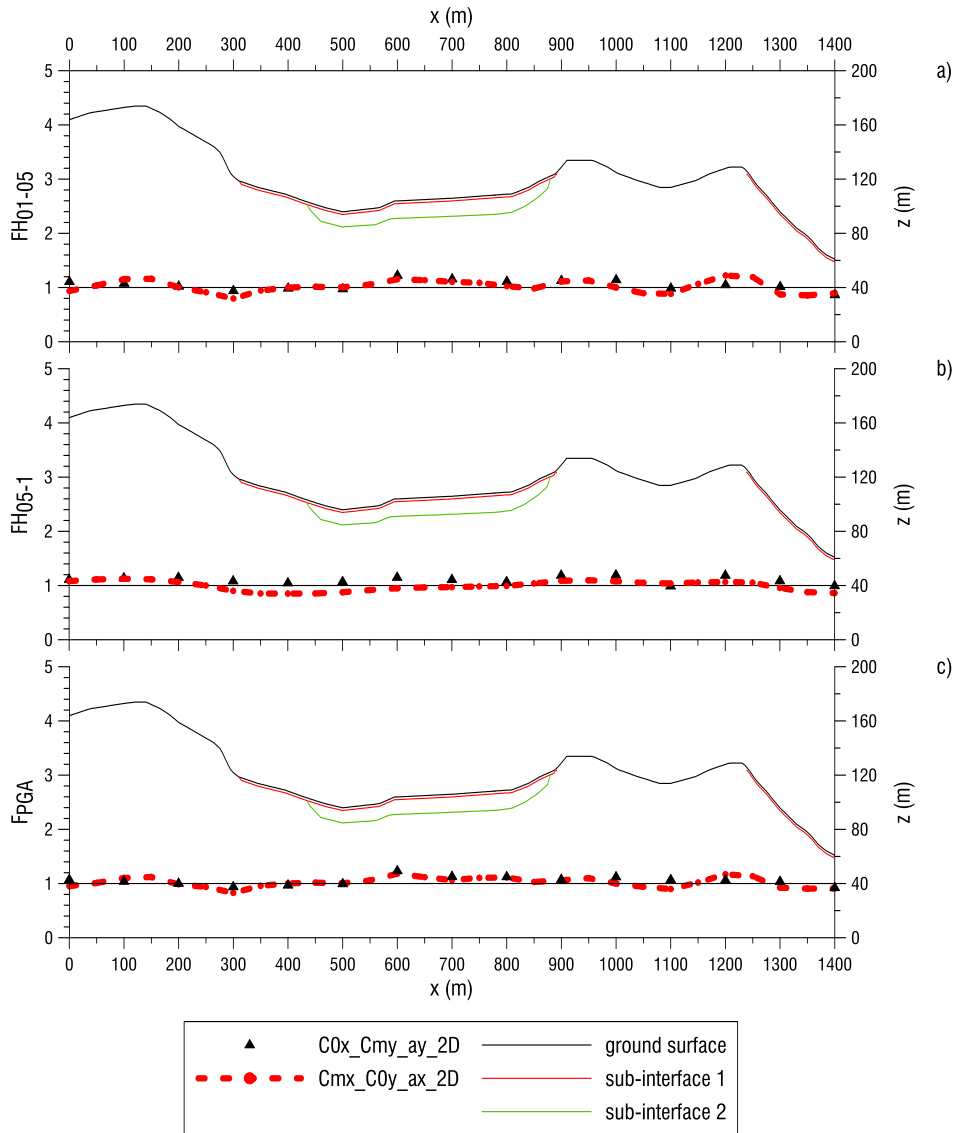


Fig. 174 Comparison between 2D mean values for section 1 and that obtained by transversal sections
a) FH_{01-05} , b) FH_{05-1} , c) F_{PGA}

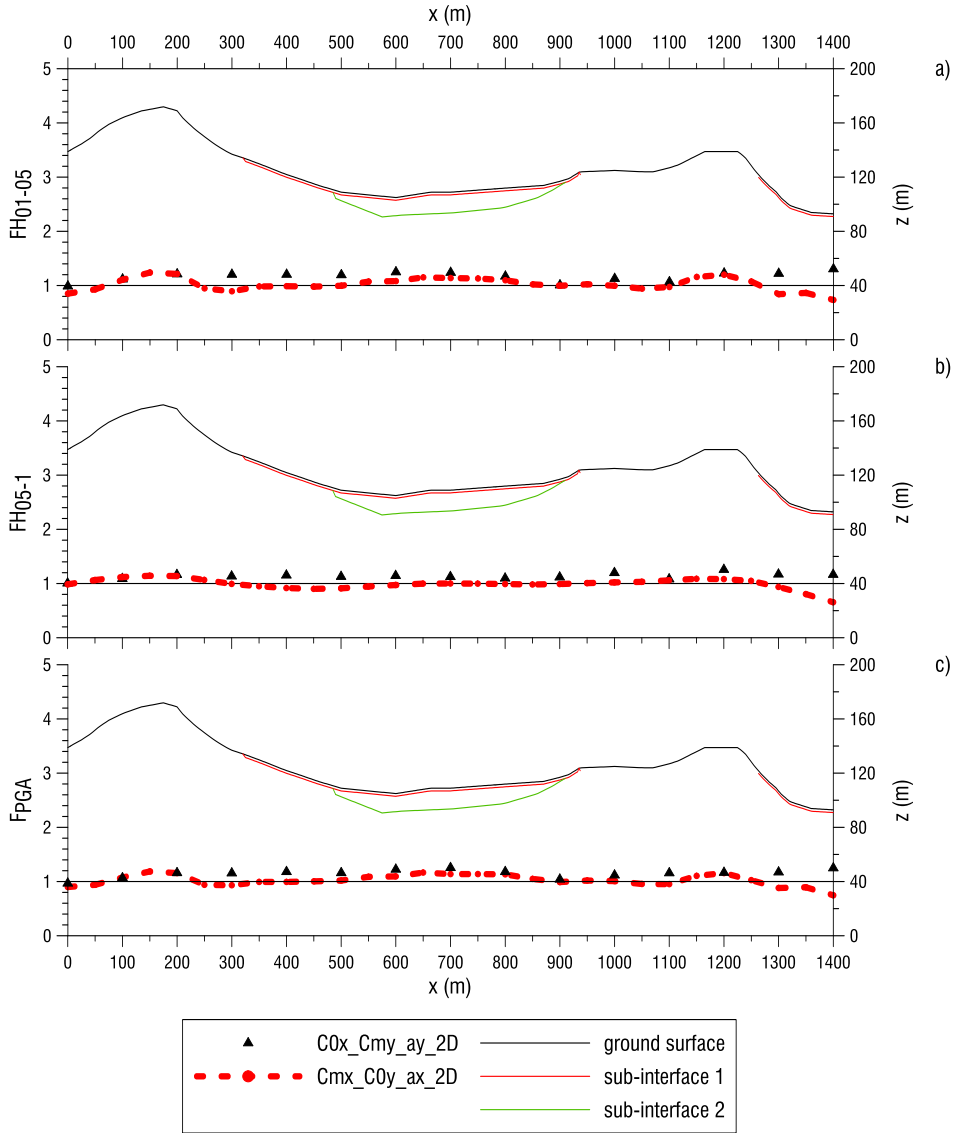


Fig. 175 Comparison between 2D mean values for section 2 and that obtained by transversal sections
a) FH_{01-05} , b) FH_{05-1} , c) F_{PGA}

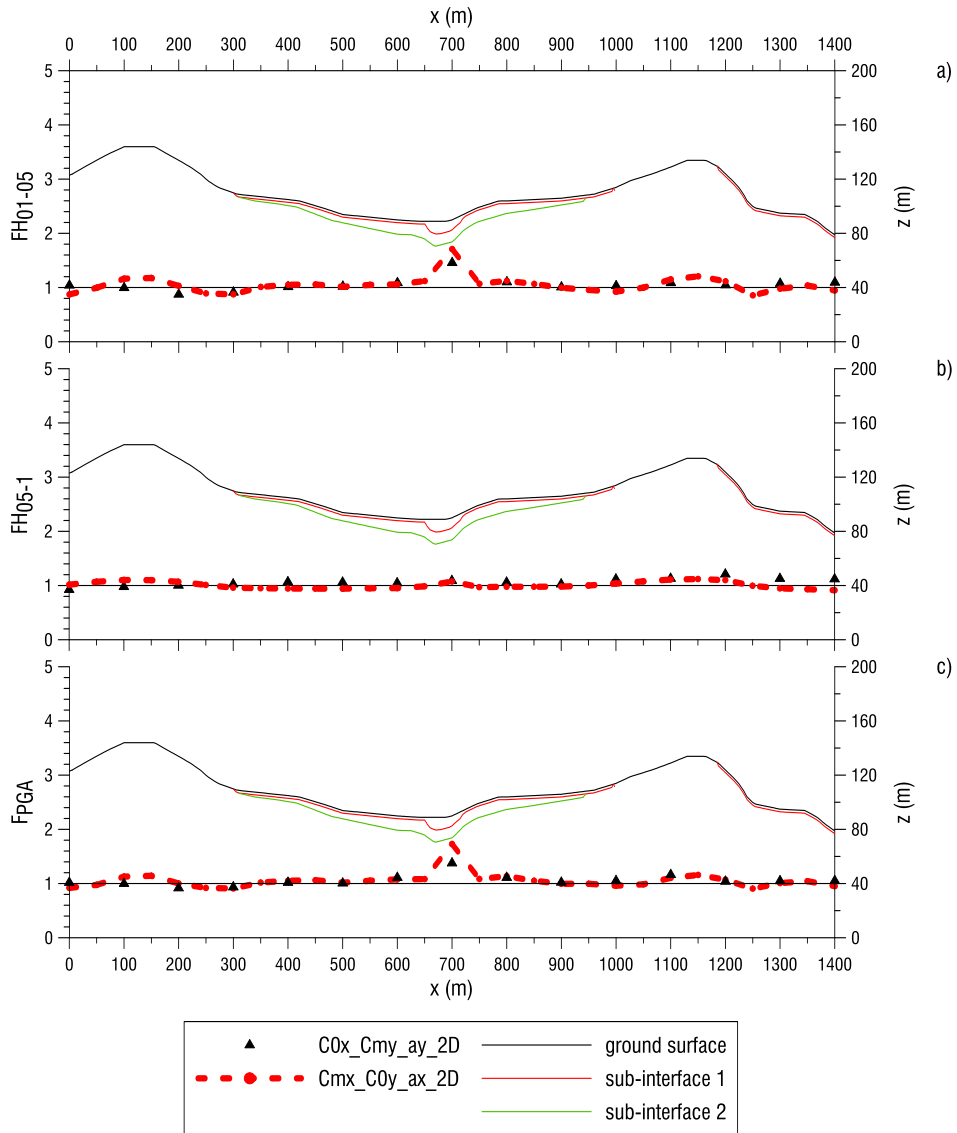


Fig. 176 Comparison between 2D mean values for section 3 and that obtained by transversal sections
a) FH_{01-05} , b) FH_{05-1} , c) F_{PGA}

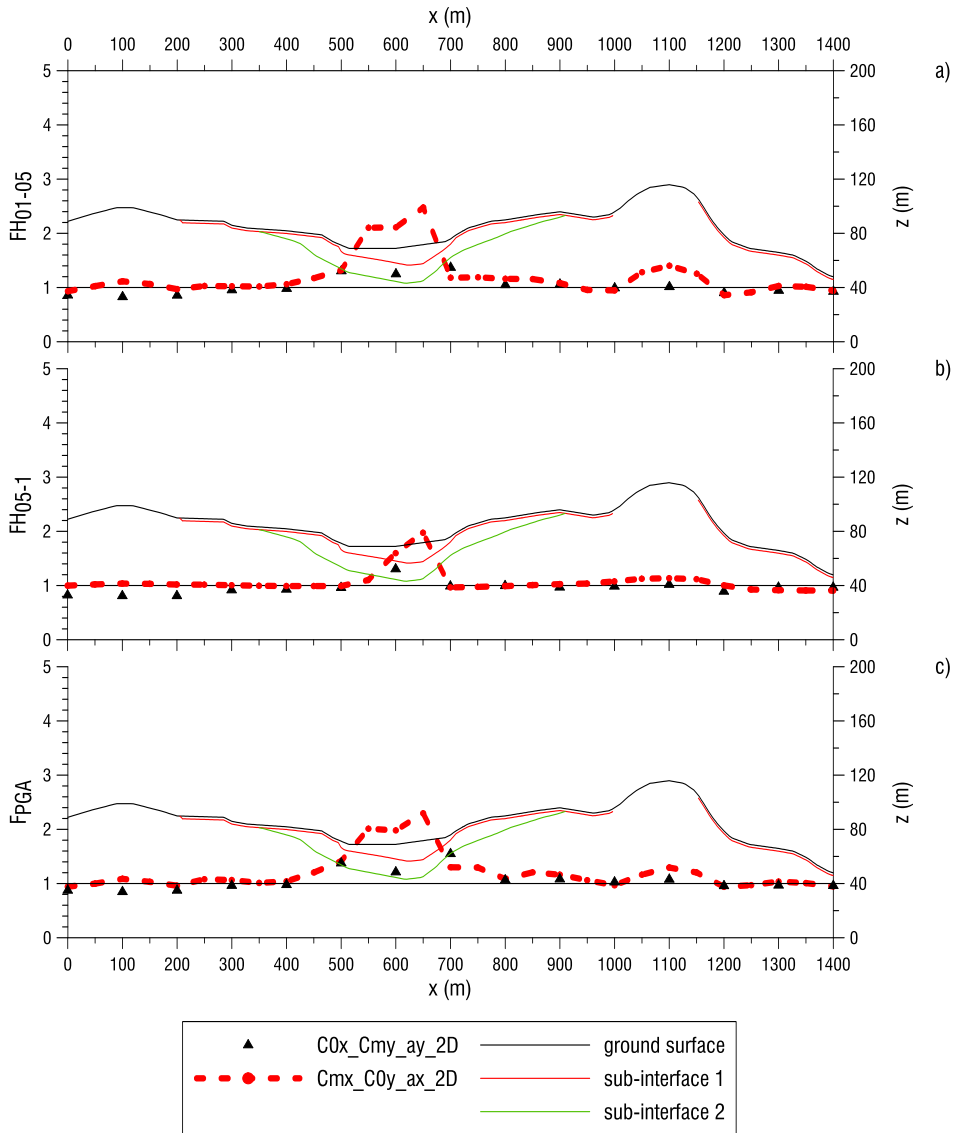


Fig. 177 Comparison between 2D mean values for section 4 and that obtained by transversal sections
a) FH_{01-05} , b) FH_{05-1} , c) F_{PGA}

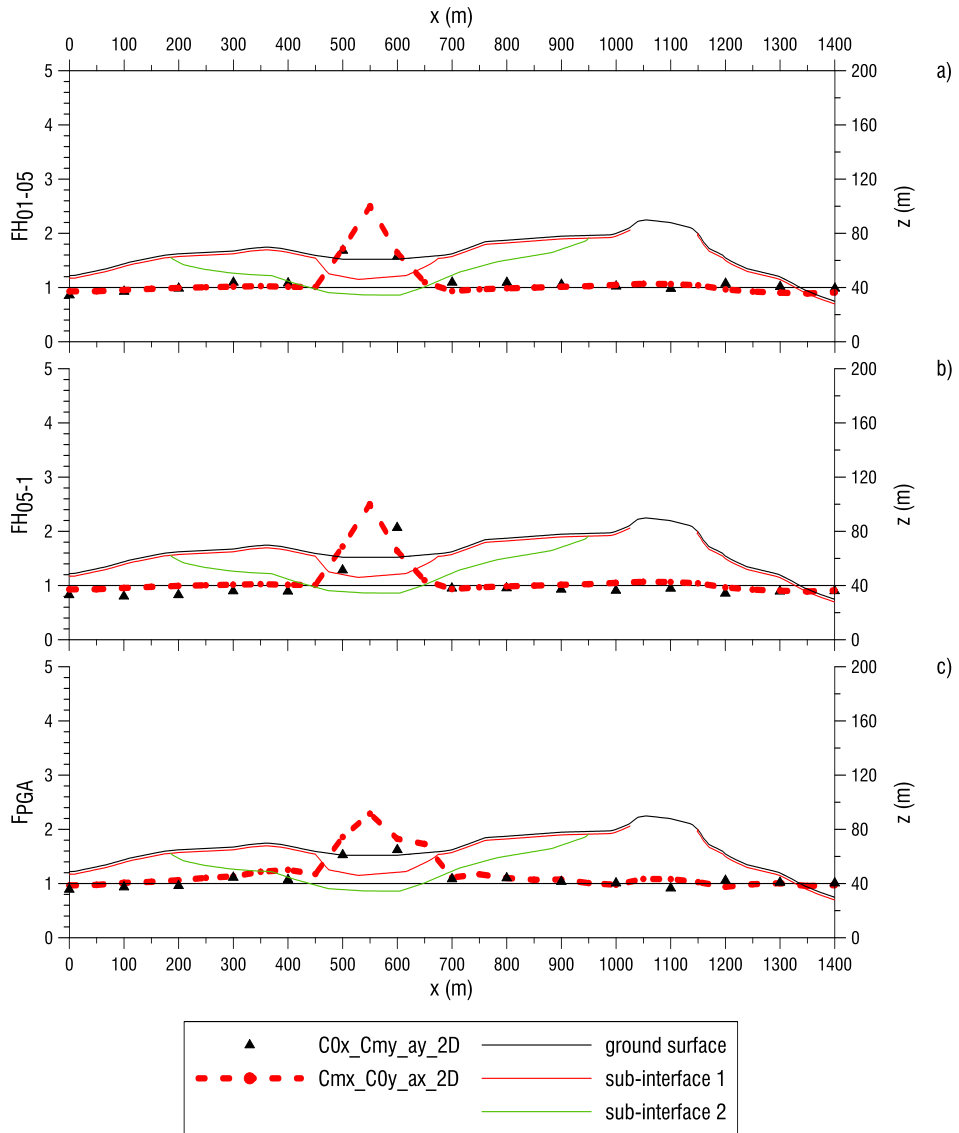


Fig. 178 Comparison between 2D mean values for section 5 and that obtained by transversal sections
a) FH_{01-05} , b) FH_{05-1} , c) F_{PGA}

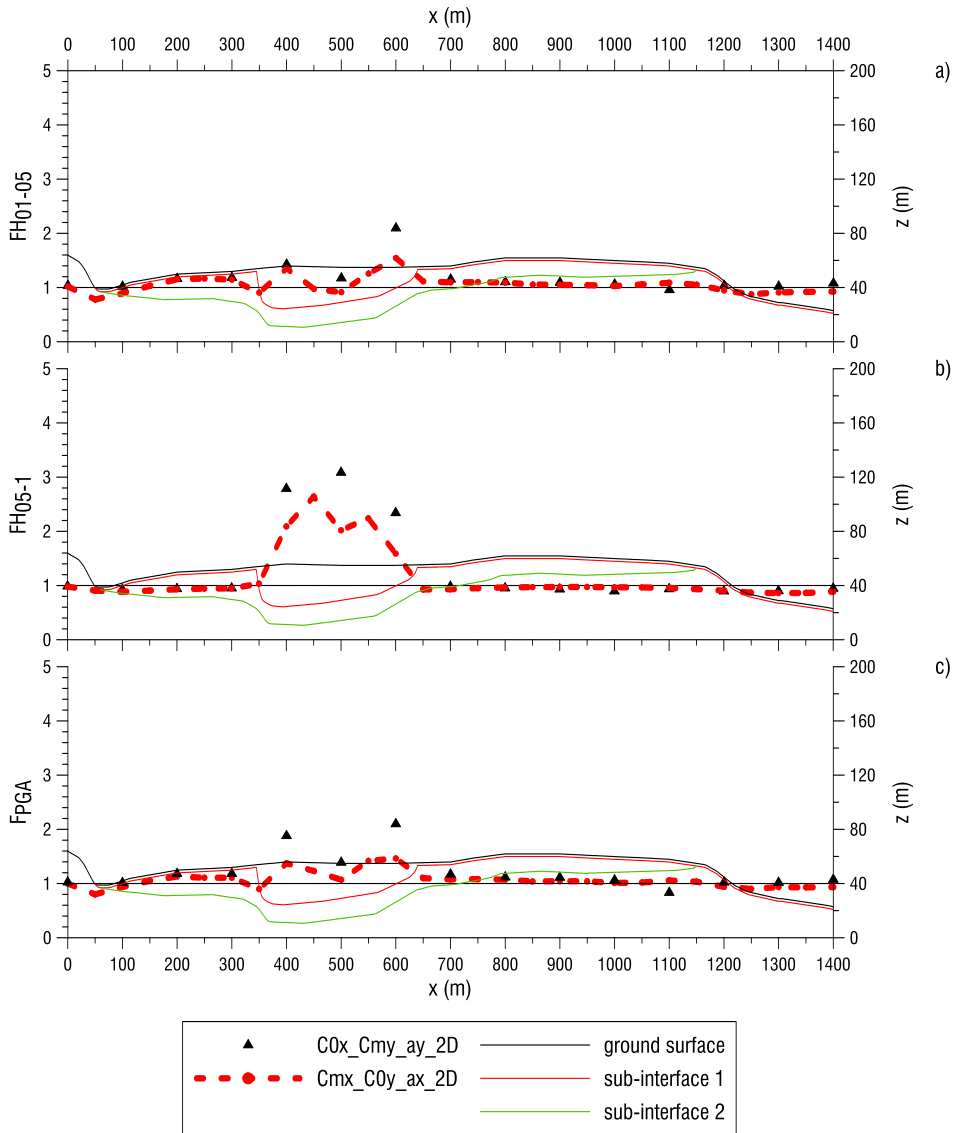


Fig. 179 Comparison between 2D mean values for section 6 and that obtained by transversal sections
a) FH₀₁₋₀₅, b) FH₀₅₋₁, c) F_{PGA}

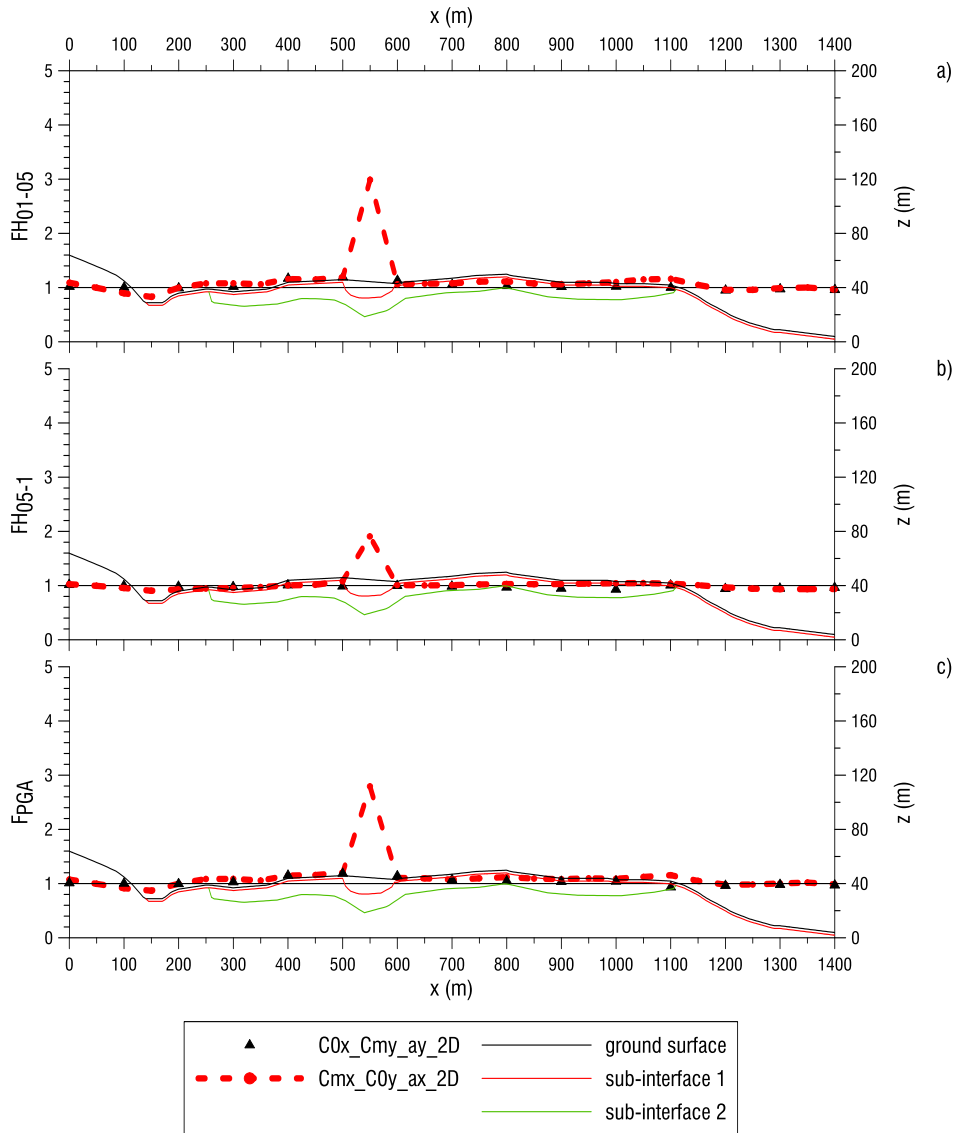


Fig. 180 Comparison between 2D mean values for section 7 and that obtained by transversal sections
 a) FH_{01-05} , b) FH_{05-1} , c) F_{PGA}

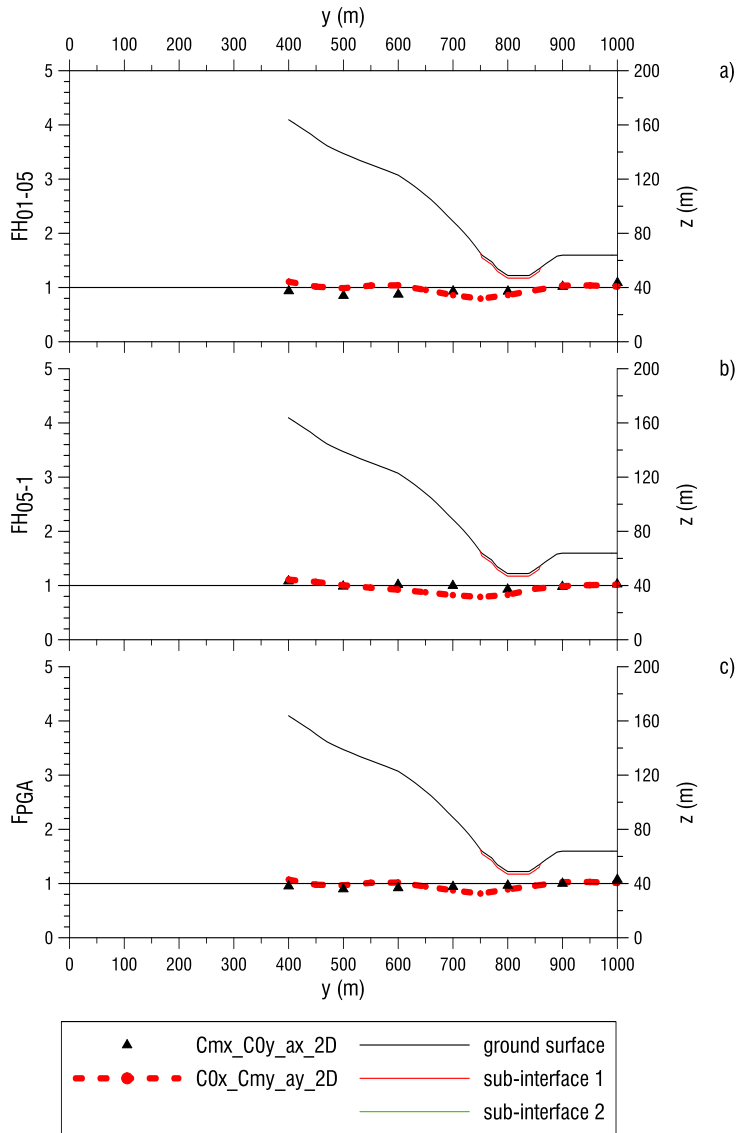


Fig. 181 Comparison between 2D mean values for section 8 and that obtained by transversal sections
a) FH_{01-05} , b) FH_{05-1} , c) F_{PGA}

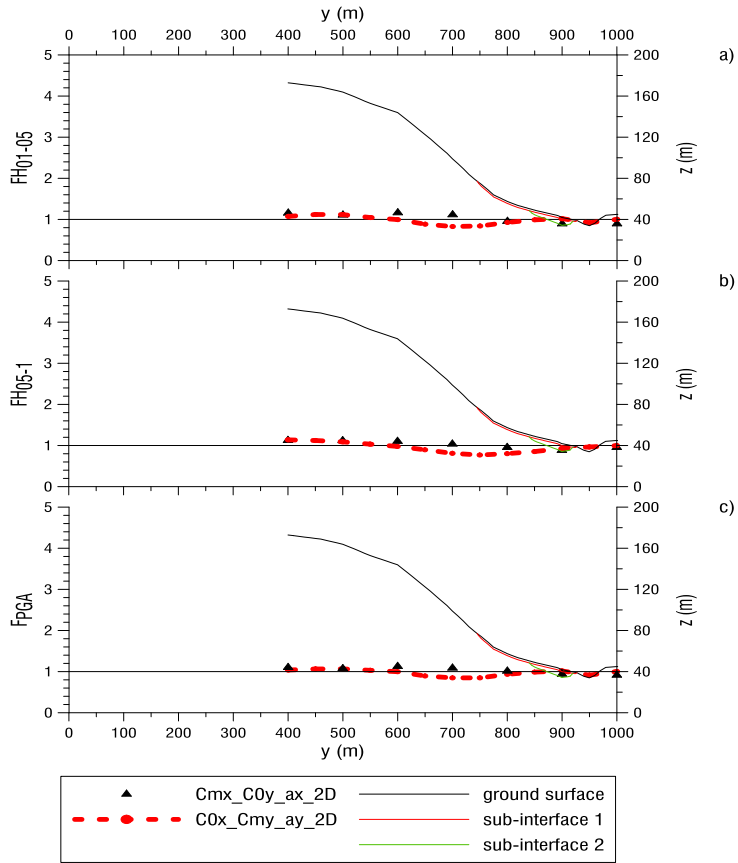


Fig. 182 Comparison between 2D mean values for section 9 and that obtained by transversal sections
 a) $F_{H_{01-05}}$, b) $F_{H_{05-1}}$, b) F_{PGA}

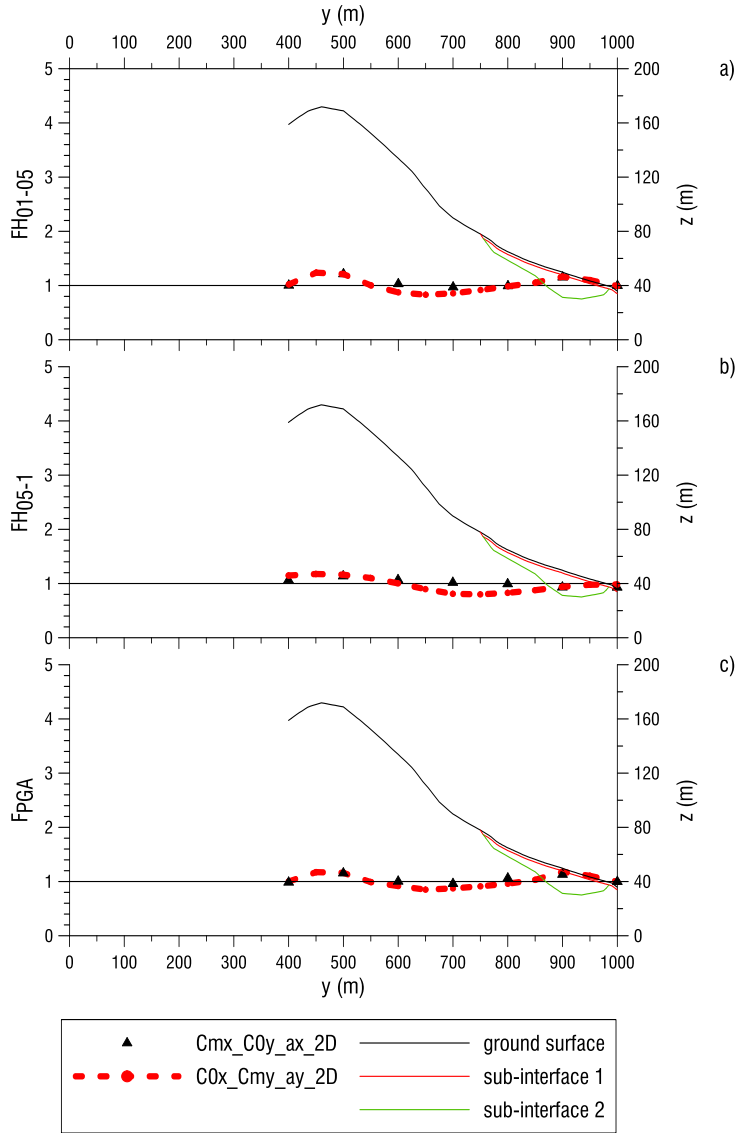


Fig. 183 Comparison between 2D mean values for section 10 and that obtained by transversal sections
a) FH_{01-05} , b) FH_{05-1} , c) F_{PGA}

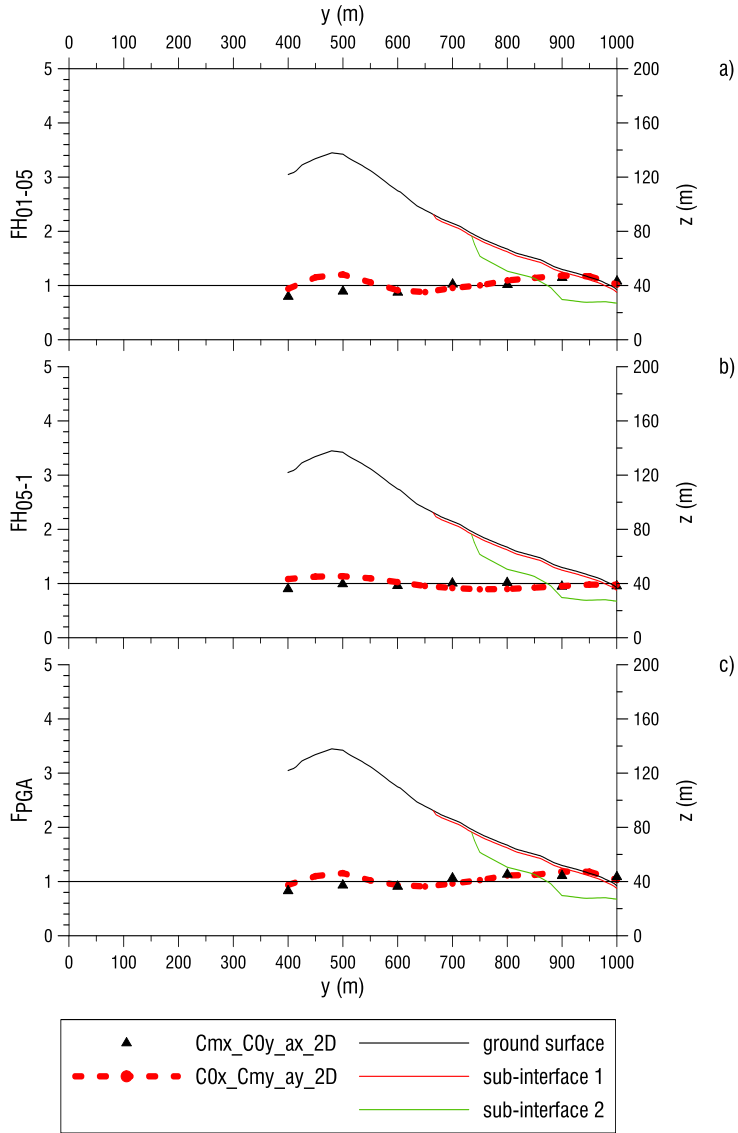


Fig. 184 Comparison between 2D mean values for section 11 and that obtained by transversal sections
a) FH_{01-05} , b) FH_{05-1} , c) F_{PGA}

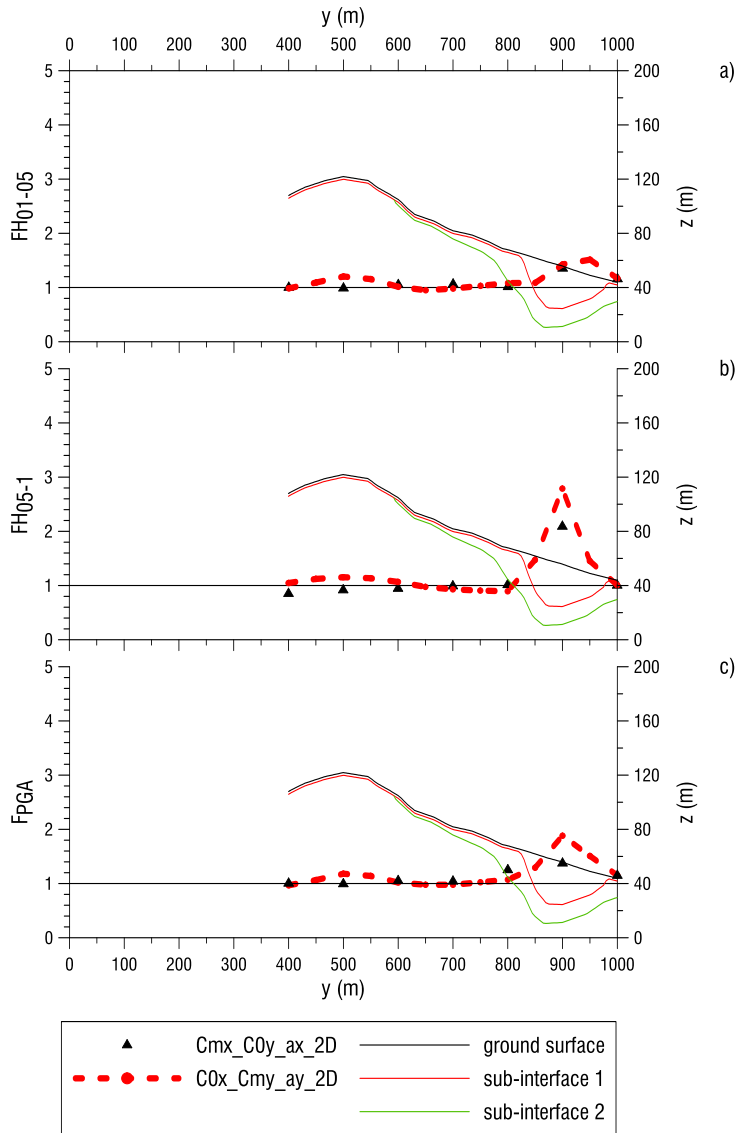


Fig. 185 Comparison between 2D mean values for section 12 and that obtained by transversal sections
a) FH_{01-05} , b) FH_{05-1} , c) F_{PGA}

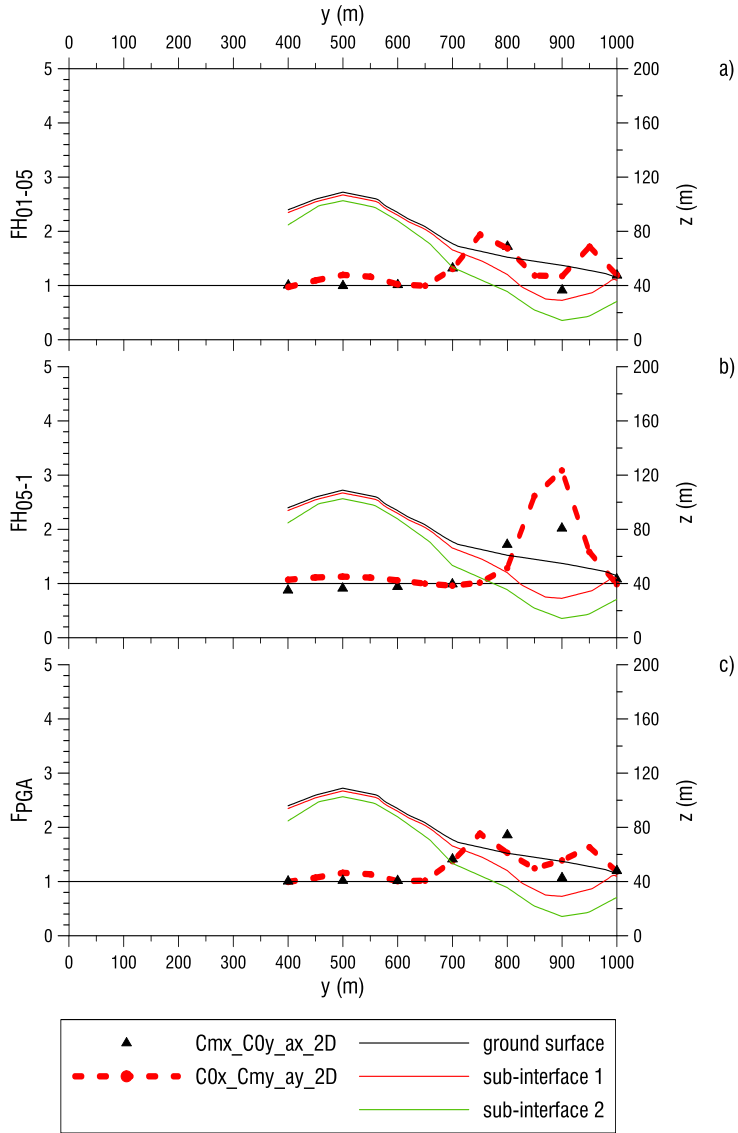


Fig. 186 Comparison between 2D mean values for section 13 and that obtained by transversal sections
a) FH_{01-05} , b) FH_{05-1} , c) F_{PGA}

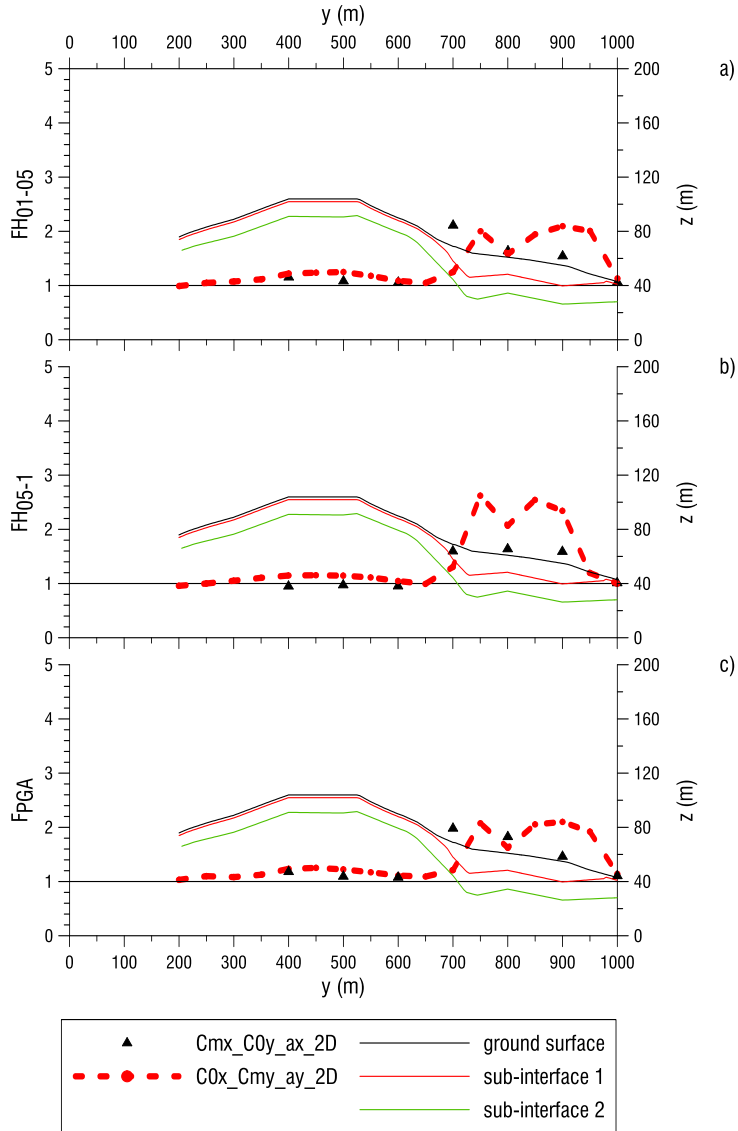


Fig. 187 Comparison between 2D mean values for section 14 and that obtained by transversal sections
 a) FH_{01-05} , b) FH_{05-1} , c) F_{PGA}

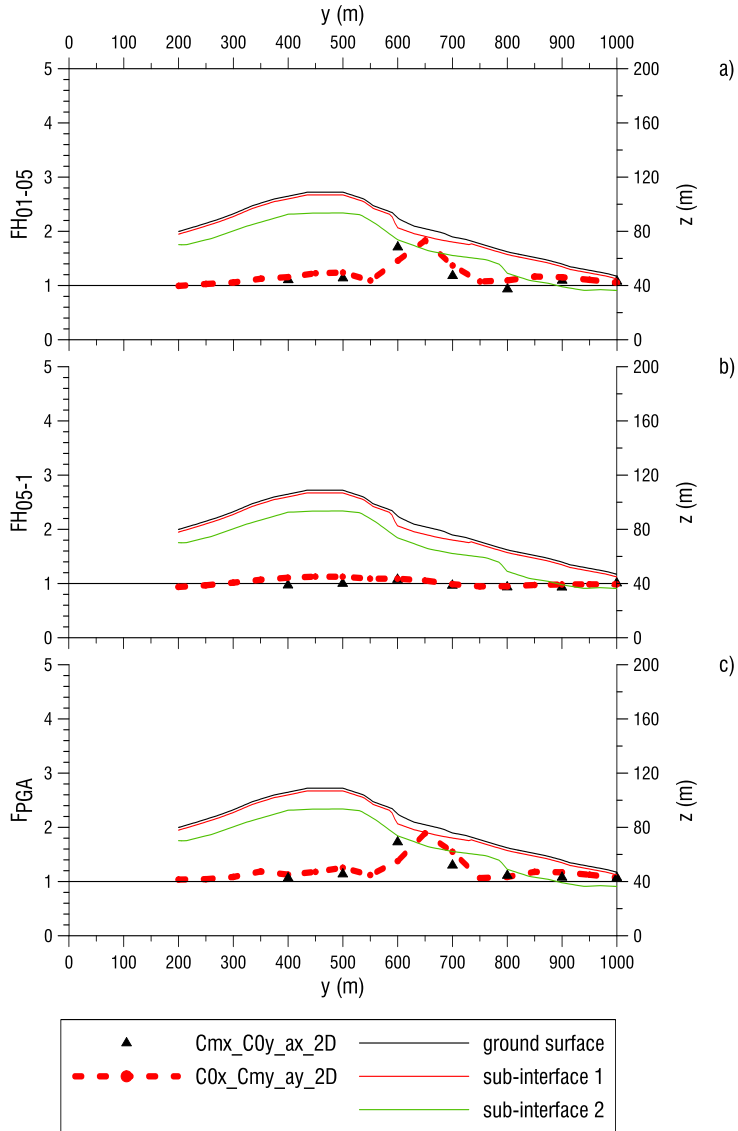


Fig. 188 Comparison between 2D mean values for section 15 and that obtained by transversal sections
a) FH_{01-05} , b) FH_{05-1} , c) F_{PGA}

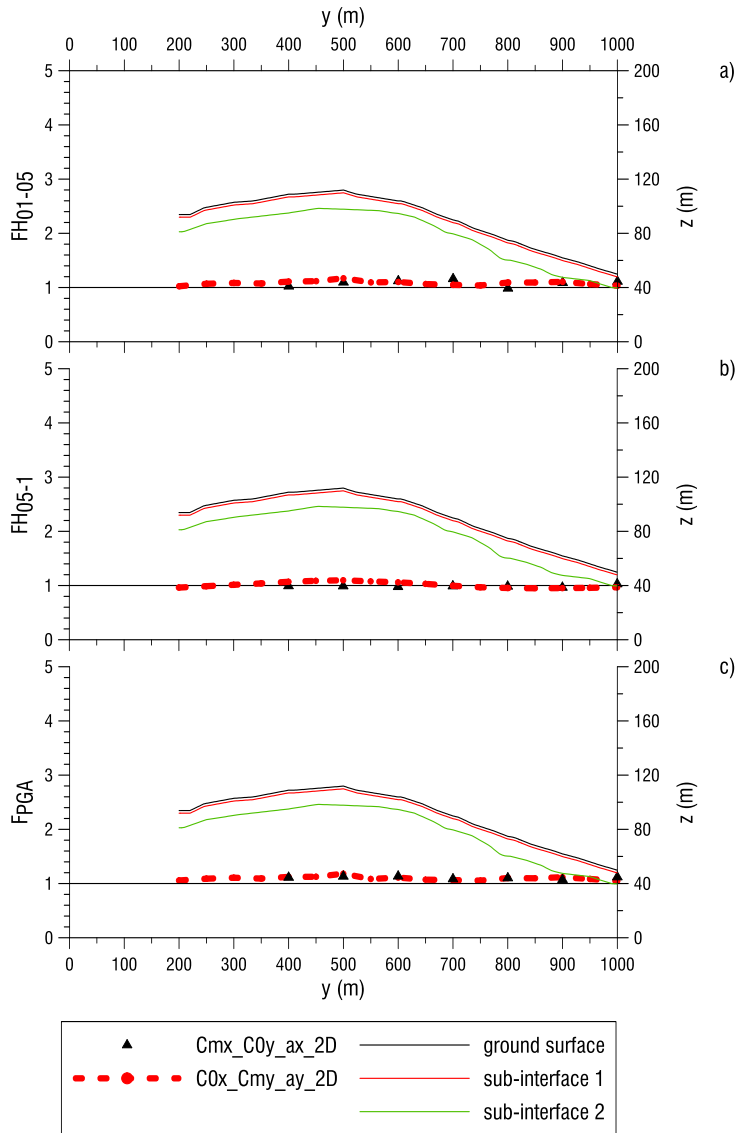


Fig. 189 Comparison between 2D mean values for section 16 and that obtained by transversal sections
 a) FH_{01-05} , b) FH_{05-1} , c) F_{PGA}

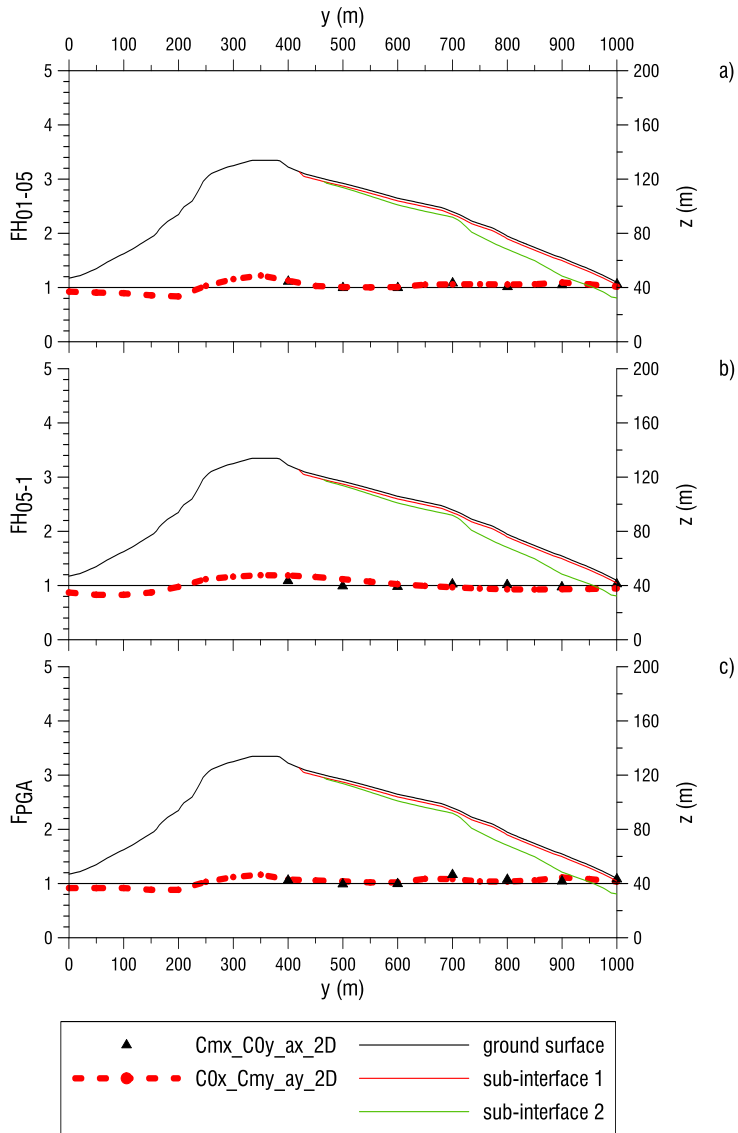


Fig. 190 Comparison between 2D mean values for section 17 and that obtained by transversal sections
a) FH₀₁₋₀₅, b) FH₀₅₋₁, c) F_{PGA}

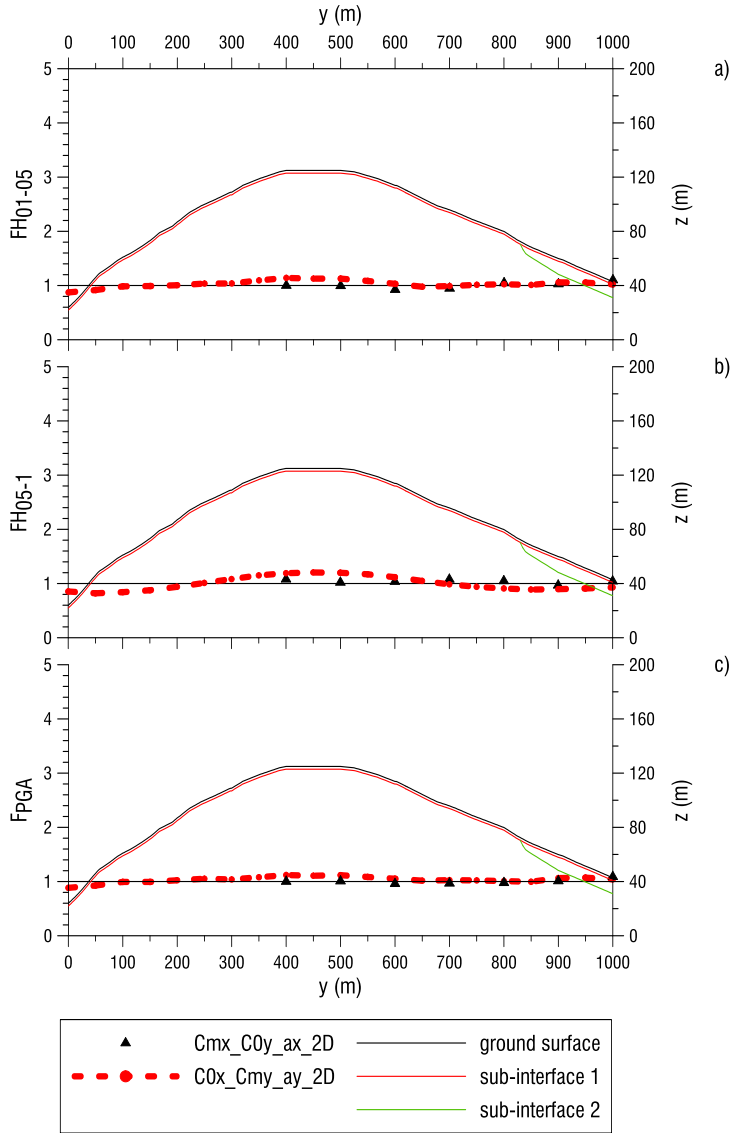


Fig. 191 Comparison between 2D mean values for section 18 and that obtained by transversal sections
a) FH_{01-05} , b) FH_{05-1} , c) F_{PGA}

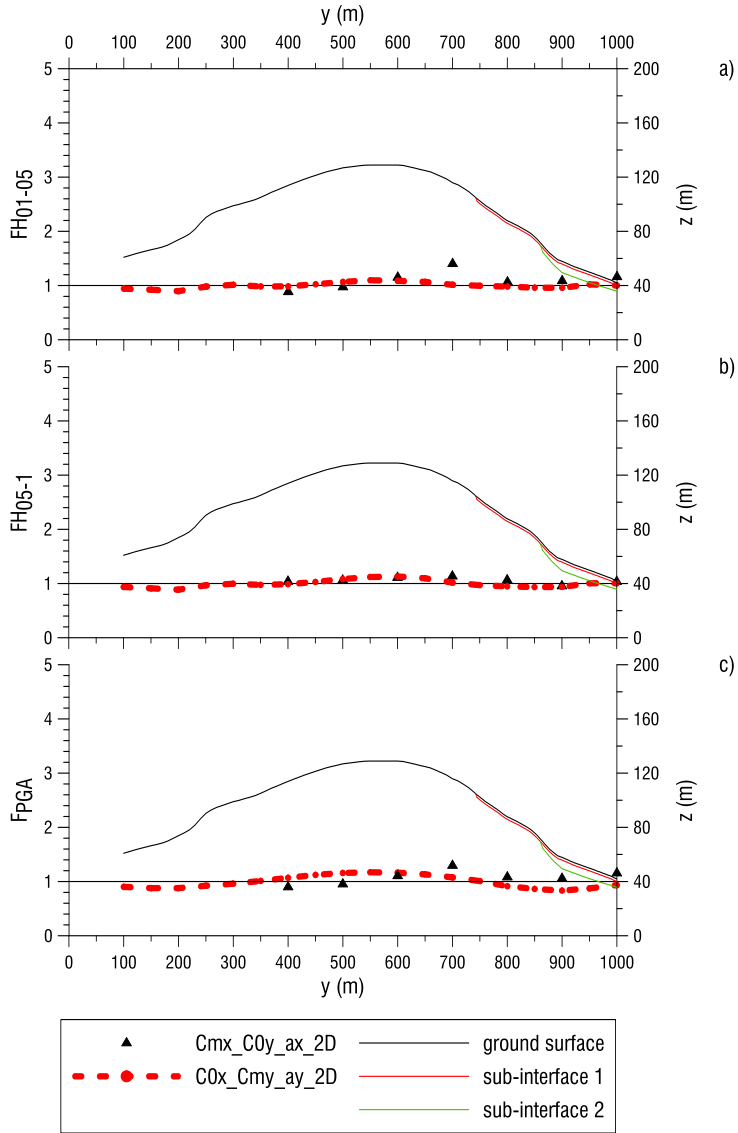


Fig. 192 Comparison between 2D mean values for section 19 and that obtained by transversal sections
a) FH_{01-05} , b) FH_{05-1} , c) F_{PGA}

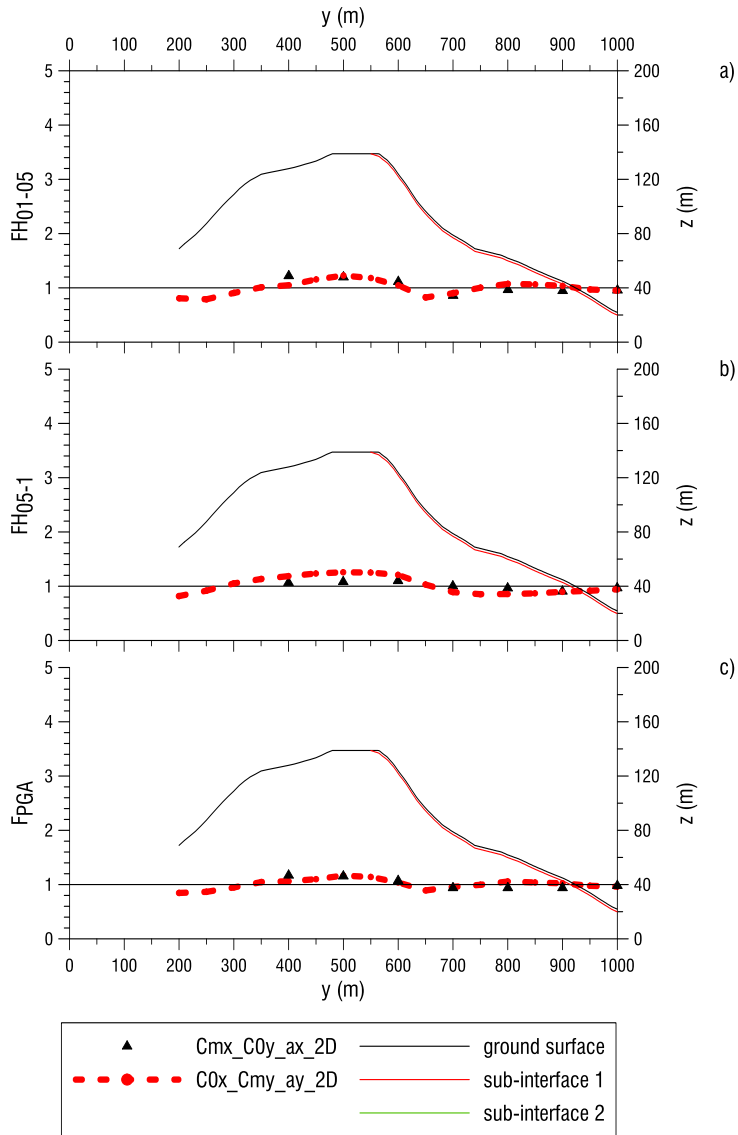


Fig. 193 Comparison between 2D mean values for section 20 and that obtained by transversal sections
a) FH_{01-05} , b) FH_{05-1} , c) F_{PGA}

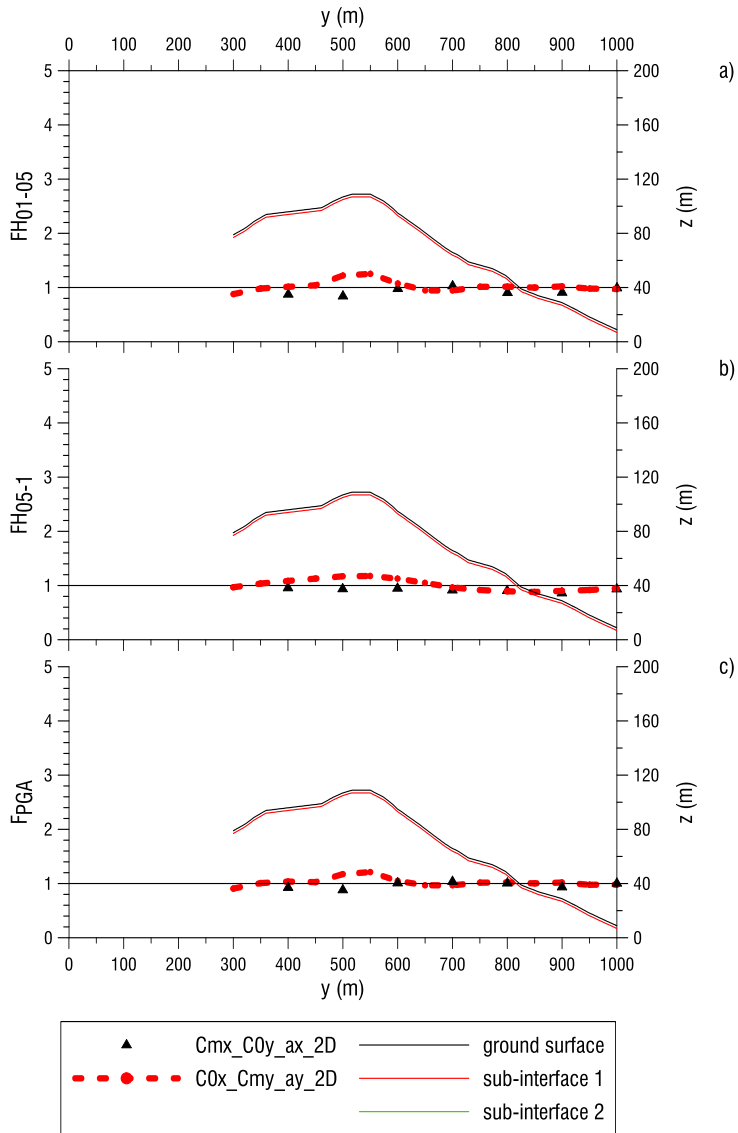


Fig. 194 Comparison between 2D mean values for section 21 and that obtained by transversal sections
a) FH_{01-05} , b) FH_{05-1} , c) F_{PGA}

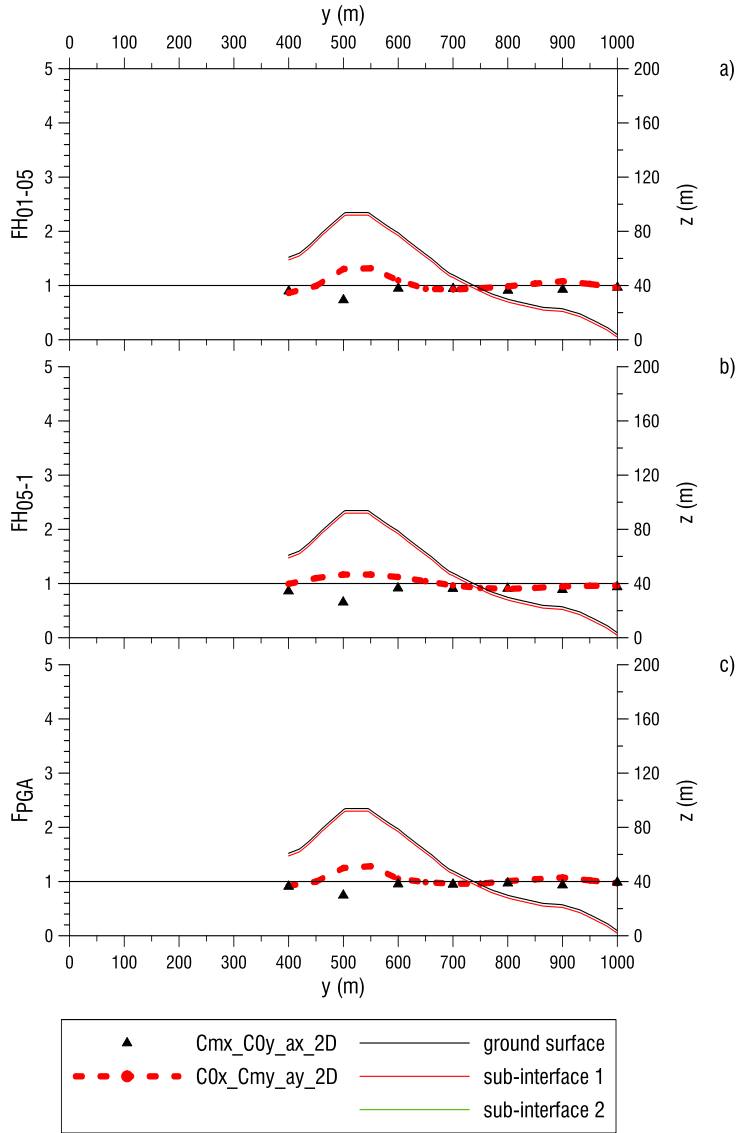


Fig. 195 Comparison between 2D mean values for section 22 and that obtained by transversal sections
a) FH_{01-05} , b) FH_{05-1} , c) F_{PGA}

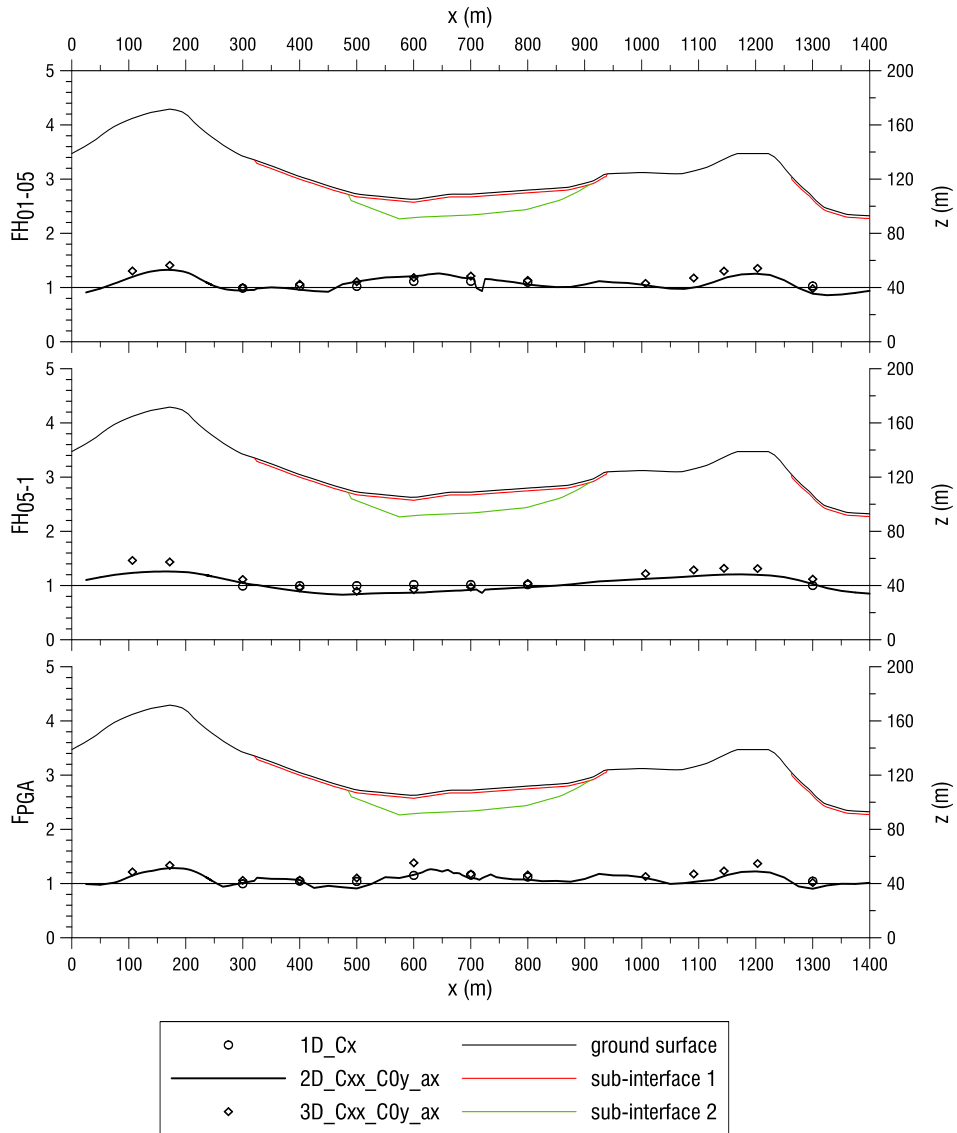


Fig. 196 Comparison A1-A3-A7 with reference to section 2, a) FH_{01-05} , b) FH_{05-1} , c) F_{PGA}

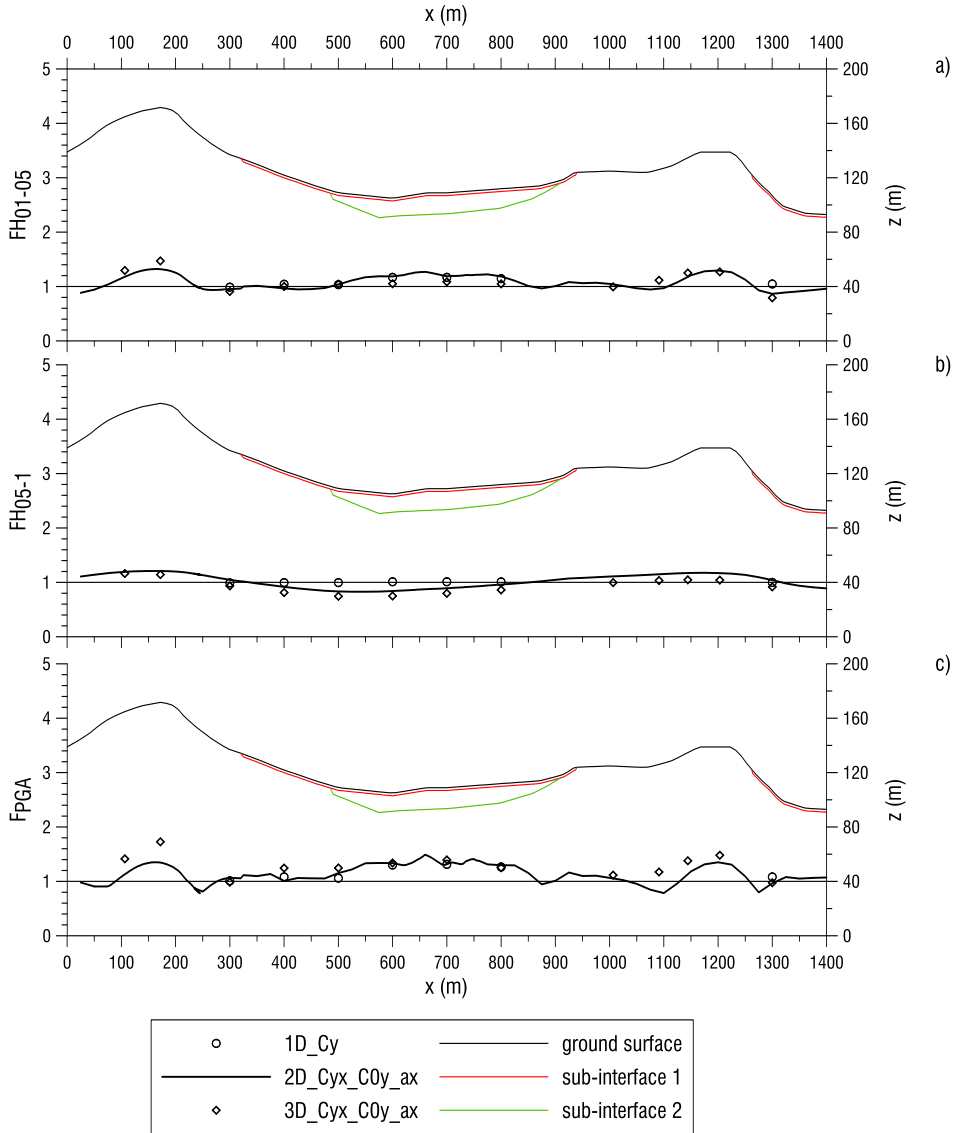


Fig. 197 Comparison A2-A4-A8 with reference to section 2, a) FH_{01-05} , b) FH_{05-1} , b) F_{PGA}

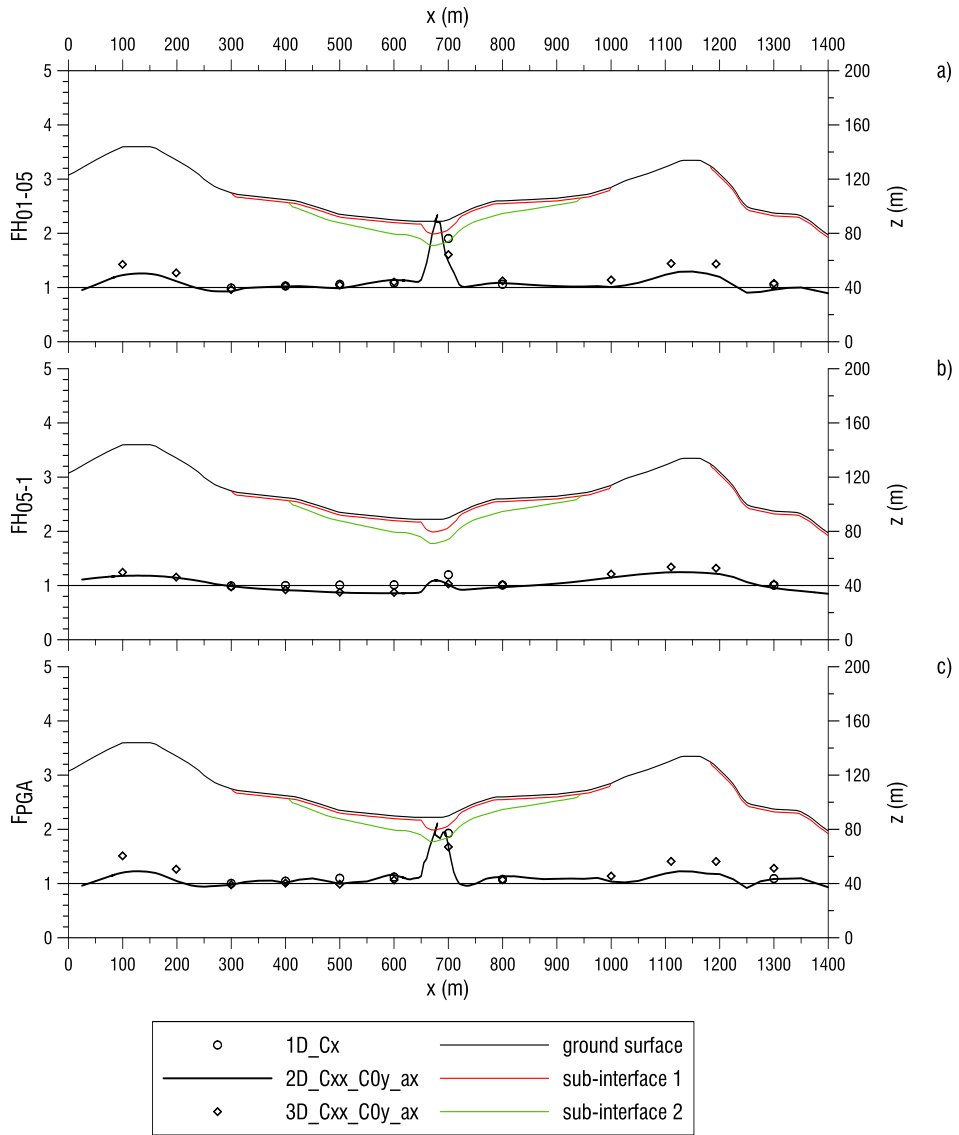


Fig. 198 Comparison A1-A3-A7 with reference to section 3, a) F_{H01-05} , b) F_{H05-1} , c) F_{PGA}

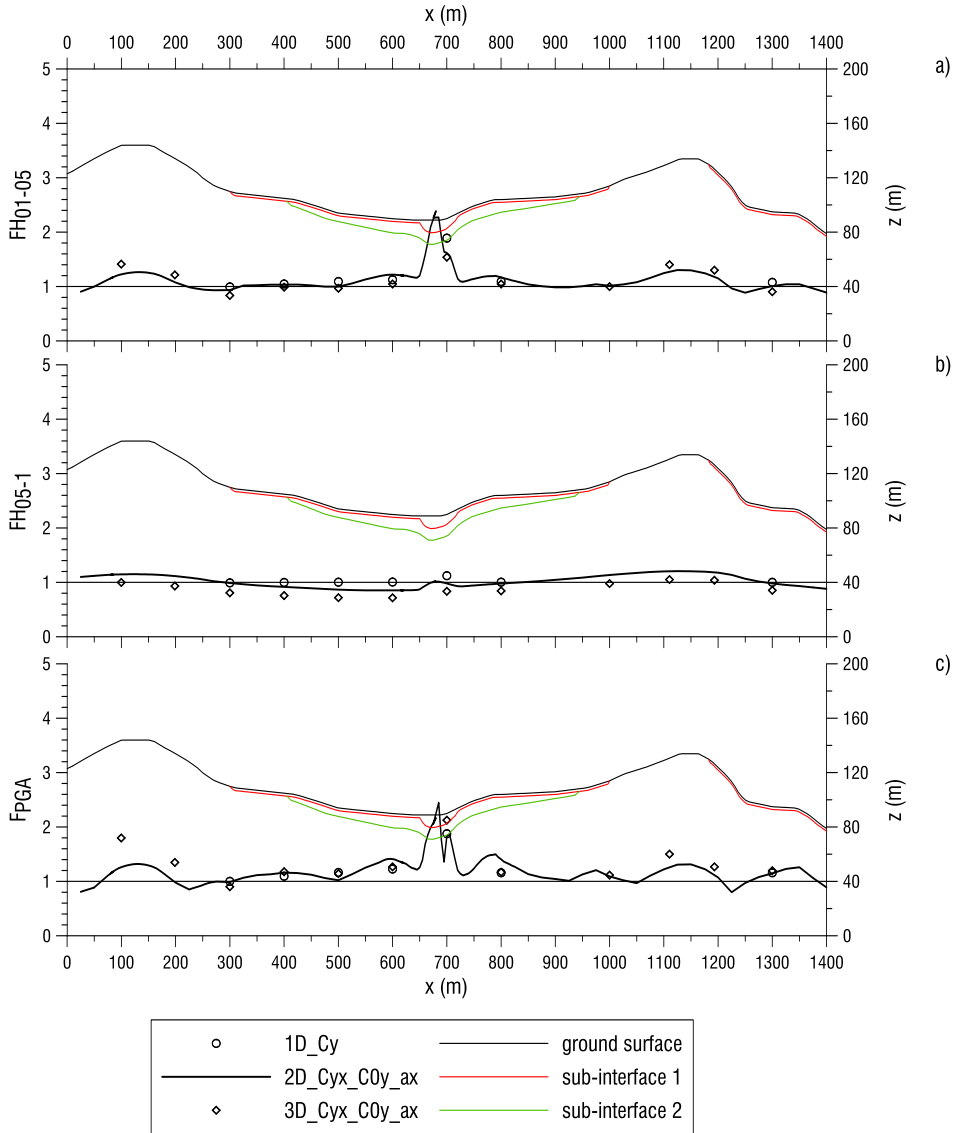


Fig. 199 Comparison A2-A4-A8 with reference to section 3, a) FH₀₁₋₀₅, b) FH₀₅₋₁, c) F_{PGA}

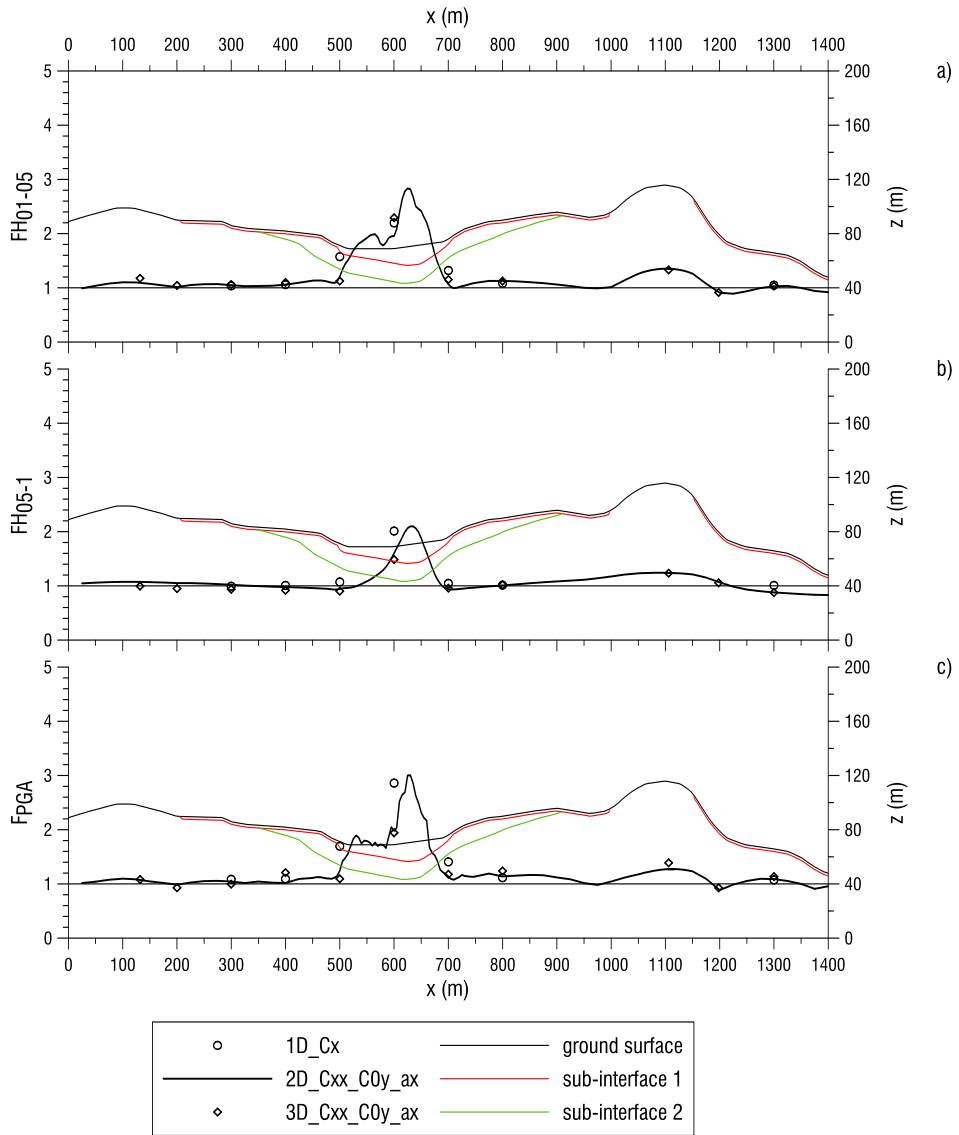


Fig. 200 Comparison A1-A3-A7 with reference to section 4, a) FH_{01-05} , b) FH_{05-1} , b) F_{PGA}

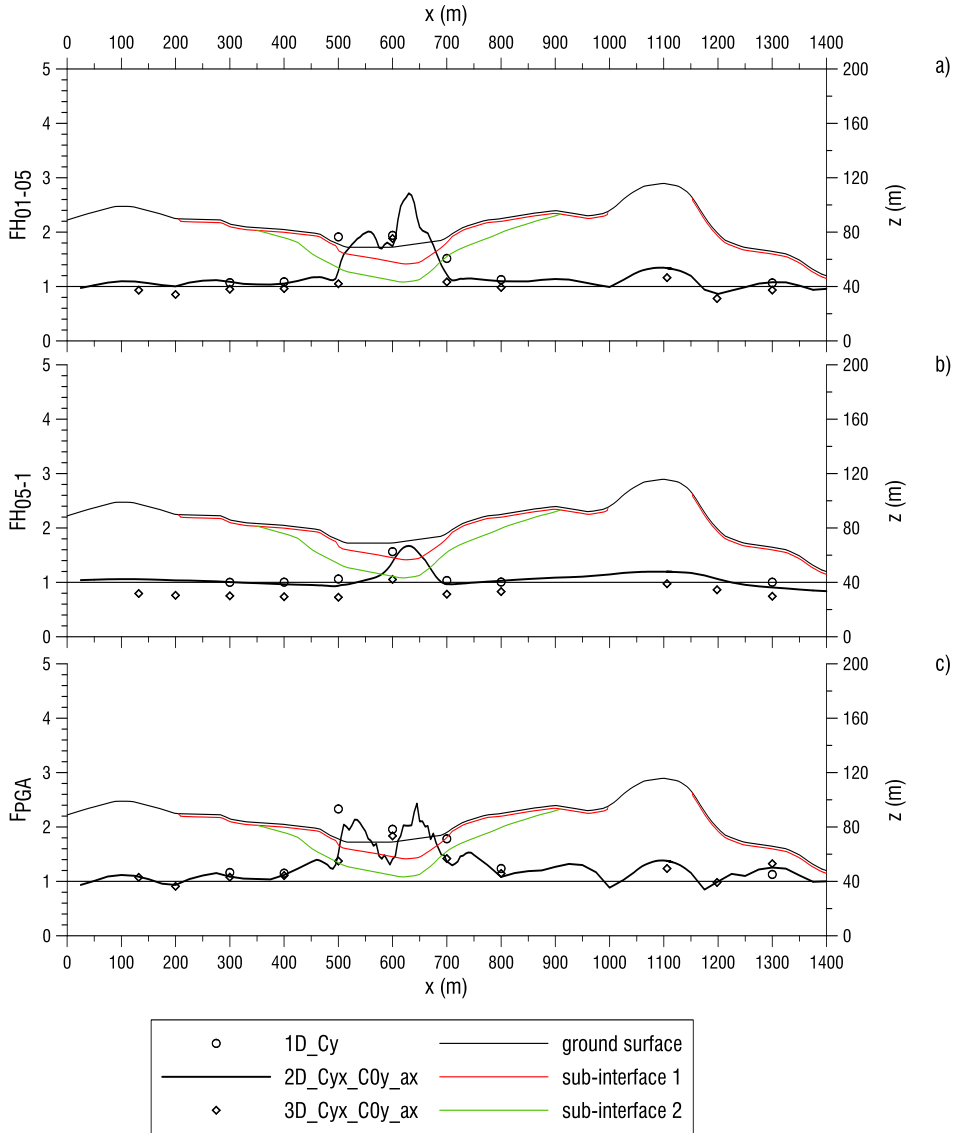


Fig. 201 Comparison A2-A4-A8 with reference to section 4, a) FH₀₁₋₀₅, b) FH₀₅₋₁, b) F_{PGA}

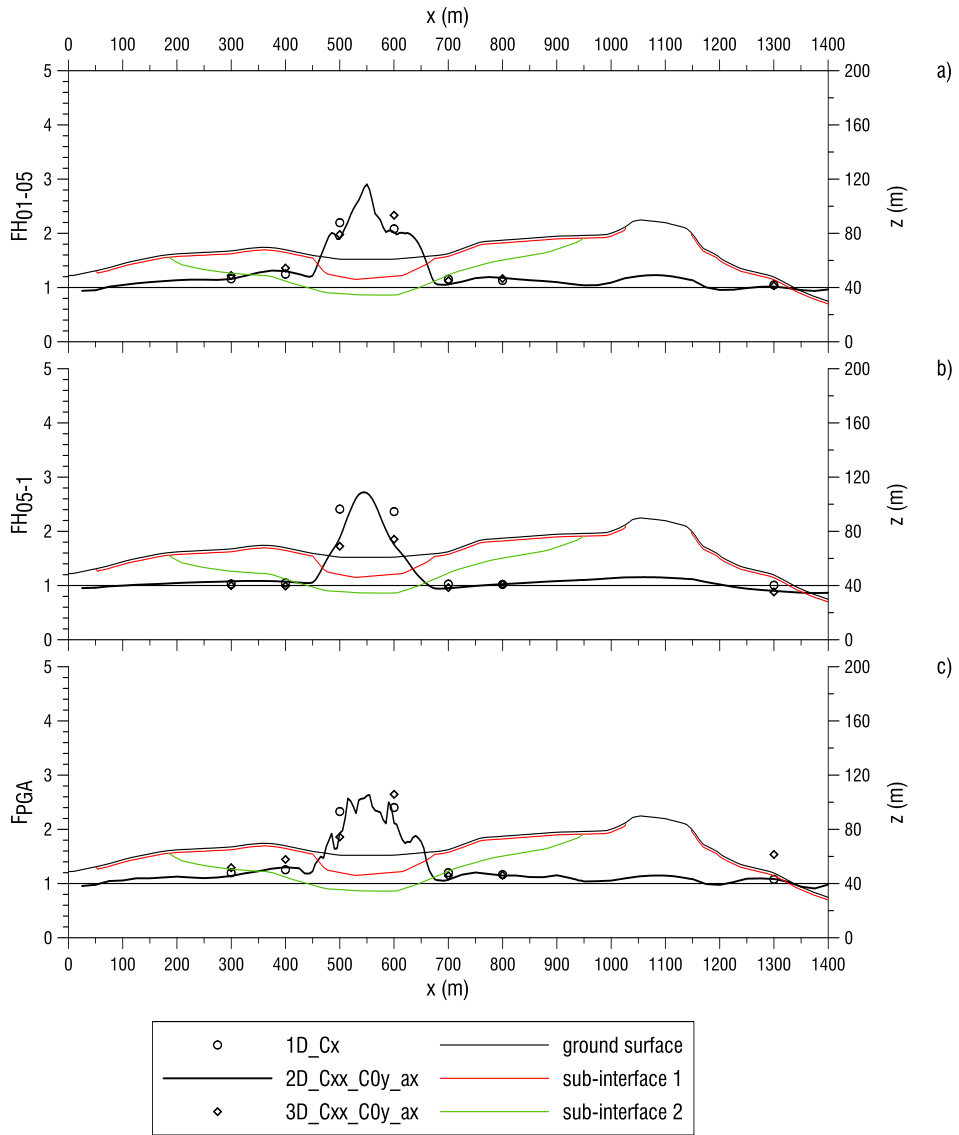


Fig. 202 Comparison A1-A3-A7 with reference to section 5, a) F_{H01-05} , b) F_{H05-1} , c) F_{PGA}

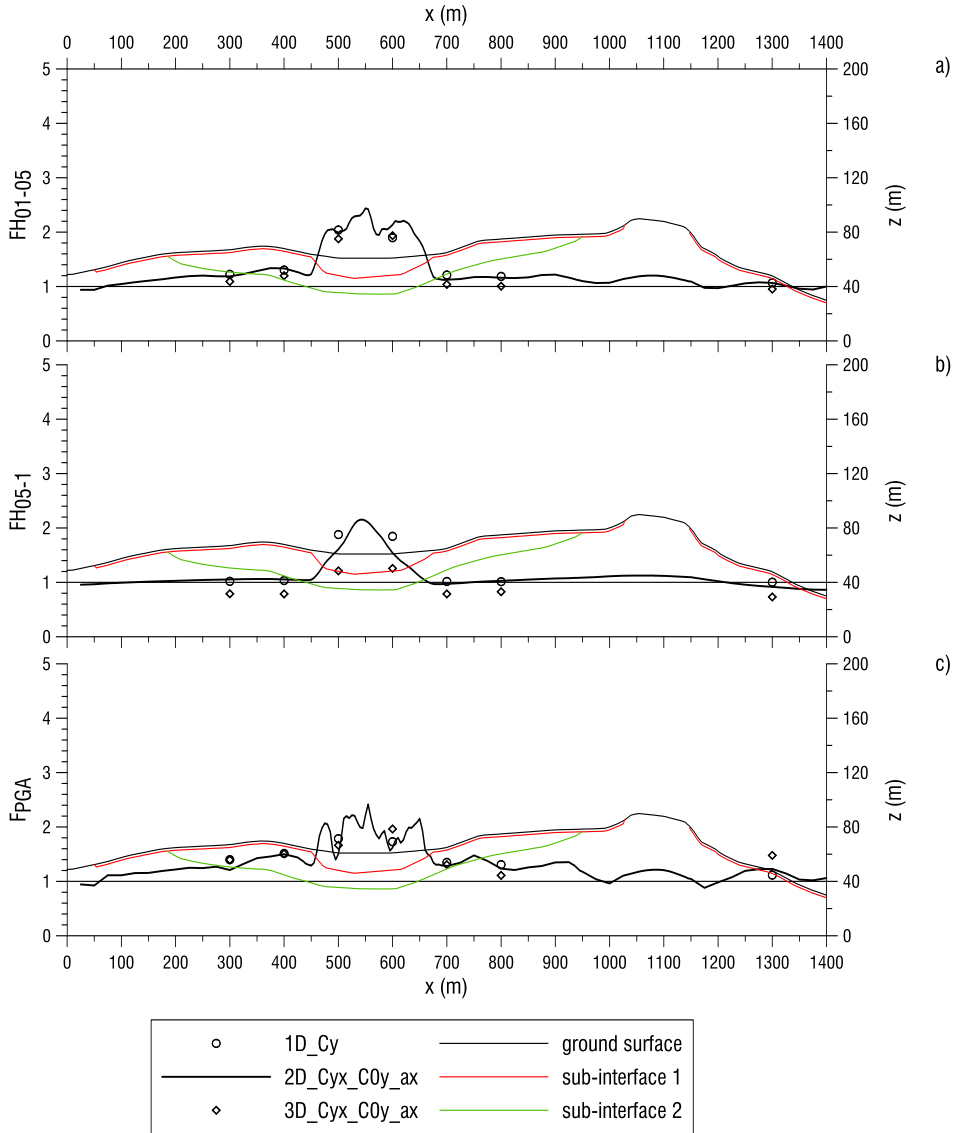


Fig. 203 Comparison A2-A4-A8 with reference to section 5, a) FH_{01-05} , b) FH_{05-1} , c) F_{PGA}

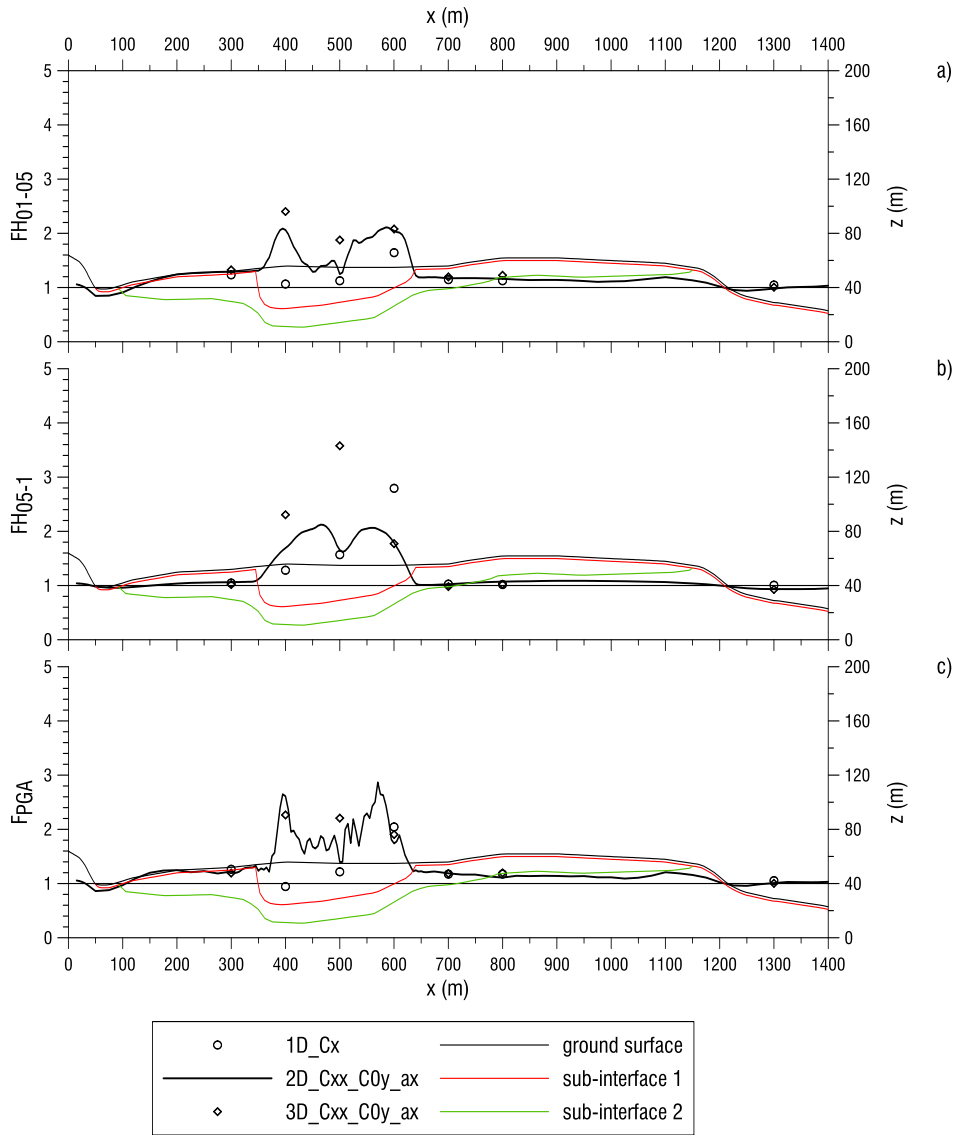


Fig. 204 Comparison A1-A3-A7 with reference to section 6, a) F_{H01-05} , b) F_{H05-1} , c) F_{PGA}

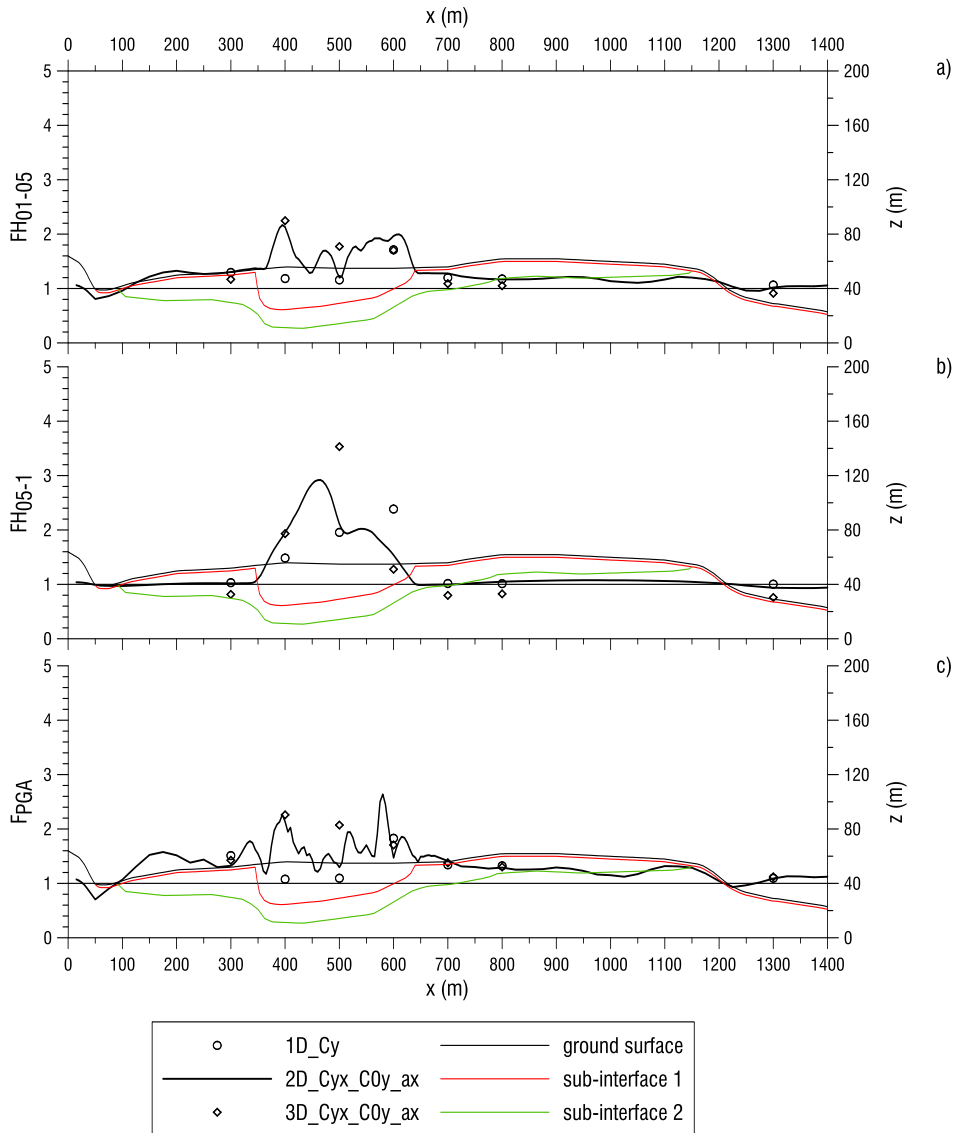


Fig. 205 Comparison A2-A4-A8 with reference to section 6, a) FH_{01-05} , b) FH_{05-1} , c) F_{PGA}

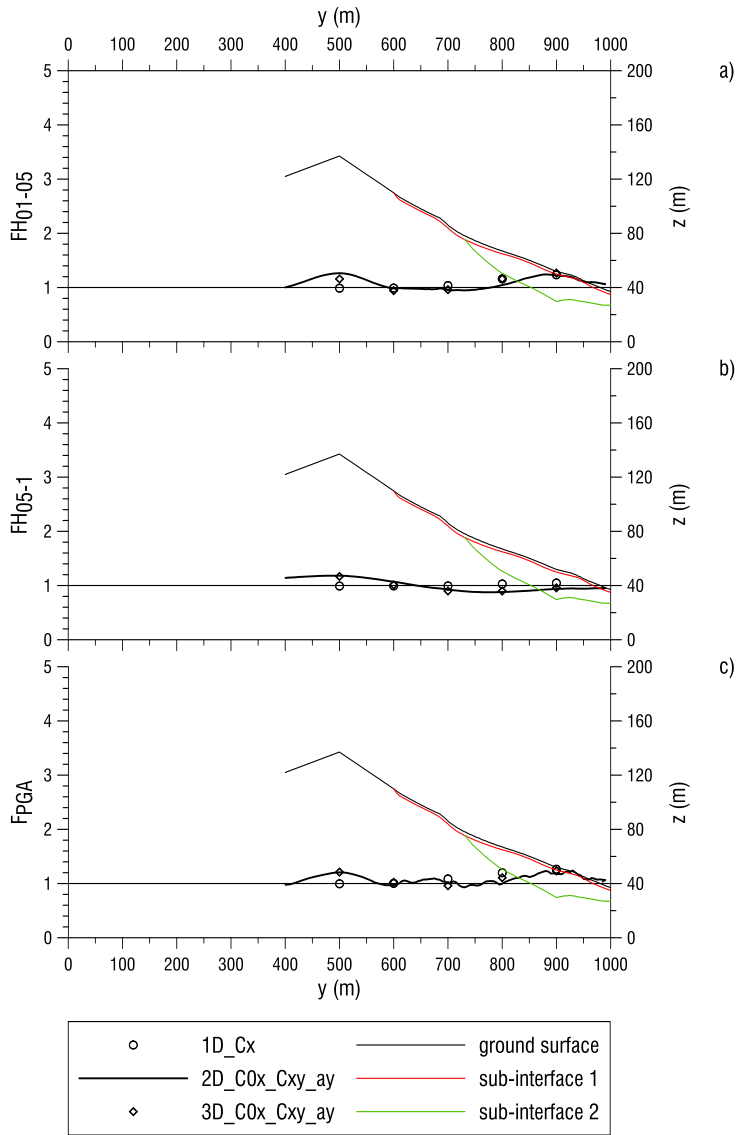


Fig. 206 Comparison A1-A3-A7 with reference to section 11, a) FH_{01-05} , b) FH_{05-1} , b) F_{PGA}

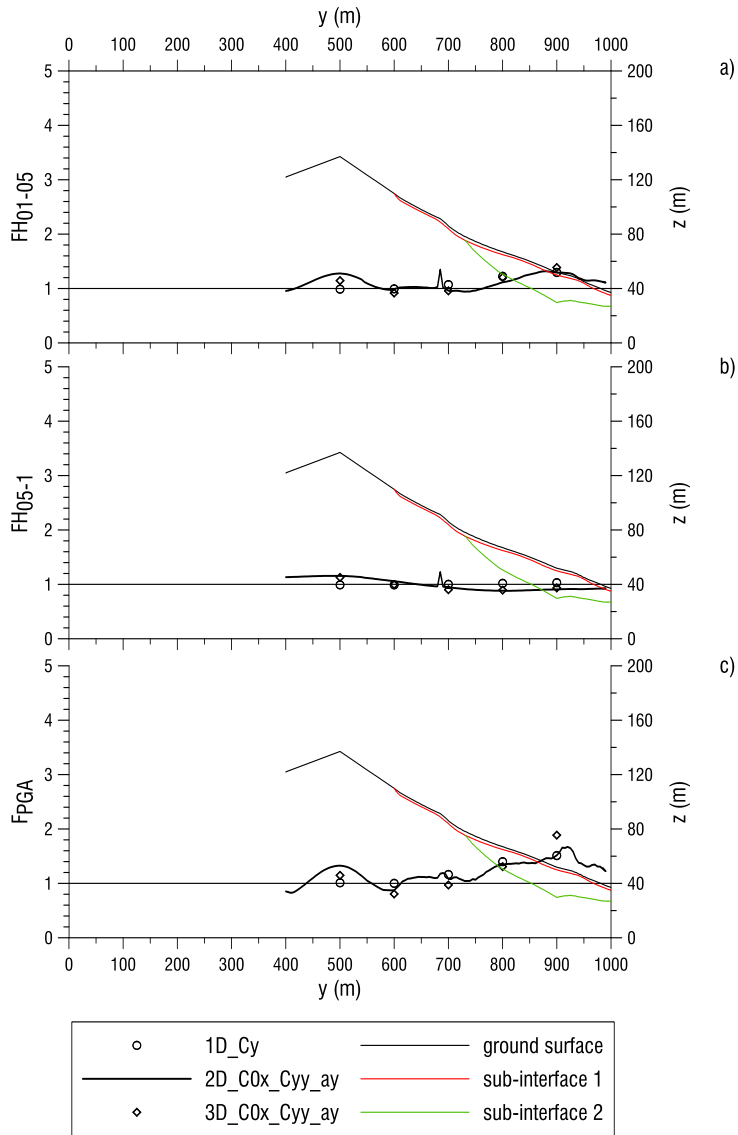


Fig. 207 Comparison A2-A4-A8 with reference to section 11, a) FH_{01-05} , b) FH_{05-1} , b) F_{PGA}

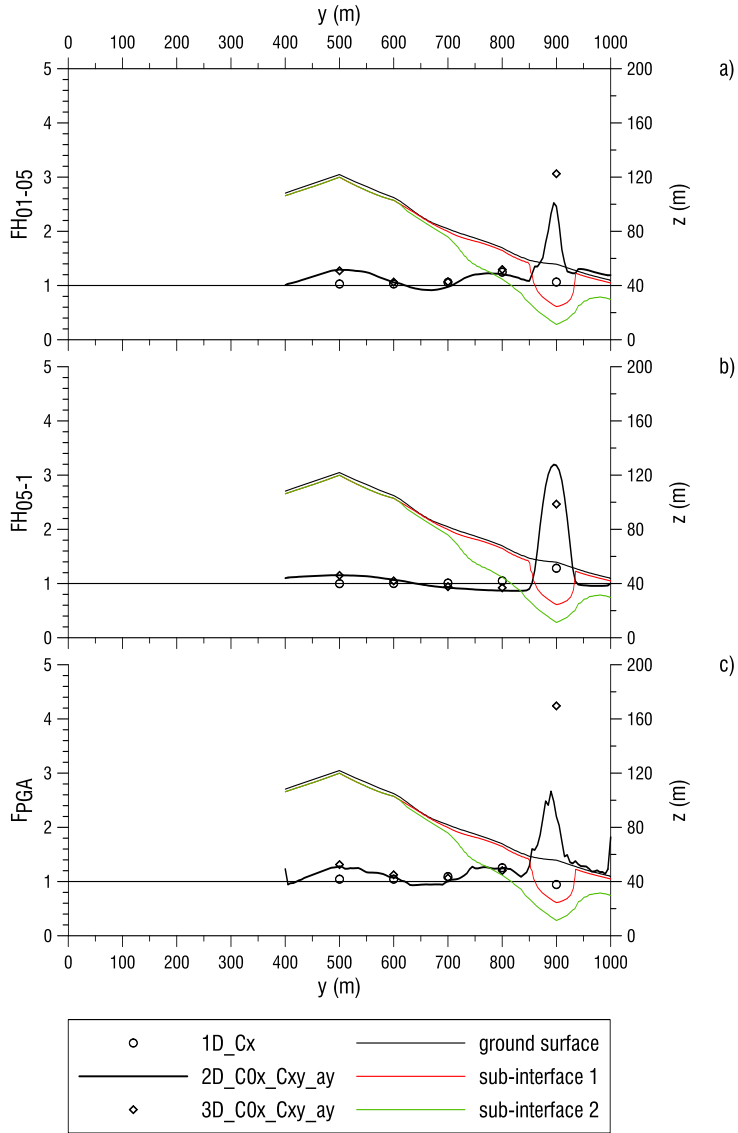


Fig. 208 Comparison A1-A3-A7 with reference to section 12, a) FH_{01-05} , b) FH_{05-1} , b) F_{PGA}

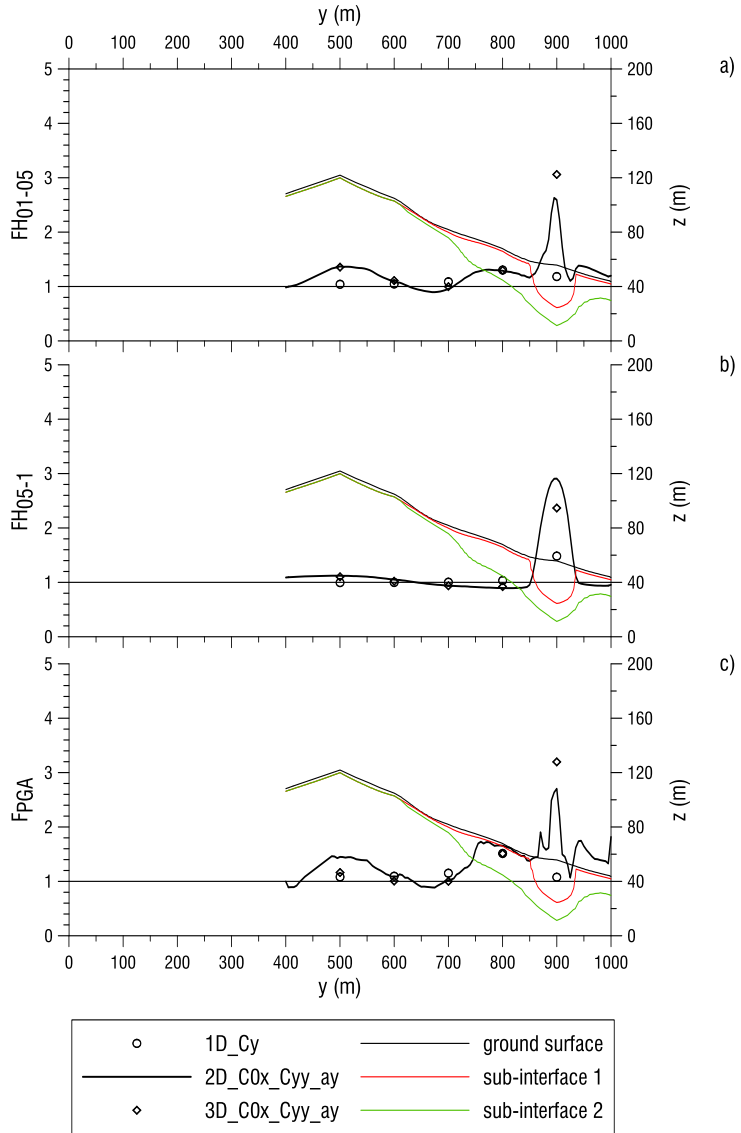


Fig. 209 Comparison A2-A4-A8 with reference to section 12, a) FH_{01-05} , b) FH_{05-1} , b) F_{PGA}

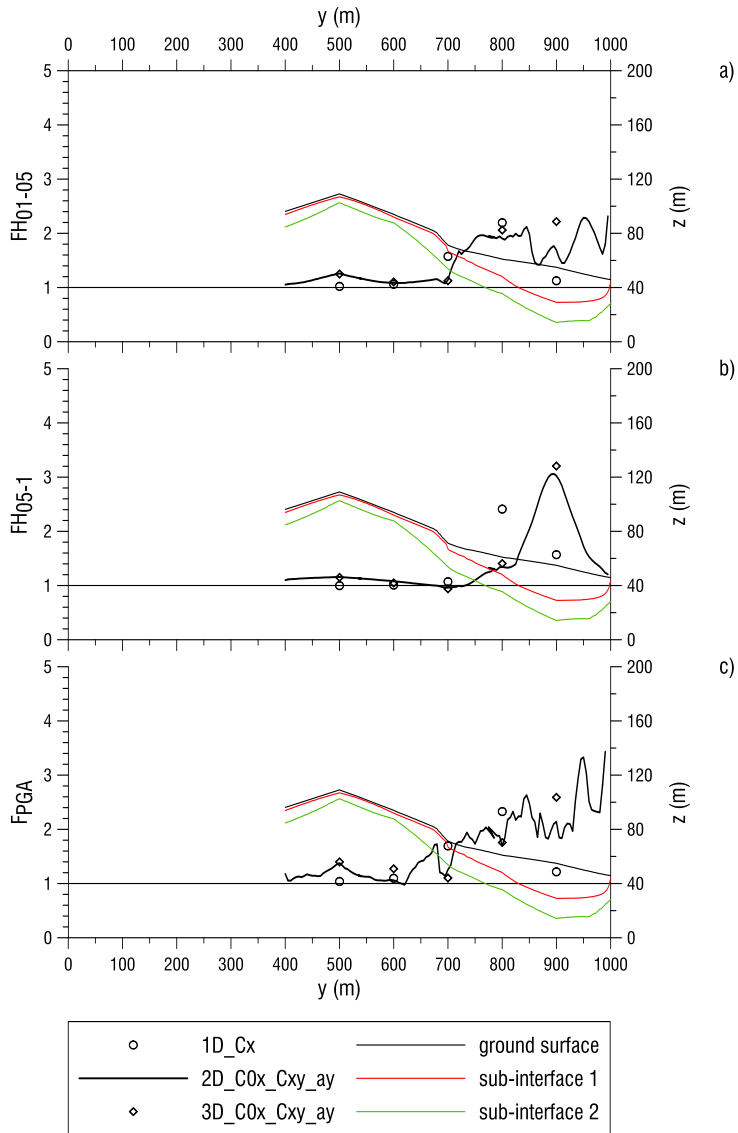


Fig. 210 Comparison A1-A3-A7 with reference to section 13, a) FH_{01-05} , b) FH_{05-1} , b) F_{PGA}

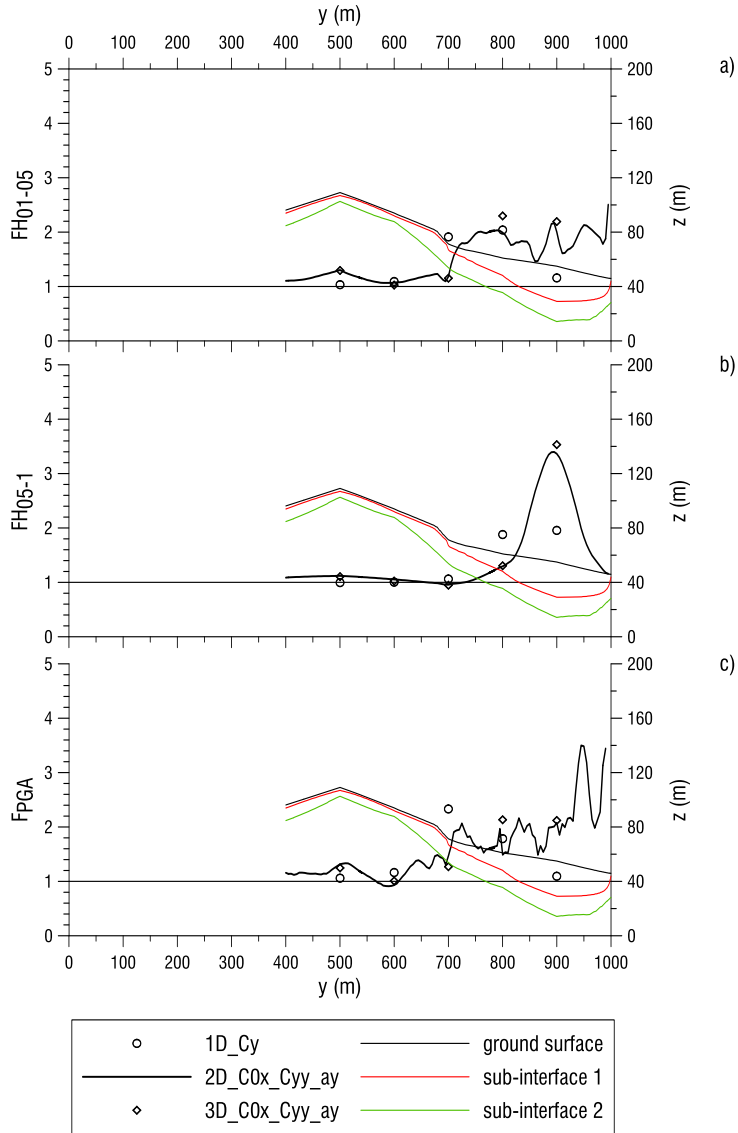


Fig. 211 Comparison A2-A4-A8 with reference to section 13, a) FH_{01-05} , b) FH_{05-1} , b) F_{PGA}

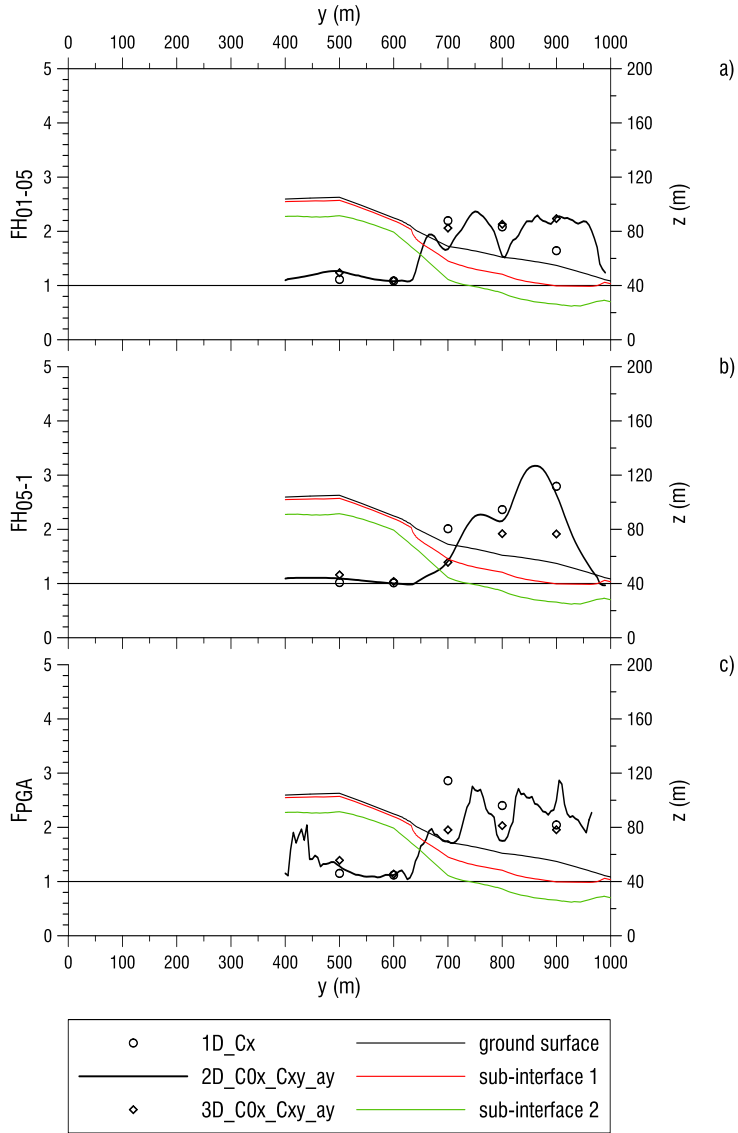


Fig. 212 Comparison A1-A3-A7 with reference to section 14, a) FH_{01-05} , b) FH_{05-1} , b) F_{PGA}

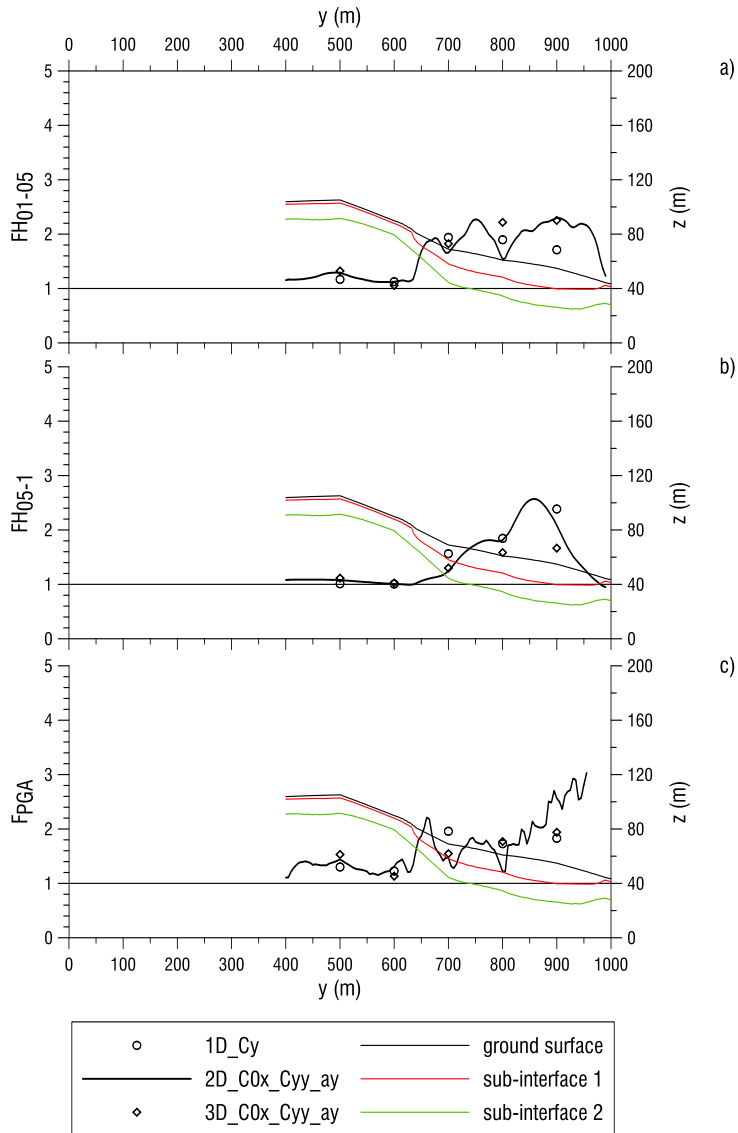


Fig. 213 Comparison A2-A4-A8 with reference to section 14, a) FH_{01-05} , b) FH_{05-1} , b) F_{PGA}

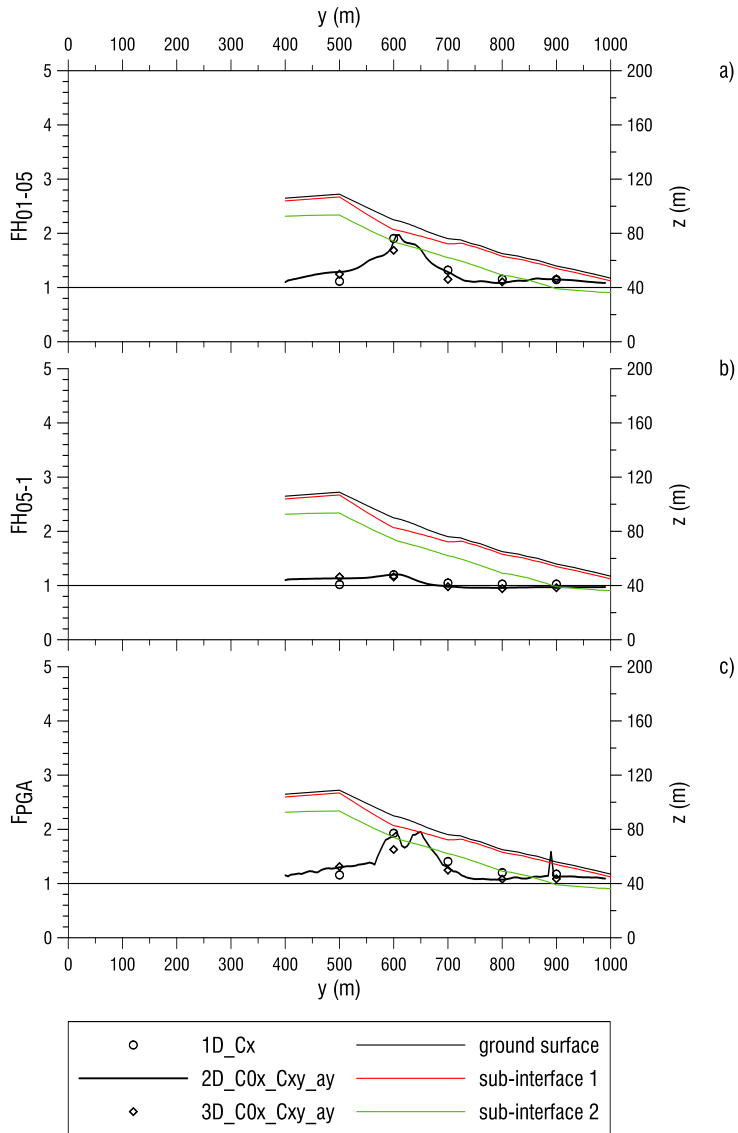


Fig. 214 Comparison A1-A3-A7 with reference to section 15, a) FH_{01-05} , b) FH_{05-1} , b) F_{PGA}

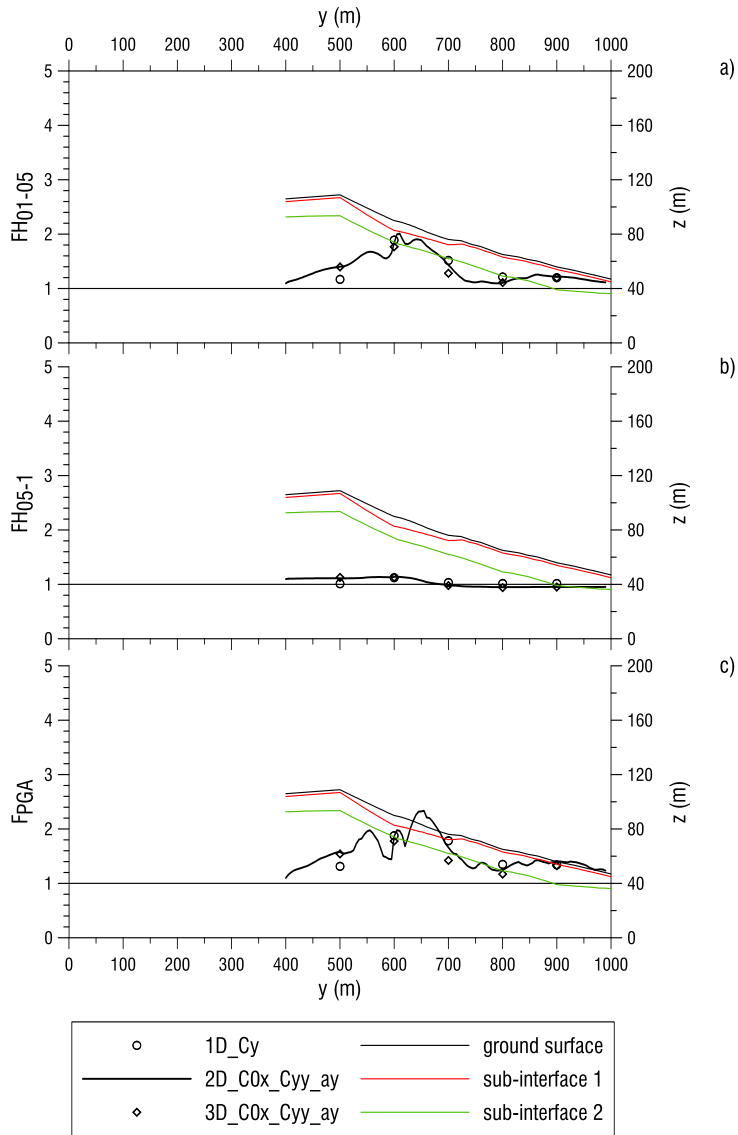


Fig. 215 Comparison A2-A4-A8 with reference to section 15, a) FH_{01-05} , b) FH_{05-1} , b) F_{PGA}

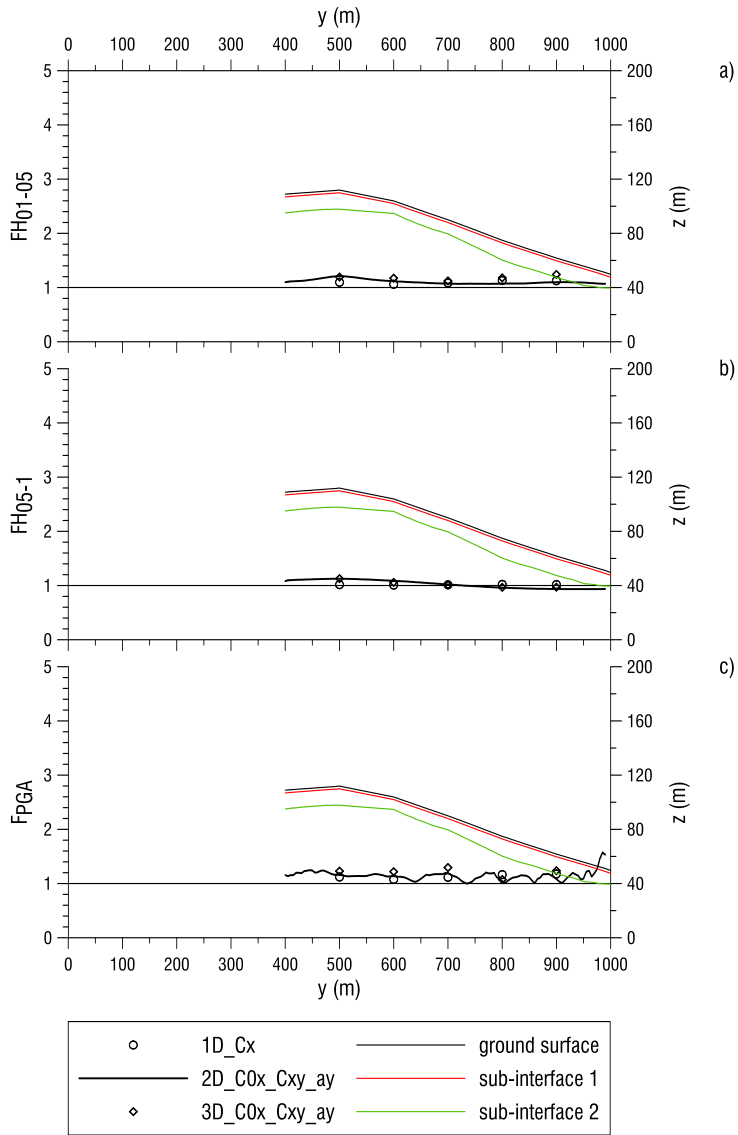


Fig. 216 Comparison A1-A3-A7 with reference to section 16, a) FH_{01-05} , b) FH_{05-1} , b) F_{PGA}

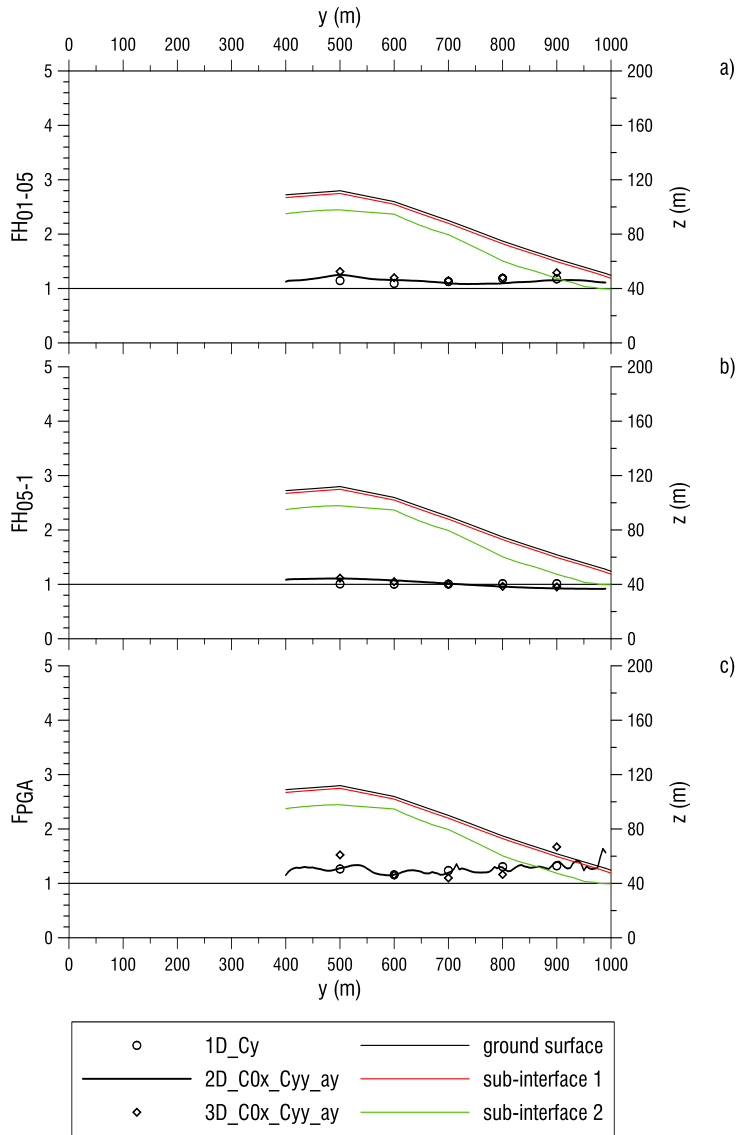


Fig. 217 Comparison A2-A4-A8 with reference to section 16, a) FH_{01-05} , b) FH_{05-1} , b) F_{PGA}

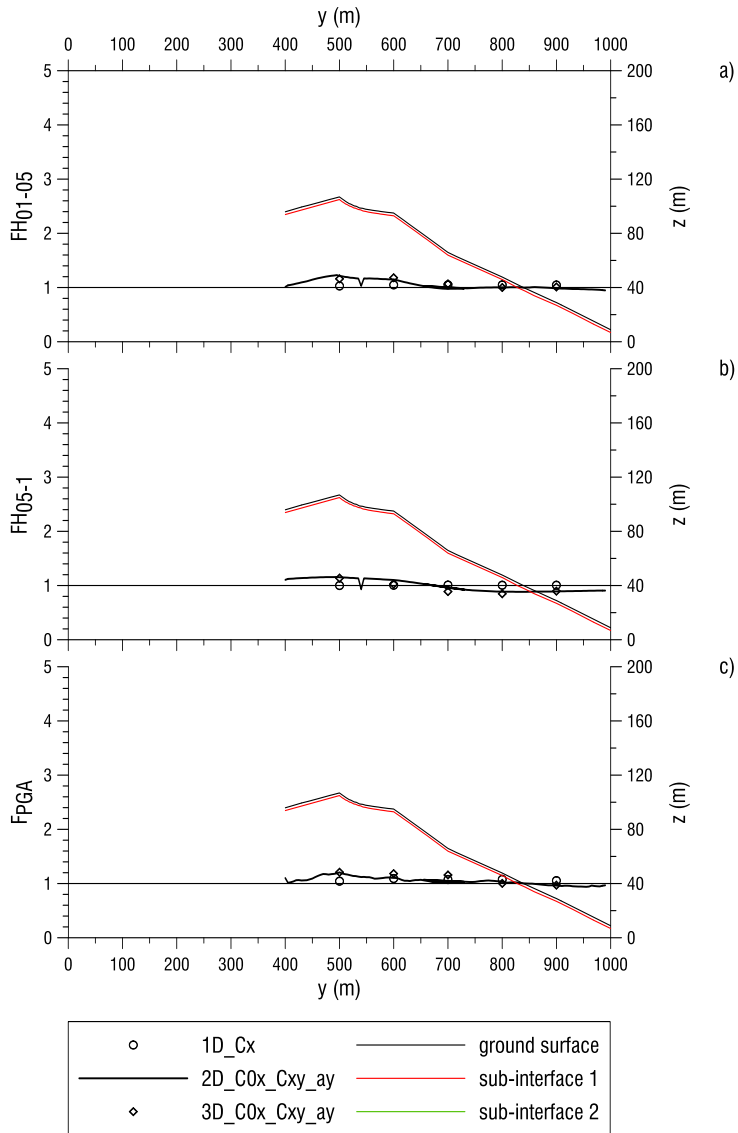


Fig. 218 Comparison A1-A3-A7 with reference to section 21, a) FH_{01-05} , b) FH_{05-1} , b) F_{PGA}

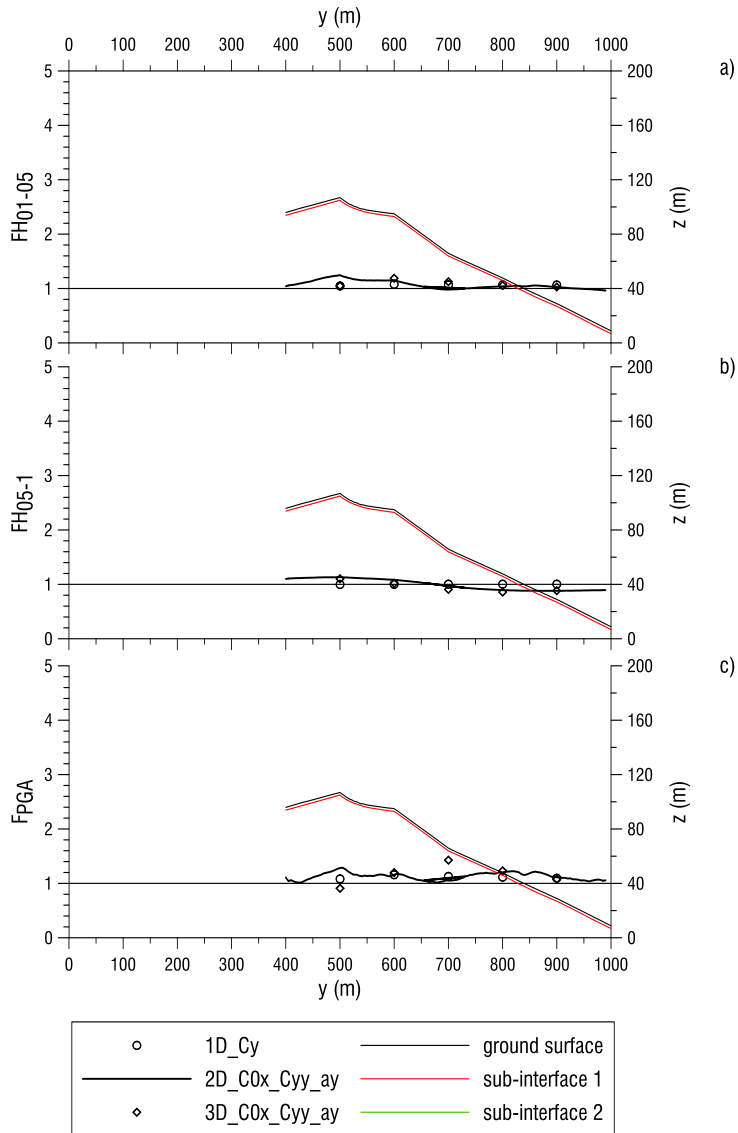


Fig. 219 Comparison A2-A4-A8 with reference to section 21, a) FH_{01-05} , b) FH_{05-1} , c) F_{PGA}

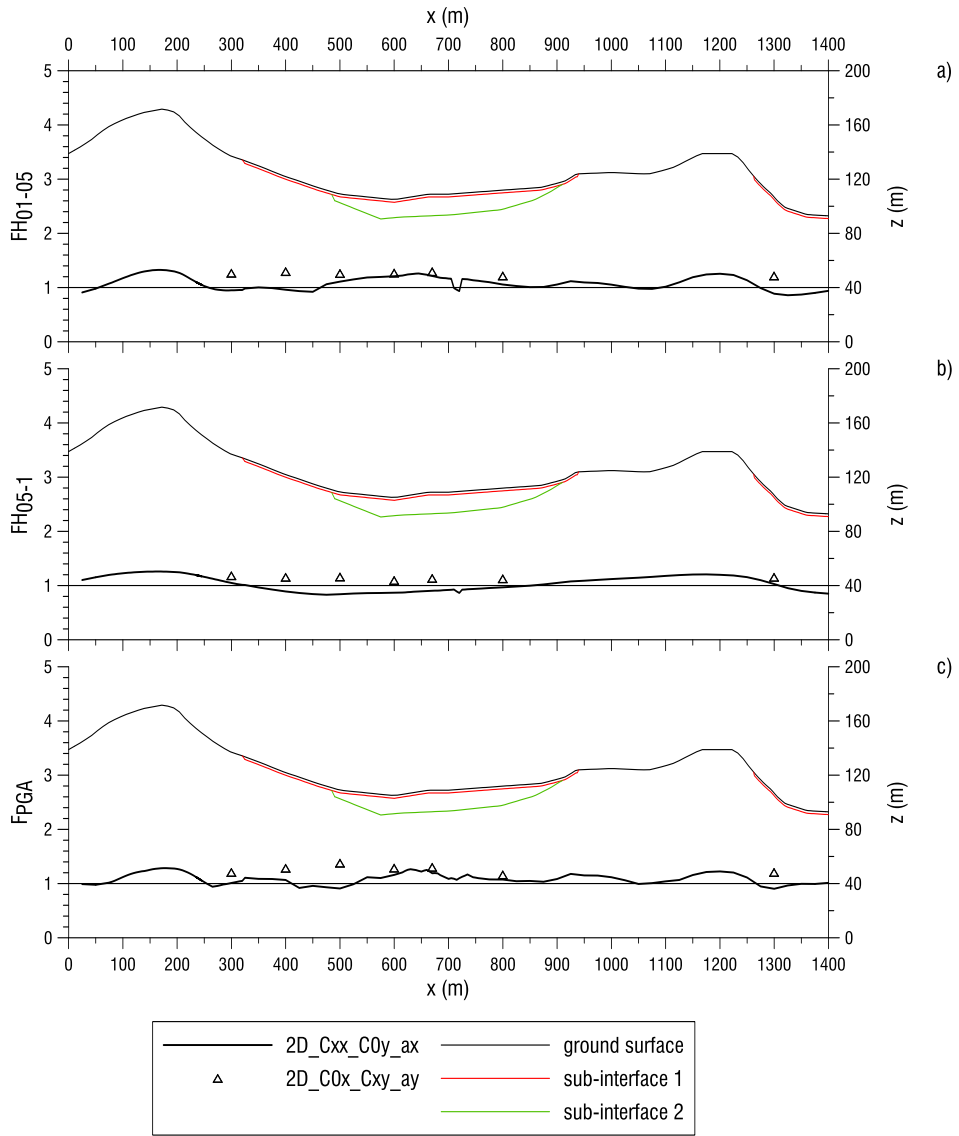


Fig. 220 Comparison A3-A5 with reference to section 2, a) FH_{01-05} , b) FH_{05-1} , b) F_{PGA}

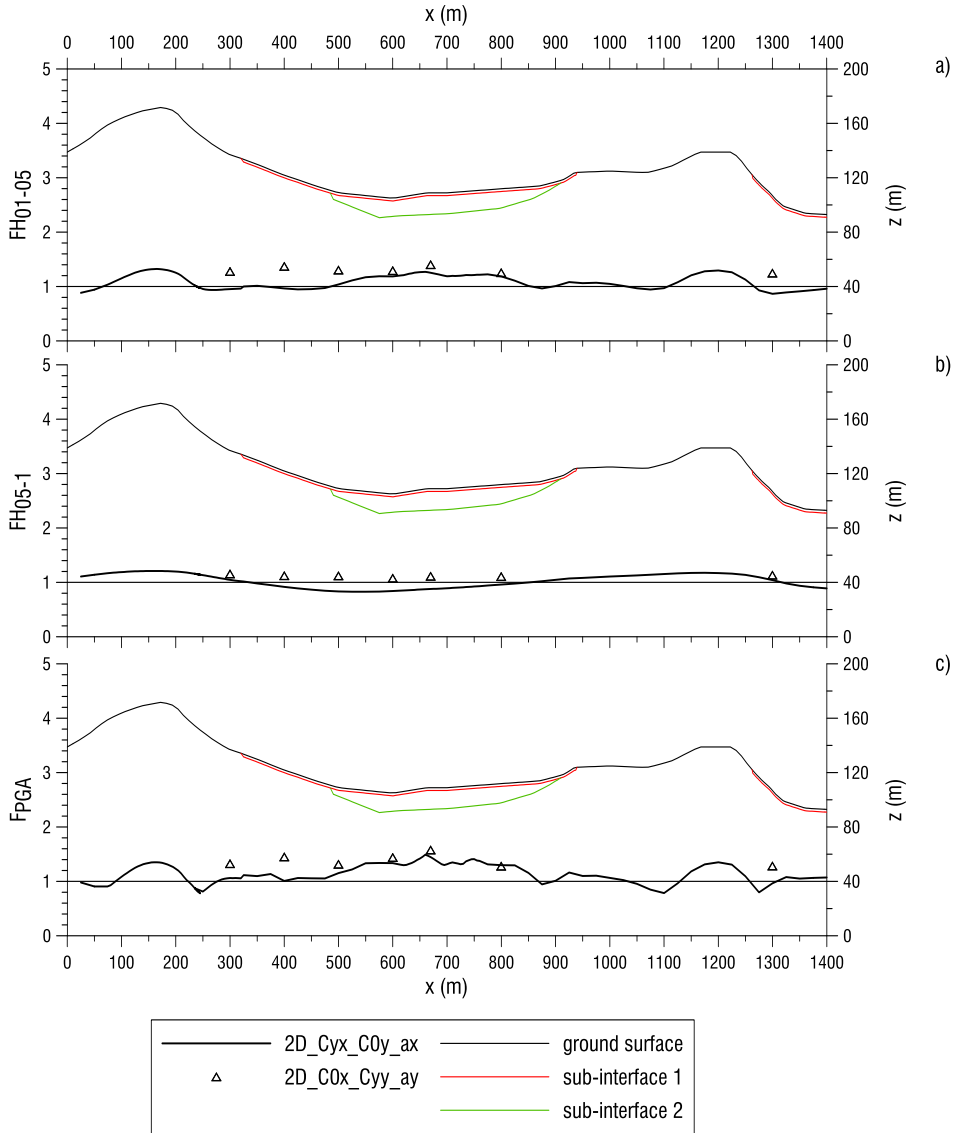


Fig. 221 Comparison A4-A6 with reference to section 2, a) FH_{01-05} , b) FH_{05-1} , c) F_{PGA}

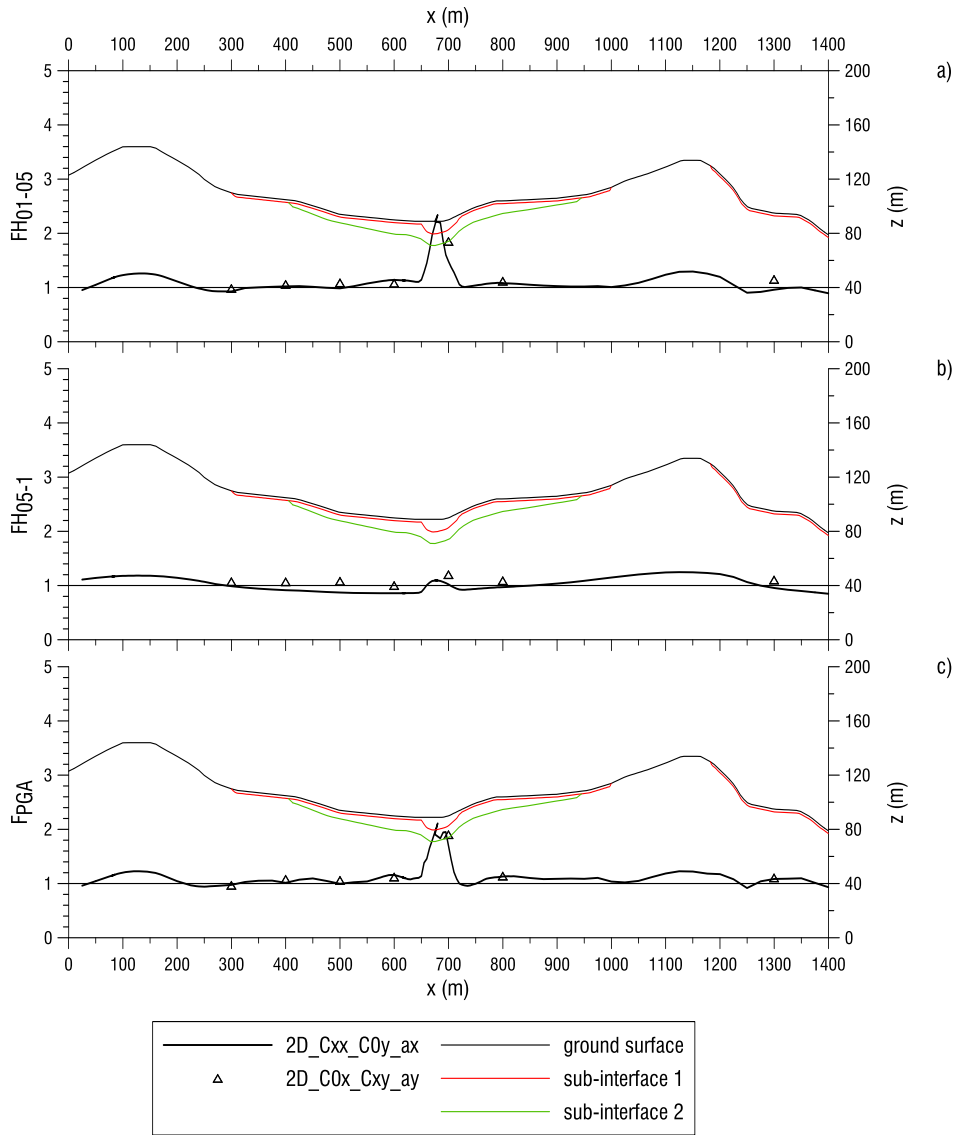


Fig. 222 Comparison A3-A5 with reference to section 3, a) FH_{01-05} , b) FH_{05-1} , c) F_{PGA}

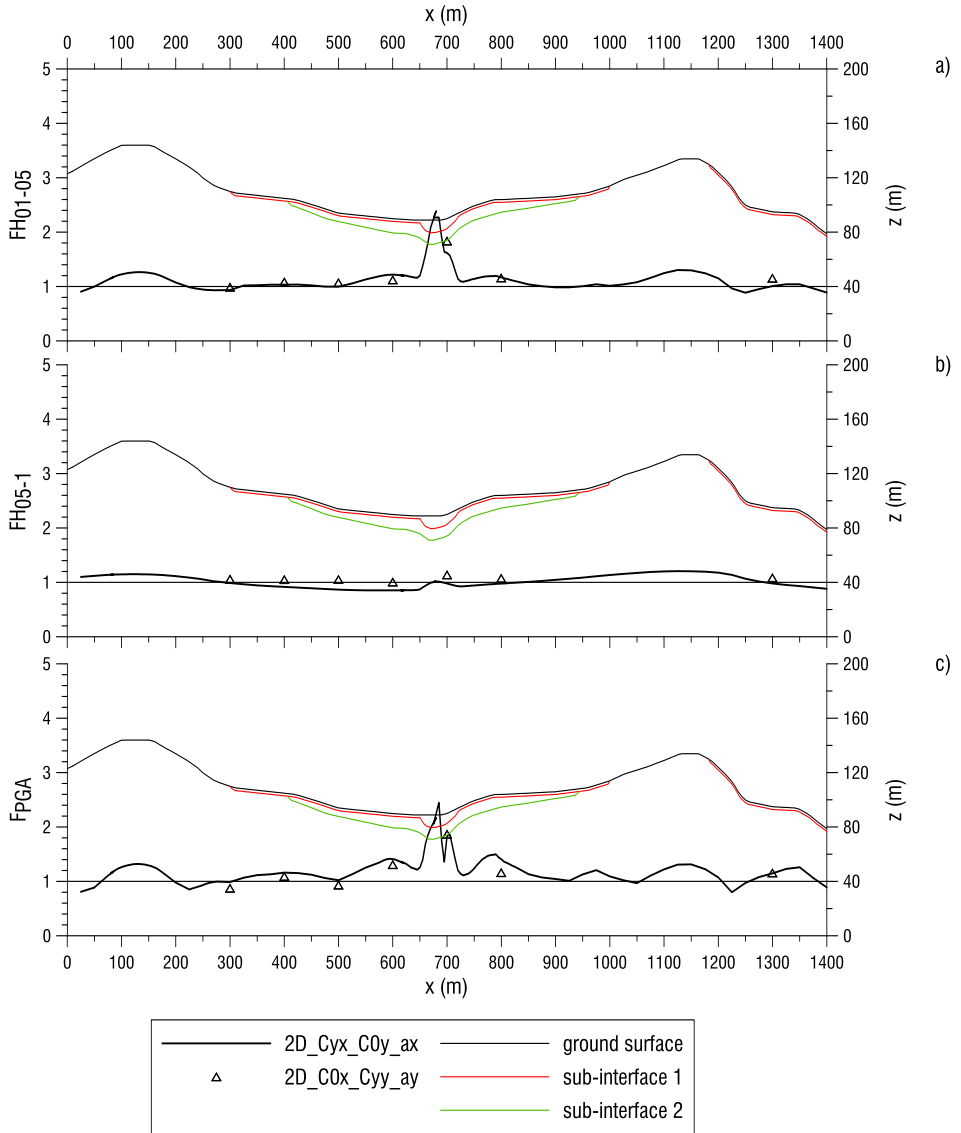


Fig. 223 Comparison A4-A6 with reference to section 3, a) FH_{01-05} , b) FH_{05-1} , c) F_{PGA}

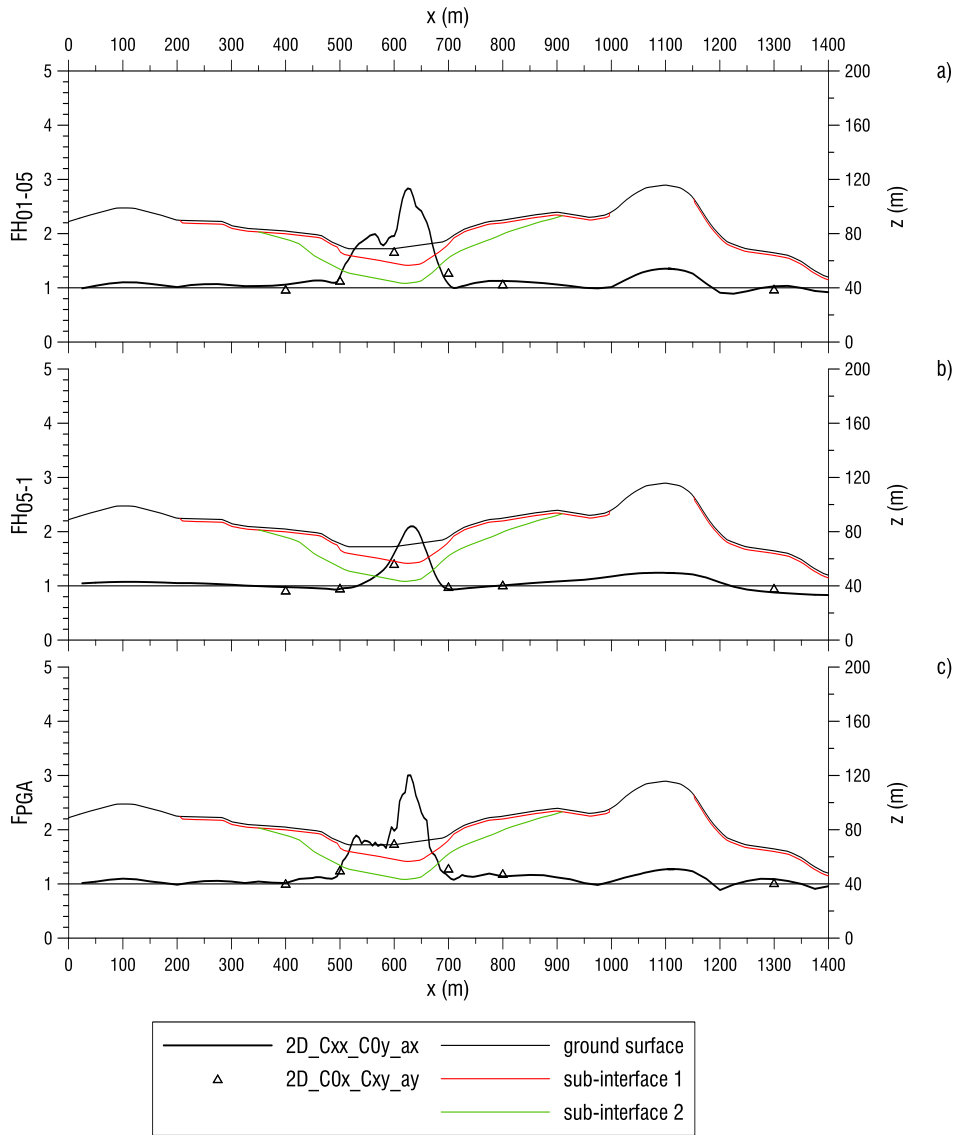


Fig. 224 Comparison A3-A5 with reference to section 4, a) FH_{01-05} , b) FH_{05-1} , b) F_{PGA}

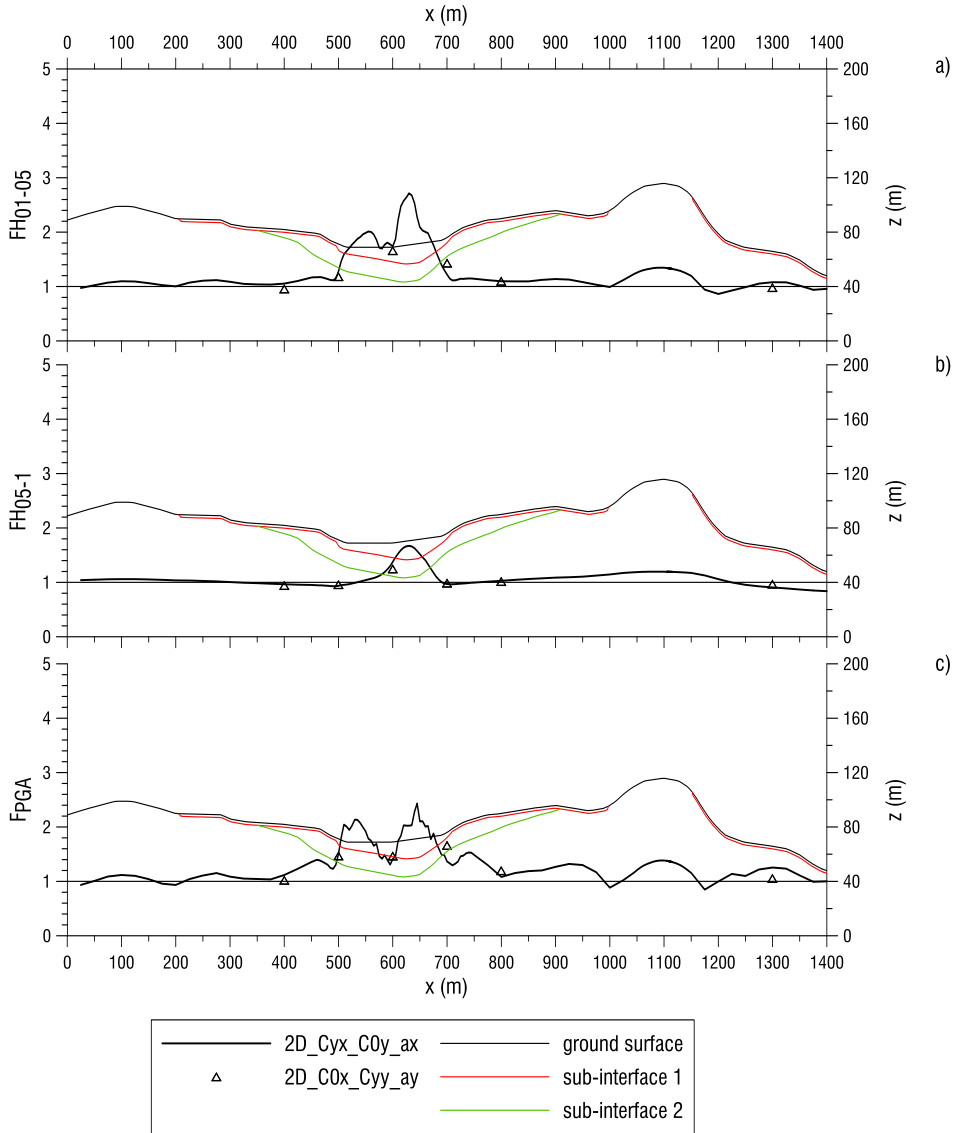


Fig. 225 Comparison A4-A6 with reference to section 4, a) FH_{01-05} , b) FH_{05-1} , c) F_{PGA}

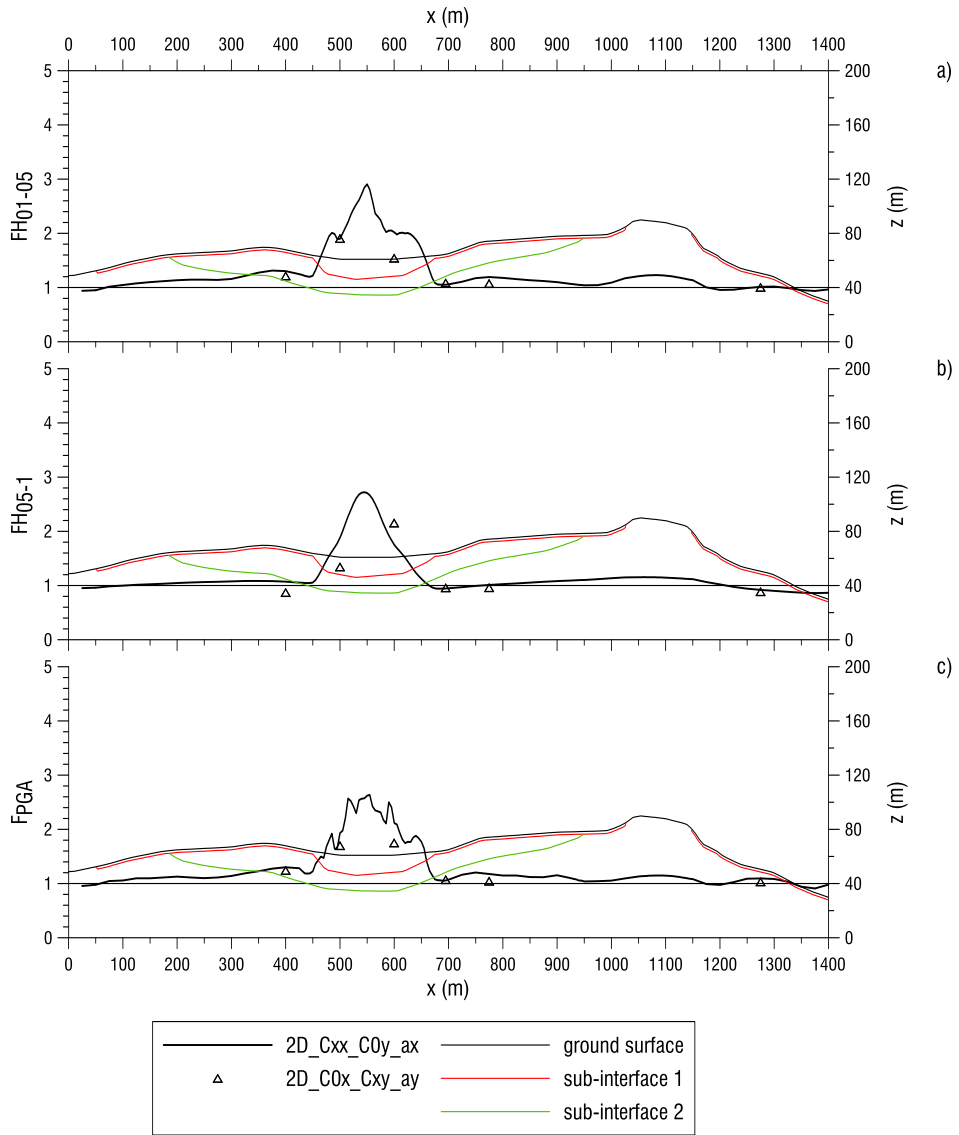


Fig. 226 Comparison A3-A5 with reference to section 5, a) FH_{01-05} , b) FH_{05-1} , c) F_{PGA}

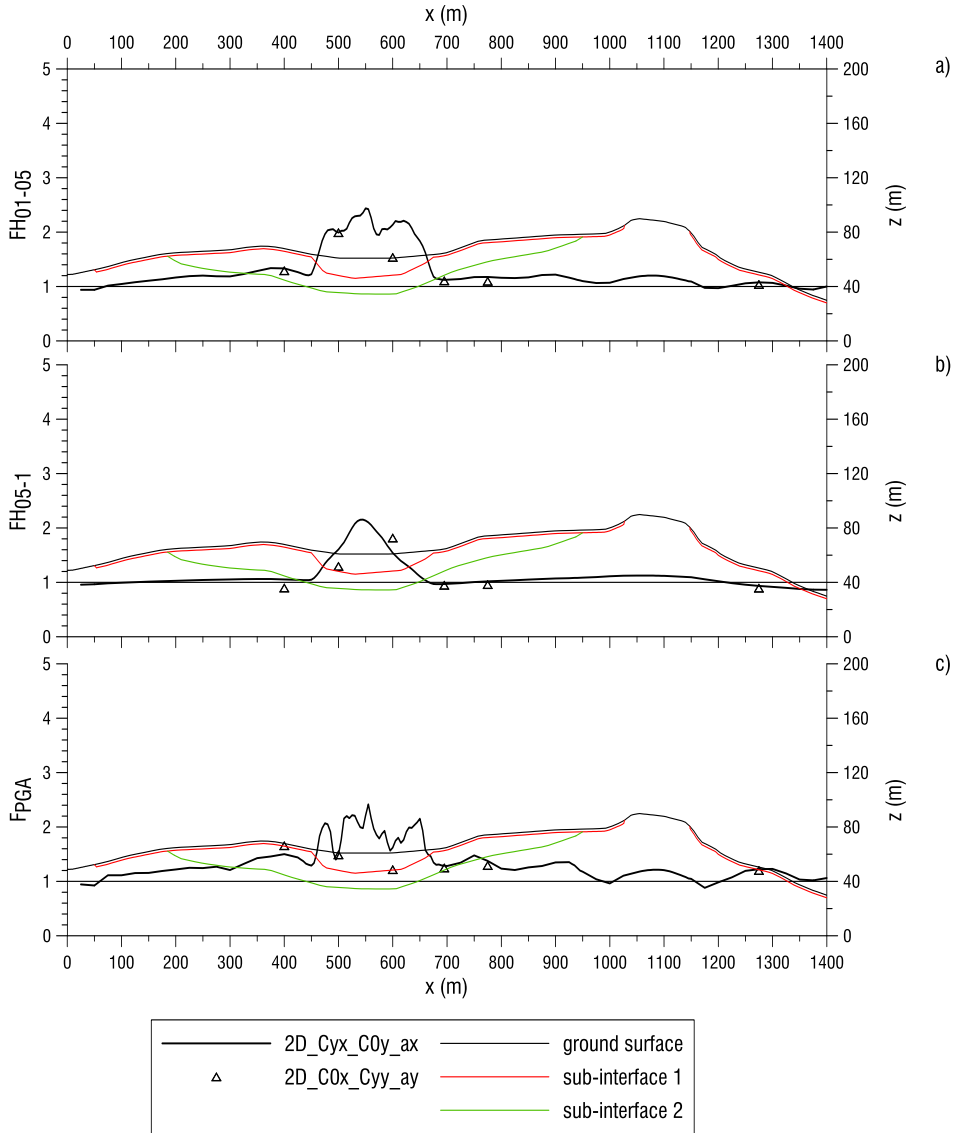


Fig. 227 Comparison A4-A6 with reference to section 5, a) FH_{01-05} , b) FH_{05-1} , c) F_{PGA}

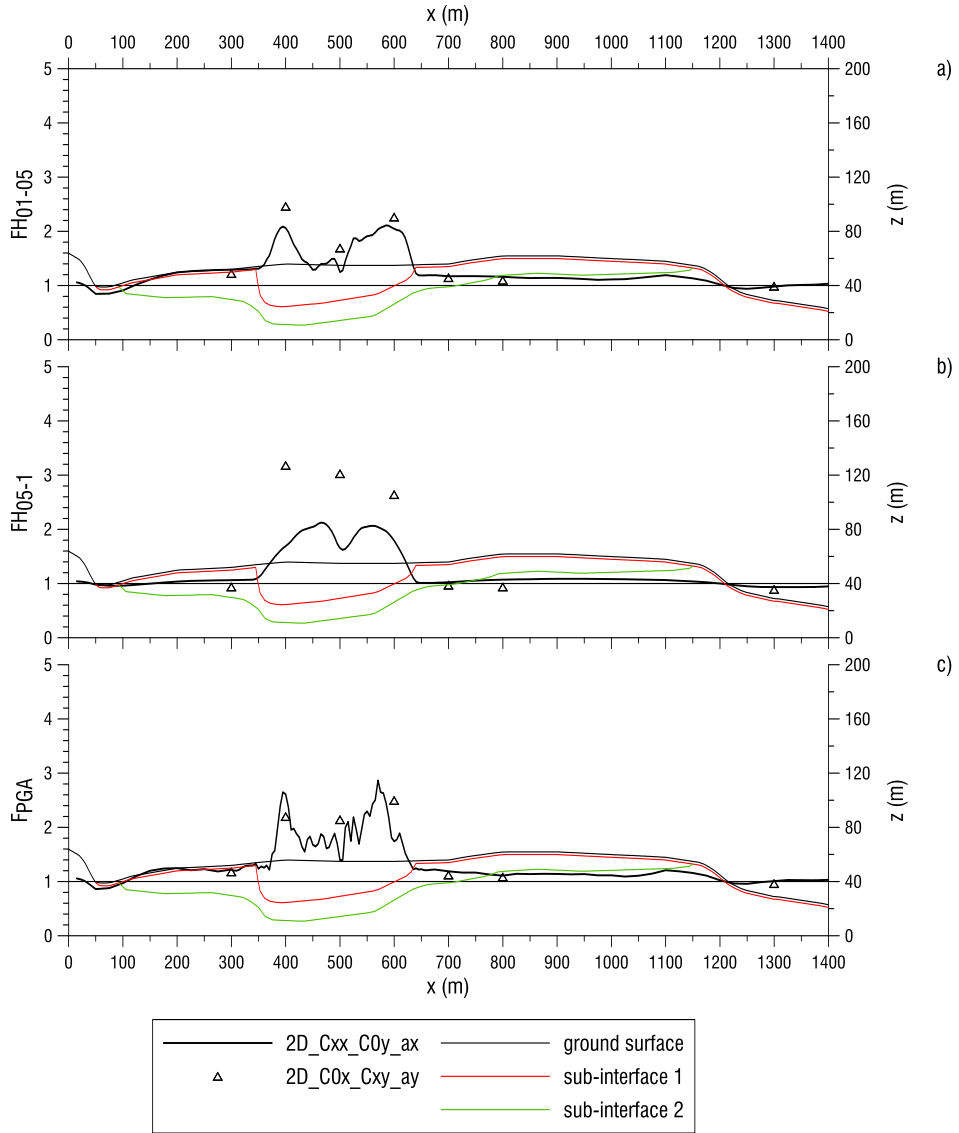


Fig. 228 Comparison A3-A5 with reference to section 6, a) F_{H01-05} , b) F_{H05-1} , c) F_{PGA}

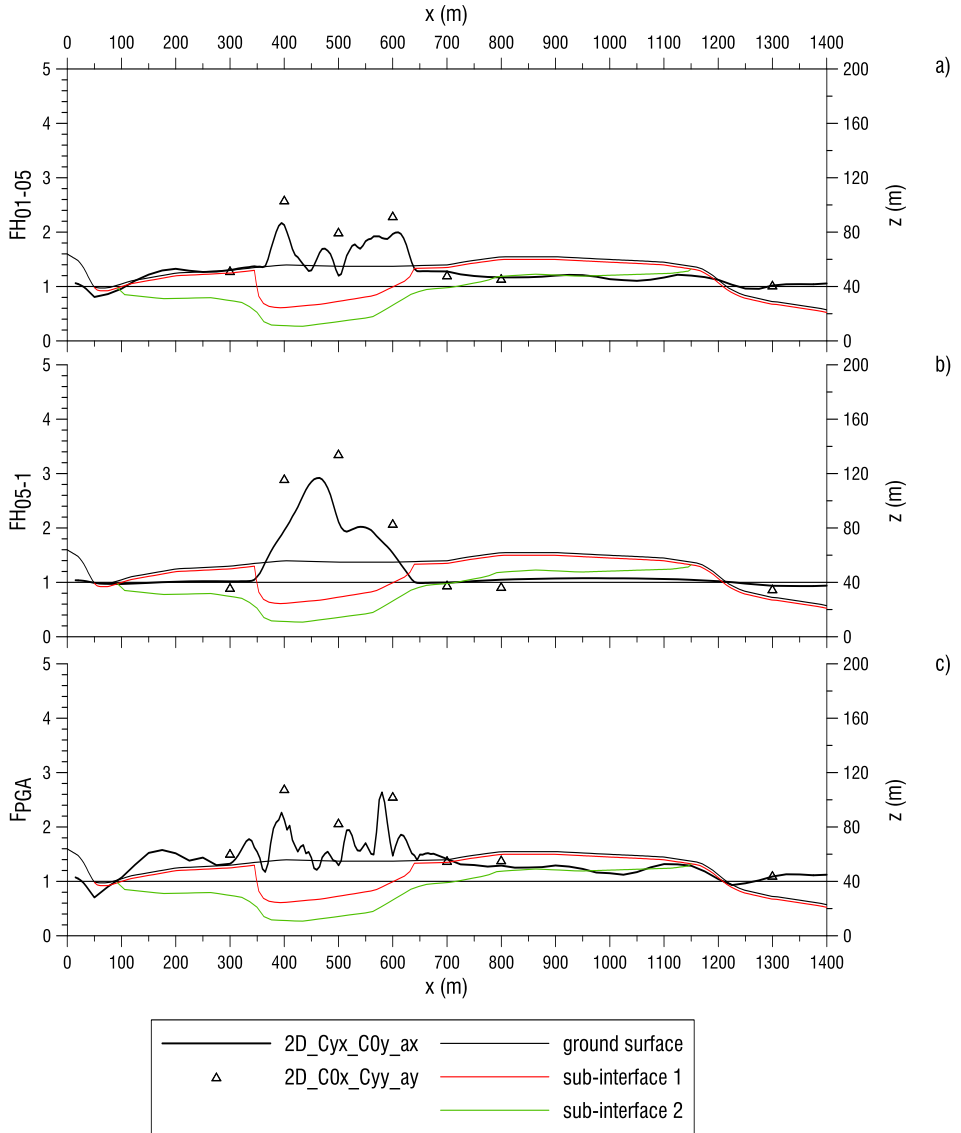


Fig. 229 Comparison A4-A6 with reference to section 6, a) FH_{01-05} , b) FH_{05-1} , c) F_{PGA}

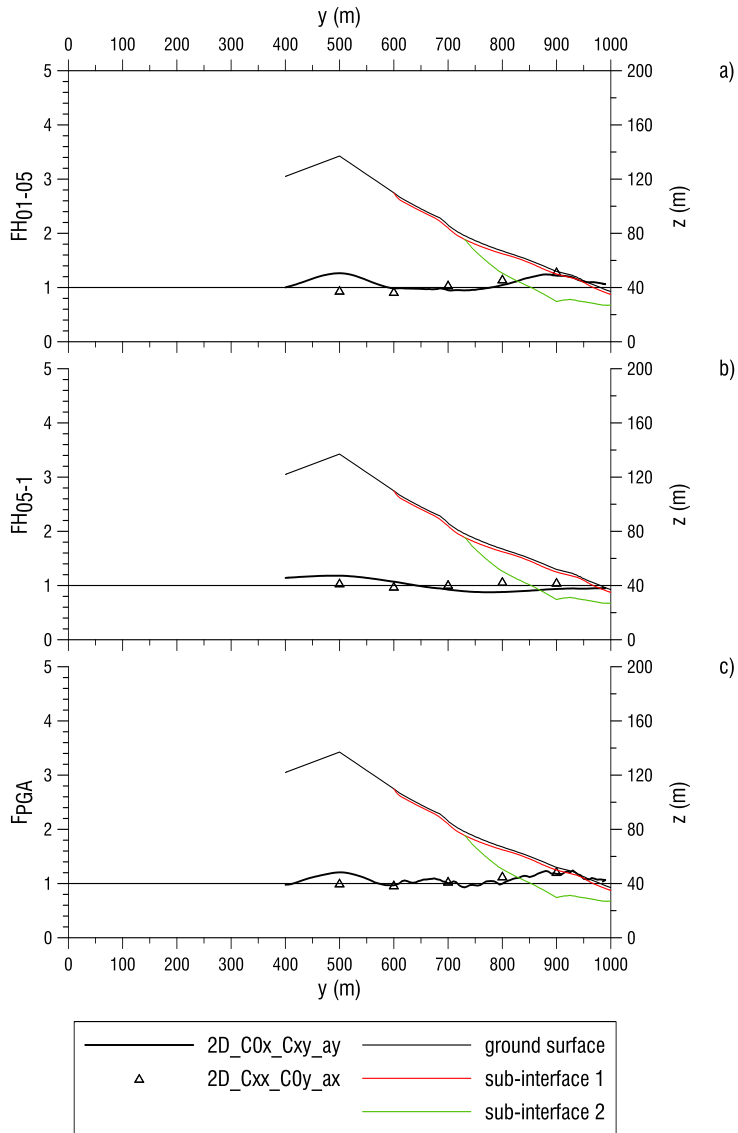


Fig. 230 Comparison A3-A5 with reference to section 11, a) FH_{01-05} , b) FH_{05-1} , b) F_{PGA}

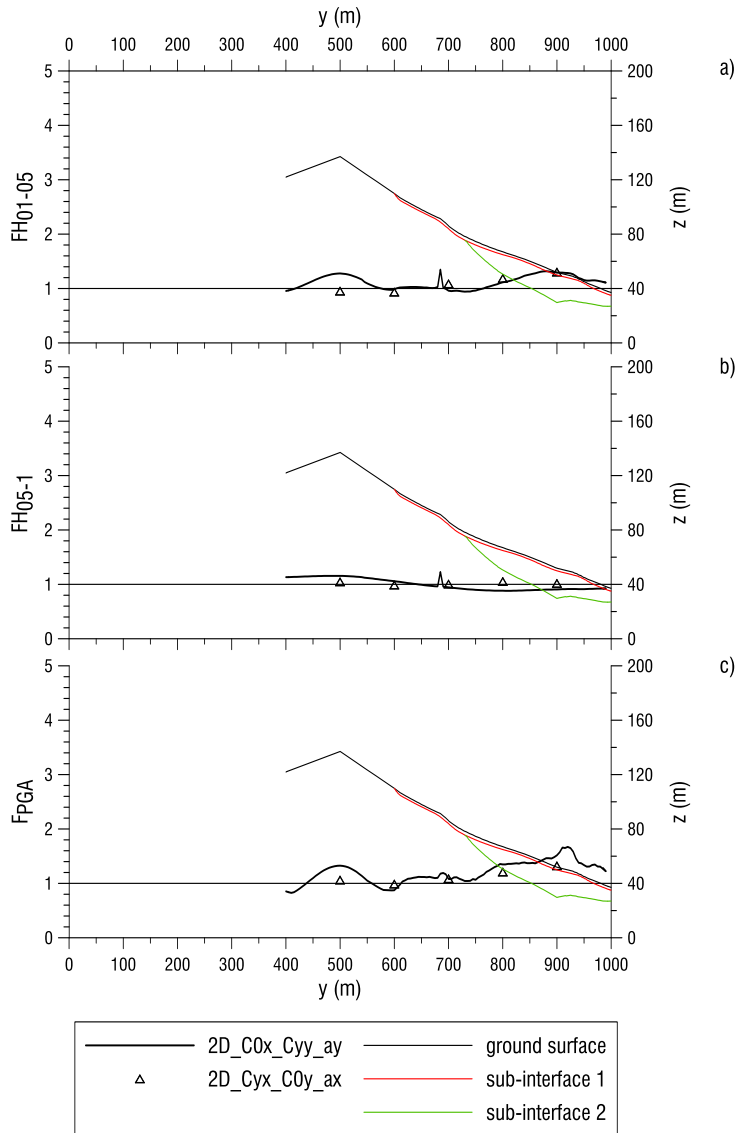


Fig. 231 Comparison A4-A6 with reference to section 11, a) FH_{01-05} , b) FH_{05-1} , b) F_{PGA}

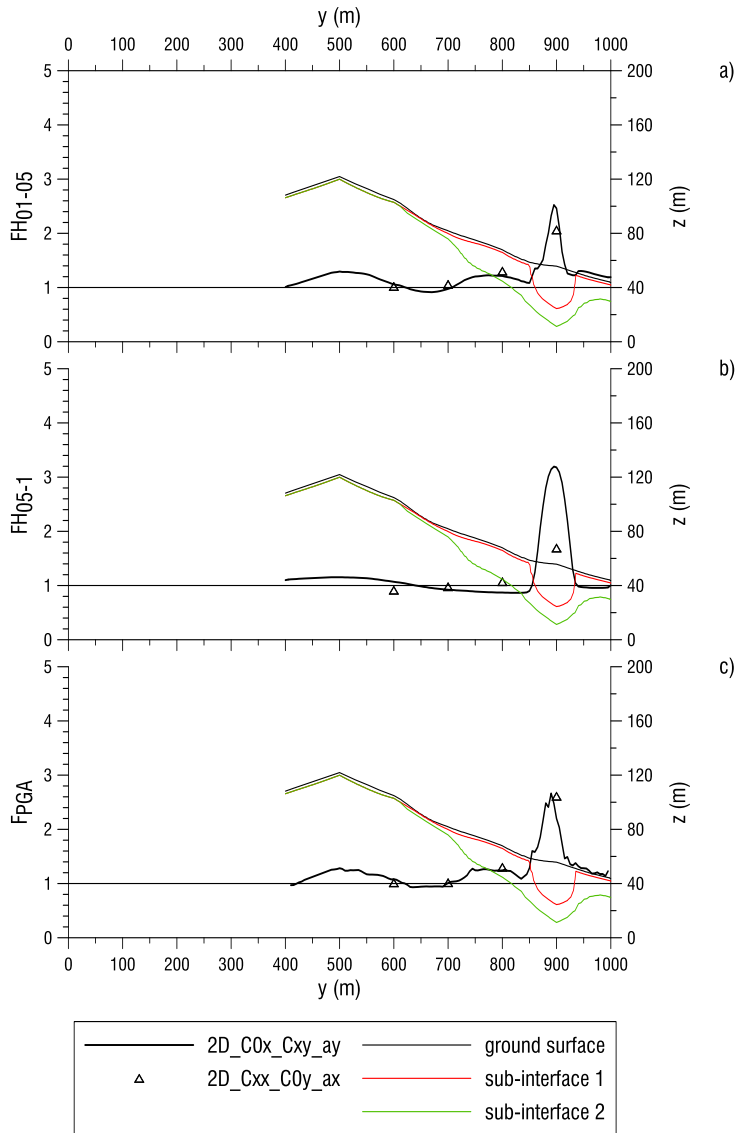


Fig. 232 Comparison A3-A5 with reference to section 12, a) FH_{01-05} , b) FH_{05-1} , b) F_{PGA}

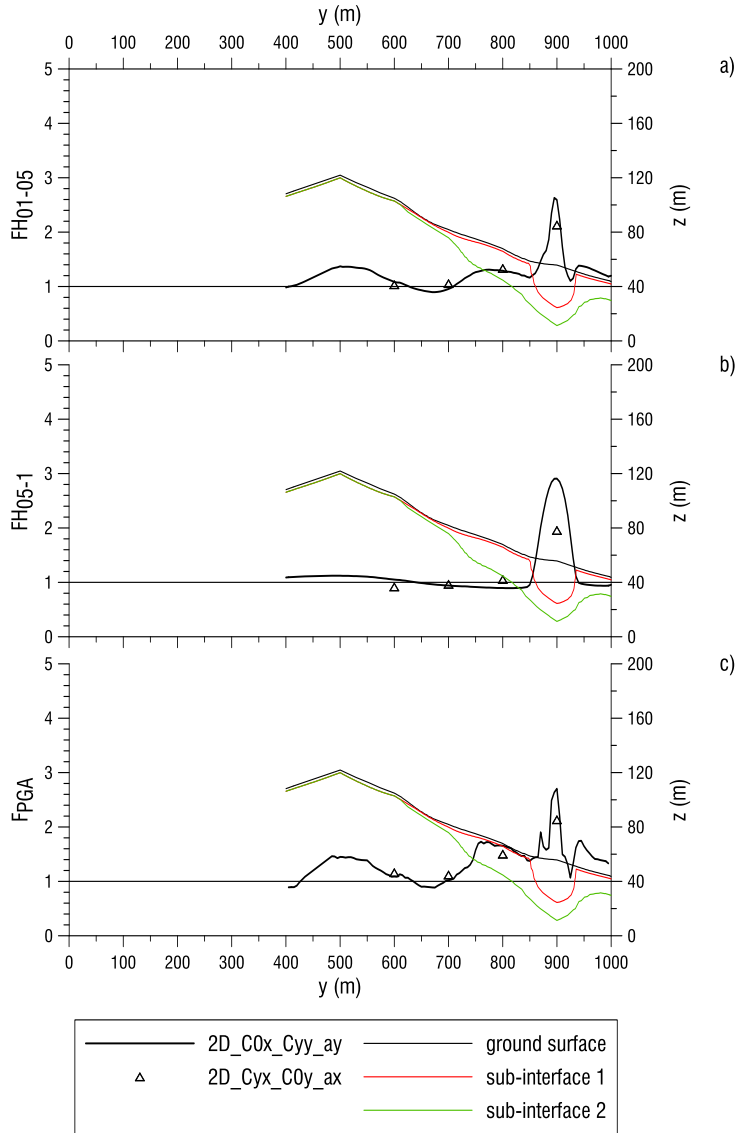


Fig. 233 Comparison A4-A6 with reference to section 12, a) FH_{01-05} , b) FH_{05-1} , c) F_{PGA}

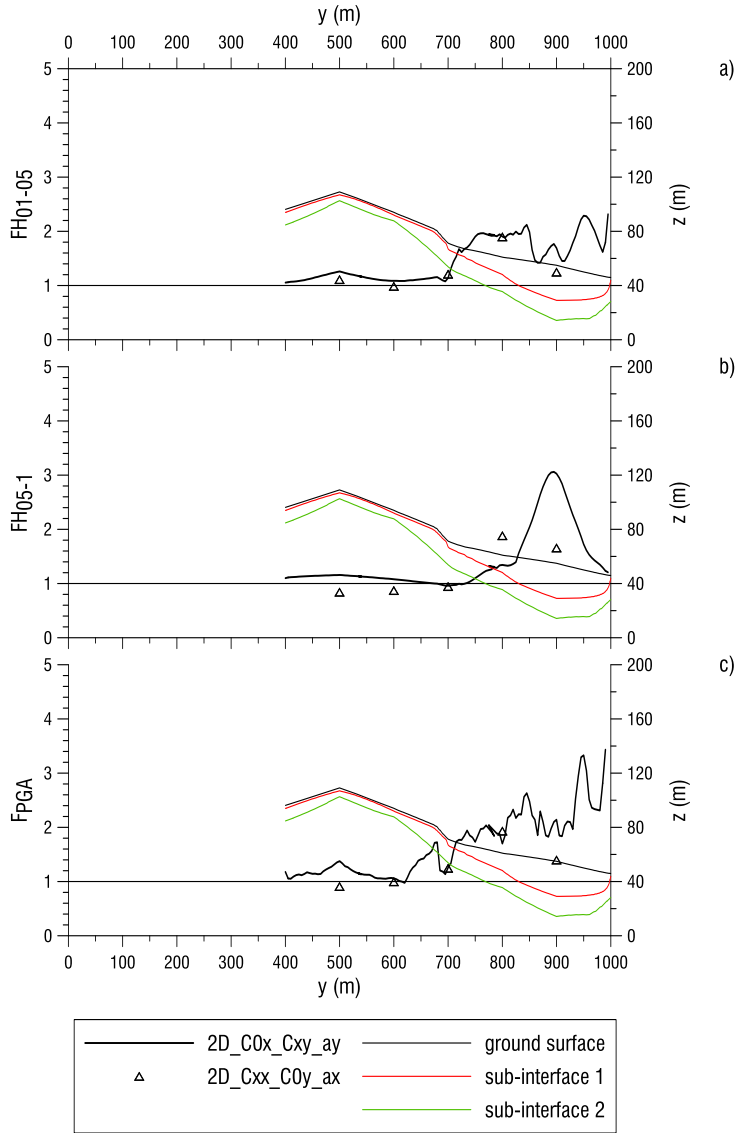


Fig. 234 Comparison A3-A5 with reference to section 13, a) FH_{01-05} , b) FH_{05-1} , b) F_{PGA}

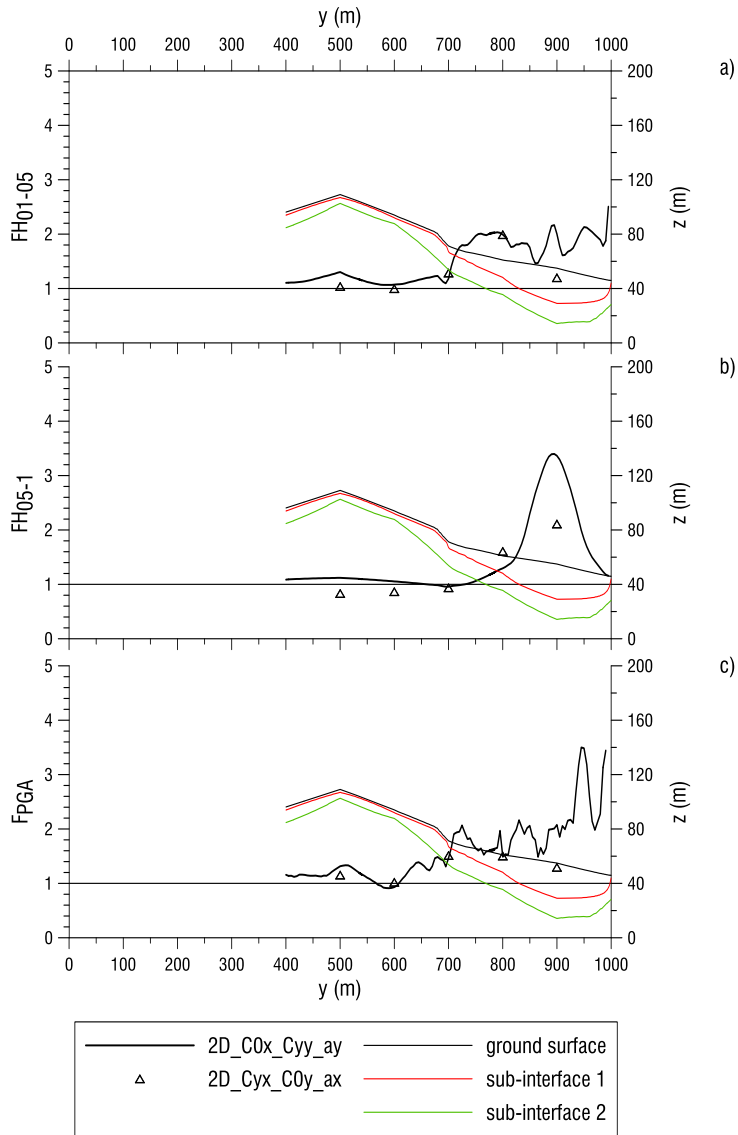


Fig. 235 Comparison A4-A6 with reference to section 13, a) FH_{01-05} , b) FH_{05-1} , c) F_{PGA}

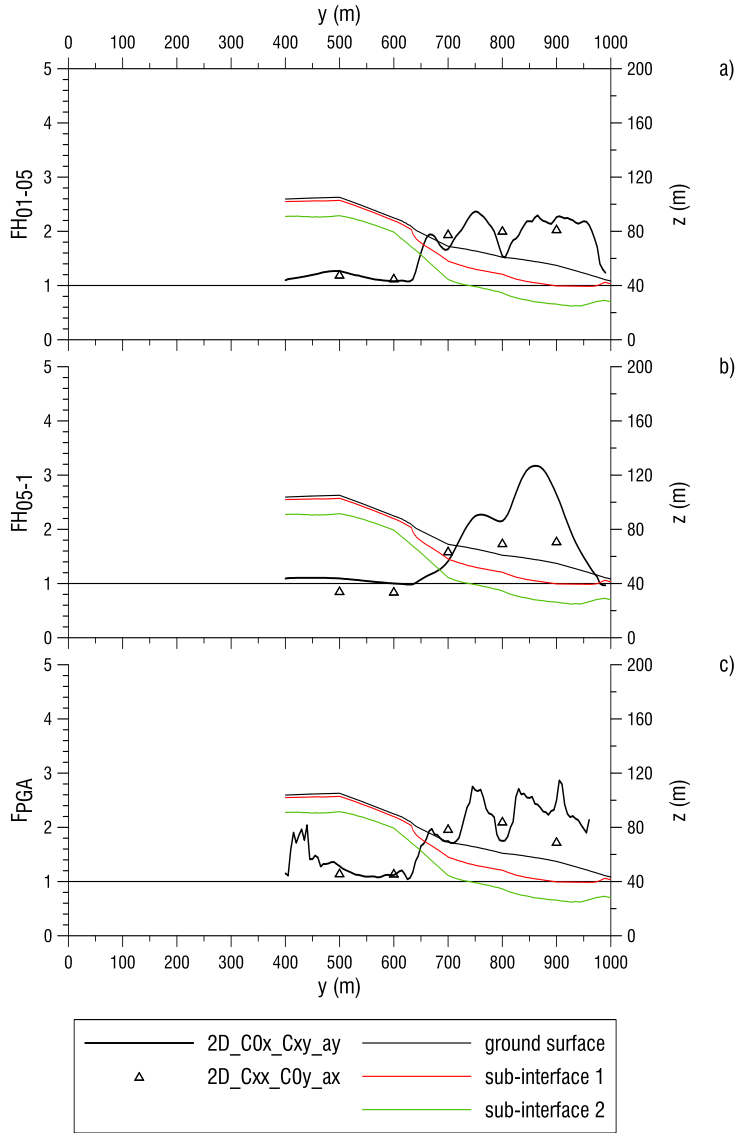


Fig. 236 Comparison A3-A5 with reference to section 14, a) FH_{01-05} , b) FH_{05-1} , b) F_{PGA}

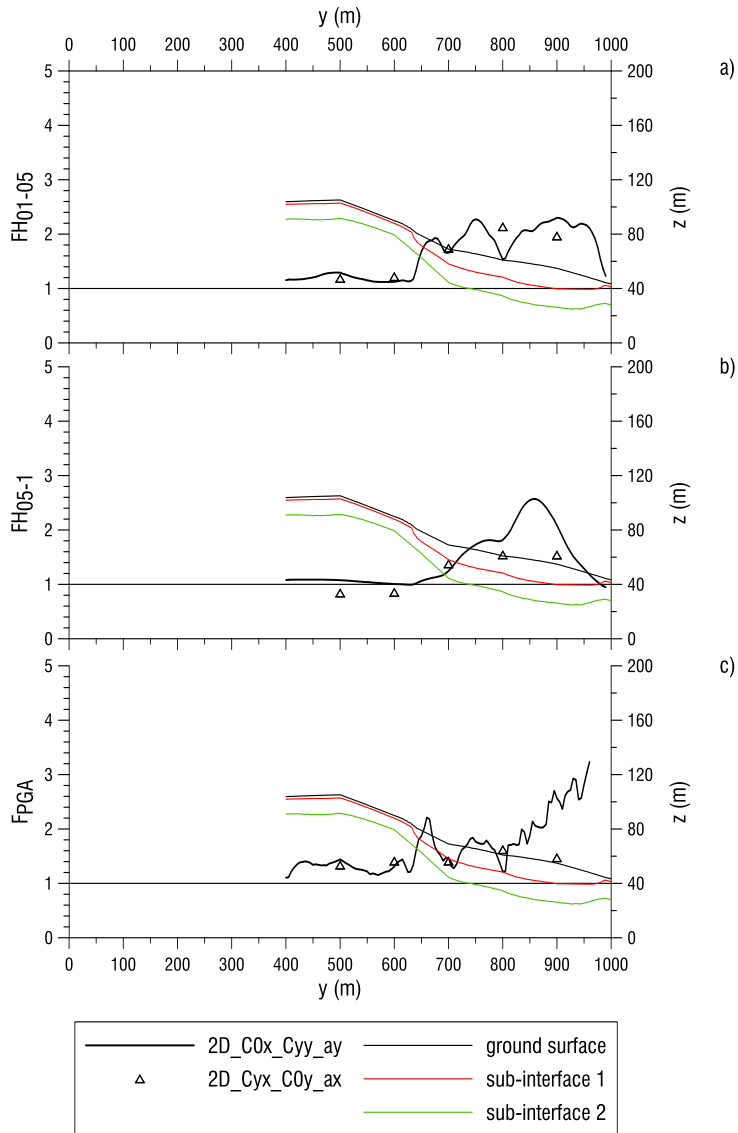


Fig. 237 Comparison A4-A6 with reference to section 14, a) $F_{H_{01-05}}$, b) $F_{H_{05-1}}$, b) F_{PGA}

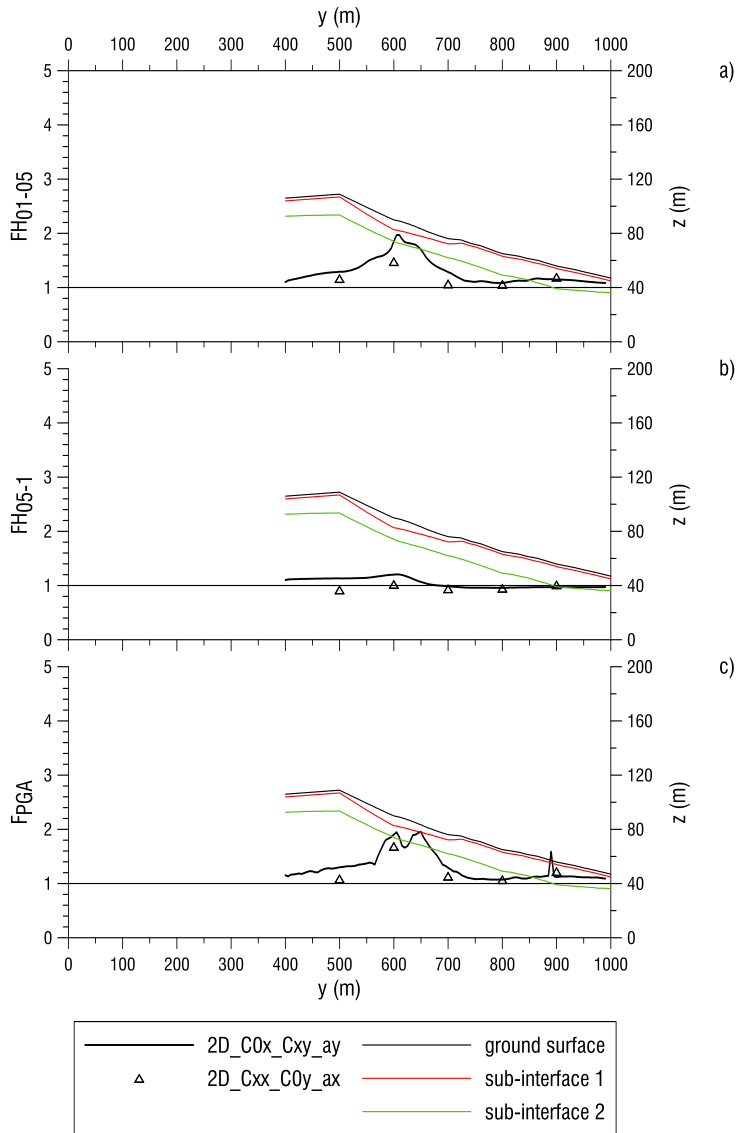


Fig. 238 Comparison A3-A5 with reference to section 15, a) FH_{01-05} , b) FH_{05-1} , c) F_{PGA}

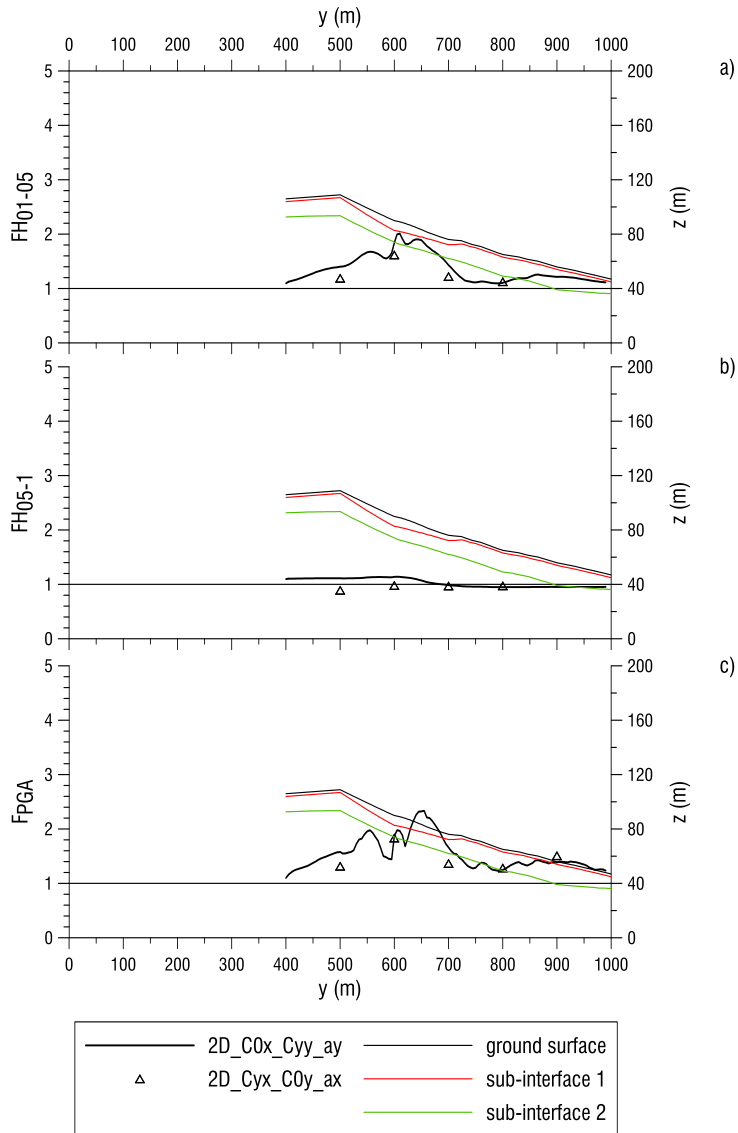


Fig. 239 Comparison A4-A6 with reference to section 15, a) FH_{01-05} , b) FH_{05-1} , b) F_{PGA}

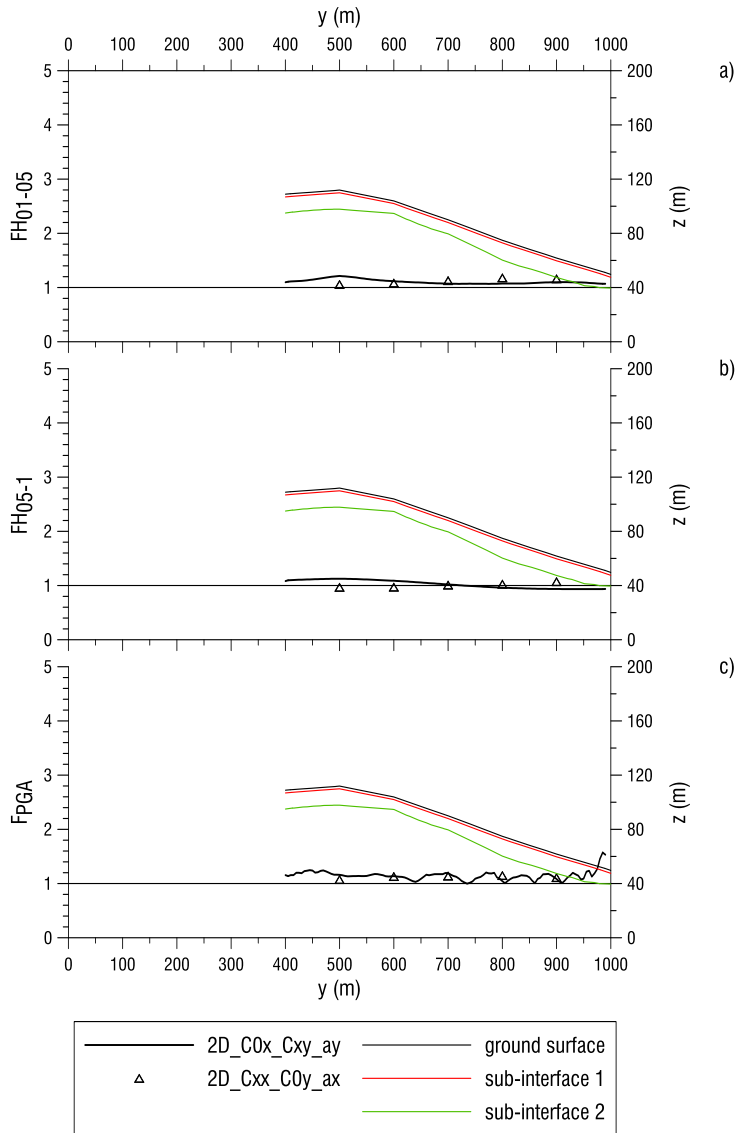


Fig. 240 Comparison A3-A5 with reference to section 16, a) FH_{01-05} , b) FH_{05-1} , b) F_{PGA}

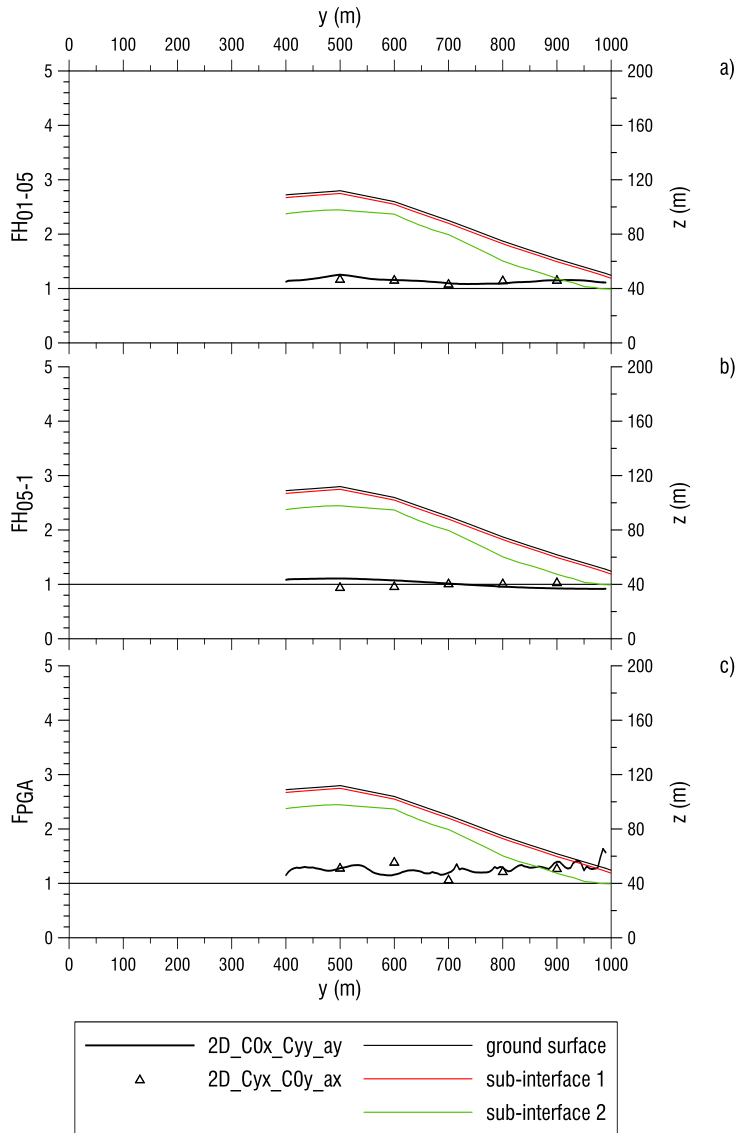


Fig. 241 Comparison A4-A6 with reference to section 16, a) FH_{01-05} , b) FH_{05-1} , c) F_{PGA}

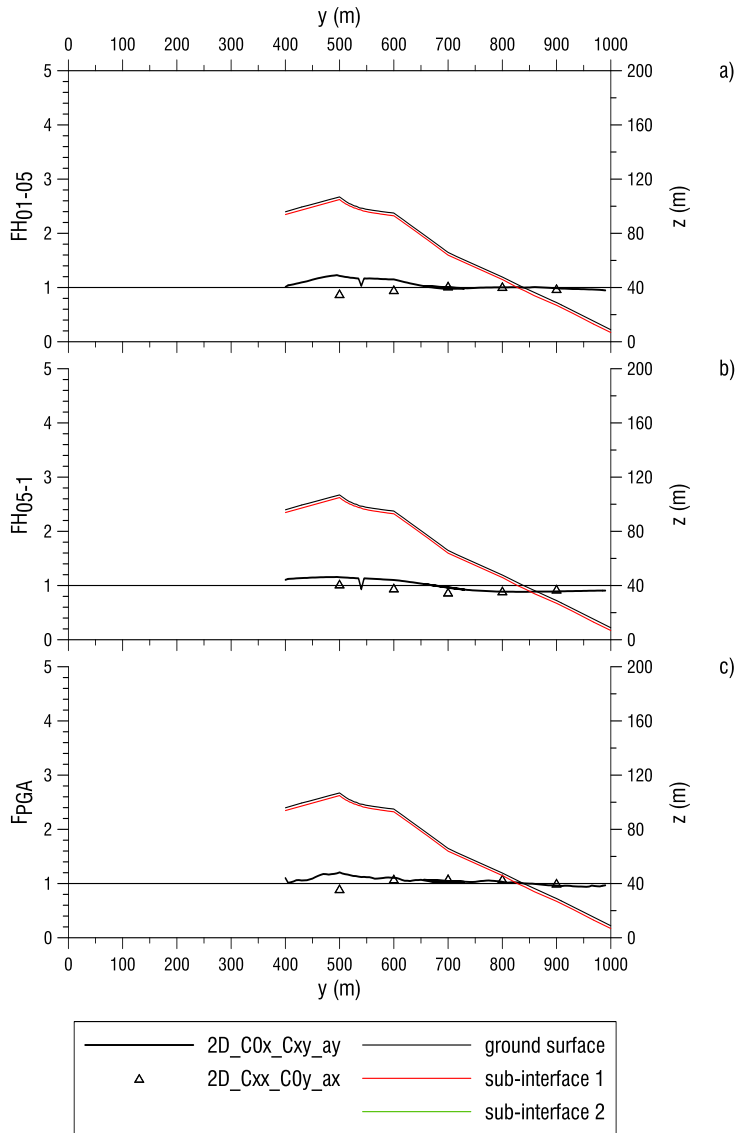


Fig. 242 Comparison A3-A5 with reference to section 21, a) FH_{01-05} , b) FH_{05-1} , b) F_{PGA}

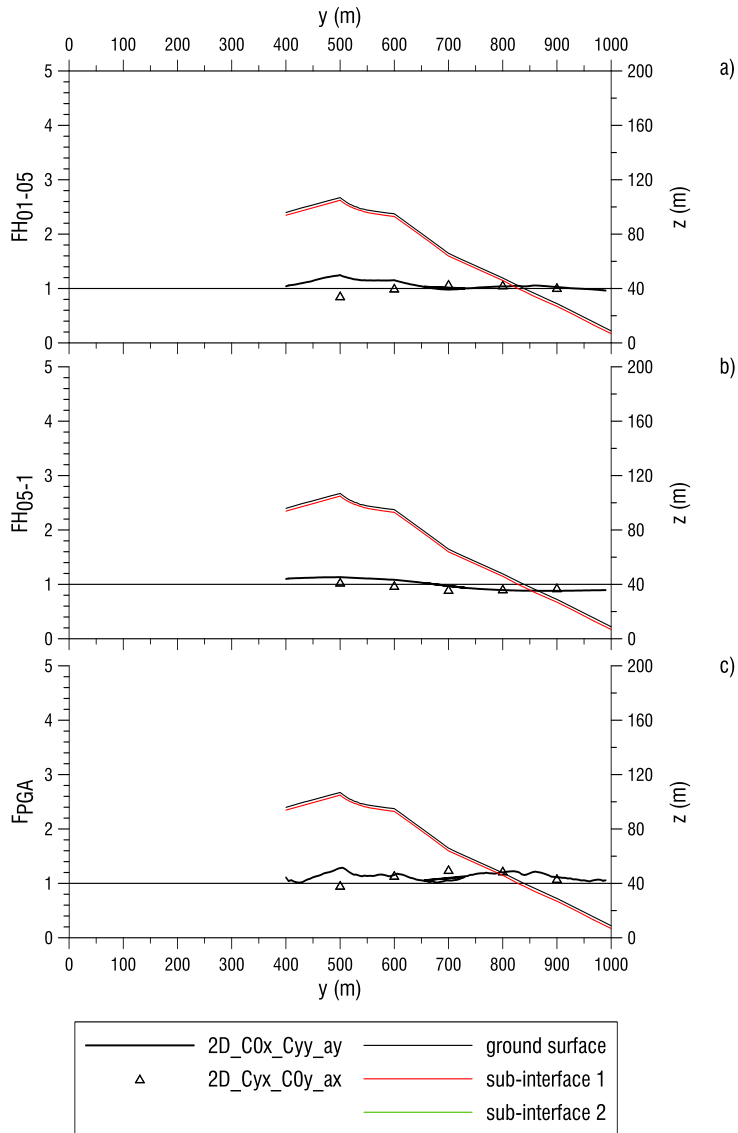


Fig. 243 Comparison A4-A6 with reference to section 21, a) F_{H01-05} , b) F_{H05-1} , c) F_{PGA}

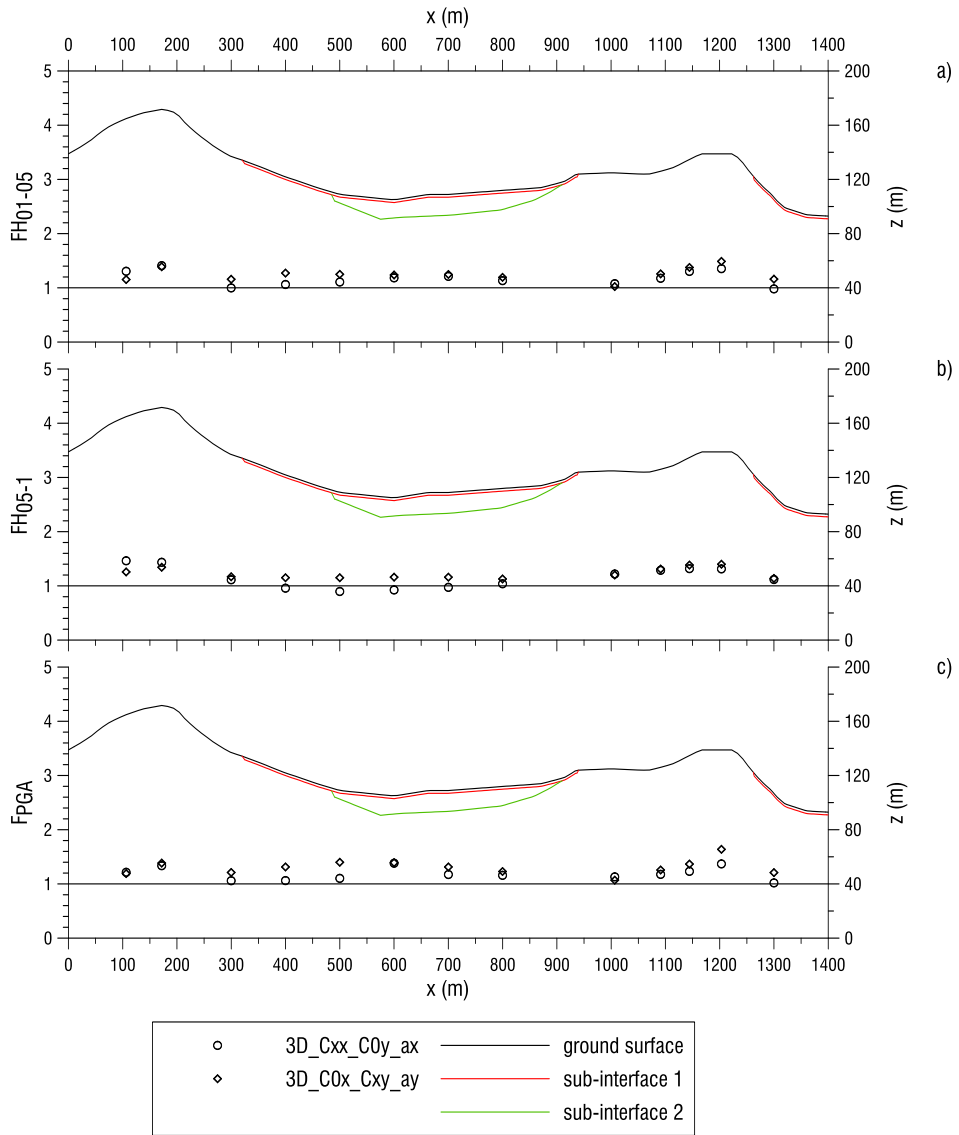


Fig. 244 Comparison A7-A9 with reference to section 2, a) FH₀₁₋₀₅, b) FH₀₅₋₁, b) F_{PGA}

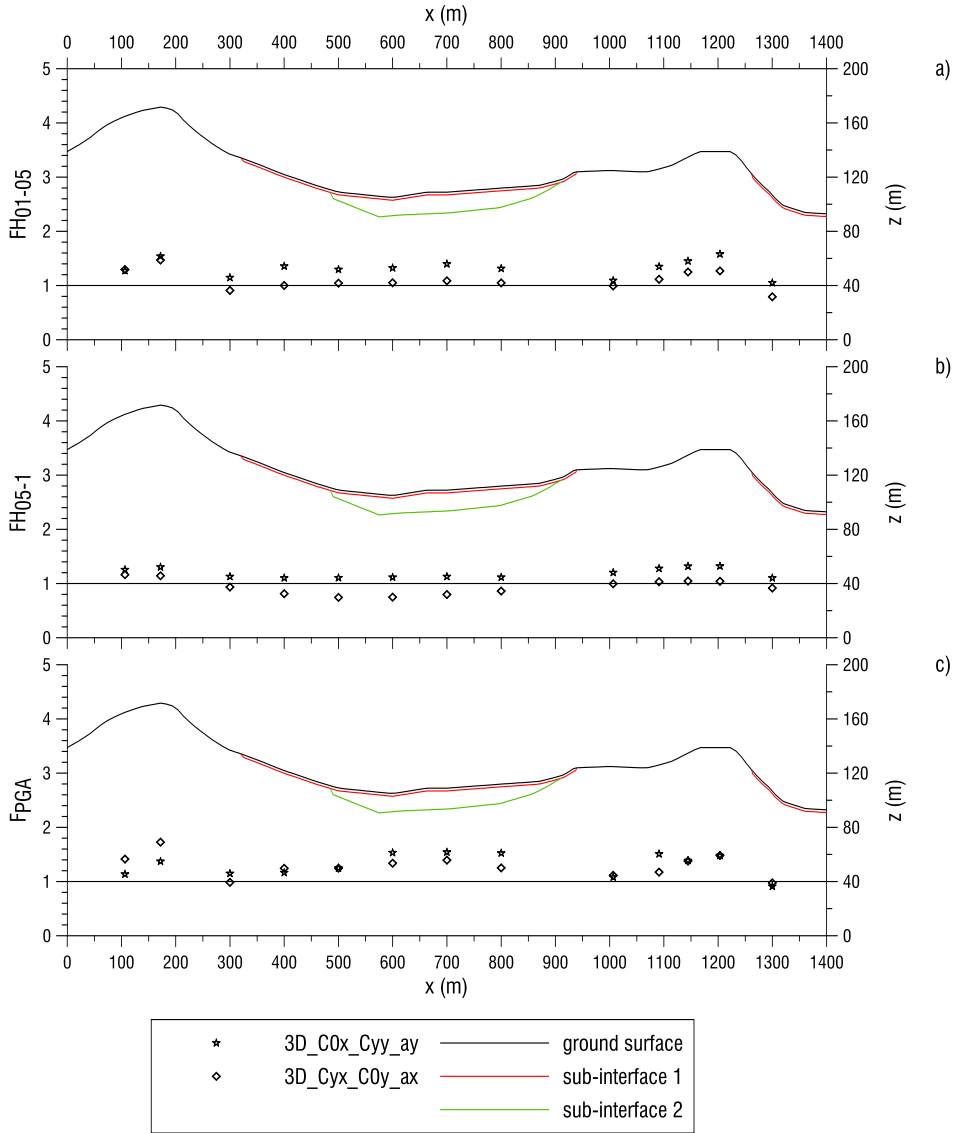


Fig. 245 Comparison A8-A10 with reference to section 2, a) $F_{H_{01-05}}$, b) $F_{H_{05-1}}$, c) F_{PGA}

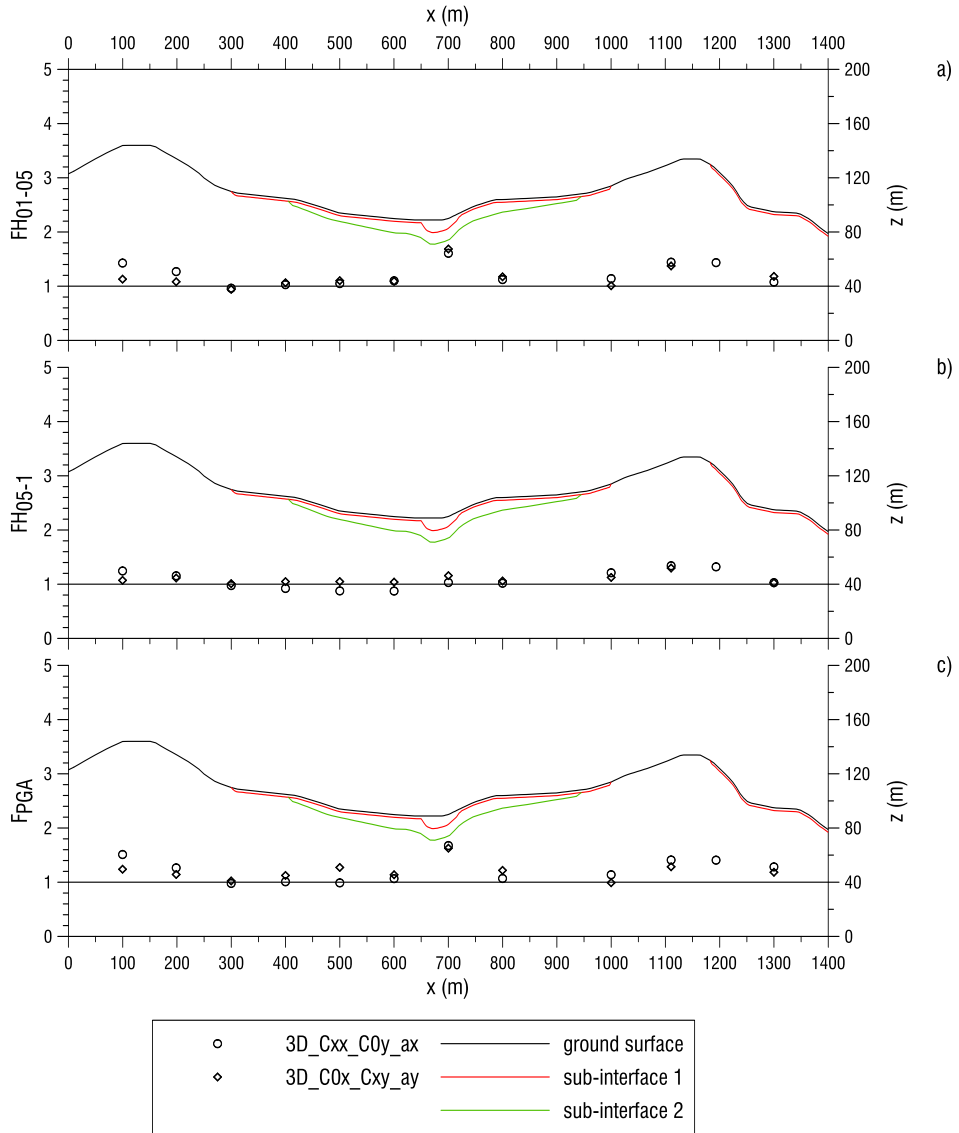


Fig. 246 Comparison A7-A9 with reference to section 3, a) FH_{01-05} , b) FH_{05-1} , b) F_{PGA}

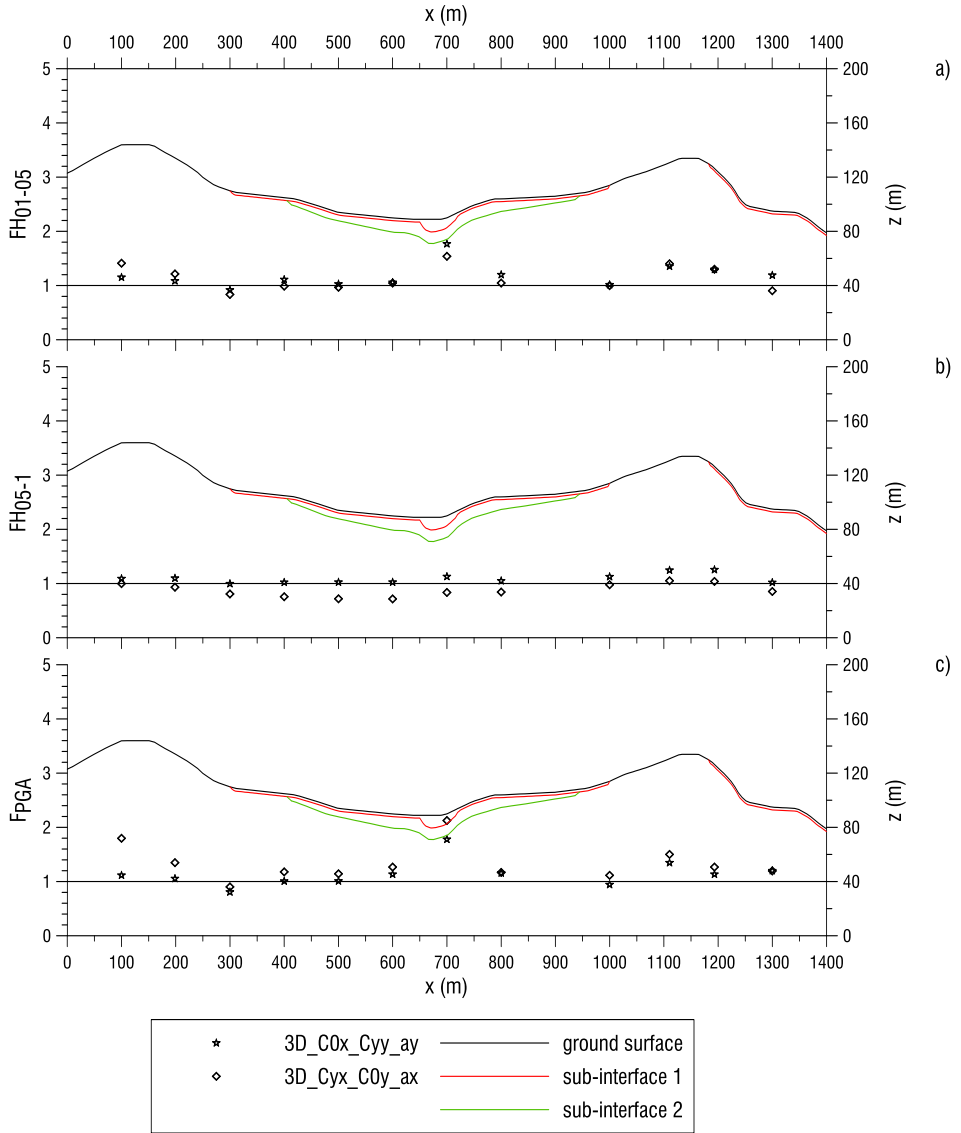


Fig. 247 Comparison A8-A10 with reference to section 3, a) FH_{01-05} , b) FH_{05-1} , c) F_{PGA}

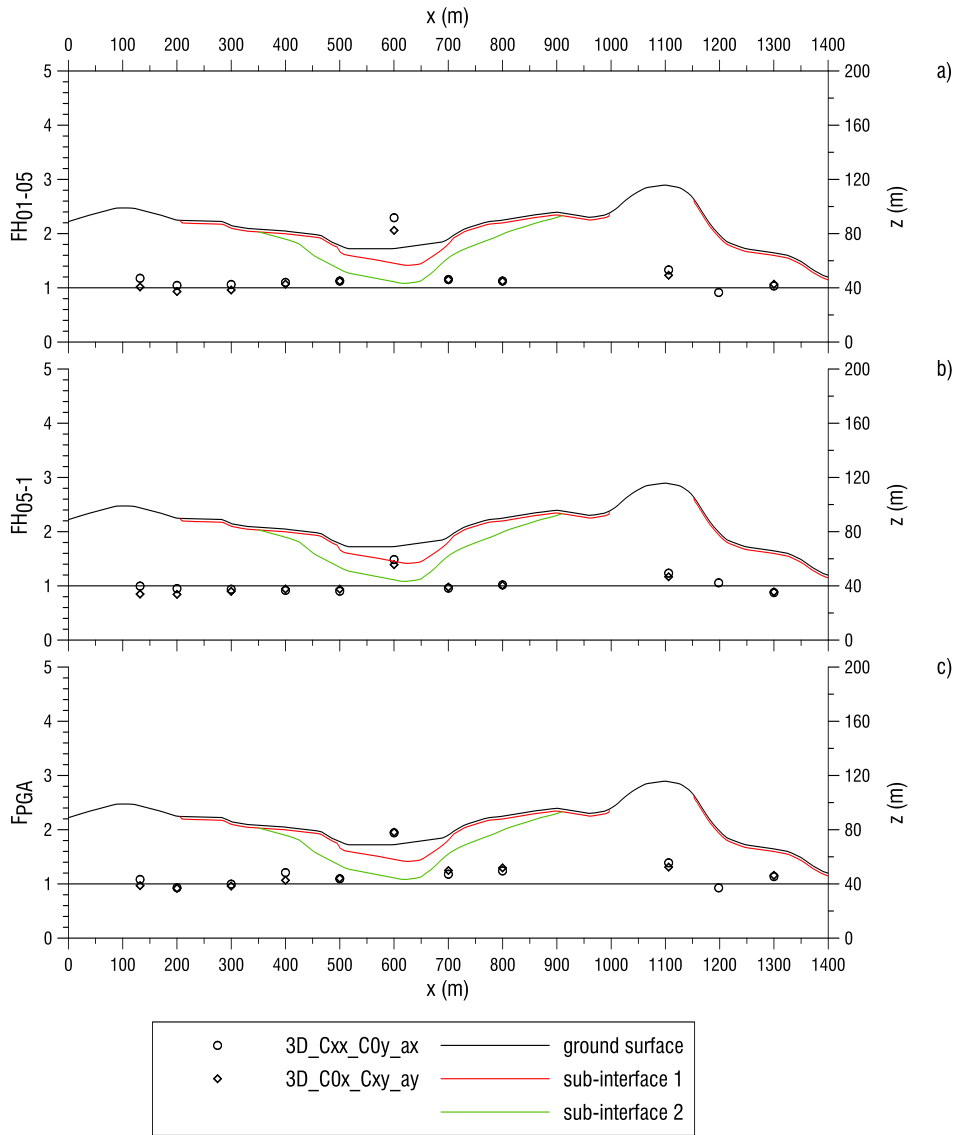


Fig. 248 Comparison A7-A9 with reference to section 4, a) F_{H01-05} , b) F_{H05-1} , b) F_{PGA}

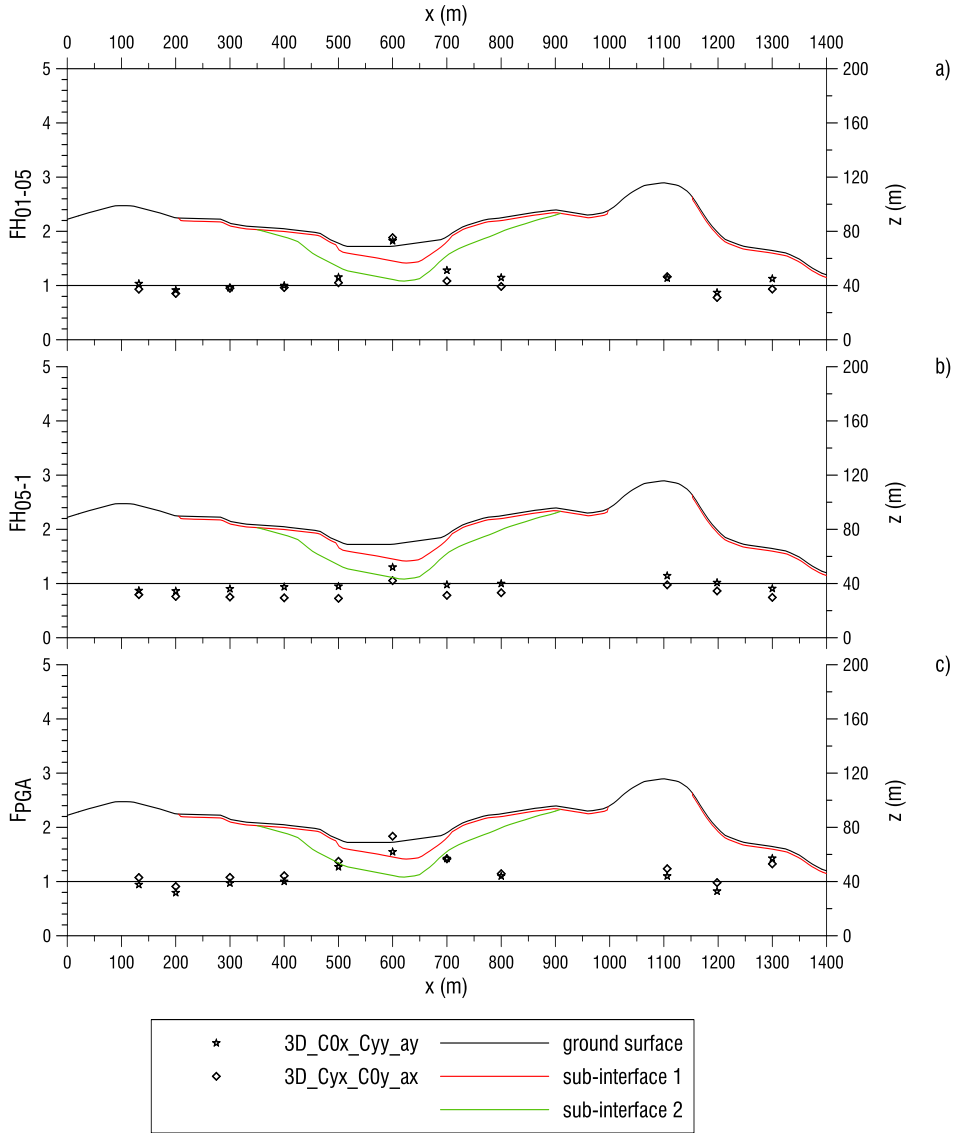


Fig. 249 Comparison A8-A10 with reference to section 4, a) FH_{01-05} , b) FH_{05-1} , c) F_{PGA}

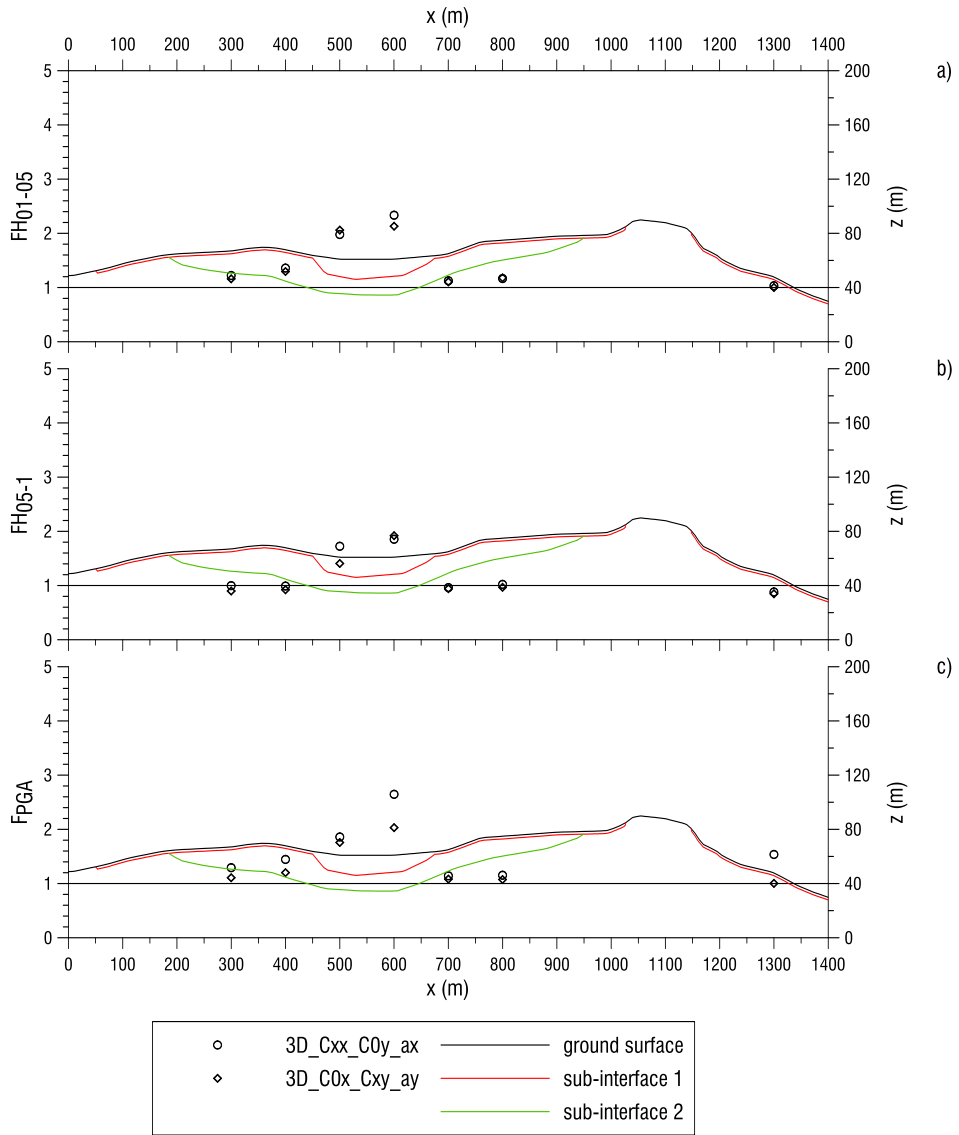


Fig. 250 Comparison A7-A9 with reference to section 5, a) $F_{H_{01-05}}$, b) $F_{H_{05-1}}$, c) F_{PGA}

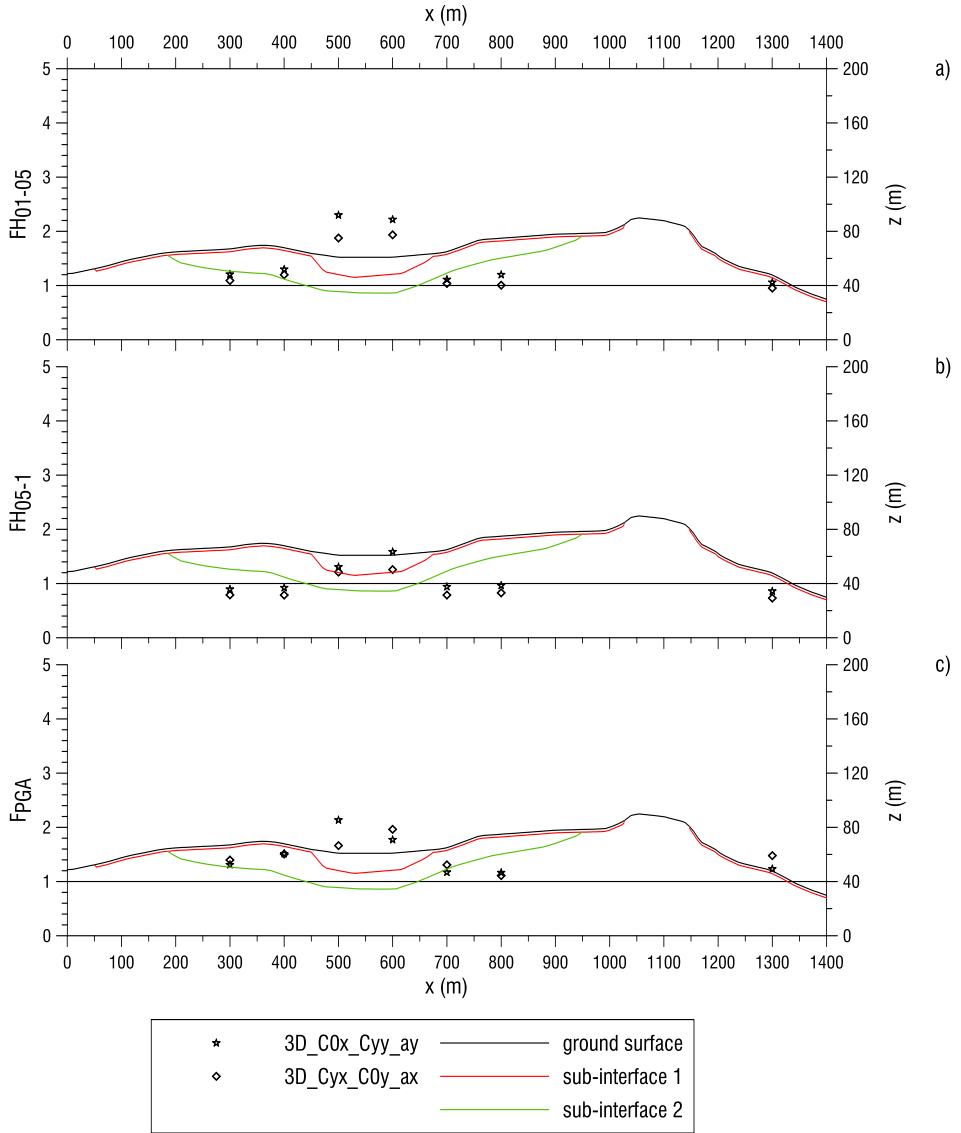


Fig. 251 Comparison A8-A10 with reference to section 5, a) FH_{01-05} , b) FH_{05-1} , c) F_{PGA}

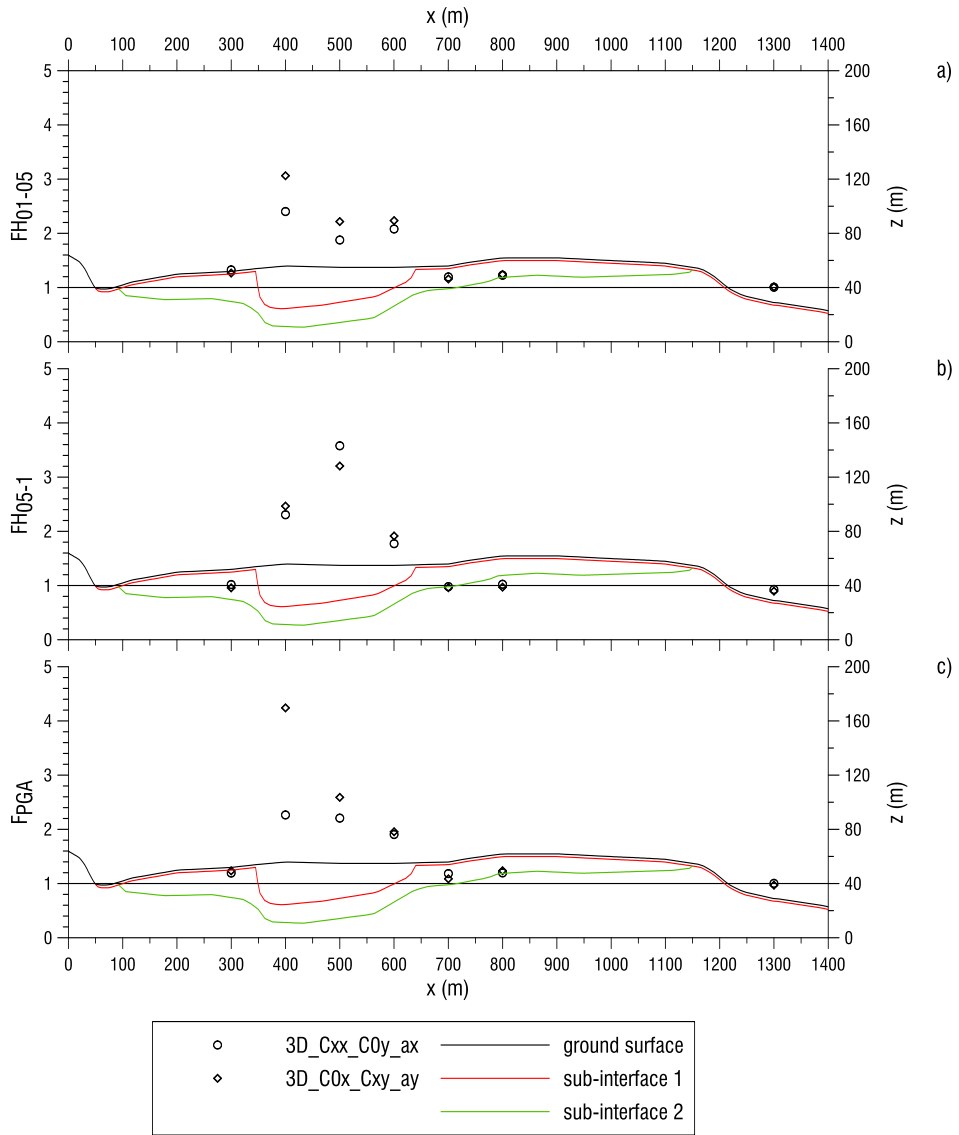


Fig. 252 Comparison A7-A9 with reference to section 6, a) FH_{01-05} , b) FH_{05-1} , b) F_{PGA}

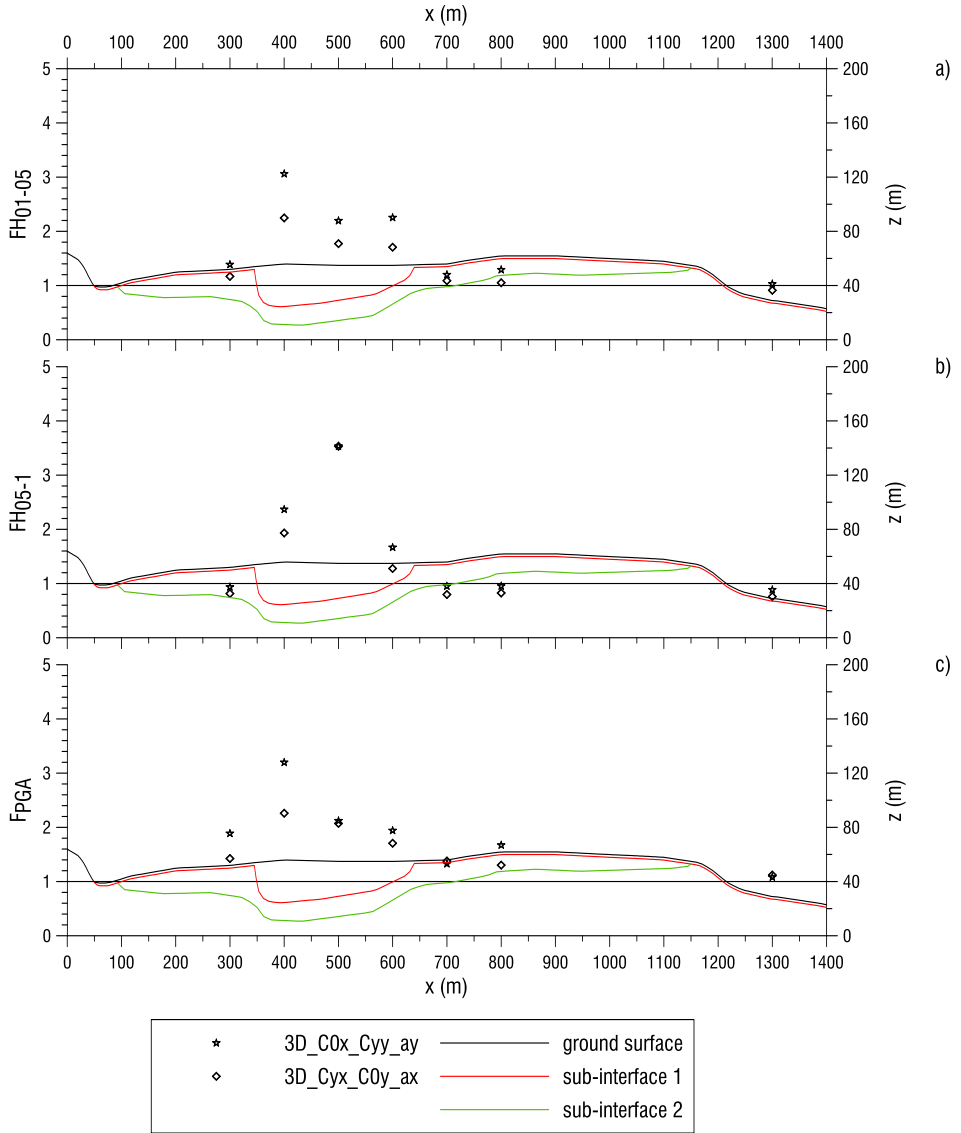


Fig. 253 Comparison A8-A10 with reference to section 6, a) F_{H01-05} , b) F_{H05-1} , c) F_{PGA}

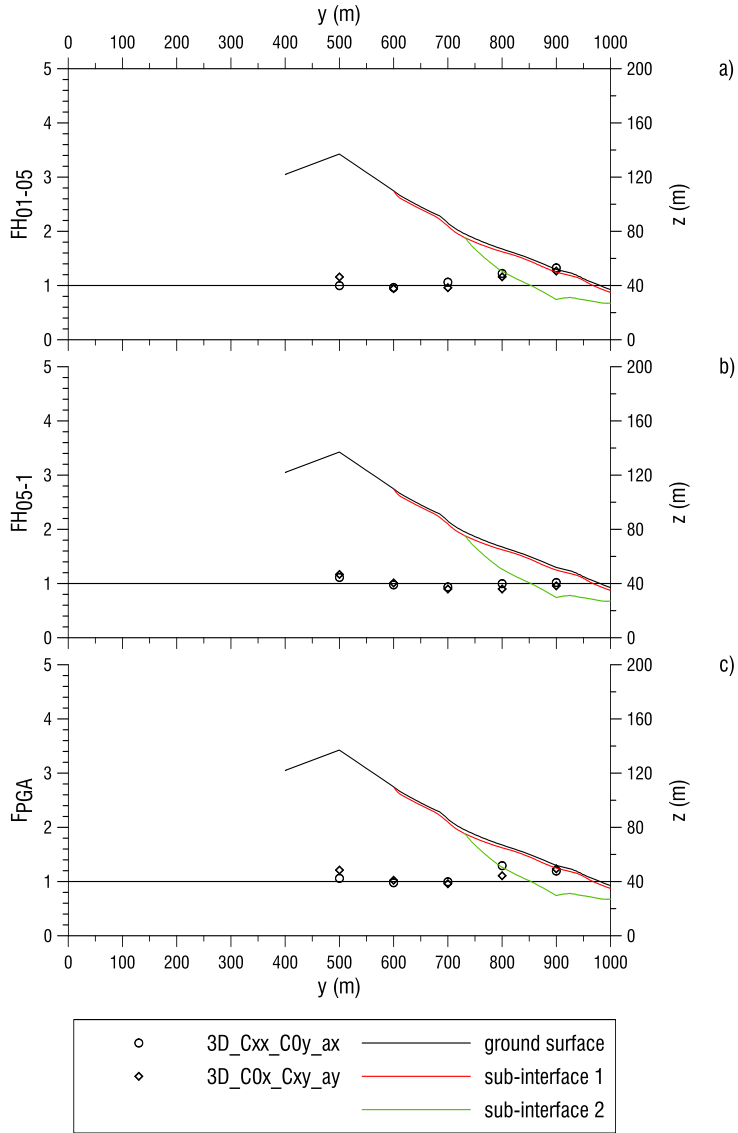


Fig. 254 Comparison A7-A9 with reference to section 11, a) FH_{01-05} , b) FH_{05-1} , b) F_{PGA}

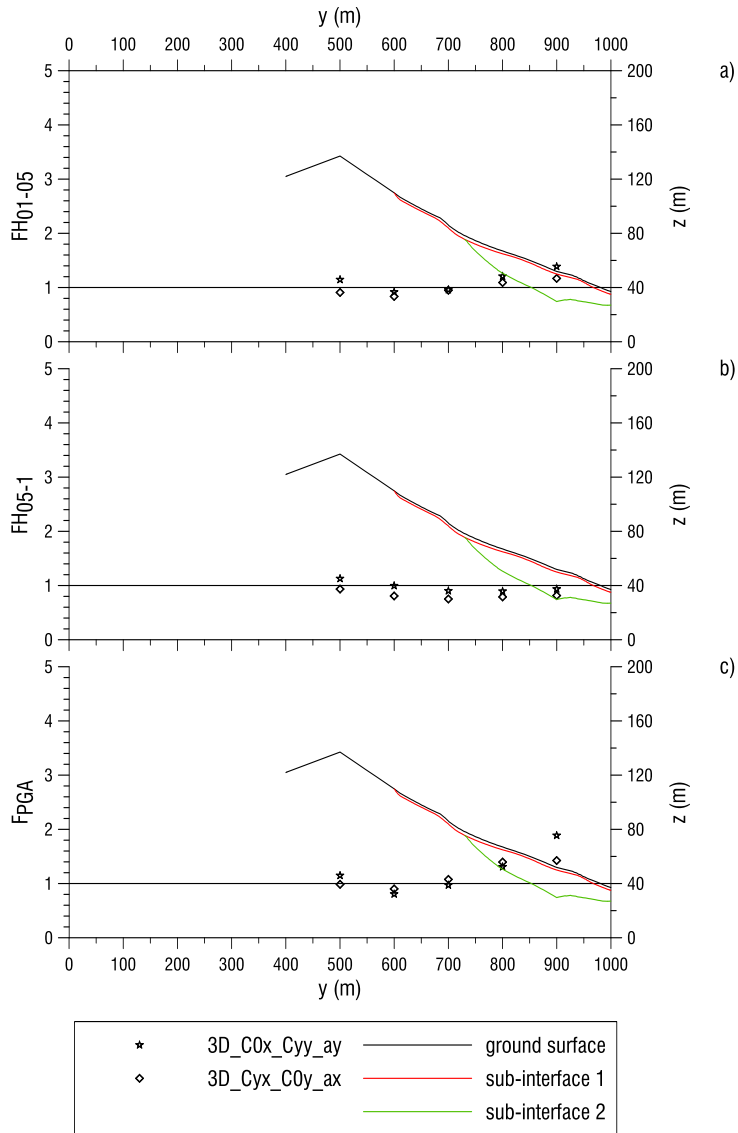


Fig. 255 Comparison A8-A10 with reference to section 11, a) FH_{01-05} , b) FH_{05-1} , b) F_{PGA}

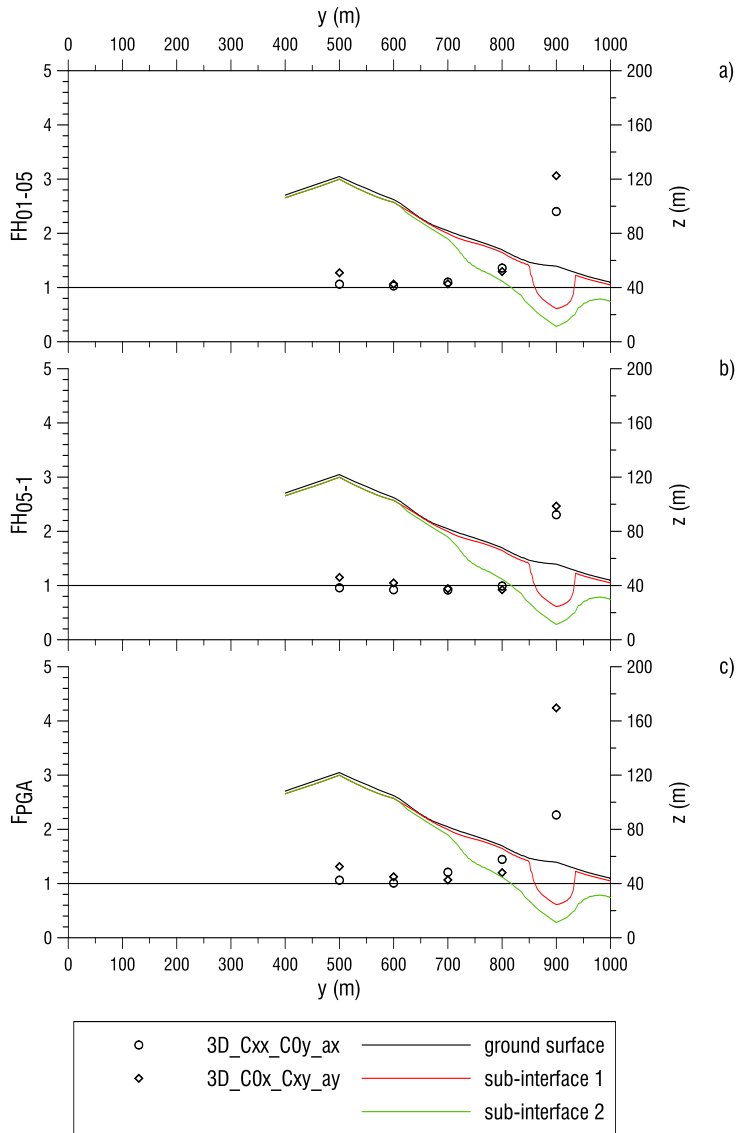


Fig. 256 Comparison A7-A9 with reference to section 12, a) FH_{01-05} , b) FH_{05-1} , b) F_{PGA}

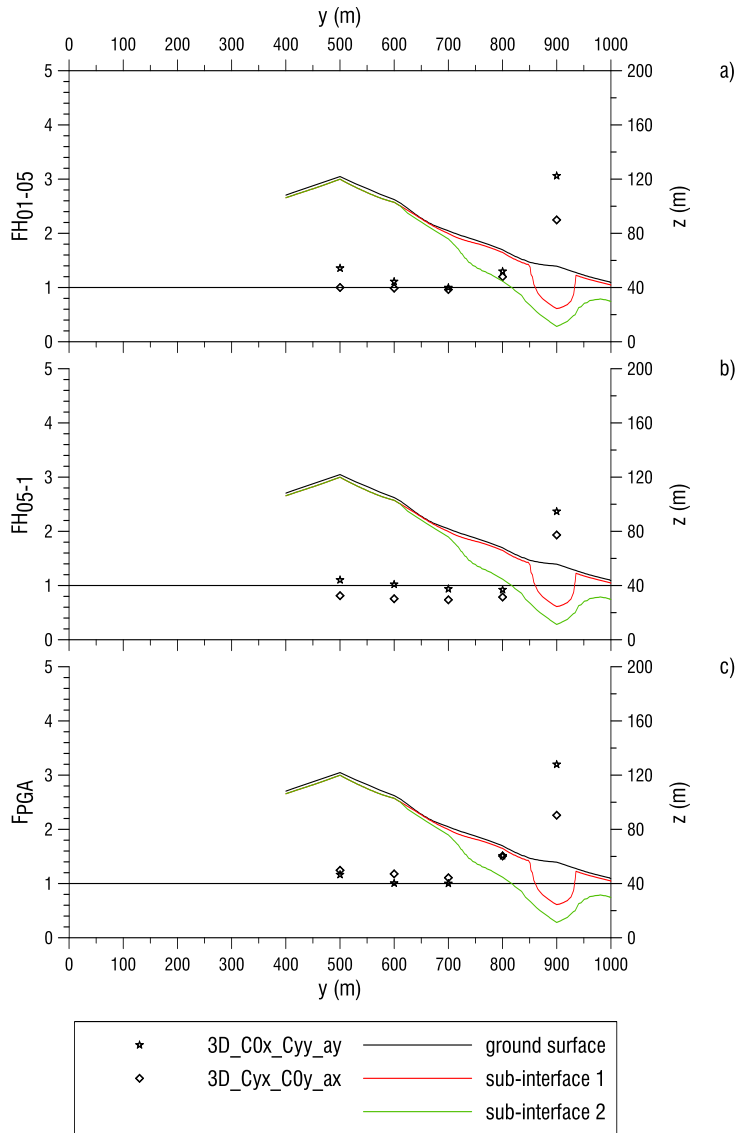


Fig. 257 Comparison A8-A10 with reference to section 12, a) F_{H01-05} , b) F_{H05-1} , c) F_{PGA}

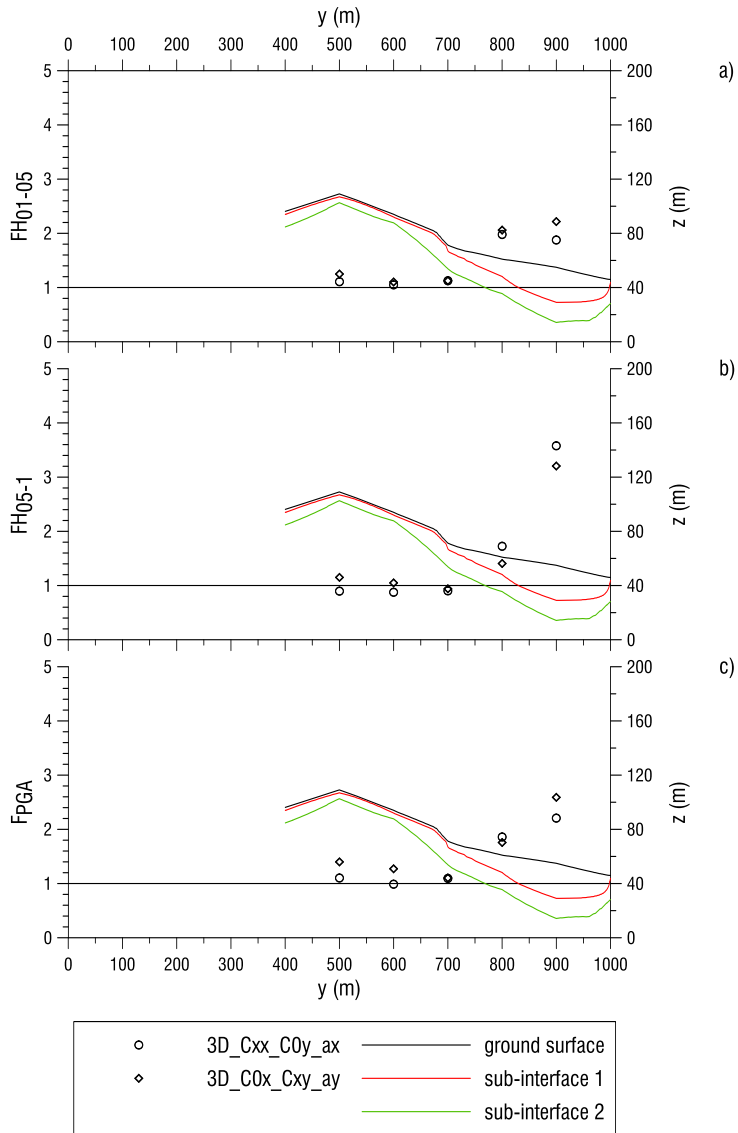


Fig. 258 Comparison A7-A9 with reference to section 13, a) FH_{01-05} , b) FH_{05-1} , b) F_{PGA}

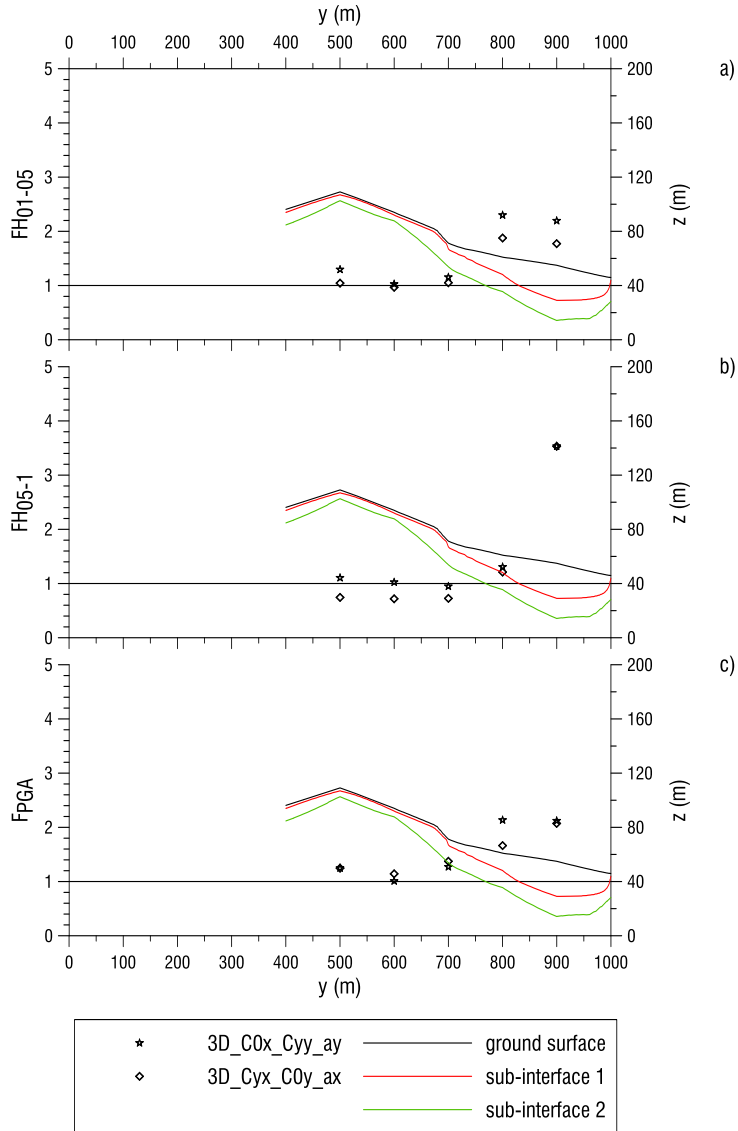


Fig. 259 Comparison A8-A10 with reference to section 13, a) F_{H01-05} , b) F_{H05-1} , b) F_{PGA}

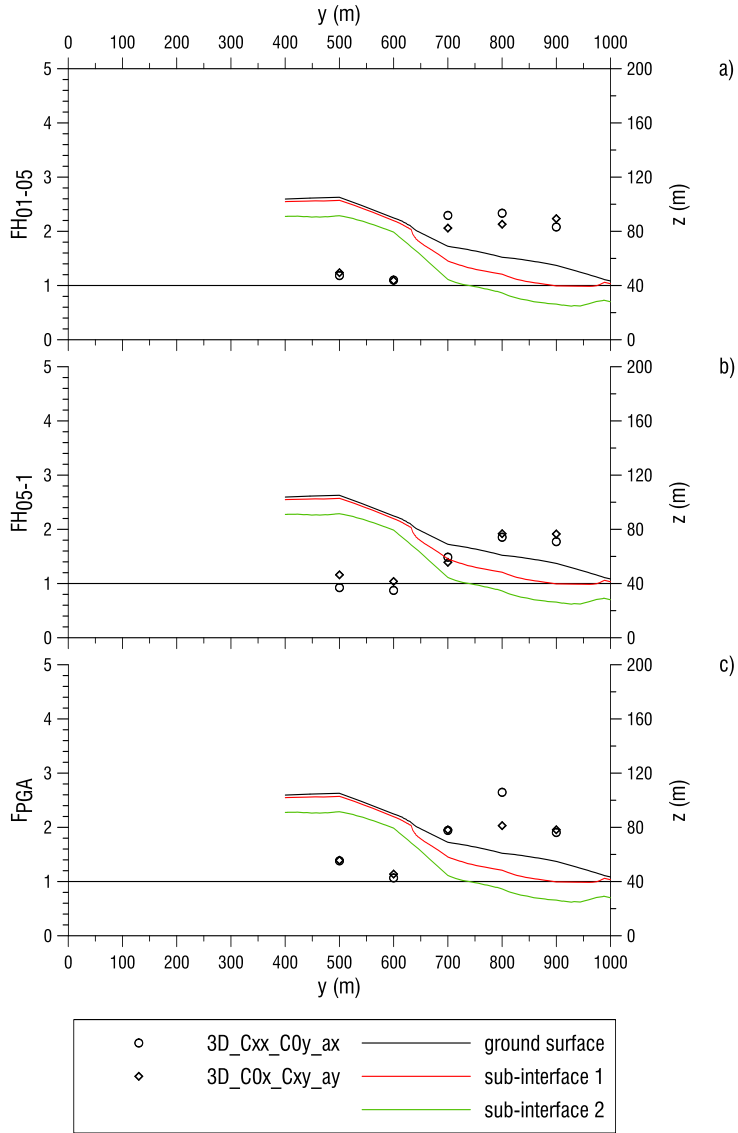


Fig. 260 Comparison A7-A9 with reference to section 14, a) FH_{01-05} , b) FH_{05-1} , b) F_{PGA}

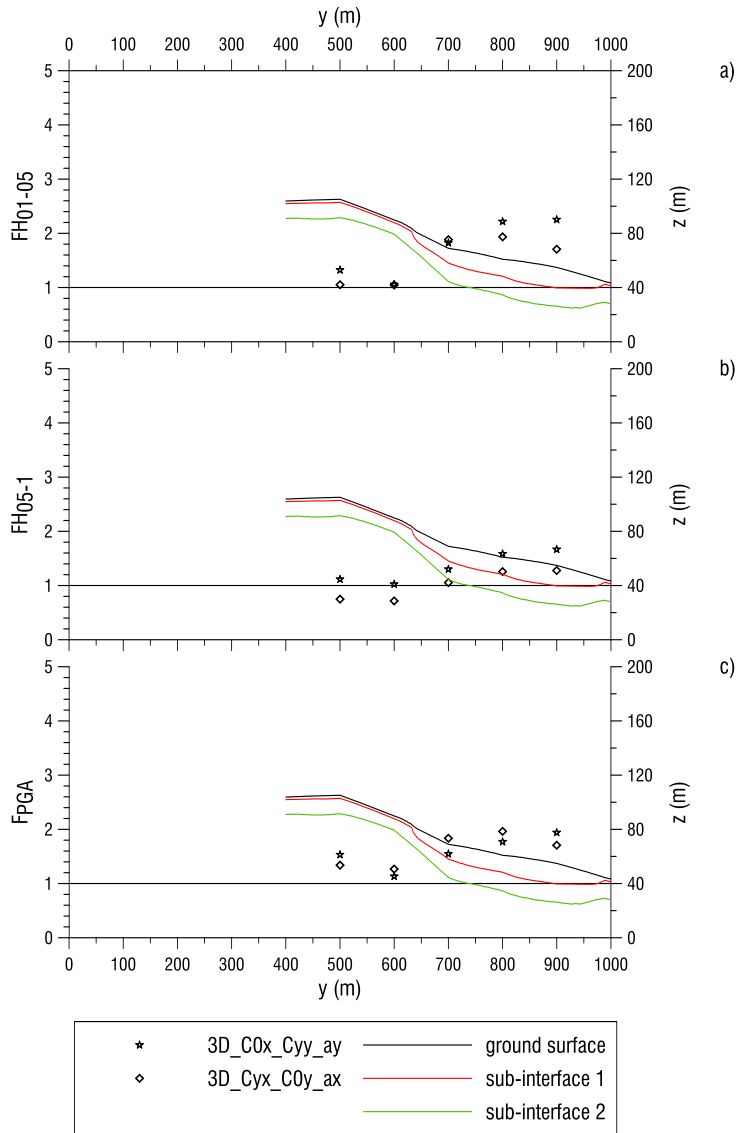


Fig. 261 Comparison A8-A10 with reference to section 14, a) F_{H01-05} , b) F_{H05-1} , c) F_{PGA}

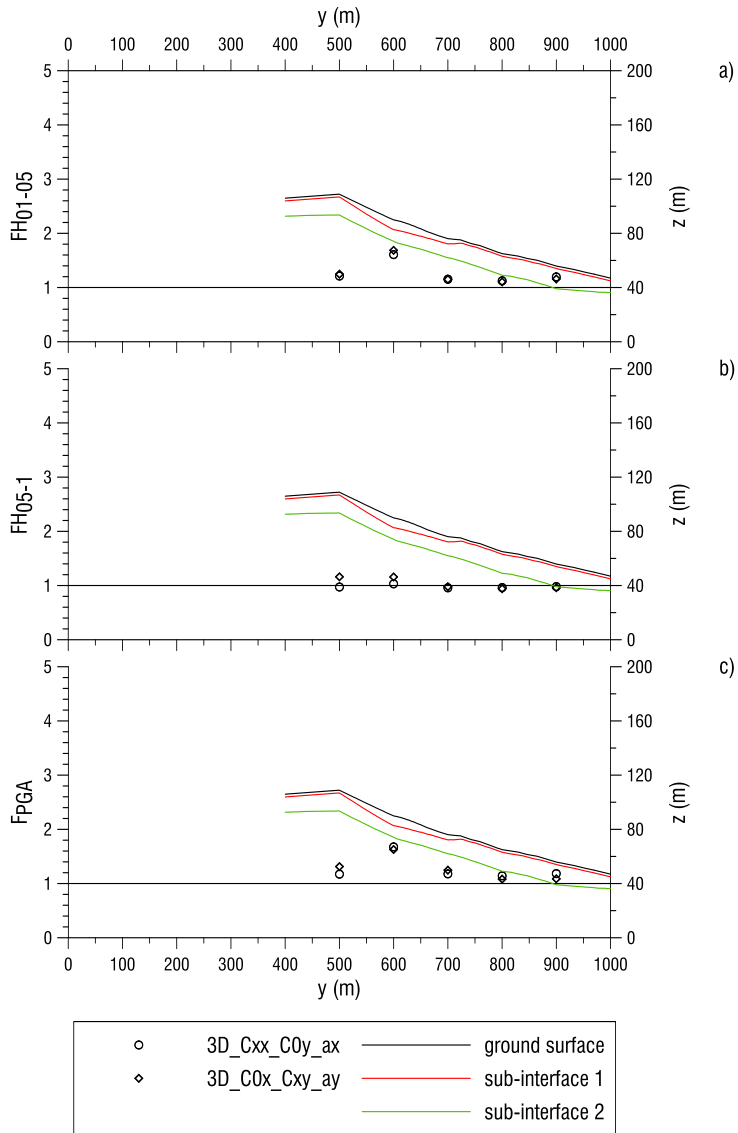


Fig. 262 Comparison A7-A9 with reference to section 15, a) FH_{01-05} , b) FH_{05-1} , b) F_{PGA}

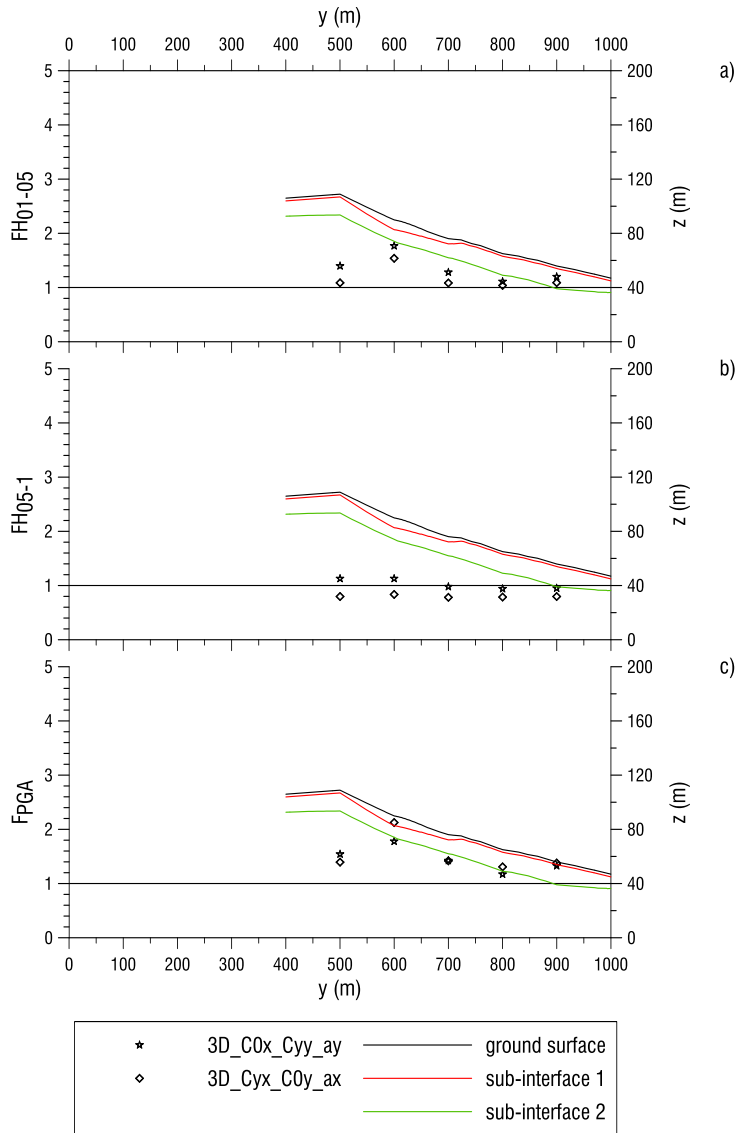


Fig. 263 Comparison A8-A10 with reference to section 15, a) F_{H01-05} , b) F_{H05-1} , c) F_{PGA}

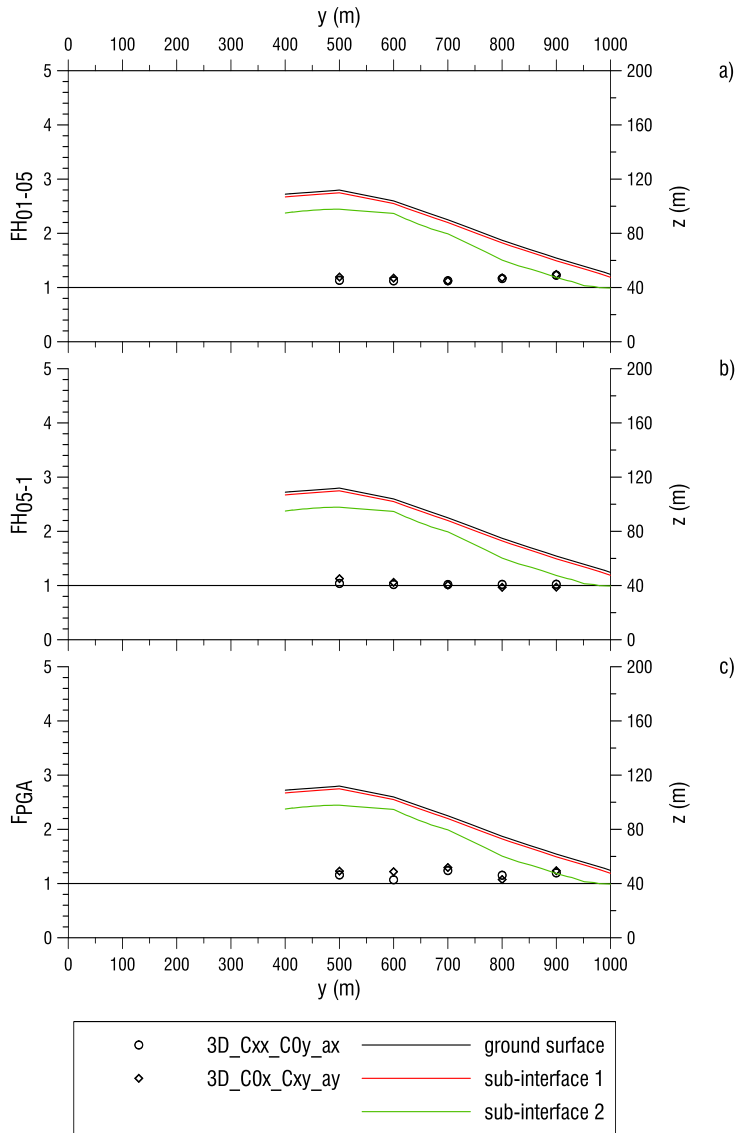


Fig. 264 Comparison A7-A9 with reference to section 16, a) FH_{01-05} , b) FH_{05-1} , b) F_{PGA}

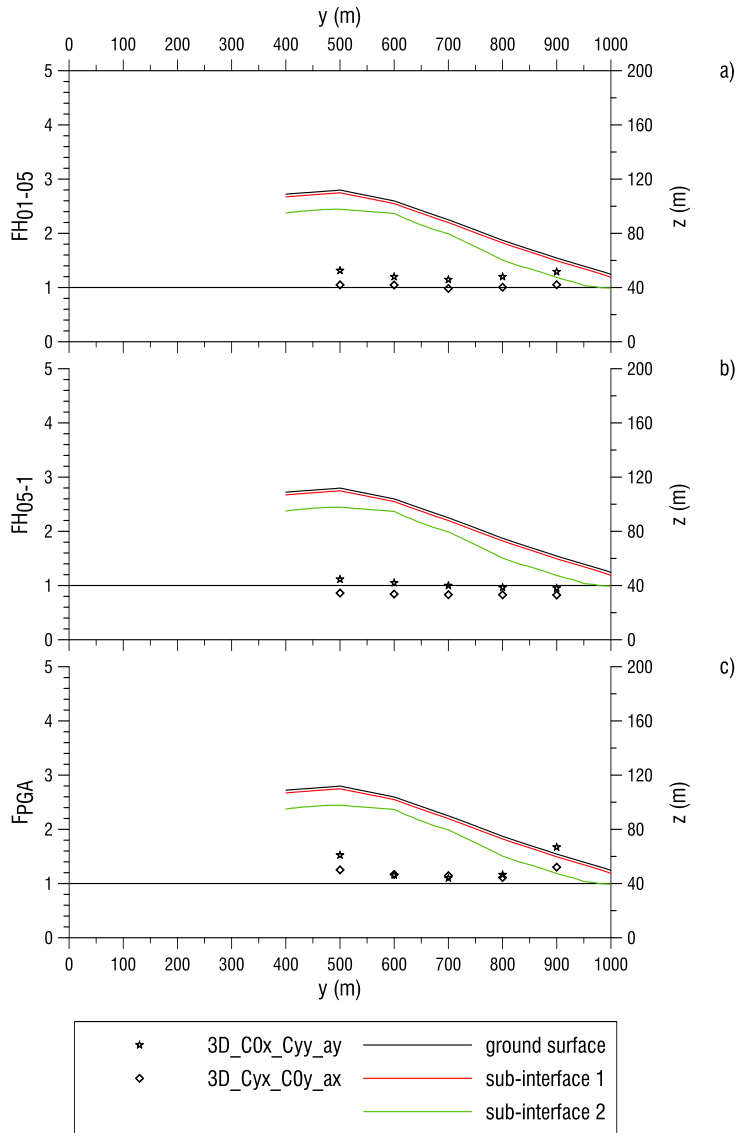


Fig. 265 Comparison A8-A10 with reference to section 16, a) FH_{01-05} , b) FH_{05-1} , c) F_{PGA}

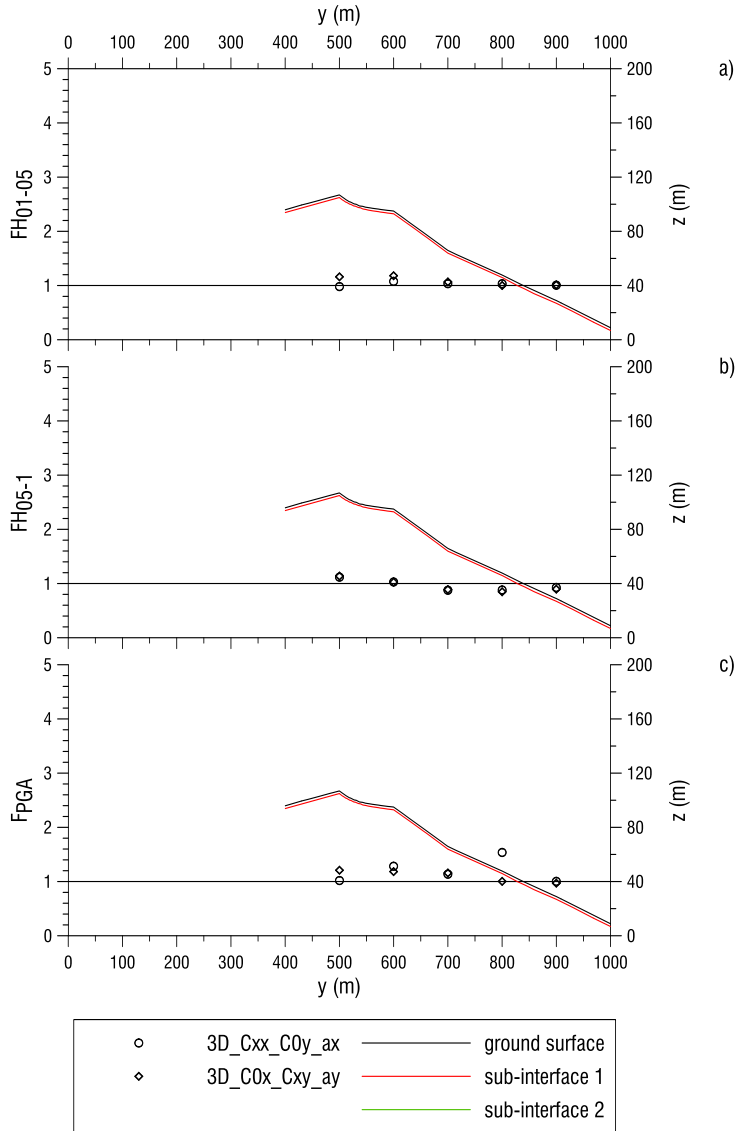


Fig. 266 Comparison A7-A9 with reference to section 21, a) FH_{01-05} , b) FH_{05-1} , b) F_{PGA}

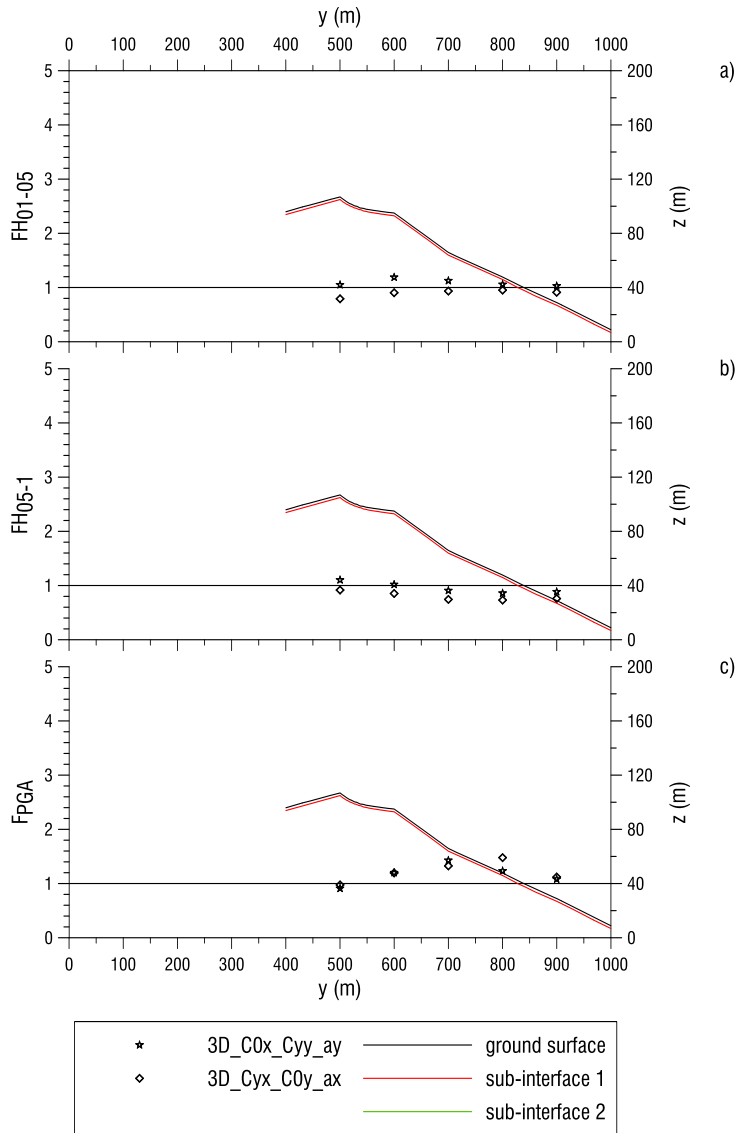


Fig. 267 Comparison A8-A10 with reference to section 21, a) FH_{01-05} , b) FH_{05-1} , b) F_{PGA}

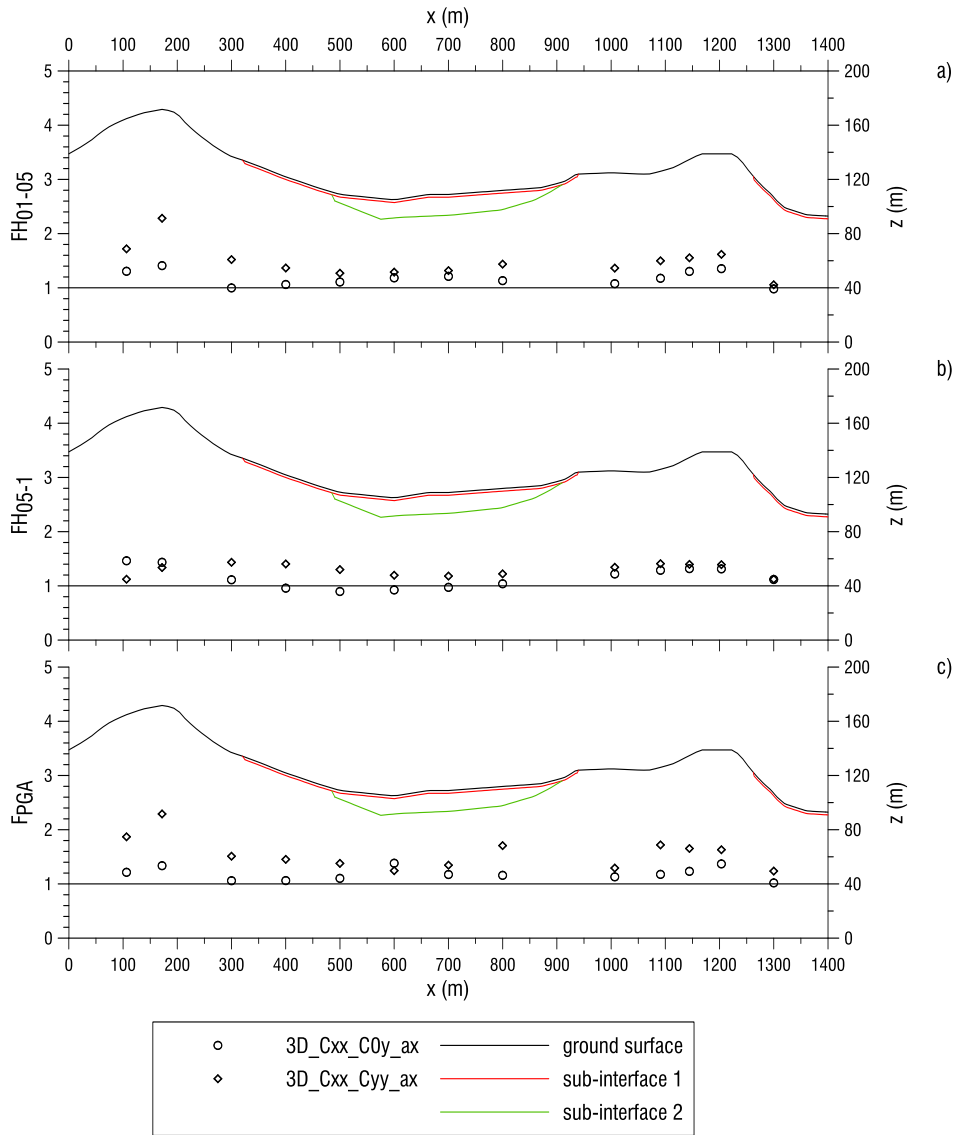


Fig. 268 Comparison A7-A11 with reference to section 2, a) FH_{01-05} , b) FH_{05-1} , b) F_{PGA}

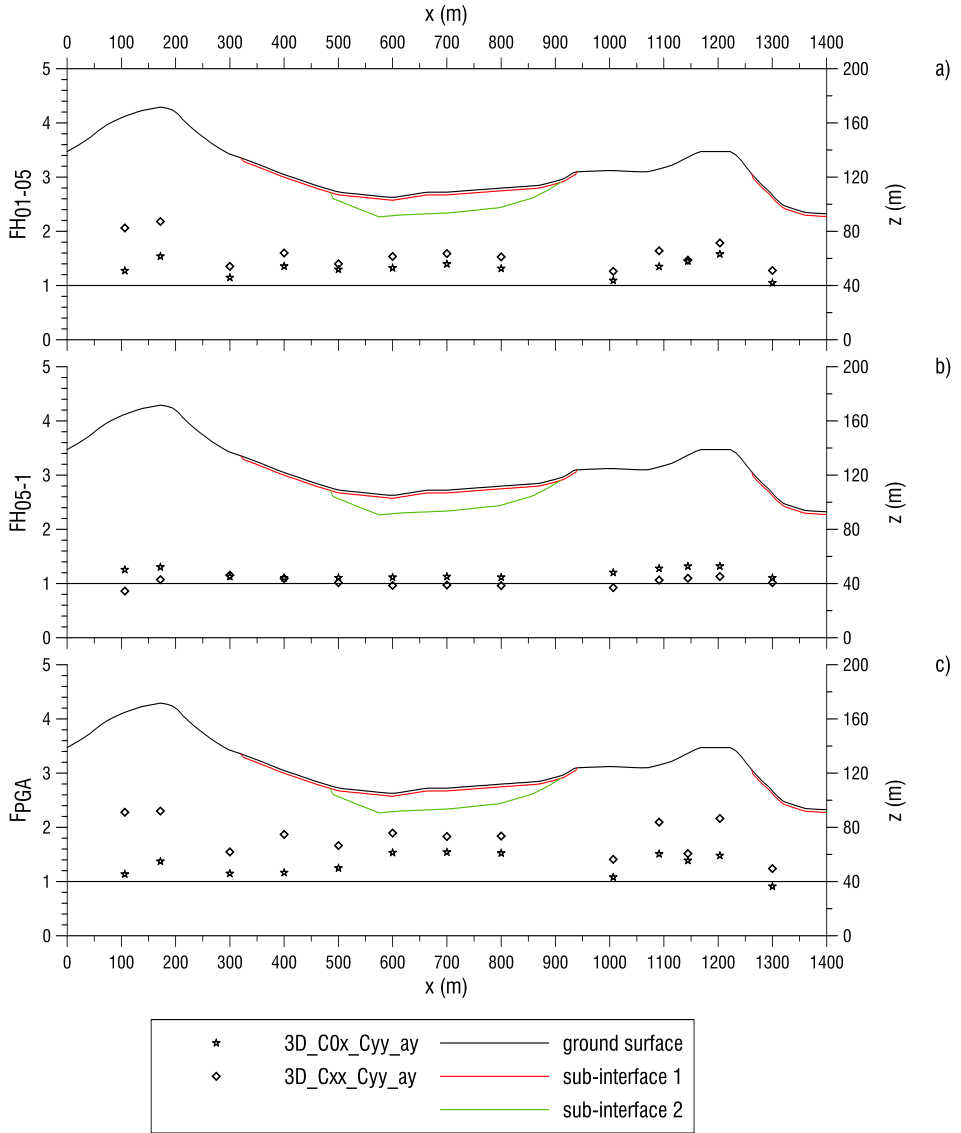


Fig. 269 Comparison A10-A11 with reference to section 2, a) F_{H01-05} , b) F_{H05-1} , c) F_{PGA}

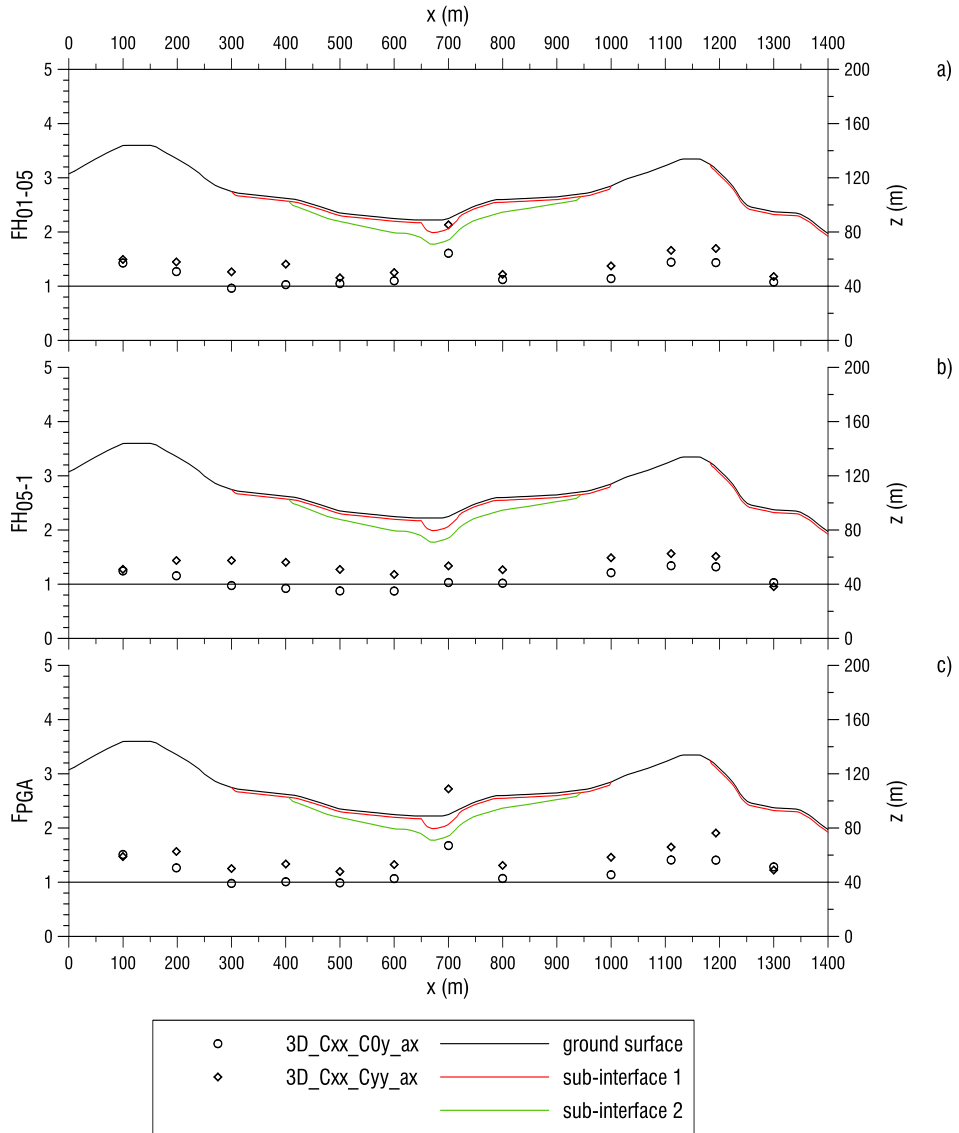


Fig. 270 Comparison A7-A11 with reference to section 3, a) FH_{01-05} , b) FH_{05-1} , c) F_{PGA}

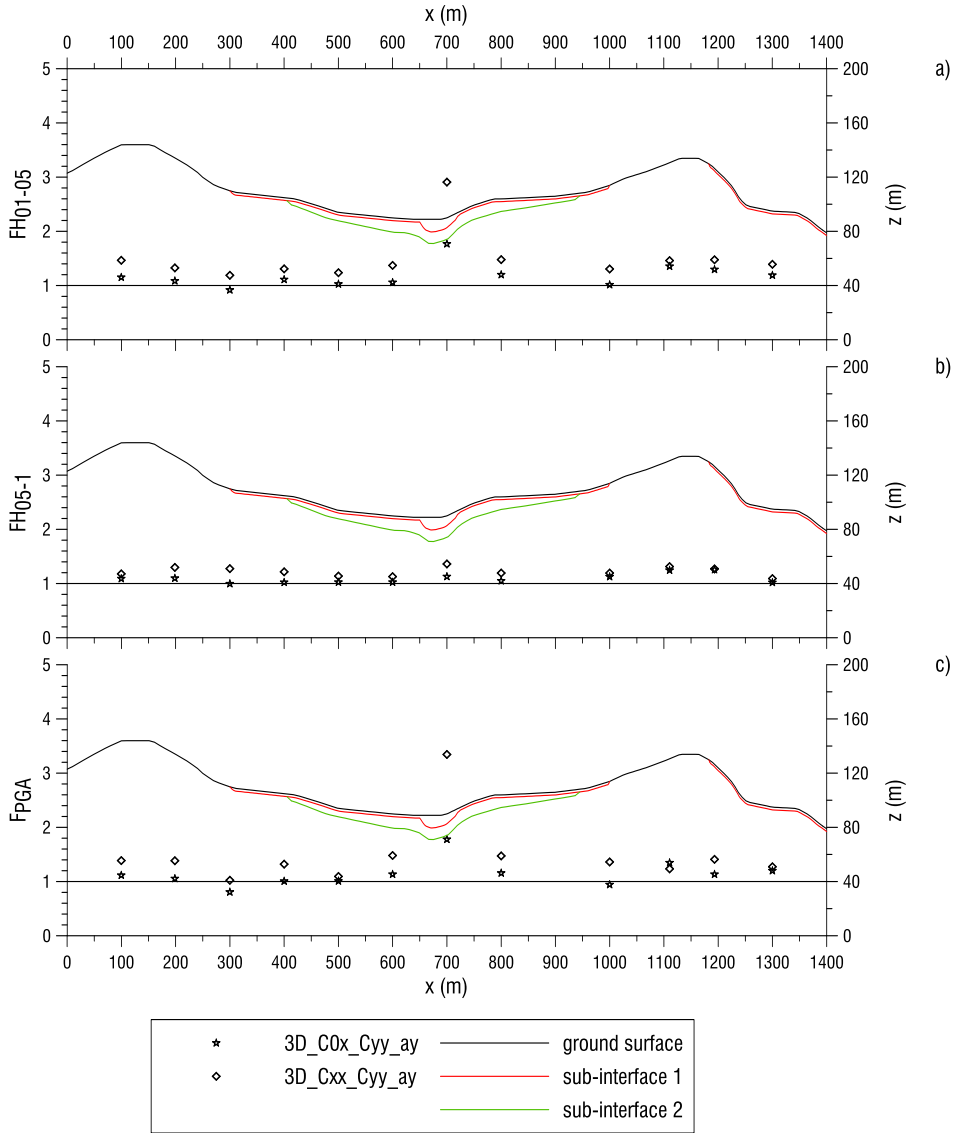


Fig. 271 Comparison A10-A11 with reference to section 3, a) F_{H01-05} , b) F_{H05-1} , b) F_{PGA}

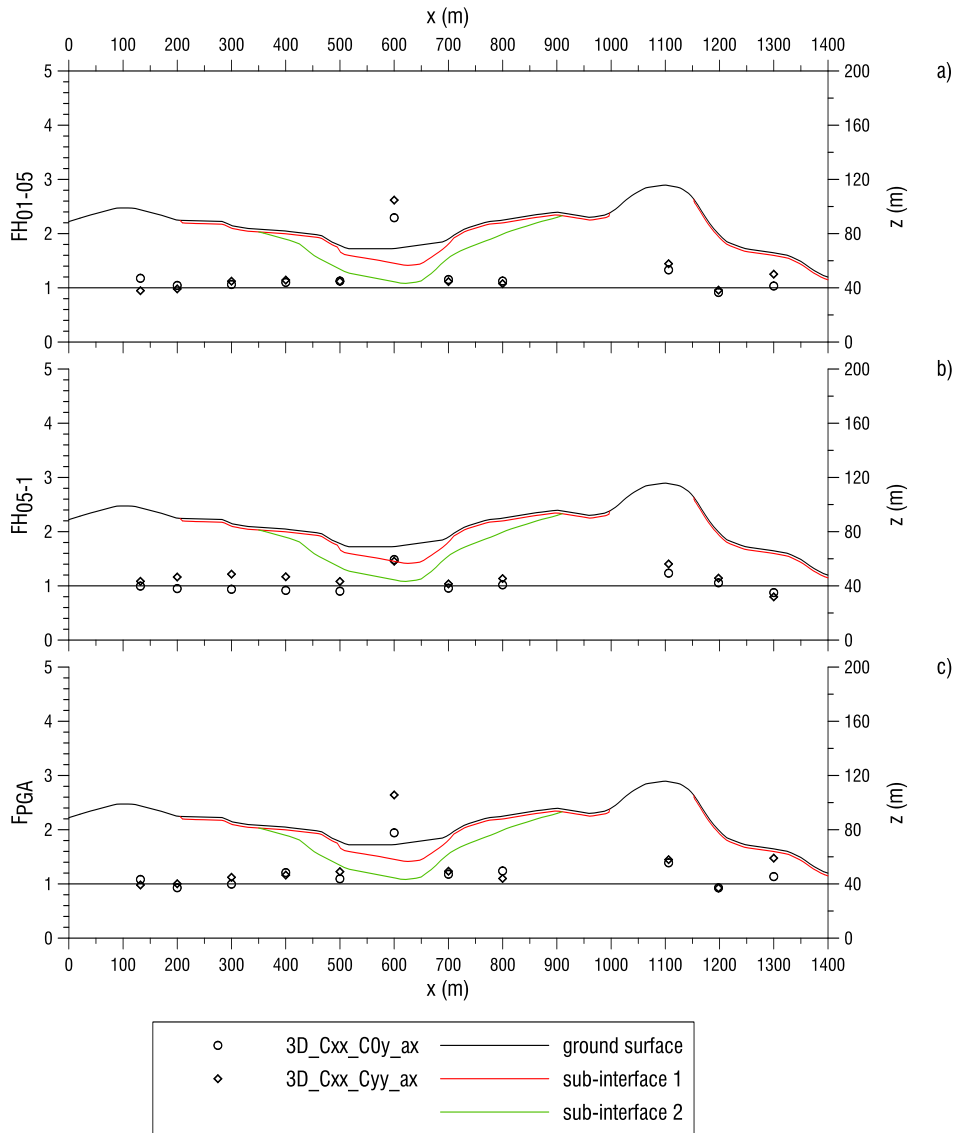


Fig. 272 Comparison A7-A11 with reference to section 4, a) FH_{01-05} , b) FH_{05-1} , c) F_{PGA}

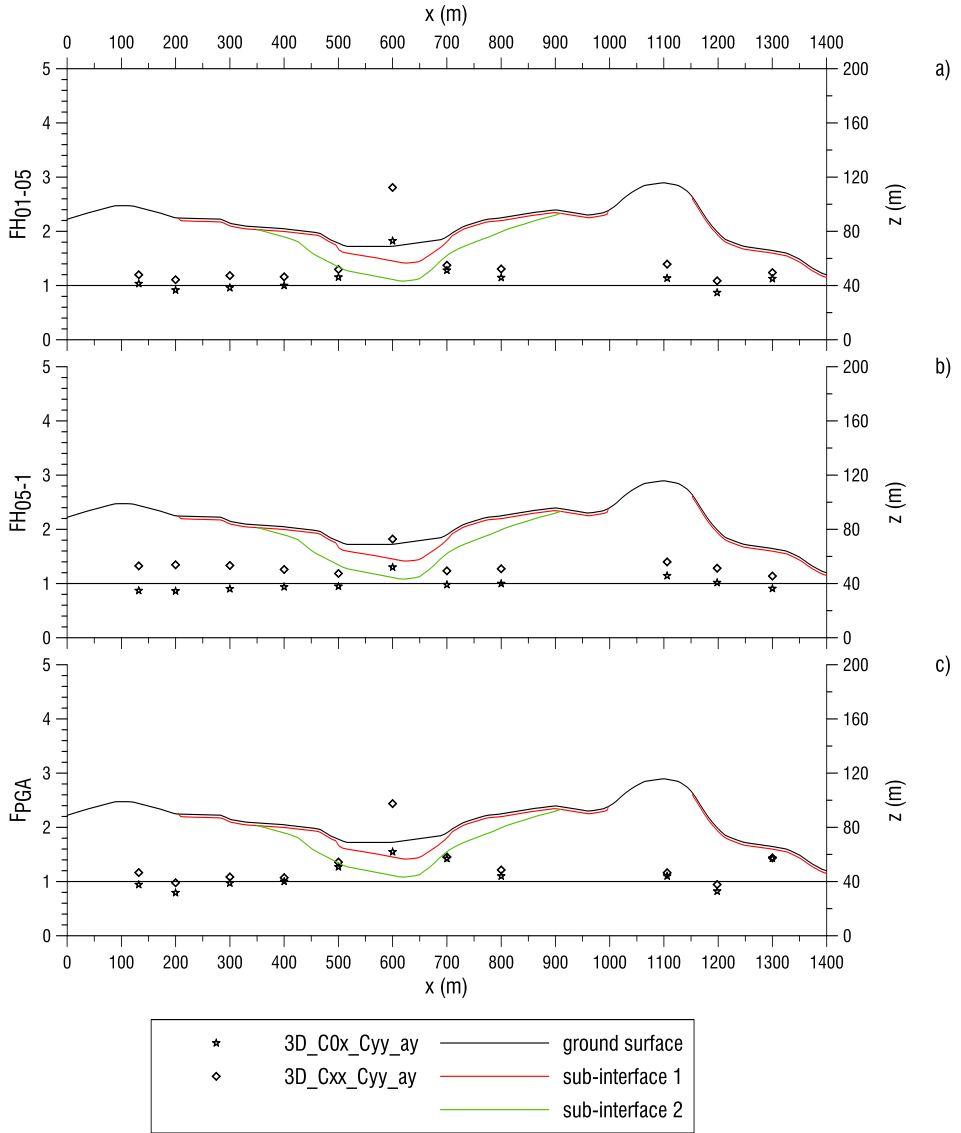


Fig. 273 Comparison A10-A11 with reference to section 4, a) FH_{01-05} , b) FH_{05-1} , b) F_{PGA}

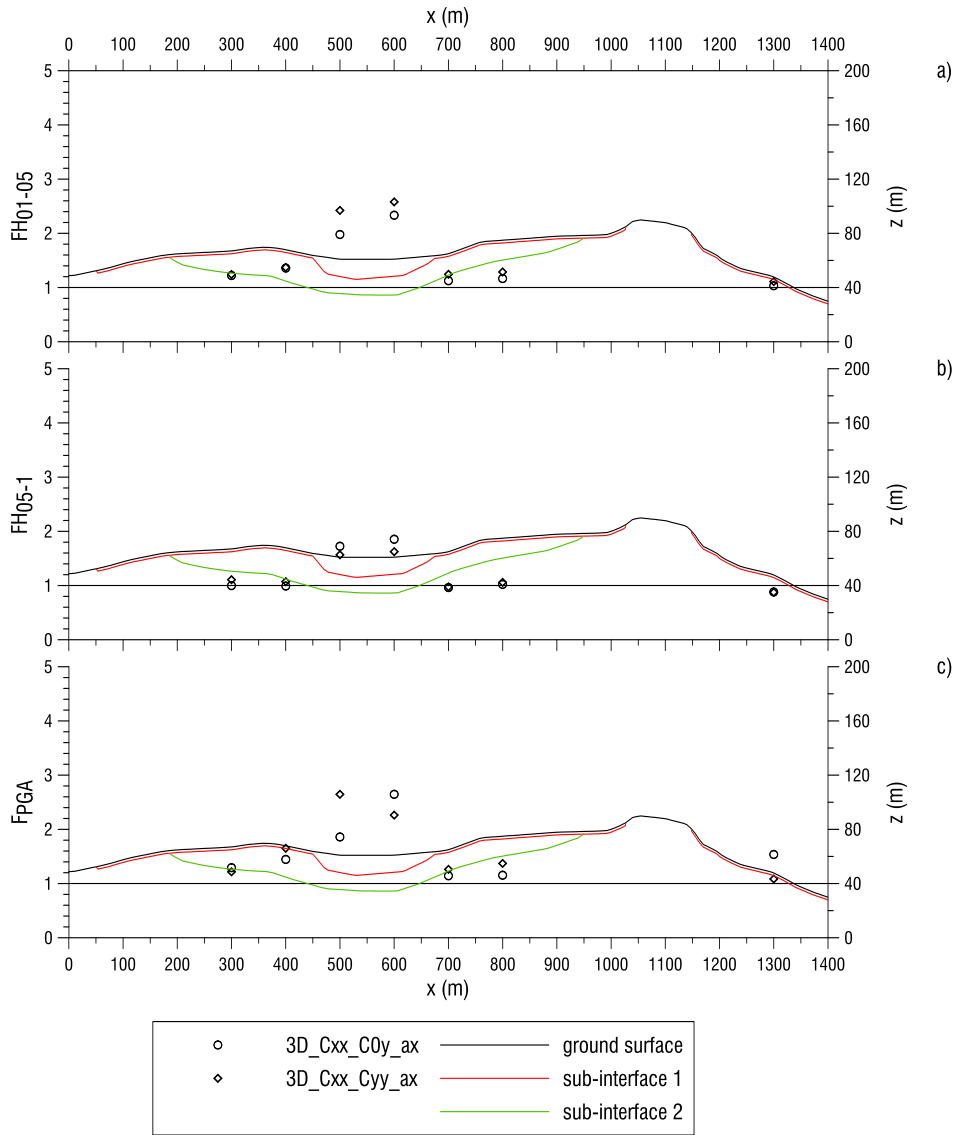


Fig. 274 Comparison A7-A11 with reference to section 5, a) FH_{01-05} , b) FH_{05-1} , c) F_{PGA}

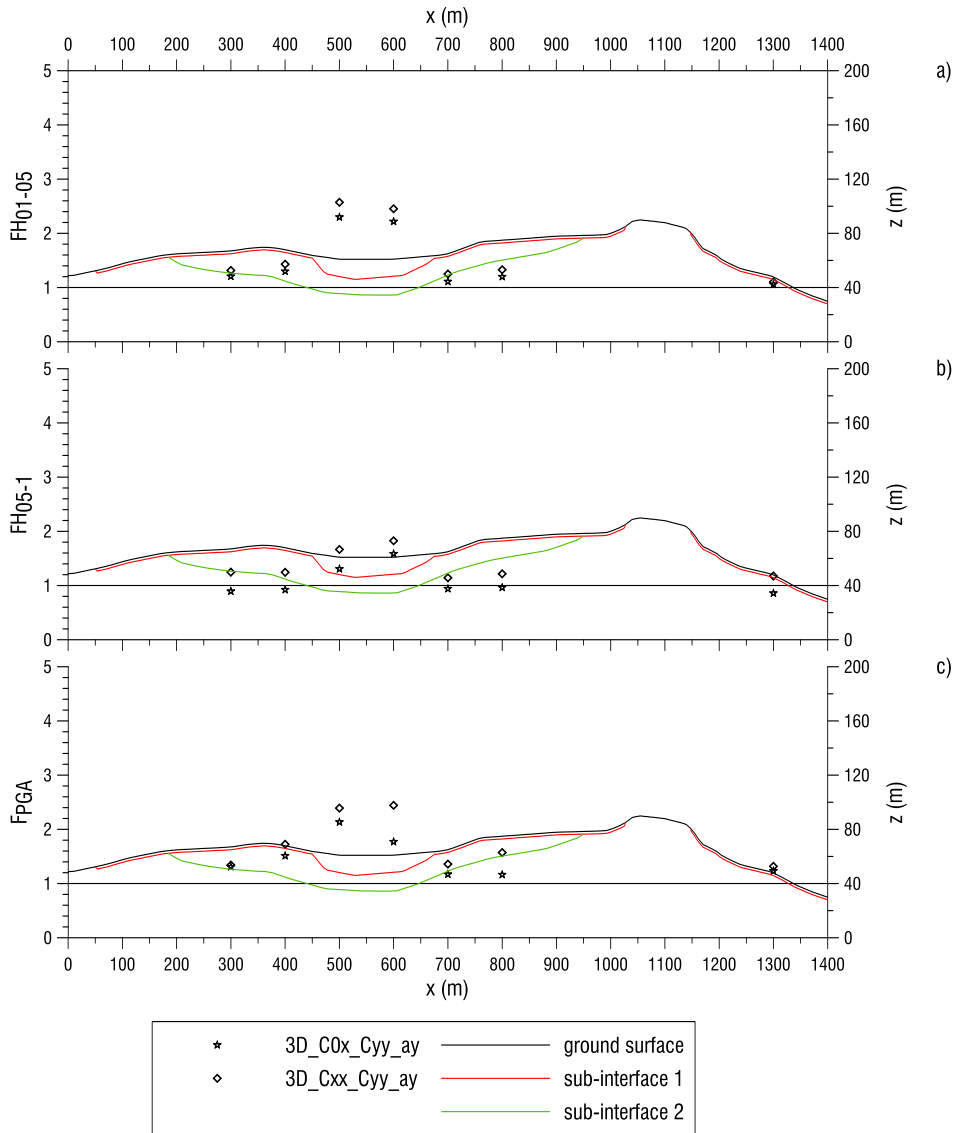


Fig. 275 Comparison A10-A11 with reference to section 5, a) FH_{01-05} , b) FH_{05-1} , b) F_{PGA}

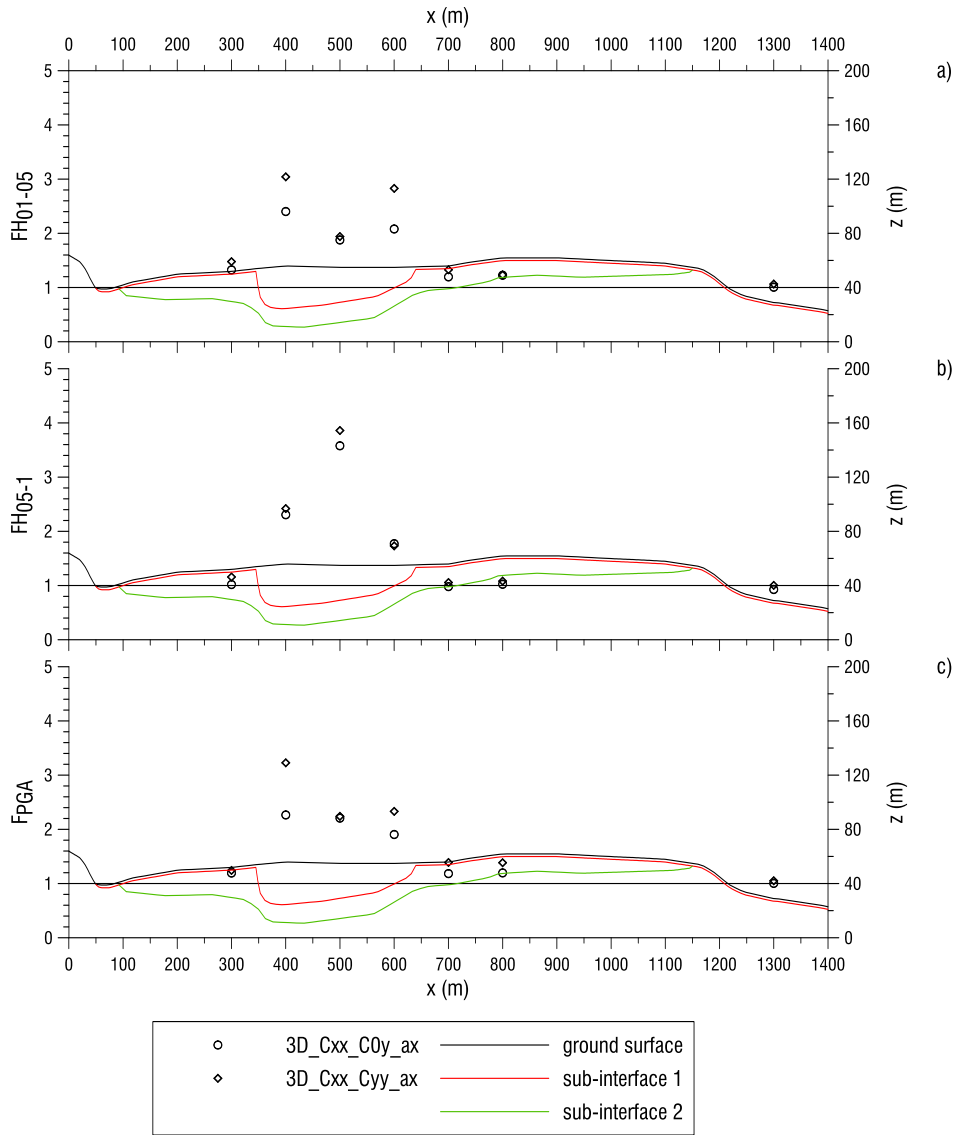


Fig. 276 Comparison A7-A11 with reference to section 6, a) FH_{01-05} , b) FH_{05-1} , c) F_{PGA}

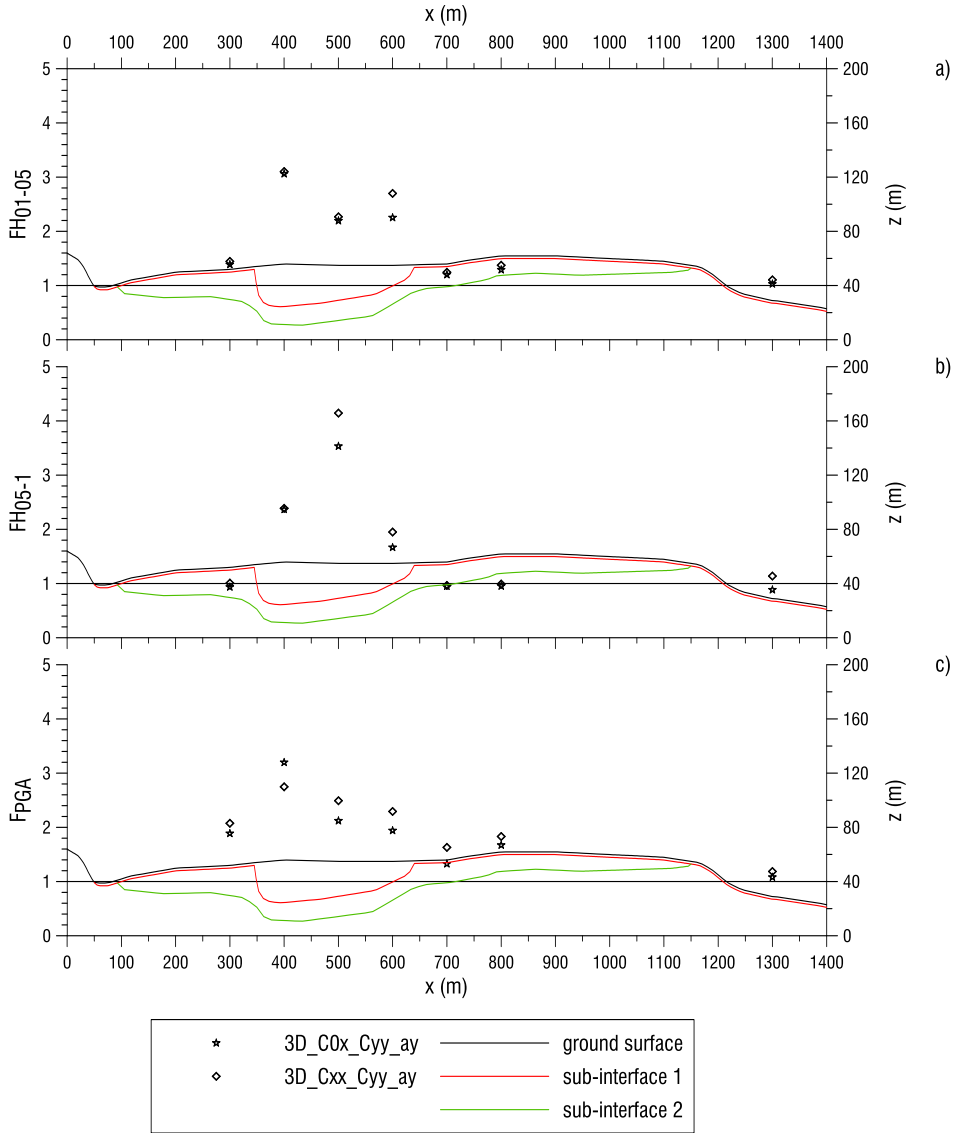


Fig. 277 Comparison A10-A11 with reference to section 6, a) FH_{01-05} , b) FH_{05-1} , c) F_{PGA}

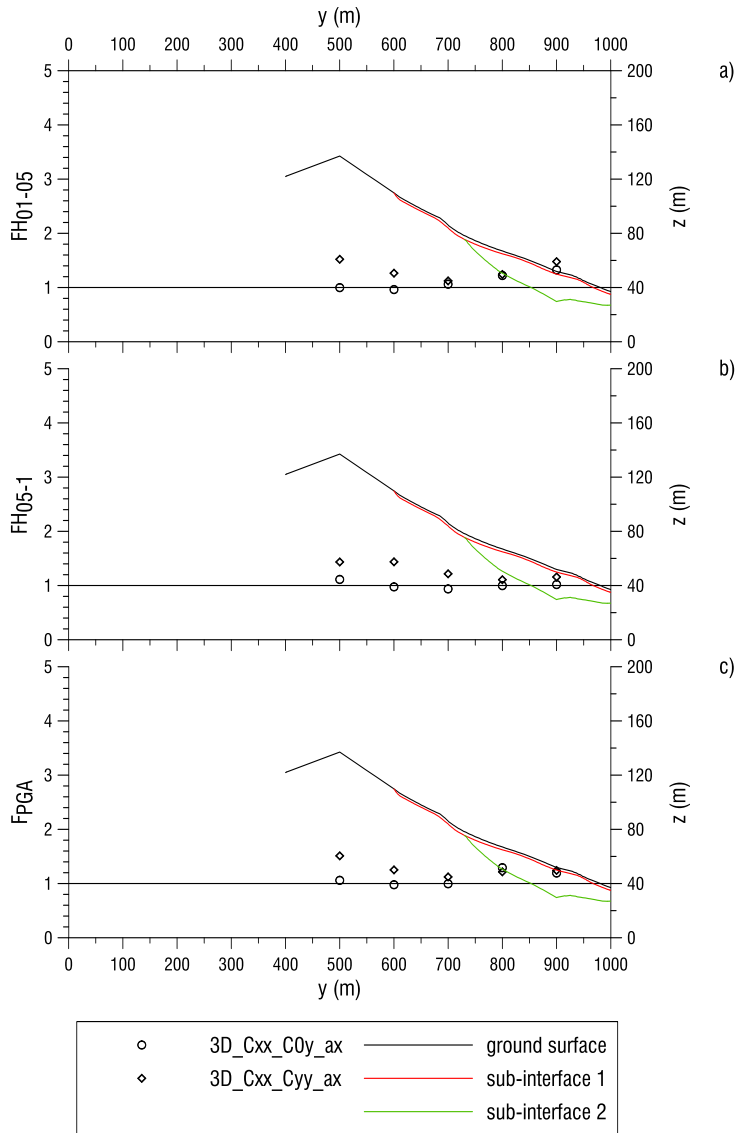


Fig. 278 Comparison A7-A11 with reference to section 11, a) FH_{01-05} , b) FH_{05-1} , c) F_{PGA}

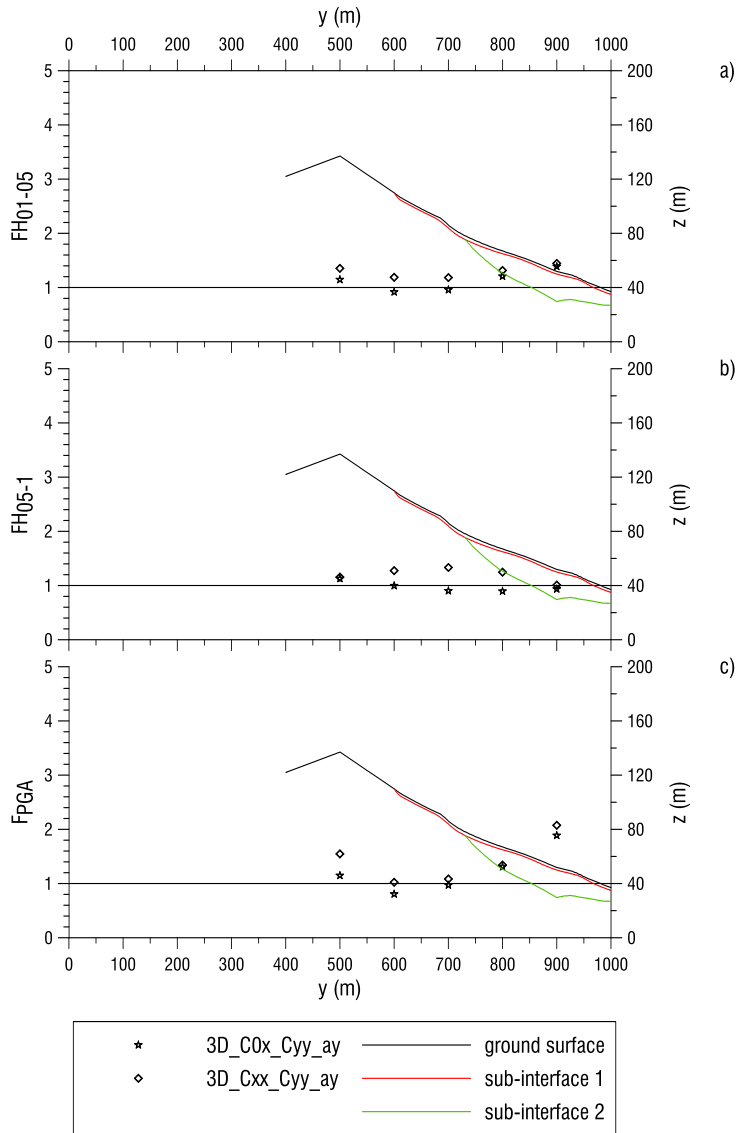


Fig. 279 Comparison A10-A11 with reference to section 11, a) FH_{01-05} , b) FH_{05-1} , b) F_{PGA}

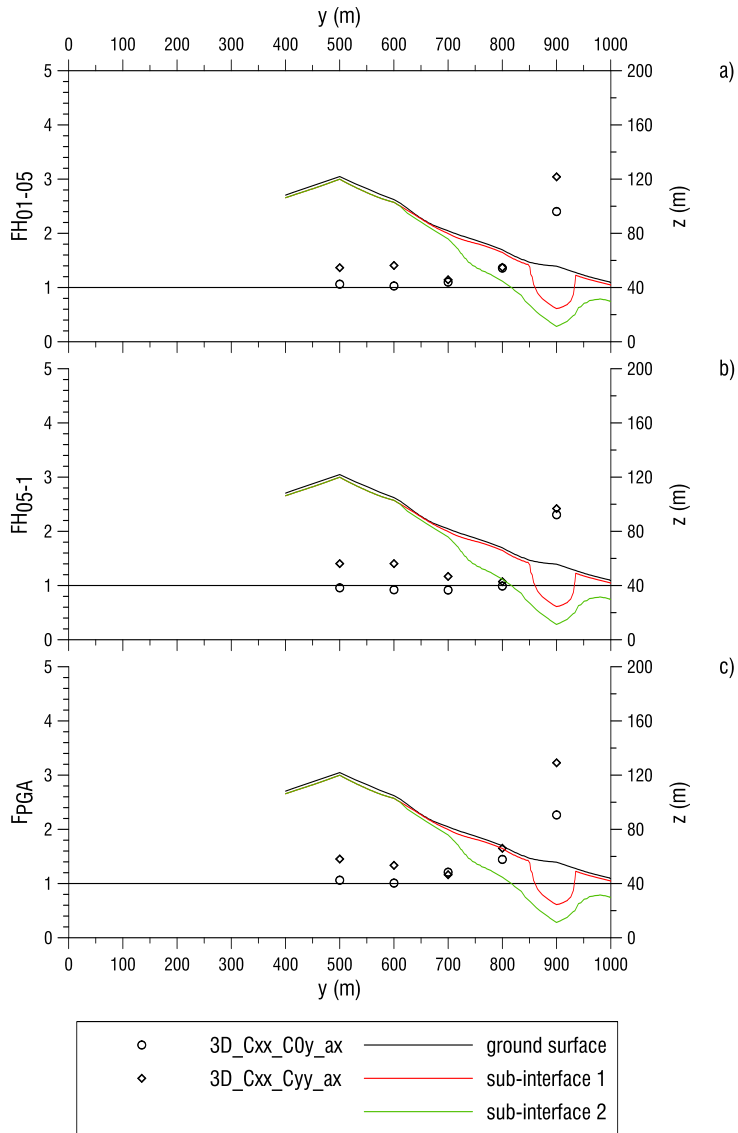


Fig. 280 Comparison A7-A11 with reference to section 12, a) FH_{01-05} , b) FH_{05-1} , c) F_{PGA}

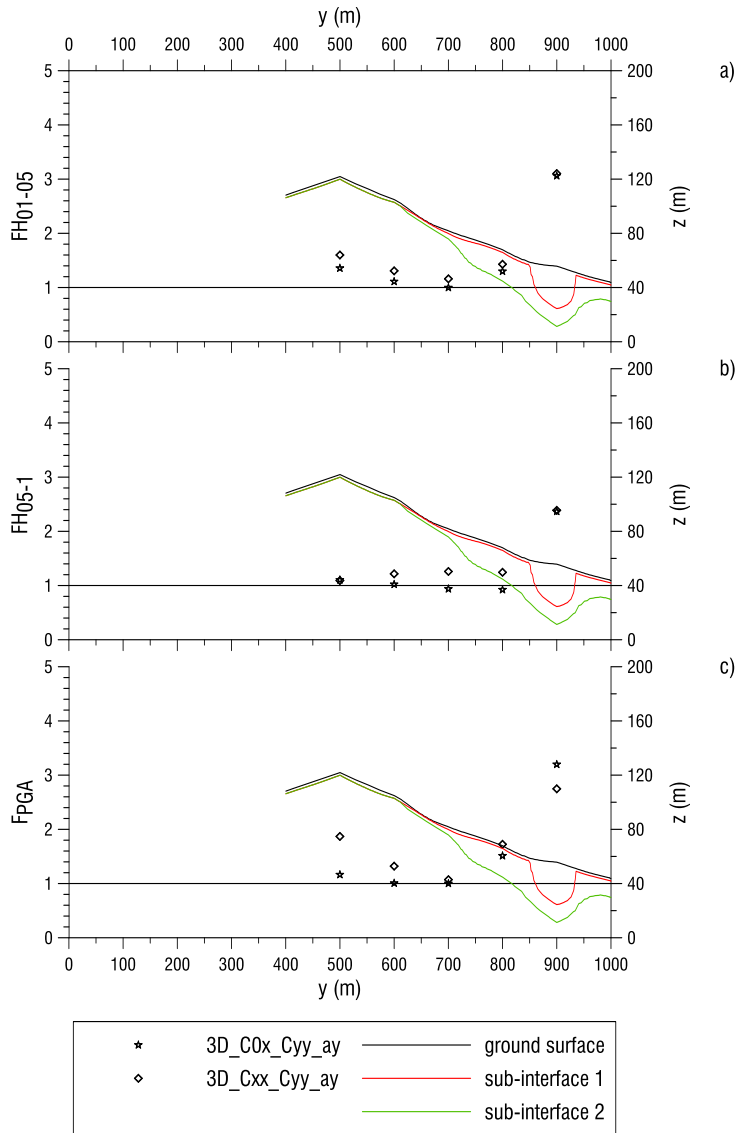


Fig. 281 Comparison A10-A11 with reference to section 12, a) FH_{01-05} , b) FH_{05-1} , b) F_{PGA}

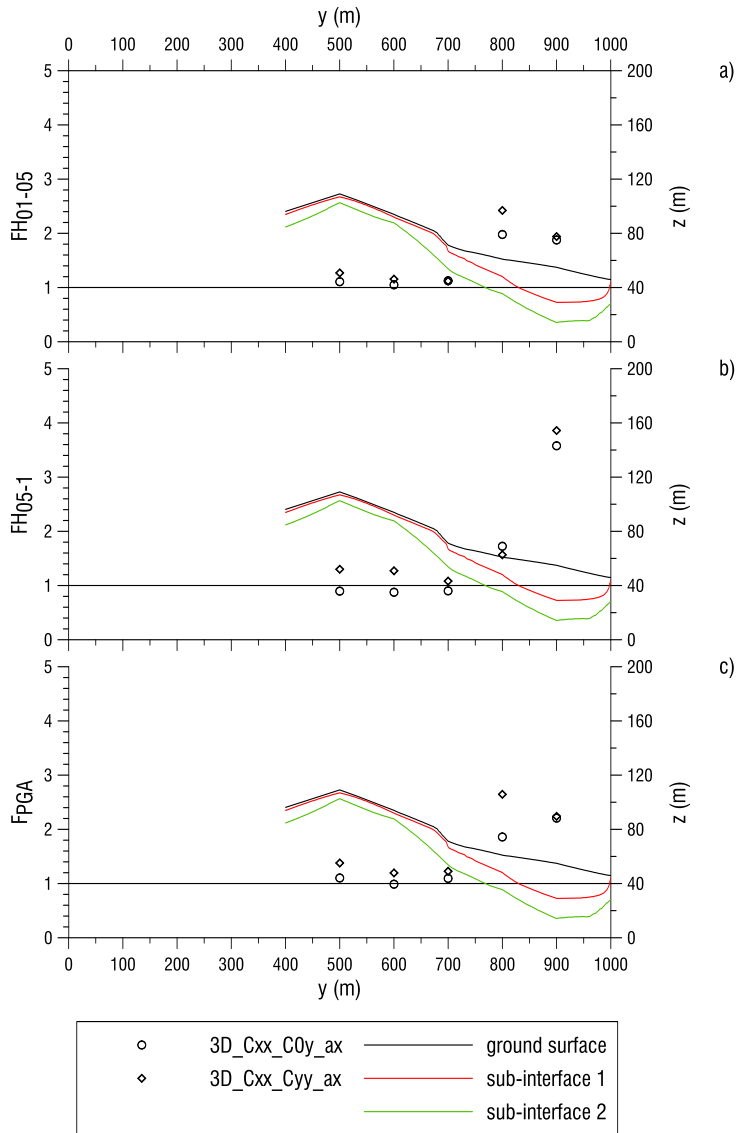


Fig. 282 Comparison A7-A11 with reference to section 13, a) FH_{01-05} , b) FH_{05-1} , c) F_{PGA}

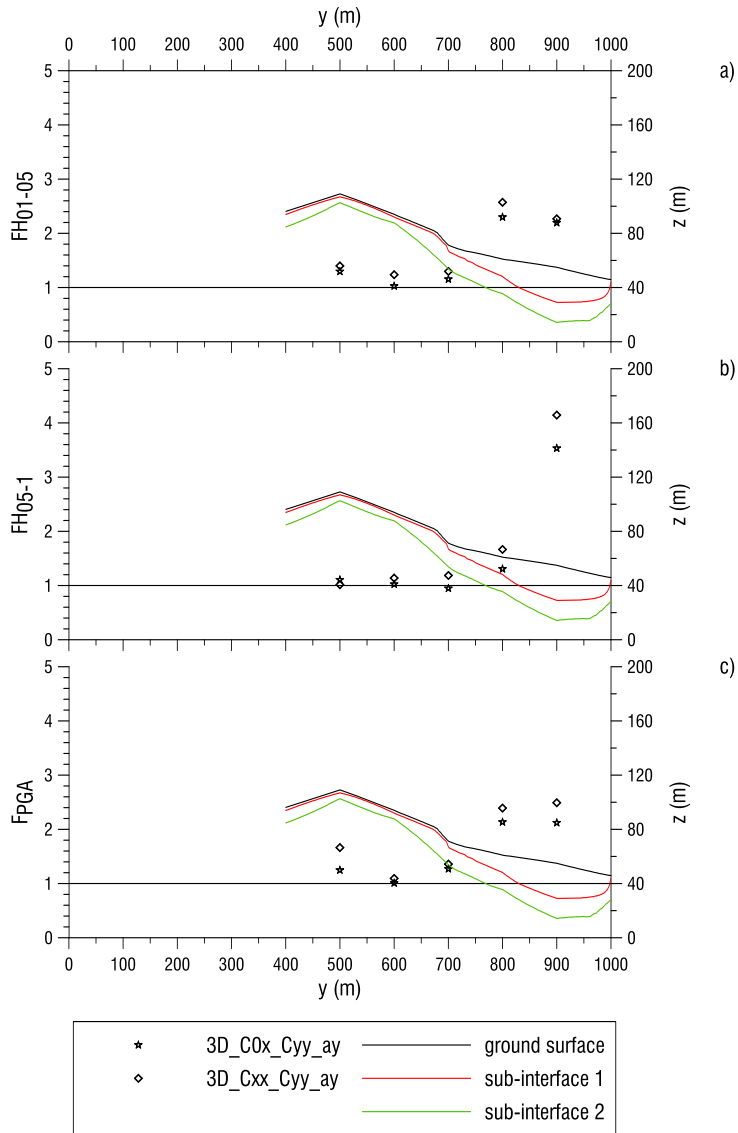


Fig. 283 Comparison A10-A11 with reference to section 13, a) FH_{01-05} , b) FH_{05-1} , b) F_{PGA}

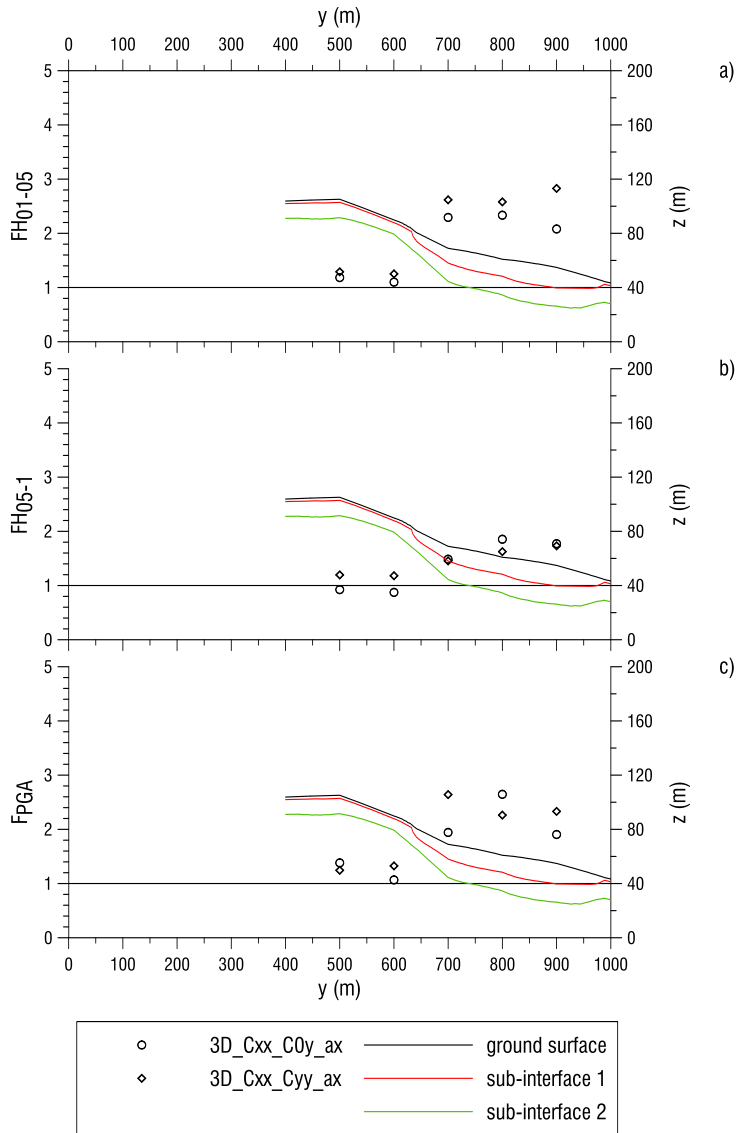


Fig. 284 Comparison A7-A11 with reference to section 14, a) FH_{01-05} , b) FH_{05-1} , c) F_{PGA}

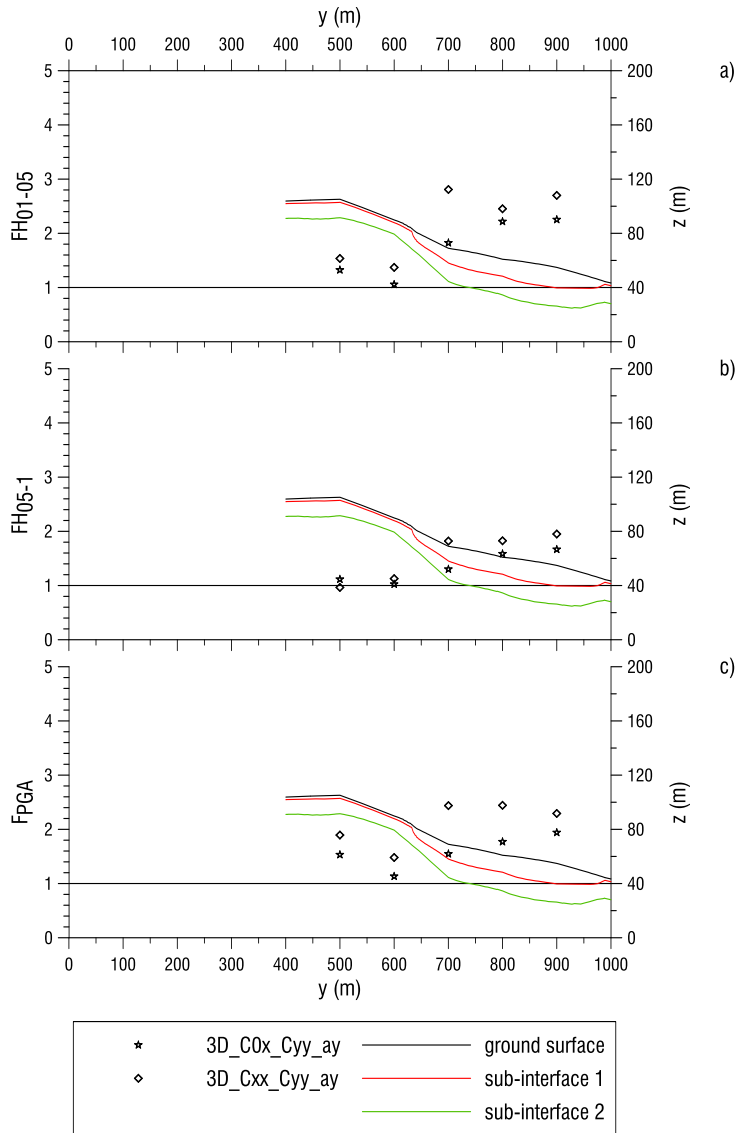


Fig. 285 Comparison A10-A11 with reference to section 14, a) FH_{01-05} , b) FH_{05-1} , b) F_{PGA}

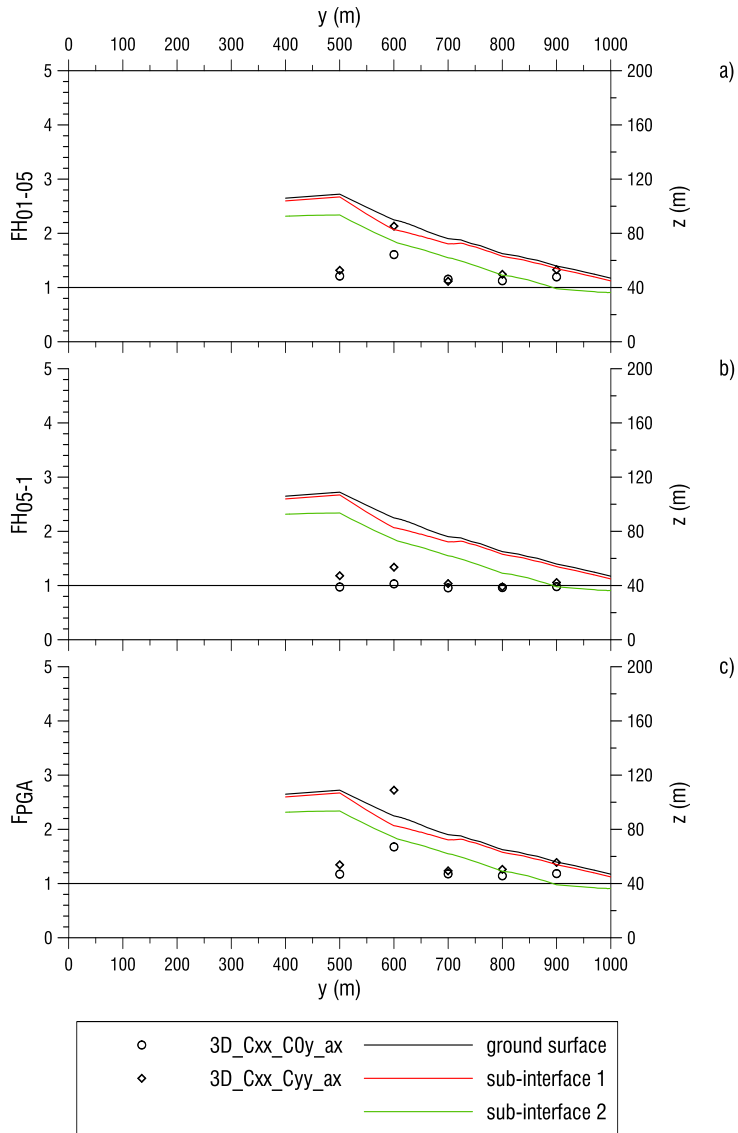


Fig. 286 Comparison A7-A11 with reference to section 15, a) FH_{01-05} , b) FH_{05-1} , c) F_{PGA}

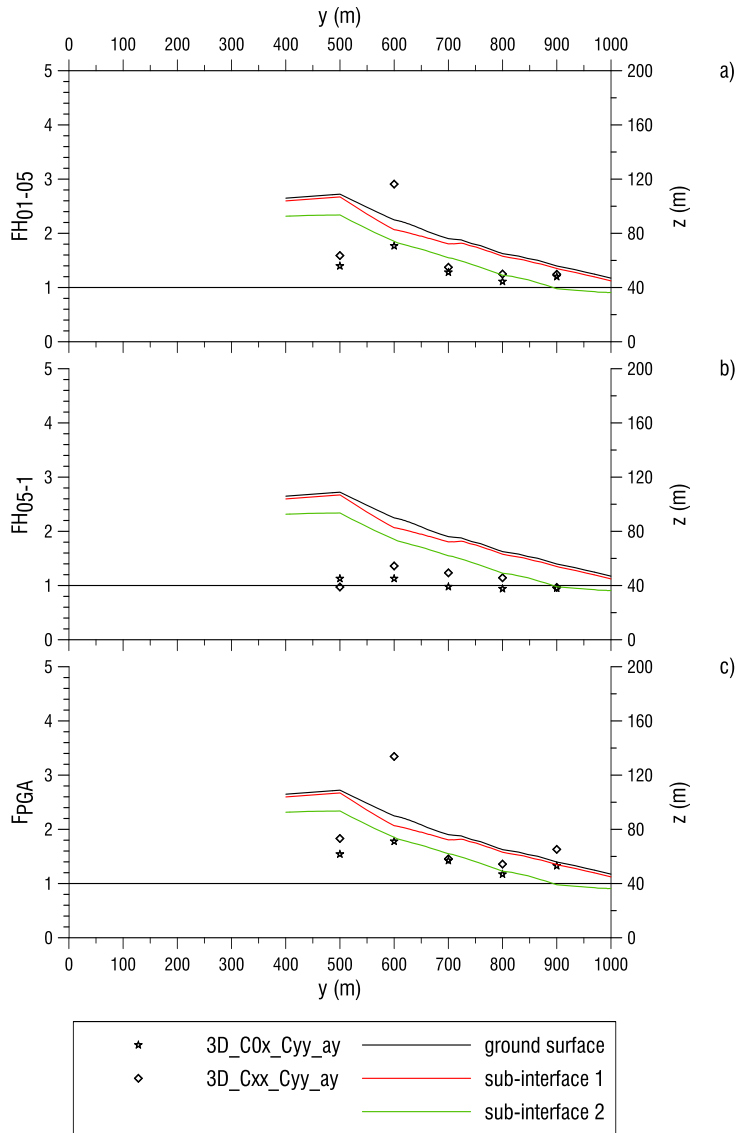


Fig. 287 Comparison A10-A11 with reference to section 15, a) F_{H01-05} , b) F_{H05-1} , c) F_{PGA}

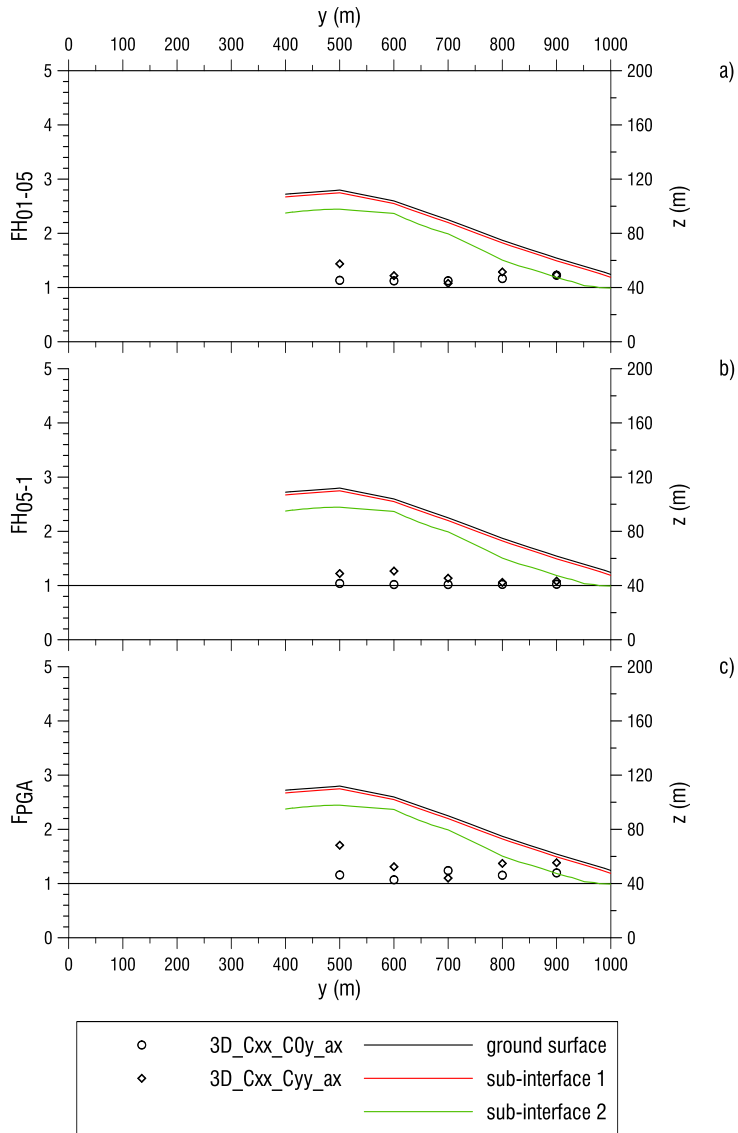


Fig. 288 Comparison A7-A11 with reference to section 16, a) FH_{01-05} , b) FH_{05-1} , c) F_{PGA}

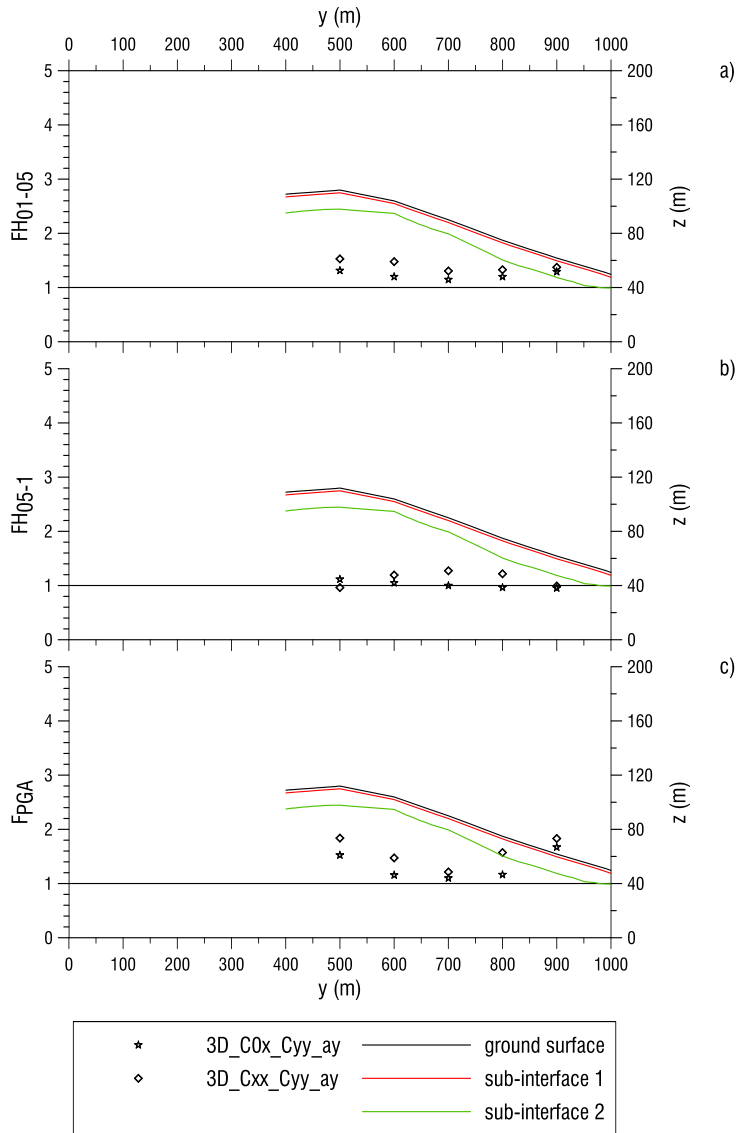


Fig. 289 Comparison A10-A11 with reference to section 16, a) FH_{01-05} , b) FH_{05-1} , b) F_{PGA}

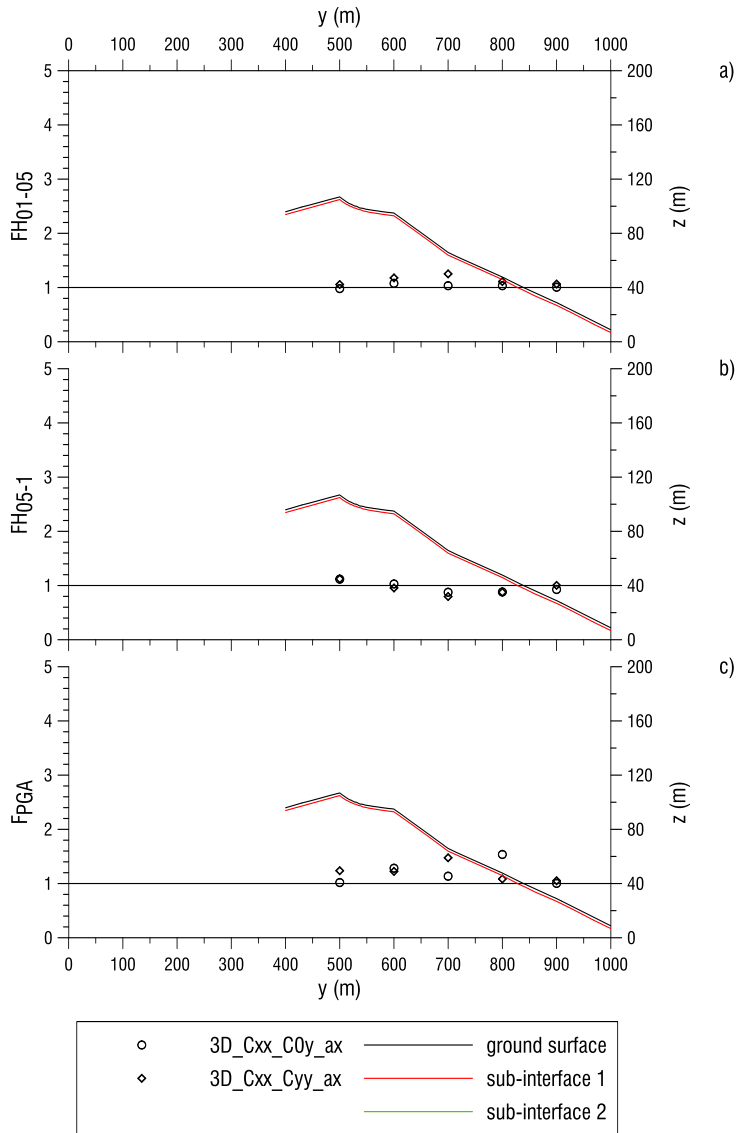


Fig. 290 Comparison A7-A11 with reference to section 21, a) FH_{01-05} , b) FH_{05-1} , c) F_{PGA}

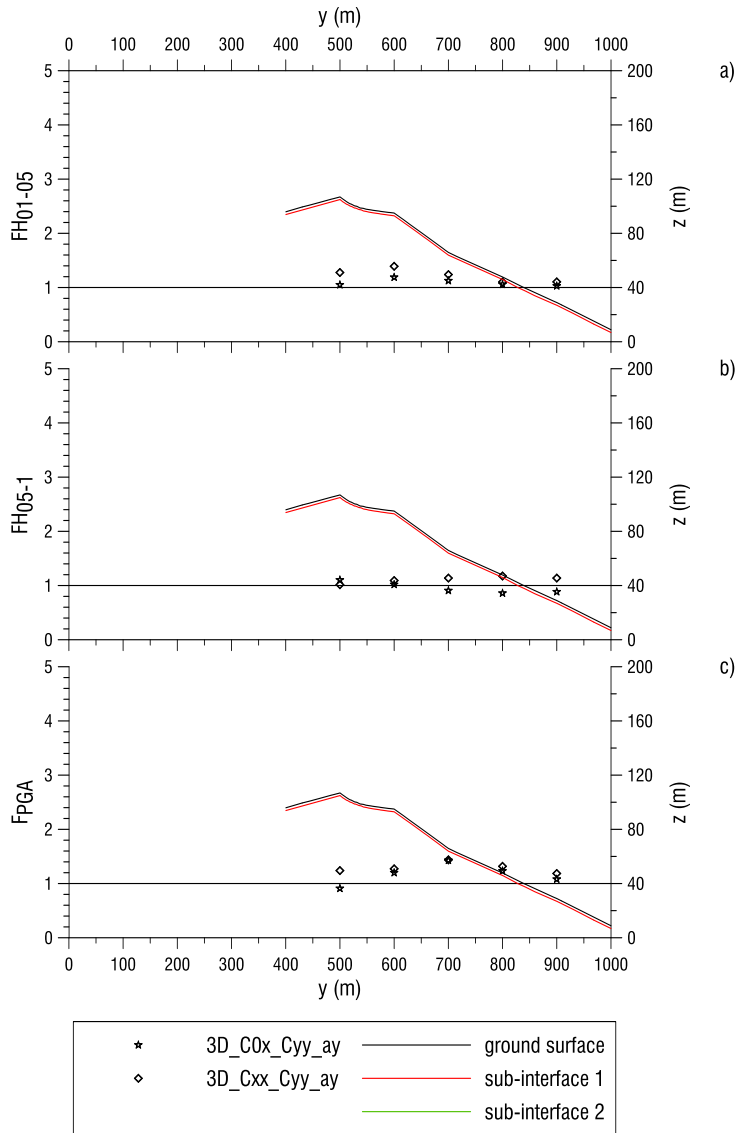


Fig. 291 Comparison A10-A11 with reference to section 21, a) FH_{01-05} , b) FH_{05-1} , b) F_{PGA}

CURRICULUM VITAE

**Europass
Curriculum Vitae**



Personal information

First name / Surname Gaetano Falcone
Address 37/C, VIA ANGELO BERTOLINI, I-70125 BARI ITALIA
Telephone Mobile: +39 3664237046
E-mail gaetano.falcone@poliba.it
gaetano.falcone1@gmail.com
Nationality Italian
Date of birth 25/06/1984
Gender Male

**Desired employment /
Occupational field**

Civil Engineer

Work experience

2015-Collaboration with Politecnico di Bari for the dissertation: "Prediction of seismic site response by means of 2D and 3D analyses using non-linear finite element code" supervised by Prof. Angelo Amorosi.

2013.-Collaboration with Politecnico di Bari for the dissertation: "Transverse response of shallow tunnel: interpretation of centrifuge dynamic tests and numerical simulations" supervised by Prof. Angelo Amorosi.

Education and training

In progress- PhD in Risk and environmental, territorial and building development tutored by Prof. A. Amorosi and Prof. D. Boldini, at Politecnico di Bari, Italy

2010-2011-Second level degree - Master of Science in Geotechnical Engineering, final degree mark:109/110.

Thesis in Soil Dynamic "Analisi numerica del comportamento trasversale di gallerie in zona sismica" (Numerical Analysis of transverse behaviour of tunnel in seismic area) supervised by Prof. A. Amorosi and Prof. D. Boldini at Politecnico di Bari, Italy

2007-2008- First level degree - Bachelor of Science in Building Engineering, final degree mark:103/110.

Thesis in Geotechnics “Verifica e progetto di muri di sostegno in condizioni statiche e dinamiche” (Design of retaining structure in static and dynamic conditions) supervised by Prof. A. Amorosi and Dr. G. Elia at Politecnico di Bari, Italy

2016- Speaker, “Evaluation of seismic local hazard by means of 1D and 2D Finite Element analyses”, to the GEST seminar series, Newcastle University, England.

2016- Occasional post graduate student at Newcastle University (England) in the School of Civil Engineering and Geosciences

2012-2015- Participation to the PRENOLIN Project, a benchmark on numerical simulation of 1D Non-Linear Site Effects.

2015- Speaker, “Numerically-based seismic microzonation: the case of Bovino (FG)”, to the Joint Summer School in Geotechnics, Technical University of Bari, Italy.

2015- Participation to the Joint Summer School in Geotechnics, Technical University of Bari, Italy.

2015- Participation to the annual meeting of Geotechnical researcher “IARG 2015”, University of Cagliari, Italy.

2014-2015- Co-tutor for the Foundations course at Technical University of Bari, Italy.

2014- Participation to the annual meeting of Geotechnical researcher “IARG 2014”, University of Chieti-Pescara, Italy.

2014- Participation to the 8th European Conference on Numerical Methods in Geotechnical Engineering “NUMGE 2014”, Technical University of Delft, Netherlands.

	<p>2014- Participation to the XXV Italian Conference of Geotechnical Engineering on Role of Geotechnical Engineering in mitigation risk from natural hazard, Baveno, Italy.</p> <p>2011-2012- Part-time collaboration at Technical University of Bari, Italy.</p> <p>2002-2003 High School Qualification Maturità Scientifica at “Istituto di istruzione superiore Fazzini-Giuliani” Macchia di Mauro, I-71019 Vieste, Italy. Final mark: 100/100.</p>				
Title of qualification awarded	Chartered Civil Engineer since 2013				
Principal subjects/ occupational skills covered	numerical modelling, soil mechanics, soil dynamics, foundation engineering, retaining structures, slope stability and a set of complementary courses in geology and hydrogeology.				
Publication	<p>Regnier, J. et al., 2016. International Benchmark on Numerical Simulations for 1D, Nonlinear Site Response (PRENOLIN): Verification Phase Based on Canonical Cases. Bulletin of the Seismological Society of America, 106 (5), pp. 2112–2135.</p> <p>Falcone, G. et al., 2015. Microzonazione sismica di livello 3 di un comune della daunia: analisi preliminari. In Proceedings of the conference IARG 2015. Cagliari, Italy.</p> <p>Amorosi, A. et al., 2014. Numerical prediction of tunnel performance during centrifuge dynamic tests. Acta Geotechnica, 9(4), pp.581–596.</p>				
Personal skills and competences					
Mother tongue	Italian				
Other language	English				
	Understanding		Speaking		Writing
	Listening	Reading	Spoken interaction	Spoken production	
	A2	A2	A2	A2	A2

Social skills and competences

Good personal relationships
Good versatility and adaptability to new situations;
Good skills in problem solving.

Organisational skills and competences

In both my academic career and my social activities emerge:
Good human interaction capability;
Good capacity of co-coordinating a work team;
Sense of responsibility.

Technical skills and competences
Computer skills and competences

Geotechnical engineering skills:
One-dimensional and multi-dimensional earthquake site response analysis;
Shallow and deep foundation design;
Slope stability analysis;
Retaining wall design.
Operating Systems: Microsoft Windows;
Software Packages: Microsoft Office, PLAXIS 2D, PLAXIS 3D, EERA, GeoStudio/SLOPE-W, GeoStudio/QUAKE-W, AutoCAD.

Artistic skills and competences

Marching ever onward to tomorrow.